

Topics in Current Chemistry 358

Pierangelo Metrangolo
Giuseppe Resnati *Editors*

Halogen Bonding I

Impact on Materials Chemistry and
Life Sciences

 Springer

Editorial Board:

H. Bayley, Oxford, UK
K.N. Houk, Los Angeles, CA, USA
G. Hughes, CA, USA
C.A. Hunter, Sheffield, UK
K. Ishihara, Chikusa, Japan
M.J. Krische, Austin, TX, USA
J.-M. Lehn, Strasbourg Cedex, France
R. Luque, Córdoba, Spain
M. Olivucci, Siena, Italy
J.S. Siegel, Nankai District, China
J. Thiem, Hamburg, Germany
M. Venturi, Bologna, Italy
C.-H. Wong, Taipei, Taiwan
H.N.C. Wong, Shatin, Hong Kong

Aims and Scope

The series Topics in Current Chemistry presents critical reviews of the present and future trends in modern chemical research. The scope of coverage includes all areas of chemical science including the interfaces with related disciplines such as biology, medicine and materials science.

The goal of each thematic volume is to give the non-specialist reader, whether at the university or in industry, a comprehensive overview of an area where new insights are emerging that are of interest to larger scientific audience.

Thus each review within the volume critically surveys one aspect of that topic and places it within the context of the volume as a whole. The most significant developments of the last 5 to 10 years should be presented. A description of the laboratory procedures involved is often useful to the reader. The coverage should not be exhaustive in data, but should rather be conceptual, concentrating on the methodological thinking that will allow the non-specialist reader to understand the information presented.

Discussion of possible future research directions in the area is welcome.

Review articles for the individual volumes are invited by the volume editors.

Readership: research chemists at universities or in industry, graduate students.

More information about this series at
<http://www.springer.com/series/128>

Pierangelo Metrangolo • Giuseppe Resnati
Editors

Halogen Bonding I

Impact on Materials Chemistry and Life
Sciences

With contributions by

C.B. Aakeröy • D.L. Bryce • G. Cavallo • T. Clark •
W. Herrebout • J.G. Hill • P.S. Ho • A.V. Jentsch •
A.C. Legon • S. Matile • P. Metrangolo • J.S. Murray •
T. Pilati • P. Politzer • G. Resnati • C.L. Spartz • G. Terraneo •
D.P. Tew • J. Viger-Gravel • N.R. Walker

 Springer

Editors

Pierangelo Metrangolo
Laboratory of Nanostructured
Fluorinated Materials (NFMLab)
Department of Chemistry, Materials,
and Chemical Engineering “Giulio Natta”
Politecnico di Milano
Milano, Italy

Giuseppe Resnati
Laboratory of Nanostructured Fluorinated
Materials (NFMLab)
Department of Chemistry, Materials, and
Chemical Engineering “Giulio Natta”
Politecnico di Milano
Milano, Italy

ISSN 0340-1022

Topics in Current Chemistry

ISBN 978-3-319-14056-8

DOI 10.1007/978-3-319-14057-5

ISSN 1436-5049 (electronic)

ISBN 978-3-319-14057-5 (eBook)

Library of Congress Control Number: 2015933504

Springer Cham Heidelberg New York Dordrecht London

© Springer International Publishing Switzerland 2015

This work is subject to copyright. All rights are reserved by the Publisher, whether the whole or part of the material is concerned, specifically the rights of translation, reprinting, reuse of illustrations, recitation, broadcasting, reproduction on microfilms or in any other physical way, and transmission or information storage and retrieval, electronic adaptation, computer software, or by similar or dissimilar methodology now known or hereafter developed.

The use of general descriptive names, registered names, trademarks, service marks, etc. in this publication does not imply, even in the absence of a specific statement, that such names are exempt from the relevant protective laws and regulations and therefore free for general use.

The publisher, the authors and the editors are safe to assume that the advice and information in this book are believed to be true and accurate at the date of publication. Neither the publisher nor the authors or the editors give a warranty, express or implied, with respect to the material contained herein or for any errors or omissions that may have been made.

Printed on acid-free paper

Springer International Publishing AG Switzerland is part of Springer Science+Business Media (www.springer.com)

Preface

Typically, halogen atoms in haloorganics are considered as sites of high electron density because of their high electronegativity. Consistent with this well-established understanding, it is commonly accepted that halogen atoms can form attractive interactions by functioning as an electron-donor site (nucleophilic site). In fact, halogen atoms can work as hydrogen-bond acceptors and some cases of these interactions were recognized as early as the 1920s [1–4]. Halogen atoms of halocarbons also function as an electron-donor site when interacting with other elements, e.g., when entering the first coordination sphere of alkali metal cations¹ or alkaline earth metal cations.

However, the electron density in covalently bound halogens is anisotropically distributed [5–7]. There is a region of higher electron density, which forms a negative belt orthogonal to the covalent bond involving the halogen atom, and a region of lower electron density, which generates a cap on the elongation of the covalent bond (the so-called σ -hole) where the electrostatic potential is frequently positive (mainly in the heavier halogens). (This description of the distribution of the electron density holds for halogen atoms forming one covalent bond. For a discussion of polyvalent halogens see [8, 9].) This region can form attractive interactions with electron-rich sites but the general ability of halogen atoms to function as the electron acceptor site (electrophilic site) in attractive interactions has been fully recognized only recently. In 2009 the International Union of Pure and Applied Chemistry (IUPAC) started a project aiming “to take a comprehensive look at intermolecular interactions involving halogens as electrophilic species and classify them” [10]. An IUPAC Recommendation defining these interactions as halogen bonds [11] was delivered in 2013 when the project was concluded: This definition

¹ A CSD search (CSD version 5.34, November 2012 plus one update, ConQuest version 1.15) for $Y\cdots X-C$ short contacts ($Y=Li^+, Na^+, K^+, Rb^+, Cs^+$ and $X=Cl, Br, I$) gave 140 hits and 296 counts, and revealed that the median value of the $Y\cdots X-C$ angle is 103.08° (only structures with $Y\cdots C > 3.0 \text{ \AA}$ were considered). Cations enter the most negative region of the halogen atom (i.e., the belt orthogonal to the $X-C$ bond), thus confirming that the halogen atom is working as the nucleophile.

states that “A halogen bond occurs when there is evidence of a net attractive interaction between an electrophilic region associated with a halogen atom in a molecular entity and a nucleophilic region in another, or the same, molecular entity.” The IUPAC definition categorizes unambiguously an interaction responsible for the formation of adducts described as early as 1814 but which had been overlooked for decades. It developed into a routinely used tool to direct self-assembly phenomena only after its effectiveness in crystal engineering was demonstrated in the mid-1990s [12].

The halogen bonding practice and concept has developed through a rather patchy course. As a consequence, it seems particularly timely to open this book with a brief history of the interaction, as a perspective of the topic may help the reader to understand better how the present situation has been reached. In the first chapter P. Metrangolo and G. Resnati examine how the halogen bonding concept emerged and became established in, and accepted by, a broad chemical community. The second chapter by P. Politzer et al. focuses on a physical interpretation of halogen bonding from a theoretical point of view. Studies on halogen-bonded complexes in the gas phase are highlighted in the third chapter by A. C. Legon and N. R. Walker, while cryogenic solutions containing halogen-bonded complexes are examined in the fourth chapter by W. Herrebout. C. B. Aakeröy and C. L. Spartz discuss the use of halogen bonding in supramolecular synthesis in the fifth chapter, and the study of such solid-state halogen-bonded complexes is described in the sixth chapter by D. L. Bryce and J. Viger-Gravel. A. V. Jentzsch and S. Matile discuss how to use halogen bonds in anion recognition and transport in the seventh chapter, while the last chapter by P. S. Ho closes the first volume of this book with a survey of biomolecular halogen bonds.

This first volume of the book “Halogen Bonding: Impact on Materials Chemistry and Life Sciences” opens with a historical perspective and a basic understanding of the halogen bond and closes showing the impact that this interaction is having in various fields such as crystal engineering, supramolecular synthesis, and medicinal chemistry. Many other fields benefit from the use of halogen bonding and will be treated in the second volume of the book.

Milan, Italy

Pierangelo Metrangolo
Giuseppe Resnati

References

1. Hantzsch A (1915) Die Chromoisomerie der p-dioxy-terephthalsäure derivate als phenol-enol-isomerie. *Chem Ber* 48:797–816
2. Nakamoto K, Margoshes M, Rundle RE (1955) Stretching frequencies as a function of distances in hydrogen bonds. *J Am Chem Soc* 77:6480–6486
3. Schleyer PR, West R (1959) Comparison of covalently bonded electro-negative atoms as proton acceptor groups in hydrogen bonding. *J Am Chem Soc* 81:3164–3165

4. Metrangolo P, Resnati G (2013) Metal-bound halogen atoms in crystal engineering. *Chem Commun* 49:1783–1785
5. Metrangolo P, Resnati G (eds) (2008) Halogen bonding: fundamentals and applications. Structure and bonding series, vol. 126. Springer-Verlag, Berlin Heidelberg
6. Murray JS, Lane P, Politzer P (2009) Expansion of the σ -hole concept. *J Mol Model* 15:723–729
7. Politzer P, Murray JS, Clark T (2013) Halogen bonding and other σ -hole interactions: a perspective. *Phys Chem Chem Phys* 15:11178–11189
8. O Hair RAJ, Williams CM, Clark T (2010) Neighboring group stabilization by sigma-holes. *J Mol Model* 16:559–565
9. Wang W (2011) Halogen bond involving hypervalent halogen: CSD search and theoretical study. *J Phys Chem A* 115:9294–9299
10. Project no. 2009-032-1-100. Categorizing halogen bonding and other noncovalent interactions involving halogen atoms. [http://www.iupac.org/nc/home/projects/project-db/project-details.html?tx_wfqbe_pi1%5Bproject_nr%5D=2009-032-1-100](http://www.iupac.org/nc/home/projects/project-db/project-details.html?tx_wfqbe_pi1%5Bproject_nr%5D=2009-032-1-100;); (2010) *Chem Int* 32(2):20–21
11. Desiraju GR, Ho PS, Kloo L, Legon AC, Marquardt R, Metrangolo P, Politzer P, Resnati G, Rissanen K (2013) Definition of the halogen bond (IUPAC Recommendations 2013). *Pure Appl Chem* 35:1711–1713
12. Metrangolo P, Resnati G (2001) Halogen bonding: a paradigm in supramolecular chemistry. *Chem Eur J* 7:2511–2519

Contents

Halogen Bond: A Long Overlooked Interaction	1
Gabiella Cavallo, Pierangelo Metrangolo, Tullio Pilati, Giuseppe Resnati, and Giancarlo Terraneo	
σ-Hole Bonding: A Physical Interpretation	19
Peter Politzer, Jane S. Murray, and Timothy Clark	
Halogen Bonding in the Gas Phase: A Comparison of the Iodine Bond in $B \cdots ICl$ and $B \cdots ICF_3$ for Simple Lewis Bases B	43
J. Grant Hill, Anthony C. Legon, David P. Tew, and Nicholas R. Walker	
Infrared and Raman Measurements of Halogen Bonding in Cryogenic Solutions	79
Wouter Herrebout	
Halogen Bonding in Supramolecular Synthesis	155
Christer B. Aakeröy and Christine L. Spartz	
Solid-State NMR Study of Halogen-Bonded Adducts	183
David L. Bryce and Jasmine Viger-Gravel	
Anion Transport with Halogen Bonds	205
Andreas Vargas Jentsch and Stefan Matile	
Biomolecular Halogen Bonds	241
P. Shing Ho	
Index	277

Halogen Bond: A Long Overlooked Interaction

Gabriella Cavallo, Pierangelo Metrangolo, Tullio Pilati, Giuseppe Resnati, and Giancarlo Terraneo

Abstract Because of their high electronegativity, halogen atoms are typically considered, in most of their derivatives, as sites of high electron density and it is commonly accepted that they can form attractive interactions by functioning as the electron donor site (nucleophilic site). This is the case when they work as hydrogen bond acceptor sites. However, the electron density in covalently bound halogens is anisotropically distributed. There is a region of higher electron density, accounting for the ability of halogens to function as electron donor sites in attractive interactions, and a region of lower electron density where the electrostatic potential is frequently positive (mainly in the heavier halogens). This latter region is responsible for the ability of halogen atoms to function as the electron-acceptor site (electrophilic site) in attractive interactions formed with a variety of lone pair-possessing atoms, anions, and π -systems. This ability is quite general and is shown by a wide diversity of halogenated compounds (e.g., organohalogen derivatives and dihalogens). According to the definition proposed by the International Union of Pure and Applied Chemistry, any attractive interactions wherein the halogen atom is the electrophile is named halogen bond (XB). In this chapter, it is discussed how the practice and the concept of XB developed and a brief history of the interaction is presented. Papers (either from the primary or secondary literature) which have reported major experimental findings in the field or which have given important theoretical contributions for the development of the concept are recollected in order to trace how a unifying and comprehensive categorization emerged encompassing all interactions wherein halogen atoms function as the electrophilic site.

G. Cavallo (✉), P. Metrangolo, T. Pilati, G. Resnati, and G. Terraneo
Laboratory of Nanostructured Fluorinated Materials (NFMLab), Department of Chemistry, Materials, and Chemical Engineering “Giulio Natta”, Politecnico di Milano, Via L. Mancinelli 7, 20131 Milano, Italy
e-mail: gabriella.cavallo@polimi.it

Keywords Crystal engineering · Halogen bond · Noncovalent interactions · Self-assembly · Supramolecular chemistry

Contents

1 A Historical Perspective	2
2 A Unifying and Unambiguous Name	10
References	13

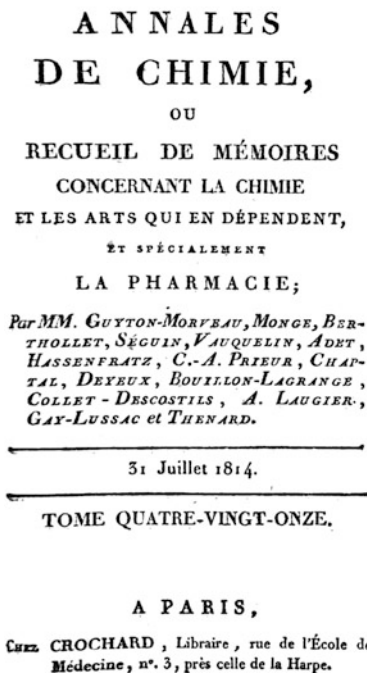
1 A Historical Perspective

The history of the halogen bonding (XB) is approximately 200 years old as the $I_2 \cdots NH_3$ adduct, probably the first halogen-bonded system ever prepared, was synthesized in Gay-Lussac's laboratory by Colin as early as 1813 [1] (Fig. 1). In two centuries, many pieces of information relevant to XB have been accumulating as a result of studies performed in quite different contexts. These pieces of information remained long fragmented, their contextualization was limited to their respective areas, and a unifying and comprehensive categorization was missing. This chapter recollects papers (either from the primary or secondary literature) which reported major experimental findings in the field or which gave important theoretical contributions for the development of the XB concept. The aim is to arrange these parts in a coherent body and to acknowledge their role in the development of the present concept of XB.

The reactivity of iodine with ammonia is quite tricky and depends heavily on the adopted conditions. Colin reported [1] that when dry gaseous ammonia and dry iodine are reacted, a liquid with a somewhat metallic luster is produced and we now understand it is formed under XB control. Fifty years after Colin's report, Guthrie obtained the same liquid in pure form by adding powdered iodine to aqueous ammonia and first proposed that the formed compound had the structure $NH_3 \cdot I_2$ [2].

Not only neutral species (i.e., ammonia in $I_2 \cdots NH_3$) but also anions were soon discovered to interact attractively and to form adducts with halogen atoms. I_3^- , formed on interaction of I^- (the nucleophile, XB-acceptor) with I_2 (the electrophile, XB-donor), is the first species ever prepared and involving I_2 and an anion. Specifically, strychnine triiodide was reported by Pelletier and Caventou in 1819 [3] and also the greater solubility of I_2 in different solvents on addition of metal iodides as well as the reaction between metal halides and iodine attracted early attention [4]. While numerous investigators suggested to rationalise these observations via the formation of triiodide ions, some others were reluctant to accept this explanation. In 1839, Jørgensen proposed that polyiodide alkaloids contain iodide ions as well as iodine and published the first systematic investigation on the topic [5].

Halocarbons were reported to give adducts similar to those formed by dihalogens, only several years later, as the quinoline/iodoform adduct, probably the first halogen-bonded adduct prepared from a halocarbon, was described by Rhoussopoulos in 1883 [6].



NOTE

Sur quelques combinaisons de l'iode ;

PAR M. COLIN, Répétiteur à l'École polytechnique (1).

Lue à l'Institut, le 27 décembre 1813.

Je me suis proposé, dans cette Note, d'éclaircir quelques phénomènes relatifs à l'action de l'iode sur l'ammoniaque et sur le mercure, et par là j'ai été conduit à examiner son action sur divers oxides. Voici quels sont les résultats de mes expériences.

On sait, d'après les observations de M. Courtois, que le mercure broyé avec

(1) Je dois prévenir ici que c'est dans le laboratoire de M. Gay-Lussac, et presque toujours sous ses yeux, que j'ai fait les expériences dont je vais avoir l'honneur de rendre compte à la Classe; par là je me suis trouvé à portée de recevoir ses conseils et de les mettre à profit; je prie donc M. Gay-Lussac de permettre que je lui en témoigne ici toute ma reconnaissance.

Fig. 1 Frontispiece of the volume (*left*) and first page of the paper (*right*) where Colin was reporting his experiments on the reaction of diiodine with ammonia

To the best of our knowledge, bromine and chlorine were reported to form halogen-bonded adducts similar to iodine only in 1896 when Remsen and Norris described the 1:1 dimers formed by Br_2 and Cl_2 with various amines [7]. It is now well established [8–10] that the XB-donor ability is greater for the heavier and more polarizable [11] halogens, namely it increases in the order $\text{Cl} < \text{Br} < \text{I}$. In the nineteenth century the three halogens were already receiving major and similar attention from the chemical community and, while the timeline reported above is limited to the very initial observations, it already suggests the scale reported above if it is assumed that the sequence of observation of related recognition processes parallels their relative robustness.

The case of fluorine (the less heavy and polarizable halogen, namely the less prone to be involved in XB) confirms the reliability of the above discussed principle. The ability of fluorine to function as a XB donor, albeit a weak donor, was first suggested at the end of the twentieth century [12–16] and fully recognized only 2 years ago, just in relation to the discussions prompted by the IUPAC project. The first $\text{F}_2 \cdots$ nucleophile neutral adducts (e.g., $\text{F}_2 \cdots \text{NH}_3$ and $\text{F}_2 \cdots \text{OH}_2$) were reported only in the 1990s ([17] and references cited therein) and F_3^- (namely $\text{F}_2 \cdots \text{F}^-$ if the XB notation is used) was first observed in 1976 (Fig. 2) [20–22]. More than 150 years

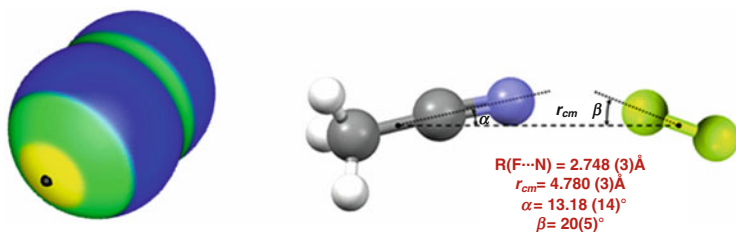


Fig. 2 *Left*: Computed electrostatic potential map (using the Wave Function Analysis-Surface Analysis Suite [18]) on the 0.001-au molecular surface of F₂. Color ranges, in kcal·mol⁻¹, are: *yellow*, between 20 and 9; *green*, between 9 and 0; *blue*, negative. *Black hemispheres* denote the positions of the most positive potentials associated with the fluorines. *Right*: Structural parameters of the halogen-bonded complex CH₃CN...F₂ as determined via microwave spectroscopy ([19] and references cited therein). Adapted from [14]

had passed from the publication of the analogous adducts formed by I₂ and, while the first halogen bonded adduct formed by iodine was reported 2 years after the discovery of the element, the first halogen-bonded adduct of fluorine was described 90 years after difluorine was isolated. Moreover, very extreme conditions (low temperatures and pressures) were required for its isolation.

Astatine is the heaviest halogen and its polarizability has been calculated higher than iodine [11]. According to the above discussed correlations, astatine may be an even better XB donor than iodine. This anticipation is supported by computational results [23, 24] but, to date, no halogen-bonded adduct has been reported for this element. This does not infringe the reliability of the heuristic principle that the sequence of observations of related phenomena usually parallels their relative robustness. Astatine is merely a very rare element and the limited attention to its chemistry has prevented an expectedly robust feature to be disclosed. A judicious use of any heuristic principle is always fundamental in chemistry as the discipline “still remains a gloriously qualitative subject” [25].

Documentation of single observations and phenomena where we are now acknowledging the role played by the XB went on during the whole of the twentieth century. The occurrence of single phenomena was conveniently described and analyzed through a variety of techniques, and compilations collecting closely related results began to appear, initially as paragraphs in papers with a more general focus, then as reviews or book chapters fully devoted to the topic (significant papers from the secondary literature which are not discussed elsewhere in this chapter are listed in [26–43]). However, single findings were understood within conceptual frames different from each other and the common features were not recognized till the end of the twentieth century. The most important discoveries reported in the last 70 years are sketched below.

The I₂...benzene complex was identified in solution thanks to its UV–vis spectrum by Benesi and Hildebrand in 1948 and 1 year later other aromatics were reported to behave analogously [44, 45]. In 1950 Mulliken described the formation of similar complexes with ethers, thioethers, and carbonyl derivatives [46], and

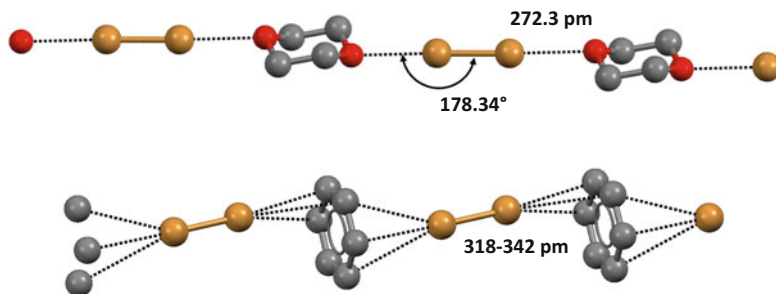


Fig. 3 Ball and stick representation (Mercury 3.3) of infinite chains formed by dibromine (working as bidentate XB donor) with 1,4-dioxane (*top*) and benzene (*bottom*). Both XB acceptors work as bidentate tectons. XB are *black dashed lines*. Color code: *gray*, carbon; *red*, oxygen; *brown*, bromine. Hydrogen atoms have been omitted for clarity

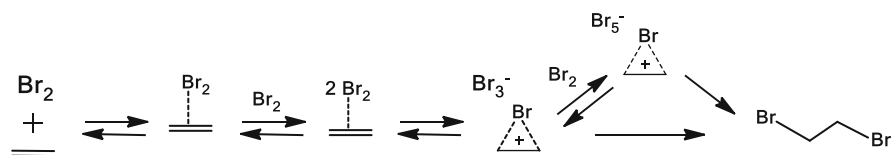


Fig. 4 Representation of a part of the mechanistic scheme for bromination of alkenes proving the formation of halogen bonded adducts

2 years later he rationalized them as a subclass of the electron donor–acceptor molecular complexes [47]. UV–vis spectroscopy also indicated that charge transfer occurs from the donor of electron density to the halogen atom in complexes involving dihalogens and aromatics ([48] and references therein) and in many other halogen bonded adducts, even as weak as the perfluorocarbon/amine complexes [49]. The solid-state structure of the $\text{Br}_2 \cdots \text{O}(\text{CH}_2\text{CH}_2)_2\text{O}$ system (Fig. 3, top) was described in 1954 by Hassel [50] who then reported the X-ray structure of several related adducts involving dihalogens and halocarbons [51, 52]. The crystal structure of $\text{Br}_2 \cdots \text{C}_6\text{H}_6$ (Fig. 3, bottom) and $\text{Cl}_2 \cdots \text{C}_6\text{H}_6$ adducts, reported in 1958 and 1959, respectively [53, 54], are particularly noteworthy as they showed that π -systems work as donors of electron density against electrophilic halogens also in the solid state [55].¹ Importantly, these systems were suggesting that halogen-bonded adducts are on the reaction pathways of halogenation reactions of aromatics and other unsaturated systems (Fig. 4). In the successive decades, the hypothesis

¹ In Hassel's structures the halogen molecules adopt a symmetrical location along the sixfold axis of benzene and form infinite $\cdots \text{C}_6\text{H}_6 \cdots \text{Br}-\text{Br} \cdots \text{C}_6\text{H}_6 \cdots \text{Br}-\text{Br} \cdots \text{C}_6\text{H}_6 \cdots$ chains. More recent X-ray measurements of the $\text{Br}_2 \cdots \text{C}_6\text{H}_6$ system at lower temperature than Hassel's [55] reveal a less symmetric arrangement where bromine atoms are positioned over the rim of the benzene ring and the calculated hapticity ($\eta = 1.52$) is midway between the "over-atom" ($\eta = 1.0$) and "over-bond" ($\eta = 2.0$) coordination. A phase transition at 203 K leads to the diffraction pattern reported by Hassel and Strømme.

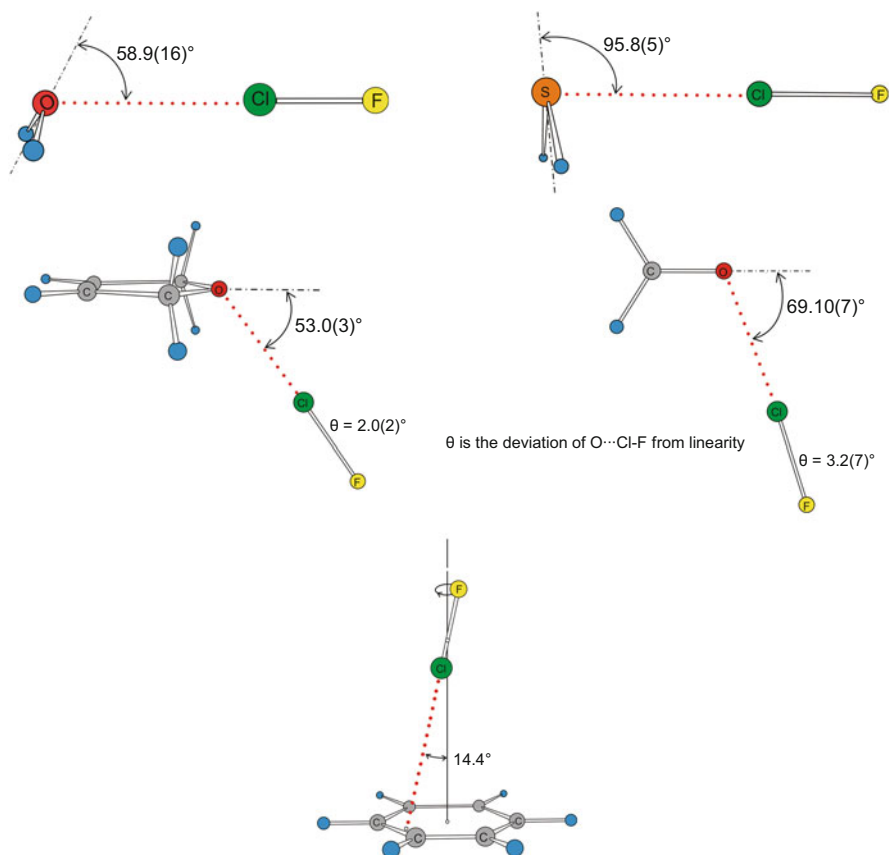


Fig. 5 Schematic representation of the halogen bonded adducts that ClF forms in the gas phase with: water (*top, left*); hydrogen sulfide (*top, right*); 2,5-dihydrofuran (*mid, left*); formaldehyde (*mid, right*); benzene (*bottom*). Geometric features (obtained via microwave spectroscopy, [17, 62]) confirm that the XB donor interacts with the lone pair or π -electrons of the acceptor

was forcefully confirmed [56, 57] and Kochi showed that π -donating moieties also form solid adducts with halocarbons [48].

In 1968, Bent [58] published a comprehensive review on the structural chemistry of donor–acceptor adducts, and halogen-bonded systems were included. He put forward the main geometric features of the XB in the solid state and 20 years later Parthasarathy and Desiraju [59, 60] convincingly validated these features through statistical analysis of the structures in the Cambridge Structural Database (CSD). Consistent indications afforded by several techniques (e.g., UV–vis, IR and Raman, NMR and NQR, dielectric polarization, etc.) allowed Dumas et al. [61] to confirm, in 1983, that the interaction features in the liquid phase parallel those in the solid phase.

Legon [17, 62] in 1998 reviewed the analysis, via microwave spectroscopy, of halogen bonded adducts formed in the gas phase (Fig. 5) and showed that the

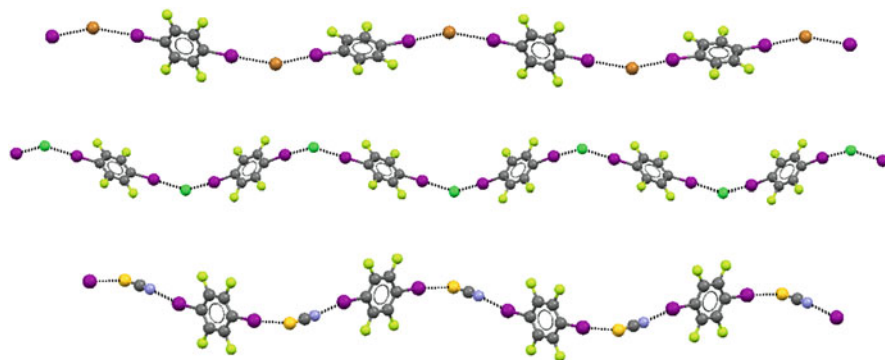


Fig. 6 Ball and stick representation (Mercury 3.3) of the halogen bonded chains formed by 1,4-diodotetrafluorobenzene when co-crystallizing with: $n\text{-Bu}_4\text{N}^+\text{Br}^-$ (top) [63]; $n\text{-Bu}_4\text{N}^+\text{Cl}^-$ (mid) [63]; $n\text{-Bu}_4\text{N}^+\text{SCN}^-$ (bottom) [64]. Quite similar infinite chains are obtained when $n\text{-Bu}_4\text{P}^+\text{Br}^-$ [64], $\text{Me}_4\text{N}^+\text{Br}^-$ [65], $n\text{-Bu}_4\text{P}^+\text{Cl}^-$ [66], and $\text{Me}_4\text{N}^+\text{Cl}^-$ [64] are used. Cations have been omitted for sake of simplicity; XBs are black dotted lines. Color code: gray, carbon; light green, fluorine; violet, iodine; brown, bromine; green, chlorine; sky blue, nitrogen; ochre, sulfur

interaction in “isolated” adducts is largely the same as in adducts in the condensed phases, namely the lattice and solvent effects present in the solid and in the liquid are non heavily affecting the interaction features. In the same period, we proved systematically that adducts formed by anions with halocarbons (Fig. 6) [63–70] are similar to those formed by lone-pair-possessing heteroatoms (Fig. 7) [71–82]. We also expanded the range of halocarbons which work as effective XB donors [83, 84] and identified the key role of residues close to covalently bound halogen atoms in determining their ability to work as electrophilic sites. It became clear that it was possible to design and fine tune the structural and functional features of adducts formed under XB control if the nature and structure of the involved modules were conveniently chosen.

Atoms in molecules have been approximated, in the past, as interpenetrating spheres and halogen atoms have long been considered neutral spheres in dihalogens and negative spheres in halocarbons (as the electronegativity of halogens is higher than that of carbon). Electrophilic halogens thus appeared strange [11], and the persistent biases resulting from the approximations described above long prevented electrophilic halogens from being recognized as responsible for the formation of relatively strong and highly directional interactions in the solid, liquid, and gas phases.

Halophilic reactions (Fig. 8) received very minor attention [85–89], probably because of the same biases. Two important contributions disproving the sphere approximation appeared towards the end of the last century. In 1986, Nyburg and Faerman [90] used a statistical analysis of crystal structures in the CSD to propose that halogen atoms in halocarbons have an ellipsoidal shape with a shorter radius on the extension of the C-halogen bond and a longer radius orthogonal to this direction. In 1992, Politzer and Murray calculated the electrostatic potential on the surface of halogen atoms and found that the electron density distribution around covalently

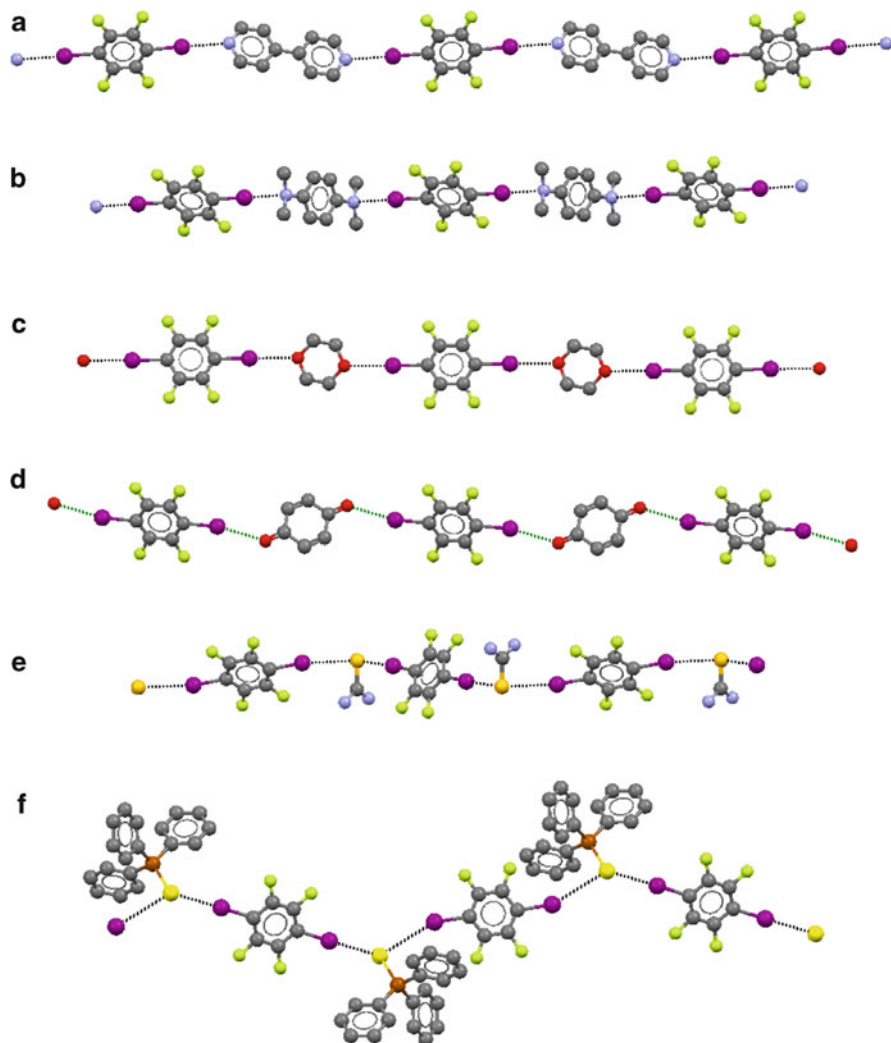


Fig. 7 Ball and stick representation (Mercury 3.3) of the halogen-bonded chains formed by 1,4-diiodotetrafluorobenzene with: (a) 4,4'-dipyridine [71], (b) *N,N,N',N'*-tetramethyl-*p*-phenylenediamine [72], (c) dioxane [73], (d) 1,4-benzoquinone [74], (e) thiourea [75], (f) triphenylphosphineselenide [76]. Hydrogen atoms have been deleted for the sake of simplicity; XBs are *black dotted lines*. Color code: *gray*, carbon; *light green*, fluorine; *violet*, iodine; *sky blue*, nitrogen; *red*, oxygen; *ochre*, sulfur; *yellow*, selenium; *brown*, phosphorus. Quite similar infinite chains are obtained when other nitrogen centered nucleophiles [77–80], oxygen centered nucleophiles [81], and sulfur centered nucleophiles [73] are used

bound halogens is anisotropic. Depletion of electronic charge occurs along the extension of the covalent bond formed by halogens and a region of positive electrostatic potential (positive σ -hole) appears, most frequently in heavier

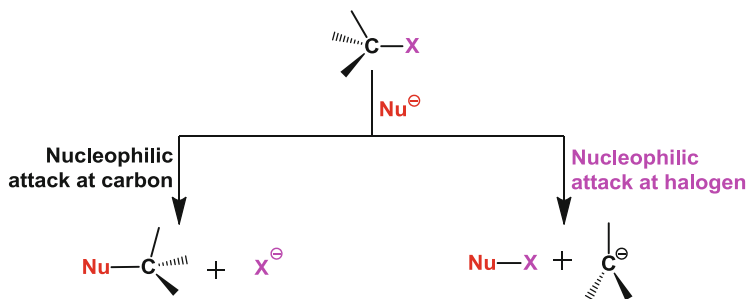
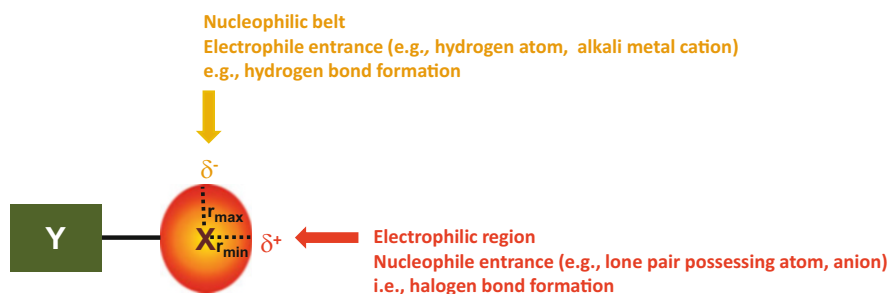


Fig. 8 A donor of electron density (represented here as the anion Nu^-) can attack a halocarbon $\text{C}-\text{X}$ ($\text{X}=\text{Cl}, \text{Br}, \text{I}$) by entering: – in the carbon atom (*left*) and the well-known nucleophilic substitution reactions at carbon occur; – in the halogen atom (*right*) and the halophilic reactions are observed. The formed NuX is frequently a reaction intermediate. Halophilic reactions can involve also halogens bound to heteroatoms (see [85, 86])



$\text{X} = \text{F}, \text{Cl}, \text{Br}, \text{I}, (\text{At}); \text{Y} = \text{C}, \text{N}, \text{F}, \text{Cl}, \text{Br}, \text{I}, \text{etc.}$

Fig. 9 Schematic representation of the anisotropic distribution of the electron density around monovalent halogen atoms and the pattern of the resulting interactions

halogens [91–93]. The position of this region accounts for the XB directionality (Fig. 9). Consistent with the high electronegativity of halogens, the rest of their surface is negative, the most negative potential forming a belt orthogonal to the covalent bond. The most positive and negative regions, identified by Politzer and Murray with modeling, correspond to the shorter (r_{min}) and longer (r_{max}) radii identified by Nyburg and Faerman via a search in the CSD. These findings gave the experimental and theoretical bases for a comprehensive process of unification which we initiated with the paper entitled “Halogen Bonding: A Paradigm in Supramolecular Chemistry” [83].

This *Concept* article put forward a single and unified model comprehensively recollecting the discoveries summarized above and many others not explicitly mentioned here. The *Concept* paper proposed the electrophilic behavior of halogen atoms as a general phenomenon impacting on “all the fields where design and manipulation of aggregation processes play a key role.” The process of unification went a further step ahead with a review article on the *Accounts of Chemical Research*

[94], where we acknowledged that differences exist in the adducts formed when dihalogens, halocarbons, or other halogenated derivatives attractively interact with lone-pair-possessing atoms, π -systems, or anions but it was also underlined that the main chemical and physical features of the formed adducts remain largely the same. The aim was to unify previously compartmentalized fields.

Finalization of this unification process required an assessment from the scientific community. A symposium devoted to the XB was organized in the frame of the 238th National Meeting of the American Chemical Society (Washington, DC; 16th August 2009) and allowed many of the leading experts in the field² to discuss the state of the art. Importantly, an operative consensus emerged that the main features of interactions involving halogen atoms as electrophilic sites remain unchanged on varying the involved modules and the physical state of the system. The relevance of the symposium was acknowledged by *Chemical & Engineering News* in a paper entitled “Halogen bonding begins to fly” [95]. This consensus was further tuned in the kick-off event of the IUPAC project aimed at proposing a definition of the XB. The event was organized in Sigüenza (20th–21st August 2011, Spain) [96, 97] as a satellite meeting to the XXII International Union of Crystallography Congress (Fig. 10). The cozy atmosphere of this charming town helped the numerous participants to tackle thoughtfully the issues critical for a definition of XB.

2 A Unifying and Unambiguous Name

The previous paragraph is an attempt to give an Ariadne’s thread for the main evidence on halogen atoms as electrophilic sites in recognition phenomena. It gives quite a linear picture of the path followed to develop the XB concept and to formulate the corresponding definition recently proposed by IUPAC. The actual path followed to correlate main experimental and theoretical evidence on interactions given by electrophilic halogen atoms was probably more patchy than presented above, but the important issue is that, independent of any ex post facto character of the path presented above, the IUPAC definition of XB registers the consensus reached by the scientific community on the endpoint of a process 200 years long.

² Lectures were given by: Peter Politzer (Cleveland State University, USA), Anthony C. Legon (University of Bristol, UK), Lee Brammer (University of Sheffield, UK), William Jones (University of Cambridge, UK), William T. Pennington (Clemson University, USA), Nancy S. Goroff (State University of New York, Stony Brook, USA), Milko E. van der Boom (The Weizmann Institute of Science, IL), Pierangelo Metrangolo (Politecnico di Milano, IT), Kari Rissanen (University of Jyväskylä, FL), Bernd Schöllhorn (Ecole Normale Supérieure Paris, FR), Duncan W. Bruce (University of York, UK), Hiroshi Yamamoto (RIKEN, JP), Shing P. Ho (Colorado State University, USA), and Patrick Lam (Bristol-Myers Squibb Research and Development, USA). Presented topics spanned modeling, crystal engineering, drug-receptor optimization, and material sciences.



Fig. 10 Picture of the participants to the meeting of the IUPAC Project (Sigüenza, 20th–21st August 2011) where the debate allowed a consensus to emerge on some issues which were controversial at the early stages of the discussion on the definition of XB. *Top*: Silhouette of participants: (1) Giancarlo Terraneo, (2) Gautam R. Desiraju, (3) Gabriella Cavallo, (4) Pierangelo Metrangolo, (5) Giuseppe Resnati, (6) Duncan W. Bruce, (7) Tatsuo Kaiho, (8) Pavel Hobza, (9) Elangannan Arunan, (10) Ibon Alkorta, (11) David L. Bryce, (12) Enrique Espinoza, (13) Stefan M. Huber, (14) Robin D. Rogers, (15) Antony C. Legon, (16) Shing P. Ho, (17) Roberto Marquardt, (18) Lee Brammer, (19) Marc Fourmigué, (20) William T. Pennigton, (21) Christer B. Aakeröy, (22) Deirdre Legon, (23) Marcos Daniel García Romero, (24) Susanta K. Najak, (25) Stefano Libri, (26) Nikolay Houbenov, (27) Wei Jun Jin, (28) Hiroshi M. Yamamoto, (29) Leonardo Belpassi, (30) Anna-Carin Carlsson, (31) Cosimo Cardellicchio, (32) Arijit Mukherjee, (33) Linda McAllister, (34) Christina Hettstedt, (35) Gabriele Manca, (36) Megan Carter, (37) Francesco Devillanova, (38) Kari Raatikainen, (39) Petra Bombicz, (40) Marijana Dakovic, (41) Catharine Esterhuysen, (42) Carlo Mealli, (43) Vera Vasylyeva, (44) Guillermo Minguez Espallargas, (45) Marta Elena González Mosquera, (46) Li-Ming Yang, (47) Matti Haukka, (48) Maura Malinska, (49) Matti Tuikka, (50) Vânia André, (51) Joao Luis Ferreira da Silva, (52) Claudio, (53) Gabriele Saleh, (54) Paulina Ivette Hidalgo Cordova, (55) Elisa Jimenez, (56) Ivan Infante, (57) Stefano Rendine, (58) Carmen Ramírez de Arellano

The recognition phenomena where we are now acknowledging the role played by XB were understood, before the late 1990s, where different and unconnected frames and erratic terms were used to designate the corresponding interactions. In 1968 Bent could already list some 20 descriptive phrases used during the “first century” of XB, illustrating the struggle to understand the phenomenon [58]. They varied from the imaginative “bumps in hollow” to the chemically meaningful “charge-transfer interaction.” The term halogen bond was probably first used to address interactions by electrophilic halogens in 1961 by Zingaro and Hedges [98] while describing the complexes formed in solution by halogens and interhalogens with phosphine oxides and sulfides.

The term then began to be used for other related systems, for instance by Martire et al. in 1976 for adducts formed in the gas phase by haloforms with ethers and amines [99], by Dumas et al. in 1978 for tetrahalomethane/pyridine complexes [100], and by Kochi et al. in 1987 for tetrahalomethane/amine adducts in the solid [101]. The use progressively became less and less occasional and an exponential growth occurred in the last 20 years in parallel with the comprehensive process of unification of all phenomena related to interactions originated by electrophilic halogens. The terms halogen bond and halogen bonding are used interchangeably.

It has also been proposed [102] that the term halogen bond could be used for any interactions formed by halogen atoms, namely when halogens are the electrophilic site (and interact with nucleophiles at the region where their electrostatic potential is most positive, i.e., the σ -hole [103]), or when they are the nucleophilic site (and interact with electrophiles at the region where their electrostatic potential is most negative, i.e., the belt orthogonal to the covalent bond). In fact, because of the anisotropic distribution of their electron density, halogen atoms frequently show an amphoteric character. The IUPAC definition recommends that the term XB is used to designate only the interactions wherein halogen atoms function as the electrophile and an electron-rich partner enters their positive region(s).

The terms fluorine bond [15, 104, 105], chlorine bond [62, 106, 107], bromine bond [108], and iodine bond [109, 110] have also been used occasionally to designate the specific sets of interactions formed when one single halogen attractively interacts with an electron-rich partner. These interactions are subsets of those encompassed by the term XB. An advantage of the term XB, relative to the aforementioned subsets, is that it gives the instruments to contrast the experimental and theoretical findings on interactions involving a single halogen, with the much wider set of related findings given by other halogens. In other words, a particularly meaningful comparison among the behavior of the four halogens becomes possible. Trends in observed or computed parameters can be obtained on changing the halogen X in an R-X \cdots Y complex while R and Y remain unchanged and these trends usefully complement information afforded by trends observed on changing R, while X and Y remain the same, or on changing Y, while R and X remain the same.

Acknowledgments We are grateful to all colleagues, graduate and Ph.D. students, and postdoctoral associates who worked with us on XB. Some of them are mentioned in the references. Their dedication and enthusiasm has been fundamental. The authors are also grateful to the IUPAC for supporting the project no. 2009-032-1-100 “Categorizing Halogen Bonding and Other Noncovalent Interactions Involving Halogen Atoms.”

References

1. Colin JJ (1814) Sur l'iode. *Ann Chim* 91:252–272
2. Guthrie F (1863) XXVIII. – On the iodide of iodammonium. *J Chem Soc* 16:239–244
3. Pelletier P, Caventou JJ (1819) Sur l'asphyxie. *Ann Chim* 10:142–177
4. Svensson PH, Kloo L (2003) Synthesis, structure, and bonding in polyiodide and metal iodide-iodine systems. *Chem Rev* 103:1649–1684
5. Jörgensen SM (1870) Ueber Einige anorganische Superjodide. *J Prakt Chem* 2:347–360
6. Roussopoulos O (1883) Einwirkung von Chinolin Auf Chloroform und Iodoform. *Ber* 16: 202–203
7. Remsen I, Norris JF (1896) Action of the halogens on the methylamines. *Am Chem J* 18: 90–95
8. Metrangolo P, Meyer F, Pilati T, Resnati G, Terraneo G (2008) Halogen bonding in supramolecular chemistry. *Angew Chem Int Ed* 47:6114–6127
9. Politzer P, Murray JS, Clark T (2010) Halogen bonding: an electrostatically-driven highly directional noncovalent interaction. *Phys Chem Chem Phys* 12:7748–7757
10. Parisini E, Metrangolo P, Pilati T, Resnati G, Terraneo G (2011) Halogen bonding in halocarbon–protein complexes: a structural survey. *Chem Soc Rev* 40:2267–2278
11. Schwerdtfeger P (2006) Atomic static dipole polarizabilities. In: Maroulis G (ed) *Atoms, molecules and clusters in electric fields*. Imperial College Press, London, pp 1–32
12. Cardillo P, Corradi E, Lunghi A, Meille SV, Messina MT, Metrangolo P, Resnati G (2000) The N···I intermolecular interaction as a general protocol for the formation of perfluorocarbon–hydrocarbon supramolecular architectures. *Tetrahedron* 56:5535–5550
13. Metrangolo P, Murray JS, Pilati T, Politzer P, Resnati G, Terraneo G (2011) Fluorine-centered halogen bonding: a factor in recognition phenomena and reactivity. *Cryst Growth Des* 11: 4238–4246
14. Metrangolo P, Murray JS, Pilati T, Politzer P, Resnati G, Terraneo G (2011) The fluorine atom as a halogen bond donor, viz. a positive site. *CrystEngComm* 13:6593–6596
15. Chopra D, Guru Row TN (2011) Role of organic fluorine in crystal engineering. *CrystEngComm* 13:2175–2186
16. Pavan MS, Durga Prasad K, Guru Row TN (2013) Halogen bonding in fluorine: experimental charge density study on intermolecular F···F and F···S donor–acceptor contacts. *Chem Commun* 49:7558–7560
17. Legon AC (1999) Prereactive complexes of dihalogens XY with Lewis bases B in the gas phase: a systematic case for the halogen analogue B–XY of the hydrogen bond B – HX. *Angew Chem Int Ed* 38:2686–2714
18. Bulat FA, Toro-Labbe A, Brinck T, Murray JS, Politzer P (2010) *J Mol Model* 16:1679–1691
19. Legon AC (1999) *Angew Chem Int Ed* 38:2686–2714
20. Ault BS, Andrews L (1976) Matrix reactions of alkali metal fluoride molecules with fluorine. Infrared and Raman spectra of the trifluoride ion in the $M^+F_3^-$ species. *J Am Chem Soc* 98: 1591–1593
21. Ault BS, Andrews L (1977) Infrared and Raman spectra of the $M^+F_3^-$ ion pairs and their mixed chlorine-fluorine counterparts in solid argon. *Inorg Chem* 16:2024–2028

22. Riedel S, Kochner T, Wang X, Andrews L (2010) Polyfluoride anions, a matrix-isolation and quantum-chemical investigation. *Inorg Chem* 49:7156–7164
23. Wentworth WE, Dojahn JG, Chen ECM (1996) Characterization of homonuclear diatomic ions by semiempirical Morse potential energy curves. 1. The halogen anions. *J Phys Chem* 100:9649–9657
24. Alkorta I, Blanco F, Solimannejad M, Elguero J (2008) Competition of hydrogen bonds and halogen bonds in complexes of hypohalous acids with nitrogenated bases. *J Phys Chem A* 112:10856–10863
25. Desiraju GR (2011) A bond by any other name. *Angew Chem Int Ed* 50:52–59
26. Andrews LJ, Keefer RM (1964) *Molecular complexes in organic chemistry*. Holden-day Inc, San Francisco London Amsterdam
27. Foster R (1969) *Organic charge-transfer complexes*. Academic, London New York
28. Foster R (ed) (1973) *Molecular complexes*, vols 1 and 2. Elek Science, London
29. Laurence C, Gal J-F (2010) *Lewis basicity and affinity scales*. Wiley, Chichester
30. Metrangolo P, Pilati T, Resnati G, Stevenazzi A (2003) Halogen bonding driven self-assembly of fluorocarbons and hydrocarbons. *Curr Opin Colloid Interface Sci* 8:215–222
31. Fox DB, Liantonio R, Metrangolo P, Pilati T, Resnati G (2004) Perfluorocarbon-hydrocarbons self-assembly: halogen bonding mediated intermolecular recognition. *J Fluorine Chem* 125: 271–281
32. Politzer P, Lane P, Concha MC, Ma Y, Murray JS (2007) An overview of halogen bonding. *J Mol Model* 13:305–311
33. Metrangolo P, Resnati G, Pilati T, Liantonio R, Meyer F (2007) Engineering functional materials by halogen bonding. *J Polym Sci A Polym Chem* 45:1–15
34. Lu Y, Shi T, Wang Y, Yang H, Yan X, Luo X, Jiang H, Zhu W (2009) Halogen bonding -a novel interaction for rational drug design? *J Med Chem* 52:2854–2862
35. Lu Y, Wang Y, Zhu W (2010) Nonbonding interactions of organic halogens in biological systems: implications for drug discovery and biomolecular design. *Phys Chem Chem Phys* 12:4543–4551
36. Rissanen K (2008) Halogen bonded supramolecular complexes and networks. *CrystEngComm* 10:1107–1113
37. Metrangolo P, Resnati G, Pilati T, Biella S (2008) Halogen bonding in crystal engineering. In: Metrangolo P, Resnati G (eds) *Halogen bonding: fundamentals and applications; structure and bonding series*, vol 126, Springer-Verlag, Berlin, Heidelberg, pp 105–136
38. Murray JS, Riley KE, Politzer P, Clark T (2010) Directional weak intermolecular interactions: sigma-hole bonding. *Aust J Chem* 63:1598–1607
39. Legon AC (2010) The halogen bond: an interim perspective. *Phys Chem Chem Phys* 12: 7736–7747
40. Bertani R, Sgarbossa P, Venzo A, Lelj F, Amati M, Resnati G, Pilati T, Metrangolo P, Terraneo G (2010) Halogen bonding in metal–organic–supramolecular networks. *Coord Chem Rev* 254:677–695
41. Wilcken R, Zimmermann M, Lange A, Joerger A, Boeckler F (2013) Principles and applications of halogen bonding in medicinal chemistry and chemical biology. *J Med Chem* 56: 1363–1388
42. Priimagi A, Cavallo G, Metrangolo P, Resnati G (2013) The halogen bond in the design of functional supramolecular materials: recent advances. *Acc Chem Res* 46:2686–2695
43. Troff RW, Mäkelä T, Topić FP, Valkonen A, Raatikainen K, Rissanen K (2013) Alternative motifs for halogen bonding. *Eur J Org Chem* 1617–1637
44. Benesi HA, Hildebrand JH (1948) Ultraviolet absorption bands of iodine in aromatic hydrocarbons. *J Am Chem Soc* 70:2832–2833
45. Benesi HA, Hildebrand JH (1949) Spectrophotometric investigation of the interaction of iodine with aromatic hydrocarbons. *J Am Chem Soc* 71:2703–2707
46. Mulliken RS (1950) Structures of complexes formed by halogen molecules with aromatic and with oxygenated solvents. *J Am Chem Soc* 72:600–608

47. Mulliken RS (1952) Molecular compounds and their spectra. III. The interaction of electron donors and acceptors. *J Phys Chem* 56:801–822
48. Rosokha SV, Kochi JK (2008) X-Ray structures and electronic spectra of the π -halogen complexes between halogen donors and acceptors with π -receptors. In: Metrangolo P, Resnati G (eds) *Halogen bonding: fundamentals and applications. Structure and bonding series*, vol. 126. Springer-Verlag, Berlin, Heidelberg, pp 137–169
49. Burdeniuc J, Sanford M, Crabtree RH (1998) Amine charge transfer complexes of perfluoroalkanes and an application to poly(tetrafluoroethylene) surface functionalization. *J Fluorine Chem* 91:49–54
50. Hassel O, Hvoslef J (1954) The structure of bromine 1,4-dioxanate. *Acta Chem Scand* 8:873
51. Hassel O, Rømming C (1962) Direct structural evidence for weak charge-transfer bonds in solid containing chemically saturated molecules. *Q Rev Chem Soc* 16:1–18
52. Hassel O (1970) Structural aspects of interatomic charge-transfer bonding. *Science* 170:497–502
53. Hassel O, Strømme KO (1958) Structure of the crystalline compound benzene-bromine (1:1). *Acta Chem Scand* 12:1146
54. Hassel O, Strømme KO (1959) Crystal structure of the addition compound benzene-chlorine (1:1). *Acta Chem Scand* 13:1781–1786
55. Vasilyev AV, Lindeman SV, Kochi JK (2001) Noncovalent binding of the halogens to aromatic donors. Discrete structures of labile Br₂ complexes with benzene and toluene. *Chem Commun* 909–910
56. Brown RS (1997) Investigation of the early steps in electrophilic bromination through the study of the reaction with sterically encumbered olefins. *Acc Chem Res* 30:131–137
57. Lenoir D, Chiappe C (2003) What is the nature of the first-formed intermediates in the electrophilic halogenation of alkenes, alkynes, and allenes? *Chem Eur J* 9:1037–1044
58. Bent HA (1968) Structural chemistry of donor–acceptor interactions. *Chem Rev* 68:587–648
59. Ramasubbu N, Parthasarathy R, Murray-Rust P (1986) Angular preferences of intermolecular forces around halogen centers: preferred directions of approach of electrophiles and nucleophiles around the carbon-halogen bond. *J Am Chem Soc* 108:4308–4314
60. Desiraju GR, Parthasarathy R (1989) The nature of halogen-halogen interactions: are short halogen contacts due to specific attractive forces or due to close packing of nonspherical atoms? *J Am Chem Soc* 111:8725–8726
61. Dumas JM, Gomet L, Guerin M (1983) Molecular interactions involving organic halides. In: Patai S, Rappoport Z (eds) *The chemistry of functional groups, supplement D*. Wiley, New York, pp 985–1020
62. Legon AC (1998) π -Electron “donor–acceptor” complexes B \cdots ClF and the existence of the “chlorine bond.” *Chem Eur J* 4:1890–1897
63. Abate A, Biella S, Cavallo G, Meyer F, Neukirch H, Metrangolo P, Pilati T, Resnati G, Terraneo G (2009) Halide anions driven self-assembly of haloperfluoroarenes: formation of one-dimensional non-covalent copolymers. *J Fluorine Chem* 130:1171–1177
64. Cauliez P, Polo V, Roisnel T, Llusar R, Fourmigue M (2010) The thiocyanate anion as a polydentate halogen bond acceptor. *CrystEngComm* 12:558–566
65. Viger-Gravel J, Leclerc S, Korobkov I, Bryce DL (2013) Correlation between ¹³C chemical shifts and the halogen bonding environment in a series of solid para-diiodotetrafluorobenzene complexes. *CrystEngComm* 15:3168–3177
66. Grebe J, Geiseler G, Harms K, Dehnicke K (1999) Donor-acceptor complexes of halide ions with 1,4-diiodotetrafluorobenzene. *Z Naturforsch B Chem Sci* 54:77–86
67. Liantonio R, Metrangolo P, Pilati RG (2003) Fluorous interpenetrated layers in a three-component crystal matrix. *Cryst Growth Des* 3:355–361
68. Cavallo MP, Pilati RG, Sansotera M, Terraneo G (2010) Halogen bonding: a general route in anion recognition and coordination. *Chem Soc Rev* 39:3772–3783
69. Metrangolo P, Pilati T, Terraneo G, Biella S, Resnati G (2009) Anion coordination and anion-templated assembly under halogen bonding control. *CrystEngComm* 11:1187–1196

70. Abate A, Martí-Rujas J, Metrangolo P, Pilati T, Resnati G, Terraneo G (2011) Tetrahedral oxyanions in halogen-bonded coordination networks. *Cryst Growth Des* 11:4220–4226
71. Walsh RB, Padgett CW, Metrangolo P, Resnati G, Hanks TW, Pennington TW (2001) Crystal engineering through halogen bonding: complexes of nitrogen heterocycles with organic iodides. *Cryst Growth Des* 1:165–175
72. Liantonio R, Luzzati S, Metrangolo P, Pilati T, Resnati G (2002) Perfluorocarbon–hydrocarbon self-assembly. Part 16: anilines as new electron donor modules for halogen bonded infinite chain formation. *Tetrahedron* 58:4023–4029
73. Cincic D, Friscic T, Jones W (2008) Isostructural materials achieved by using structurally equivalent donors and acceptors in halogen-bonded cocrystals. *Chem Eur J* 14:747–753
74. Liu P, Ruan C, Li T, Ji B (2012) Cyclo-hexa-2,5-diene-1,4-dione-1,2,4,5-tetra-fluoro-3,6-diiodo-benzene (1/1). *Acta Crystallogr Sect E Struct Rep* 68:o1431
75. Arman HD, Gieseking RL, Hanks TW, Pennington WT (2010) Complementary halogen and hydrogen bonding: sulfuriodine interactions and thioamide ribbons. *Chem Commun* 46:1854–1856
76. Arman HD, Rafferty ER, Bayse CA, Pennington WT (2012) Complementary selenium···iodine halogen bonding and phenyl embraces: cocrystals of triphenylphosphine selenide with organoiodides. *Cryst Growth Des* 12:4315–4323
77. Corradi E, Meille SV, Messina MT, Metrangolo P, Resnati G (2000) Halogen bonding versus hydrogen bonding in driving self-assembly processes. *Angew Chem Int Ed* 39:17821786
78. Sgarbossa P, Bertani R, Di Noto V, Piga M, Giffin GA, Terraneo G, Pilati T, Metrangolo P, Resnati G (2012) Interplay between structural and dielectric features of new low k hybrid organic–organometallic supramolecular ribbons. *Cryst Growth Des* 12:297–305
79. Aakeroy CB, Desper J, Helfrich BA, Metrangolo P, Pilati T, Resnati G, Stevenazzi A (2007) Combining halogen bonds and hydrogen bonds in the modular assembly of heteromeric infinite 1-D chains. *Chem Commun* 4236–4238
80. Meazza L, Foster JA, Fucke K, Metrangolo P, Resnati G, Steed JW (2013) Halogen-bonding-triggered supramolecular gel formation. *Nat Chem* 5:42–47
81. Messina MT, Metrangolo P, Panzeri W, Pilati T, Resnati G (2001) Intermolecular recognition between hydrocarbon oxygen-donors and perfluorocarbon iodine-acceptors: the shortest O···I non-covalent bond. *Tetrahedron* 57:8543–8550
82. Britton D, Gleason WB (2002) Dicyanodurene-p-tetrafluorodiodobenzene (1/1). *Acta Crystallogr Sect E Struct Rep* 58:o1375–o1377
83. Metrangolo P, Resnati G (2001) Halogen bonding: a paradigm in supramolecular chemistry. *Chem Eur J* 7:2511–2519
84. Lunghi A, Cardillo P, Messina T, Metrangolo P, Panzeri W, Resnati G (1998) Perfluorocarbon–hydrocarbon self assembling. Thermal and vibrational analyses of one-dimensional networks formed by α , ω -diiodoperfluoroalkanes with K₂.2. and K₂.2.2. *J Fluorine Chem* 91:191–194
85. Foucaud A (1983) Positive halogen compounds. In: Patai S, Rappoport Z (eds) *The chemistry of functional groups, supplement D*. Wiley, New York, pp 441–480
86. Du Mont WW, Ruthe F (1999) Iodophosphonium salt structures: homonuclear cation–anion interactions leading to supramolecular assemblies. *Coord Chem Rev* 189:101–133
87. Grinblat J, Ben-Zion M, Hoz S (2001) Halophilic reactions: anomalies in bromine transfer reactions. *J Am Chem Soc* 123:10738–10739
88. Zefirov NS, Makhon'kov D (1982) X-Philic Reactions. *Chem Rev* 82:615–624
89. Koser GF (1983) Halonium ions. In: Patai S, Rappoport Z (eds) *The chemistry of functional groups, supplement D*. Wiley, New York, pp 1265–1352
90. Nyburg SC, Faerman CH (1985) A revision of van der Waals atomic radii for molecular crystals: N, O, F, S, Cl, Se, Br and I bonded to carbon. *Acta Cryst B* 41:274–279
91. Murray JS, Paulsen K, Politzer P (1994) Molecular-surface electrostatic potentials in the analysis of non-hydrogen-bonding noncovalent interactions. *Proc Indian Acad Sci Ser Chim* 106:267–275

92. Brinck T, Murray JS, Politzer P (1992) Surface electrostatic of halogenated methanes as indicators of directional intermolecular interactions. In *J Quantum Chem* 44:57–64
93. Brinck T, Murray JS, Politzer P (1993) Molecular-surface electrostatic potentials and local ionization energies of group V-VII hydrides and their anions – relationships for aqueous and gas-phase acidities. *Int J Quantum Chem* 48:73–88
94. Metrangolo P, Neukirch H, Pilati T, Resnati G (2005) Halogen bonding based recognition processes: a world parallel to hydrogen bonding. *Acc Chem Res* 38:386–395
95. Ritter SK (2009) Halogen bonding begins to fly. *Chem Eng News* 87:39–42
96. Rogers RD (2011) Halogen bonding: weak interactions result in strong opinions. *Cryst Growth Des* 11:4721–4722
97. Metrangolo P, Resnati G (2012) Halogen bonding: where we are and where we are going. *Cryst Growth Des* 12:5835–5838
98. Zingaro R, Hedges R (1961) Phosphine oxide-halogen complexes: effect on P–O and P–S stretching frequencies. *J Phys Chem* 65:1132–1138
99. Martire DE, Sheridan JP, King JW, O'Donnell SE (1976) Thermodynamics of molecular association. 9. An NMR study of hydrogen bonding of CHCl_3 and CHBr_3 to di-n-octyl ether, di-n-octyl thioether, and di-n-octylmethylamine. *J Am Chem Soc* 98:3101–3106
100. Dumas JM, Peurichard H, Gomel M (1978) $\text{CX}_4 \cdots$ base interactions as models of weak charge-transfer interactions: comparison with strong charge-transfer and hydrogen-bond interactions. *J Chem Res (S)* 54–55; *J Chem Res (M)* 0649–0663
101. Blackstock SC, Lorand JP, Kochi JK (1987) Charge-transfer interactions of amines with tetrahalomethanes. X-Ray crystal structures of the donor-acceptor complexes of quinuclidine and diazabicyclo[2.2.2]octane with carbon tetrabromide. *J Org Chem* 52:1451–1460
102. Glaser R, Murphy RF (2006) What's in a name? Noncovalent $\text{Ar}-\text{Cl} \cdots (\text{H}-\text{Ar})_n$ interactions and terminology based on structure and nature of the bonding. *CrystEngComm* 8:948–951
103. Metrangolo P, Pilati T, Resnati G (2006) Halogen bonding and other noncovalent interactions involving halogens: a terminology issue. *CrystEngComm* 8:946–947
104. Laurence C, Graton J, Gal J-F (2011) An overview of Lewis basicity and affinity scales. *J Chem Educ* 88:1651–1657
105. Lu YX, Zou JW, Yu QS, Jiang YJ, Zhao WN (2007) Ab initio investigation of halogen bonding interactions involving fluorine as an electron acceptor. *Chem Phys Lett* 449:6–10
106. Raghavendra B, Arunan E (2007) Unpaired and σ bond electrons as H, Cl, and Li bond acceptors: an anomalous one-electron blue-shifting chlorine bond. *J Phys Chem A* 111: 9699–9706
107. Karan NK, Arunan E (2004) Chlorine bond distances in ClF and Cl_2 complexes. *J Mol Struct* 688:203–205
108. Rosokha SV, Neretin IS, Rosokha TY, Hecht J, Kochi JK (2006) Charge-transfer character of halogen bonding: molecular structures and electronic spectroscopy of carbon tetrabromide and bromoform complexes with organic σ - and π -donors. *Heteroatom Chem* 17:449–459
109. Imakubo T, Tajima N, Tamura M, Kato R, Nishio Y, Kajita K (2003) Crystal design of organic conductors using the iodine bond. *Synth Met* 135–136:601–602
110. Laurence C, Graton J, Berthelot M, El Ghomari MJ (2011) The diiodine basicity scale: toward a general halogen-bond basicity scale. *Chem Eur J* 17:10431–10444

σ -Hole Bonding: A Physical Interpretation

Peter Politzer, Jane S. Murray, and Timothy Clark

Abstract The anisotropic electronic densities of covalently-bonded Group IV–VII atoms frequently give rise to regions of positive electrostatic potential on the extensions of covalent bonds to these atoms. Through such positive “ σ -holes,” the atoms can interact attractively and highly directionally with negative sites such as the lone pairs of Lewis bases, anions, π electrons, etc. In the case of Group VII this is called “halogen bonding.” Hydrogen bonding can be viewed as a less directional subset of σ -hole interactions. Since positive σ -holes often exist in conjunction with regions of negative potential, the atoms can also interact favorably with positive sites. In accordance with the Hellmann–Feynman theorem, all of these interactions are purely Coulombic in nature (which encompasses polarization and dispersion). The strength of σ -hole bonding increases with the magnitudes of the potentials of the positive σ -hole and the negative site; their polarizabilities must sometimes also be taken explicitly into account.

Keywords Coulombic interactions · Halogen bonding · σ -Hole bonding

P. Politzer (✉) and J.S. Murray
Department of Chemistry, University of New Orleans, New Orleans, LA 70148, USA
CleveThcoComp, 1951 W. 26th Street, Cleveland, OH 44113, USA
e-mail: ppolitze@uno.edu

T. Clark
Computer-Chemie-Centrum, Department Chemie und Pharmazie, Friedrich-Alexander-Universität Erlangen-Nürnberg, Nögelsbachstrasse 25, 91052 Erlangen, Germany
Centre for Molecular Design, University of Portsmouth, King Henry Building, King Henry I Street, Portsmouth PO1 2DY, UK

Contents

1	Newton, the Hellmann–Feynman Theorem and Coulomb’s Law	20
2	The σ -Hole: Halogens	22
3	σ -Holes: Groups IV–VI	25
4	σ -Hole Interactions	28
5	The Nature of σ -Hole Interactions	31
6	Hydrogen Bonding	34
7	Thermodynamic Stability	36
8	“Anomalously” Strong Interactions	36
9	William of Occam, Einstein, and Newton	37
	References	38

1 Newton, the Hellmann–Feynman Theorem and Coulomb’s Law

The formation of chemical bonds, wherever they may fall in the continuum between covalent and non-covalent, involves a balancing of attractive and repulsive forces within the system. At equilibrium, according to Newton, the resultant force on each nucleus must be zero (within the Born–Oppenheimer approximation of treating the nuclei as fixed, with the electrons moving among them [1, 2]). What are the natures of the forces felt by the nuclei?

The Hellmann–Feynman theorem [3, 4] tells us that these forces are given rigorously by purely classical electrostatics – the Coulombic repulsion of the other nuclei and the Coulombic attraction of the electrons. As Levine put it [5]: “The fact that the effective forces on the nuclei are electrostatic affirms that there are no ‘mysterious quantum-mechanical forces’ acting in molecules.” All that is required are the positions of the nuclei, the electronic density distribution $\rho(\mathbf{r})$, and Coulomb’s Law – a distressingly simple conclusion. It provoked some objections [6], but these were refuted [7] and the theorem is alive and well.

However, what about such hallowed quantum-mechanical concepts as exchange, antisymmetry, correlation, Pauli repulsion, etc.? These are important, but their role is in obtaining the electronic density of the system computationally. Once it is available, along with the nuclear positions, only Coulomb’s Law is needed. (For further discussion of this, see Berlin [7] and Bader [8].) The Hellmann–Feynman theorem can in fact be regarded as a forerunner to Hohenberg and Kohn showing that the electronic density is the fundamental determinant of the properties of a system of nuclei and electrons [9].

Coulomb’s law states that the force \mathbf{F} between two point charges Q_a and Q_b separated by a distance R is given by

$$\mathbf{F}(R) = k \frac{Q_a Q_b}{R^2}, \quad (1)$$

where k is a constant. The energy $\Delta E(R)$ of the interaction between Q_a and Q_b can be obtained by integrating $\mathbf{F}(R)$ from infinite separation to R :

$$\Delta E(R) = \int_{R=\infty}^R \mathbf{F}(R) \cdot d\mathbf{R} = \int_{R=\infty}^R k \frac{Q_a Q_b}{R^2} \cos\theta dR, \quad (2)$$

where θ is the angle between the vector \mathbf{F} and the vector \mathbf{R} representing the path of Q_b . If Q_a and Q_b have the same sign, then \mathbf{F} is repulsive and opposite in direction to \mathbf{R} ; thus $\theta = 180^\circ$. If Q_a and Q_b have different signs, then \mathbf{F} is attractive and in the same direction as \mathbf{R} ; $\theta = 0^\circ$. Either way,

$$\Delta E(R) = k \frac{Q_a Q_b}{R}, \quad (3)$$

where $\Delta E(R) > 0$ when Q_a and Q_b have the same sign, and $\Delta E(R) < 0$ when they have opposite signs.

A point charge Q_a creates both an “electric field” $\boldsymbol{\varepsilon}(R)$ and an “electrical potential” $V(R)$ in the surrounding space:

$$\boldsymbol{\varepsilon}(R) = k \frac{Q_a}{R^2}, \quad (4)$$

$$V(R) = k \frac{Q_a}{R}. \quad (5)$$

Their significance is that another point charge Q placed at a distance R from Q_a feels a force $\mathbf{F}(R) = Q\boldsymbol{\varepsilon}(R)$ and the interaction energy with Q_a is $\Delta E(R) = QV(R)$. Both \mathbf{F} and $\boldsymbol{\varepsilon}$ are vectors.

In extending Coulomb’s Law to molecules, complexes, etc., the nuclei and electrons can normally be viewed as point charges. The electrical potential $V(\mathbf{r})$ which they create at any point \mathbf{r} can therefore be obtained, in principle, by summing (5) over all of the nuclei and electrons. However, the electrons, unlike the nuclei, cannot be treated as having fixed positions; accordingly, instead of summing (5) over the electrons, it is necessary to integrate over the electronic density $\rho(\mathbf{r})$:

$$V(\mathbf{r}) = \sum_A \frac{Z_A}{|\mathbf{R}_A - \mathbf{r}|} - \int \frac{\rho(\mathbf{r}') d\mathbf{r}'}{|\mathbf{r}' - \mathbf{r}|}. \quad (6)$$

In (6), Z_A is the charge on nucleus A, located at \mathbf{R}_A . The denominators are the distances from each nucleus A and each unit of electronic charge $\rho(\mathbf{r}') d\mathbf{r}'$ from the point of interest \mathbf{r} . Equation (6) is written in atomic units (au), in which the Coulomb’s Law constant k and the charge on an electron or proton are equal to one. A potential $V(\mathbf{r})$ of 1 au is equivalent to 27.21 V (a more common unit for potential).

We emphasize that $V(\mathbf{r})$ is a real property of a system, a physical observable. It can be determined both experimentally, by diffraction methods [10–12], and computationally. The sign of $V(\mathbf{r})$ in any region depends upon whether the positive contribution of the nuclei or the negative contribution of the electrons is dominant there. In the absence of any perturbing effect, $\rho(\mathbf{r})$ is static and $V(\mathbf{r})$ is then commonly known as the “electrostatic” potential.

If a point charge Q is placed at \mathbf{r} , then its interaction energy with the system is, by extension of the earlier discussion, $\Delta E(\mathbf{r}) = QV(\mathbf{r})$. When Q and $V(\mathbf{r})$ are of the same sign, then the interaction is repulsive, $\Delta E(\mathbf{r}) > 0$; when they are of different signs, it is attractive, $\Delta E(\mathbf{r}) < 0$. It is important to recognize, however, that the electric field of Q perturbs (i.e., polarizes) the electronic density of the system and the $V(\mathbf{r})$ appropriate for calculating $\Delta E(\mathbf{r})$ is not the same as $V(\mathbf{r})$ in the absence of Q .

(Traditionally, molecular electrostatic potentials have often been expressed in energy units, e.g., kcal/mol. When this is done, the stated value of $V(\mathbf{r})$ actually corresponds to the interaction energy of the molecule with a positive point charge at the position \mathbf{r} . However, this is misleading because the electric field of the positive point charge would perturb the electronic density of the system and hence change $V(\mathbf{r})$ from what it is for the isolated molecule, for which it was computed. To avoid this unfortunate confusion, we give $V(\mathbf{r})$ in units of potential, i.e., volts (V).)

The electrostatic potential is a property of fundamental significance [13–15], as well as being very useful in interpreting and predicting non-covalent interactions [13, 15, 16]; regions of positive $V(\mathbf{r})$ on one molecule are attracted to regions of negative $V(\mathbf{r})$ on another. For such purposes, $V(\mathbf{r})$ is frequently computed on the surface of the molecule, which is taken to be defined by the 0.001 au (electrons/bohr³) contour of its $\rho(\mathbf{r})$, as suggested by Bader et al. [17]. This surface encompasses approximately 97% of the electronic charge, and has the important feature of being specific to the particular molecule, reflecting lone pairs, π electrons, strained bonds, atomic anisotropies, etc. The electrostatic potential on the surface is labeled $V_S(\mathbf{r})$. Its locally most positive and most negative values are designated by $V_{S,\max}$ and $V_{S,\min}$, respectively, and there may be several of each.

2 The σ -Hole: Halogens

Consider a free halogen atom. Its electronic density distribution is, on average, spherically symmetrical [18] and the electrostatic potential $V(\mathbf{r})$ created by its nucleus and electrons is positive for all $r < \infty$ [19]; the positive contribution of the nucleus, which is usually treated as a point charge, outweighs the negative contribution of the dispersed electrons. When the atom participates in forming a covalent bond, however, its electronic density undergoes a redistribution which causes it to become anisotropic [20–25], less on the outer side of the atom (i.e., along the extension of the bond) than on the lateral sides. This can be seen, for instance, for the chlorine in Cl-OH in Fig. 1. The term “polar flattening” has

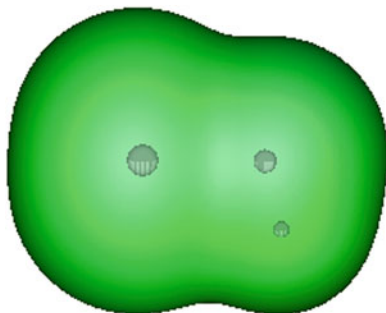


Fig. 1 Calculated 0.001-au molecular surface of ClOH. The positions of the nuclei are shown by *light circles*; chlorine is on the *left*. Distance from chlorine nucleus to surface along extension of O–Cl bond is 1.85 Å; distance from chlorine nucleus to lateral surface is 2.10 Å. Computational level: M06-2X/aug-cc-pVTZ

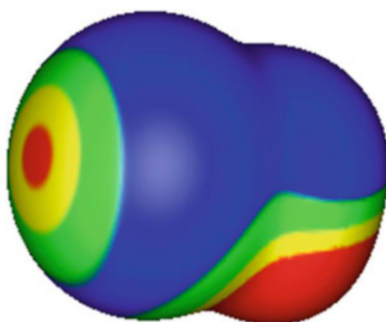


Fig. 2 Calculated electrostatic potential on the 0.001-au molecular surface of ClOH. Chlorine is on the *left*. Color ranges, in volts: *red*, greater than 0.87; *yellow*, from 0.87 to 0.43; *green*, from 0.43 to 0; *blue*, less than 0 (negative). The most positive potential on the chlorine surface (*red*) has a $V_{S,\max}$ of 0.99 V, and corresponds to a σ -hole on the extension of the O–Cl bond. Note also the positive region associated with the hydrogen (*lower right*); the $V_{S,\max}$ is 2.51 V. Computational level: M06-2X/aug-cc-pVTZ

sometimes been used to describe this. The outer region of diminished electronic density has been labeled a “ σ -hole” [26].

This rearrangement of electronic density is, of course, reflected in the electrostatic potential $V_S(\mathbf{r})$ on the surface of the covalently-bonded halogen. What is often found is that $V_S(\mathbf{r})$ is positive in the σ -hole region, which has the lesser electronic density, and is negative on the lateral sides, which have the greater electronic densities. This is shown in Fig. 2 for the chlorine in Cl–OH. The σ -hole corresponds to a local maximum in the molecular surface electrostatic potential, a $V_{S,\max}$. (It should be remembered that the σ -hole is a region in space, not simply a point.)

In general, the more polarizable the halogen atom and the more electron-attracting the remainder of the molecule, the more positive is the halogen σ -hole [27–30]. This is illustrated by the computed $V_{S,\max}$ in Table 1. For instance, the

Table 1 Most positive σ -hole potentials ($V_{S,max}$) and most negative potentials ($V_{S,min}$) on 0.001-au surfaces of indicated halogen atoms, in volts. Computational method: M06-2X/6-311G(d)

Molecule	Atom	Bond producing σ -hole	$V_{S,max}$	$V_{S,min}$	References
<i>Focus on general trends</i>					
H ₃ C-F	F	C-F	-1.07	-1.10	[31]
H ₃ C-Cl	Cl	C-Cl	-0.04	-0.68	[31]
H ₃ C-Br	Br	C-Br	0.25	-0.65	[31]
H ₃ C-I	I	C-I	0.56	-0.56	[31]
F ₃ C-F	F	C-F	-0.06	-0.12	[31]
F ₃ C-Cl	Cl	C-Cl	0.86	-0.03	[31]
F ₃ C-Br	Br	C-Br	1.10	-0.09	[31]
F ₃ C-I	I	C-I	1.38	-0.08	[31]
NC-F	F	C-F	0.56	0.47	Present work
NC-Cl	Cl	C-Cl	1.56	0.45	Present work
NC-Br	Br	C-Br	1.85	0.37	Present work
NC-I	I	C-I	2.11	0.31	Present work
<i>Dihalogens</i>					
F-F	F	F-F	0.49	-0.11	Present work
Cl-Cl	Cl	Cl-Cl	1.11	-0.12	[30]
Br-Br	Br	Br-Br	1.26	-0.18	[30]
<i>Focus on bromine</i>					
H ₃ Ge-Br	Br	Ge-Br	-0.07	-0.58	[31]
H ₃ Si-Br	Br	Si-Br	0.02	-0.51	[31]
H ₂ P-Br	Br	P-Br	0.15	-0.62	[30]
H ₃ C-Br	Br	C-Br	0.25	-0.65	[31]
F ₂ P-Br	Br	P-Br	0.42	-0.33	[30]
HS-Br	Br	S-Br	0.75	-0.42	[30]
H ₂ N-Br	Br	N-Br	0.77	-0.35	[30]
F ₃ Si-Br	Br	Si-Br	0.79	0.09	[31]
FS-Br	Br	S-Br	0.98	-0.20	[30]
Br ₂ C=CBr ₂	Br	C-Br	1.05	-0.25	Present work
F ₃ C-Br	Br	C-Br	1.10	-0.09	[31]
Br-Br	Br	Br-Br	1.26	-0.18	[30]
Br-C≡C-Br	Br	C-Br	1.31	-0.09	Present work
HO-Br	Br	O-Br	1.42	-0.46	[30]
F ₂ N-Br	Br	N-Br	1.48	-0.07	[30]
Cl-Br	Br	Cl-Br	1.54	-0.10	[30]
FO-Br	Br	O-Br	1.99	-0.02	[30]
F-Br	Br	F-Br	2.31	-0.004	[30]

$V_{S,max}$ of iodine is greater in H₃C-I than that of bromine in H₃C-Br but it is less than that of iodine in NC-I. Table 1 also gives the value of the most negative surface potential, $V_{S,min}$, on the portion of the surface attributable to the indicated halogen atom.

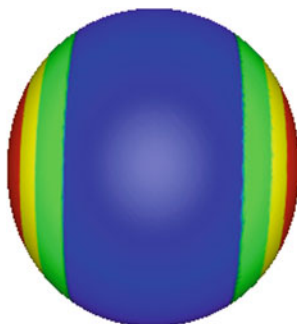


Fig. 3 Calculated electrostatic potential on the 0.001-au molecular surface of a chlorine atom in the $s^2p_x^2p_y^2p_z^1$ valence state configuration. Color ranges, in volts: *red*, greater than 0.43; *yellow*, from 0.43 to 0.22; *green*, from 0.22 to 0; *blue*, less than 0 (negative). The most positive potentials on the chlorine surface, shown in *red* at *left* and *right*, have $V_{S,\max}$ of 0.95 V. Computational level: M06-2X/aug-cc-pVTZ

The less polarizable and more electronegative halogens, fluorine and chlorine, tend to have less positive σ -holes than the others. In fact, they are sometimes negative (although less so than their surroundings); see Table 1. On the other hand, a very strongly electron-attracting bonding partner can cause the potential $V_S(\mathbf{r})$ of the entire surface of the halogen to be positive (the σ -hole being still more so). This can be the case even for fluorine. In F-CN, for instance, the $V_S(\mathbf{r})$ of fluorine is entirely positive (Table 1), with the maximum being in the σ -hole [32]; the $V_{S,\min}$ of fluorine is also positive.

It is interesting that positive σ -holes can even be seen in a free halogen atom if it is in the asymmetric valence state configuration $s^2p_x^2p_y^2p_z^1$ which it has when participating in a covalent bond [26, 28, 33, 34]. The half-filled p_z orbital is the one that is directly involved in the bonding and, in Fig. 3, positive σ -holes are clearly visible in both the $+z$ and $-z$ directions for the valence state of chlorine. In contrast, there is an equatorial ring of negative potential caused by the doubly-occupied p_x and p_y orbitals.

3 σ -Holes: Groups IV–VI

σ -Holes are not limited to halogens. This has been demonstrated for covalently-bonded atoms of Group VI [35], Group V [36], and Group IV [37]. This is again caused by the anisotropic charge distributions of the atoms [21, 25, 38, 39], which result in σ -holes on the extensions of single (and sometimes multiple) bonds to these atoms. Accordingly Group VI, V, and IV atoms can have two, three, and four σ -holes, respectively (or more if the atoms are hypervalent [37, 40]). The electrostatic potentials of these σ -holes show the same trends as for the halogens: within a

given Group, the σ -hole $V_{S,max}$ becomes more positive in going from the lighter to the heavier (more polarizable) atoms and as the bonding partner is more electron-attracting. The latter factor means that the σ -holes on a given atom may have different $V_{S,max}$, depending upon the partners in the covalent bonds; see Figs. 4, 5, and 6. For a more general discussion of factors affecting σ -hole potentials, see Murray et al. [30].

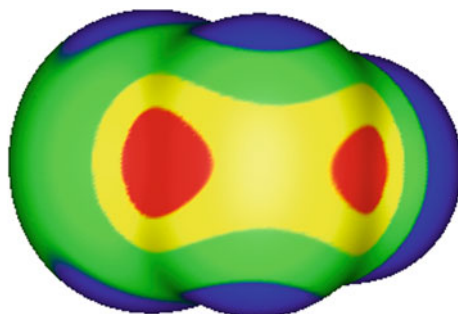


Fig. 4 Calculated electrostatic potential on the 0.001-au molecular surface of BrSF. Sulfur is *in the middle facing the viewer*, bromine is *on the left* and fluorine is *on the right*. Color ranges, in volts: *red*, greater than 0.87; *yellow*, from 0.87 to 0.43; *green*, from 0.43 to 0; *blue*, less than 0 (negative). The most positive potentials on the sulfur surface, shown in *red*, have $V_{S,max}$ of 1.31 V (*left*) and 1.10 V (*right*). These correspond to σ -holes on the extensions of the F–S and Br–S bonds, respectively. Computational level: M06-2X/aug-cc-pVTZ

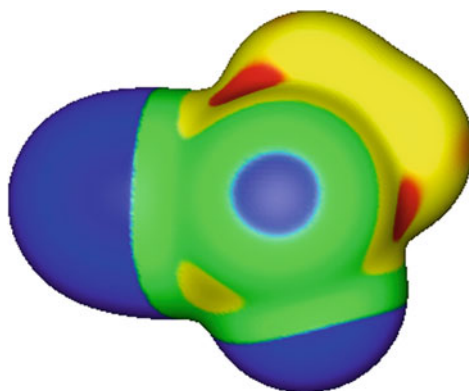


Fig. 5 Calculated electrostatic potential on the 0.001-au molecular surface of PF(CH₃)(CN). Phosphorus is *in the middle facing the viewer*, the cyano group is *on the left*, the methyl group is *at the top right*, and fluorine is *at the bottom right*. Color ranges, in volts: *red*, greater than 1.26; *yellow*, from 1.26 to 0.65; *green*, from 0.65 to 0; *blue*, less than 0 (negative). The most positive potentials on the phosphorus surface, shown in *red* or *yellow*, have $V_{S,max}$ of 1.52 V (*top*), 1.41 V (*right*), and 0.95 V (*bottom left*). These correspond to σ -holes on the extensions of the F–P, NC–P and H₃C–P bonds, respectively. Note that the phosphorus has a negative region facing the viewer. Computational level: M06-2X/aug-cc-pVTZ

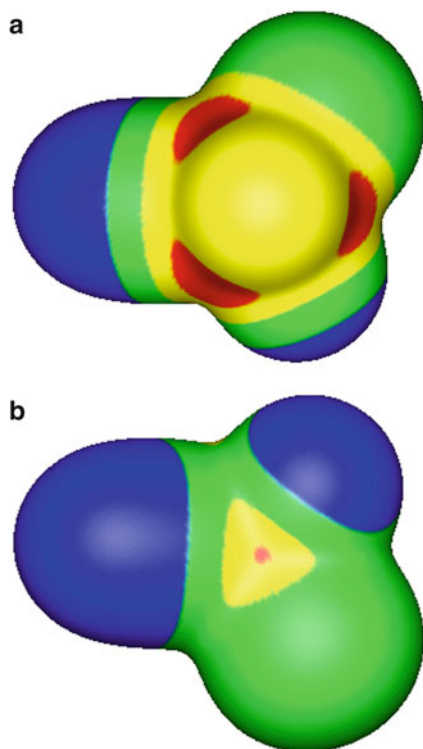


Fig. 6 Calculated electrostatic potential on the 0.001-au molecular surface of HSiF(Cl)(CN). Color ranges, in volts: *red*, greater than 1.26; *yellow*, from 1.26 to 0.65; *green*, from 0.65 to 0; *blue*, less than 0 (negative). Two views are shown: In (a), hydrogen is in the middle facing the viewer, the cyano group is *on the left*, chlorine is *at the top right* and fluorine is *at the bottom right*. The most positive potentials on the silicon surface, shown in *red*, have $V_{S,\max}$ of 1.76 V (*right*), 1.90 V (*bottom left*), and 1.77 V (*top left*). There correspond to σ -holes on the extensions of the NC–Si, Cl–Si and F–Si bonds, respectively. In (b), silicon is *in the middle*, the cyano group is *on the left*, the chlorine is *at the bottom right*, and fluorine is *at the top right*. The most positive potential on the silicon surface, shown in *red*, has $V_{S,\max} = 1.31$ V. It is on the extension of the H–Si bond. Computational level: M06-2X/aug-cc-pVTZ

As with the halogens, positive σ -holes on Group V and VI atoms (but not Group IV) are often found in conjunction with regions of negative potential. This is evident in Figs. 4 and 5 and in Table 2, which lists the σ -hole $V_{S,\max}$ and the $V_{S,\min}$ of various covalently-bonded Group IV–VI atoms. For the first-row members of each Group, which are the least polarizable and most electronegative, the $V_{S,\max}$ are often negative, just as for fluorine. At the other extreme, the surface potential of the Group V or Group VI atom may be completely positive if the atom is bonded to highly electron-withdrawing partners, e.g., in AsF₂Br (Table 2); however the σ -holes are still local maxima. With tetravalent Group IV atoms, our experience has been that their $V_S(\mathbf{r})$ are always entirely positive, regardless of the bonding partners (Fig. 6), with four σ -holes as local maxima.

Table 2 Most positive σ -hole potentials ($V_{S,max}$) and most negative potentials ($V_{S,min}$) on 0.001-au surfaces of indicated atoms from Groups IV–VI, in volts. (The Group IV atoms have no local minima.) Computational method: M06-2X/6-311G(d)

Molecule	Atom	Bond producing σ -hole	$V_{S,max}$	$V_{S,min}$	References
FOBr	O	F–O	0.46	–0.51	Present work
	O	Br–O	–0.15	–0.51	Present work
FSBr	S	F–S	1.56	–0.17	Present work
	S	Br–S	1.18	–0.17	Present work
FSeBr	Se	F–Se	1.89	–0.22	Present work
	Se	Br–Se	1.52	–0.22	Present work
F ₂ NBr	N	F–N	0.57	–0.40	Present work
	N	Br–N	0.52	–0.40	Present work
F ₂ PBr	P	F–P	1.40	0.49	Present work
	P	Br–P	1.53	0.49	Present work
F ₂ AsBr	As	F–As	1.72	0.91	Present work
	As	Br–As	1.67	0.91	Present work
F ₃ CBr	C	F–C	0.69	–	[31]
	C	Br–C	0.94	–	[31]
F ₃ SiBr	Si	F–Si	1.76	–	[31]
	Si	Br–Si	2.06	–	[31]
F ₃ GeBr	Ge	F–Ge	1.96	–	[31]
	Ge	Br–Ge	1.93	–	[31]

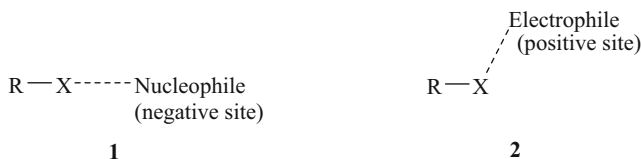
4 σ -Hole Interactions

The existence of positive σ -holes on many covalently-bonded atoms suggests that these can give rise to attractive non-covalent interactions, both inter- and intramolecular, with negative sites such as the lone pairs of Lewis bases, π electrons, anions, etc. Because of the focused nature of the positive region, the σ -hole, these interactions should be highly directional, approximately along the extensions of the covalent bonds giving rise to the σ -holes. They should also be stronger as the σ -hole is more positive. Interactions of this sort have in fact been known experimentally for Groups IV–VII for decades, as summarized elsewhere [28, 29, 41]. However, these were not described as σ -hole interactions until 2007 [26, 32, 35–37].

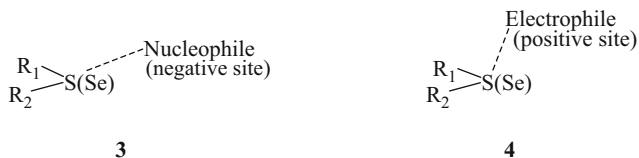
When Group VII is involved, this has been labeled “halogen bonding,” and it was often viewed as puzzling that a covalently-bonded halogen – normally presumed to be negative in character – would be attracted to a negative site. Much of the evidence for this involved crystallographic observations of close contacts in organic halides and in complexes between halides and oxygen/nitrogen Lewis bases. A series of the latter studies, particularly by Hassel et al., was reviewed by Bent in 1968 [42].

Especially significant were surveys of organic halide crystal structures in the Cambridge Structural Database by Murray-Rust et al. [43–45]. They found numerous halogen close contacts, which were highly directional. For a halogen X in a

molecule R–X, close contacts with nucleophilic components of other molecules (negative sites) were approximately linear, along the extension of the R–X bond (**1**), while close contacts with electrophilic components (positive sites) involved the lateral sides of the halogen (**2**).



At roughly the same time, analogous findings were reported by Parthasarathy et al. for sulfides and selenides [38, 39, 46]. For compounds $R_1R_2S(\text{Se})$, crystallographic surveys showed that close contacts with nucleophilic (negative) sites were along the extensions of the $R_1-S(\text{Se})$ and/or $R_2-S(\text{Se})$ bonds (**3**), and those with electrophilic (positive) sites were above or below the $R_1-S(\text{Se})-R_2$ plane (**4**).



It is clear that the close contacts with nucleophiles, **1** and **3**, can readily be explained as positive σ -holes interacting with negative sites, while **2** and **4** involve the negative lateral sides of the halogen, sulfur, or selenium (Figs. 1 and 4). This was first pointed out by Brinck et al. for halogen bonding [47, 48] and by Burling and Goldstein for S–O and Se–O close contacts [49]; Auffinger et al. [50] and Awwadi et al. [23] subsequently offered similar interpretations of halogen bonding. However, none of these persons used the term “ σ -hole,” which was introduced later, in 2007 [26].

Numerous Group IV–VII non-covalent interactions which fit the characteristic directional criterion for σ -hole bonding have now been documented, both computationally and experimentally; several overviews are available [27–29, 41]. Some computational examples are presented in Table 3. The interactions are all approximately linear (i.e., along the extension of the covalent bond to the atom) and the separations between the atoms with the σ -holes and the negative sites are less than or similar to the sums of the respective van der Waals radii. The interaction energies ΔE were obtained via (7):

$$\Delta E = E(\text{A—B}) - [E(\text{A}) + E(\text{B})], \quad (7)$$

in which $E(\text{A—B})$ is the energy of the complex A–B and $E(\text{A})$ and $E(\text{B})$ are the energies of the isolated components.

Table 3 σ -Hole $V_{S,\max}$ for atoms shown in bold and interaction energies ΔE for some gas phase complexes with NH_3 and HCN .^a Computational methods: electrostatic potentials, M06-2X/6-311G(d); interaction energies, M06-2X/aug-cc-pVTZ

Complex	Bond producing σ -hole	σ -Hole $V_{S,\max}$ (volts)	ΔE (kcal/mol)	Separation ^b (Å)	Angle (deg)
F-F— NH_3	F-F	0.49	-1.5	2.59 (3.0)	179.9
F ₃ C-Cl— NH_3	C-Cl	0.86	-2.5	3.03 (3.3)	180.0
F ₃ C-Br— NH_3	C-Br	1.10	-3.7	3.07 (3.5)	179.9
BrC≡C-Br— NH_3	C-Br	1.31	-4.2	2.99 (3.5)	179.8
H ₂ FP— NH_3	F-P	1.68	-7.2	2.71 (3.4)	166.5
H ₂ FAs— NH_3	F-As	1.93	-8.7	2.73 (3.5)	165.0
F-Cl— NH_3	F-Cl	1.98	-10.3	2.59 (3.3)	179.9
F ₃ C-Cl—NCH	C-Cl	0.86	-1.6	3.13 (3.3)	179.1
BrC≡C-Br—NCH	C-Br	1.31	-2.7	3.05 (3.5)	180.0
Cl ₂ Se—NCH	Cl-Se	1.57	-4.0	2.92 (3.5)	176.1
H ₂ FP—NCH	F-P	1.68	-4.7	2.81 (3.4)	164.0
H ₃ FGe—NCH	F-Ge	1.87	-4.9	2.89 (-)	179.8
F-Br—NCH	F-Br	2.31	-7.1	2.60 (3.5)	180.0

^aComputed $V_{S,\max}$ and ΔE were reported in [29]

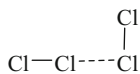
^bValues in parentheses are the sums of the van der Waals radii of the σ -hole-containing atom and nitrogen [108, 109]. No van der Waals radius was found for germanium

For a given negative site, ΔE has been found to correlate reasonably well with the $V_{S,\max}$ of the σ -hole [28, 29, 31, 51, 52]; ΔE becomes more negative (stronger interaction) as $V_{S,\max}$ is more positive. When the ΔE correspond to two or more different negative sites, as in Table 3, then their $V_{S,\min}$ must be taken into account. One way of doing this is by plotting ΔE against the product of $V_{S,\max}$ (σ -hole) and $V_{S,\min}$ (negative site). When this was done for a series of 20 complexes with NH_3 and HCN , including the 13 in Table 3, the R^2 was a very satisfactory 0.96 [29].

The first-row atoms of Groups IV–VII (carbon, nitrogen, oxygen, and fluorine) tend to have relatively weakly-positive or negative σ -holes, because of their lower polarizabilities and higher electronegativities compared to the other members of their groups. Attractive σ -hole interactions are therefore less common for these four atoms. Thus it was formerly thought that fluorine does not form halogen bonds. This has been disproved [32, 53, 54]. It was in fact shown some years ago that carbon [37], nitrogen [36], oxygen [35], and fluorine [32] can all have positive σ -holes if covalently bonded to strongly electron-attracting partners. From this it follows that they can indeed form σ -hole bonds, and this has been demonstrated computationally [31, 32, 35–37] and to some extent experimentally [41, 53, 54].

Since a positive σ -hole is frequently surrounded by a negative surface potential (except for Group IV), a given atom can interact favorably and directionally with both negative and positive sites, as is seen in the crystallographic close contacts discussed above, 1–4. It is even possible to have “like attracting like,” whereby the positive σ -hole on an atom in one molecule interacts with the negative potential on

the same atom in another identical molecule. This has been observed both computationally [25, 29, 55, 56] and experimentally [22, 38, 57, 58]. Examples are crystalline Cl_2 , **5** [22], and $\text{ClH}_2\text{P}-\text{PH}_2\text{Cl}$ [56]. (Note that “like attracting like” cannot happen with tetravalent Group IV atoms, which have entirely positive surface potentials.)



5

The fact that many atoms have surface regions of both positive and negative potentials, and can interact through either or both, demonstrates anew the fallacy of trying to assign a point positive or negative charge to an atom in a molecule (i.e., an atomic monopole). While numerous different procedures for doing so have been invented [59] (including one by an author of this paper [60], a youthful folly), there is no rigorous basis for doing so, and the results are likely to be physically misleading, as shown by Figs. 2, 4, 5, and 6, and Tables 1 and 2. For example, traditional atomic charges cannot in general account for or predict halogen bonding and other σ -hole interactions. In this respect, as has been pointed out [50, 55], force fields that assign single charges to atoms in molecules are inadequate; recognition of this has led to efforts to make them more realistic [61–65].

5 The Nature of σ -Hole Interactions

The interaction energy ΔE of a σ -hole-bonded complex A—B can be determined by (7). ΔE is a real physical property, an observable which can be obtained experimentally. It tells us how much energy is released when the complex is formed, or alternatively, the negative of ΔE tells us how much energy is required to break the A—B bond and separate A and B, i.e., the binding energy.

Unfortunately, it has become quite popular in recent years to dissect ΔE into various components. This is viewed as a means of better “understanding” the interaction; the fact that the process is physically meaningless is not taken to be a deterrent. The assumed components are usually some subset of a group which includes electrostatics, dispersion, polarization, charge transfer, exchange repulsion (which Bader called an oxymoron [8]), induction, orbital interaction, Pauli repulsion, exchange, distortion, etc. While each of these can be claimed to have some conceptual significance, they are not observables, are not uniquely defined, and are not independent of each other.

There is no physically rigorous or “correct” way to make such a dissection of ΔE , which has the advantage that everyone can feel free to invent their own scheme (a situation akin to that of atomic charges) and their own set of assumed components. A recent summary by Mo et al. [66] lists at least 16 different procedures

which have been proposed, and they invoke different subsets of the group of supposed components listed above. They can be quite contradictory, as exemplified by two separate dissections of the interaction energies of the complexes $\text{H}_3\text{C-X-OCH}_2$ and $\text{F}_3\text{C-X-OCH}_2$. By one procedure, the primary stabilizing components were found to be electrostatics and dispersion [67]. The other energy dissection scheme concluded, *for the same complexes*, that charge transfer and polarization are dominant and that electrostatics contributes only “slightly” [68]. (So what causes the polarization?)

The Hellmann–Feynman theorem tells us that the forces acting within the complex A—B are purely Coulombic attractions and repulsions involving the nuclei and electrons, and can be determined exactly from the electronic density and the positions of the nuclei [3, 4]. How do we reconcile this rigorous statement with the various interaction components commonly invoked in different analyses of non-covalent bonding, even if we resist the urge to try to quantify them?

The answer to this lies in the fact that the Hellmann–Feynman theorem refers to the actual electronic density of the system; this is what is to be used in evaluating the Coulombic interactions of the electrons. In energy dissection schemes, on the other hand, the electrostatic term pertains to an imaginary situation: A and B being at the separation that they have in the complex but with the unperturbed charge distributions that they would have at infinite separation. Accordingly, the electrostatic component of the interaction energy is typically computed without including the polarizing effects that A and B have upon each other and that perturb their electronic densities and hence their electrostatic interactions. Polarization is treated as another component, separate from the electrostatic, which is completely unrealistic.

Polarization is an intrinsic part of any Coulombic interaction (unless only point charges are involved) [25, 28, 29, 69, 70]; it cannot be viewed separately. The electric fields of the participants polarize each other’s charge distributions. Consider the formation of a σ -hole complex A—B in which the positive σ -hole is on A and the negative site on B. Then the shifting (polarization) of the electronic densities of A and B are as shown in **6**.



The importance of polarization is confirmed by plots showing the difference between the computed electronic density of a σ -hole complex A—B and that of the imaginary unperturbed system mentioned above: free A and free B placed at the same separation as in the complex [25, 69, 71, 72]. Such plots all show the qualitative features depicted in **6**: the electric field of the negative site on B polarizes the electronic density near the σ -hole of A away from B, while the electric field of the σ -hole polarizes the electronic charge of B toward A.

The polarization shown in **6** helps to interpret the “cooperativity” sometimes observed in systems involving more than one non-covalent interaction [32, 71, 73, 74]. For example, ΔE for the formation of NC-Br-NC-Br-NC-Br has more than

twice the magnitude of that for NC-Br—NC-Br [32], because each NC-Br—NC-Br interaction in the trimer strengthens either the σ -hole or the negative site for the other.

Polarization also nicely explains the changes that σ -hole interactions produce in the stretching frequencies of the covalent bonds to the atoms having the σ -holes (i.e., the bonds that give rise to them). In some complexes these frequencies increase (blue shifts) but more often they decrease (red shifts) [75, 76]. These observations have frequently been rationalized in terms of “charge transfer” from orbitals on the negative sites B to various orbitals on the σ -hole molecules A. However it has been demonstrated [75, 76] that both blue and red shifts can be explained and predicted, using the formalisms of Hermansson [77] or Qian and Krimm [78], from the electric field produced by B and the permanent and induced dipole moments of A. No orbital factors need be invoked.

Dispersion is an intrinsic part of the Coulombic interaction in a complex A—B, as is polarization. Dispersion is commonly considered to be associated with electronic correlation [79–81], i.e., the instantaneous correlated movements of the electrons in response to their mutual Coulombic repulsions. These movements create temporary dipoles which interact attractively, accounting for the stabilizing contribution of dispersion.

Feynman proposed a different (often overlooked) interpretation of dispersion [4], involving nuclear-electronic rather than dipole interactions. Support for his conjecture was reported by Hirschfelder and Eliason [82], and a proof was offered by Hunt [83].

Either explanation is consistent with the Hellmann–Feynman theorem: The forces acting within the complex are purely Coulombic and can be determined from the electronic density and the nuclear positions. What the energy dissection procedures view as three separate components of ΔE – electrostatics, polarization, and dispersion – are really just one, the Coulombic, which rigorously encompasses all the forces within the complex.

The electronic density and the nuclear positions can in principle be obtained either experimentally or computationally. It is in doing the latter that factors such as antisymmetry, exchange, Pauli repulsion, etc., enter the picture, as consequences of the mathematical model being used. However, the distinction between physical reality and a mathematical model should always be kept in mind.

An example of a frequent failure to do this relates to the notion of charge transfer. This is often invoked in regard to non-covalent bonding, although without explaining how, physically, this is stabilizing. (On the other hand, some energy dissection schemes do not even include it in their subsets of components.) Charge-transfer formalism was introduced by Mulliken to describe the electronic transition from the ground state of a complex to an excited state, which is largely dative [84]; his focus was upon this transition, not upon the physical nature of the bonding in the ground state. The idea that a σ -hole interaction involves some small fraction of an electron being transferred from the negative site on B into an orbital on the molecule A having the positive σ -hole is purely mathematical modeling, not physical reality. Orbitals are not real, they are mathematical expressions which

are useful in constructing wave functions [85]; electrons cannot be sliced up into fragments. The overlap of an occupied orbital of the “donor” with an unoccupied orbital of the “acceptor” is simply one mathematical technique (not the only one) for describing the physical event, which is the mutual polarization of A and B, as in **6**.

This point can be illustrated by considering another perfectly valid mathematical approach, discussed by Stone and Misquitta [86]. Quite a satisfactory quantum chemical representation of the complex A—B could be obtained using only orbitals of either A or B, provided that enough of them were used. The polarization depicted in **6** would be adequately described. However, the charge transfer, as evaluated by any orbital-based method, would necessarily be zero, since one of the participants was not assigned any orbitals! It is indeed increasingly becoming recognized that the distinction between polarization and charge transfer is an artificial one [87–90].

6 Hydrogen Bonding

There is an obvious structural similarity between hydrogen bonding, R—H—B, and halogen bonding, R—X—B, in that both involve a univalent covalently-bonded atom interacting with a negative site. For a given R and B, hydrogen bonding is generally the stronger if X=F or Cl, but they are comparable when X=Br and halogen bonding is often the stronger when X=I [91–93]. Halogen bonding dominating over hydrogen bonding has been observed experimentally, for instance in solution studies [94] and in co-crystallization [95].

In recent years, hydrogen bonding has fallen victim to intense theoretical scrutiny, and so one can now find references to classical and nonclassical hydrogen bonding, proper and improper, blue shifted and red shifted, dihydrogen bonding, anti-hydrogen bonding, H— σ and H— π hydrogen bonding, positive and negative charge-assisted hydrogen bonding, resonance-assisted and polarization-assisted hydrogen bonding, etc. However, all of these fit the same basic pattern: a Coulombic interaction involving a region of positive electrostatic potential on the hydrogen and a negative site.

It is in fact justifiable to view hydrogen bonding as a subset of σ -hole interactions [25, 28, 33, 34]. Since a hydrogen atom has only one valence electron, and that is participating in the R—H bond, it can be anticipated that the outer portion of the hydrogen has a positive potential with its maximum along the extension of the R—H bond (a σ -hole). Because of the absence of any other valence electrons on the hydrogen, its lateral sides also have relatively low electronic densities and therefore the positive σ -hole potential extends farther back toward the bonding partner than is typical of Group V–VII atoms. Hydrogen σ -holes are more hemispherical and less narrowly focused. These features are clearly apparent in Fig. 2 and especially in Fig. 7, and can also be seen in earlier reports [27, 28, 33, 81]. They help to explain why hydrogen bonds tend overall to be less directional than other σ -hole interactions [33, 96, 97].

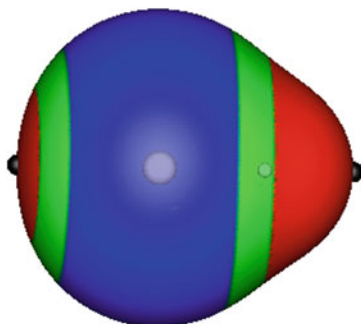
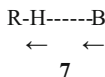


Fig. 7 Calculated electrostatic potential on the 0.001-au molecular surface of HI. The hydrogen is *on the right*. The positions of the nuclei are indicated by the *light circles*. Color ranges, in volts: *red*, greater than 0.43; *green*, between 0.43 and 0; *blue*, less than 0 (negative). The most positive values of the electrostatic potential, the $V_{S,max}$, are shown by *black hemispheres*; they are 1.26 V (hydrogen) and 0.91 V (iodine). Note that these surface maxima are along the extensions of the covalent bond. Computational level: M06-2X/6-311G(d)

Plots of electronic-density changes accompanying hydrogen bond formation show polarization as represented in 7 [98–100]. This is fully analogous to what is observed for other σ -hole interactions, discussed earlier and depicted in 6.



Both the minor differences in directionality and the fundamentally similar Coulombic natures of hydrogen bonding and halogen bonding in particular were brought out in a recent computational study [33]. This involved the halogen-bonded complexes of NC-Br and F₃C-Br with the two bases NH₃ and HCN, and the hydrogen-bonded complexes of NC-H and F₃C-H with the same two bases. For each complex, the interaction energy ΔE was computed as a function of the C-Br—N or C-H—N angle over the range 100°–180°. The most negative ΔE (strongest interactions) were for angles of 180°, since these involved the most positive potentials (the $V_{S,max}$) of the σ -holes of both the bromines and the hydrogens. ΔE was more negative for the hydrogen bonds than for the corresponding halogen bonds, reflecting the more positive potentials of the hydrogens compared to the bromines, and the NH₃ interactions were stronger than the HCN, caused by the nitrogen in the former having a more negative $V_{S,min}$.

The results showed the greater tendency of halogen bonding for linearity: the halogen bond ΔE rapidly became more negative as angles of 180° were approached, even in the NC-Br complexes, in which the bromine is completely positive (Table 1), whereas the hydrogen bond ΔE variation was more gradual. This demonstrates the role of the nonbonding valence electrons on the lateral sides of the halogen in focusing the interaction.

Particularly striking were plots of ΔE vs the positive potentials created by the four isolated R-Br and R-H molecules at the various distances and angles where the nitrogens of NH_3 and HCN were situated in the complexes; these were the potentials felt by the nitrogens in the complexes. Excellent linear correlations were obtained: $R^2 = 0.986$ for the NH_3 complexes and $R^2 = 0.990$ for the HCN. In each case, and for both $\text{R}=\text{NC}$ and $\text{R}=\text{F}_3\text{C}$, the hydrogen-bonded and the halogen-bonded complexes fit on the *same* correlation! All of this certainly strengthens the argument that these are basically similar Coulombic interactions.

7 Thermodynamic Stability

It is customary to use the energy change ΔE or the enthalpy change ΔH as a measure of the strength of the interaction in forming a complex A—B. The more negative are ΔE and ΔH , the more strongly bound is the complex.

From a thermodynamic standpoint, however, it is the free energy change ΔG that is important. Thermodynamic stability requires that ΔG be negative. Since at a fixed absolute temperature T ,

$$\Delta G = \Delta H - T\Delta S, \quad (8)$$

this introduces the entropy change ΔS as an additional factor. The formation of A—B diminishes the degrees of freedom of A and B, causing ΔS to be negative. Accordingly, even for an attractive interaction having $\Delta H < 0$, if $|T\Delta S| > |\Delta H|$, then $\Delta G > 0$ and the complex is thermodynamically unstable.

This is in fact the case for the formation of many σ -hole complexes in the gas phase at 298 K [29, 101, 102]. In solution or a solid phase, additional factors are involved which may make ΔG negative even when it is positive in the gas phase. However, it should be remembered that $\Delta G > 0$ does not completely preclude the formation of a complex; it simply means that the equilibrium constant for the process is less than one. (More extensive discussions of the thermodynamic stabilities of σ -hole complexes are given elsewhere [28, 29, 102].)

8 “Anomalously” Strong Interactions

There have sometimes been encountered, at least computationally, σ -hole complexes having properties suggesting unusually strong interactions – e.g., significantly more negative ΔE and shorter A—B separations than are commonly obtained. It might be inferred that the bonding in these systems differs in some fundamental manner from that in the weaker complexes; however, that is not the case. These “anomalously” strong interactions can be explained quite well in terms

of the usual suspects: the $V_{S,\max}$ of the σ -hole, the $V_{S,\min}$ of the negative site, and the polarizabilities of both.

For example, the computed ΔE of the complexes F-Cl—CN-Q and F-Cl—SiN-Q, where Q is an atom or group, range from -1.9 to -33.4 kcal/mol [103, 104]. This remarkably large variation must reflect the properties of the negative sites, since the σ -hole molecule is in all instances the same. Indeed, when the ΔE were expressed by double regression analysis as functions of the $V_{S,\min}$ and the local ionization energies of the CN-Q carbons and the SiN-Q silicons, the relationship between predicted and computed ΔE had $R^2 = 0.99$ [104]. (The local ionization energy was being used as a measure of polarizability [105].) The combination of a strong electric field produced by a large positive σ -hole $V_{S,\max}$ plus a highly polarizable negative site (as indicated by a low local ionization energy) can result in polarization to an extent which might be described (in less physical and more ambiguous terms) as a significant degree of dative sharing of electrons, or coordinate covalence. However, this is just terminology and does not imply a “transfer” of electronic charge or some other new factor; it is still a Coulombic interaction, but with a higher level of polarization. (An analogous explanation applies to “anomalously strong” π -hole interactions, in which the region of positive electrostatic potential is perpendicular to an atom in a planar portion of a molecular framework, e.g., the boron in BCl_3 and the sulfur in SO_2 [106]). For more detailed discussions, see Politzer et al. [29].

9 William of Occam, Einstein, and Newton

A great many non-covalent interactions of covalently-bonded atoms of Groups IV–VII, as well as hydrogen bonding, can be explained as Coulombic interactions (which encompasses polarization and dispersion) involving positive σ -holes and negative sites. We resist forlornly the current tendency to subject σ -hole bonding to the fate of compartmentalization which has befallen hydrogen bonding. Thus we do not separate σ -hole interactions on the basis of the atom having the σ -hole (i.e., chalcogen bonding, pnictogen bonding, tetrel bonding, carbon bonding, etc.) nor on the basis of the negative site (lone pair, anion, π electrons, etc.). They are all σ -hole interactions, and we believe that it is important to focus upon this fundamental unifying similarity rather than upon differences in detail. In the spirit of William of Occam: *Lex parsimoniae: Pluralitas non est ponenda sine necessitate* (plurality is not to be posited without necessity), Occam’s Razor.

We have tried to emphasize the importance of distinguishing between mathematical models and physical reality. This can be challenging, because mathematical models are often pleasingly elegant and complex, whereas physical reality may be distressingly simple and straightforward. Newton was aware of this failing on the part of Nature; he observed, “Nature is pleased with simplicity.” [107]. Einstein concurred: “Nature is the realization of the simplest conceivable mathematical ideas.” [107]. (To Newton and Einstein, “Nature” meant physical laws. Biological

“Nature” often finds seemingly unnecessarily complicated solutions to problems; evolution simply stops changing what works well enough.) Newton, Einstein, and William of Occam provide excellent guiding principles for those wishing to understand physical phenomena.

Acknowledgements This work was supported by the Deutsche Forschungsgemeinschaft as part of the Excellence Cluster “Engineering of Advanced Materials” and SFB953 “Synthetic Carbon Allotropes”.

References

1. Born M, Oppenheimer JR (1927) Zur Quantentheorie der Molekeln. *Ann Physik* 389:457–484
2. Born M, Huang K (1954) *Dynamical theory of crystal lattices*. Oxford University Press, New York
3. Hellmann H (1937) *Einführung in die Quantenchemie*. Franz Deuticke, Leipzig
4. Feynman RP (1939) Forces in molecules. *Phys Rev* 56:340–343
5. Levine IN (1970) *Quantum chemistry*. Volume I: quantum mechanics and molecular electronic structure. Allyn and Bacon, Boston, p 449
6. Coulson CA, Bell RP (1945) Kinetic energy, potential energy and force in molecule formation. *Trans Faraday Soc* 41:141–149
7. Berlin T (1951) Binding regions in diatomic molecules. *J Chem Phys* 19:208–213
8. Bader RFW (2006) Pauli repulsions exist only in the eye of the beholder. *Chem Eur J* 12:2896–2901
9. Hohenberg P, Kohn W (1964) Inhomogeneous electron gas. *Phys Rev* 136:B864–B871
10. Stewart RF (1979) On the mapping of electrostatic properties from Bragg diffraction data. *Chem Phys Lett* 65:335–342
11. Politzer P, Truhlar DG (eds) (1981) *Chemical applications of atomic and molecular electrostatic potentials*. Plenum, New York
12. Klein CL, Stevens ED (1988) Charge density studies of drug molecules. In: Liebman JF, Greenberg A (eds) *Structure and reactivity*. VCH, New York, Ch 2, pp 25–64
13. Politzer P, Murray JS (2002) The fundamental nature and role of the electrostatic potential in atoms and molecules. *Theor Chem Acc* 108:134–142
14. Ayers PW (2007) Using reactivity indicators instead of the electron density to describe Coulomb systems. *Chem Phys Lett* 438:148–152
15. Murray JS, Politzer P (2011) The electrostatic potential: an overview. *WIREs Comput Mol Sci* 1:153–163
16. Murray JS, Politzer P (1998) Statistical analysis of the molecular surface electrostatic potential: an approach to describing noncovalent interactions in condensed phases. *J Mol Struct (Theochem)* 425:107–114
17. Bader RFW, Carroll MT, Cheeseman JR, Chang C (1987) Properties of atoms in molecules: atomic volumes. *J Am Chem Soc* 109:7968–7979
18. Delgado-Barrio G, Prat RF (1975) Deformed Hartree–Fock solutions for atoms. III. Convergent iterative process and results for O^{-} . *Phys Rev A* 12:2288–2297
19. Sen KD, Politzer P (1989) Characteristic features of the electrostatic potentials of singly-negative monoatomic ions. *J Chem Phys* 90:4370–4372
20. Stevens ED (1979) Experimental electron density distribution of molecular chlorine. *Mol Phys* 37:27–45

21. Nyburg SC, Faerman CH (1985) A revision of van der Waals atomic radii for molecular crystals: N, O, F, S, Cl, Se, Br and I bonded to carbon. *Acta Cryst B* 41:274–279
22. Tsirelson VG, Zou PF, Tang T-H, Bader RFW (1995) Topological definition of crystal structure: determination of the bonded interactions in solid molecular chlorine. *Acta Cryst A* 51:143–153
23. Awwadi FF, Willett RD, Peterson KA, Twamley B (2006) The nature of halogen–halogen synthons: crystallographic and theoretical studies. *Chem Eur J* 12:8952–8960
24. Bilewicz E, Rybarczyk-Pirek AJ, Dubis AT, Grabowski SJ (2007) Halogen bonding in crystal structure of 1-methylpyrrol-2-yl trichloromethyl ketone. *J Mol Struct* 829:208–211
25. Politzer P, Riley KE, Bulat FA, Murray JS (2012) Perspectives on halogen bonding and other σ -hole interactions: *lex parsimoniae* (Occam's Razor). *Comput Theoret Chem* 998:2–8
26. Clark T, Hennemann M, Murray JS, Politzer P (2007) Halogen bonding: the σ -hole. *J Mol Model* 13:291–296
27. Politzer P, Murray JS, Clark T (2010) Halogen bonding: an electrostatically-driven highly directional noncovalent interaction. *Phys Chem Chem Phys* 12:7748–7757
28. Politzer P, Murray JS (2013) Halogen bonding: an interim discussion. *ChemPhysChem* 14:278–294
29. Politzer P, Murray JS, Clark T (2013) Halogen bonding and other σ -hole interactions: a perspective. *Phys Chem Chem Phys* 15:11178–11189
30. Murray JS, Macaveiu L, Politzer P (2014) Factors affecting the strengths of σ -hole electrostatic potentials. *J Comput Sci.* doi:10.1016/j.jocs.2014.01.002
31. Bundhun A, Ramasami P, Murray JS, Politzer P (2013) Trends in σ -hole strengths and interactions of F_3MX molecules ($M=C, Si, Ge$ and $X=F, Cl, Br, I$). *J Mol Model* 19:2739–2746
32. Politzer P, Murray JS, Concha MC (2007) Halogen bonding and the design of new materials: organic chlorides, bromides and even fluorides as donors. *J Mol Model* 13:643–650
33. Shields ZP, Murray JS, Politzer P (2010) Directional tendencies of halogen and hydrogen bonds. *Int J Quantum Chem* 110:2823–2832
34. Clark T (2013) σ -Holes. *WIREs Comput Mol Sci* 3:13–20
35. Murray JS, Lane P, Clark T, Politzer P (2007) σ -Hole bonding: molecules containing group VI atoms. *J Mol Model* 13:1033–1038
36. Murray JS, Lane P, Politzer P (2007) A predicted new type of directional interaction. *Int J Quant Chem* 107:2286–2292
37. Murray JS, Lane P, Politzer P (2009) Expansion of the σ -Hole concept. *J Mol Model* 15:723–729
38. Guru Row TN, Parthasarathy R (1981) Directional preferences of nonbonded atomic contacts with divalent sulfur in terms of its orbital orientations. 2. S–S interactions and nonspherical shape of sulfur in crystals. *J Am Chem Soc* 103:477–479
39. Ramasubbu N, Parthasarathy R (1987) Stereochemistry of incipient electrophilic and nucleophilic reactions at divalent selenium center: electrophilic – nucleophilic pairing and anisotropic shape of Se in Se–Se Interactions. *Phosphorus Sulfur* 31:221–229
40. Clark T, Murray JS, Lane P, Politzer P (2008) Why are dimethyl sulfoxide and dimethyl sulfone such good solvents? *J Mol Model* 14:689–697
41. Politzer P, Murray JS, Janjić GV, Zarić SD (2014) σ -Hole interactions of covalently-bonded nitrogen, phosphorus and arsenic: a survey of crystal structures. *Crystals* 4:12–31
42. Bent HA (1968) Structural chemistry of donor–acceptor interactions. *Chem Rev* 68:587–648
43. Murray-Rust P, Motherwell WDS (1979) Computer retrieval and analysis of molecular geometry. 4. Intermolecular interactions. *J Am Chem Soc* 101:4374–4376
44. Murray-Rust P, Stallings WC, Monti CT, Preston RK, Glusker JP (1983) Intermolecular interactions of the carbon-fluorine bond: the crystallographic environment of fluorinated carboxylic acids and related structures. *J Am Chem Soc* 105:3206–3214

45. Ramasubbu N, Parthasarathy R, Murray-Rust P (1986) Angular preferences of intermolecular forces around halogen centers: preferred directions of approach of electrophiles and nucleophiles around carbon-halogen bonds. *J Am Chem Soc* 108:4308–4314
46. Rosenfield RE Jr, Parthasarathy R, Dunitz JD (1977) Directional preferences of nonbonded atomic contacts with divalent sulfur. 1. Electrophiles and nucleophiles. *J Am Chem Soc* 99:4860–4862
47. Brinck T, Murray JS, Politzer P (1992) Surface electrostatic potentials of halogenated methanes as indicators of directional intermolecular interactions. *Int J Quantum Chem* 44 (Suppl 19):57–64
48. Brinck T, Murray JS, Politzer P (1993) Molecular surface electrostatic potentials and local ionization energies of group V–VII hydrides and their anions: relationships for aqueous and gas-phase acidities. *Int J Quantum Chem* 48:73–88
49. Burling FT, Goldstein BM (1992) Computational studies of nonbonded sulfur-oxygen and selenium-oxygen interactions in the thiazole and selenazole nucleosides. *J Am Chem Soc* 114:2313–2320
50. Auffinger P, Hays FA, Westhof E, Shing Ho P (2004) Halogen bonds in biological molecules. *Proc Natl Acad Sci* 101:16789–16794
51. Riley KE, Murray JS, Politzer P, Concha MC, Hobza P (2009) Br–O complexes as probes of factors affecting halogen bonding: interactions of bromobenzenes and bromopyrimidines with acetone. *J Chem Theory Comput* 5:155–163
52. Riley KE, Murray JS, Fanfrlík J, Rezáč J, Solá RJ, Concha MC, Ramos FM, Politzer P (2011) Halogen bond tunability I: the effects of aromatic fluorine substitution on the strengths of halogen-bonding interactions involving chlorine, bromine and iodine. *J Mol Model* 17:3309–3318
53. Chopra D, Guru Row TN (2011) Role of organic fluorine in crystal engineering. *CrystEngComm* 13:2175–2186
54. Metrangolo P, Murray JS, Pilati T, Politzer P, Resnati G, Terraneo G (2011) Fluorine-centered halogen bonding: a factor in recognition phenomena and reactivity. *Cryst Growth Des* 11:4238–4246
55. Politzer P, Murray JS, Concha MC (2008) σ -Hole bonding between like atoms: a fallacy of atomic charges. *J Mol Model* 14:659–665
56. Politzer P, Murray JS (2013) Molecular electrostatic potentials: some observations. In: Ghosh K, Chattaraj P (eds) *Concepts and methods in modern theoretical chemistry*, vol. 1: electronic structure and reactivity. Taylor & Francis, New York, pp 181–199
57. Widhalm M, Kratky C (1992) Synthesis and X-ray structure of binaphthyl-based macrocyclic diphosphanes and their Ni(II) and Pd(II) complexes. *Chem Ber* 125:679–689
58. Sundberg MR, Ugglar R, Viñas C, Teixidor F, Paavola S, Kivekäs R (2007) Nature of intramolecular interactions in hypercoordinate C-substituted 1,2-dicarba-closododecaboranes with short P–P distances. *Inorg Chem Comm* 10:713–716
59. Meister J, Schwarz WHE (1994) Principal components of ionicity. *J Phys Chem* 98:8245–8252
60. Politzer P, Harris RR (1970) Properties of atoms in molecules. I. A proposed definition of the charge on an atom in a molecule. *J Am Chem Soc* 92:6451–6454
61. Ibrahim MAA (2011) Molecular mechanical study of halogen bonding in drug discovery. *J Comput Chem* 32:2564–2574
62. Kolař M, Hobza P (2012) On extension of the current biomolecular empirical force field for the description of halogen bonds. *J Chem Theory Comput* 8:1325–1333
63. Carter M, Rappé AK, Shing Ho P (2012) Scalable anisotropic shape and electrostatic models for biological bromine halogen bonds. *J Chem Theory Comput* 8:2461–2473
64. Jorgensen WL, Schyman P (2012) Treatment of halogen bonding in the OPLS-AA force field: application to potent anti-HIV agents. *J Chem Theory Comput* 8:3895–3901
65. Liem SY, Popelier PLA (2014) The hydration of serine: multipole moments *versus* point charges. *Phys Chem Chem Phys* 16:4122–4134

66. Mo Y, Bao P, Gao J (2011) Energy decomposition analysis based on a block-localized wavefunction and multistate density functional theory. *Phys Chem Chem Phys* 13:6760–6775
67. Riley KE, Hobza P (2008) Investigations into the nature of halogen bonding including symmetry adapted perturbation theory analyses. *J Chem Theory Comput* 4:232–242
68. Palusiak M (2010) On the nature of the halogen bond – the Kohn-Sham molecular orbital approach. *J Mol Struct (Theochem)* 945:89–92
69. Clark T, Murray JS, Politzer P (2014) Role of polarization in halogen bonds. *Aust J Chem.* doi:10.1071/ch13531
70. Clark T (2014) Directional electrostatic bonding. In: Frenking G, Shaik S (eds) *The chemical bond: chemical bonding across the periodic table*. Wiley-VCH, KGaA, Ch 18
71. Solimannejad M, Malekani M, Alkorta I (2010) Cooperative and diminutive unusual weak bonding in F3CX...HMgH...Y and F3CX...Y...HMgH trimers (X = Cl, Br; Y = HCN and HNC). *J Phys Chem A* 114:12106–12111
72. Scheiner S (2011) On the properties of X–N noncovalent interactions for first-, second-, and third-row X atoms. *J Chem Phys* 134(1–9):164313
73. Grabowski SJ, Bilewicz E (2006) Cooperative halogen bonding effect – ab initio calculations on H₂CO...(ClF)_n complexes. *Chem Phys Lett* 427:51–55
74. Li Q, Li R, Zhou Z, Li W, Cheng J (2012) S–X halogen bonds and H–X hydrogen bonds in H₂CS–XY (XY = FF, ClF, ClCl, BrF, BrCl and BrBr) complexes: cooperativity and solvent effect. *J Chem Phys* 136(1–8):14302
75. Wang W, Wang NB, Zheng W, Tian A (2004) Theoretical study on the blueshifting halogen bond. *J Phys Chem A* 108:1799–1805
76. Murray JS, Concha MC, Lane P, Hobza P, Politzer P (2008) Blue shifts vs red shifts in σ -hole bonding. *J Mol Model* 14:699–704
77. Hermansson K (2002) Blue-shifting hydrogen bonds. *J Phys Chem A* 106:4695–4702
78. Qian W, Krimm S (2002) Vibrational spectroscopy of hydrogen bonding: origin of the different behavior of the C–H–O hydrogen bond. *J Phys Chem A* 106:6628–6636
79. Hobza P, Zahradnik R (1992) An essay on the theory and calculations of intermolecular interactions. *Int J Quantum Chem* 42:581–590
80. Cramer CJ (2002) *Essentials of computational chemistry*. Wiley, Chichester
81. Riley KE, Murray JS, Fanfrlík J, Rezáč J, Solá RJ, Concha MC, Ramos FM, Politzer P (2013) Halogen bond tunability ii: the varying roles of electrostatic and dispersion contributions to attraction in halogen bonds. *J Mol Model* 19:4651–4659
82. Hirschfelder JO, Eliason MA (1967) Electrostatic Hellmann–Feynman theorem applied to the long-range interaction of two hydrogen atoms. *J Chem Phys* 47:1164–1169
83. Hunt KLC (1990) Dispersion dipoles and dispersion forces: proof of Feynman’s “conjecture” and generalization to interacting molecules of arbitrary symmetry. *J Chem Phys* 92:1180–1187
84. Mulliken RS (1952) Molecular compounds and their spectra II. *J Am Chem Soc* 74:811–824
85. Scerri ER (2000) Have orbitals really been observed? *J Chem Ed* 77:1492–1494
86. Stone AJ, Misquitta AJ (2009) Charge-transfer in symmetry-adapted perturbation theory. *Chem Phys Lett* 473:201–205
87. Stone AJ, Price SL (1988) Some new ideas in the theory of intermolecular forces: anisotropic atom-atom potentials. *J Phys Chem* 92:3325–3335
88. Reed AE, Curtiss LA, Weinhold F (1988) Intermolecular interactions from a natural bond orbital, donor-acceptor viewpoint. *Chem Rev* 88:899–926
89. Sokalski WA, Roszak SM (1991) Efficient techniques for the decomposition of intermolecular interaction energy at SCF level and beyond. *J Mol Struct (Theochem)* 234:387–400
90. Chen J, Martínez TJ (2007) QTPIE: charge transfer with polarization current equalization. A fluctuating charge model with correct asymptotics. *Chem Phys Lett* 438:315–320
91. Politzer P, Murray JS, Lane P (2007) σ -Hole bonding and hydrogen bonding: competitive interactions. *Int J Quantum Chem* 107:3046–3052

92. Aakeröy CB, Fasulo M, Shultheiss N, Desper J, Moore C (2007) Structural competition between hydrogen bonds and halogen bonds. *J Am Chem Soc* 129:13772–13773
93. Alkorta I, Blanco F, Solimannejad M, Elguero J (2008) Competition of hydrogen bonds and halogen bonds in complexes of hypohalous acids with nitrogenated bases. *J Phys Chem A* 112:10856–10863
94. Di Paolo T, Sandorfy C (1974) On the biological importance of the hydrogen bond breaking potency of fluorocarbons. *Chem Phys Lett* 26:466–469
95. Corradi E, Meille SV, Messina MT, Metrangolo P, Resnati G (2000) Halogen bonding versus hydrogen bonding in driving self-assembly processes. *Angew Chem Int Ed* 39:1782–1786
96. Legon AC (1999) Prereactive complexes of dihalogens XY with Lewis bases B in the gas phase: a systematic case for the halogen analogue B–XY of the hydrogen bond B–HX. *Angew Chem Int Ed* 38:2686–2714
97. Legon AC (2010) The halogen bond: an interim perspective. *Phys Chem Chem Phys* 12:7736–7747
98. Joseph J, Jemmis ED (2007) Red-, blue-, or no-shift in hydrogen bonds: a unified explanation. *J Am Chem Soc* 129:4620–4632
99. Sánchez-Sanz G, Trujillo C, Alkorta I, Elguero J (2012) Electron density shift description of non-bonding intramolecular interactions. *Comput Theor Chem* 991:124–133
100. Wang J, Giu J, Leszczynski J (2012) The electronic spectra and the H-bonding pattern of the sulfur and selenium substituted guanines. *J Comput Chem* 33:1587–1593
101. Lu X, Li H, Zhu X, Zhu W, Liu H (2011) How does halogen bonding behave in solution? A theoretical study using implicit solvation model. *J Phys Chem A* 115:4467–4475
102. Politzer P, Murray JS (2013) Enthalpy and entropy factors in gas phase halogen bonding: compensation and competition. *CrystEngComm* 15:3145–3150
103. Del Bene JE, Alkorta I, Elguero J (2010) Do traditional, chlorine-shared and ion-pair halogen bonds exist? An ab initio investigation of FCl:CNX complexes. *J Phys Chem A* 114:12958–12962
104. Politzer P, Murray JS (2012) Halogen bonding and beyond: factors influencing the nature of CN-R and SiN-R complexes with FCl and Cl₂. *Theor Chem Acc* 131(1–10):1114
105. Politzer P, Murray JS, Bulat FA (2010) Average local ionization energy: a review. *J Mol Model* 16:1731–1742
106. Murray JS, Lane P, Clark T, Riley KE, Politzer P (2012) σ -Holes, π -holes and electrostatically-driven interactions. *J Mol Model* 18:541–548
107. Isaacson W (2007) Einstein: his life and universe. Simon and Schuster, New York, p 549
108. Bondi A (1964) van der Waals volumes and radii. *J Phys Chem* 68:441–451
109. Rowland RS, Taylor R (1996) Intermolecular nonbonded contact distances in organic crystal structures: comparison with distances expected from van der Waals radii. *J Phys Chem* 100:7384–7391

Halogen Bonding in the Gas Phase: A Comparison of the Iodine Bond in $B \cdots ICl$ and $B \cdots ICF_3$ for Simple Lewis Bases B

J. Grant Hill, Anthony C. Legon, David P. Tew, and Nicholas R. Walker

Abstract Methods for observing the rotational spectra of the halogen-bonded complexes $B \cdots ICl$ and $B \cdots ICF_3$ ($B = N_2, CO, HC \equiv CH, H_2C = CH_2, H_2O, H_2S, PH_3$ or NH_3) and deriving from them properties such as angular geometry, radial geometry, the strength of the intermolecular bond, and the extent of electron redistribution on complex formation are described. Comparison of various properties reveals several similarities between the two series. Thus, the $B \cdots ICF_3$ obey a set of rules which were originally proposed to rationalise the angular geometries of hydrogen-bonded complexes of the type $B \cdots HX$, but which were subsequently found to apply to their halogen-bonded analogues $B \cdots XY$, where XY is a dihalogen molecule, including ICl . Important for establishing the validity of these rules in both series $B \cdots ICl$ and $B \cdots ICF_3$ were the complexes with $B = H_2O$ or H_2S . The configuration at O in $H_2O \cdots ICF_3$ and $H_2O \cdots ICl$ is effectively planar. On the other hand, the configuration at S in $H_2S \cdots ICF_3$ and $H_2S \cdots ICl$ is permanently pyramidal. Ab initio calculations of potential energy functions for inversion at O or S performed at the CCSD(T)(F12*)/cc-pVDZ-F12 level of theory confirmed these conclusions. Comparison of the intermolecular stretching force constants k_σ show that the series $B \cdots ICF_3$ is systematically more weakly bound than $B \cdots ICl$. Interpretation of k_σ in terms of nucleophilicities N_B of B and electrophilicities E_{IR} of ICl and ICF_3 reveals that $E_{ICF_3} \approx E_{ICl}/3$. Experimental and ab initio values of distances $r(Z \cdots I)$, where Z is the acceptor atom/

J.G. Hill

Department of Chemistry, University of Sheffield, Sheffield S3 7HF, UK
e-mail: grant.hill@sheffield.ac.uk

A.C. Legon (✉) and D.P. Tew

School of Chemistry, University of Bristol, Bristol BS8 1TS, UK
e-mail: a.c.legon@bristol.ac.uk; david.tew@bristol.ac.uk

N.R. Walker

School of Chemistry, Bedson Building, Newcastle University, Newcastle-upon-Tyne NE1 7RU, UK
e-mail: nick.walker@newcastle.ac.uk

region of B, show that, for a given B, the intermolecular bond of $B \cdots ICF_3$ is longer than that of $B \cdots ICl$. The electronic charge redistributed from B to ICF_3 on formation of $B \cdots ICF_3$ is probably negligibly small.

Keywords Ab initio calculations · Angular and radial geometry · Intermolecular force constants · Iodine bond · Iodine monochloride · Iodo-trifluoromethane · Lewis bases · Potential energy functions · Rotational spectroscopy

Contents

1	Introduction	44
2	Methods of Observing Rotational Spectra of Complexes $B \cdots ICl$ and $B \cdots ICF_3$	46
2.1	Pulsed-Jet, Fourier-Transform Microwave Spectroscopy Conducted in a Fabry–Perot Cavity	47
2.2	Chirped-Pulse, Fourier-Transform Microwave Spectroscopy	49
3	Molecular Properties of $B \cdots ICl$ and $B \cdots ICF_3$ Available from Spectroscopic Constants Obtained from Analysis of Rotational Spectra	50
3.1	Geometry from Rotational Constants	51
3.2	Intermolecular Stretching Force Constant k_σ from Centrifugal Distortions Constants	52
3.3	Electric Charge Redistribution on Formation of $B \cdots ICl$ from I and Cl Nuclear Quadrupole Coupling Constants	53
4	Comparison of Observed Properties of $B \cdots ICl$ and $B \cdots ICF_3$	55
4.1	Angular Geometry: Do Complexes $B \cdots ICF_3$ Obey the Rules?	55
4.2	Radial Geometry: How Do the Halogen Bond Distances $Z \cdots I$ Vary from $B \cdots ICl$ to $B \cdots ICF_3$?	66
4.3	Intermolecular Stretching Force Constants k_σ : How Does Replacement of Cl in $B \cdots ICl$ by CF_3 Change the Electrophilicity of the Halogen Bond Donor Molecule?	68
4.4	Electric Charge Rearrangement on Formation of $B \cdots ICl$ and $B \cdots ICF_3$ Complexes	71
	Conclusions	73
	References	74

1 Introduction

This chapter compares the gas-phase properties of two groups of binary complexes, in both of which the components are held together by means of an iodine bond. The two groups of complexes are of the general type $B \cdots I-R$, where B is one of a range of simple Lewis bases and R is either the atom Cl [1–9] or the group CF_3 [10–16]. Some generalisations appropriate to both groups are discussed.

Only relatively small complexes in which the components are linked by a halogen bond have been investigated in the gas phase. In particular, only those of the type $B \cdots X-R$, where B is a simple Lewis base, X is the atom forming the halogen bond to the acceptor atom/centre Z of B, and R is either another halogen atom [17–20] or the groups CF_3 [10–16, 21–23], have been examined spectroscopically. Among the $B \cdots XCF_3$ groups, the series with $X=I$ is the most extensive and

is the focus of this chapter. The technique predominantly employed for gas-phase studies has been microwave spectroscopy, which is conducted under conditions where the complexes $B \cdots X-R$ can be investigated in effective isolation, unperturbed by either the solvent or lattice effects that are present in condensed phases. In the work described here, the results are derived from pure rotational spectra, which are usually observed in the microwave region. Also related to the content of this chapter are the systematic investigations of the vibrational spectra of complexes of the type $B \cdots XCF_3$ when dissolved in liquid noble gases (described in chapter “Infrared and Raman measurements of halogen bonding in cryogenic solutions”). The solvent–solute interactions are then present but small. Recently, Bevan et al. have carried out some very high-resolution vibration-rotation spectroscopy of gas-phase, halogen-bonded complexes such as $OC \cdots Cl_2$ [24] by using quantum cascade lasers.

Analysis of rotational spectra provides very precise spectroscopic constants which can be interpreted to give various properties of the isolated complexes $B \cdots X-R$, and therefore such properties are the most appropriate for comparison with the results of ab initio electronic structure calculations. The series of halogen-bonded complexes involving Lewis bases with dihalogen molecules $B \cdots XY$ ($XY = F_2, ClF, Cl_2, BrCl, Br_2$ or ICl) is, so far, the series most completely characterised by means of rotational spectroscopy; this work is conveniently summarised in [18]. An advantage of dihalogens acting as the halogen-bond donor lies in the absence (for F_2, Cl_2 and Br_2) or sparseness (for $ClF, BrCl$ and ICl) of their rotational spectra. Comparisons of the way derived properties change as first B and then XY are systematically varied have led to some generalisations about the halogen bond [25–30]. These generalisations are concerned with the geometry of the complex, the strength of its intermolecular bond and, in suitable cases, the extent of the electric charge rearrangement that accompanies complex formation. Examples of these generalisations are some rules for the interpretation and prediction of angular geometry [18] (i.e. the relative orientation of the B and XY subunits within $B \cdots XY$) and an expression which allows the prediction of the intermolecular stretching force constant k_σ (one measure of the strength of the interaction of B and XY) from properties assigned to the isolated molecules B and XY, namely the nucleophilicity N_B of B and the electrophilicity E_{XY} of XY [18, 28]. The experimental results and generalisations for $B \cdots XY$ have been thoroughly reviewed elsewhere [17–20]. In these reviews, attention was drawn to a set of identical generalisations previously developed from investigations of the rotational spectra of hydrogen-bonded complexes $B \cdots HX$ in which both B and X were systematically varied. This parallelism between the hydrogen bond and the halogen bond suggests a common origin for these two types of interaction, but such a conclusion must be tempered with caution [31].

The rotational spectra of the halogen-bonded complexes $B \cdots XCF_3$ having a trifluorohalogenomethane XCF_3 as the X donor [10–16, 21–23] have been observed and analysed more recently than those in which a dihalogen molecule XY is the halogen-bond donor, this order being dictated, at least in part, by an instrumental development discussed in Sect. 2.2. Of the series of $B \cdots XCF_3$ complexes, the one

to be discussed here involves $X = \text{I}$ as the halogen donor atom and $\text{B} = \text{N}_2$, CO , $\text{HC}\equiv\text{CH}$, $\text{H}_2\text{C}=\text{CH}_2$, H_2O , H_2S , PH_3 or NH_3 as the Lewis bases. The reason for the particular interest in ICF_3 lies in its role as the tractable prototype for those molecules, such as tetrafluoro-diiodobenzene, employed in crystal engineering applications of the halogen bond [32]. The multiple fluorination is used as a means of withdrawing electrons from the I atom, thereby enhancing the strength of the halogen bond that it forms. In this chapter, we take the opportunity to compare the results for the series $\text{B}\cdots\text{ICF}_3$ with those of the corresponding series $\text{B}\cdots\text{ICl}$, to examine the extent to which replacement of Cl by CF_3 affects the iodine bond, and to find out whether the generalisations previously identified for the latter group of complexes also apply to the former.

The structure of the remainder of this chapter is as follows. In Sect. 2, the two methods used to observe the rotational spectra of complexes $\text{B}\cdots\text{ICl}$ and $\text{B}\cdots\text{ICF}_3$ are briefly outlined, namely pulsed-jet, Fourier-transform microwave spectroscopy in a Fabry–Perot cavity (Sect. 2.1), and chirped-pulse, Fourier-transform microwave spectroscopy (Sect. 2.2), with the emphasis on their advantages and disadvantages. Section 3 describes the properties of the $\text{B}\cdots\text{ICl}$ and $\text{B}\cdots\text{ICF}_3$ molecules that can be derived from spectroscopic constants obtained from analysis of rotational spectra, i.e. the geometry from rotational constants (Sect. 3.1), the intermolecular stretching force constant k_σ from centrifugal distortion constants (Sect. 3.2) and the electric charge redistribution on formation of $\text{B}\cdots\text{ICl}$ from the I and Cl nuclear quadrupole coupling constants (Sect. 3.3). The comparison of observed properties of $\text{B}\cdots\text{ICl}$ and $\text{B}\cdots\text{ICF}_3$ is given in Sect. 4 in which we consider (1) whether $\text{B}\cdots\text{ICF}_3$ complexes, as do their $\text{B}\cdots\text{ICl}$ counterparts, obey the rules for angular geometry (Sect. 4.1), (2) radial geometry and in particular how the halogen bond distances $\text{Z}\cdots\text{I}$ vary from $\text{B}\cdots\text{ICl}$ to $\text{B}\cdots\text{ICF}_3$ (Sect. 4.2) and (3) (in Sect. 4.3) whether the intermolecular stretching force constants k_σ for the $\text{B}\cdots\text{ICF}_3$ series allow an electrophilicity E_{ICF_3} to be determined for ICF_3 and, if so, how replacement of $\text{R} = \text{Cl}$ by CF_3 affects the electrophilicity of the halogen donor molecule. A brief argument to establish that the extent of electric charge rearrangement on formation of $\text{B}\cdots\text{ICF}_3$ complexes from B and ICF_3 is probably very small is given in Sect. 4.4. Section “Conclusions” presents a summary of the conclusions.

2 Methods of Observing Rotational Spectra of Complexes $\text{B}\cdots\text{ICl}$ and $\text{B}\cdots\text{ICF}_3$

Two methods [33–36], having several features in common, have been used to observe the rotational spectra of complexes of the type $\text{B}\cdots\text{ICl}$ and $\text{B}\cdots\text{ICF}_3$. Both employ supersonic expansion of a mixture of B and I–R diluted in an inert gas (argon) to produce a short gas pulse (≈ 1 ms duration) containing a sufficient number density of the complexes $\text{B}\cdots\text{I–R}$ which then expand into a vacuum

chamber. The important properties of the supersonic expansion in this context are (1) that the $B \cdots I-R$ molecules so formed rapidly achieve collisionless expansion in the chamber with an effective translational temperature of only ≈ 1 K, so that even very weakly bound complexes survive until the gas pulse collides with part of the vacuum chamber/pumping system, and (2) that complexes are usually in their vibrational ground state (unless very low energy vibrational states such as those caused by hindered rotation exist) and in their lower energy rotational states. Both techniques then involve the polarization of rotational transitions in a macroscopic ensemble of molecules $B \cdots IR$ by means of a short pulse of microwave radiation, both recording the amplitude of the spontaneous coherent emission from the polarized ensemble as a function of time (time-domain experiment) after the polarizing radiation has decayed sufficiently in intensity that there is no significant background radiation against which to discriminate. Both employ Fourier transformation of the time-domain signal, usually to yield the intensity vs frequency spectrum. In both, the physics of the creation of the macroscopic polarization and its decay are very similar to that involved in the NMR experiment, the main differences being (1) that the microwave experiment involves an electric polarization while the NMR experiment relies on a magnetic polarization and (2) that the decay of the electric polarization is much faster ($T_2 \approx 100 \mu\text{s}$) than that of the magnetic polarization ($T_2 \approx 10$ s). Each technique has Fourier-transform microwave spectroscopy in its title, but they differ in the frequency bandwidth of the polarizing microwave pulse. An outline of each technique is given below, with emphasis on their differences, together with an indication of their advantages and disadvantages.

2.1 Pulsed-Jet, Fourier-Transform Microwave Spectroscopy Conducted in a Fabry–Perot Cavity

The essential features of the pulsed-jet, Fourier-transform, Fabry–Perot (F–P) cavity technique [33, 34] are as follows. A short pulse (duration ≈ 1 –2 ms) of the gas mixture (usually about 1% each of B and I–R in argon at a total pressure of 2 bar) is produced by a solenoid valve and enters an evacuated microwave F–P cavity along its axis. The F–P cavity consists of a pair of confocal, spherical aluminium mirrors having a high Q and an acceptance bandwidth of ≈ 1 MHz. After a suitable delay to allow the gas pulse to arrive at the centre of the mirrors, monochromatic microwave radiation (produced by a microwave synthesizer) is formed into a pulse of $\approx 1 \mu\text{s}$ duration and carries with it into the F–P cavity a range of frequencies covering about 1 MHz, thereby matching the cavity bandwidth. The microwave pulse, if of sufficient power, can therefore polarize all rotational transitions of the target molecules whose frequencies fall within approx. 1 MHz of the frequency to which the Fabry–Perot cavity is tuned. After a short delay to ensure that the polarizing microwave pulse has decayed, the spontaneous coherent

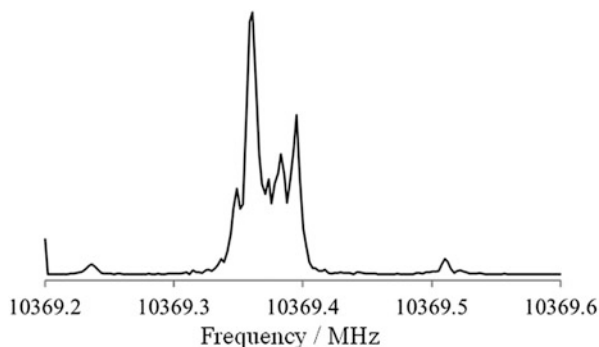


Fig. 1 A small part of the nuclear quadrupole hyperfine structure of the $J=6 \rightarrow 5$, $K=0 \rightarrow 0$ transition of $\text{H}_3^{14}\text{N} \cdots ^{127}\text{ICF}_3$ recorded with a pulsed-jet, F-T microwave spectrometer incorporating a Fabry–Perot cavity. The feature at 10,369.365 MHz is a combination of the $F_1=3.5 \rightarrow 4.5$, $F_2=2.5 \rightarrow 3.5$ and the $F_1=3.5 \rightarrow 4.5$, $F_2=4.5 \rightarrow 5.5$ hyperfine components (each appearing as a Doppler doublet) arising from the presence of the ^{127}I and ^{14}N nuclei in the molecule. The spectrum is the average of the signals collected from 11,500 gas pulses

emission from the rotationally polarized gas is recorded in the time domain, Fourier transformed and the power spectrum displayed. The parallel propagation of the gas and microwave pulses along the cavity axis leads to a so-called Doppler doublet (the centre frequency of which is the transition frequency), but has the advantage that it reduces the full-width at half-maximum intensity of each component to approx. 5 kHz. This instrument therefore has a very high resolution and a correspondingly high accuracy of frequency measurement (typically 0.5 kHz). In addition, only a relatively low microwave power is needed to polarize rotationally a large fraction of the gas pulse when within the F–P cavity and this ensures a high sensitivity. Disadvantages include (1) slow searching because every time the radiation is changed (usually in 0.5 MHz steps to ensure no transitions are missed) the cavity must be re-tuned to the radiation frequency and (2) difficulty in extracting relative intensities because the intensity of an observed signal depends critically on the mode of the F–P cavity in use and on the how far the radiation is offset from the exact resonant frequency of the cavity. As an example of the resolution and sensitivity, part of the extensive hyperfine structure arising from coupling of the ^{14}N and ^{127}I nuclear spins to the overall rotational angular momentum in the $J=6 \rightarrow 5$ transition of $\text{H}_3^{14}\text{N} \cdots ^{127}\text{IF}_3$ is shown in Fig. 1. Each transition is split into a doublet by the Doppler effect mentioned earlier.

2.2 *Chirped-Pulse, Fourier-Transform Microwave Spectroscopy*

The sequence of events comprising a gas pulse, microwave pulse, detection of the spontaneous coherent emission and Fourier-transformation of the detected radiation is also used in the chirped-pulse version of FTMW spectroscopy. Chirped-pulse (CP) FTMW spectroscopy [35, 36] additionally entails the use of a microwave polarization pulse which is rapidly swept over a very broad frequency range. Such experiments have only recently become possible as a result of advances in the technology available for the digital generation and processing of waveforms. Compared with typical FTMW experiments exploiting an F–P cavity, the polarization pulse duration is unchanged. However, a pulse of significantly higher intensity must be used to polarize efficiently molecules across the broader bandwidth of the experiment. The intensity required in the chirped polarization pulse is directly proportional to its bandwidth.

When implemented within a spectrometer that exploits fixed-frequency microwave pulses (i.e. of the type described in Sect. 2.1), a Fabry–Perot cavity comprising confocal, spherical mirrors allows higher sensitivity and resolution than could otherwise be achieved. However, the acceptance bandwidth of such a cavity is too narrow to gain any advantage when a microwave polarization pulse spanning 12 GHz in frequency is used. For this reason, the polarizing pulse is introduced and the molecular emission detected using broadband horn antennae in a chirped-pulse FTMW spectrometer. The principal advantage of the CP-FTMW technique undoubtedly arises from the opportunity to excite all transitions across a broad bandwidth in a single measurement. At microwave frequencies, all transitions between 6 and 18 GHz can be probed simultaneously, representing a very significant expansion of the frequency range which can be probed compared with experiments that exploit a Fabry–Perot cavity. An additional, related advantage arises because the intensity of the chirped pulse in a CP-FTMW spectrometer is highly uniform across the frequency range under examination. It is thus easier to compare the relative intensities of different transitions across a broad frequency range. The intensities of transitions measured by FTMW experiments exploiting a Fabry–Perot cavity are dependent on a greater range of factors, as described in

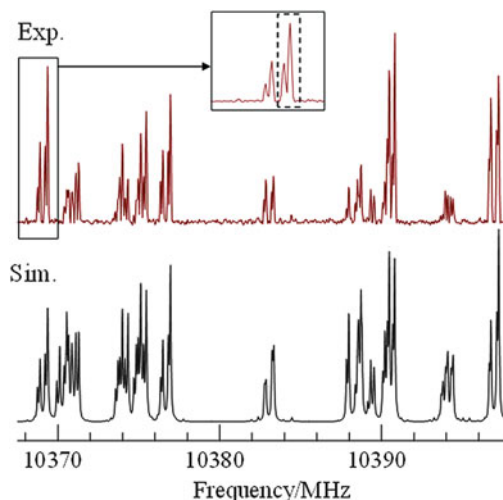


Fig. 2 Part of the $J=6 \rightarrow 5$ transition of $\text{H}_3^{14}\text{N} \cdots ^{127}\text{ICF}_3$ recorded with a chirped-pulse F-T microwave spectrometer in the frequency range 10,365–10,400 MHz is shown in the *upper panel* while the *lower panel* is a simulation obtained with the aid of the spectroscopic constants given in [15]. A small section of the spectrum is expanded within the *inset*. The features at 10,369.365 MHz, further expanded and enclosed within the *dashed box*, are those displayed in Fig. 1. The spectrum resulted from the averaging of the signals from 13,000 gas pulses

Sect. 2.1. Figure 2 shows a recording of the rotational spectrum of $\text{H}_3\text{N} \cdots \text{ICF}_3$ observed with the CP-FTMW spectrometer when the frequency range displayed is successively decreased. A small part of the same spectrum recorded with a spectrometer of the type discussed in Sect. 2.1 is shown in Fig. 1. The smaller line widths and accompanying increased resolution are apparent.

3 Molecular Properties of $\text{B} \cdots \text{ICl}$ and $\text{B} \cdots \text{ICF}_3$ Available from Spectroscopic Constants Obtained from Analysis of Rotational Spectra

The techniques discussed in Sects. 2.1 and 2.2 lead to the rotational spectra of the $\text{B} \cdots \text{I-R}$ ($\text{R} = \text{Cl}$ or CF_3) complexes of good intensity but usually in their ground vibrational states only. Sometimes, however (with $\text{H}_3\text{N} \cdots \text{ICF}_3$, $\text{H}_2\text{O} \cdots \text{ICF}_3$, for example), the corresponding spectra in excited internal rotation states are also observed. Here we shall be concerned only with molecular properties pertaining to vibrational ground states. Analysis of the ground-state spectra lead to ground-state spectroscopic constants, among which are included rotational constants, centrifugal distortion constants and nuclear quadrupole coupling constants. The spectroscopic constants can be interpreted, at various levels of approximation, to give properties of

the complexes with which they are associated. These properties and the approximations involved in obtaining them are discussed in Sects. 3.1, 3.2 and 3.3.

3.1 Geometry from Rotational Constants

Ground-state rotational constants A_0 , B_0 and C_0 are simply related to the zero-point principal moments of inertia I_a^0 , I_b^0 and I_c^0 through the equations $A_0 = h/8\pi^2 I_a^0$, $B_0 = h/8\pi^2 I_b^0$ and $C_0 = h/8\pi^2 I_c^0$, where a , b and c delineate the three principal inertia axes. The principal moments of inertia associated with the equilibrium geometry (indicated by a superscript e) are simple functions of only the masses and the equilibrium principal-axis coordinates of the atoms. The expression for the equilibrium principal moment of inertia I_a^e , for example, is just $I_a^e = \sum_i m_i (b_i^2 + c_i^2)$,

with corresponding expressions for I_b^e and I_c^e . If an isotopic substitution is made at a particular atom, the changes ΔI_a^e , ΔI_b^e and ΔI_c^e in the moments of inertia which accompany the substitution are related by exact equations (called Kraitchman's equations [37]) to the principal-axis coordinates of the atom in question. Isotopic substitution at each atom in turn thus leads to a complete geometry for the molecule.

Unfortunately, equilibrium moments of inertia are very rarely available experimentally, except for the simplest of molecules and certainly not for weakly bound complexes such as those under discussion here. The approach usually adopted then is to use zero-point moments of inertia as if they were equilibrium values. When isotopic substitutions are made and the geometry is fitted to the minimum number of zero-point moments of inertia by the least-squares method, the result is called an r_0 geometry. Since isotopic substitution changes the zero-point motion, the geometry obtained varies depending on the isotopologues chosen, and therefore inconsistencies occur when r_0 geometries are over-determined, i.e. determined from different sets of isotopologues. When changes in zero-point moments of inertia ΔI_a^0 , ΔI_b^0 and ΔI_c^0 are used in Kraitchman's equations [37] in place of equilibrium values (ΔI_a^e , ΔI_b^e , ΔI_c^e), however, the resulting coordinates are referred to as substitution coordinates and the geometry as the r_s geometry [38]. The advantage of r_s geometries is that they exhibit greater internal consistency when over-determined and are closer to equilibrium values than r_0 geometries (for diatomic molecules there is an exact relation $r_s = (r_e + r_0)/2$). Even r_s geometries are not available for the type of molecules considered here, however. In view of the weak intermolecular binding, it is usually assumed that the geometry of each of the two component molecules B and I-R is unperturbed by complex formation. The parameters defining the separation of the two subunits B and I-R and their relative orientation in space, i.e. the radial and angular geometries of the complex, respectively, are obtained by a least-squares fit of the zero-point moments of inertia of the various isotopologues. All molecular geometries of B ··· I-R considered here are of this pseudo- r_0 type.

3.2 Intermolecular Stretching Force Constant k_σ from Centrifugal Distortions Constants

Chemical bonds are elastic and, therefore, when a molecule is in its zero-point vibrational state and a rotational state having a quantum number $J > 0$ (i.e. it is rotating), the bonds distort. The higher the rotational energy (i.e. the higher J), the larger the distortion and therefore the geometry changes (very slightly) with the rotational state. In the usual expressions for the energy of rotation of a molecule in its zero-point state, the main part of the energy is expressed in terms of the zero-point rotational constants A_0 , B_0 and C_0 (often referred to as the effective rigid rotor energy) while the centrifugal distortion contribution is described by small additional terms consisting of centrifugal distortion constants which multiply simple functions of the rotational quantum number J for diatomic and linear molecules or quantum numbers J and K for symmetric-top molecules [39]. The expressions for asymmetric-top molecules are more complicated but the principles are the same. For a diatomic or linear molecule, this energy expression is simply

$$E(J) = hB_0J(J+1) - hD_JJ^2(J+1)^2, \quad (1)$$

in which the second term on the right-hand side takes account of the change of geometry (and therefore rotational energy) with J . D_J is called the (quartic) centrifugal distortion constant. There are higher order (sextic, etc.) centrifugal distortion constants but these are usually negligible unless the molecule is unusually floppy or very high J value transitions are observed. The expressions for symmetric-top and asymmetric-top molecules contain three and five (quartic) centrifugal constants, respectively, because there are other ways in which such molecules change geometry with rotational state, corresponding to rotations about principal inertia axes other than b . However, the term corresponding to D_J for linear/diatomic molecules is also present for symmetric-top and asymmetric-top molecules. It is given the same symbol D_J in symmetric-top molecules but is labelled Δ_J in the latter group.

To a reasonable approximation, the components of a weakly bound complex (such as one of the $B \cdots I-R$ considered here) may be modelled as a pair of rigid molecules held together by a weak intermolecular bond. In the crudest approximation, B and I-R can be taken as point masses and $B \cdots I-R$ becomes a pseudo-diatomic molecule. Clearly in that case the centrifugal distortion constant depends on only one force constant, namely the intermolecular stretching force constant k_σ . The expression relating k_σ and D_J for a complex $B \cdots I-R$ is simply related to that for a diatomic molecule [40] and is given in the pseudo-diatomic approximation by

$$k_\sigma = 16\pi^2\mu \left[\frac{1}{2}(B+C) \right]^3 / D_J, \quad (2)$$

where $\mu = M_B M_{IR} / (M_B + M_{IR})$ and M_B and M_{IR} are the masses of B and I-R, respectively. A more realistic approximation, made by Millen [41], treats the two component molecules as rigid but takes into account their spatial extension of mass.

The expressions are different for different types of molecular rotor. For a symmetric-top complex, such as $\text{H}_3\text{N} \cdots \text{ICl}$ [8], the appropriate expression is

$$k_\sigma = (16\pi^2\mu B^3/D_J)[1 - B/C_{\text{NH}_3} - B/B_{\text{ICl}}], \quad (3)$$

in which the rotational constants in the denominators of the expressions in square brackets refer to the indicated free molecules and B is that of the complex. Strictly, these rotational constants should be equilibrium values but it is a good approximation to use zero-point quantities. When the complex is a planar asymmetric-top molecule of C_{2v} symmetry, for example ethyne $\cdots \text{ICl}$ [3], having rotational constants B and C and the centrifugal distortion constant Δ_J , the expression for k_σ takes the form

$$k_\sigma = (8\pi^2\mu/\Delta_J)[B^3(1-b) + C^3(1-c)], \quad (4)$$

in which $b = (B/B_{\text{C}_2\text{H}_2}) + (B/B_{\text{ICl}})$, $c = (C/B_{\text{C}_2\text{H}_2}) + (C/B_{\text{ICl}})$. The expression given by Millen [41] for planar C_{2v} molecules of this type actually refers to D_J , which was the nomenclature employed in an earlier approach to the centrifugal distortion Hamiltonian than that used in the work reported here. D_J so determined differs from Δ_J by a small term. As a consequence, Millen's expression relating D_J and k_σ differs from Eq. (4) by a small additional term within the square brackets. Here we are concerned only with Δ_J values for asymmetric-top molecules and hence Eq. (4) is appropriate. If the complex is an asymmetric-top molecule such as $\text{C}_2\text{H}_4 \cdots \text{ICl}$ [4], in which ICl lies along the C_2 axis that is perpendicular to the plane of the ethene subunit, Eq. (4) also applies. Millen's original derivations were for complexes in which the Lewis acid is a diatomic or linear molecule, but it is readily shown that Eqs. (3) and (4) also apply when the Lewis acid is a symmetric-top molecule, such as ICF_3 .

3.3 *Electric Charge Redistribution on Formation of $\text{B} \cdots \text{ICl}$ from I and Cl Nuclear Quadrupole Coupling Constants*

It has been shown elsewhere [2, 8] that, in a complex $\text{B} \cdots \text{ICl}$, the iodine and chlorine nuclear quadrupole coupling constants can be interpreted on the basis of a simple model (the Townes–Dailey model [42]) to provide information about the electron redistribution which occurs on formation of the complex from its two components.

Nuclei with a spin quantum number $I \geq 1$ can possess an electric quadrupole moment. Since $I = 3/2$ for ^{35}Cl and $I = 5/2$ for ^{127}I , both nuclei in $\text{XY} = ^{127}\text{I}^{35}\text{Cl}$ are quadrupolar. As a result of the electrostatic interaction of the nuclear electric quadrupole moment \mathbf{Q}_X of nucleus X with any electric field gradient $q_{zz} = \partial^2 V^X / \partial z^2$ existing at that nucleus along the intermolecular axis direction

z in the molecule XY, the nuclear spin angular momentum \mathbf{I}_X associated with X couples to the overall rotational angular momentum \mathbf{J} , and similarly for nucleus Y. Only a limited number of orientations of the X and Y nuclear spin axes with respect to z are allowed and each of these corresponds to a different energy of interaction of \mathbf{Q}_X with $\partial^2 V^X/\partial z^2$ and \mathbf{Q}_Y with $\partial^2 V^Y/\partial z^2$. The result is a splitting of the rotational energy levels of XY into several so-called *nuclear quadrupole hyperfine components*. By measuring the resulting nuclear quadrupole hyperfine structure of the rotational transitions, the nuclear quadrupole coupling constants $\chi_{zz}(X)$ and $\chi_{zz}(Y)$ defined by

$$\chi_{zz}(X) = eQ_X \left(\partial^2 V^X / \partial z^2 \right), \quad (5)$$

and

$$\chi_{zz}(Y) = eQ_Y \left(\partial^2 V^Y / \partial z^2 \right), \quad (6)$$

can be determined accurately. Since the proton charge e and the conventional nuclear electric quadrupole moments Q_X and Q_Y are known constants, Eqs. (5) and (6) lead to the electric field gradients (efgs) at X and Y along the z axis. The efg at a given nucleus X is determined entirely by the electron charge distribution in the molecule XY outside a small sphere surrounding the X nucleus.

The Townes–Dailey model [42] is a simple way of interpreting nuclear quadrupole coupling constants in terms of the electron distribution within the molecule XY. The model makes the following approximations:

1. Filled inner-core electrons associated with an atom remain spherically symmetric when the atom is subsumed into a molecule and therefore the efg at its nucleus remains zero. Thus, only valence electrons contribute to the efg. Of these, s electrons are assumed to remain spherically symmetric when in a molecule and therefore do not contribute.
2. Because the efg at a nucleus arising from a given electron varies with the distance of the electron from the nucleus according to $\langle r^{-3} \rangle$, the contributions to $q_{zz} = \partial^2 V^X / \partial z^2$ from electrons centred on atom Y are neglected.
3. Hence, only p,d,... valence electrons centred on X contribute to $\partial^2 V^X / \partial z^2$. These are, moreover, assumed to be in orbitals unperturbed from the free-atom orbitals. If the contribution of an electron characterised by quantum numbers n, l , and m to the efg in the free atom X is written as $q_{n,l,m}$, and recognising that for a p electron $2q_{n,1,1} = 2q_{n,1,-1} = -q_{n,1,0}$, it follows that, according to the Townes–Dailey approximation, the efg along the z direction at the nucleus of the halogen atom X (electronic configuration np^5) in the molecule XY is just $2q_{n,1,1} + 2q_{n,1,-1} + q_{n,1,0} = -q_{n,1,0}$ which is that arising from an absence of an np_z electron. Clearly, if we define the nuclear quadrupole coupling constant of free atom X as $\chi_A(X) = -eQ_X q_{n,1,0}^X$, then when the atom X is in the XY

molecule, the coupling constant of X is $\chi_{zz}(X) = -eQ_X q_{n,1,0}^X = \chi_A(X)$ in the Townes–Dailey approximation.

When a complex $B \cdots XY$ is formed by bringing up the Lewis base B to XY along the internuclear axis z of XY, the efgs at X and Y change. If we assume that the changes arise from a fraction δ_i of an electron transferred from B into the np_z orbital of X and a fraction δ_p of an electron transferred from X into the np_z orbital of Y, it follows that the nuclear quadrupole coupling constants in the equilibrium (e) geometry of $B \cdots XY$ are given by

$$\chi_{zz}^e(X) = \chi_0(X) - (\delta_i - \delta_p)\chi_A(X), \quad (7)$$

and

$$\chi_{zz}^e(Y) = \chi_0(Y) - \delta_p\chi_A(Y), \quad (8)$$

in which $\chi_0(X)$ and $\chi_0(Y)$ are the zero-point coupling constants of the free molecule XY but should strictly be equilibrium values $\chi_e(X)$ and $\chi_e(Y)$. This approximation can be used without introducing significant error, however. It is necessary to modify Eqs. (7) and (8) to allow for the fact that the XY subunit, when within the complex, undergoes zero-point vibrations, particularly an angular oscillation with respect to its centre of mass. These angular oscillations are small for $XY = \text{ICl}$ because of the large mass, but the very small corrections of Eqs. (7) and (8) resulting from the motion have been made and are discussed elsewhere [1–9, 19]. Equations (7) and (8) then provide a route to the values of δ_i and δ_p , but only for those complexes in which both X and Y carry quadrupolar nuclei. Such an approach is therefore possible for the complexes $B \cdots \text{ICl}$ under discussion in this chapter but not for $B \cdots \text{ICF}_3$. Nevertheless, we can use the (mainly small) δ_i for the former series to argue that net intermolecular charge transfer in the latter is probably going to be negligible. The fact that the δ_i values are usually small means that the approximations inherent in the Townes–Dailey model are not too serious here.

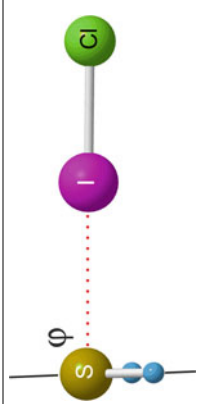

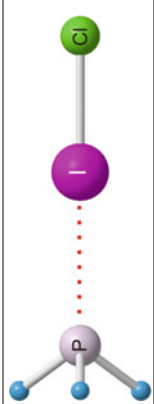


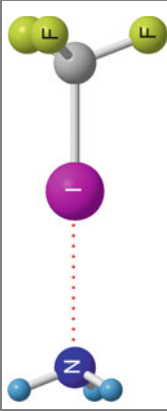
4 Comparison of Observed Properties of $B \cdots \text{ICl}$ and $B \cdots \text{ICF}_3$

4.1 Angular Geometry: Do Complexes $B \cdots \text{ICF}_3$ Obey the Rules?

The angular geometries determined for the two series of complexes $B \cdots \text{ICl}$ [1–9] and $B \cdots \text{ICF}_3$ [10–16], where $B = \text{N}_2, \text{CO}, \text{H}_2\text{O}, \text{C}_2\text{H}_2, \text{C}_2\text{H}_4, \text{H}_2\text{S}, \text{PH}_3$ and NH_3 , are shown in Table 1. Each was determined in the approximation that the r_0 geometries of the two separate components are unchanged by complex formation. The species when $B = \text{N}_2, \text{CO}, \text{PH}_3$ and NH_3 are either linear or symmetric-top molecules for

Table 1 Angular geometries of $B \cdots ICl$ and $B \cdots ICF_3$ in the gas phase

$B \cdots ICl$	Point group, Refs.	$B \cdots ICF_3$	Point group, Refs.
	C_{8v} , [1]		C_{3v} , [10]
	C_{8v} , [2]		C_{3v} , [11]
	C_{2v} , [3]		Highest symmetry ^a C_{2v} [12]
	C_{2v} , [4]		Highest symmetry ^a C_{2v} [13]
	C_s at equilibrium, C_{2v} in zero-point state, $\varphi = 46(2)^\circ$, [5]		Highest symmetry ^a C_s $\varphi = 34(2)^\circ$, [14]

	C_s at equilibrium and in zero-point state. $\varphi = 91.9(2)^\circ$, [6]		Highest symmetry ^a C_s , $\varphi = 93.7(2)^\circ$, [14]
	C_{3v} [9]		Highest symmetry ^a C_{3v} , [16]
	C_{3v} [8]		Highest symmetry ^a C_{3v} , [15]

^aThese molecules possess low barriers to internal rotation/other motion. The point group of highest symmetry achieved during the motion is given

both $B \cdots ICl$ and $B \cdots ICF_3$. Therefore their angular geometries are known and, under the approximation mentioned, only the internuclear distances $r_0(Z \cdots I)$ need to be determined to characterise the geometry completely. When $B = C_2H_2$ or C_2H_4 , various observations concerning nuclear spin statistical weight effects and relationships among the principal moments of inertia allow the conclusions that the complex is C_{2v} , T-shaped for $B = C_2H_2$, and that $C_2H_4 \cdots ICl$ has C_{2v} symmetry, with ICl lying along the C_2 axis of C_2H_4 that is perpendicular to the plane containing all the C_2H_4 nuclei. For $B = H_2O$, and H_2S , only the angles defined in each case in Table 1 are necessary in addition to determine the geometry fully, if unperturbed monomer geometries are again assumed. In the case of the $B \cdots ICF_3$ series (excluding $B = N_2$ and CO), there is a complication not present in the $B \cdots ICl$ series, namely that in each case there exists a very low potential energy barrier hindering the internal rotation of the CF_3 group against B . Such motion manifests itself in the observed rotational spectra as *vibrational satellites*, in this case rotational spectra in low-lying energy states associated with the hindered internal rotation. The ground-state spectra and the satellites were readily identified in the cases $B = NH_3$ [15] and PH_3 [16] and were analysed according to existing theory for such molecules. Only conclusions drawn from ground-state spectra are discussed here. When $B = H_2O$ [14], C_2H_2 [12], C_2H_4 [13] or H_2S [14] in $B \cdots ICF_3$, a satisfactory theory to account for internal rotation is not available, and it was more difficult to identify the ground-state rotational spectrum. For each, two sets of rotational spectra were observed, one of which could be fitted as a symmetric-top type spectrum while the other was of the expected asymmetric-top type. Each spectral analysis has its own difficulties and the reader is referred to the primary articles for detailed accounts of the fitting process and for detailed methods of interpreting the spectroscopic constants to give the molecular properties. The important point to note in connection with geometry for $B \cdots ICF_3$ for $B = H_2O$, C_2H_2 , C_2H_4 or H_2S is that, whichever of the two types of spectrum was fitted, the geometry obtained was not significantly different.

It is clear from an examination of Table 1 that, for a given B , the pair of complexes $B \cdots ICl$ and $B \cdots ICF_3$ are isomorphic in the sense that they have similar angular geometries. A simple model which accounts for this isomorphism is given below. It is based on a set of empirical rules first proposed for rationalising/predicting angular geometries of hydrogen-bonded complexes $B \cdots HX$ [43–45], but was later extended to include halogen-bonded species [17, 18, 26–30]. The original rules were based on electrostatics in the sense that the electrophilic end δ^+H of the HX molecules is assumed to seek out the most nucleophilic region of B . Nucleophilic regions of B are usually associated with non-bonding electron pairs or π -bonding electron pairs. The rules are as follows:

The angular geometries of hydrogen-bonded complexes $B \cdots HX$ in the gas phase can be predicted by assuming that in the equilibrium conformation the internuclear axis of the HX molecule lies:

1. Along the axis of a non-bonding electron pair (n -pair) carried by B , or
2. Along the local symmetry axis of a π orbital, if B carries no n -pairs or
3. If B carries both n - and π -pairs, rule 1 takes precedence

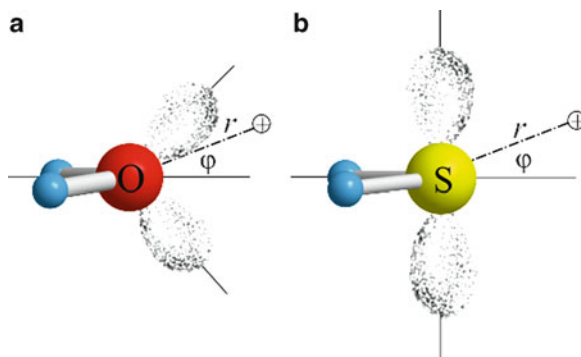


Fig. 3 The chemist's conventional model of the nonbonding electron pairs in (a) H_2O and (b) H_2S . The angle φ is defined in each case as the angle made by a line, of length r , joining a unit positive non-perturbing charge \oplus and the O or S atom with the C_2 axis. The line lies in the plane containing the n -pair axes. r , φ and \oplus are used in the description of the electrostatic potentials shown in Figs. 4 and 5

With these rules, the angular geometries of the hydrogen-bonded complexes $\text{B} \cdots \text{HX}$, where $\text{X} = \text{F}, \text{Cl}, \text{Br}, \text{I}, \text{CN}$ or CCH , have been rationalised for a wide range of Lewis bases B , as described elsewhere [43–45]. It has also been shown more recently that the rules, when modified by replacing $\text{B} \cdots \text{HX}$ and HX by $\text{B} \cdots \text{XY}$ and XY , respectively, also apply to halogen-bonded complexes of the type $\text{B} \cdots \text{XY}$, in which XY is one of the dihalogen molecules $\text{F}_2, \text{ClF}, \text{Cl}_2, \text{BrCl}, \text{Br}_2$ or ICl [17, 18]. The range of Lewis bases B investigated was the most extensive in the case of $\text{XY} = \text{ClF}$ and was similar to that used for the $\text{B} \cdots \text{HCl}$ series. A close parallelism between the angular geometries of $\text{B} \cdots \text{HX}$ and $\text{B} \cdots \text{XY}$ was identified and led to the proposal [17, 18] of a halogen bond $\text{B} \cdots \text{XY}$ in the gas phase which is the analogue of the more familiar hydrogen bond.

Do these rules apply to complexes formed by halogen bond donors such as ICF_3 as well as by dihalogen molecules XY ? The similarity of the angular geometries of the $\text{B} \cdots \text{ICl}$ and the $\text{B} \cdots \text{ICF}_3$ evident in Table 1 suggests that they do. The angular geometries of $\text{H}_2\text{Z} \cdots \text{ICl}$ and $\text{H}_2\text{Z} \cdots \text{ICF}_3$ when Z is either O or S are particularly important in establishing this result, as indeed were the angular geometries of $\text{H}_2\text{Z} \cdots \text{HX}$ and $\text{H}_2\text{Z} \cdots \text{XY}$ in first formulating the rules for the hydrogen bond and the halogen bond. Given simple electronic models of H_2O and H_2S , the rules also provide an explanation of why the complexes $\text{H}_2\text{S} \cdots \text{HX}$ [45] and $\text{H}_2\text{S} \cdots \text{XY}$ [18] (including $\text{XY} = \text{ICF}_3$ [14]) are permanently pyramidal on the microwave timescale, while their H_2O analogues [14, 18, 45] are inverting and effectively planar.

In the electronic model of H_2O , we assume sp^3 hybridisation of the 2s and 2p orbitals of O. A diagram of this model of H_2O is shown in Fig. 3a and has been drawn with the exaggerated n -pair electron density distributions frequently employed in chemistry. This familiar approach accounts for an HOH angle that is not far from tetrahedral and it implies a similar angle between the axes of the two n -pairs carried by O, which therefore requires an angle φ (see Table 1 for definition of the angle φ) close to 50° for $\text{H}_2\text{O} \cdots \text{HX}$ and $\text{H}_2\text{O} \cdots \text{XY}$ complexes. On the other hand, to explain the HSH angle close to 90° in free H_2S , we might invoke S–H bonds formed by

overlap of two 3p orbitals ($3p_x$ and $3p_y$, say) on S with 1s orbitals of H and then place each n -pair in a sp hybrid orbital formed from 3s and $3p_z$ on S. Such a model then requires an angle of 180° between the n -pairs on S, and consequently an angle φ close to 90° (see Fig. 3b and Table 1). Moreover, the larger angle implies a much wider potential energy barrier to inversion of the configuration at S in $\text{H}_2\text{S}\cdots\text{HX}$ and $\text{H}_2\text{S}\cdots\text{XY}$ than that at O in $\text{H}_2\text{O}\cdots\text{HX}$ and $\text{H}_2\text{O}\cdots\text{XY}$. Alternatively, in an unhybridised model for H_2S , one n -pair is viewed as occupying a $3p_z$ orbital while the other occupies the 3s orbital. If the weak interaction is via the n -pair in $3p_z$, the geometrical consequences are identical to those of the hybridised version.

It was pointed out some time ago [45] that this difference in the n -pair angular electron density distributions of H_2O and H_2S is consistent with simple electrostatics. The electric charge distribution of a molecule can be accurately described by sets of point multipoles (charges, dipoles and quadrupoles) placed on atoms and sometimes at the centres of bonds. The values of the multipoles are determined by a *distributed multipole analysis*, as proposed by Stone [46], of the ab initio wavefunction of the molecule. Buckingham and Fowler [47] have provided accurate electric charge distributions for H_2O and H_2S by using this approach. Once the DMA is available, it is straightforward to calculate the electrostatic potential, electric field, etc. at any point outside the molecule in question (by using the **T** tensor formalism set out by Buckingham [48]) without any of the convergence problems experienced when the molecular electric moments are used instead of the DMA to describe the charge distribution. Figure 4 shows the electrostatic potential (the potential energy of a non-perturbing, unit point positive charge \oplus) $V(\varphi)$ plotted against the angle φ (as defined in Fig. 3a) at each of two distances ($r = 1.50$ and 1.75 Å) of \oplus from the O atom. The unit charge \oplus lies at all times in the plane of the n -pair axes and is kept at a fixed distance from the oxygen atom of H_2O . The distance $r = 1.50$ Å is similar to that of the $\delta^+\text{H}$ atom of HF from O in the complex $\text{H}_2\text{O}\cdots\text{HF}$. Figure 4 shows that the electrostatic potential $V(\varphi)$ for $r = 1.50$ Å has two minima at φ ca. $\pm 45^\circ$, i.e. at approximately the angle defined by the n -pair axis directions, and has a low barrier at the planar ($\varphi = 0$) arrangement. The minima deepen and separate as r decreases. The reasons why the minima in the energy do not occur closer to the $\pm 54^\circ$ required by a tetrahedral disposition of electron pairs in H_2O are understood and have been discussed elsewhere [45]. As r increases to 1.75 Å, the minima draw together and the barrier height decreases rapidly but is still non-zero. The results of applying the same procedure to H_2S at each of two different distances $r = 2.33$ and 2.80 Å, the first of which corresponds to the $\text{S}\cdots\delta^+\text{H}$ distance in $\text{H}_2\text{S}\cdots\text{HF}$, are shown in Fig. 5 (see Fig. 3b for the corresponding definitions of r and φ). At both distances, two minima occur at ca. $\pm 85^\circ$, very similar to that (90°) expected of the n -pair model shown in Fig. 3b. It should be noted that the potential energy barrier is higher and the angle between the minima is much larger than is the case for H_2O (see Fig. 4), even when r is increased from 2.33 to 2.80 Å. The diagrams in Figs. 4 and 5 (and similar diagrams in [45]) demonstrate that the experimental observations about angular geometry and the rules deduced from them are consistent with an electrostatic model of the hydrogen bond. It is also of interest to note that although n -pairs are difficult to discern in the total electron densities of H_2S and H_2O ,

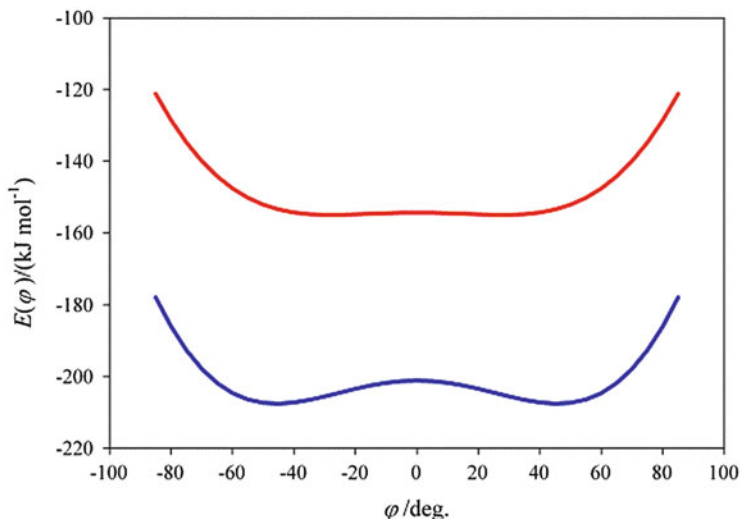


Fig. 4 The electrostatic potential $E(\varphi)$ near to the oxygen atom in H_2O as a function of the angle φ defined in Fig. 3a. The electrostatic potential is the potential energy of a non-perturbing unit positive charge at (r, φ) . The *upper curve* is generated by taking \oplus around the O atom in the plane containing the n -pair axes at the fixed distance $r = 1.5 \text{ \AA}$. The *lower curve* is obtained in a similar way at the distance $r = 1.75 \text{ \AA}$. See text for discussion

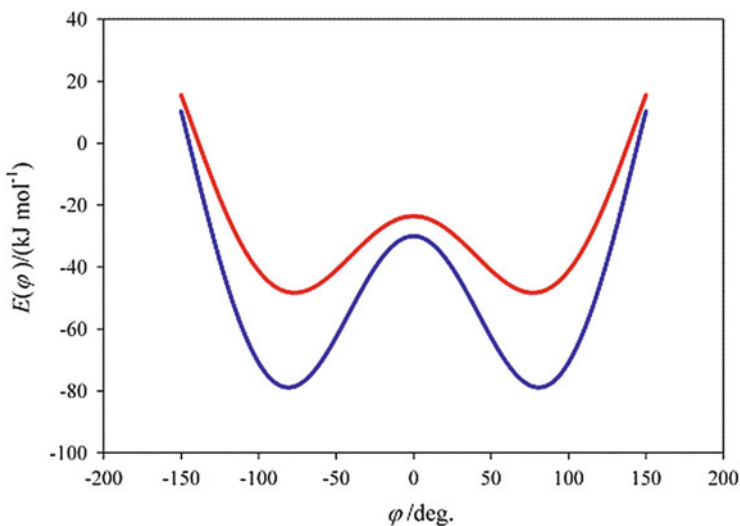


Fig. 5 The electrostatic potential $E(\varphi)$ close to the sulfur atom in H_2S as a function of the angle φ defined in Fig. 3b. The electrostatic potential is the potential energy of a non-perturbing unit positive charge at (r, φ) . The *upper curve* is generated by taking \oplus around the S atom in the plane containing the n -pair axes at the fixed distance $r = 2.33 \text{ \AA}$. The *lower curve* is obtained in a similar way at the distance $r = 2.80 \text{ \AA}$. See text for discussion

the electrostatic potentials around S and O show minima along those directions normally associated with n -pairs in the exaggerated models of Fig. 3.

The complexes $\text{H}_2\text{Z} \cdots \text{ICl}$ and $\text{H}_2\text{Z} \cdots \text{ICF}_3$ ($\text{Z}=\text{O}$ or S) can be examined in more detail in the light of the foregoing discussion of electronic models of H_2O and H_2S . It was shown by means of observations in the rotational spectra of both $\text{H}_2\text{O} \cdots \text{ICl}$ [5] and $\text{H}_2\text{O} \cdots \text{ICF}_3$ [14] that the H, O and I atoms must be effectively coplanar in the zero-point state, i.e. the potential energy as a function of the angle φ (see Table 1 for definition of φ) is either of the single minimum type with $\varphi = 0$ at the minimum or is of the double minimum type ($|\varphi_{\min}| > 0$) but with a barrier at $\varphi = 0$ sufficiently low that inversion of the configuration at O is rapid on the microwave timescale. Thus, the ground-state vibrational wavefunction reflects the symmetry of the coplanar arrangement. On the other hand, interpretations of the rotational spectra of both $\text{H}_2\text{S} \cdots \text{ICl}$ [6] and $\text{H}_2\text{S} \cdots \text{ICF}_3$ [14] reveal that in these complexes the potential energy barrier to the coplanar arrangement of the H, S and I atoms is sufficiently high and wide that inversion of the configuration is slow on the microwave timescale and the configuration at S is therefore permanently pyramidal on that timescale. Similar contrasting results were found experimentally for $\text{H}_2\text{O} \cdots \text{HF}$ [49] and $\text{H}_2\text{S} \cdots \text{HF}$ [50, 51] and provide further evidence that the simple electrostatic n -pair model is appropriate for $\text{H}_2\text{Z} \cdots \text{ICl}$ and $\text{H}_2\text{Z} \cdots \text{ICF}_3$ ($\text{Z}=\text{O}$ or S). These semi-quantitative conclusions about the general forms of the potential energy functions $V(\varphi)$ available from the rotational spectra and from the simple electrostatic model were confirmed and made quantitative by means of ab initio calculations as follows.

The geometry of each $\text{H}_2\text{Z} \cdots \text{IR}$ ($\text{Z} = \text{O}$ or S ; $\text{R} = \text{Cl}$ or CF_3) was optimised at a fixed angle φ at the CCSD(T)(F12*)/cc-pVDZ-F12 level of theory to give the energy $V(\varphi)$ using the MOLPRO program [52]. A collinear arrangement $\text{Z} \cdots \text{I}-\text{R}$ of the halogen bond was assumed. The explicitly correlated (F12*) level of theory [53, 54] was the best compromise between accuracy and computational time available. For iodine, the cc-pVDZ-PP-F12 basis set, where PP indicates a pseudopotential replacing the 28 inner core electrons, was used [55]. The CF_3I and H_2Z molecules were assumed to retain their C_{3v} and C_{2v} symmetries, respectively, when subsumed into the complex. In the cases of $\text{H}_2\text{O} \cdots \text{ICF}_3$ and $\text{H}_2\text{S} \cdots \text{ICF}_3$ there is the additional degree of vibrational (torsional) freedom associated with the internal rotation of the H_2Z molecule with respect to the CF_3 group. In fact, the potential energy barrier to internal rotation is extremely small in these molecules. At the level of theory employed, the difference in energy (expressed as a wavenumber here) between the two limiting forms in which the $\text{Z}-\text{H}$ bonds are eclipsed and staggered with respect to the $\text{C}-\text{F}$ bonds is at most a few cm^{-1} , whatever the angle φ . In the calculations reported here, the energy obtained refers to the fixed angle φ with the $\text{C}-\text{F}$ and $\text{Z}-\text{H}$ bonds fully staggered. This procedure was repeated for a sufficient range of φ values to give $V(\varphi)$ as a function of φ . Corrections for basis set superposition error are small for basis functions optimised for F12 methods (for example, the BSSE corrections to the PE barrier heights of 115 and $1,175 \text{ cm}^{-1}$ in $\text{H}_2\text{O} \cdots \text{HF}$ and $\text{H}_2\text{S} \cdots \text{HF}$, respectively, corresponded to only 4 and 16 cm^{-1} (Legon and Tew (2014), unpublished observations)) and have

not been applied here. Potential energy functions generated in this manner for various $\text{H}_2\text{O} \cdots \text{HX}$, $\text{H}_2\text{O} \cdots \text{XY}$, $\text{H}_2\text{S} \cdots \text{HX}$ and $\text{H}_2\text{S} \cdots \text{XY}$ complexes [49, 56–58] can be fitted (by the least-squares method) with reasonable accuracy to an analytical, double-minimum potential energy function of the type

$$V(\varphi) = \alpha\varphi^4 - \beta\varphi^2, \quad (9)$$

where α and β are positive constants. This type of function can be readily converted to the form

$$V(z) = a(z^4 - bz^2), \quad (10)$$

in which z is a dimensionless, reduced coordinate related to φ by means of the expression

$$\varphi = (r_{\text{H}} \cos \frac{1}{2}\theta)^{-1} (2\mu/\hbar^2)^{-\frac{1}{2}} a^{-\frac{1}{2}} z, \quad (11)$$

In Eq. (11), r_{H} is the Z–H distance, θ is the angle HZH and μ is the reduced mass for the inversion in question. When a curvilinear motion is assumed for the H atoms of H_2Z in $\text{H}_2\text{Z} \cdots \text{IR}$ ($\text{R} = \text{Cl}$ or CF_3), the definition of the reduced mass appropriate to the form $V(\varphi) = \alpha\varphi^4 - \beta\varphi^2$ is [49, 59]

$$\begin{aligned} \frac{1}{\mu} = & \frac{1}{M_{\text{XY}}} \left(\frac{r_{\text{H}} \cos \frac{1}{2}\theta}{r_{\text{cm}}} \right)^2 + \frac{1}{4M_{\text{H}}} + \frac{1}{4M_{\text{X}}} \\ & + \frac{1}{M_{\text{Z}}} \left\{ \left(\frac{r_{\text{H}} \cos \frac{1}{2}\theta}{r_{\text{cm}}} \right)^2 + \frac{2r_{\text{H}} \cos \frac{1}{2}\theta \cos \varphi}{r_{\text{cm}}} + 1 \right\}. \end{aligned} \quad (12)$$

The expressions that relate the coefficients α , β , a and b are

$$\alpha = (r_{\text{H}} \cos \frac{1}{2}\theta)^4 (2\mu/\hbar^2)^2 a^3, \quad (13)$$

and

$$\beta = (r_{\text{H}} \cos \frac{1}{2}\theta)^2 (2\mu/\hbar^2) a^2 b. \quad (14)$$

The energy levels associated with the one-dimensional motion described by the reduced coordinate z and governed by the potential energy expression Eq. (10) can be calculated by using the program *Anharm*.¹ These energy levels (expressed as wavenumbers) for $\text{H}_2\text{O} \cdots \text{ICl}$ and $\text{H}_2\text{O} \cdots \text{ICF}_3$ are shown together with the

¹The program *Anharm* was originally developed by Johan Mj6berg (see [60]). The version used here is the one modified by Kisiel Z. <http://www.ifpan.edu.pl/~kisiel/prospe.htm>

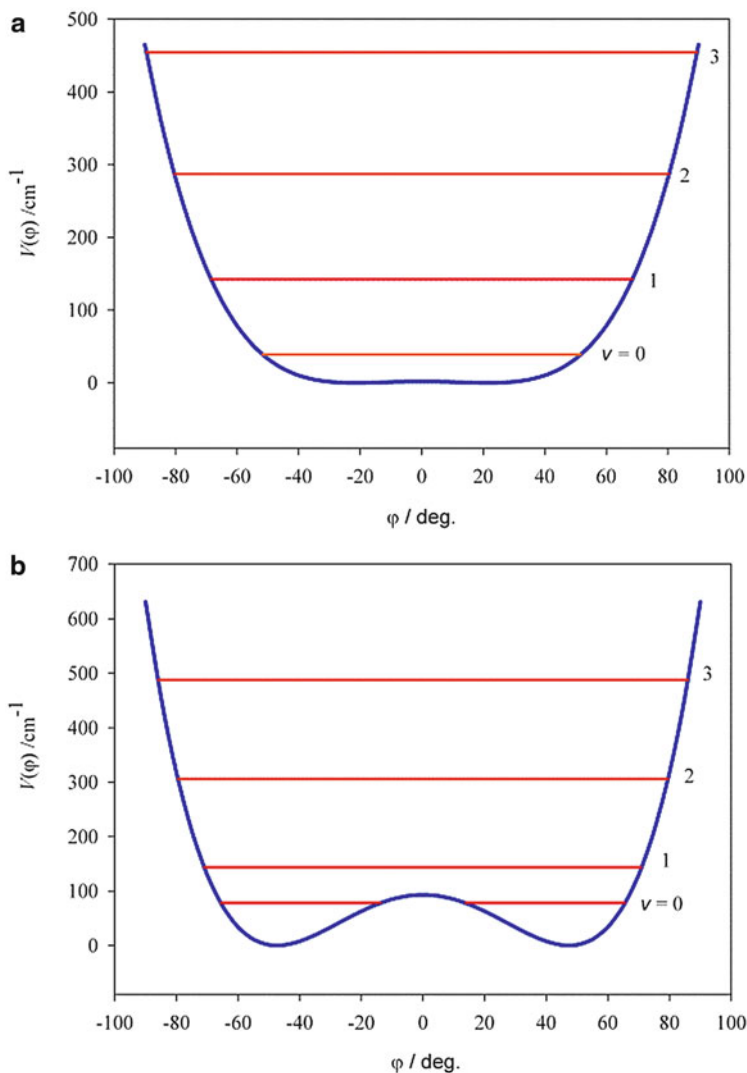


Fig. 6 The potential energy $V(\varphi)$ of the molecules (a) $\text{H}_2\text{O}\cdots\text{ICl}$ and (b) $\text{H}_2\text{O}\cdots\text{ICF}_3$ as a function of the angle φ made by the extension of the C_2 axis of the H_2O molecule with the $\text{O}\cdots\text{I}$ internuclear axis (as defined in Table 1). Each curve corresponds to a spline-function fit of the energies of the optimized geometry obtained at each of a series of angles φ , when varied in 5° steps from 0° to 100° . The geometry was optimized at the CCSD(T)(F12*)/cc-pVDZ-F12 level of theory at each angle. The method of obtaining the vibrational energy levels v associated with the potential energy curve is discussed in the text

corresponding fitted functions $V(\varphi) = \alpha\varphi^4 - \beta\varphi^2$ in Fig. 6a, b, respectively, while the results for $\text{H}_2\text{S}\cdots\text{ICl}$ and $\text{H}_2\text{S}\cdots\text{ICF}_3$ are in Fig. 7a, b, respectively. We note that the functions and their associated energy levels confirm that both $\text{H}_2\text{O}\cdots\text{ICl}$

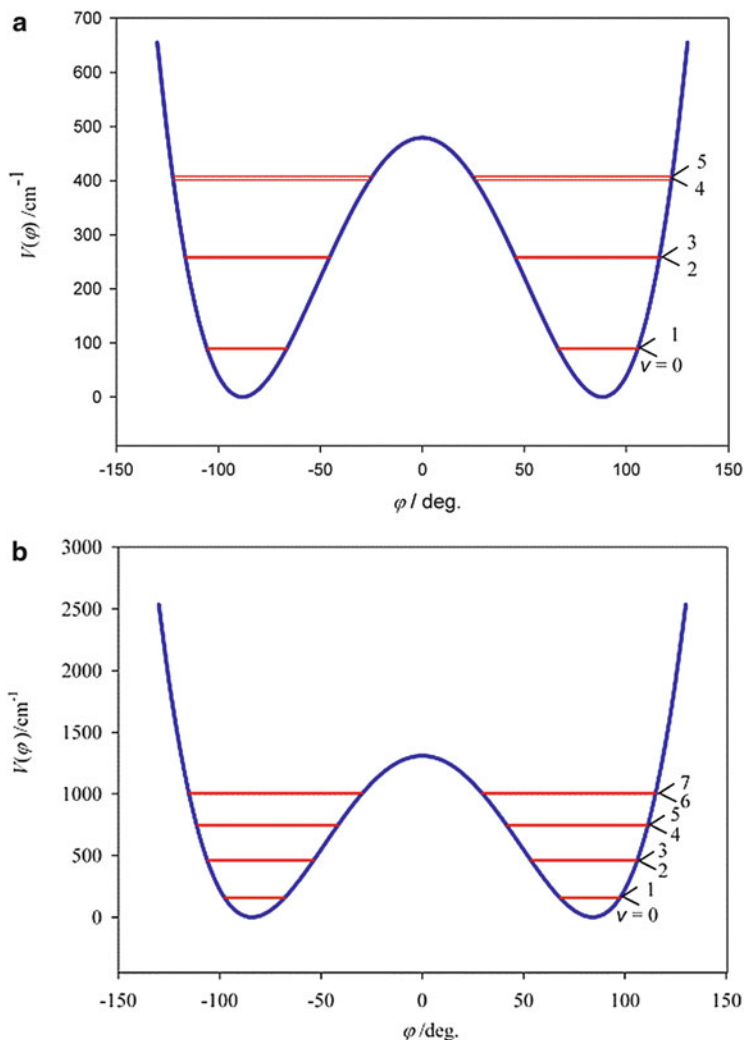


Fig. 7 The potential energy $V(\varphi)$ of the molecules (a) $\text{H}_2\text{S} \cdots \text{ICl}$ and (b) $\text{H}_2\text{S} \cdots \text{ICF}_3$ as a function of the angle φ made by the extension of the C_2 axis of the H_2S molecule with the $\text{S} \cdots \text{I}$ internuclear axis (as defined in Table 1). The method of obtaining the potential energy curve and its associated vibrational energy levels is as referred to in the legend for Fig. 6

and $\text{H}_2\text{O} \cdots \text{ICF}_3$ have a sufficiently low potential energy barrier to the planar configuration at O to ensure that the molecules are effectively planar in the sense defined earlier. Indeed, the PE barrier in the case of $\text{H}_2\text{O} \cdots \text{ICF}_3$ is so close to zero ($< 2 \text{ cm}^{-1}$) that the $\text{H}_2\text{O} \cdots \text{I}-\text{C}$ group of atoms may be taken as planar. The frequency associated with the motion that inverts the configuration at O (or S) corresponds to the separation between the two lowest energy levels ($v = 0$ and 1). The inversion frequency for both $\text{H}_2\text{O} \cdots \text{ICl}$ and $\text{H}_2\text{O} \cdots \text{ICF}_3$ is very much greater

than the (microwave) frequencies associated with rotational transitions and in that sense the molecule is planar on the microwave timescale but pyramidal at equilibrium. This conclusion holds for all halogen-bonded complexes $\text{H}_2\text{O} \cdots \text{XY}$ and all hydrogen-bonded complexes $\text{H}_2\text{O} \cdots \text{HX}$ so far investigated and the potential energy functions for all $\text{H}_2\text{O} \cdots \text{HX}$ (Legon AC, Tew DP (2014), unpublished observations) [49, 56–58] are similar to those for $\text{H}_2\text{O} \cdots \text{ICl}$ and $\text{H}_2\text{O} \cdots \text{ICF}_3$.

It is a well-known property of double minimum functions such as those discussed here that, as the associated energy levels drop below the top of the potential energy barrier, they draw together rapidly in pairs and in the limit of a high, wide barrier the members of each pair become degenerate. Both $\text{H}_2\text{S} \cdots \text{ICl}$ and $\text{H}_2\text{S} \cdots \text{ICF}_3$ have potential energy functions $V(\varphi)$ in which the barrier is sufficiently high and broad that the lower energy levels exhibit this effect (see Fig. 7a, b). In both cases, the separation between the lowest energy pair ($\nu = 0$ and 1) corresponds to a frequency of less than a few kilohertz, i.e. very small on the microwave timescale. Clearly, both $\text{H}_2\text{S} \cdots \text{ICl}$ and $\text{H}_2\text{S} \cdots \text{ICF}_3$ have non-inverting pyramidal configurations at S. This difference in the height and width of the potential energy barrier at $\varphi = 0$ between the H_2S and H_2O complexes can be understood in the light of the discussion of the electrostatic potential outside these molecules given earlier.

The near-degeneracy of the $\nu = 0$ and 1 levels has been noted for all halogen-bonded complexes $\text{H}_2\text{S} \cdots \text{XY}$ and hydrogen-bonded complexes $\text{H}_2\text{S} \cdots \text{HX}$ investigated so far (Legon and Tew (2014), unpublished observations) and leads to consequences (e.g. absence of certain transitions) in the rotational spectra when observed at very low temperatures in supersonically expanded gas pulses. When identified, such consequences allow the conclusion that these molecules are pyramidal at S.

4.2 Radial Geometry: How Do the Halogen Bond Distances $Z \cdots I$ Vary from $B \cdots \text{ICl}$ to $B \cdots \text{ICF}_3$?

Table 2 compares the distances $r(Z \cdots I)$ in $B \cdots \text{ICl}$ and $B \cdots \text{ICF}_3$ obtained through interpretation of spectroscopic constants (see Sect. 3.1) with those calculated ab initio at the CCSD(T)(F12*)/cc-pVDZ-F12 level of theory, where Z is either the halogen bond acceptor atom or centre (in those cases where B is a π electron donor). In the geometry optimisations, collinear $Z \cdots \cdots \text{I}-\text{C}$ and $Z \cdots \text{I}-\text{Cl}$ nuclei were assumed for $B = \text{H}_2\text{O}$ and H_2S , i.e. in those complexes for which these systems were not constrained by symmetry to be collinear. In the complexes $\text{C}_2\text{H}_2 \cdots \text{IR}$ and $\text{C}_2\text{H}_4 \cdots \text{IR}$, small angular distortions ($< 1^\circ$) resulting from a symmetrical movement of the H atoms away from the line of the two C atoms were detected.

Table 2 Observed and calculated intermolecular bond lengths $r(Z \cdots I)$ in complexes $B \cdots ICF_3$ and $B \cdots ICl$

Lewis base B	$r_0(Z \cdots I)/\text{\AA}$ from experiment			$r_e(Z \cdots I)/\text{\AA}$ calculated ab initio ^a			$\sigma(Z) + \sigma(I)/\text{\AA}^b$
	$B \cdots ICF_3$	$B \cdots ICl$	Δr	$B \cdots ICF_3$	$B \cdots ICl$	Δr	
N ₂	3.441(1) ^c	3.180(2) ^d	0.258(3)	3.467	3.187	0.280	3.53
OC	3.428(1) ^e	3.011(1) ^f	0.417(2)	3.456	3.003	0.453	3.68
HCN	...	2.850(1) ^g	...	3.168	2.840	0.328	3.53
C ₂ H ₄	3.434(2) ^h	3.032(2) ⁱ	0.402(4)	3.428	2.959	0.469	3.68
C ₂ H ₂	3.442(2) ^j	3.115(2) ^k	0.327(4)	3.453	3.090	0.363	3.68
H ₂ O	3.053(2) ^l	2.828(1) ^m	0.225(3)	3.044	2.776	0.268	3.50
H ₂ S	3.559(1) ^l	3.154(3) ⁿ	0.405(4)	3.559	3.120	0.439	3.78
H ₃ P	3.571(3) ^o	2.963(1) ^p	0.608(4)	3.597	2.898	0.699	3.78
H ₃ N	3.038(1) ^q	2.711(2) ^r	0.327(3)	2.991	2.599	0.392	3.53

^aCalculations at the CCSD(T)(F12*)/cc-pVDZ-F12 level of theory^bFrom [62], ^c[10], ^d[1], ^e[11], ^f[2], ^g[7], ^h[13], ⁱ[4], ^j[12], ^k[3], ^l[14], ^m[5]. The value 2.838 Å quoted in [5] is a misprint. ⁿ[6], ^o[16], ^p[9], ^q[15], ^r[8]

Also recorded in Table 2 are the experimental and calculated differences $\Delta r(Z \cdots I)$ in the length of the halogen bonds of $B \cdots ICF_3$ and $B \cdots ICl$. It is known (see Section 3.1) that the experimental distances are of the r_0 variety, while those from the ab initio calculations are r_e values. We note several points in connection with Table 2. First, the distances $r(Z \cdots I)$ are well predicted by the ab initio calculations for the complexes $B \cdots ICl$, with the exception of $B = NH_3$ for which the experimental value is ~ 0.1 Å longer than that calculated. The complex $H_3N \cdots ICF_3$ is, however, well-behaved in this respect. Of relevance here is the distance $r_e(N \cdots I) = 2.605$ Å obtained from a geometry optimisation of $H_3N \cdots ICl$ conducted at the counterpoise corrected, CCSD(T)(F12b)/VTZ level of theory [61]. This differs by only 0.006 Å from the value reported in Table 2. Mostly, the r_0 quantities are slightly longer than the calculated r_e values but not always. For diatomic molecules, it is known that $r_0 > r_e$ and this order is expected for normal polyatomic molecules. Second, the $Z \cdots I$ bond is systematically longer in $B \cdots ICF_3$ than in $B \cdots ICl$ complexes, a result consistent with the finding reported in Sect. 4.3 that, for a given B, the intermolecular bond is stronger in $B \cdots ICl$ complexes than in their $B \cdots ICF_3$ analogues, as measured by the intermolecular stretching force constant k_σ . The ab initio values of Δr are always larger than the experimental quantities. In both $B \cdots ICl$ and $B \cdots ICF_3$ the distances $r(Z \cdots I)$ are significantly shorter than the sums of the van der Waals radii $\sigma(Z)$ and $\sigma(I)$ [62] of the atoms Z and I, which are also given in Table 2. This is readily understood in terms of the σ -hole concept for the halogen bond (see Sect. 4.3) introduced by Politzer et al. [63]. The σ -hole is closely related to the reduced van der Waals radius along the bond in Cl_2 , for example, relative to that perpendicular to it, as discussed by Stone [64] and others [65], and to the known sign of the molecular electric quadrupole moment of Cl_2 .

4.3 Intermolecular Stretching Force Constants k_σ : How Does Replacement of Cl in $B \cdots ICl$ by CF_3 Change the Electrophilicity of the Halogen Bond Donor Molecule?

The measure of the binding strength of $B \cdots ICF_3$ and $B \cdots ICl$ complexes in the gas phase that is most commonly available experimentally is the intermolecular stretching force constant k_σ , the method for the determination of which from centrifugal distortion constants was set out in Sect. 3.2. Values of k_σ obtained in this way for both series are set out in Table 3.

It is clear from Table 3 that complexes $B \cdots ICl$ are systematically stronger than the corresponding complexes $B \cdots ICF_3$ according to the k_σ criterion (i.e. the restoring force required for infinitesimal increase of the intermolecular bond length $Z \cdots I$), with the ratio $k_\sigma(B \cdots ICl)/k_\sigma(B \cdots ICF_3)$ of the order 2 or 3.

It has been shown [66] that the intermolecular stretching force constant k_σ for hydrogen-bonded complexes $B \cdots HX$ ($X=F, Cl, Br, I$ or CN) can be reproduced with reasonable accuracy by means of the expression

$$k_\sigma = cN_B E_{HX}, \quad (15)$$

in which N_B is a numerical nucleophilicity assigned to the Lewis base B , E_{HX} is a numerical electrophilicity of the acid HX and $c = 0.25 \text{ N m}^{-1}$ is a constant. A similar expression (but with E_{HX} replaced by E_{XY}) also holds for the halogen-bonded complexes $B \cdots XY$ ($XY = F_2, ClF, Cl_2, BrCl, Br_2$ or ICl). Figure 8 shows the value of k_σ plotted against N_B for the six series $B \cdots F_2$, $B \cdots ClF$, $B \cdots Cl_2$,

Table 3 Experimental values of k_σ intermolecular stretching force constants for the series $B \cdots ICl$ and $B \cdots ICF_3$; a measure of binding strength

B	$k_\sigma/(\text{N m}^{-1})^a$		$D_e/(\text{kJ mol}^{-1})^b$	
	$B \cdots ICF_3$	$B \cdots ICl$	$B \cdots ICF_3$	$B \cdots ICl$
N_2	2.954(1) ^c	5.35(2) ^d	4.2	7.1
OC	3.950(2) ^e	7.96(3) ^f	6.2	12.7
HCN	...	14.5(1) ^g	13.9	23.7
C_2H_4	4.95(1) ^h	14.0(1) ⁱ	10.2	21.5
C_2H_2	4.96(7) ^j	12.1(1) ^k	9.2	17.2
H_2O	8.8(1) ^l	15.9(2) ^m	14.9	24.7
H_2S	6.7(1) ^l	16.55(5) ⁿ	10.5	22.6
H_3P	6.27(2) ^o	20.7(1) ^p	10.4	28.9
H_3N	11.6(2) ^q	30.4(3) ^r	22.5	46.8

^aCalculated from centrifugal distortion constant D_J or Δ_J using the appropriate expression given in Sect. 3.2. Errors reflect only the experimental error in the centrifugal distortion constants

^bCalculated at the CCSDT(T)(F12*)/cc-pVDZ-F12 level of theory and corrected for BSSE. See also [67] for D_e values for the complexes $B \cdots ICl$, ^c[10], ^d[1], ^e[11], ^f[2], ^g[7], ^h[13], ⁱ[4], ^j[12], ^k[3], ^l[14], ^m[5], ⁿ[6], ^o[16], ^p[9], ^q[15], ^r[8]

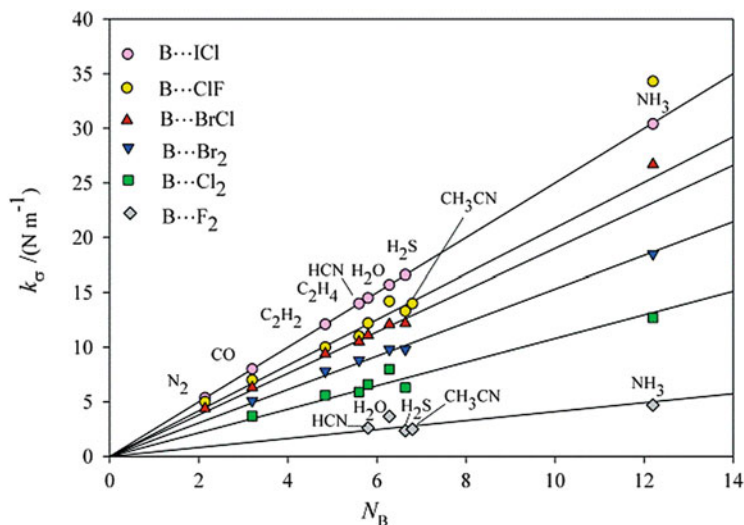


Fig. 8 The intermolecular force constant k_σ plotted against the nucleophilicity N_B of the Lewis base B for six series of halogen-bonded complexes $B \cdots XY$ ($XY = F_2, ClF, Cl_2, BrCl, Br_2$ or ICl). The values of N_B were defined by arranging the k_σ of the series $B \cdots ICl$ to lie on a straight line. The slope of each line yields the electrophilicity E_{XY} by means of Eq. (15) and the value $c = 0.25 \text{ N m}^{-1}$

$B \cdots BrCl$, $B \cdots Br_2$ and $B \cdots ICl$ [18, 28] for a range of simple Lewis bases B. The scale of N_B was defined by setting $E_{ICl} = 10.0$ and requiring that all points for the $B \cdots ICl$ plot lie on a perfectly straight line $k_\sigma = cN_B E_{ICl}$. The other five series of k_σ values are seen to lie on reasonably straight lines which pass through the origin when plotted against the N_B values so defined, although the points $B = NH_3$ are less well-behaved, probably because of significant polarization of charge on complex formation. The slopes of the lines in Fig. 8 are proportional to E_{XY} and indicate that the order of electrophilicity of the dihalogen molecules is $F_2 < Cl_2 < Br_2 < BrCl \sim ClF < ICl$. This order is in agreement with chemical intuition. The non-dipolar dihalogens have the smaller electrophilicities and these are in the order of their molecular electric quadrupole moments. The three polar species are more electrophilic. The question that now arises is whether Eq. (15) applies to $B \cdots ICF_3$ complexes and, if so, how does the electrophilicity of ICF_3 as a halogen bond donor compare with those of the dihalogen molecules in general and ICl in particular?

Figure 9 again shows k_σ plotted against N_B for the series $B \cdots ICl$, with $E_{ICl} = 10.0$ and the N_B values as defined in connection with Fig. 8. Also shown in Fig. 9 is the corresponding plot for the series $B \cdots ICF_3$. It is a reasonably straight line, with a slope which is about three times smaller than that for ICl but similar to that for the $B \cdots Cl_2$ series shown in Fig. 8. Evidently, the CF_3 group is less electron-withdrawing than Cl when bound to I and reduces the halogen bond donor ability of I to make it similar to that of Cl in Cl_2 .

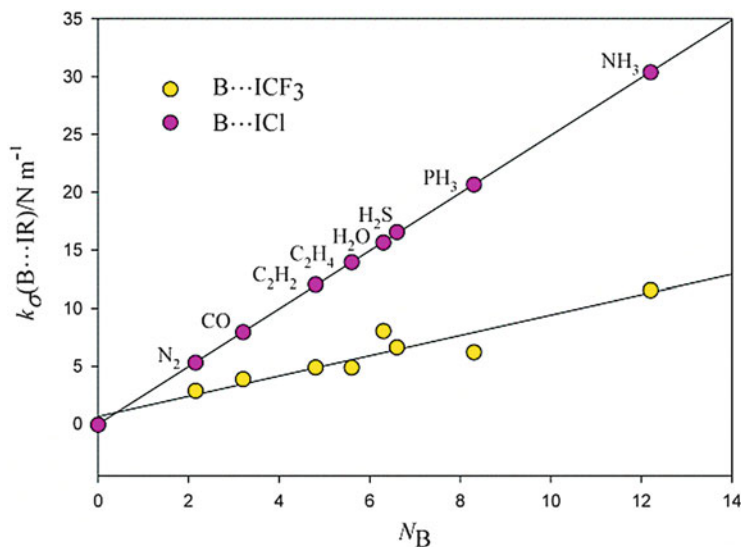
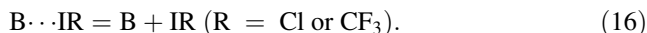


Fig. 9 k_σ plotted against N_B for the two series $B \cdots ICl$ and $B \cdots ICF_3$. The values of N_B were defined by arranging for the k_σ of the series $B \cdots ICl$ to lie on a straight line

Another measure of binding strength is the equilibrium dissociation energy D_e for the process



Values of D_e calculated at the explicitly correlated level of theory CCSD(T)(F12*)/cc-pVDZ-F12 are included in Table 3 for all $B \cdots ICF_3$ and $B \cdots ICl$. The calculations for the $B \cdots ICl$ series were carried out in connection with a detailed analysis of D_e values for many $B \cdots XY$ and $B \cdots HX$ [67]. Corrections for basis set superposition error, although much reduced for F12-optimised basis functions, have been applied by using the Boys–Bernardi method [68]. The values of D_e shown in Table 3 for $C_2H_2 \cdots ICF_3$ and $C_2H_4 \cdots ICF_3$ are similar to those implied by measurement of ΔH for the process in liquid argon solution by Herrebout et al. and also D_e calculated by them at the MP2/aug-cc-pVTZ level of theory [69, 70]. Recent calculations at the MP2/DZVP level for $H_3N \cdots ICF_3$ and at the CCSDT(F12b)/VTZ-F12 level for $H_3N \cdots ICl$ yield $D_e = 24.3$ [71] and 54.0 kJ mol^{-1} [61], respectively. In general, the D_e values presented in Table 3 confirm the conclusion based on k_σ values, namely that, for a given B, the complex $B \cdots ICF_3$ is more weakly bound than the $B \cdots ICl$ complex. Moreover, k_σ and D_e appear to be proportional, as noted for the $H_3N \cdots XY$ series discussed in ref. [61] and established for a wide range of $B \cdots XY$ and $B \cdots HX$ in ref. [67].

This conclusion, based on two measures of binding strength (k_σ and D_e), is consistent with the σ -hole concept introduced by Politzer and co-workers [63]. The

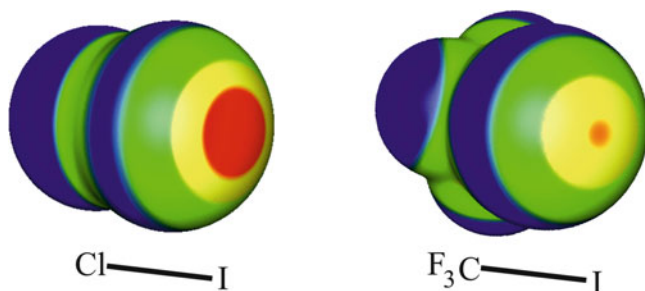


Fig. 10 The molecular electrostatic surface potentials (MESP) of ICl and ICF₃. Electrostatic potentials were computed on the 0.001 electron bohr⁻³ molecular surfaces using M06-2X/6-311G* optimisations for each molecule (see [63] for method of calculation). Colour ranges, in kJ mol⁻¹, are: red > 125, 125 > yellow > 63, 63 > green > 0 and blue < 0 (negative). The most positive MESPs are along the extensions of the Cl-I and C-I bonds and are 192 and 133 kJ mol⁻¹ for ICl and ICF₃, respectively. This diagram was kindly provided by Jane Murray and Peter Politzer

σ -hole is the positive region of molecular electrostatic surface potential (MESP) that occurs at I on the symmetry axes of ICl and ICF₃, as displayed in Fig. 10. The σ -holes are evident as the red spots. The axial MESP for ICl is larger, more positive than that of ICF₃, a result consistent with the greater electrophilicity of ICl than ICF₃ and the greater values of k_σ and D_e for a given B in the B ···ICl series.

4.4 Electric Charge Rearrangement on Formation of B ···ICl and B ···ICF₃ Complexes

It was shown in Sect. 3.3 that the I and Cl nuclear quadrupole coupling constants χ_{zz}^e (I) and χ_{zz}^e (Cl) (defined in Eqs. (5) and (6)) of the ICl subunit within the complex B ···ICl can be used in Eqs. (7) and (8) together with the free atom coupling constants χ_A (I) and χ_A (Cl) and the free ICl molecule constants χ_0 (I) and χ_0 (Cl) to obtain an estimate of δ_i , the fraction of an electronic charge that is transferred from the acceptor atom/centre Z of the Lewis base B to I. It was also indicated that Eqs. (7) and (8) must be corrected for the zero-point oscillations of the ICl subunit when within the complex if the zero-point (observed) coupling constants χ_{zz}^0 (I) and χ_{zz}^0 (Cl) are to be related to their equilibrium counterparts. The values of δ_i that result [9] for the series B ···ICl, where B = N₂, CO, H₂O, C₂H₂, C₂H₄, H₂S, PH₃ and NH₃, when this procedure is applied are shown in Fig. 11. The values on the abscissa are the first ionization energies, I_B , of the Lewis bases; these were used to order the δ_i values because I_B provides a measure of the ease with which the highest energy electron may be removed from B. Also shown in Fig. 11 is the corresponding curve for the series B ···Cl₂.

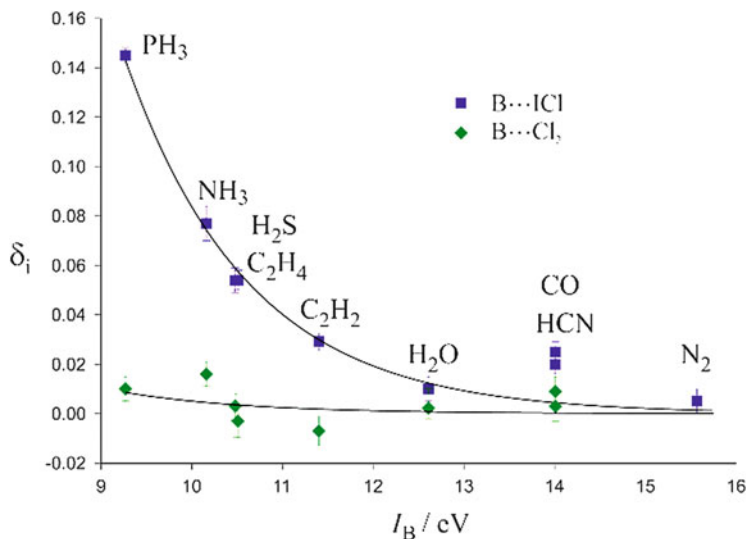


Fig. 11 The fraction δ_i of an electronic charge transferred from B to XY on formation of $B \cdots XY$ from B and XY plotted against the first ionization energy I_B of the Lewis base B for the two series of halogen-bonded complexes $B \cdots ICl$ and $B \cdots Cl_2$. δ_i was determined, by the method described in Sect. 3.3, from the changes in X and Y nuclear quadrupole coupling constants when XY is subsumed into the complex

The important points about the curves in Fig. 11 are that the value of δ_i increases reasonably smoothly as B becomes easier to ionize (and presumably more polarizable) and that the curve for $B \cdots Cl_2$ is much shallower than that of $B \cdots ICl$ (as might be expected from the more polar nature of ICl). Indeed, the value of δ_i is effectively zero for all but $H_3N \cdots Cl_2$ and $H_3P \cdots Cl_2$.

Unfortunately, this approach is not possible for the $B \cdots ICF_3$ complexes because ICF_3 does not possess a second quadrupolar nucleus, as required by Eq. (8). Then only the difference ($\delta_i - \delta_p$) can be obtained from Eq. (7). Since δ_p is unknown, δ_i is unavailable. Some progress is possible, however, when we note that the strength of the intermolecular binding is considerably less in $B \cdots ICF_3$ than in the corresponding $B \cdots ICl$. In fact, a comparison of Figs. 8 and 9 reveals that the binding strength for $B \cdots ICF_3$ (as measured by k_σ) is similar to that of $B \cdots Cl_2$ for a given B or, put another way, $E_{ICF_3} \approx E_{Cl_2}$. Moreover, the distance of the atom I from the acceptor atom Z of B is always considerably greater in $B \cdots ICF_3$ than in $B \cdots ICl$ for a given B (see Table 2). Both of these observations suggest that the values of δ_i for the $B \cdots ICF_3$ series are much reduced from those of the $B \cdots ICl$ and are probably negligibly small, as they are for the $B \cdots Cl_2$.

Conclusions

This chapter first describes how to observe the rotational spectra of pairs of molecules held together by a weak intermolecular bond, as exemplified by the halogen bonds in the series of complexes $B \cdots ICl$ and $B \cdots ICF_3$. The various properties of such complexes in the gas phase that can be determined from their rotational spectra under various levels of approximation are next discussed. A comparison of the angular geometries, radial geometries and strength of the intermolecular bond, the last of these as defined by the intermolecular force constants k_σ , reveals several similarities between the two series of complexes. It is shown that the complexes $B \cdots ICF_3$ also obey a set of rules originally enunciated to rationalise the angular geometries of hydrogen-bonded complexes of the type $B \cdots HX$, but which were subsequently found to apply to their halogen-bonded analogues $B \cdots XY$, where XY is a dihalogen molecule such as ICl . Important in establishing the validity of these rules in the case of the $B \cdots ICF_3$ series are the complexes in which $B = H_2O$ and H_2S . These exhibit out-of-plane angles φ which differ markedly from $B = H_2O$ to $B = H_2S$. Thus, H_2O forms a complex $H_2O \cdots ICF_3$ in which the configuration at O is either planar or effectively planar, i.e. rapidly inverting between equivalent pyramidal arrangements. On the other hand, the configuration at S in $H_2S \cdots ICF_3$ is permanently pyramidal. This contrast is also found for the pair $H_2O \cdots ICl$ and $H_2S \cdots ICl$. Ab initio calculations performed at the CCSD(T)(F12*)/cc-pVDZ-F12 level of theory generated potential energy functions governing the inversion of configuration at O or S. For both $H_2O \cdots ICF_3$ and $H_2O \cdots ICl$ each function has a low barrier to the planar arrangement but the barriers are much higher and wider in the corresponding H_2S complexes. In the lowest states, the rates of inversion are high compared with the timescale of molecular rotations for the two H_2O complexes but are negligible for the H_2S pair.

The values of the intermolecular stretching force constants k_σ for the two series $B \cdots ICF_3$ and $B \cdots ICl$ show that the former series is systematically more weakly bound than the latter. Interpretation of k_σ values in terms of a nucleophilicity N_B assigned to the Lewis bases B and an electrophilicity E_{IR} assigned to the Lewis acids/halogen bond donors $IR = ICl$ and ICF_3 reveals that replacement of the chlorine atom in ICl by a CF_3 group leads to an E_{ICF_3} value which is approximately $E_{ICl}/3$ and which is similar to that of Cl_2 . Finally, it is argued that amount of electronic charge redistributed from B to ICF_3 on formation of $B \cdots ICF_3$ is probably negligibly small.

Acknowledgements Support by the EPSRC of various aspects of the work reported here is gratefully acknowledged (NRW for Grant No. EP/G026424/1 and ACL for a Senior Fellowship). We are also pleased to acknowledge a Senior Research Fellowship of the University of Bristol, a Leverhulme Emeritus Fellowship (ACL) and Royal Society University Research Fellowships (DPT and NRW). We also thank Jane Murray and Peter Politzer for providing Fig. 10.

References

1. Davey JB, Legon AC, Waclawik ER (2000) Measurement of inter- and intramolecular charge transfer in the complex $N_2 \cdots ICl$ from analysis of halogen nuclear quadrupole hyperfine structure in the rotational spectrum. *J Mol Struct* 500:391–402
2. Davey JB, Legon AC, Waclawik ER (1999) Inter- and intra-molecular electron transfer in the complex $OC \cdots ICl$ determined from iodine and chlorine nuclear quadrupole hyperfine structure in its rotational spectrum. *Phys Chem Chem Phys* 1:3097–3102
3. Davey JB, Legon AC (1999) Rotational spectroscopy of mixtures of ethyne and iodine monochloride: isolation and characterisation of the π -type complex $C_2H_2 \cdots ICl$. *Phys Chem Chem Phys* 1:3721–3726
4. Thumwood JMA, Legon AC (1999) A π -electron donor-acceptor complex of ethene and iodine monochloride: geometry, binding strength and charge redistribution determined by rotational spectroscopy. *Chem Phys Letts* 310:88–96
5. Davey JB, Legon AC, Waclawik ER (2000) An investigation of the gas-phase complex of water and iodine monochloride by microwave spectroscopy: geometry, binding strength and electron redistribution. *Phys Chem Chem Phys* 2:1659–1665
6. Legon AC, Waclawik ER (1999) Angular geometry, binding strength and charge transfer for the complex $H_2S \cdots ICl$ determined by rotational spectroscopy. *Chem Phys Letts* 312:385–393
7. Herrebout WA, Legon AC, Waclawik ER (1999) Is there a significant intermolecular charge transfer in the ground state of the $HCN \cdots ICl$ complex? An answer from rotational spectroscopy. *Phys Chem Chem Phys* 1:4961–4966
8. Waclawik ER, Legon AC (1999) Halogen nuclear quadrupole coupling in the rotational spectrum of $H_3N \cdots ICl$ as a probe of inter- and intramolecular transfer. *Phys Chem Chem Phys* 1:4695–4700
9. Davey JB, Legon AC, Waclawik ER (2000) Inter- and intramolecular electronic transfer on formation of $H_3P \cdots ICl$ as determined by rotational spectroscopy. *Phys Chem Chem Phys* 2:2265–2269
10. Anable JP, Hird DE, Stephens SL, Zaleski DP, Walker NR, Legon AC (2014) The rotational spectrum of $N_2 \cdots ICF_3$ observed with a broadband, chirped-pulse FT microwave spectrometer. Manuscript in preparation
11. Stephens SL, Walker NR, Legon AC (2011) Rotational spectra and properties of complexes $B \cdots ICF_3$ ($B=Kr$ or CO) and a comparison of the efficacy of ICl and ICF_3 as iodine donors in halogen bond formation. *J Chem Phys* 135:224309
12. Stephens SL, Walker NR, Legon AC (2014) Broadband rotational spectroscopy of the ethyne $\cdots ICF_3$ complex in the microwave region. Manuscript in preparation
13. Stephens SL, Mizukami W, Tew DP, Walker NR, Legon AC (2012) The halogen bond between ethene and a simple perfluoroiodoalkane: $C_2H_4 \cdots ICF_3$ identified by broadband rotational spectroscopy. *J Mol Spectrosc* 280:47–53
14. Stephens SL, Walker NR, Legon AC (2011) Molecular geometries of $H_2S \cdots ICF_3$ and $H_2O \cdots ICF_3$ characterised by broadband rotational spectroscopy. *Phys Chem Chem Phys* 13:21093–21101
15. Stephens SL, Walker NR, Legon AC (2011) Internal rotation and halogen bonds in $CF_3I \cdots NH_3$ and $CF_3I \cdots N(CH_3)_3$ probed by broadband rotational spectroscopy. *Phys Chem Chem Phys* 13:20736–20744
16. Stephens SL, Walker NR, Legon AC (2014) The broadband rotational spectrum of $H_3P \cdots ICF_3$ and internal rotation. Manuscript in preparation
17. Legon AC (1998) π -Electron ‘donor-acceptor’ complexes $B \cdots ClF$ and the existence of the ‘chlorine’ bond. *Chem Eur J* 4:1890–1897
18. Legon AC (1999) Pre-reactive complexes of dihalogens XY with Lewis bases B in the gas phase: a systematic case for the ‘halogen’ analogue $B \cdots XY$ of the hydrogen bond $B \cdots HX$. *Angew Chem Int Ed Engl* 38:2686–2714

19. Legon AC (2008) The interaction of dihalogens and hydrogen halides with Lewis bases in the gas phase: an experimental comparison of the halogen bond and the hydrogen bond. In: Metrangolo P, Resnati G (eds) Halogen bonding: fundamentals and applications. Structure and bonding, vol 126. Springer, Berlin, pp 17–64
20. Legon AC (2010) The halogen bond: an interim perspective. *Phys Chem Chem Phys* 12:7736–7747
21. Evangelisti L, Feng G, Eciija P, Cocinero EJ, Fernando Castaño F, Caminati WA (2011) The halogen bond and internal dynamics in the molecular complex of CF_3Cl and H_2O . *Angew Chem Int Ed Engl* 50:7807–7810
22. Feng G, Evangelisti L, Gasparini N, Caminati W (2012) On the $\text{Cl}\cdots\text{N}$ halogen bond: a rotational study of $\text{CF}_3\text{Cl}\cdots\text{NH}_3$. *Chem Eur J* 18:1364–1368
23. Evangelisti L, Feng G, Gou Q, Guidetti G, Caminati W (2012) Orientation of the water moiety in $\text{CF}_4\text{-H}_2\text{O}$. *J Mol Spectrosc* 282:39–41
24. Springer SD, Rivera-Rivera LA, Scott KW, McElmurry BA, Wang Z, Leonov II, Lucchese RR, Legon AC, Bevan JW (2012) A CMM-RS potential for characterization of the properties of the halogen-bonded OC-Cl_2 complex. *J Phys Chem A* 116:1213–1223
25. Legon AC (1995) Mulliken $n.\text{a}\sigma^*$ and $b\pi.\text{a}\sigma^*$ complexes $\text{B}\cdots\text{Cl}_2$ in the gas phase: rules for predicting angular geometries and nature of the interaction. *Chem Phys Lett* 237:291–298
26. Legon AC (1995) Donor-acceptor complexes of Lewis bases with bromine monochloride in the gas phase: some generalisations from rotational spectroscopy. *J Chem Soc Faraday Trans* 91:1881–1883
27. Legon AC (1997) Nature of complexes $\text{B}\cdots\text{ClF}$ in the gas phase: conclusions from systematic variation of the Lewis base B and a comparison of the $\text{B}\cdots\text{ClF}/\text{B}\cdots\text{HCl}$ series. *Chem Phys Lett* 279:55–64
28. Legon AC (1998) Quantitative gas-phase electrophilicities of the dihalogen molecules $\text{XY}=\text{F}_2, \text{Cl}_2, \text{Br}_2, \text{BrCl}$ and ClF . *J Chem Soc Chem Commun* 2585–2586
29. Legon AC (1999) Angular and radial geometries, charge transfer and binding strength in isolated complexes $\text{B}\cdots\text{ICl}$: some generalisations. *Chem Phys Lett* 314:472–480
30. Legon AC (1998) The nature of the interaction of molecular fluorine and Lewis bases B from a comparison of the properties of $\text{B}\cdots\text{F}_2$ and $\text{B}\cdots\text{HF}$. *J Chem Soc Chem Commun* 2737–2738
31. Stone AJ (2013) Are halogen bonds electrostatically driven? *J Am Chem Soc* 135:7005–7009
32. Metrangolo P, Meyer F, Pilati T, Resnati G, Terraneo G (2008) Halogen bonding in supramolecular chemistry. *Angew Chem Int Ed Engl* 47:6114–6127
33. Balle TJ, Flygare WH (1981) Fabry-Perot cavity Fourier transform microwave spectroscopy with a pulsed nozzle particle source. *Rev Sci Instrum* 52:33–45
34. Legon AC (1992) Fourier transform microwave spectroscopy. In: Scoles G (ed) Atomic and molecular beam methods, vol 2. Oxford University Press, New York, pp 289–308
35. Brown GG, Dian BC, Douglass KO, Geyer SM, Shipman SS, Pate BH (2008) A broadband Fourier transform microwave spectrometer based on chirped pulse excitation. *Rev Sci Instrum* 79:053103-1-13
36. Stephens SL, Walker NR (2010) Determination of nuclear spin-rotation coupling constants in CF_3I by chirped-pulse Fourier-transform microwave spectroscopy. *J Mol Spectrosc* 263:27–33
37. Kraitchman J (1953) Determination of molecular structures from microwave spectroscopic data. *Am J Phys* 21:17–24
38. Costain CC (1958) Determination of molecular structure from ground-state spectroscopic constants. *J Chem Phys* 29:864–874
39. Gordy W, Cook RL (1984) Microwave molecular spectra. In: Weissberger A (ed) Techniques of chemistry, vol 56. Wiley, New York, pp 726–795
40. Herzberg G (1950) Molecular spectra and molecular structure. I. Spectra of diatomic molecules, 2nd edn. Van Nostrand, New York, p 103
41. Millen DJ (1985) Determination of stretching force constants of weakly bound dimers from centrifugal distortion constants. *Can J Chem* 63:1477–1479

42. Townes CH, Schawlow AL (1955) *Microwave spectroscopy*. McGraw-Hill, New York, Chap 9, p 225
43. Legon AC, Millen DJ (1982) Determination of properties of hydrogen-bonded dimers by rotational spectroscopy and a classification of dimer geometries. *Faraday Discuss Chem Soc* 73:71–87
44. Legon AC, Millen DJ (1987) Directional character, strength and nature of the hydrogen bond in gas-phase dimers. *Acc Chem Res* 20:39–46
45. Legon AC, Millen DJ (1987) Angular geometries and other properties of hydrogen-bonded dimers: a simple electrostatic interpretation based on the success of the electron-pair model. *Chem Soc Rev* 16:467–498
46. Stone AJ (1981) Distributed multipole analysis or how to describe molecular charge distributions. *Chem Phys Lett* 83:233–239
47. Buckingham AD, Fowler PW (1985) A model for the geometries of van der Waals complexes. *Can J Chem* 63:2018–2025
48. Buckingham AD (1967) Permanent and induced molecular moments and long-range intermolecular forces. *Adv Chem Phys* 12:107–142
49. Kisiel Z, Legon AC, Millen DJ (1982) Spectroscopic investigations of hydrogen bonding interactions in the gas phase. VII. The equilibrium conformation and out-of-plane bending potential energy function of the hydrogen-bonded heterodimer $\text{H}_2\text{O} \cdots \text{HF}$ determined from its microwave rotational spectrum. *Proc R Soc Lond A* 381:419–442
50. Viswanathan R, Dyke TR (1982) The structure of $\text{H}_2\text{S} \cdots \text{HF}$ and the stereochemistry of the hydrogen bond. *J Chem Phys* 77:1166–1174
51. Willoughby LC, Fillery-Travis AJ, Legon AC (1984) An investigation of the rotational spectrum of $\text{H}_2\text{S} \cdots \text{HF}$ by pulsed-nozzle, Fourier-transform microwave spectroscopy: determination of the hyperfine coupling constants $\chi_{aa}(\text{}^3\text{S})$, χ_{aa}^{D} and $D_{aa}^{\text{H(D)F}}$. *J Chem Phys* 81:20–26
52. Werner HJ, Knowles PJ, Knizia G, Manby FR, Schütz M et al (2012) MOLPRO, version 2012.1, a package of ab initio programs. <http://www.molpro.net>
53. Hättig C, Tew DP, Köhn A (2010) Accurate and efficient approximations to explicitly correlated coupled-cluster singles and doubles, CCSD-F12. *J Chem Phys* 132:231102
54. Peterson KA, Adler TB, Werner H-J (2008) Systematically convergent basis sets for explicitly correlated wavefunctions: The atoms H, He, B–Ne and Al–Ar. *J Chem Phys* 128:084102
55. Hill JG, Peterson KA (2014) Correlation consistent basis sets for explicitly correlated wavefunctions: Pseudopotential-based basis sets for the post-d main group elements Ga–Rn. *J Chem Phys* 141:094106
56. Kisiel Z, Pietrewicz BA, Fowler PW, Legon AC, Steiner E (2000) Rotational spectra of the less common isotopomers, electric dipole moment and double-minimum inversion potential of $\text{H}_2\text{O} \cdots \text{HCl}$. *J Phys Chem* 104:6970–6978
57. Davey JB, Legon AC, Thumwod JMA (2001) Interaction of water and dichlorine in the gas phase: an investigation of $\text{H}_2\text{O} \cdots \text{Cl}_2$ by rotational spectroscopy and ab initio calculations. *J Chem Phys* 114:6190–6202
58. Cooke SA, Cotti G, Evans CM, Holloway JH, Kisiel Z, Legon AC, Thumwood JMA (2001) Pre-reactive complexes in mixtures of water vapour with halogens: characterisation of $\text{H}_2\text{O} \cdots \text{ClF}$ and $\text{H}_2\text{O} \cdots \text{F}_2$ by a combination of rotational spectroscopy and ab initio calculations. *Chem Eur J* 7:2295–2305
59. Tyler JK, Sheridan J, Costain CC (1972) Microwave spectra of cyanamide-conclusions from μ_a transitions. *J Mol Spectrosc* 43:248–261
60. Mjoberg PJ, Almlöf J (1978) *Chem Phys* 29:201–208
61. Hill JG, Hu X (2013) Theoretical insights into the nature of halogen bonding in pre-reactive complexes. *Chem Eur J* 19:3620–3628
62. Bondi A (1964) van der Waals volumes and radii. *J Phys Chem* 68:441–451
63. Murray JS, Politzer P, Clark T (2010) Halogen bonding: an electrostatically driven highly directional non-covalent interaction. *Phys Chem Chem Phys* 12:7748–7757

64. Price SL, Stone AJ (1982) The anisotropy of the Cl₂-Cl₂ pair potential as shown by the crystal structure. Evidence for intermolecular bonding or lone pair effects? *Mol Phys* 47:1457–1470
65. Peebles SA, Fowler PW, Legon AC (1995) Anisotropic repulsion in complexes B ··· Cl₂ and B ··· HCl: the shape of the chlorine atom-in-a molecule. *Chem Phys Lett* 240:130–134
66. Legon AC, Millen DJ (1987) Hydrogen bonding as a probe for electron densities: limiting gas phase nucleophilicities and electrophilicities of B and HX. *J Am Chem Soc* 109:356–358
67. Legon AC (2014) A reduced radial potential energy function for halogen- and hydrogen-bonded complexes B ··· XY and B ··· HX, where X and Y are halogen atoms. *Phys Chem Chem Phys* 16:25199–25199
68. Boys SF, Bernadi F (1970) The calculation of small molecular interactions by the differences of separate total energies. Some procedures with reduced errors. *Mol Phys* 19:553–566
69. Nagels N (2013) Building cryospectroscopic bridges: halogen bonding, hydrogen bonding and lone pair ··· π interactions. Ph.D. thesis, Departement Chemie, Universiteit Antwerpen
70. Hauchecorne D, Nagels N, van der Veken BJ, Herrebout WA (2012) C–X ··· π halogen and C–X ··· π hydrogen bonding: interactions of CF₃X (X=Cl, Br, I or H) with ethane and propene. *Phys Chem Chem Phys* 14:681–690
71. Valerio G, Raos G, Meille SV, Metrangolo P, Resnati G (2000) Halogen bonding in fluoroalkylhalides: a quantum chemical study of increasing fluorine substitution. *J Phys Chem A* 104:1617–1620

Infrared and Raman Measurements of Halogen Bonding in Cryogenic Solutions

Wouter Herrebout

Abstract Because they create a weakly interacting environment which, combined with the low temperatures used, leads to small bandwidths and thus facilitates the detection of complex bands only slightly shifted from the monomer modes, solutions in liquefied inert gases have proven to be an ideal medium to study molecular complexes held together by weak and medium-strong C–X...Y (with X=I, Br, Cl and Y=O, N, S, F, Cl, π ,...) halogen bonds. In this chapter, experimental setups for infrared and Raman study of cryosolutions are described, and general methodologies used to examine weakly bound molecular complexes are discussed. The methods are illustrated using data obtained for a variety of halogen-bonded complexes involving, amongst others, the trifluorohalomethanes CF₃Cl, CF₃Br, and CF₃I, and a variety of Lewis bases. The results are compared with theoretical data obtained from ab initio calculations, and with experimental and theoretical data obtained for complexes involving weak C–H proton donors such as CHF₃. Preliminary data for mixed proton donor/halogen donors such as CHClF₂, CHBrF₂ are also discussed.

Keywords Cryosolutions · Halogen bonding · Infrared spectroscopy · Raman spectroscopy · Trifluorohalomethanes CF₃X

Contents

1	Introduction	80
2	Experimental Setups	83
2.1	Infrared Spectroscopy of Cryosolutions	83
2.2	Raman Spectroscopy of Cryosolutions	90
3	General Methodology Used for Studying Weakly Bound Molecular Complexes	92

W. Herrebout (✉)

Department of Chemistry, University of Antwerp, Groenenborgerlaan 171, 2020 Antwerp, Belgium

e-mail: wouter.herrebout@uantwerpen.be

3.1	General Methodology	93
3.2	Separating Monomers and Complexes: Subtraction Procedures	95
3.3	Confirming the Stoichiometry: Concentration Studies	96
3.4	Determining the Relative Stability: Temperature Studies	98
3.5	Ab Initio Calculations and Statistical Thermodynamics	101
3.6	Monte Carlo-Free Energy Perturbation Simulations	102
4	Weak C–X...Y Halogen-Bonded Complexes Involving CF ₃ X	104
4.1	Infrared and Raman Spectra of Isolated CF ₃ X Molecules	105
4.2	C–X...N-Bonded Complexes: Trimethylamine	106
4.3	C–X...O and C–X...S-Bonded Complexes: Dimethyl Ether, Dimethyl Sulfide	112
4.4	C–X...F and C–X...Cl-Bonded Complexes: Alkyl Fluorides and Alkyl Chlorides	121
4.5	C–X... π -Bonded Complexes: Alkenes, Alkynes, and Aromatic Compounds;	126
5	Analyzing Trends	138
5.1	Complexation Enthalpies	139
5.2	Blue- and Red-Shifting C–X Halogen Bonds	142
6	Conclusions and Future Perspectives	144
6.1	Different Interaction Sites in the Donor Molecule	144
6.2	Mixed Halogen/Hydrogen Donors: Simultaneous Occurrence of C–X...Y Halogen- and C–H...Y Hydrogen-Bonded Complexes	145
	References	146

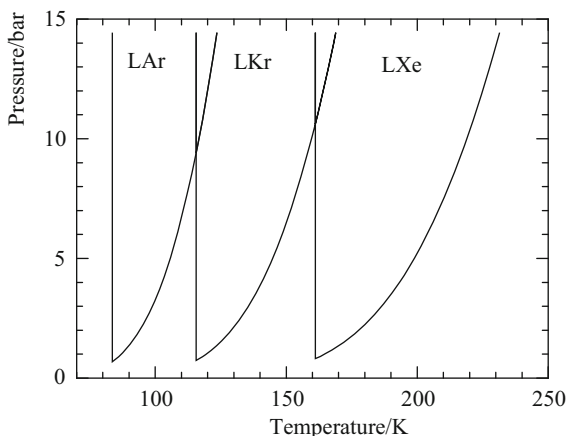
Abbreviations

DME	Dimethyl ether
DMS	Dimethyl sulfide
IR	Infrared
LAr	Liquid argon
LKr	Liquid krypton
LNe	Liquid neon
LN ₂	Liquid nitrogen
LXe	Liquid xenon
TMA	Trimethylamine

1 Introduction

During the last few decades, matrix isolation spectroscopy has certainly been one of the most active fields in low temperature vibrational spectroscopy [1]. Although the technique remains unsurpassed for a variety of applications including, e.g., the study of free radicals and other unstable species, several disadvantages remain. For example, absorption bands produced by matrix isolated species are often complicated by multiplet structures arising from the presence of different trapping sites in the matrix, from aggregation of solute molecules, from rotation of the solute molecule in its trapping site, etc. These splittings are often difficult to distinguish from other spectral effects arising from the formation of molecular complexes or

Fig. 1 Fusion and vaporization curves for argon, krypton, and xenon



the occurrence of multiple conformations. Because it is difficult to produce sufficiently thick samples and because of strong scattering of the infrared (IR) beam by thicker matrixes, matrix-isolation spectroscopy is also rarely used to explore weak bands. Moreover, because the species under study are trapped in a solid, rigid medium, no information on their thermodynamic properties is accessible.

Information complementary to that derived using solid matrixes can be obtained by studying solutions of molecules dissolved in liquefied inert gases, such as rare gases, nitrogen, or oxygen. Apart from the relatively low temperatures used during these experiments and the weak solute–solvent interactions, a major advantage of these cryosolutions is their transparency over a broad spectral interval, ranging from far-IR to ultraviolet. Therefore, in contrast to solid matrices, the solutions in cryogenic solvents can be used for the study of weak phenomena. As cryosolutions in general are in thermodynamical equilibrium, they are also ideally suited to determine thermodynamical and other physical properties.

The main obstacle to using liquefied inert gases as solvents is their limited solvability: a large number of molecules dissolve well in liquid xenon (LXe), but substantially fewer compounds dissolve in liquid krypton (LKr) or liquid argon (LAr). A second drawback is related to the fact that at atmospheric pressure the liquid ranges of the rare gases are very narrow, varying from 3.3 K for LAr to 3.8 K for LXe. Taking into account the transparency of the RGs, the first obstacle can often be overcome by using longer optical path lengths, up to several centimeters or even longer. Expanding the temperature range typically involves the use of higher pressures, the liquid range at a pressure of 15 bar as derived from Fig. 1 being 88–128 K for LAr, 118–170 K for LKr, and 168–223 K for LXe.

Over the last few decades, many experiments have been performed where liquid RGs are used as solvents and the results have been summarized in earlier reviews [2–10]. The items covered not only include the studies of isolated molecules, but also describe studies on solute–solute and solute–solvent interactions, and on (photo)chemical reactions. In this chapter, we concentrate on experimental results

obtained for molecular complexes held together by weak to medium-strong C–X...Y halogen-bonded complexes involving, among others, the trifluorohalomethanes CF₃Cl, CF₃Br, and CF₃I, and a variety of Lewis bases containing electron-rich atoms such as N, O, S, F, and Cl. The driving force behind the experimental studies was that, although the formation of halogen bonds had been suggested in various theoretical and experimental studies including single crystal X-ray diffraction experiments, spectroscopic data on halogen bond complexes is very limited, the main results being IR and NMR studies on the complexes of CF₃I and CF₃Br with trimethylamine (TMA) reported by Pullin and co-workers [11–17]. Although these studies yielded unique information on the existence of halogen bonding, it was soon realized that, because the interactions observed in crystal structures studied are involved in a three-dimensional network in which important cooperative effects can be present, and because the available NMR and IR data on C–X...N (X=I, Br) halogen-bonded complexes could be disturbed by solvent effects, the experimental studies on halogen bonding reported in the literature did not yield detailed information on the intrinsic properties of the halogen bond and thus could hardly be used to assess reliably the theoretical developments in this field. With the study of halogen bonds formed between the trifluorohalomethanes CF₃X, and a variety of weak, medium, and strong Lewis bases dissolved in LRGs, we therefore aimed at proving the existence of well isolated halogen-bonded complexes and, at the same time, establishing their main spectroscopic, structural, and thermodynamic properties.

An interesting phenomenon which caught our attention was related to the observation that, despite the various theoretical studies suggesting that the C–X bond can be either strengthened or weakened during complexation, and thus could lead to blue-shifting halogen-bonded complexes [18–20], no experimental data for such systems were available. The lack of observed blue-shifting C–X stretching fundamentals was considered somewhat surprising, as C–X...Y halogen bonds were generally accepted [21–28] to mimic the structural and spectroscopic properties of blue- and red-shifting C–H...Y hydrogen bonds [29–38].

The lack of experimental data for the C–X stretching fundamental supporting the similarity idea with blue- and red-shifting C–H...Y hydrogen bonds, in our opinion, was for two reasons. First, the experimental results reported in the literature had been limited to the stronger complexes involving a C–I...N or C–Br...N halogen bond, while for these species the C–X bond length was always predicted [18–20] to elongate with complexation. Second, for the CF₃X halogen donors involving chlorine or bromine, the C–X stretching modes were known to have a very low IR intensity, in the order of 0.01 km mol⁻¹ or less [39–47]. Combined with the fact that for weak complexes in general only a minor fraction of the monomers is converted into complex, it was not really surprising that traditional IR spectroscopy had failed to give reliable data on the C–Br or C–Cl stretches. From the complementarities of Raman and IR spectroscopy, we expected the C–X stretching vibrations to be intense in Raman, and there was reason to assume, for the first time ever, that the Raman spectra of the halogen-bonded complexes occurring in cryogenic

solutions would provide experimental information on blue-shifting halogen bonds. As summarized below, this indeed proved to be the case.

Before discussing the methodology used and the results obtained during the cryospectroscopic experiments, it is worth noting that, since the first experiments reported in 2009 [48], a variety of complexes strongly related to those studied in the cryosolutions have now also been investigated using traditional and chirped-pulsed microwave studies [49–55], and that additional information on complexes between more complex perfluoro alkyl iodides and pyridine has also been obtained using low-temperature IR and NMR experiments [56].

2 Experimental Setups

Ever since their discovery, the rare gases have attracted the interest of researchers, and their chemical and physical properties have been studied in great detail. Because of the complete absence of intramolecular vibrations in these monoatomic gases, their potential as solvents for vibrational studies of solutes was explored in the 1940s. However, the actual use as solvents met with considerable difficulty. In the first place, the relative low boiling points of LAr (87.3 K), LKr (119.9 K), and LXe (165.0 K) necessitate the systematic use of cryogenic equipment, making their handling difficult. The study of such solutions as function of temperature is also not trivial because of the limited liquid range at environmental pressures. Expanding the temperature ranges available thus necessitates the use of cells which can be used at pressures of up to 50 bar.

Over the last decade we have developed and optimized an extended set of cryostats with path lengths of 0.6–70.0 mm and equipped with a range of window materials. The cryostats are fitted into the sample area of Bruker IFS 66 V FTIR spectrometers which are available in the group and allow the complete IR spectrum to be recorded between 10 and 25,000 cm^{-1} . For the mid-IR spectra, a Globar source is used in combination with a Ge/KBr beam splitter and an LN₂-cooled broadband MCT detector. For the far-IR spectra, a Mylar beam splitter and an LHe-cooled bolometer is typically used, while for the near-NIR spectra, Si/CaF₂ and quartz beamsplitters are used in combination with an InSb detector. In the following paragraphs, typical experimental setups are described. Subsequently, the procedures used to record the IR spectra and the choice of the optimal experimental conditions are discussed.

2.1 Infrared Spectroscopy of Cryosolutions

Figure 2 shows a typical experimental setup used for the IR study of cryosolutions. It consists of four main parts: (1) a pressure manifold to fill and evacuate the cell and to monitor the amount of solute gas in a particular experiment, (2) the actual

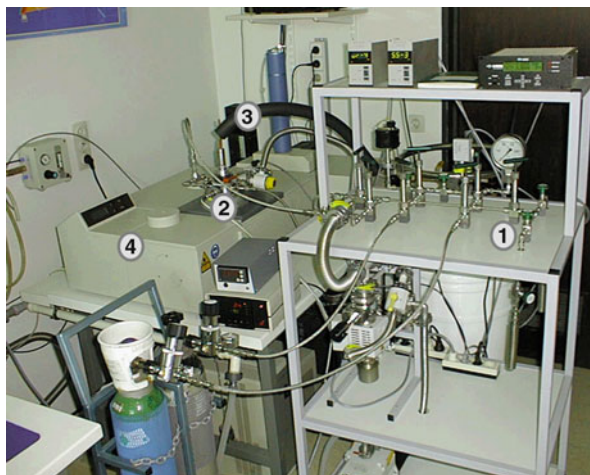


Fig. 2 Overview of an experimental setup used for infrared studies: (1) pressure manifold, (2) liquid cell, (3) cooling accessories, (4) spectrometer

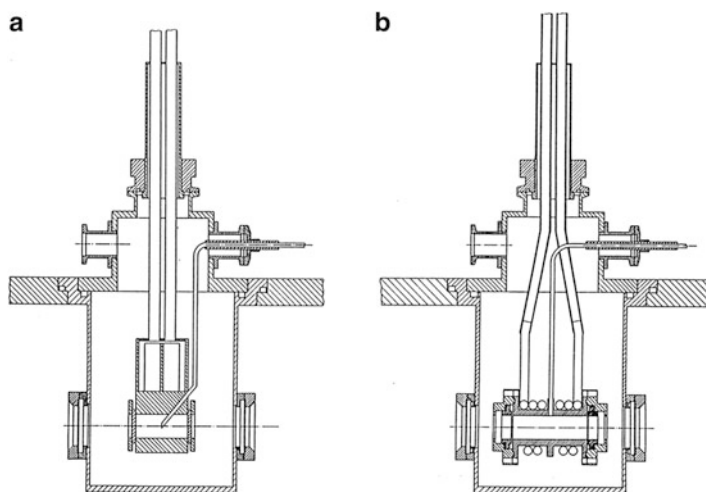


Fig. 3 Schematic drawing of the two different cell types used for liquefied noble gas cryostats: (a) low-pressure cryostat with clamped-on windows; (b) cryostat with high-pressure window holders

liquid cell, (3) additional equipment to control the temperature of the cell, and (4) the spectrometer.

The two different cell designs in use are shown in Fig. 3. In both cases, the actual cell is suspended, via a stainless steel LN₂ feedthrough, in a vacuum shroud to avoid condensation of H₂O and CO₂ on the outside of the cell. The vacuum shroud is equipped with polyethylene windows for the far-IR, KBr windows for mid-IR, and

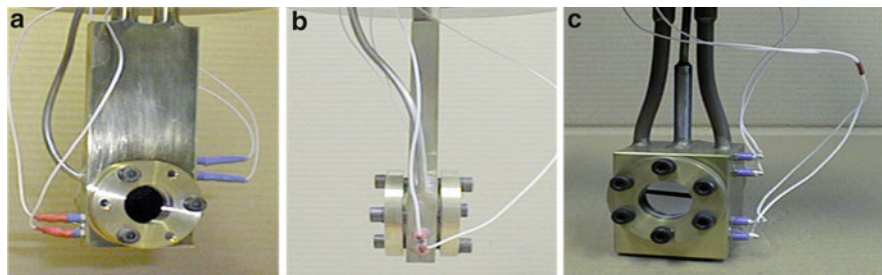


Fig. 4 Liquid cells based on low-pressure design: (a, b) cell with silicon windows and an optical path length of 10 mm; (c) cell with silicon windows and an optical path length of 40 mm

quartz or CaF_2 windows for the near-IR, and is hermetically sealed to the vacuum spectrometer.

The first type of cryostat, with a low-pressure design, is shown schematically in Fig. 3a. For these cells, the IR window is fixed on the outside of the cell body using an indium gasket. Because of the difference in expansion coefficients of the materials used to construct the cell body and the window material, and because the pressurized solvent inside the cell tends to break the seal, the preparation of the latter is critical. The cells can withstand an internal pressure of 15 bar at 80 K and can be used in different temperature intervals, ranging from 93 to 125 K for LAr, from 120 to 155 K for LKr, and from 152 to 223 K for LXe. The minimal path length achieved is 5 mm and the largest 40 mm. Examples of liquid cells, equipped with Si windows and characterized by path lengths of 10 and 40 mm are shown in Fig. 4.

The second type of cryostat, with a high-pressure design similar to those described in [57], is shown schematically in Fig. 3b. In these cells, the IR windows are fitted into the cell body using two window holders. These holders are then sealed to a central cell body. These cells have the advantage that the pressurized solvent inside the cell tends to improve the indium seal between the IR window and the window holder. Because these cells involve a central cell body and two different window holders, the minimal path length obtainable is sufficiently larger than that described above. Typical examples of cryostats with a high-pressure design are shown in Fig. 5. The first cell has a path length of 70 mm, is equipped with ZnSe windows, and can be used for pressures as high as 15 bar. The second cell also has a path length of 70 mm, is equipped with 5 mm thick Si windows, and can withstand an internal pressure of 140 bar.

In principle, any window material of sufficient strength can be used in liquid cells if simple rules for selecting the thickness are followed [58]. A popular window material often used in the construction of liquid cells is Si, because this material is quite strong and transparent through most of the IR region, including the far-IR. Unfortunately, silicon has a fairly high index of refraction. Therefore, substantial reflections may occur so the actual transmittance of the cell is rather low. To avoid internal reflections in the windows and to avoid the resulting interference fringes, Si windows which are slightly wedged, typically by 0.5° or 1° , are recommended.

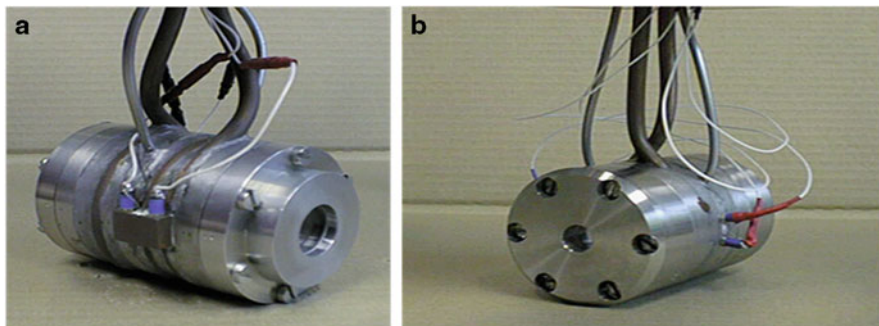


Fig. 5 Liquid cells based on high-pressure design: (a) cell with ZnSe windows, an optical path length of 70 mm, an inner diameter of 19 mm, and a maximum operating pressure of 15 bar; (b) cell with silicon windows, an optical path length of 70 mm, an inner diameter of 19 mm and a maximum operating pressure of 140 bar

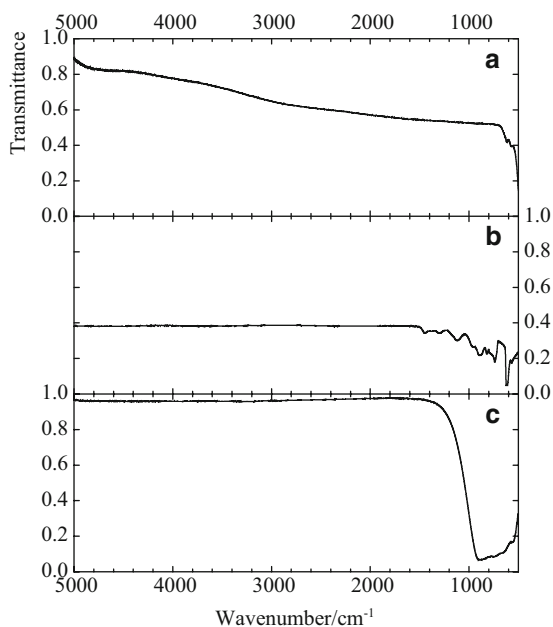
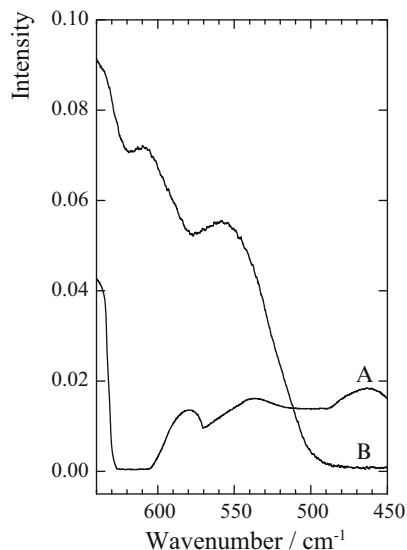


Fig. 6 Transmittance of classical window materials in the mid-IR region: (a) ZnSe; (b) Si; (c) CaF₂. The thickness of all windows is 5 mm. To avoid interference, a Si window with 0.5° wedge was used

The spectral characteristics of the commonly used window materials Si, ZnSe, and CaF₂ are compared in Figs. 6 and 7. CaF₂ provides excellent transmittance for frequencies above 1,000 cm⁻¹, and is commonly used for experiments in the mid- and near-IR regions. Because of the differences in the index of refraction, the transparency for Si and ZnSe in general is significantly smaller than that of CaF₂.

Fig. 7 Single-beam spectra of a liquid cell equipped with Si (a) and ZnSe (b) windows. Because of the complete absorption by Si, ZnSe is preferred for measurements around 600 cm^{-1} . However, because of complete absorption by ZnSe, Si windows are required for measurements below 500 cm^{-1} . The single-beam spectra were recorded using KBr windows in the vacuum shroud



The transmittance of ZnSe is further limited to approximately 500 cm^{-1} while Si shows a significant loss below $1,000\text{ cm}^{-1}$ and almost complete absorption near 600 cm^{-1} . In contrast to ZnSe, Si shows a significant transmittance in the far-IR region. CaF_2 , ZnSe, and Si windows have their specific advantages and are strongly complementary.

The different cryocells described above are cooled with bursts of liquid nitrogen from a slightly pressurized Dewar. In all cases, the LN_2 flow is regulated by a solenoid valve, which is controlled via a Pt-100 thermoresistor embedded in the cell body. The temperature of the solution is measured using a second Pt-100 thermoresistor located close to the solution. Cells similar to those described above can also be constructed by combining a cell body and a double-stage cryostat involving closed cycle helium cooling, or by combining a cell body with an LN_2 Dewar, heating cartridge, and proportional-integral-derivative (PID) controller. A typical cell of the first type, recently developed for experiments in LNe [59–61], is shown in Fig. 8. The setup consists of a cell similar to that shown in Fig. 2 which is connected to the cold head of a Leybold ROK 10–300 double-stage closed-cycle helium refrigerator. The temperature of the cell is controlled using a set of two Si diodes, located at the top and at the bottom of the cell body. The main advantages of this design are related to the improvement in temperature stability and the ability to conduct experiments at temperatures below 77 K . The combination with the closed-cycle helium refrigerator, however, also has disadvantages. Because double-stage cryostats show severe mechanical vibrations, the cryostat cannot be sealed hermetically to a vacuum spectrometer, so weak absorptions caused by water vapor and CO_2 cannot be completely avoided. The use of this type of cryostat also results in a much more complicated setup which is less flexible than those with LN_2 cooling. Finally, the cooling power of closed-cycle cryostats is significantly smaller than that of LN_2 , so longer times are required to cool down the cell.

Fig. 8 Liquid cell based on low-pressure design in combination with a double-stage cryostat involving closed cycle helium cooling. The cell has an optical path length of 40 mm, and, because an optimal signal-to-noise ratio is required at $4,000\text{ cm}^{-1}$, it is equipped with sapphire windows

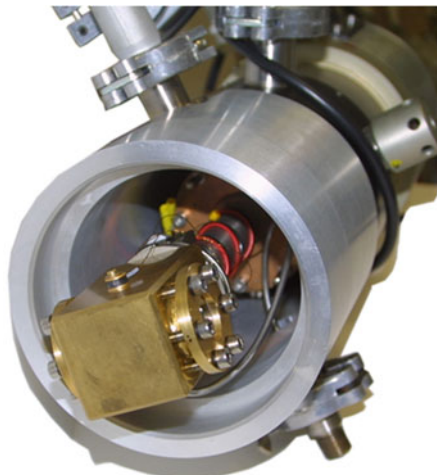
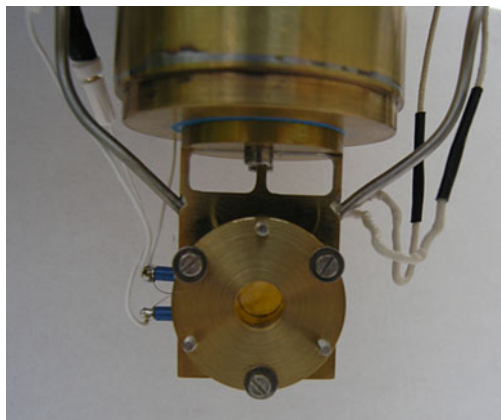


Fig. 9 Liquid cell based on low-pressure design in combination with an LN₂ Dewar/Sunrod electric minicartridge heater. The cell has an optical path length of 10 mm, and is equipped with ZnSe windows. To control the temperature of the cell body with limited power three cold bridges were used to connect the cell body and the LN₂ Dewar



A typical cell produced by combining a cell body, an LN₂ Dewar, and a PID controlled heating cartridge is shown in Fig. 9. The liquid cell is characterized by path length of 10 mm, is equipped with ZnSe windows, and is mounted below an LN₂ Dewar. The temperature of the cell body is measured using a Pt-100 thermoresistor. The SunRod electric 30 W minicartridge heater is controlled using a Eurotherm 3504 PID controller. The time required to stabilize the temperature depends on the temperature change requested, but typically is in the order of 5–10 min. The temperature variation during a typical experiment is less than 0.05°C .

For the low-pressure cells, filling and evacuating of the cell is performed using a $1/8''$ stainless steel tube brazed into the cell body and connected to the pressure manifold. For the high pressure cryostats, two different $1/8''$ tubes are brazed into the cell body. The first tube connects the cell with the pressure manifold; the second is connected to a safety relief valve.

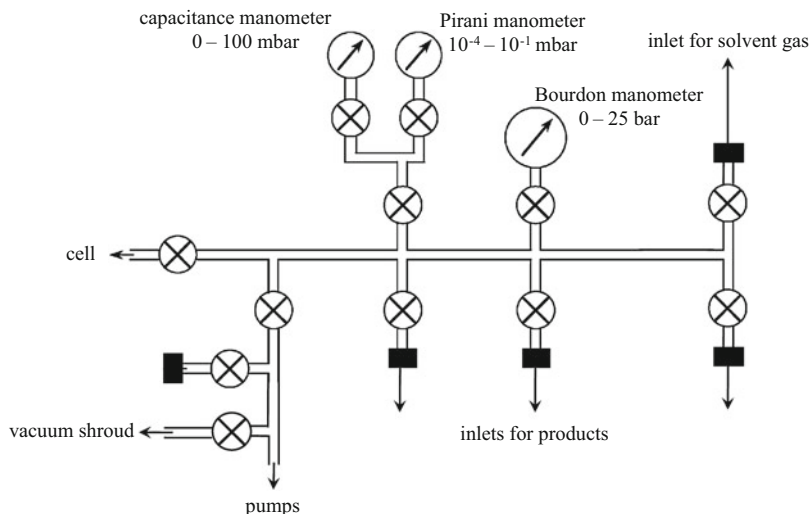


Fig. 10 Schematic overview of the pressure manifolds used to fill and evacuate the liquid cells

The pressure manifolds, schematically represented in Fig. 10, are equipped with Swagelok SS-4H or SS-4UK bellows valves and allow the handling of pressures up to 145 bar. The manifolds are connected to a fore pump–turbo molecular pump combination and are equipped with Pirani vacuum meters, capacitance manometers, and Bourdon-type high-pressure gauges. The vacuum meters are used to check the vacuum in the manifold and in the actual cell, while the capacitance manometers are used to monitor the amount of gas used in a particular experiment. The Bourdon manometers are used to control the pressure of the solvent gas. All pressure meters can be isolated from the manifold using bellows valves, essential in the case of the Pirani and capacity gauges when the manifold is put under high pressure. Safety relief valves also protect the gauges. The manifolds have several inlets through which compounds and solvent gases can be admitted to the system.

In a typical experiment, the evacuated cell is positioned in the spectrometer and vacuum shroud, and the cell and the pressure manifold are evacuated. Subsequently, the solutions are prepared in the following way. After cooling the cell to the required temperature, some of the solute gas, monitored by the capacitance manometer, is admitted into an isolated part (with accurately known volume) of the pressure manifold. Upon opening the valve connecting the actual cell and the pressure manifold, the vapors condense in the cell or on the walls of the filling tube. If necessary, this procedure is repeated for other species. The manifold and the cell are then pressurized with the solvent gas, which immediately starts to condense. This condensation takes place in the cold part of the filling tube and in the actual cell, allowing the deposited compounds to dissolve. When the filling and evacuation of a liquid cell is followed visually, the condensation of the rare gas into the liquid cell is quite vigorous: the turbulence created thus suffices to homogenize the solution so that no additional stirring is required. After stabilizing the temperature,

the solution in most cases is ready for immediate spectroscopic examination. The exceptions are caused by species with limited solubility and which often give rise to small crystalline particles suspended in the solvent. The appearance of such crystalline particles is readily observed through deviations of the base line and can usually be avoided by performing additional temperature cycles in which the temperature is systematically varied between the highest and lowest points of the temperature range used for the noble gas being used. For all experiments, IR single-beam spectra of the cell filled with solvent gas only and recorded at exactly the same temperature as that used for the sample is used as a reference.

An important characteristic of a solution is the concentration of the solutes. Unfortunately, because it cannot be verified whether the compound deposited into the cell has completely dissolved and because the level of the solvent in the filling tube is not precisely known, an accurate determination of the actual concentrations is very difficult.

Because cryosolutions often are studied in cryostats with long path lengths, special attention should be paid to possible impurities in the solvent gases used. Experiments with LAr or LN₂ as a solvent are typically performed by using gases with a purity of 99.9999%. The highest purity available for Kr or Xe is substantially less, resulting in several weak absorption bands caused by, amongst other substances, CO₂, CF₄, and SiF₄.

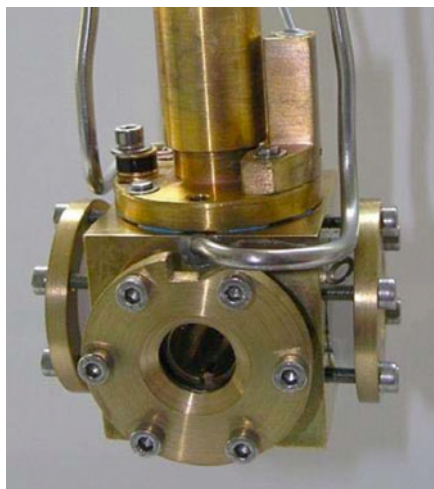
2.2 Raman Spectroscopy of Cryosolutions

To record Raman spectra of cryosolutions, a high-pressure liquid cell has been constructed [62–68]. The cell body, shown in Fig. 11, is machined from a brass block, is equipped with four quartz windows at right angles, and is attached to the cold head of a CRYO Industries of America RC102 continuous flow cryostat cooled with LN₂ or LHe. As before, the actual cell is suspended in a vacuum shroud while filling and evacuating of the cell is performed using two separate 1/8" stainless steel tubes brazed into the cell body. The cell is cooled by pumping small amounts of LN₂ from a Dewar to the cryostat by means of an isolated liquid transfer line. The flow is controlled by a diaphragm membrane pump, and is regulated by a precision needle valve. The cooling is balanced by a heating element attached to the cold head of the cryostat. The temperature is controlled and measured through a Cryocon 32B PID temperature controller.

To maximize the number of scattered photons, the cell is aligned within a multipass arrangement which allows the incident laser beam to pass through the same liquid several times. Because of the double set of windows through which the laser beam has to pass, experience shows the increase of the signal is limited to a factor close to 6.

The Raman spectra are recorded using a TriVista 557 spectrometer consisting of a double $f = 50$ cm monochromator equipped with 300/1,500/2,000 lines mm⁻¹ gratings and an $f = 70$ cm spectrograph equipped with 500/1,800/2,400 lines mm⁻¹

Fig. 11 High-pressure liquid cell constructed for Raman scattering experiments. The use of four quartz windows at right angles allows the use of a multipass arrangement in which the incident laser beam passes through the liquid several times



gratings and a back-end illuminated LN₂-cooled CCD detector. The 514.5 nm line of a Spectra-Physics argon ion laser is used for Raman excitation. To compensate for local heating of the solution appearing when greater laser powers are used, the power of the incident laser beam is typically varied between 0.5 W and 0.8 W. Frequencies are calibrated using Ne emission lines and, depending on the exact setup used, are expected to be accurate to 0.2–0.5 cm⁻¹.

The spectrometer can be used in three different setups: triple additive, triple subtractive, or third stage mode. To typify these settings, the $\nu_{C=C}$ vibration situated near 1,620 cm⁻¹ observed in the Raman spectrum of ethene dissolved in LAr was used (Hauchecorne and Herrebout, unpublished results). The full width at half-height and the intensity of the band, obtained using a power of 0.6 W for the incident laser beam, are 0.79 cm⁻¹ and 5.7 counts s⁻¹ in triple additive mode, 1.29 cm⁻¹ and 7.4 counts s⁻¹ in triple subtractive mode, and 1.27 cm⁻¹ and 50.6 counts s⁻¹ in third stage mode. These characteristics clearly indicate the differences between the different setups: the triple additive mode provides the best resolution while the third stage mode is better suited to detect weak features. Moreover, the spectral range for the third stage mode, 320 cm⁻¹, is more than twice the range for the triple additive mode, 135 cm⁻¹. However, using only the third monochromator comes with a few disadvantages such as the low stray light rejection resulting in a higher background signal and a difficult characterization of the modes close to the excitation line. The choice of setup is thus influenced by the specific requirements of an experiment. A schematic overview of the spectrometer in third stage mode is shown in Fig. 12.

The general workflow described above for the infrared experiments can in principle also be used for Raman experiments. During the initial experiments, however, it was soon realized that optimal experimental conditions involved pre-mixing of the solutes with a large excess of solvent gas in a stainless steel cylinder. After cooling the cell to the desired temperature, the homogenized gas

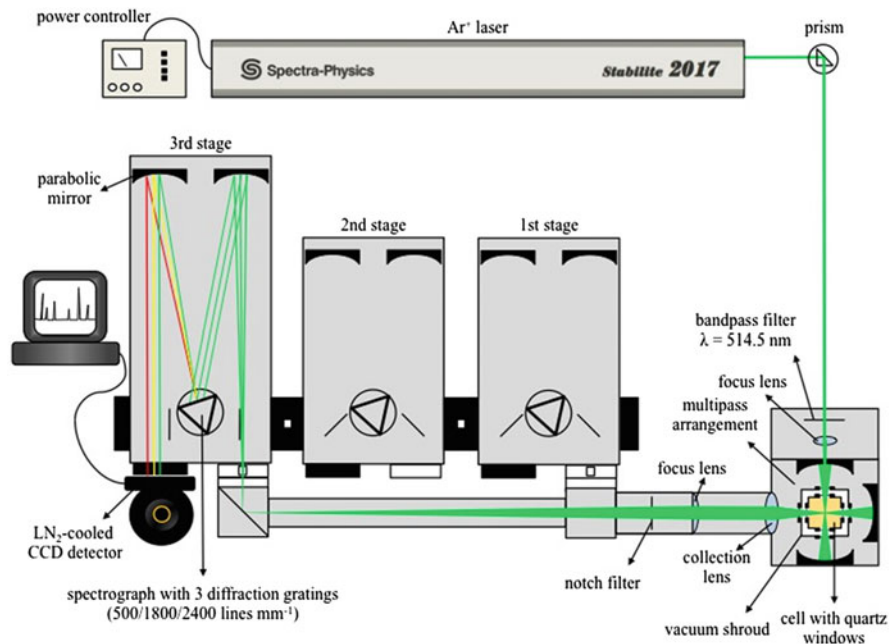


Fig. 12 Schematic overview of the experimental setup used for Raman experiments. For clarity, only the setup using the third stage spectrograph is given

mixture is allowed to condense in the cell and the cell is pressurized further with additional solvent gas. The reason for the better signal-to-noise ratio is not fully understood, but most probably is because with a pre-mixing setup the compounds under investigation do not require any additional turbulence of the solvent gas to dissolve and thus are more easily transferred into the liquid cell.

3 General Methodology Used for Studying Weakly Bound Molecular Complexes

Because of the changes in the electron distribution appearing upon complexation, and because of the resulting changes in vibrational frequencies, vibrational spectroscopy combined with matrix-isolation is a commonly used technique for the study of weakly bound molecular complexes. While it cannot compete with the precision and structural definition of gas phase studies, matrix isolation combined with IR and/or Raman spectroscopy provides valuable, often unique, information complementary to that derived from gas phase experiments. Unfortunately, because solid matrices are not in thermodynamical equilibrium, no direct information about the relative stability of the species can be deduced. This shortcoming can be avoided by studying the complexes in cryogenic solutions. Because these solutions

often make it possible to study the complexes over a broad temperature range and under equilibrium conditions, they can, in principle, be used to obtain information about their stoichiometry, their relative stability, and, to some extent, even their angular geometry.

During the past two decades, experimental studies of solutions in LRGs using IR and/or Raman spectroscopy have led to a wealth of information on weakly bound molecular complexes involving, amongst other substances, the Lewis acids HX ($X=F, Cl, Br, \text{ and } I$), BF_3 , BCl_3 , and CO_2 [69–97]. Solutions in LRGs have also proven to be an ideal medium to study the spectroscopic and thermodynamical properties of complexes held together by weak red- or blue-shifting C–H...X hydrogen bonds, typical Lewis acids studied so far [31, 64, 67, 98–132] being CHF_3 , CHF_2Cl , $CHFCl_2$, $CHCl_3$, CF_2CFH , C_2H_2 , and CF_3CCH .

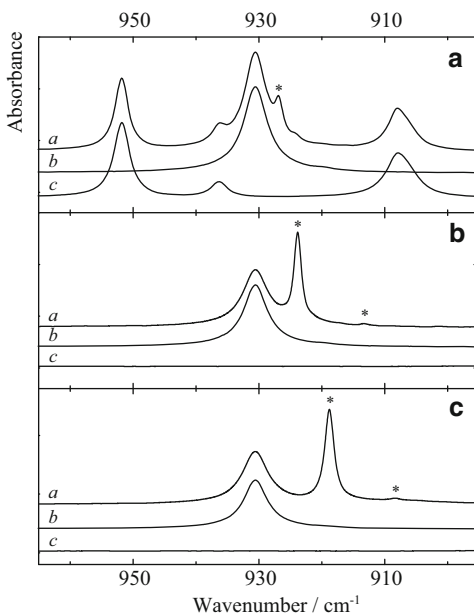
In the following paragraphs, the general methodologies used while studying weakly bound molecular complexes formed in solutions in LAr, LKr, and/or LXe are discussed. Where applicable, the procedures are illustrated with results obtained while studying mixed solutions containing the trifluorohalomethanes CF_3Cl , CF_3Br , or CF_3I , and the Lewis bases studied so far. A more complete survey of the results obtained so far and the trends observed are discussed in Sect. 4. It is shown that by combining theoretical data derived from ab initio molecular orbital calculations and experimental data obtained from cryosolutions, valuable data on the complexes can be obtained.

3.1 General Methodology

The study of complexes formed in cryosolutions is typically divided into several phases. In the first step, spectra of monomer solutions of the compounds under study are recorded to investigate their solubility, and to monitor whether homodimers and higher oligomers are formed. Next, spectra of mixed solutions are recorded and new bands, not present in the single-monomer spectra, are taken to signal the formation of complexes. The studies typically involve the recording of spectra of solutions with different monomer concentrations, and the recording of spectra at different temperatures. The analysis often also requires the combination of cells with different path lengths and/or window materials, and the use of different beamsplitters and detectors.

As an example, in Fig. 13, IR spectra of mixed solutions containing CF_3Cl , CF_3Br , or CF_3I , and dimethyl ether (DME) and those of solutions containing only monomers are compared. For each halogen donor studied a complex band caused by the symmetric C–O–C stretching mode in the complex can be observed [48] on the low frequency side of the 930.6 cm^{-1} band of monomer DME. The data also show that for the complex with CF_3Cl , only a small red shift, by -3.8 cm^{-1} , occurs, while for the complexes with CF_3Br and CF_3I the frequency changes are significantly larger. The increase in complexation shift, from -3.8 cm^{-1} for CF_3Cl to -6.8 cm^{-1} for CF_3Br and -11.7 cm^{-1} for CF_3I , is in line with theoretical results

Fig. 13 Infrared spectra of the symmetric C–O–C stretching region ν_6 (DME) for solutions of mixtures of CF_3Cl (**a**), CF_3Br (**b**), and CF_3I (**c**) with dimethyl ether dissolved in LAr, at 96 K. In each panel, trace *a* represents the spectrum of the mixed solution while traces *b* and *c* refer to the spectra of the solutions containing only dimethyl ether or CF_3X , respectively. The new bands appearing in the spectra of the mixture assigned to the 1:1 complex are marked with an *asterisk* (*). Reprinted with permission from [48]. Copyright (2013) John Wiley & Sons, Inc



derived from *ab initio* calculations. The data also nicely reflect the changes in relative stability of the complexes while substituting the halogen donor. Apart from the bands reported above, in the spectra of the mixed solutions containing CF_3Br and CF_3I , weak spectral features caused by the 1:1 complexes are also observed near 913.6 cm^{-1} and 908.3 cm^{-1} , respectively. These bands are assigned to the C–O–C stretching mode in the complexes with the ^{13}C isotopomer $^{12}\text{CH}_3\text{O}^{13}\text{CH}_3$. The complexation shifts observed, -6.4 cm^{-1} for the complex with CF_3Br and -11.7 cm^{-1} for the complex with CF_3I , compare favorably with those obtained above.

Because the cryosolutions are in chemical equilibrium, and because all complexation reactions studied are exothermic, small changes in temperature can result in relatively large changes in the relative intensity of monomer and complex bands. The observation of new complex bands, therefore, is facilitated by carefully comparing spectra of mixed solutions recorded at a variety of temperatures, typical temperature ranges and intervals being at least $20\text{--}25^\circ\text{C}$, and 1°C or 2°C , respectively.

An example of a typical temperature series obtained for a mixed solution in LAr containing DME and a large excess of CF_3Br [48] is depicted in Fig. 14. Apart from the bands at 930.6 cm^{-1} and 923.8 cm^{-1} , assigned above to the monomer DME and the 1:1 complex of DME with CF_3Br , at lower temperatures an additional feature arises near 916.8 cm^{-1} . This band is assigned to a 1:2 complex involving one DME molecule and two CF_3Br units simultaneously bound to the oxygen atom. The assignment of the bands at 923.8 cm^{-1} and 916.8 cm^{-1} to two different species showing different relative stabilities and different stoichiometries is confirmed by

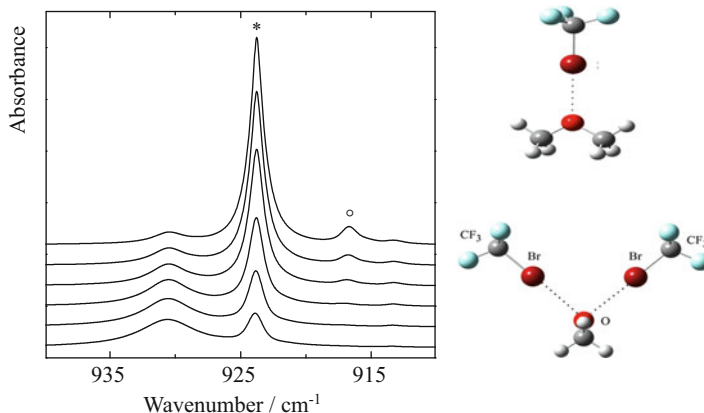


Fig. 14 Temperature dependence for the symmetric C–O–C stretching region obtained by studying a mixed solution in LAr containing dimethyl ether, and a large excess of CF_3Br . From *top to bottom*, the temperature of the solution increases with a 3 K interval, from 87 to 102 K. The band assigned to the 1:1 complex is marked with an *asterisk* (*); the band assigned to the 1:2 complex is marked with a *circle* (°)

temperature studies and concentration studies, to be discussed below. The experimental data are also in excellent agreement with calculated harmonic vibrational frequencies, the unscaled *ab initio* values for the COC stretching mode reported [48] being 971.7 cm^{-1} for monomer DME and 965.2 cm^{-1} and 955.4 cm^{-1} for the 1:1 and 1:2 complexes, respectively.

3.2 *Separating Monomers and Complexes: Subtraction Procedures*

From the data in Fig. 13 it is clear that, because of the weakness of the complexes studied, new bands often are only slightly shifted from the corresponding monomer bands. Consequently, complex and monomer bands tend to show considerable overlap.

To separate the contributions from the monomers and complexes, subtraction techniques are often used, in which spectra of the monomer solutions, recorded at similar concentrations and at identical temperatures, are rescaled and subtracted from the spectra of the mixture. Typical results obtained for a solution in LAr containing both DME and CF_3Cl [48] as in Fig. 13 are summarized in Fig. 15.

It is of interest to note that, by using subtracting procedures, the band areas of the monomer and complex bands can be accurately determined using a simple numerical integration and the inaccuracies inherently connected to resolving strongly overlapping bands with least square band fitting procedures can be avoided. This result is important, as accurate band areas of monomer or complex bands are

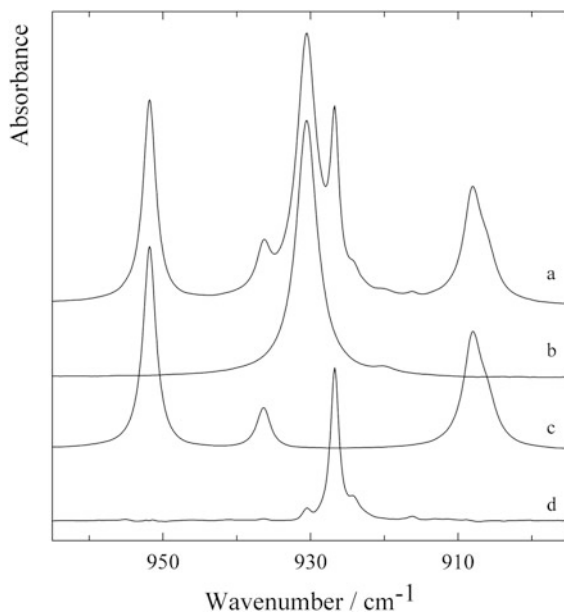


Fig. 15 Decomposition of an experimental spectrum of a solution in LAr containing dimethyl ether and CF_3Cl , at 88 K. Trace *a* shows the spectrum recorded for a solution of DME and CF_3Cl . Traces *b* and *c* are the rescaled monomer spectra showing the contributions of monomer DME and monomer CF_3Cl . Trace *d* shows the isolated spectrum of the complex obtained by subtracting traces *b* and *c* from trace *a*

required during further analyses, including confirmation of the stoichiometry of the complex and determination of the complexation enthalpy. As illustrated in the following sections, the use of subtraction procedures also allows the identification of weak spectral features not immediately visible in the original spectra.

3.3 Confirming the Stoichiometry: Concentration Studies

Using the Lambert–Beer law combined with the equilibrium constant for the formation of a complex A_mB_n



it is easily shown that the band area of a complex band is linearly related to the product of the m th power of the monomer band area I_A and the n th power of the monomer band area I_B :

$$I_{A_mB_n} = C(I_A)^x(I_B)^y \quad (2)$$

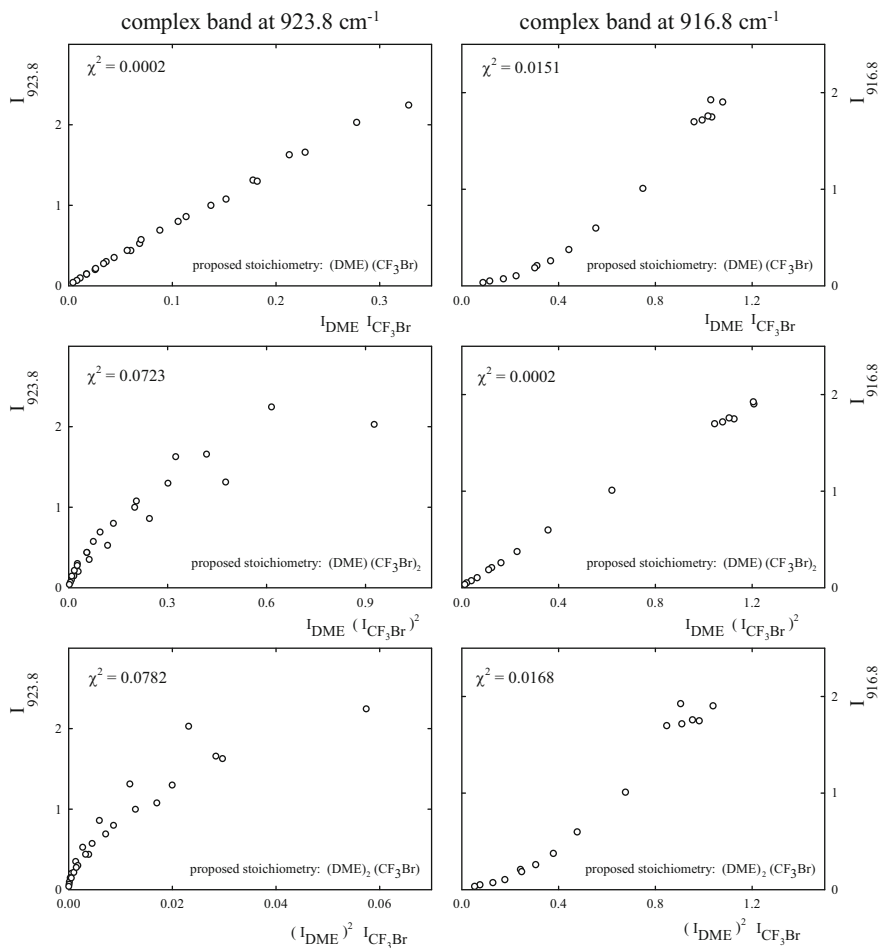


Fig. 16 Concentration studies for the 923.8 cm⁻¹ (left) and 916.3 cm⁻¹ (right) complex bands observed for mixed solutions in LAr containing dimethyl ether and CF₃Br. The integrated band areas of the complex bands were plotted against the intensity products corresponding to a 1:2, 1:1, and 2:1 stoichiometry

where C is a constant related to the equilibrium constant. This equation shows that for an isothermal concentration study in which spectra are recorded for solutions where the concentrations of the solutes are systematically varied, a plot of the complex band area vs the product of the monomer band areas $(I_A)^x(I_B)^y$ yields a linear dependence only when $x = m$ and $y = n$. By preparing a series of plots for various integer values of x and y , and by comparing the degrees of linearity observed, the stoichiometry of the complex can be established.

Typical examples of such a procedure, obtained for the two complexes formed between DME and CF₃Br reported above, are shown in Fig. 16. The data obtained were obtained by recording spectra of solutions in LAr containing different mole

fractions of DME, varying between 1.3×10^{-5} and 2.6×10^{-4} , and of CF_3Br , varying between 0.3×10^{-6} and 5.6×10^{-5} , at a constant temperature of 93.0(1) K. It can be seen that for the 923.8 cm^{-1} band, a linear correlation is obtained for a proposed 1:1 stoichiometry only, while for the band at 916.8 cm^{-1} , a linear dependence is observed for a proposed 1:2 stoichiometry only. These results obviously confirm the suggested stoichiometry of the different complexes. In many studies, for each combination of n and m , the degree of linearity is expressed by calculating the χ^2 value of the linear regression line. The resulting values obtained for the different plots are also included in the panels of Fig. 16. It can be seen that, for both the 923.6 cm^{-1} and the 916.8 cm^{-1} complex bands, the values obtained for the correct stoichiometry are significantly smaller than those obtained for the other combinations.

3.4 Determining the Relative Stability: Temperature Studies

Standard complexation enthalpies are traditionally derived from temperature studies in which spectra of a solution are recorded at a variety of temperatures, and in which the resulting band areas of monomer and complex bands of different solutions are analyzed using the Van't Hoff relation. The key element of the analysis is the approximation that, in a limited temperature interval, the standard complexation enthalpies and the corresponding values for the complexation entropies are independent of temperature.

For traditional solvents, the complexation enthalpy for a complex can be obtained by plotting the logarithm of the intensity ratio of complex and monomer intensities vs the inverse of temperature $1/T$. The relation between both quantities, derived from the Van't Hoff isochore, is given by

$$\ln \left[\frac{I_{A_mB_n}}{I_A^m \times I_B^n} \right] = -\frac{\Delta H^\circ}{RT} + c^{st} \quad (3)$$

This approach is valid when the temperature variation of the spectral intensities is fully accounted for by the shift in the chemical equilibrium as a consequence of a change in temperature. For cryosolutions such as solutions in liquid rare gases, this condition is not fulfilled as a consequence of the pronounced variation in liquid density of these solvents over the available temperature interval.

Corrections to account for the changes in liquid density have been described by Bertsev et al. [133] and by Van der Veken [134]. These studies have shown that for an ideal solution, the equilibrium constant of a complex $A_m - B_n$ can be written as

$$K_{eq} = \frac{I_{AmBn}}{I_A^m I_B^n} \frac{\varepsilon_A^m \varepsilon_B^n}{\varepsilon_{AmBn}} \frac{\rho^{n+m-1} d^{n+m-1}}{M_a^{n+m-1}} \quad (4)$$

in which I_{AmBn} , I_A , and I_B are the band areas of bands assigned to the complex and the monomer species, ε_{AmBn} , ε_A , and ε_B are the corresponding IR intensities, ρ and M_a are the average density and the average molar mass of the solution, and d is the path length of the liquid cell. Combination of this expression with

$$-RT \ln K_{eq} = \Delta G^o = \Delta H^o - T \Delta S^o \quad (5)$$

leads to the following expression:

$$-\frac{\Delta H^o}{RT} = \ln \left[\frac{I_{AmBn}}{I_A^m I_B^n} \right] + (n+m-1) \ln \rho + C \quad (6)$$

with C a constant equal to

$$C = \ln \left[\frac{\varepsilon_A^m \varepsilon_B^n}{\varepsilon_{AmBn}} \left(\frac{d}{M_a} \right)^{n+m-1} \right] - \frac{\Delta S^o}{R} \quad (7)$$

The influence of the solvent density on the slope of a Van't Hoff plot can be compensated for by using two different procedures. The first is based on the fact that for the temperature ranges envisaged, the logarithm of the density of the cryosolvents is approximately inversely related to the temperature:

$$\ln \rho = a + \frac{b}{T} \quad (8)$$

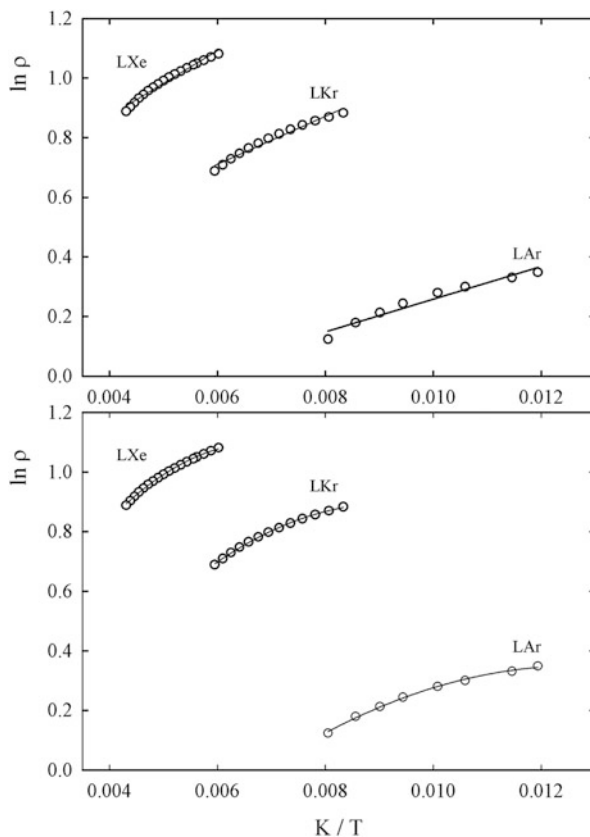
in which a and b are temperature-independent constants. With this, (6) can be written as

$$\ln \left[\frac{I_{AmBn}}{I_A^m I_B^n} \right] = - \left[\frac{\Delta H^o + (n+m-1)Rb}{R} \right] \frac{1}{T} - (cst + a) \quad (9)$$

This relation shows that the slope of the Van't Hoff plot, multiplied by R , equals $-(\Delta H^o + (n+m-1)Rb)$, and not $-\Delta H^o$ as in the simple approximation. The value of b is the slope of the plot of $\ln \rho$ vs $1/T$. Typical plots, obtained for LAr, LKr, and LXe in the temperature ranges in which vapor pressure is below 15 bar, are shown in Fig. 17. In the upper panel, the resulting linear regression lines are also shown. The corresponding values for Rb are 0.46(8) kJ mol⁻¹ for LAr, 0.623(4) kJ mol⁻¹ for LKr, and 1.359(6) kJ mol⁻¹ for LXe [134].

The complexation enthalpies for 1:1 complexes observed in cryosolutions typically exceed 3 kJ mol⁻¹, with uncertainties for the more accurate determinations in the order of 0.2–0.3 kJ mol⁻¹. From this, it follows that, for the solutions in LAr and

Fig. 17 Scatter plots obtained for $\ln \rho$ vs the inverse temperature: (*top*) regression lines obtained by assuming a linear dependence; (*bottom*) regression lines obtained by assuming a quadratic dependence



LKr, the value of Rb is small compared to ΔH^o . However, the values exceed the average uncertainty, so the corrections are small but statistically significant. For complexes with a higher stoichiometry, or for solutions in LXe, the density influences are obviously more prominent.

Close scrutiny of the data in Fig. 17 shows that the correct description of the relation between $\ln \rho$ and $1/T$ requires not only a first-order term and small higher order terms may be necessary. In view of the typical error margins, these small higher order terms are expected not to disrupt markedly the linearity of the Van't Hoff plot, so the complexation enthalpy can be obtained in the way suggested by (9), i.e., by constructing the Van't Hoff plot using the logarithm of the intensity ratios, and correcting the slope by the term $(n + m - 1)Rb$.

As an alternative to the method described above, for pronounced cases where changes in solvent densities cause the simple Van't Hoff plot to deviate from linearity, it is better to follow a procedure suggested by (6). In the second method, it is therefore recommended to obtain the values for the logarithm of the intensity ratio and $(n + m - 1)\ln \rho$ for each temperature separately, and plot the sum of both terms against the inverse temperature. For such analysis, the complexation enthalpy

Fig. 18 Van't Hoff plots for the 1:1 complexes of CF_3I (A), CF_3Br (B), and CF_3Cl (C) with TMA dissolved in LXe, LKr, and LAr, respectively. Reprinted from [135] with permission from Elsevier

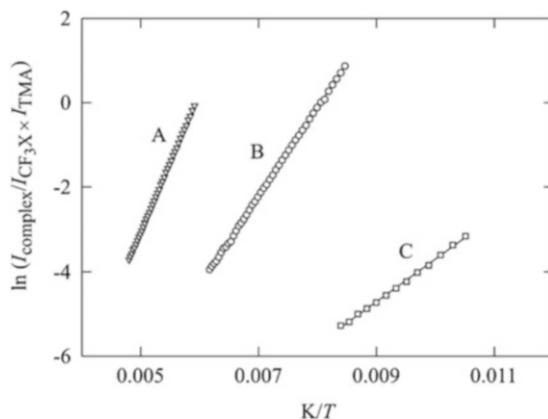
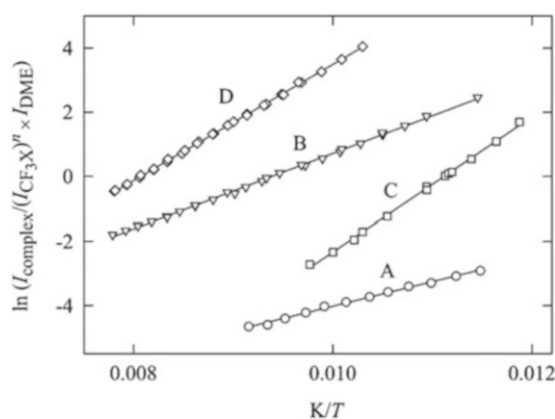


Fig. 19 Van't Hoff plots for the complexes of CF_3Cl (A), CF_3Br (1:1, B; 2:1, C), and CF_3I (D) with DME dissolved in LAr. Reprinted with permission from [48]. Copyright (2013) John Wiley & Sons, Inc



is obtained by calculating the slope of the linear regression line directly, and no subsequent correction is required.

Typical Van't Hoff plots obtained for the complexes of CF_3X ($\text{X}=\text{Cl}$, Br , and I) with the Lewis bases trimethylamine (TMA) and DME are reproduced in Figs. 18 and 19. The results obtained for TMA (Fig. 18) illustrate the use of the different solvents LXe, LKr, and LAr. The results obtained for DME shown in Fig. 19 reflects the use of Van't Hoff plots to characterize complexes with 1:1 and 1:2 complexes which can simultaneously appear in the solutions studied

3.5 *Ab Initio* Calculations and Statistical Thermodynamics

To assist in the interpretation of the experimental data and the rationalization of the results obtained, the experimental data are supported by a variety of quantum chemical calculations, in which the structural, thermodynamic, and spectroscopic

properties of the species under study are predicted. A detailed description of the different methodologies and basis sets applicable to weak and medium strong C–X...Y halogen-bonded complexes involving, among other compounds, CF₃Cl, CF₃Br, and CF₃I was deemed beyond the scope of this chapter, and interested readers are referred to other chapters in this book. It is of interest, however, to note that since the first experiments performed on weak halogen-bonded complexes, various combinations of basis sets and pseudo-potentials have been evaluated. In the initial stages of the studies, SDD and Lanl2DZ* basis sets were used for all halogens, while the 6–311++G(*d,p*) basis set was used for all atoms other than chlorine, bromine, and iodine. More recently, the aug-cc-pV(D)(T)Z-PP basis set was used for bromine and iodine while the standard aug-cc-pV(D)(T)Z basis set was used for any other atom including chlorine. During all calculations, corrections for Basis Set Superposition Error (BSSE) were accounted for explicitly using counterpoise (CP) corrected gradients and Hessians.

It should be noted that to be able to compare experimental and calculated values on the relative stability of the complexes, the predicted complexation energies should be converted into complexation enthalpies. For the weak complexes studied here, corrections for zero-point vibrational and thermal influences typically yield a vapor phase enthalpy which, in absolute values, is 2–3 kJ mol⁻¹ smaller than the initial energy. It is also worth noting that the vibrational spectra are traditionally predicted using the double harmonic approximation, and that effects caused by mechanical and/or optical anharmonicities are thus neglected. Taking into account that in some cases, including, for example, CF₃I, the experimental spectra can be heavily perturbed by Fermi resonances, the effects of these approximations cannot always be neglected.

3.6 Monte Carlo-Free Energy Perturbation Simulations

Although solutions in liquefied rare gases were originally described as pseudo-gas phases, it is now generally accepted that, in cryosolutions, significant solute–solvent interactions can occur. These interactions not only influence the frequencies of monomers and complexes, but also perturb the relative stability of the complexes studied. The *ab initio* complexation energies and the vapor phase enthalpies derived should therefore not be directly compared with the experimental values deduced from cryosolutions.

To be able to estimate the solvent effects, and to predict the complexation enthalpies in the solutions, new methodologies involving Monte Carlo Free Energy Perturbation (MC-FEP) simulations were introduced [125, 136]. The optimized procedure involves a calculation of the Gibbs free energy of solvation $\Delta_{sol}G$ for the monomers and for the complexes, at a variety of temperatures, varying between 88 K and 138 K for solutions in LAr, between 119 K and 179 K for solutions in LKr, and between 171 K and 231 K for solutions in LXe. The calculation of the Gibbs energies is then followed by an enthalpy–entropy decomposition involving the expressions

$$\Delta_{\text{sol}}H = \Delta_{\text{sol}}G + T\Delta_{\text{sol}}S \quad (10a)$$

$$\Delta_{\text{sol}}S = -(\partial\Delta_{\text{sol}}G/\partial T)_p \quad (10b)$$

According to statistical perturbation theory, the Gibbs free energy of solvation is calculated as the energy difference between a reference system *A* representing a box containing only solvent molecules and a perturbed system *B* with a single solute molecule surrounded by the same number of solvent molecules. To avoid numerical instabilities, the introduction of the solute molecule is not carried out in a single step, but involves *k* intermediate (virtual) states between *A* and *B* introduced by means of a coupling parameter $\lambda_i (0 \leq \lambda_i \leq 1)$. The change in free energy can then be written as the sum of all intermediate energy differences:

$$\Delta_{\text{sol}}G(0 \rightarrow 1) = \sum_{i=1}^{k-1} \Delta_{\text{sol}}G(\lambda_i \rightarrow \lambda_{i+1}) = -k_{\text{B}}T \sum_{i=1}^{k-1} \ln \left\langle e^{-\frac{H_{\lambda_{i+1}} - H_{\lambda_i}}{k_{\text{B}}T}} \right\rangle \quad (11)$$

in which the angle brackets indicate averaging over the ensemble considered and *H* is the Hamiltonian describing the perturbed, λ_{i+1} , and unperturbed, λ_i , systems for each species involved.

The calculations are usually done in the binary approximation, meaning the interaction potential between any two species is assumed not to be affected by the presence of further species in their neighborhood. In this approximation, and because of the nature of rare gases, the solvent–solvent interactions are satisfactorily described by Lennard–Jones potentials, accounting for long-range dispersion attraction and short range exchange repulsion. Solute–solvent interactions are typically described by a sum of two contributions. The first is obtained by using one Lennard–Jones function between each solvent atom and each atom of the solute molecule. The second contribution accounts for the polarization of the solvent atoms by the solute and is calculated in a non-iterative first-order approximation as

$$E_{\text{pol}} = -\frac{1}{2} \vec{\mu}_{\text{ind}} \cdot \vec{E} = -\frac{1}{2} \alpha_{\text{solvent}} (\vec{E} \cdot \vec{E}) \quad (12)$$

where α_{solvent} is to the polarizability of the rare gas studied, and \vec{E} is the electric field generated by the solute. The partial charges on the different nuclei, used to mimic the electric field generated by the solute, are optimized so as to reproduce the dipole moment and the electric potential around the molecule [125, 136]. The ϵ and σ parameters for the Lennard–Jones potentials are typically taken from the OPLS (Optimized Potentials for Liquid Simulation) all-atom force field. For an interaction between two different atoms *i* and *j*, traditional mixing rules are applied:

$$\epsilon_{ij} = \sqrt{\epsilon_{ii}\epsilon_{jj}} \quad \sigma_{ij} = \frac{1}{2}(\sigma_{ii} + \sigma_{jj}) \quad (13)$$

As an example, in Fig. 20, the calculated values for the Gibbs energy of solvation obtained for the complexes of TMA with the trifluorohalomethanes and the

Fig. 20 Gibbs free energies of solvation obtained for the complexes of trimethylamine with CF_3X ($\text{X}=\text{Cl}$, Br , and I) and for the monomers involved. For each trifluorohalomethane, the solvent gas used in the experimental studies was also used for the calculations

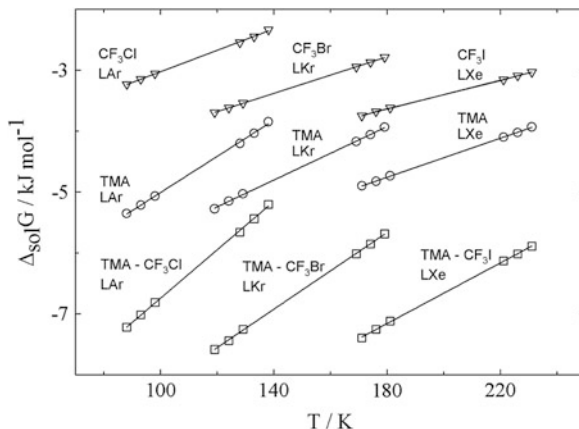


Table 1 Enthalpies of solvation, in kJ mol^{-1} , obtained for the complexes of trimethyl amine (*TMA*) with the different trifluorohalomethanes CF_3X ($\text{X}=\text{Cl}$, Br , I)

$\Delta_{\text{sol}}H/\text{kJ mol}^{-1}$	TMA – CF_3Cl (LAr)	TMA – CF_3Br (LKr)	TMA – CF_3I (LXe)
CF_3X	–20.04 (25)	–22.93 (9)	–24.15 (17)
TMA	–33.39 (42)	–32.98 (25)	–32.01 (18)
TMA – CF_3X	–44.86 (42)	–47.46 (22)	–48.71 (33)
Destabilization	8.6 (6)	8.5 (3)	7.4 (4)

For completeness, the net destabilization of the complexes in the solutions studied is also given

corresponding monomers are summarized. The data for TMA- CF_3Cl were obtained [135] using LAr as a solvent, while the data for the complexes with CF_3Br and CF_3I were obtained in LKr and LXe, respectively. The values for $\Delta_{\text{sol}}H$ and $\Delta_{\text{sol}}S$ obtained from the linear regression lines derived are summarized in Table 1. Close scrutiny of the data shows that for all trifluorohalomethanes the sum of the solvent stabilizations of the monomers is greater than that of the complex, the difference being approximately 8.6 kJ mol^{-1} for TMA- CF_3Cl , 8.5 kJ mol^{-1} for TMA- CF_3Br , and 7.4 kJ mol^{-1} for TMA- CF_3I . It thus follows that in the solutions, the complexes are destabilized with respect to the monomers. Similar destabilizations are also observed for the other halogen complexes studied.

4 Weak C–X...Y Halogen-Bonded Complexes Involving CF_3X

In the following paragraph, the main results obtained during a detailed study in which the complexes of the trifluorohalomethanes CF_3Cl , CF_3Br , or CF_3I with a variety of weak, medium, and strong Lewis bases were examined experimentally using cryosolutions are summarized. It is shown that by combining theoretical data

derived from *ab initio* molecular orbital calculations and experimental data obtained from cryosolutions, and by exploiting the complementarity of IR and Raman spectroscopy, valuable data on all different complexes can be obtained. It should be noted we focus mainly on the vibrational spectra obtained and on the complexation enthalpies derived from them, while only little attention is paid to the supporting data derived from *ab initio* and MC-FEP calculations. These results are available from the original papers.

4.1 Infrared and Raman Spectra of Isolated CF_3X Molecules

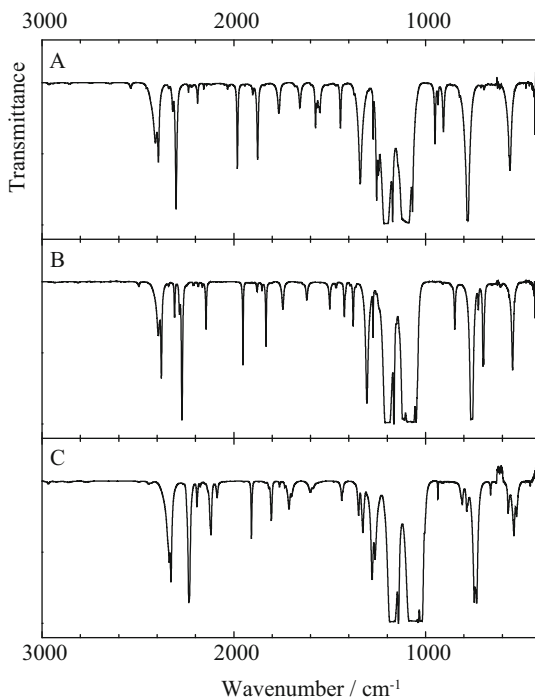
The vibrational spectra of the monomer trifluorohalomethanes CF_3Cl , CF_3Br , and CF_3I in the gas phase and in liquid rare gases have been thoroughly studied [39–47]. As a consequence, extensive information has been gathered on the harmonic and anharmonic frequencies of CF_3X , on the effects of Fermi and higher resonances, and on corrections related to the appearance of vibrational angular momentum. Because of C_{3v} symmetry, all compounds give rise to $3N - 6 = 9$ vibrational degrees of freedom. The first three modes ν_1 , ν_2 , and ν_3 are non-degenerate and have A_1 symmetry. The remaining modes give rise to degenerated modes and have E symmetry.

Figure 21 shows the IR spectra of CF_3Cl (Fig. 21A), CF_3Br (Fig. 21B), and CF_3I (Fig. 21C) dissolved in LKr at 123 K. Apart from the fundamentals, combination bands, and overtones, for all species, additional features caused by ^{13}C isotopomers are observed, the intensity ratios with the bands of the $^{12}CF_3X$ parent molecule being close to the natural abundance of 1.1%. In addition, significant isotope splittings with approximate intensity ratios of 3:1 and 1:1 are observed for all transitions involving the $C-^{35/37}Cl$ or $C-^{79/81}Br$ stretching vibrations.

The harmonic vibrational frequencies, IR intensities, and Raman scattering activities for CF_3Cl , CF_3Br , and CF_3I , calculated at the MP2/6–311++G(*d,p*)/LanL2DZ* and MP2/aug-cc-pVDZ(-PP) levels, and the corresponding frequencies observed for solutions in LKr, at 123 K, are summarized in Table 2. It should be stressed that, in agreement with literature data [39–47], the different C–X stretching vibrations are calculated to have an extremely small IR intensity. It is also of interest to note that, for CF_3I , a complex resonance pattern involving ν_1 , $2\nu_5$, $\nu_5 + 2\nu_6$, and $4\nu_6$ is observed. The quadruple resonance obviously influences the spectra in the ν_1 and $2\nu_1$ regions.

Last but not least, it is worth mentioning that the spectra of the different monomer solutions were scrutinized for evidence of self-associations, but no indications of such a process were found.

Fig. 21 Infrared spectra for a solution in LKr, at 123 K, containing CF₃Cl (A), CF₃Br (B), and CF₃I (C). The mole fractions of the trifluorohalomethanes used are 3.5×10^{-4} , 4.6×10^{-4} , and 2.8×10^{-4} , respectively



4.2 C–X...N-Bonded Complexes: Trimethylamine

Experimental results on halogen-bonded complexes of trimethylamine with CF₃Br and CF₃I were first reported by Pullin and co-workers [11–17]. The studies, involving vapor pressure measurements, IR, ¹H, and ¹⁹F NMR spectroscopy, led to the identification of the complexes of TMA with CF₃Br and CF₃I. In addition, using NMR spectroscopy in the temperature range 263–313 K, the standard complexation enthalpy for TMA-CF₃I in a benzene solution was determined to be $-25(3) \text{ kJ mol}^{-1}$.

Triggered by the work of Pullin et al., by the experimental observation that TMA has an excellent solubility in all liquid rare gases, and by the fact that at the start of the experimental studies no experimental information on molecular complexes held together by a weak C–Cl...N halogen bond was reported, a study on the formation of halogen-bonded complexes between TMA and CF₃I, CF₃Br, and CF₃Cl dissolved in LXe, LKr, and LAr was initiated [135]. For all halogen donors, evidence was found for the formation of C–X...N halogen-bonded 1:1 complexes, and experimental information on their relative stability was derived by determining their standard complexation enthalpy. The study provided the first experimental characterization of a complex formed under thermodynamic equilibrium conditions in solution via a C–Cl...N halogen bond. The renewed interest in C–X...N halogen-bonded complexes has also triggered other experimentalists. Typical

Table 2 Harmonic vibrational frequencies ν , in cm^{-1} , infrared intensities ϵ , in km mol^{-1} , and Raman scattering activities S , in $\text{\AA}^4 \text{amu}^{-1}$, for CF_3Cl , CF_3Br , and CF_3I calculated at the MP2/6-311++G(*d,p*)+Lanl2DZ* and MP2/aug-cc-pVDZ(-PP) level

		Lanl2DZ*			aug-cc-pVDZ(-PP)			Experiment LKr, 123 K
		N	ϵ	S	nu	ϵ	S	
CF_3Cl	ν_1	1,142.1	485.3	0.7	1,096.4	469.6	1.5	1,099.7
	ν_2	799.2	21.0	5.2	764.7	24.8	9.3	781.2
	ν_3	499.9	0.2	4.5	479.9	0.1	4.8	476.6/468.9
	ν_4	1,226.1	713.4	1.5	1,192.5	564.4	3.0	1,207.5
	ν_5	569.5	5.0	2.6	545.9	2.8	1.6	560.3
	ν_6	363.9	0.03	2.9	347.1	0.004	1.7	347.7
CF_3Br	ν_1	1,102.7	530.2	1.7	1,078.3	496.2	3.1	1,075.2
	ν_2	767.5	35.9	5.0	739.5	30.4	9.0	759.4
	ν_3	360.4	0.007	5.8	360.9	0.03	5.9	352.1/350.3
	ν_4	1,215.6	624.5	1.8	1,180.2	509.7	3.3	1,198.1
	ν_5	554.3	3.2	2.0	531.4	1.8	1.5	546.3
	ν_6	313.2	0.001	2.3	305.5	0.02	1.5	303.4
CF_3I	ν_1	1,085.6	597.5	16.0	1,059.6	547.3	9.6	1,067.4
	ν_2	751.6	42.7	6.5	722.3	34.7	10.9	740.7
	ν_3	293.3	0.02	9.5	294.9	0.3	8.2	286.4
	ν_4	1,197.9	564.2	3.7	1,162.6	455.5	3.5	1,175.6
	ν_5	544.0	2.2	1.6	518.8	1.1	1.4	539.9
	ν_6	279.2	0.01	2.3	269.1	0.05	1.5	266.0

For completeness, the values for the fundamental transitions observed in LKr, at 123 K, are also given

complexes for which a detailed microwave study is now reported include the complex of ammonia with CF_3Cl [50] and the 1:1 adducts of CF_3I with ammonia and trimethylamine [53]. Related complexes recently investigated using IR and NMR spectroscopy [56] are formed between pyridine and the perfluoroalkyl iodides heptafluoro-2-iodopropane (iso- $\text{C}_3\text{F}_7\text{I}$) and heptafluoro-1-iodopropane (1- $\text{C}_3\text{F}_7\text{I}$).

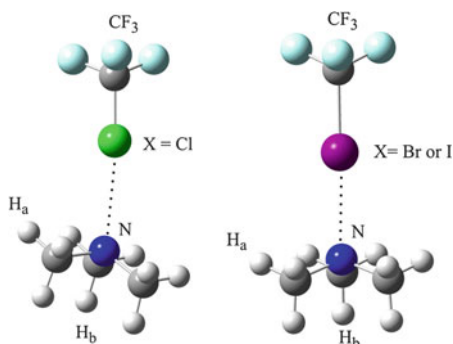
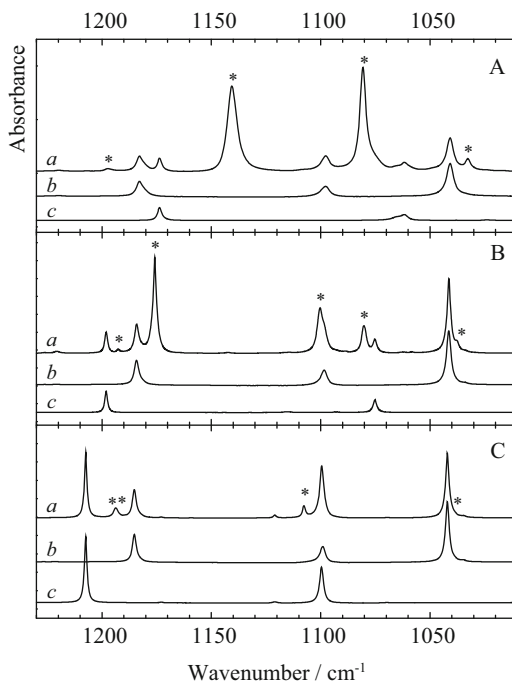


Fig. 22 Infrared spectra of the 1,230–1,010 cm^{-1} region for solutions of mixtures of CF_3I (A), CF_3Br (B), and CF_3Cl (C) with TMA dissolved in LXe (173 K), LKr (123 K), and LAr (96 K), respectively. Trace *a* represents the spectrum of the mixed solution and traces *b* and *c* are the spectra of the monomer TMA and CF_3X solution, respectively. The new bands appearing in the spectra of the mixture assigned to the 1:1 complex are marked with an *asterisk* (*). Reprinted from [135] with permission from Elsevier



4.2.1 Vibrational Spectra

To measure the complexation enthalpies, IR spectra of different series of mixtures of CF_3X and TMA dissolved in liquid rare gases were investigated. The success of the temperature studies largely depends on the availability of spectra in which monomer and complex bands are present with a similar intensity. For the weaker complex with CF_3Cl , this required the lower temperatures provided by LAr as a solvent, while for the complexes with CF_3Br and CF_3I the optimum relative intensities were achieved in LKr and LXe, respectively.

Apart from the monomer bands in the spectra of the mixed solutions of CF_3X and TMA, new bands caused by 1:1 complexes were observed for a variety of modes localized in the CF_3X or TMA moieties. In Fig. 22A, the CF_3 stretching region for a solution containing TMA and CF_3I dissolved in LXe, trace *a*, is compared with the spectra of the respective monomers in traces *b* and *c*. The new bands in the spectra of the mixture, marked with an asterisk, are assigned to the 1:1 complex. It can be seen that, in the region concerned, two strong and two weak complex bands are detected. Ab initio calculations suggest that the C–F stretches must give rise to the strongest bands in that region, and it is, therefore, straightforward to assign the high frequency component of the strong doublet to the antisymmetric $\nu_4(\text{CF}_3\text{I})$ and the low frequency component to the symmetric $\nu_1(\text{CF}_3\text{I})$ CF_3 stretching mode. It follows that the complexation shifts for $\nu_4(\text{CF}_3\text{I})$ and $\nu_1(\text{CF}_3\text{I})$ in LXe are -32.9 cm^{-1} and $+15.1 \text{ cm}^{-1}$, respectively. These shifts are in good agreement with those observed in CCl_4 solution [11–17], -31 cm^{-1} and

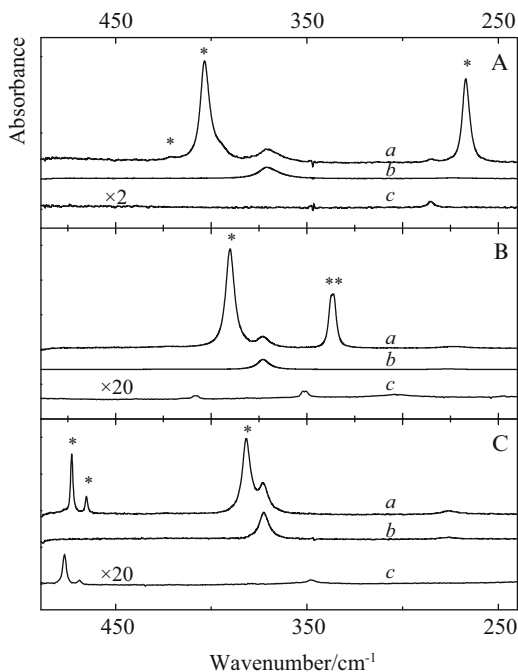
+15 cm⁻¹, and with ab initio predictions [135], -31.4 cm⁻¹ and +17.8 cm⁻¹. It should be noted that in the solid phase the corresponding shifts are significantly larger, the reported shifts being -62 cm⁻¹ and +24 cm⁻¹, respectively [11–17].

Similar arguments allow the complex bands at 1,175.9 cm⁻¹ and 1,080.3 cm⁻¹ in the spectrum of CF₃Br/TMA mixed solutions in LKr (Fig. 22B) to be associated with $\nu_4(\text{CF}_3\text{Br})$ and $\nu_1(\text{CF}_3\text{Br})$. This results in complexation shifts of -22.2 cm⁻¹ and +5.1 cm⁻¹, in good agreement with the ab initio values of -21.6 cm⁻¹ and +10.2 cm⁻¹, respectively, but differing significantly from the shifts of -39 cm⁻¹ and +32 cm⁻¹ observed by Pullin for the same complex in the solid phase [11–17]. This discrepancy, however, is likely produced by a solid state effect on the complexation shifts similar to the one pointed out in the previous paragraph for TMA-CF₃I.

The corresponding spectral region for a mixture of CF₃Cl and TMA dissolved in LAr is shown in Fig. 22C. Although of considerably weaker intensity, new bands are observed for this mixture as well. A weak shoulder appears on the low frequency side of the $\nu_{20}(\text{TMA})$ band situated at 1,042.1 cm⁻¹. This band must be identified as the $\nu_{20}(\text{TMA})$ complex band. Another new band is seen at 1,107.8 cm⁻¹. This band is caused by either $\nu_{19}(\text{TMA})$ or $\nu_1(\text{CF}_3\text{Cl})$. In analogy with the assignments made above for the CF₃I and CF₃Br complexes, this complex band should be assigned to $\nu_1(\text{CF}_3\text{Cl})$. Two more complex bands can be seen in Fig. 22C, at 1193.7 cm⁻¹, and as a shoulder on this band at 1,189.8 cm⁻¹. The vibrations expected in this region are $\nu_4(\text{CF}_3\text{Cl})$ and $\nu_5(\text{TMA})$. With the ab initio intensities for $\nu_4(\text{CF}_3\text{Cl})$ equal to 670.8 km mol⁻¹ and for $\nu_5(\text{TMA})$ equal to 24.0 km mol⁻¹, it is clear that the weaker feature, i.e., the shoulder at 1,189.8 cm⁻¹, must be assigned as $\nu_5(\text{TMA})$ and the stronger band at 1,193.7 cm⁻¹ as $\nu_4(\text{CF}_3\text{Cl})$. The complex bands in this region are a first proof that a complex between CF₃Cl and TMA is formed in sufficient concentration to be detectable by IR spectroscopy.

From the discussion of their IR spectra, it is clear that the assignments by Pullin in the 450–350 cm⁻¹ region, where $\nu_7(\text{TMA})$ and $\nu_{21}(\text{TMA})$ are expected, are somewhat speculative. This region for the solutions in liquid rare gases is shown in Fig. 23, with Fig. 23A giving the results for CF₃I. The frequency interval has been chosen to include bands produced by the C–X stretching mode. In each panel trace *a* gives the spectrum of the mixed solution, while traces *b* and *c* give the single-monomer solution spectra of TMA and CF₃X, respectively. Trace *a* of the top panel shows two prominent complex bands, at 403.6 cm⁻¹ and 267.3 cm⁻¹, and a much weaker one at 421.6 cm⁻¹. Comparison with traces *b* and *c*, which were recorded with concentrations similar to those used for trace *a*, shows that the complex bands must have considerably higher IR intensities than the corresponding monomer modes. This is the case for the $\nu_3(\text{CF}_3\text{I})$ monomer mode seen at 285.4 cm⁻¹, which is calculated to red shift by -18.3 cm⁻¹ upon complexation with a 900-fold intensity increase. The complex band at 267.3 cm⁻¹ evidently has to be assigned to this C–I stretching mode. The ab initio relative intensities for $\nu_7(\text{TMA})$, 43.4 km mol⁻¹, and $\nu_{21}(\text{TMA})$, 0.5 km mol⁻¹, however, are such that with high certainty the prominent 403.6-cm⁻¹ band may be assigned to $\nu_7(\text{TMA})$ in the complex, blue shifted from the corresponding monomer mode at 370.9 cm⁻¹ in

Fig. 23 Infrared spectra of the 490–240 cm^{-1} region for solutions of mixtures of CF_3I (A), CF_3Br (B), and CF_3Cl (C) with TMA dissolved in LXe (208 K), LKr (123 K), and LAr (103 K), respectively. Trace *a* represents the spectrum of the mixed solution and traces *b* and *c* are the spectra of the monomer TMA and CF_3X solution, respectively. The spectra of the CF_3X monomer solutions are magnified by the given factor. The new bands appearing in the spectra of the mixture assigned to the 1:1 complex are marked with an asterisk (*). Reprinted from [135] with permission from Elsevier

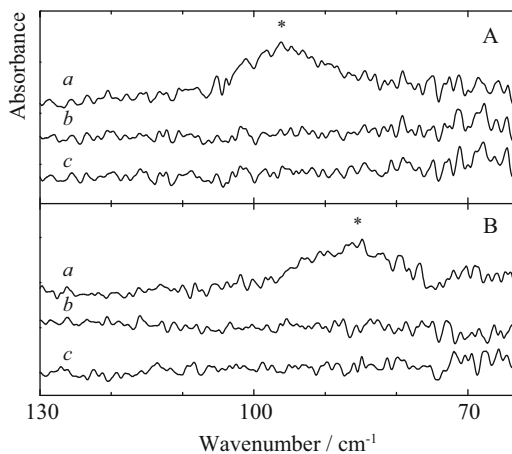


trace *b*. The weak band at 421.6 cm^{-1} then remains to be assigned to $\nu_{21}(\text{TMA})$ in the complex, with the corresponding monomer band remaining unobserved.

Figure 23B shows the results for the solutions of CF_3Br and TMA in LKr. Also here, two clear complex bands are present, at 390.3 cm^{-1} and 336.5 cm^{-1} . The first of these is assigned to $\nu_7(\text{TMA})$, in analogy with the CF_3I complex. Upon closer inspection, the band at 336.5 cm^{-1} is seen to be a strongly overlapping doublet, with maxima at 337.1 cm^{-1} and 336.2 cm^{-1} . These bands are assigned as $\nu_3(\text{CF}_3\text{Br})$ in the complex, with the splitting caused by the $^{79}\text{Br}/^{81}\text{Br}$ isotopes. The weak CF_3Br monomer bands in trace *c* are not found back in trace *a*, which, in view of the magnification by a factor of 20 applied to trace *c*, is not surprising. Their absence is supported by the calculated intensity ratio $\epsilon_{\text{complex}}/\epsilon_{\text{monomer}}$ of the $\nu_3(\text{CF}_3\text{Br})$ mode being close to 1,300.

The spectrum of the mixture of CF_3Cl and TMA in LAr, shown in Fig. 23C, reveals the presence of three complex bands, a doublet at 472.7 cm^{-1} and 465.0 cm^{-1} and a singlet at 381.5 cm^{-1} . The latter is assigned as $\nu_7(\text{TMA})$ and shows a blue shift of $+9 \text{ cm}^{-1}$. Comparison with Fig. 23A, B shows that the complexation shift of $\nu_7(\text{TMA})$ decreases from CF_3I to CF_3Cl , in agreement with the anticipation that the complexation shift decreases with decreasing stability of the complex. The $472.7/465.0 \text{ cm}^{-1}$ doublet is assigned as the $^{35}\text{Cl}/^{37}\text{Cl}$ isotopic doublet of the C–Cl stretching frequencies. They are shifted by -3.9 cm^{-1} from their frequencies in the monomer. The comment for the monomer CF_3Br bands can be repeated for the transitions in trace *c* of Fig. 23C.

Fig. 24 Infrared spectra of the 130–65 cm^{-1} region for solutions of mixtures of CF_3I (A) and CF_3Br (B) with TMA dissolved in LXe (208 K) and LKr (123 K), respectively. Trace *a* represents the spectrum of the mixed solution and traces *b* and *c* are the spectra of the monomer TMA and CF_3X solution, respectively. The new bands appearing in the spectra of the mixture assigned to the 1:1 complex are marked with an *asterisk* (*)



The 130–65 cm^{-1} regions obtained for solutions in LXe and LKr containing mixtures of CF_3I and CF_3Br with TMA are shown in Fig. 24A and B, respectively. In each panel, the spectrum of the mixed solution is given as trace *a*, while those of the solutions containing only TMA and CF_3X are shown as traces *b* and *c*, respectively. It can be seen that for both CF_3I and CF_3Br a broad band produced by the van der Waals stretching mode of the 1:1 complex is observed in the spectra of the mixed solutions. The maxima of the complex bands are situated near 97 cm^{-1} (Fig. 24A) and 87 cm^{-1} (Fig. 24B), in good agreement with calculated values of 96.2 cm^{-1} and 79.2 cm^{-1} .

4.2.2 Relative Stability

The relative stabilities for the 1:1 complexes were derived from temperature studies of different solutions using the Van't Hoff relation, as described in Sect. 3.3. The average complexation enthalpies, obtained from the Van't Hoff plots shown in Fig. 18, and the theoretical values for the complexation enthalpies obtained by combining the MP2 complexation energies with data obtained from statistical thermodynamics and MC-FEP simulations are summarized in Table 3. A detailed comparison of the data obtained and those obtained for the other complexes is considered in Sect. 5.1. It is worth mentioning, however, that, taking into consideration the rather different environments and temperatures and the rather large experimental uncertainty, the value of $-28.7(1) \text{ kJ mol}^{-1}$ obtained for TMA- CF_3I in solutions in LXe compares favorably with the value of $-25(3) \text{ kJ mol}^{-1}$ in benzene solution studied by Mc Naught [16] in the temperature range 263–313 K.

Table 3 Experimental and predicted complexation enthalpies, in kJ mol^{-1} , obtained for the complexes of trimethylamine (TMA) with the different trifluorohalomethanes CF_3X ($\text{X}=\text{Cl}, \text{Br}, \text{I}$)

		$\Delta_{\text{exp}}\text{H}/\text{kJ mol}^{-1}$	$\Delta_{\text{calc}}\text{H}/\text{kJ mol}^{-1}$
TMA – CF_3Cl	LAr	–8.9 (2)	–7.0 (6)
TMA – CF_3Br	LKr	–18.3 (1)	–18.6 (3)
TMA – CF_3I	LXe	–28.7 (1)	–31.9 (4)
TMA – $\text{CF}_3\text{H}^{\text{a}}$	LKr	–14.6 (8)	

For reason of comparison, the experimental values obtained for the complex of TMA and fluoroform, CHF_3 , are also given

^aMeasured by Bertsev et al. [133]

4.3 C–X...O and C–X...S-Bonded Complexes: Dimethyl Ether, Dimethyl Sulfide

Although C–X...O and C–X...S halogen-bonded interactions are known to play an active role in many biochemical processes, including, amongst others, thyroid chemistry [138–140], little experimental information on the nature of these type of interactions is available in the literature. Triggered by the results obtained for trimethylamine, a study of the complexes involving dimethyl ether (DME) and dimethyl sulfide (DMS) was initiated. The main goals of the study were to collect data allowing tendencies to be observed while descending down group VI in the periodic table, and to compare the results for typical halogen-bonded complexes with data obtained for similar hydrogen-bonded complexes. It was shown that the halogen-bonded complexes involving a divalent sulfur atom have a strength generally comparable with, or even slightly larger than, that of the complexes involving oxygen. The results obtained for the halogen-bonded complexes, therefore, contrasted with observations on hydrogen bonds indicating that substitution of the oxygen by a sulfur atom results in weaker interactions [68].

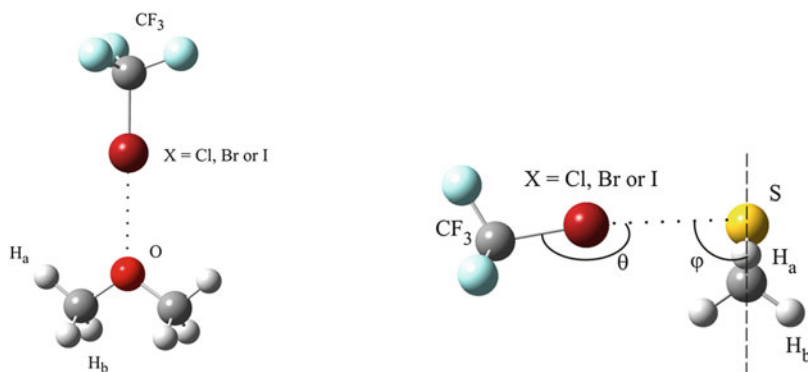
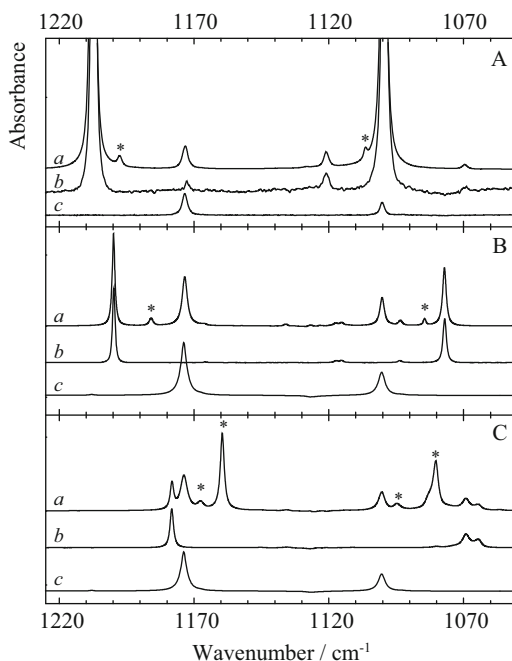


Fig. 25 Infrared spectra of the 1,225–1,050 cm^{-1} region for solutions of mixtures of CF_3Cl (A), CF_3Br (B), and CF_3I (C) with DME dissolved in LAr, at 89 K. Trace *a* represents the spectrum of the mixed solutions, and traces *b* and *c* are the spectra of the monomer CF_3X and DME solution, respectively. The new bands appearing in the spectra of the mixture assigned to the 1:1 complex are marked with an asterisk (*). Reprinted with permission from [48]. Copyright (2013) John Wiley & Sons, Inc

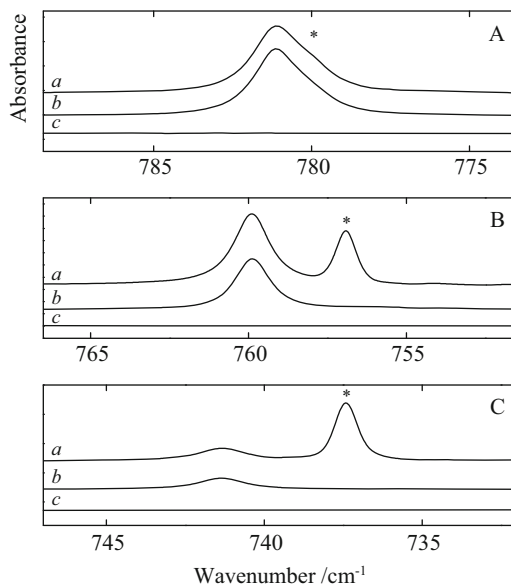


4.3.1 Vibrational Spectra: Complexes with Dimethyl Ether

In Fig. 25, the CF_3 stretching region of a solution containing mole fractions of 1.3×10^{-4} of CF_3Cl and 8.8×10^{-4} of DME dissolved in LAr, trace *a*, is compared with the spectra of the monomers in traces *b* and *c*, respectively. The new bands in the spectrum of the mixture, marked with an asterisk, are assigned to the 1:1 complex. Inspection shows that in the mixed solution new bands can be seen at 1,197.4 cm^{-1} and 1,106.4 cm^{-1} . They are assigned as the antisymmetric $\nu_4(\text{CF}_3\text{Cl})$ and symmetric $\nu_1(\text{CF}_3\text{Cl})$ CF_3 stretching modes, respectively. These vibrations can be seen to give rise to the saturated absorptions at 1,208.0 cm^{-1} and 1,099.4 cm^{-1} in the monomer. Similar new bands can be seen in trace *a* in Fig. 25B, where the corresponding region of a solution containing mole fractions of 4.1×10^{-6} of CF_3Br and 9.1×10^{-4} of DME is given. In view of the much lower concentration of CF_3Br compared to CF_3Cl , it is appreciated that the similar relative intensities of the complex bands in Fig. 25A, B suggest the complex with CF_3Br is significantly more stable than that with CF_3Cl .

Trace *a* in Fig. 25C depicts the same region for a solution containing mole fractions of 3.8×10^{-6} of CF_3I and 8.2×10^{-4} of DME. In the region near 1,180 cm^{-1} , where $\nu_4(\text{CF}_3\text{I})$ and $\nu_{20}(\text{DME})$ are present in the monomers, new bands in the mixed solution are seen at 1,166.0 cm^{-1} and 1,158.5 cm^{-1} . Identifying the latter as $\nu_4(\text{CF}_3\text{I})$ in the complex results in observed complexation shifts of -18.8 cm^{-1} for $\nu_4(\text{CF}_3\text{I})$ and -7.5 cm^{-1} for $\nu_{20}(\text{DME})$. This assignment is

Fig. 26 Infrared spectra of the $\nu_2(\text{CF}_3\text{X})$ region for solutions of mixtures of CF_3Cl (**A**), CF_3Br (**B**), and CF_3I (**C**) with DME dissolved in LAr, at 89 K. Trace *a* represents the spectrum of the mixed solution and traces *b* and *c* are the spectra of the monomer CF_3X and DME solution, respectively. The new bands appearing in the spectra of the mixture assigned to the 1:1 complex are marked with an asterisk (*). Reprinted with permission from [48]. Copyright (2013) John Wiley & Sons, Inc



supported by the calculated complexation shifts of these modes of -20.2 cm^{-1} and -6.9 cm^{-1} , respectively, and by the predicted IR intensities of the modes in the complexes, 546 km mol^{-1} for $\nu_4(\text{CF}_3\text{I})$ and 97.6 km mol^{-1} for $\nu_{20}(\text{DME})$. It is further obvious from trace *a* in Fig. 25C that the $\nu_4(\text{CF}_3\text{I})$ band in the complex is much more intense than the corresponding monomer band. The concentrations of the monomers in this case are of the same order as in the case of CF_3Br in Fig. 25B, so from the relative intensities it is inferred that the complex with CF_3I is much more stable than the complex with CF_3Br .

For all halomethanes, red shifts are predicted for the CF_3 deformation mode $\nu_2(\text{CF}_3\text{X})$. The corresponding spectral regions are given in Fig. 26. For CF_3Cl (Fig. 26A) the complex band appears as a very weak low frequency shoulder of the 781.0 cm^{-1} monomer band. The complex bands for CF_3Br and CF_3I are increasingly more intense and show larger red shifts, as is clear from Fig. 26B, C. The mixed solutions used to record the spectra contained similar concentrations of DME, but decreasing concentrations of the halomethane, with ratios 1:0.77:0.27 from CF_3Cl to CF_3I . With the ab initio intensities of the complexes similar to those in the corresponding monomers, the relative intensities of the complex bands in Fig. 26 neatly confirm the increasing stability of the complex from CF_3Cl to CF_3I .

The C–X stretching mode in the respective monomers is calculated with a limited IR intensity, but in the complexes the intensities are somewhat enhanced. This is illustrated in Fig. 27. In each panel, trace *a* represents the spectrum of the mixed solution and trace *b* was recorded from a solution in which only CF_3X was dissolved in LAr. In some panels, trace *c* shows the spectrum of the complex, obtained by subtracting trace *b* from trace *a*. The IR and Raman spectra for the solutions containing CF_3Cl are shown in Fig. 27A, B. Trace *a* clearly shows the

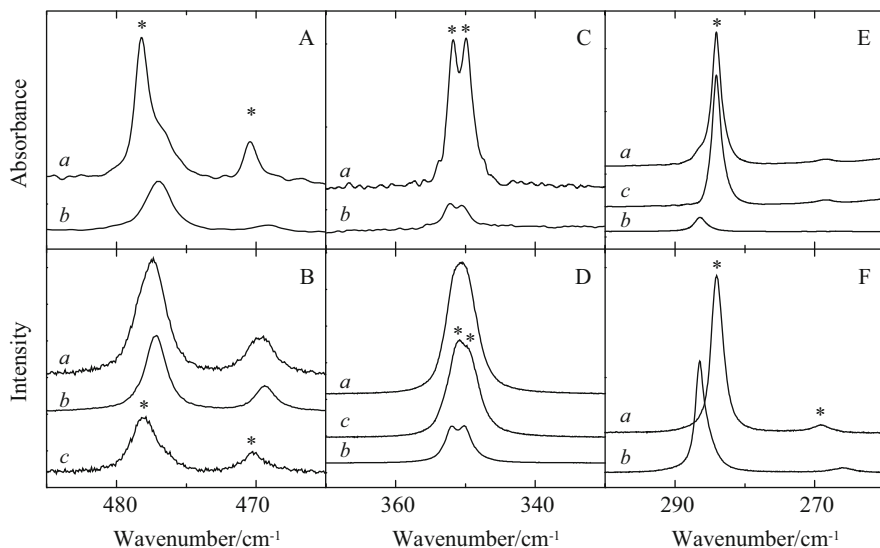


Fig. 27 Infrared (A, C, E) and Raman (B, D, F) spectra of the $\nu_3(\text{CF}_3\text{X})$ region for solutions of mixtures of CF_3Cl (A, B), CF_3Br (C, D), and CF_3I (E, F) with DME dissolved in LAr, at 89 K. Trace *a* represents the spectrum of the mixed solution, trace *b* is the spectrum of the monomer CF_3X , and trace *c* is the spectrum of the 1:1 complex, obtained by subtracting trace *b* from trace *a*. The new bands appearing in the spectra of the mixture assigned to the 1:1 complex are marked with an *asterisk* (*). Reprinted with permission from [48]. Copyright (2013) John Wiley & Sons, Inc

presence of a $^{35}\text{Cl}/^{37}\text{Cl}$ isotopic doublet, with maxima at 478.3 cm^{-1} and 470.5 cm^{-1} . This doublet is assigned as $\nu_3(\text{CF}_3\text{Cl})$ in the complex and is blue shifted by $+2.0\text{ cm}^{-1}$ from their frequencies in the monomer. The assignments are confirmed by the Raman spectra in Fig. 27B.

The CF_3Br analogue is shown in Fig. 27C, D. Trace *a* in the IR spectra, Fig. 27C, shows a clear doublet with maxima at 351.5 cm^{-1} and 349.6 cm^{-1} . These bands are assigned as $\nu_3(\text{CF}_3\text{Br})$ in the complex, with the splitting because of the $^{79}\text{Br}/^{81}\text{Br}$ isotopes. The CF_3Br monomer bands appear as very weak features in the IR spectra but are much more pronounced in the Raman spectra, Fig. 27D. It is clear from these panels that the bromine isotopic structure can be distinguished both in monomer and complex, although the Raman spectra show that in the former the isotope bands are somewhat better resolved. The complexation shifts are to the red by -0.7 cm^{-1} .

The IR and Raman spectra for the CF_3I complex are shown in panels Fig. 27E, F, respectively. It is clear that the $\nu_3(\text{CF}_3\text{I})$ bands in the monomer and in the complex are present in both the IR and the Raman spectra. The $\nu_3(\text{CF}_3\text{I})$ complex band can be seen to red shift by -2.6 cm^{-1} . In the Raman spectra, a weak feature at 268.4 cm^{-1} can be observed in addition to the intense $\nu_3(\text{CF}_3\text{I})$ transitions. This band is assigned as the $\nu_6(\text{CF}_3\text{I})$ complex band, blue shifted by $+2.1\text{ cm}^{-1}$ from the frequency in the monomer.

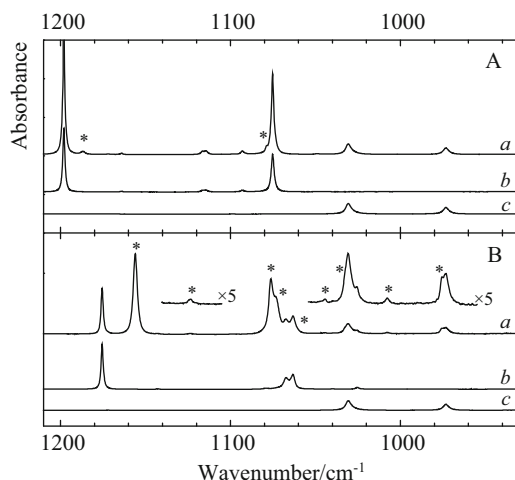


Fig. 28 Infrared spectra of the 1,210–930 cm^{-1} region for solutions of mixtures of CF_3Br (A) and CF_3I (B) with DMS dissolved in LKr, at 123 K. Trace *a* represents the spectrum of the mixed solution and traces *b* and *c* are the spectra of the monomer CF_3X and DMS solution, respectively. The new bands appearing in the spectra of the mixture assigned to the 1:1 complex are marked with an asterisk (*). Reproduced from [137] with permission from the PCCP Owner Societies

4.3.2 Vibrational Spectra: Complexes with Dimethyl Sulfide

In Fig. 28A, the CF_3 stretching region of a solution containing mole fractions of 4.3×10^{-5} of CF_3Br and 1.2×10^{-3} of DMS dissolved in LKr, trace *a*, is compared with the spectra of the monomers in traces *b* and *c*, respectively. The new bands in the spectra of the mixture, marked with an asterisk, are assigned to the 1:1 complex. It can be seen that weak bands, assigned as the antisymmetric $\nu_4(\text{CF}_3\text{Br})$ and symmetric $\nu_1(\text{CF}_3\text{Br})$ stretching modes in the complex, are detected at 1,187.0 cm^{-1} and 1,079.0 cm^{-1} . The experimental shifts for these bands, -11.1 cm^{-1} for $\nu_4(\text{CF}_3\text{Br})$ and $+3.8 \text{ cm}^{-1}$ for $\nu_1(\text{CF}_3\text{Br})$, compare favorably with the ab initio values of -11.8 cm^{-1} and $+4.8 \text{ cm}^{-1}$.

Similar, but much more pronounced, complex bands can be observed in the top trace in Fig. 28B, where the corresponding region of a solution containing mole fractions of 4.0×10^{-5} of CF_3I and 7.1×10^{-3} of DMS is given. The complex bands assigned to $\nu_4(\text{CF}_3\text{I})$ and $\nu_1(\text{CF}_3\text{I})$, and those assigned to the same modes in the ^{13}C -isotopomer, are observed at 1,156.1 cm^{-1} and 1,076.2 cm^{-1} , and at 1,123.5 cm^{-1} and 1,044.6 cm^{-1} . The experimental shifts, -19.5 cm^{-1} and $+8.8 \text{ cm}^{-1}$, in the ^{12}C -isotopomer agree nicely with the theoretical values of -17.2 cm^{-1} and $+9.5 \text{ cm}^{-1}$. These shifts are significantly larger than those observed for the CF_3Br complex. New bands are also observed in the spectra of the mixed solutions at 1,073.4 cm^{-1} , 1,061.9 cm^{-1} , 1,030.7 cm^{-1} , 1,007.8 cm^{-1} , and 973.3 cm^{-1} . The last three are assigned as the $\nu_5(\text{DMS})$, $\nu_2(\text{CF}_3\text{I}) + \nu_3(\text{CF}_3\text{I})$, and $\nu_{14}(\text{DMS})$ modes, respectively. The experimental complexation shifts for these

modes are $+2.0\text{ cm}^{-1}$, -17.6 cm^{-1} , and $+2.5\text{ cm}^{-1}$ to be compared with the calculated values of $+1.2\text{ cm}^{-1}$, -16.9 cm^{-1} (obtained by summing the harmonic shifts of ν_2 and ν_3), and $+2.4\text{ cm}^{-1}$. The assignment of the first two is not so straightforward because of the presence of a Fermi quadruplet in CF_3I consisting of $\nu_5(\text{CF}_3\text{I}) + 2\nu_6(\text{CF}_3\text{I})$ ($1,079.3\text{ cm}^{-1}$), $\nu_1(\text{CF}_3\text{I})$ ($1,067.3\text{ cm}^{-1}$), $2\nu_5(\text{CF}_3\text{I})$ ($1,063.5\text{ cm}^{-1}$), and $4\nu_6(\text{CF}_3\text{I})$ ($1,052.4\text{ cm}^{-1}$) [39, 47]. As a result of the calculated frequency shifts and the intensity differences, the complex band at $1,061.9\text{ cm}^{-1}$ is assigned to $\nu_5(\text{CF}_3\text{I})$. The complex band at $1,073.4\text{ cm}^{-1}$, present as a weak shoulder on the $\nu_1(\text{CF}_3\text{I})$ complex band, remains unassigned. It is of interest to stress that, while the spectra of the mixed solutions were recorded for solutions containing similar concentrations of the monomers involved, the complex bands in Fig. 28B are much more intense than those in Fig. 28A. These differences are a clear indication of the higher stability of the CF_3I complex.

Figure 29A,C gives the IR spectra and Fig. 29B, D the Raman spectra of the $\nu_2(\text{CF}_3\text{Br})$ (Fig. 29A, B) and $\nu_6(\text{DMS})$ (Fig. 29C, D) modes in mixed and monomer solutions. Similarly, Fig. 29E–H give the corresponding regions for solutions containing CF_3I . In both IR and Raman, for the mixed CF_3Br solutions, weak bands red shifted from their monomer counterparts are observed. The shifts, -3.8 cm^{-1} for $\nu_2(\text{CF}_3\text{Br})$ and -1.6 cm^{-1} for $\nu_6(\text{DMS})$, are in agreement with the predicted values of -5.3 cm^{-1} and -1.9 cm^{-1} , respectively. Just as for the CF_3 stretches, Fig. 29E–H shows that, in comparison with CF_3Br , the relative intensities of the complex bands in the mixed CF_3I solutions are much more intense, confirming the above conclusion on relative stabilities. In each region of the IR spectra, Fig. 29E, G, a single complex band is detected. The observed shifts, with the ab initio values given in brackets, are -6.5 (-6.4) cm^{-1} for $\nu_2(\text{CF}_3\text{I})$ and -3.6 (-3.3) cm^{-1} for $\nu_6(\text{DMS})$.

The Raman spectra of the mixed solutions in Fig. 29F, H were recorded for two different analytical concentrations of DMS: for trace *a* the concentration was 8.8×10^{-4} mol fraction, for trace *a'* it was 3.1×10^{-3} , and in both cases the analytical concentration of CF_3I was 2.4×10^{-3} . For clarity, trace *a'* has been rescaled to correspond to the intensities of the 1:1 complex bands in trace *a*. For trace *a'* the excess DMS causes virtually only the 1:1 complex band to be present in the $\nu_2(\text{CF}_3\text{I})$ region, the monomer CF_3I concentration being reduced to below the detection limit. In trace *a* in both regions a second complex band, marked with an open circle, is present. In this solution the CF_3I was in excess, and this promotes the formation of complexes with higher $\text{CF}_3\text{I}/\text{DMS}$ ratios. Therefore, these second complex bands are assigned to a 2:1 complex in which two molecules of CF_3I interact with the sulfur atom of the same DMS molecule.

IR and Raman spectra in the C–X stretching regions are given in Fig. 30. Figure 30A (IR) and Fig. 30B (Raman) contain spectra for the CF_3Br complex, while Fig. 30C (IR) and Fig. 30D (Raman) refer to the CF_3I complex. Complex bands for the 1:1 complex are marked with an asterisk. It can be seen that in the IR spectrum, the C–Br stretching mode of the complex in trace *a* is much stronger than the monomer CF_3Br doublet. The doublet structure remains unresolved in the broad complex bands. A similar remark on the intensities can be made for the 1:1 Raman

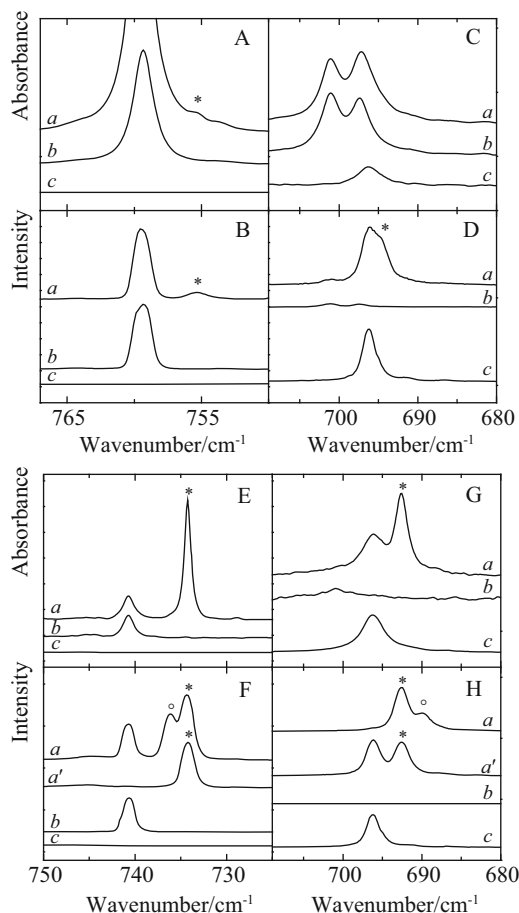


Fig. 29 Top: IR (A, C) and Raman (B, D) spectra in the $\nu_2(\text{CF}_3\text{X})$ (A, B) and $\nu_6(\text{DMS})$ (C, D) region for solutions of mixtures of CF_3Br with DMS dissolved in LKr, at 123 K. Trace *a* represents the spectrum of the mixed solution and traces *b* and *c* are the spectra of the monomer CF_3Br and DMS solution, respectively. The new bands appearing in the spectra of the mixture assigned to the 1:1 complex are marked with an asterisk (*). Bottom: Infrared (E, G) and Raman (F, H) spectra in the $\nu_2(\text{CF}_3\text{X})$ (E, F) and $\nu_6(\text{DMS})$ (G, H) region for solutions of mixtures of CF_3I with DMS dissolved in LKr, at 123 K. Traces *a* and *a'* represent the spectrum of a mixed solution and traces *b* and *c* are the spectra of the monomer CF_3I and DMS solution, respectively. The new bands appearing in the spectra of the mixture assigned to the 1:1 complex are marked with an asterisk (*); the bands assigned to the 2:1 complex are marked with a circle (°). Reproduced from [137] with permission from the PCCP Owner Societies

band in Fig. 30B, although it is clear that in this case the complex/monomer activity ratio is much lower than in Fig. 30A. These observations show a significant enhancement of the intensity/activity of the $\nu_3(\text{CF}_3\text{Br})$ mode in the complex and at the same time suggest that the complexation influence on the IR intensity is higher than on the Raman scattering activity. This is substantiated by ab initio

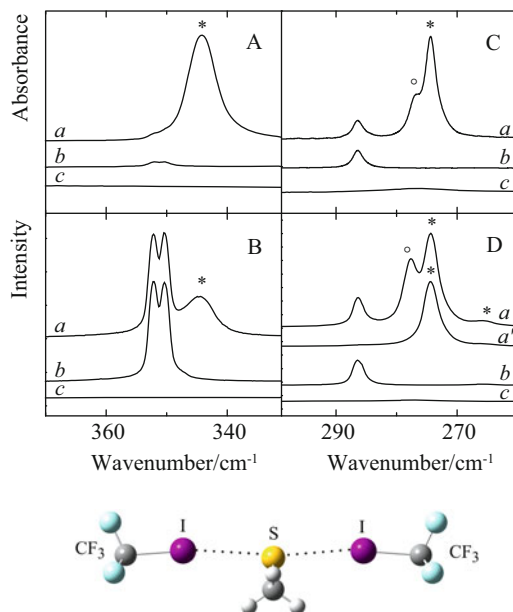


Fig. 30 Infrared (A, C) and Raman (B, D) spectra of the $\nu_3(\text{CF}_3\text{X})$ region for solutions of mixtures of CF_3Br (A, B) and CF_3I (C, D) with DMS dissolved in LKr, at 123 K. Traces *a* and *a'* represent the spectrum of a mixed solution and traces *b* and *c* are the spectra of the monomer CF_3X and DMS solution, respectively. The new bands appearing in the spectra of the mixture assigned to the 1:1 complex are marked with an *asterisk* (*); the bands assigned to the 2:1 complex are marked with a *circle* (°). For completeness, the MP2/aug-cc-pVDZ(-PP) equilibrium geometry for the 2:1 complex is also shown. Reproduced from [137] with permission from the PCCP Owner Societies

calculations where the complexation was calculated to enhance the IR intensity by a factor of 125, compared to an enhancement by a factor of 4.4 for the Raman scattering activity.

Trace *a'* of Fig. 30D was recorded from the same solution as that used for trace *a'* in Fig. 29. It can be seen that a single complex band, assigned to the 1:1 complex, is observed. Although the above shows that the complex with CF_3I is stronger than the one with CF_3Br , the virtual absence of the monomer bands in that trace shows that also here the complexation induces a considerable enhancement, by a factor of 135, of the Raman scattering activity. If, however, the mole fraction of CF_3I is chosen to be much higher than that of DMS, 2.4×10^{-3} against 8.8×10^{-4} , respectively, for trace *a* of Fig. 30D, and 3.8×10^{-3} against 1.8×10^{-3} , respectively, for trace *a* of Fig. 30C, a new complex band appears on the high frequency side of the band caused by the 1:1 complex. The new bands are again assigned to the 2:1 complex $(\text{CF}_3\text{I})_2\text{DMS}$. Least squares band fittings of the spectra in Fig. 30C, D result in a frequencies of 276.6 cm^{-1} and 277.6 cm^{-1} , respectively. Frequency differences between IR and Raman spectra may occur as a consequence of poor calibration of the Raman spectrum, but the calibration run made in this case shows that the frequencies of other spectral features in the same region differed from the

corresponding IR values by not more than 0.1 cm^{-1} . Therefore, the frequency difference between the 2:1 bands is accepted to be real. This observation is interpreted as follows. For the 2:1 complex two $\nu_3(\text{CF}_3\text{I})$ bands are expected. The symmetry of that complex is such that the sulfur atom comes close to being a local inversion center, so that the $\nu_3(\text{CF}_3\text{I})$ modes of the monomers couple to an anti-symmetric and symmetric vibration. A near-mutual exclusion effect must be at work which means that in IR the spectrum is dominated by the antisymmetric component and in Raman by the symmetric component. The presence of the sulfur atom combined with the relative weakness of the halogen bonds means that the coupling between the antisymmetric and symmetric components is small, i.e., the frequency difference between the IR and Raman bands must be expected to be small, as is indeed observed. The ab initio calculations support this interpretation: the predicted frequencies are 285.9 cm^{-1} for the antisymmetric component and 286.6 cm^{-1} for the symmetric component, and the calculated antisymmetric/symmetric intensity ratio is 228 for the IR components against 6×10^{-5} for the Raman doublet.

Theoretical information confirming the above assignment was obtained by performing additional geometry optimizations and frequency calculations for the 2:1 complex. The equilibrium geometry for this complex is shown in Fig. 30. It can be seen that the 2:1 complex has a bifurcated structure with C_s symmetry in which the fluorine atoms of the two CF_3I molecules appear in the eclipsed conformation. Both CF_3I moieties are bound to the sulfur atom in such a way that the two C-I...S halogen bonds are almost collinear. The bifurcation leads to an anti-cooperative effect, as can be seen from the calculated energy, structure, and vibrational frequencies. Thus, the 2:1 complexation enthalpy is some 8% smaller than twice the 1:1 value, in the 2:1 complex the I...S interatomic distances are slightly higher, the structural perturbation of the Lewis acids is smaller, and their complexation shifts are smaller than in the 1:1 complex. In agreement with the expectations, the central DMS moiety is slightly more perturbed in the 2:1 than in the 1:1 complex, yielding complexation shifts which in general are somewhat larger than for the 1:1 complex

It is of interest to note that no indications were found for the formation of 1:1 complexes between DMS and CF_3Cl for any of the solutions studied. The reason for this is related to the limited solubility of DMS in LAr, with mole fractions being less than 1.0×10^{-6} [2], so mixed solutions of CF_3Cl and DMS could only be studied in LKr or LXe. Taking into consideration that for TMA and DME, complexes with CF_3Cl were only observed at the lowest temperatures in LAr, it is not surprising that in LKr the complex between DMS and CF_3Cl is too weak to be observed.

4.3.3 Relative Stability

The relative stabilities for the 1:1 and 1:2 complexes, derived from temperature studies of different solutions, and the theoretical values for the complexation enthalpies obtained by combining the MP2 complexation energies with data obtained from statistical thermodynamics and MC-FEP simulations are

Table 4 Experimental and predicted complexation enthalpies, in kJ mol^{-1} , obtained for the complexes of dimethyl ether (*DME*) and of dimethyl sulfide (*DMS*) with the trifluorohalomethanes CF_3X ($\text{X}=\text{Cl}, \text{Br}, \text{I}$)

		$\Delta_{\text{exp}}\text{H}/\text{kJ mol}^{-1}$	$\Delta_{\text{calc}}\text{H}/\text{kJ mol}^{-1}$
DME – CF_3Cl	LAr	–6.8 (3)	–5.1 (6)
DME – CF_3Br	LAr	–10.2 (1)	–11.1 (3)
DME – CF_3I	LAr	–15.5 (1)	–17.6 (6)
DMS – CF_3Cl	LKr	–	–4.0 (4)
DMS – CF_3Br	LKr	–9.5 (6)	–9.4 (2)
DMS – CF_3I	LKr	–17.4 (1)	–15.2 (2)
DME (– CF_3Br) ₂	LAr	–18.3 (5)	–
DMS (– CF_3I) ₂	LKr	–30.8 (16)	–
DME – $\text{CF}_3\text{H}^{\text{a}}$	LKr	–12.5 (2)	–10.2 (6)

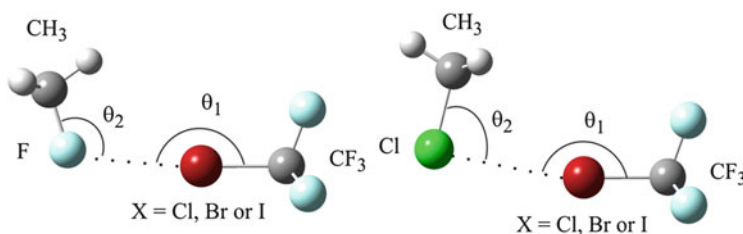
For reason of comparison, the experimental values obtained for the complex of DME and fluoroform, CHF_3 , are also given

^aTaken from [125, 141]

summarized in Table 4. As before, a detailed comparison of the data obtained is postponed to Sect. 5.1.

4.4 C–X...F and C–X...Cl-Bonded Complexes: Alkyl Fluorides and Alkyl Chlorides

To obtain information on halogen–halogen C–X...Y halogen bonds, interactions involving the fluorine and chlorine atoms in methyl fluoride (CH_3F), ethyl fluoride ($\text{C}_2\text{H}_5\text{F}$), methyl chloride (CH_3Cl), and ethyl chloride ($\text{C}_2\text{H}_5\text{Cl}$) were also studied. The choice for these alkyl halides was based on earlier observations [97, 110, 113, 130–132, 143] showing that these compounds can act as Lewis bases, and in earlier studies were observed to form complexes with C–H donors such as CHF_3 , CHCl_3 , CHBrClCF_3 , and other Lewis acids such as HCl , HBr , BF_3 , and BCl_3 . The Lewis bases studied were limited to alkyl fluorides and alkyl chlorides, as measurable concentrations of the weak halogen-bonded complexes could only be observed at temperatures below 145 K, i.e., in LAr and LKr, while alkyl bromides and iodides show a limited solubility in these conditions.



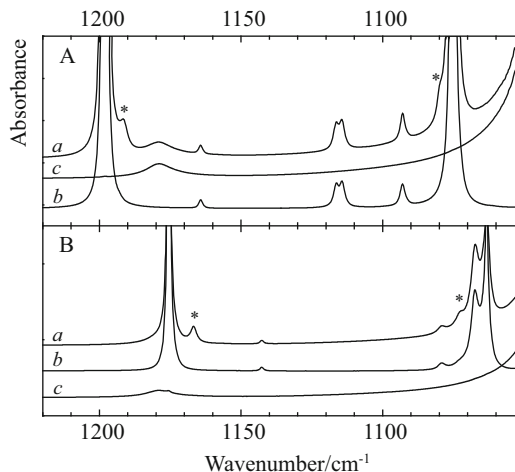


Fig. 31 Infrared spectra of the 1,220–1,050 cm^{-1} region for solutions of mixtures of CF_3Br (A) and CF_3I (B) with CH_3F dissolved in LKr, at 123 K. Trace *a* represents the spectrum of the mixed solution and traces *b* and *c* are the spectra of the monomer CF_3X and CH_3F solution, respectively. The new bands appearing in the spectra of the mixture assigned to the 1:1 complex are marked with an asterisk (*). Reprinted with permission from [142]. Copyright (2013) American Chemical Society

4.4.1 Vibrational Spectra

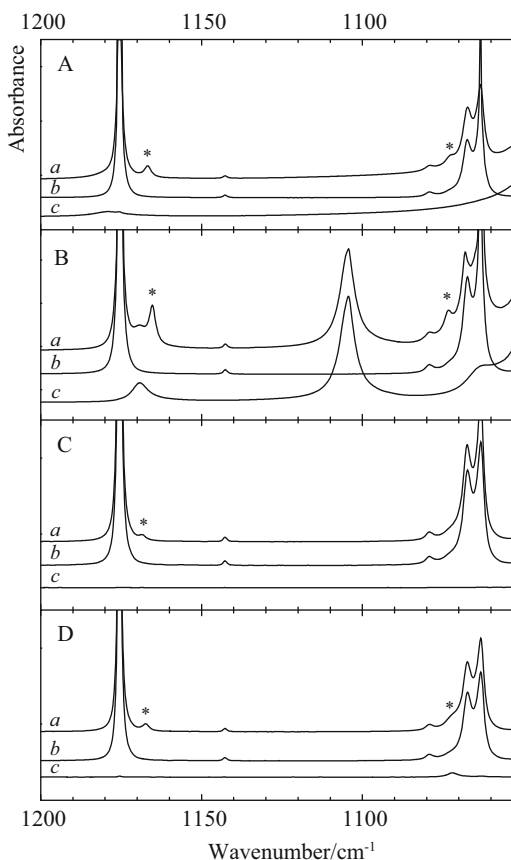
Apart from the bands assigned to the monomers involved, new bands illustrating the formation of weak C–X...Y halogen...halogen bonds were observed for CF_3I and CF_3Br . In contrast, no features suggesting the formation of a complex with CF_3Cl were detected for any of the solutions. In agreement with the data for DMS described above, the obvious conclusion is that these complexes are also too weak to be observed.

In Fig. 31A the CF_3 stretching region of a solution containing mole fractions of 3.2×10^{-4} of CF_3Br and 1.3×10^{-2} of CH_3F dissolved in LKr, trace *a*, is compared with the spectra of the monomers in traces *b* and *c*, respectively. The new bands in the spectra of the mixture, marked with an asterisk, are assigned to the 1:1 complex. It can be seen that weak bands, assigned as the antisymmetric $\nu_4(\text{CF}_3\text{Br})$ and symmetric $\nu_1(\text{CF}_3\text{Br})$ stretching modes in the complex, are detected at 1,191.5 cm^{-1} and 1079.7 cm^{-1} . The experimental shifts for these bands, -6.6 cm^{-1} for $\nu_4(\text{CF}_3\text{Br})$ and $+4.5 \text{ cm}^{-1}$ for $\nu_1(\text{CF}_3\text{Br})$, compare favorably with the ab initio values of -9.2 cm^{-1} and $+6.5 \text{ cm}^{-1}$. Similar, but more pronounced, complex bands can be observed in the top trace in Fig. 31B, where the corresponding region of a solution containing mole fractions of 9.4×10^{-5} of CF_3I and 5.6×10^{-3} of CH_3F is given. The complex bands assigned to $\nu_4(\text{CF}_3\text{I})$ and $\nu_1(\text{CF}_3\text{I})$ are observed at 1,166.8 cm^{-1} and 1,072.9 cm^{-1} . The experimental complexation shifts, -8.8 cm^{-1} and $+5.5 \text{ cm}^{-1}$, agree nicely with the theoretical values of -9.8 cm^{-1} and $+8.5 \text{ cm}^{-1}$. Even though the monomer concentrations in

Fig. 31B are about three times smaller as those in Fig. 31A, the complex bands in the former panel are slightly more pronounced, so that from the relative intensities it is inferred that the complex with CF_3I is more stable than the complex with CF_3Br .

In order to visualize the differences between the four Lewis bases, Fig. 32 depicts the IR spectra of the CF_3 stretching region for the complexes of CF_3I with CH_3F (Fig. 32A), $\text{C}_2\text{H}_5\text{F}$ (Fig. 32B), CH_3Cl (Fig. 32C) and $\text{C}_2\text{H}_5\text{Cl}$ (Fig. 32D) observed in LKr. In each panel, trace *a* gives the spectrum of the mixed solution, while traces *b* and *c* were recorded from a solution in which only CF_3I or the Lewis base was dissolved in LKr, respectively. Complex bands for the 1:1 complex are marked with an asterisk. The spectra in Fig. 32A are the same as those depicted in Fig. 31B and thus need no further discussion. Similar, but more pronounced, complex bands can be observed in the top trace of Fig. 32B, where the corresponding region of a solution containing mole fractions of 9.4×10^{-5} of CF_3I and 2.1×10^{-3} of $\text{C}_2\text{H}_5\text{F}$ is given. It can be seen that this region is more complicated by the presence of three relatively intense $\text{C}_2\text{H}_5\text{F}$ monomer bands, located at

Fig. 32 Infrared spectra of the 1,200–1,050 cm^{-1} region for solutions of mixtures of CF_3I with CH_3F (A), $\text{C}_2\text{H}_5\text{F}$ (B), CH_3Cl (C), and $\text{C}_2\text{H}_5\text{Cl}$ (D), dissolved in LKr, at 123 K. Trace *a* represents the spectrum of the mixed solution and traces *b* and *c* are the spectra of the monomer CF_3I and CH_3Y or $\text{C}_2\text{H}_5\text{Y}$ solution, respectively. The new bands appearing in the spectra of the mixture assigned to the 1:1 complex are marked with an *asterisk* (*). Reprinted with permission from [142]. Copyright (2013) American Chemical Society



1,169.4 cm^{-1} , 1104.7 cm^{-1} , and 1,062.8 cm^{-1} . The first two are assigned to $\nu_8(\text{C}_2\text{H}_5\text{F})$ and $\nu_9(\text{C}_2\text{H}_5\text{F})$, while the latter is produced by an overtone or combination band. Except for a more difficult subtraction, the $\text{C}_2\text{H}_5\text{F}$ bands barely influence the interpretation of this spectral region. The complex band observed at 1,165.3 cm^{-1} can either be assigned to $\nu_8(\text{C}_2\text{H}_5\text{F})$ or to $\nu_4(\text{CF}_3\text{I})$. The ab initio relative intensities for these complex bands, 3.9 km mol^{-1} and 450.1 km mol^{-1} , respectively, are such that with high certainty the 1,165.3 cm^{-1} band should be assigned to $\nu_4(\text{CF}_3\text{I})$, as expected from Fig. 32A. The other complex band, observed at 1,073.5 cm^{-1} is assigned to $\nu_1(\text{CF}_3\text{I})$. The observed shifts, -10.3 and $+6.1$ cm^{-1} , agree nicely with the theoretical values of -10.7 cm^{-1} and $+10.8$ cm^{-1} . The differences in complexation shifts and relative intensities between Fig. 32A, B are a clear indication of the higher stability of the $\text{C}_2\text{H}_5\text{F}$ complex.

Figure 32C shows the spectra of a solution containing mole fractions of 7.5×10^{-5} of CF_3I and 3.8×10^{-3} of CH_3Cl . In Fig. 32C, the only complex band observed is $\nu_4(\text{CF}_3\text{I})$ at 1,168.5 cm^{-1} . The experimental complexation shift of -7.1 cm^{-1} agrees nicely with the theoretical value of -7.5 cm^{-1} . Because of the low concentration of CH_3Cl , the complex band produced by $\nu_1(\text{CF}_3\text{I})$ remains undetected in Fig. 32C. By using higher concentrations of both monomers, this complex band was seen at 1,070.8 cm^{-1} . The resulting complexation shift of $+3.4$ cm^{-1} agrees nicely with the calculated shift of $+5.2$ cm^{-1} . Finally, the spectra of a solution containing mole fractions of 7.5×10^{-5} of CF_3I and 1.9×10^{-3} of $\text{C}_2\text{H}_5\text{Cl}$ are shown in Fig. 32D. Although the Lewis base concentration in this panel is only half the concentration used in Fig. 32C, both $\nu_4(\text{CF}_3\text{I})$ and $\nu_1(\text{CF}_3\text{I})$ are present here. They give rise to absorptions at 1,167.4 cm^{-1} and 1,070.5 cm^{-1} , respectively. The experimental complexation shifts, -8.2 cm^{-1} and $+3.1$ cm^{-1} , agree well with the calculated values of -7.9 cm^{-1} and $+5.0$ cm^{-1} . The differences in complexation shifts and relative intensities between Fig. 32C and Fig. 32D are a clear indication of the higher stability of the $\text{C}_2\text{H}_5\text{Cl}$ complex.

Infrared spectra in the C–X stretching regions for the C–X...F complexes are given in Fig. 33. In each panel, trace *a* gives the spectrum of the mixed solution and trace *b* was recorded from a solution in which only CF_3X was dissolved in LKr. Trace *c* shows the spectrum of the 1:1 complex, obtained by subtracting trace *b* from trace *a*. Complex bands for the 1:1 complex are marked with an asterisk. The infrared spectra for the $\text{CH}_3\text{F}-\text{CF}_3\text{Br}$ and $\text{C}_2\text{H}_5\text{F}-\text{CF}_3\text{Br}$ complexes are shown in Fig. 33A, B, respectively. Trace *a* in Fig. 33A clearly shows the presence of a $^{79}\text{Br}/^{81}\text{Br}$ isotopic doublet, with maxima at 353.4 cm^{-1} and 351.6 cm^{-1} . This doublet is assigned as $\nu_3(\text{CF}_3\text{Br})$ in the complex and is blue shifted by $+1.3$ cm^{-1} from the frequencies in the monomer. A similar blue shift can be seen in trace *a* of Fig. 33B, the $^{79}\text{Br}/^{81}\text{Br}$ isotopic doublet showing maxima at 353.6 cm^{-1} and 351.7 cm^{-1} , leading to a blue shift of $+1.5$ cm^{-1} . These results are in agreement with the calculated complexation shifts of $+1.0$ cm^{-1} and $+0.7$ cm^{-1} , respectively. The weak CF_3Br monomer bands in trace *b* of both panels are not found back in trace *a*, which, in view of the magnification by a factor of 5 applied to trace *b*, is not surprising. The IR spectra for the CF_3I analogues are shown in Fig. 33C, D,

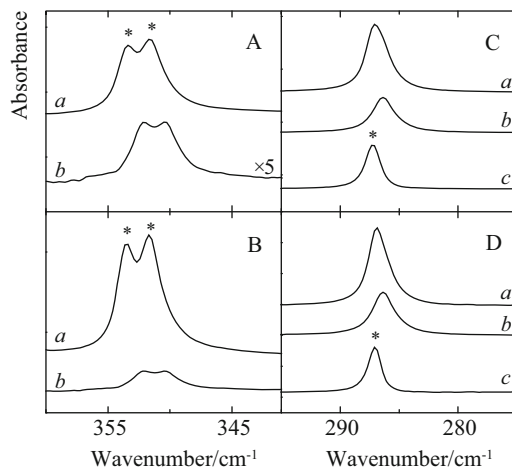


Fig. 33 Infrared spectra of the $\nu_3(\text{CF}_3\text{X})$ region for solutions of mixtures of CF_3Br (**A, B**) and CF_3I (**C, D**) with CH_3F (**A, C**) and $\text{C}_2\text{H}_5\text{F}$ (**C, D**) dissolved in LKr, at 123 K. Trace *a* represents the spectrum of the mixed solution, trace *b* is the spectrum of the monomer CF_3X solution, and trace *c* is the spectrum of the 1:1 complex, obtained by subtracting trace *b* from trace *a*. The new bands appearing in the spectra of the mixture assigned to the 1:1 complex are marked with an asterisk (*). Reprinted with permission from [142]. Copyright (2013) American Chemical Society

respectively. The $\nu_3(\text{CF}_3\text{I})$ complex band in Fig. 33C, D can be seen to blue shift by $+0.8\text{ cm}^{-1}$ and $+0.6\text{ cm}^{-1}$, respectively.

IR spectra in the C–X stretching regions for the C–X...Cl complexes are given in Fig. 34. In each panel, trace *a* gives the spectrum of the mixed solution, and traces *b* and *c* were recorded from a solution in which only CF_3X or $\text{C}_2\text{H}_5\text{Cl}$ was dissolved in LKr. Trace *d* shows the spectrum of the 1:1 complex, obtained by subtracting traces *b* and *c* from trace *a*. Complex bands for the 1:1 complex are marked with an asterisk. The IR spectra for the CH_3Cl – CF_3Br and $\text{C}_2\text{H}_5\text{Cl}$ – CF_3Br complexes are shown in Fig. 34A, B, respectively. Trace *a* in Fig. 34A clearly shows the presence of a $^{79}\text{Br}/^{81}\text{Br}$ isotopic doublet, with maxima at 352.0 cm^{-1} and 350.1 cm^{-1} . This doublet is assigned as $\nu_3(\text{CF}_3\text{Br})$ in the complex and is red shifted by -0.1 cm^{-1} from their frequencies in the monomer. A similar red shift can be seen in trace *a* of Fig. 34B, the $^{79}\text{Br}/^{81}\text{Br}$ isotopic doublet showing maxima at 351.9 cm^{-1} and 350.0 cm^{-1} , leading to a red shift of -0.2 cm^{-1} . These results are in agreement with the calculated complexation shifts of -1.1 cm^{-1} and -1.2 cm^{-1} , respectively. The weak CF_3Br monomer bands in trace *b* of both panels are not found back in trace *a*, which, in view of the magnification by a factor of 5 applied to trace *b*, is not surprising. The IR spectra for the CF_3I analogues are shown in Fig. 34C, D, respectively. The $\nu_3(\text{CF}_3\text{I})$ complex band in Fig. 34C, D can be seen to red shift by -1.0 cm^{-1} and -1.2 cm^{-1} , respectively.

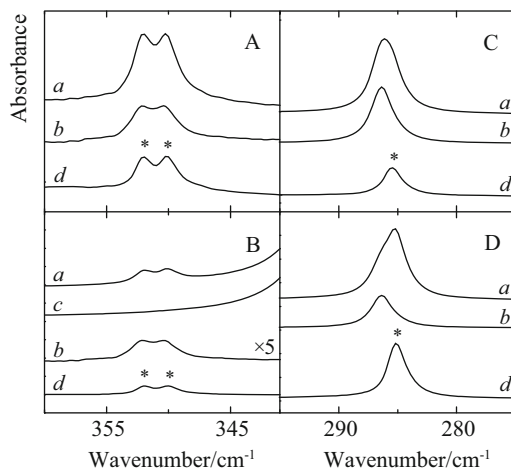


Fig. 34 Infrared spectra of the $\nu_3(\text{CF}_3\text{X})$ region for solutions of mixtures of CF_3Br (**A**, **B**) and CF_3I (**C**, **D**) with CH_3Cl (**A**, **C**) and $\text{C}_2\text{H}_5\text{Cl}$ (**C**, **D**) dissolved in LKr, at 123 K. Trace *a* represents the spectrum of the mixed solution, traces *b* and *c* are the spectra of the monomer CF_3X and $\text{C}_2\text{H}_5\text{Cl}$ solution, respectively, and trace *d* is the spectrum of the 1:1 complex, obtained by subtracting traces *b* and *c* from trace *a*. The new bands appearing in the spectra of the mixture assigned to the 1:1 complex are marked with an *asterisk* (*). Reprinted with permission from [142]. Copyright (2013) American Chemical Society

4.4.2 Relative Stability

The relative stabilities for the $\text{C}-\text{X} \cdots \text{Y}$ ($\text{X}=\text{Br}$, I and $\text{Y}=\text{F}$ and Cl) halogen-bonded complexes, derived from temperature studies of different solutions, and the theoretical values for the complexation enthalpies obtained by correcting the MP2 complexation energies for zero-point vibrational, thermal, and solvent influences are summarized in Table 5. As before, a detailed comparison of the data obtained is postponed to Sect. 5.1.

4.5 $\text{C}-\text{X} \cdots \pi$ -Bonded Complexes: Alkenes, Alkynes, and Aromatic Compounds;

Because of their role in biomolecular systems and protein–ligand binding and in supramolecular chemistry in general, the nature of $\text{C}-\text{X} \cdots \text{Y}$ halogen-bonded interactions has attracted widespread interest from chemists and biochemists. Apart from interactions where the donor atom is an oxygen, a nitrogen, a sulfur, or a halogen atom, an important role is assigned to the interactions of organic halogen atoms with aromatic amino acid side chains, the relative importance derived from a recent survey of protein databases being [138, 140, 146] in the

Table 5 Experimental and predicted complexation enthalpies, in kJ mol^{-1} , obtained for the complexes of methyl fluoride, ethyl fluoride, methyl chloride, and ethyl chloride with the different trifluorohalomethanes CF_3X ($\text{X}=\text{Cl}, \text{Br}, \text{I}$)

		$\Delta_{\text{exp}}\text{H}/\text{kJ mol}^{-1}$	$\Delta_{\text{calc}}\text{H}/\text{kJ mol}^{-1}$
$\text{CH}_3\text{F} - \text{CF}_3\text{Cl}$	LAr	–	–3.3 (2)
$\text{CH}_3\text{F} - \text{CF}_3\text{Br}$	LAr	–7.0 (3)	–7.6 (2)
$\text{CH}_3\text{F} - \text{CF}_3\text{I}$	LAr	–7.6 (1)	–9.7 (2)
$\text{C}_2\text{H}_5\text{F} - \text{CF}_3\text{Cl}$	LKr	–	–5.7 (2)
$\text{C}_2\text{H}_5\text{F} - \text{CF}_3\text{Br}$	LKr	–7.1 (1)	–7.6 (2)
$\text{C}_2\text{H}_5\text{F} - \text{CF}_3\text{I}$	LKr	–8.7 (2)	–10.0 (3)
$\text{CH}_3\text{Cl} - \text{CF}_3\text{Cl}$	LKr	–	–0.4 (2)
$\text{CH}_3\text{Cl} - \text{CF}_3\text{Br}$	LKr	–5.9 (2)	–6.3 (3)
$\text{CH}_3\text{Cl} - \text{CF}_3\text{I}$	LKr	–8.3 (3)	–8.8 (2)
$\text{C}_2\text{H}_5\text{Cl} - \text{CF}_3\text{Cl}$	LKr	–	–5.1 (2)
$\text{C}_2\text{H}_5\text{Cl} - \text{CF}_3\text{Br}$	LKr	–6.5 (2)	–7.5 (3)
$\text{C}_2\text{H}_5\text{Cl} - \text{CF}_3\text{I}$	LKr	–8.8 (3)	–10.4 (4)
$\text{CH}_3\text{F} - \text{CF}_3\text{H}^{\text{a}}$	LKr	–7.2 (5)	
$\text{CH}_3\text{Cl} - \text{CF}_3\text{H}^{\text{a}}$	LKr	–6.5 (5)	

For reason of comparison, the experimental values obtained for the complexes of MF and MCl and fluoroform, CHF_3 , are also given

^aTaken from [131, 132]

order of 53%, 9%, and 5% for $\text{C-X}\dots\text{O}$, $\text{C-X}\dots\text{N}$, and $\text{C-X}\dots\text{S}$ interactions, respectively, and up to 33% for $\text{C-X}\dots\pi$ interactions.

To characterize the nature of various $\text{C-X}\dots\pi$ interactions, a study of the complexes with the aromatic model compounds benzene and toluene, and the non-aromatic alkenes and alkynes ethene, propene, ethyne, propyne, and 2-butyne was initiated.

4.5.1 Vibrational Spectra: Ethene and Propene

In Fig. 35A, the CF_3 stretching region of a mixed solution in LAr containing CF_3Br and of ethene, trace *a*, is compared with the spectra of the monomers in traces *b* and *c*, respectively. The new bands in the spectra of the mixture, marked with an asterisk, are assigned to the 1:1 complex. It can be seen that weak bands, assigned as the antisymmetric $\nu_4(\text{CF}_3\text{Br})$ and symmetric $\nu_1(\text{CF}_3\text{Br})$, stretching modes in the complex, are detected at $1,195.4 \text{ cm}^{-1}$ and $1,079.2 \text{ cm}^{-1}$. The experimental shifts for these bands, -4.4 cm^{-1} for $\nu_4(\text{CF}_3\text{Br})$ and $+2.0 \text{ cm}^{-1}$ for $\nu_1(\text{CF}_3\text{Br})$, compare favorably with the ab initio values of -7.5 cm^{-1} and $+3.6 \text{ cm}^{-1}$.

Similar, but much more pronounced, complex bands can be observed in the top trace in Fig. 35B, where the corresponding region of a solution containing mole fractions of 9.4×10^{-5} of CF_3I and 1.9×10^{-2} of ethene is given. The complex bands assigned to $\nu_4(\text{CF}_3\text{I})$ and $\nu_1(\text{CF}_3\text{I})$ and those assigned to the same modes in the ^{13}C -isotopomer are observed at $1,170.2 \text{ cm}^{-1}$ and $1,073.6 \text{ cm}^{-1}$, and at

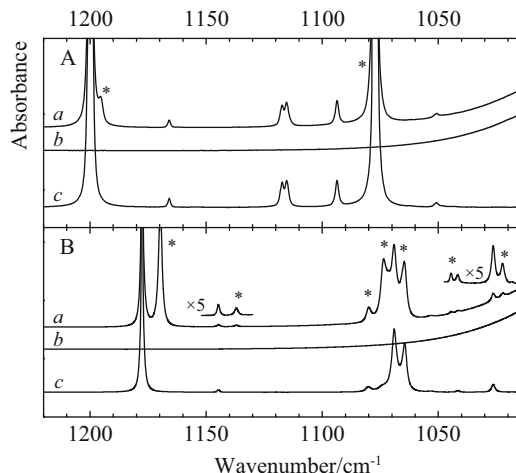


Fig. 35 Infrared spectra of the 1,220–1,010 cm^{-1} region for solutions of mixtures of CF_3Br (A) and CF_3I (B) with ethene dissolved in LAr, at 93 K. Trace *a* represents the spectrum of the mixed solution and traces *b* and *c* are the spectra of the monomer ethene and CF_3X solution, respectively. The new bands appearing in the spectra of the mixture assigned to the 1:1 complex are marked with an asterisk (*). Reproduced from [144] with permission from the PCCP Owner Societies

1,136.9 cm^{-1} and 1,044.5 cm^{-1} . The experimental complexation shifts, -7.9 cm^{-1} and $+4.8 \text{ cm}^{-1}$, agree nicely with the theoretical values of -9.1 cm^{-1} and $+5.5 \text{ cm}^{-1}$. It is obvious from trace *a* in Fig. 35B that the complex bands are much more intense than the corresponding complex bands in Fig. 35A. The concentrations of the monomers in this case are of the same order as in the case of CF_3Br , so here, from the relative intensities, it is inferred that the complex with CF_3I is much more stable than the complex with CF_3Br . New bands are also observed at 1,079.9 cm^{-1} , 1,065.7 cm^{-1} , and 1,022.3 cm^{-1} . The latter is assigned as the $\nu_2(\text{CF}_3\text{I}) + \nu_3(\text{CF}_3\text{I})$, and the experimental complexation shift equals -4.1 cm^{-1} compared with the calculated value of -6.8 cm^{-1} (i.e., the sum of the harmonic shifts of $\nu_2(\text{CF}_3\text{I})$ and $\nu_3(\text{CF}_3\text{I})$). Based on the calculated frequency shifts and the intensity differences, the complex bands at 1,079.9 cm^{-1} and 1,065.7 cm^{-1} are assigned to $\nu_5(\text{CF}_3\text{I}) + 2\nu_6(\text{CF}_3\text{I})$ and $2\nu_5(\text{CF}_3\text{I})$, respectively.

The CF_3 stretching region for the propene complexes is shown in Fig. 36. Figure 36A compares a solution containing mole fractions of 1.9×10^{-4} of CF_3Br and 3.8×10^{-3} of propene dissolved in LAr, trace *a*, with the spectra of the monomers in traces *b* and *c*, respectively. The new bands in the spectra of the mixture, marked with an asterisk, are assigned to the 1:1 complex. It can be seen that weak bands, assigned as the antisymmetric $\nu_4(\text{CF}_3\text{Br})$ and symmetric $\nu_1(\text{CF}_3\text{Br})$ stretching modes in the complex, are detected at 1193.8 cm^{-1} and 1079.4 cm^{-1} . The experimental shifts for these bands, -6.0 cm^{-1} for $\nu_4(\text{CF}_3\text{Br})$ and $+2.2 \text{ cm}^{-1}$ for $\nu_1(\text{CF}_3\text{Br})$, compare favorably with the ab initio values of -8.3 cm^{-1} and $+3.4 \text{ cm}^{-1}$. Even though the used propene concentration is about

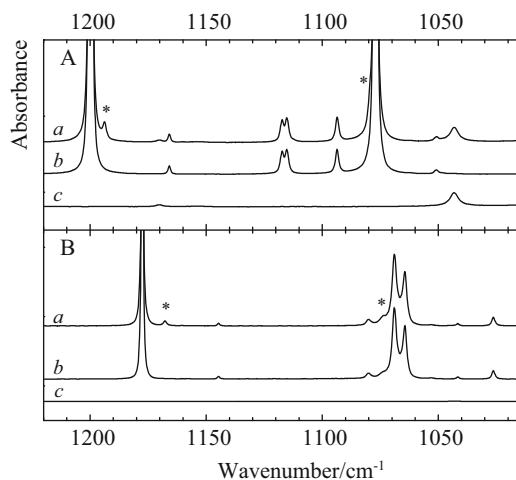
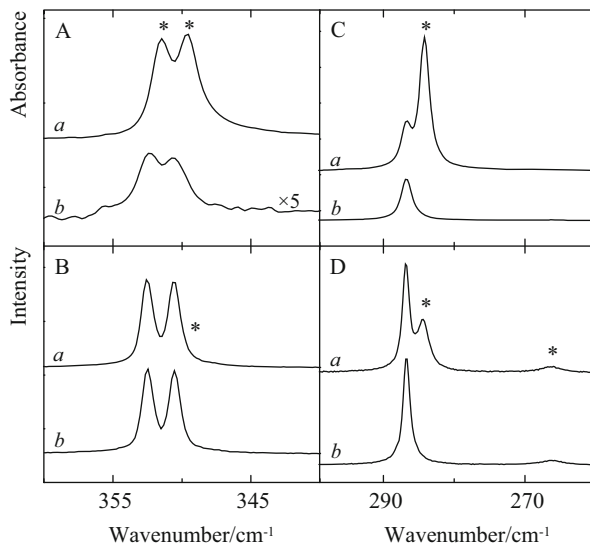


Fig. 36 Infrared spectra of the 1,220–1,010 cm^{-1} region for solutions of mixtures of CF_3Br (A) and CF_3I (B) with propene dissolved in LAr, at 93 K. Trace *a* represents the spectrum of the mixed solution and traces *b* and *c* are the spectra of the monomer propene and CF_3X solution, respectively. The new bands appearing in the spectra of the mixture assigned to the 1:1 complex are marked with an *asterisk* (*). Reproduced from [144] with permission from the PCCP Owner Societies

five times smaller than the ethene concentration in Fig. 35A, the complex bands here are slightly more pronounced and show a larger complexation shift. This indicates the difference in strength between the ethene and propene complexes. Similar complex bands can be observed in the top trace in Fig. 36B, where the corresponding region of a solution containing mole fractions of 7.5×10^{-5} of CF_3I and 3.4×10^{-3} of propene is given. The complex bands assigned to $\nu_4(\text{CF}_3\text{I})$ and $\nu_1(\text{CF}_3\text{I})$ are observed at 1,168.1 cm^{-1} and 1,073.7 cm^{-1} . The experimental complexation shifts, -10.0 cm^{-1} and $+4.9 \text{ cm}^{-1}$, agree nicely with the theoretical values of -10.6 cm^{-1} and $+6.7 \text{ cm}^{-1}$. In view of the low concentrations of CF_3I and propene, it is not surprising that only a few complex bands occur and with a lower intensity than those in Fig. 35B. Nevertheless, the complexation shifts for the propene complex are larger than those for the ethene complex, indicating the difference in strength between the two complexes.

IR and Raman spectra in the C–X stretching regions for the ethene complexes are given in Fig. 37. In each panel, trace *a* represents the spectrum of the mixed solution, while traces *b* and *c* were recorded from a solution in which only CF_3X or ethene was dissolved in liquid argon. Trace *d* is the spectrum of the 1:1 complex, obtained by subtracting traces *b* and *c* from trace *a*. Complex bands for the 1:1 complex are marked with an asterisk. The IR and Raman spectra for the CF_3Br complex are shown in Fig. 37A, B, respectively. Trace *a* in Fig. 37A clearly shows the presence of a $^{79}\text{Br}/^{81}\text{Br}$ isotopic doublet, with maxima at 351.4 cm^{-1} and 349.6 cm^{-1} . This doublet is assigned as $\nu_3(\text{CF}_3\text{Br})$ in the complex and is red shifted by -1.0 cm^{-1} from their frequencies in the monomer. The weak CF_3Br monomer

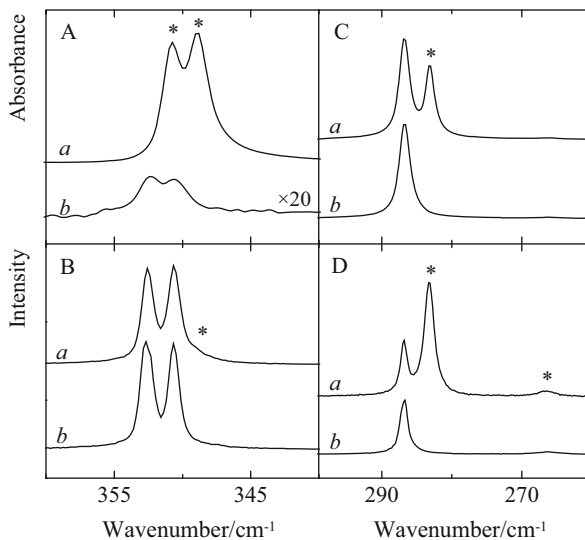
Fig. 37 Infrared (A, C) and Raman (B, D) spectra of the C–X stretching region for solutions of mixtures of CF₃Br (A, B), CF₃I (C, D) with ethene dissolved in LAr, at 93 K. Traces *a* and *b* represent the spectrum of the mixed solution and of the monomer CF₃X solution, respectively. The new bands appearing in the spectra of the mixture assigned to the 1:1 complex are marked with an *asterisk* (*). Reproduced from [144] with permission from the PCCP Owner Societies



bands in trace *b* of the IR panel are not found back in trace *a*, which, in view of the magnification by a factor of 5 applied to trace *b*, is not surprising. The assignments are confirmed by the Raman spectra, albeit that only the ⁸¹Br-isotopomer is visible here as a very weak shoulder on the intense monomer doublet. The IR and Raman spectra for the CF₃I complex are shown in Fig. 37C, D, respectively. It is clear that the $\nu_3(\text{CF}_3\text{I})$ bands in the monomer and in the complex are present in the IR and the Raman spectra. The $\nu_3(\text{CF}_3\text{I})$ complex band can be seen to red shift by -2.6 cm^{-1} . In the Raman spectra, a weak feature at 266.5 cm^{-1} can be observed in addition to the intense $\nu_3(\text{CF}_3\text{I})$ transitions. This band is assigned as the $\nu_6(\text{CF}_3\text{I})$ complex band, blue shifted by $+0.4 \text{ cm}^{-1}$ from the frequency in the monomer.

Figure 38 shows the C–X stretching regions for the propene complexes. The IR and Raman spectra for the CF₃Br complex are again shown in Fig. 38A, B, respectively. Trace *a* in Fig. 38A clearly shows the presence of a ⁷⁹Br/⁸¹Br isotopic doublet, with maxima at 350.7 cm^{-1} and 348.9 cm^{-1} . This doublet is assigned as $\nu_3(\text{CF}_3\text{Br})$ in the complex and is red shifted by -1.7 cm^{-1} from their frequencies in the monomer. The weak CF₃Br monomer bands in trace *b* are not found back in trace *a*, which, in view of the magnification by a factor of 20 applied to trace *b*, is not surprising. The assignments are confirmed by the Raman spectra, albeit only the ⁸¹Br-isotopomer is visible here as a weak shoulder on the intense monomer doublet. The IR and Raman spectra for the CF₃I complex are shown in Fig. 38C, D, respectively. It is clear that the $\nu_3(\text{CF}_3\text{I})$ bands in the monomer and in the complex are present in the IR and the Raman spectra. The $\nu_3(\text{CF}_3\text{I})$ complex band can be seen to red shift by -3.6 cm^{-1} . In the Raman spectra, a weak feature at 266.8 cm^{-1} can be observed in addition to the intense $\nu_3(\text{CF}_3\text{I})$ transitions. This band is assigned

Fig. 38 Infrared (A, C) and Raman (B, D) spectra of the C–X stretching region for solutions of mixtures of CF₃Br (A, B), CF₃I (C, D) with propene dissolved in LAr, at 93 K. Trace *a* and *b* represents the spectrum of the mixed solution and of the monomer CF₃X solution, respectively. The new bands appearing in the spectra of the mixture assigned to the 1:1 complex are marked with an *asterisk* (*). Reproduced from [144] with permission from the PCCP Owner Societies



as the $\nu_6(\text{CF}_3\text{I})$ complex band, blue shifted by $+0.6 \text{ cm}^{-1}$ from the frequency in the monomer.

Figure 39A shows the temperature dependence in the $1,010\text{--}985 \text{ cm}^{-1}$ and $940\text{--}900 \text{ cm}^{-1}$ regions for a solution in LAr with mole fractions of 1.3×10^{-2} for CF₃I and 5.6×10^{-4} for propene. From top to bottom, the temperature increases from 93 to 103 K. The two lowest traces represent the single-monomer spectra of propene and CF₃I recorded at 103 K, respectively. In the regions shown, propene gives rise to four fundamental monomer bands situated at 990.5 cm^{-1} , 934.4 cm^{-1} , 918.6 cm^{-1} , and 910.7 cm^{-1} . They are assigned as the $\nu_{18}(\text{propene})$, $\nu_{12}(\text{propene})$, $\nu_{13}(\text{propene})$, and $\nu_{19}(\text{propene})$ monomer vibrations, respectively, and can be seen to conform to the ab initio IR intensities of 16 km mol^{-1} , 3 km mol^{-1} , 2 km mol^{-1} , and 39 km mol^{-1} , respectively. The bands assigned to the 1:1 complex are marked with an asterisk and can be seen to give rise to absorptions at 995.2 cm^{-1} , 934.9 cm^{-1} , 919.6 cm^{-1} , and 916.5 cm^{-1} . The first two are straightforwardly assigned as the $\nu_{18}(\text{propene})$ and $\nu_{12}(\text{propene})$ complex bands, respectively. For an unambiguous assignment of the last two absorptions, the spectra in Fig. 39B are required. Figure 39B panel shows the Raman spectra of a solution in liquid argon with mole fractions of 1.2×10^{-3} for CF₃I and 1.8×10^{-3} for propene. Trace *a* gives the spectrum of the mixed solution and trace *b* was recorded from a solution in which only propene was dissolved in LAr. In trace *b*, only one band is present, situated at 918.6 cm^{-1} , which corresponds to the $\nu_{13}(\text{propene})$ monomer vibration. In the mixed spectrum, trace *a*, a complex band produced by this mode appears at 916.5 cm^{-1} , so that the complex band seen at 919.6 cm^{-1} in Fig. 39A has to be assigned as the $\nu_{19}(\text{propene})$ complex band. At low temperatures, additional bands, marked with an open circle (\circ), appear at 999.6 cm^{-1} and 924.7 cm^{-1} . The intensity behavior of these bands is found to differ from the 1:1 complex bands. These bands

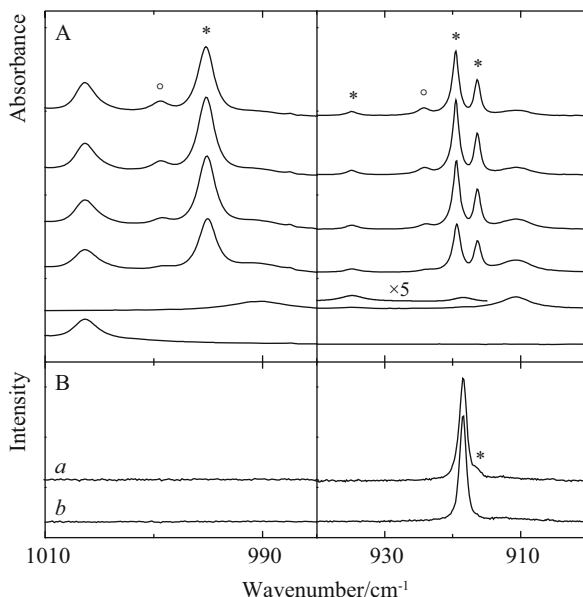


Fig. 39 Infrared (A) and Raman (B) spectra of the 1,010–900 cm^{-1} region for solutions of mixtures of CF_3I and propene dissolved in LAr. A depicts the temperature dependence of this region. From top to bottom, the temperature of the solution increases from 93 to 103 K. The two lowest traces represent the spectrum of the propene and CF_3I monomer, recorded at 103 K. The spectra in B are recorded at 93 K. Trace *a* represents the spectrum of the mixed solution and trace *b* is the spectrum of the monomer propene solution. The new bands appearing in the spectra of the mixture assigned to the 1:1 complex are marked with an *asterisk* (*); the bands assigned to the 2:1 complex are marked with a *circle* (°). Reproduced from [144] with permission from the PCCP Owner Societies

are, therefore, assigned to a 2:1 complex in which two molecules of CF_3I interact with the π -system of the same propene molecule.

4.5.2 Vibrational Spectra: Ethyne, Propyne, and 2-Butyne

In agreement with the data for ethene and propene, and for the mixed solution containing ethyne, propyne, and 2-butyne, complexation shifts were observed for the symmetric and the antisymmetric CF_3 stretching modes in the halogen donors used. For the solutions containing ethyne and CF_3I , a weak complex band assigned to $\nu_4(\text{CF}_3\text{I})$ was observed at 1,168.5 cm^{-1} . In addition, for the solutions containing propyne and 2-butyne, bands assigned to the stretching modes $\nu_4(\text{CF}_3\text{I})$ and $\nu_1(\text{CF}_3\text{I})$ in the complex with CF_3I were observed at 1,165.4 cm^{-1} and 1,072.6 cm^{-1} , and at 1,163.0 cm^{-1} and 1,073.6 cm^{-1} , respectively. The experimental shifts, -6.8 cm^{-1} for ethyne, -10.0 cm^{-1} and $+7.1 \text{ cm}^{-1}$ for propyne, and -12.4 cm^{-1} and $+8.1 \text{ cm}^{-1}$ for 2-butyne, again compare favorably with the

predicted values of -7.1 cm^{-1} , -9.6 cm^{-1} and $+6.1\text{ cm}^{-1}$, and -12.0 cm^{-1} and $+7.1\text{ cm}^{-1}$, respectively. Apart from the bands reported above, for the solutions containing propyne and 2-butyne, weak features caused by the CF_3 stretching modes in the ^{13}C isotopomers were also observed near $1,132.8\text{ cm}^{-1}$ and $1,043.6\text{ cm}^{-1}$ and near $1,130.5$ and $1,044.2\text{ cm}^{-1}$, respectively.

In agreement with the results for ethene and propene and with the values derived from the harmonic vibrational frequencies, for both the mixtures containing propyne and 2-butyne, new bands caused by the C–I stretching mode in the complexes are also observed. The complexation shifts derived are -2.7 cm^{-1} for ethene- CF_3I and -3.4 cm^{-1} for propene- CF_3I .

In Fig. 40, the spectral regions for the various $\text{C}\equiv\text{C}$ stretching modes, obtained by studying the IR and Raman spectra of mixed solutions in LKr containing CF_3I and ethyne, propyne, or 2-butyne, and of solutions containing only monomers, are compared. The data derived from the Raman experiments with ethyne, propyne, and 2-butyne are given in Fig. 40A, C, E, respectively. The corresponding IR data are given in Fig. 40B, D, F. In Fig. 40A, B, C, E, traces *a*, *b*, and *c* refer to the spectra obtained for the mixed solution, for the monomer alkyne, and for monomer CF_3I , respectively. In Fig. 40D, F, traces *a*, *b*, and *c* refer to the spectra obtained for the mixed solution, for monomer propyne or 2-butyne, and for monomer CF_3I , while trace *d* gives the spectrum of the isolated complex obtained by subtracting the spectrum of the mixed solution with the rescaled monomer spectra of 2-butyne and CF_3I . The Raman data in Fig. 40A, C, E, show that, apart from the monomer transitions at $1,970.1\text{ cm}^{-1}$, $2,136.7\text{ cm}^{-1}$, and $2,247.8\text{ cm}^{-1}$, new bands produced by the stretching modes in the complexes can be observed near $1,966.5\text{ cm}^{-1}$, $2,130.0\text{ cm}^{-1}$, and $2,237.6\text{ cm}^{-1}$, respectively. The additional weak features observed at $2,129.6\text{ cm}^{-1}$ in trace *b* and at $2,123.0\text{ cm}^{-1}$ and $2,128.3\text{ cm}^{-1}$ in trace *c* of Fig. 40C are caused by an as yet unassigned combination band or overtone in propyne, and by combination bands involving the CF_3 stretching modes in the halogen donor. These bands, at first glance, have no direct counterpart in the spectra of the complexes. The intense feature at $2,229.2\text{ cm}^{-1}$, marked with an open circle (°) in the spectrum of the mixed solutions containing 2-butyne and CF_3I , is discussed in more detail below.

The Raman data for propyne can directly be compared with the IR data in Fig. 40D showing the appearance of monomer and complex bands at exactly the same frequencies as those observed in the Raman spectra. The analysis of the IR data obtained for ethyne and 2-butyne is less straightforward as the $\text{C}=\text{C}$ stretching mode in these species is IR forbidden in the monomer and gains a relatively small, induced intensity in the complex. Inspection of the data in Fig. 40B shows that in the IR spectra of the solutions containing mixtures of ethyne and CF_3I , a weak feature caused by the induced $\text{C}\equiv\text{C}$ stretching mode in the complex can be observed near $1,966.5\text{ cm}^{-1}$, i.e., at a frequency closely resembling that derived from the Raman studies. The appearance of a weak feature caused by the induced $\text{C}\equiv\text{C}$ stretching vibration is in line with predicted IR intensities suggesting a weak IR intensity of some 1.7 km mol^{-1} for the stretching mode in the complex with CF_3I . The results are also in line with previous experimental observations showing

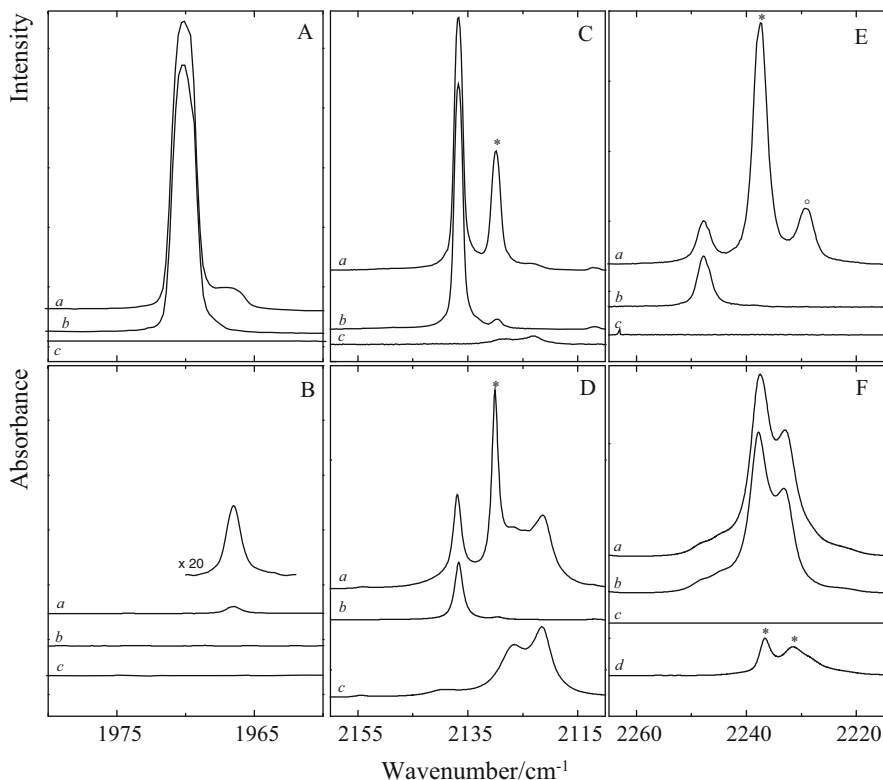


Fig. 40 Raman spectra (panels A, C, E) and infrared spectra (panels B, D, F) of the $\nu_{\text{C}\equiv\text{C}}$ spectral region for solutions of mixtures of CF_3I with ethyne (A, B), propyne (C, D), and 2-butyne (E, F) dissolved in liquid krypton at 120 K. In each panel, trace *a* represents the mixed solution while traces *b* and *c* show the solution containing only CF_3I or ethyne, propyne or 2-butyne. Trace *d* in D, F is obtained by subtracting traces *b* and *c* from trace *a*. New bands due to the 1:1 complex appearing in the spectrum of the mixture are marked with an *asterisk*. Bands marked with a *circle* are assigned to the 2:1 complex

the appearance of induced $\text{C}\equiv\text{C}$ stretching modes while forming complexes of ethyne with Lewis bases such as HCl and BF_3 [99, 100] and the appearance of induced $\text{C}=\text{C}$ stretching modes while forming complexes of ethene with, among others compounds, CHF_3 and CHBrClCF_3 [63, 144]. The predicted IR intensities also suggest that for 2-butyne, complexation with CF_3I leads to an induced IR intensity of some 4.7 km mol^{-1} for the $\text{C}\equiv\text{C}$ stretching mode. Unfortunately, the appearance of relatively strong absorption features related to the $\nu_4 + \nu_5 + 2\nu_6/\nu_1 + \nu_4/\nu_4 + 2\nu_5/\nu_4 + 4\nu_6$ resonances in monomer CF_3I [39, 47] and in the complex with 2-butyne hampered the observation of the spectral features related to the induced $\text{C}\equiv\text{C}$ stretching mode in this complexes.

It was noted above that, apart from the bands assigned to the monomers and to the 1:1 complexes, an additional spectral feature at $2,229.2 \text{ cm}^{-1}$ is observed in the

Raman spectra of the mixed solutions containing 2-butyne and CF_3I . This band, marked with an open circle ($^\circ$) in Fig. 40E, is only observed at lower temperatures and at higher concentrations of CF_3I , in agreement with similar observations made for mixed solutions containing dimethyl sulfide and CF_3I , and dimethyl ether and CF_3Br , and is assigned to the $\text{C}\equiv\text{C}$ stretching mode in a 2:1 complex consisting of one 2-butyne molecule and two CF_3I moieties. Additional experimental evidence for the formation of such a complex was derived from the $2\nu_8$ and $\nu_2 + \nu_4$ spectral regions of 2-butyne and of CF_3I , respectively.

4.5.3 Vibrational Spectra : Benzene and Toluene

In agreement with the results reported above, and with the results derived from *ab initio* calculations in which the harmonic frequencies of monomer and complexes are calculated, red shifts, varying between -7.7 cm^{-1} and -10.3 cm^{-1} for the complexes of benzene with CF_3Br and CF_3I and between -8.3 cm^{-1} and -10.8 cm^{-1} for the complexes of toluene with CF_3Br and CF_3I are observed for the antisymmetric stretches $\nu_4(\text{CF}_3\text{X})$. In addition, small blue shifts, of $+2.7\text{ cm}^{-1}$ and $+3.1\text{ cm}^{-1}$ were observed for the $\nu_1(\text{CF}_3\text{I})$ symmetric stretching modes in benzene- CF_3I and toluene- CF_3I , respectively.

Careful analysis of the IR and Raman spectra of the mixed solutions and of the monomers shows that for the mixtures of benzene and toluene, indications for complex bands can be observed in the C-X stretching region. The experimental complexation shifts for the C- ^{79}Br , the C- ^{81}Br , and the C-I stretching modes are in the order of -0.1 cm^{-1} to -0.8 cm^{-1} for the complexes with benzene and in the order of -0.6 cm^{-1} to -1.3 cm^{-1} for the complexes with toluene.

Analysis of the data in the different panels of Fig. 41 reveals that for both CF_3Br and CF_3I a complex band appears on the high frequency side of the 674.8 cm^{-1} monomer vibration assigned to the C-H out of plane bending mode $\nu_4(\text{benzene}, A_{2u})$. The blue shifts of $+2.6\text{ cm}^{-1}$ for the CF_3Br complex and $+4.6\text{ cm}^{-1}$ for CF_3I are in line with *ab initio* complexation shifts and agree favorably with data reported in earlier studies showing that the C-H out of plane bending mode in benzene is largely perturbed by C-H proton donors such as halothane, CF_3CBrClH [67], and sevoflurane, $(\text{CF}_3)_2\text{CHOCH}_2\text{F}$ [64], and other Lewis acids such as hexafluorobenzene, C_6F_6 [136].

Apart from the bands assigned to the monomers and to the 1:1 complexes, in the IR spectra of the mixed solutions containing higher concentrations of benzene and CF_3I an additional spectral feature is observed near 683.2 cm^{-1} . This band, which in Fig. 41C is marked with an open circle ($^\circ$), is observed at lower temperatures and in highly concentrated solutions only. Supported by the results of the *ab initio* calculations, a concentration study, and the appearance of similar features for solutions containing benzene and halothane [67], this band is assigned to the C-H out of plane bending mode of benzene in a 1:2 complex consisting of one benzene molecule and two CF_3I moieties.

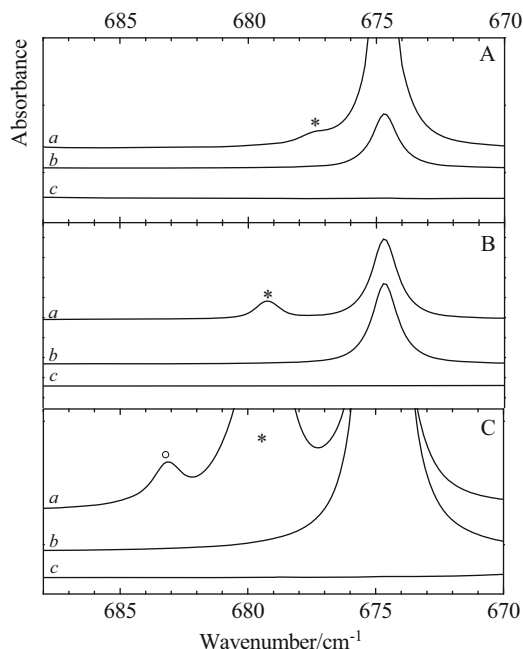


Fig. 41 Infrared spectra of the C–H out of plane bending mode $\nu_4(A_{2u})$ of benzene for LKr solutions of mixtures of CF_3Br (A) or CF_3I (B, C) with benzene at 120 K. In each panel trace *a* represents the mixed solution while traces *b* and *c* show the solution containing only benzene and CF_3X (with $\text{X}=\text{Br}, \text{I}$), respectively. New bands appearing in the spectrum of the mixtures are marked with an *asterisk* (*) and are assigned to the 1:1 complex. C is obtained by using higher concentrations of both CF_3I and benzene. In this panel, the band marked with a *circle* (°) is assigned to the 2:1 complex with two molecules CF_3I and a single molecule benzene. Reprinted from [145] with permission from MDPI

Upon complexation with CF_3I and CF_3Br , a small red shift was predicted for the ring breathing mode of benzene. In addition, a significant increase in IR intensity, from zero up to 1.6 km mol^{-1} for benzene- CF_3Br and 3.1 km mol^{-1} for benzene- CF_3I , was encountered. To shed light on the appearance of induced spectral features and to rationalize further the behavior of the ring breathing mode in the complexes formed with benzene, special attention was paid to IR and Raman spectra in the ν_2 spectral region. Typical spectra obtained for mixed solutions of benzene with CF_3Br and CF_3I , and of the monomers involved, are summarized in Fig. 42. The IR and Raman data are given in Fig. 42A, C and in Fig. 42B, D, respectively. The data for CF_3Br are shown in Fig. 42A, B while the data obtained for CF_3I are given in Fig. 42C, D. In each panel, trace *a* refers to the spectrum of the mixed solution, while traces *b* and *c* are the spectra of monomer benzene and CF_3X , respectively. Trace *d* is the spectrum of the 1:1 complex, obtained by subtracting the rescaled monomer traces *b* and *c* from the mixture trace *a*.

Inspection of the difference spectra shown in traces *d* of Fig. 42B, D shows that for CF_3Br and CF_3I , a new band appears red-shifted from the 992.7 cm^{-1} monomer

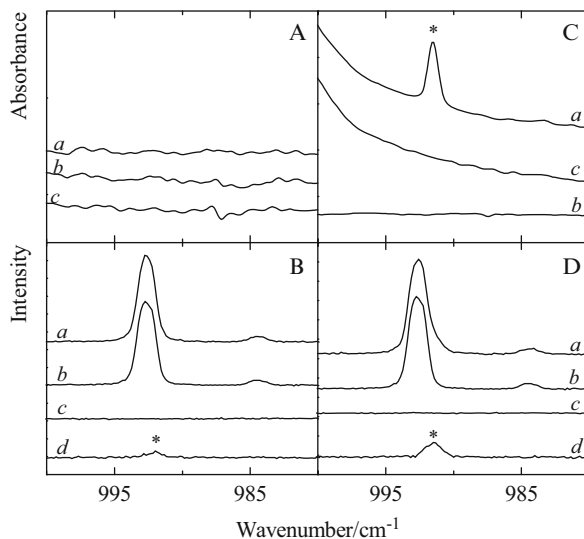


Fig. 42 Infrared spectra (A, C) and Raman spectra (B, D) of the so-called ring breathing mode ν_2 of benzene for solutions with CF_3Br (A, B) and CF_3I (C, D). Trace *a* gives the spectrum of the mixed solution while traces *b* and *c* are the spectra of the monomer benzene and CF_3X (with $\text{X}=\text{Br}, \text{I}$), respectively. Trace *d* is the spectrum of the 1:1 complex, obtained by subtracting the rescaled monomer traces *b* and *c* from the mixture trace *a*. New bands appearing in the spectrum of the complex are marked with an *asterisk* (*) and are assigned to the 1:1 complex. Reprinted from [145] with permission from MDPI

transition, by -0.7 cm^{-1} and -1.3 cm^{-1} , respectively. The frequency of the complex band observed for benzene- CF_3I is in excellent agreement with that of the induced spectral feature observed in the IR spectra in Fig. 42C, and confirms its assignment. Even for a large excess of CF_3Br , no counterpart of the 992.0-cm^{-1} complex band observed in the Raman spectra could be detected in the IR spectra in Fig. 42A. The occurrence of an induced ring breathing mode in the complex with CF_3I and the lack of such a feature for the complex with CF_3Br is not fully understood. The observations, however, are in line with the differences in predicted IR intensity, suggesting the induced ring breathing mode in the complex with CF_3I is almost twice as large as that in the complex with CF_3Br , and with the above observations showing that even when a large excess of CF_3Br is used, the equilibrium concentrations of the complexes formed remain rather small.

4.5.4 Relative Stability

The relative stabilities for the $\text{C-X}\dots\pi$ ($\text{X}=\text{Br}, \text{I}$) halogen-bonded complexes, derived from temperature studies of different solutions, and the theoretical values for the complexation enthalpies obtained by correcting the MP2 energies

Table 6 Experimental and predicted complexation enthalpies, in kJ mol^{-1} , obtained for the complexes of ethene, propene, ethyne, propyne, 2-butyne, benzene, and toluene with the different trifluorohalomethanes CF_3X ($\text{X}=\text{Cl}, \text{Br}, \text{I}$). For reason of comparison, the experimental values obtained for the complexes of ethane and propene with fluoroform, CHF_3 , are also given

		$\Delta_{\text{exp}}\text{H}/\text{kJ mol}^{-1}$	$\Delta_{\text{calc}}\text{H}/\text{kJ mol}^{-1}$
Ethene – CF_3Cl	LAr		–0.6 (4)
Ethene – CF_3Br	LAr	–5.3 (2)	–3.1 (4)
Ethene – CF_3I	LAr	–7.5 (2)	–5.0 (4)
Propene – CF_3Cl	LAr		–2.5 (5)
Propene – CF_3Br	LAr	–5.6 (1)	–5.6 (5)
Propene – CF_3I	LAr	–8.8 (1)	–8.5 (5)
Ethyne – CF_3Cl	LKr		–4.1 (3)
Ethyne – CF_3Br	LKr		–6.0 (4)
Ethyne – CF_3I	LKr	–5.9 (3)	–8.8 (4)
Propyne – CF_3Cl	LKr		–4.8 (5)
Propyne – CF_3Br	LKr	–5.6 (3)	–7.8 (4)
Propyne – CF_3I	LKr	–8.1 (2)	–11.6 (6)
2-Butyne – CF_3Cl	LKr		–7.7 (4)
2-Butyne – CF_3Br	LKr	–7.3 (2)	–10.9 (5)
2-Butyne – CF_3I	LKr	–10.9(2)	–15.4 (6)
Benzene – CF_3Cl	LKr		–7.5 (4)
Benzene – CF_3Br	LKr	–6.5(3)	–9.4 (5)
Benzene – CF_3I	LKr	–7.6(2)	–12.4 (5)
Toluene – CF_3Cl	LKr		–8.5 (5)
Toluene – CF_3Br	LKr	–6.2(5)	–10.9 (5)
Toluene – CF_3I	LKr	–7.4(5)	–15.1 (6)
Propene – $(\text{CF}_3\text{I})_2$	LAr	–16.5 (6)	
2-Butyne – $(\text{CF}_3\text{I})_2$	LKr	–20.9(7)	
Benzene – $(\text{CF}_3\text{I})_2$	LKr	–14.5(9)	
Ethene – CF_3H	LKr	–4.6 (4)	
Propene – CF_3H	LKr	–5.1 (2)	

for zero-point vibrational, thermal, and solvent influences are summarized in Table 6. As before, a detailed comparison of the data obtained is postponed to Sect. 5.1.

5 Analyzing Trends

In this section, the properties of the studied halogen bonds are compared and trends observed are discussed. These characteristics are also compared with the equivalent properties of the corresponding $\text{C-H} \cdots \text{X}$ hydrogen-bonded complexes formed with fluoroform, CHF_3 .

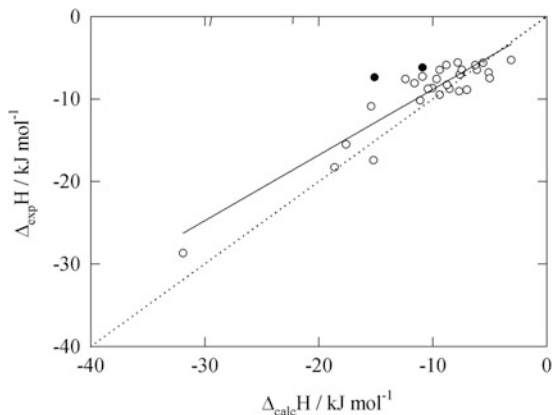


Fig. 43 Scatter plot obtained by plotting the experimental and calculated complexation enthalpies. The experimental values are determined using temperature studies in liquid argon, liquid krypton, or liquid xenon. The calculated values are obtained by correcting MP2/aug-cc-pVTZ(-PP) complexation energies for zero-point vibrational, thermal and solvent influences. The *solid line* refers to the linear regression line obtained. The *filled symbols* refer to the data obtained for the complexes of CF_3I with benzene and toluene for which the largest deviations are observed

5.1 Complexation Enthalpies

In the quest for general trends in the characteristic features of non-covalent interactions, it has always been attractive to find predictive tools for the stability of the interactions studied. For hydrogen-bonded complexes, for example, attempts have been made [147–150] to plot the X–H stretching vibrational shift vs the experimentally determined complexation enthalpy.

Figure 43 shows the correlation of the experimental complexation enthalpies and theoretical values obtained by correcting the *ab initio* energies for zero-point vibrational, thermal and solvent influences. The coefficients of the linear regression line $\Delta_{\text{exp}}H = a + b\Delta_{\text{calc}}H$ are $a = -0.87(85) \text{ kJ mol}^{-1}$ and $b = 0.796(73)$. These results illustrate that although most theoretical values overestimate the strength of the halogen bond, a good correlation is obtained. The largest deviations are observed for the complexes of CF_3I with benzene and toluene. These deviations are in line with earlier observations showing that for other complexes involving the aromatic model compounds including, amongst other compounds, the complexes of benzene with the anesthetics halothane [67] and sevoflurane [63], MP2 *ab initio* calculations tend to overestimate seriously the complexation energies and the corresponding complexation enthalpies. In view of these results, the overestimation for benzene– CF_3X and toluene– CF_3X , most likely, is due to imperfections related to the MP2 second order perturbation approach used.

Correlation plots studying the dependence of the complexation enthalpies determined and the complexation shifts observed or the modes in the CF_3X moieties are shown in Figs. 44 and 45. The first plot relates to the shifts observed for the C–X

Fig. 44 Scatter plot showing the correlation between the complexation shifts observed for the C–X stretching modes $\nu_3(\text{CF}_3\text{X})$ in the different complexes and the experimental enthalpies in cryosolution: *triangles*, CF_3I , *squares*, CF_3Br

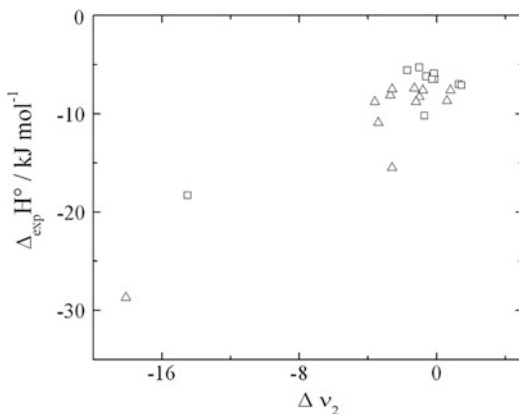
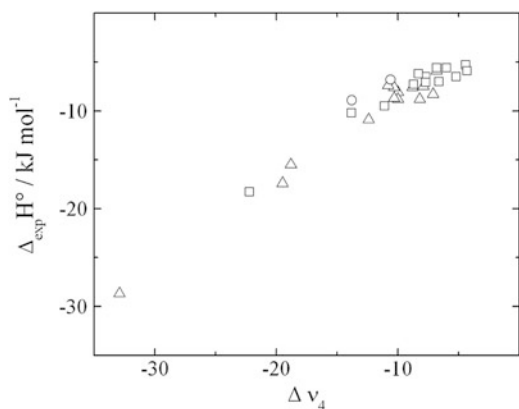


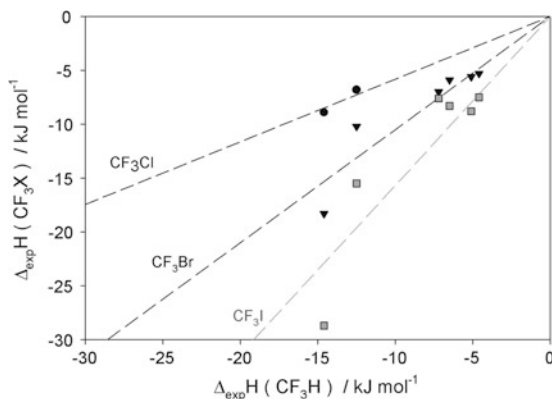
Fig. 45 Scatter plot showing the correlation between the complexation shifts observed for the CF_3 antisymmetric stretching modes $\nu_4(\text{CF}_3\text{X})$ in the different complexes and the experimental enthalpies in cryosolution: *triangles*, CF_3I , *squares*, CF_3Br , *circles*, CF_3Cl



stretching mode $\nu_3(\text{CF}_3\text{X})$; the second plot is obtained by using the complexation shifts derived for the antisymmetric CF_3 stretching modes $\nu_4(\text{CF}_3\text{X})$. The results clearly illustrate that, for the $\nu_3(\text{CF}_3\text{X})$, little or no correlation is found, while the data for $\nu_4(\text{CF}_3\text{X})$ show an intriguing correlation between the experimental complexation enthalpies and the shifts observed. The limited correlation, if any, observed for the $\nu_3(\text{CF}_3\text{X})$ mode is explained by the fact that the C–X stretching modes in the monomer and in the complexes are far from isolated, and are often strongly perturbed because of couplings with other low-frequency vibrations. The excellent correlation for $\nu_4(\text{CF}_3\text{X})$, most presumably, is related to the fact that the CF_3 stretching modes are easily perturbed by the partner molecule and at the same time often give rise to larger complexation shifts.

To be able compare the relative stabilities of the different C–X...Y halogen-bonded complexes with those of the equivalent C–H...X hydrogen-bonded complexes, and to shed light on the parallelisms between both types of interaction, the experimental complexation enthalpies for the different trifluorohalomethanes studied are plotted in Fig. 46 vs the values obtained for the respective complexes formed

Fig. 46 Scatter plot obtained for the complexation enthalpies for the trifluorohalomethanes CF_3X ($\text{X}=\text{Cl}$, Br and I) and the corresponding C–H donor CF_3H . The plots and linear regression lines are based on the experimental values reported in Tables 2, 3, 4, 5, and 6



with fluoroform, CHF_3 . The slopes of the linear regression lines, obtained by assuming a regression line that passes through the origin, are:

$$\Delta_{\text{exp}}\text{H}(\text{CF}_3\text{I}..B) = 1.58(42)\Delta_{\text{exp}}\text{H}(\text{CF}_3\text{H}..B) \quad (14a)$$

$$\Delta_{\text{exp}}\text{H}(\text{CF}_3\text{Br}..B) = 1.06(23)\Delta_{\text{exp}}\text{H}(\text{CF}_3\text{H}..B) \quad (14b)$$

$$\Delta_{\text{exp}}\text{H}(\text{CF}_3\text{Cl}..B) = 0.57(8)\Delta_{\text{exp}}\text{H}(\text{CF}_3\text{H}..B) \quad (14c)$$

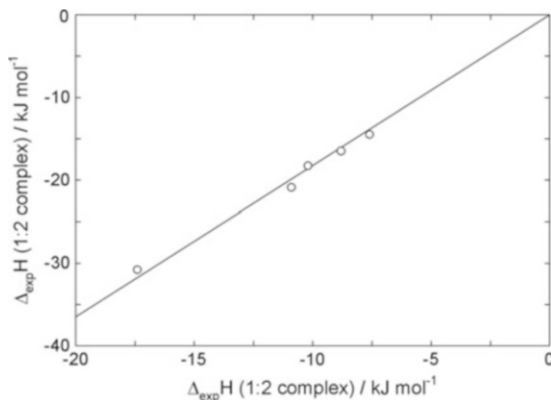
Although the available data are still quite limited, and obtaining more experimental data is certainly required to allow a more reliable analysis, these data show that, for all Lewis bases studied, a similarity in strength is observed for the complexes of CHF_3 and CF_3Br . Within current error margins, the differences in slope observed when passing from CF_3Br to CF_3I and from CF_3Br to CF_3Cl are both in the order of 50%.

An interesting, somewhat surprising, correlation obtained by comparing the enthalpies for the 1:1 and the 1:2 complexes observed is shown in Fig. 47. The linear regression line shown was obtained by assuming a regression line that passes through the origin, and is given by

$$\Delta_{\text{exp}}\text{H}(\text{CF}_3\text{X}..B..X\text{CF}_3) = 1.82(8)\Delta_{\text{exp}}\text{H}(\text{CF}_3\text{X}..B) \quad (15)$$

Analysis of the original data in Fig. 47 and the data derived from the regression line shows that for all 1:2 complexes, a weak anti-cooperative effect occurs in which the second C–X...Y halogen bond weakens the first bond, and vice versa. The weak anti-cooperative effect is in line with the observations showing that, for a 1:2 complex, the complexation shifts induced in the CF_3X moieties are slightly smaller than those obtained for the corresponding 1:1 complexes. The larger complexation shifts for the 1:2 complexes observed for the vibrational modes in the Lewis base are in line with the general idea of a bifurcated structure, in which the central Lewis base is simultaneously perturbed by both interacting CF_3X units.

Fig. 47 Scatter plot comparing the complexation enthalpies for the 1:1 and 1:2 complexes formed between a single Lewis base and one or two trifluorohalomethanes. The data and the linear regression line derived is based on the experimental values reported in Tables 2, 3, 4, 5, and 6



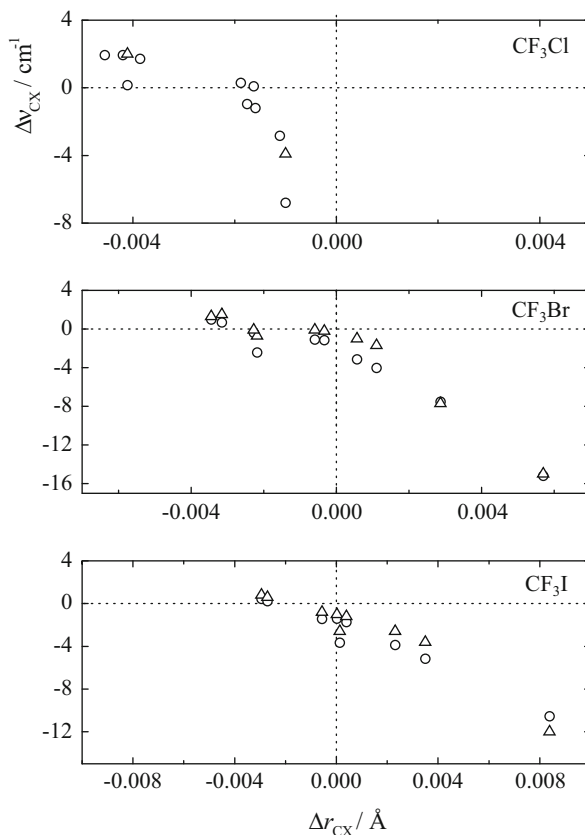
5.2 Blue- and Red-Shifting C–X Halogen Bonds

Several theoretical studies comparing the properties of C–H...Y hydrogen bonds and C–X...Y halogen bonds have drawn attention [18–20, 151] to the fact that blue shifts for the C–X stretching vibration are possible for both CF_3Cl and CF_3Br . Wang and Hobza also suggested [18] that the iodoperfluoroalkanes are only involved in red-shifting halogen bonds.

The experimental data reported for the cryosolutions provide the first experimental evidence for blue-shifting halogen bonds, and, taking into account the observation of blue-shifting C–I stretching modes in the complexes of CF_3I with CH_3F , also allows Wang and Hobza's statement to be refuted. Before discussing the predicted changes in the C–X bond length and the complexation shift derived for the corresponding stretching mode, it is interesting to note that complexation also has its repercussions on the IR intensities of the C–X stretching mode. These modes are known to be extremely small in the monomers and to gain a significant intensity in the complex. For the complexes studied here, the predicted intensity $\epsilon_{\text{complex}}/\epsilon_{\text{monomer}}$ varies from 7 for $\text{C}_2\text{H}_5\text{Cl}-\text{CF}_3\text{Cl}$ to 1300 for $\text{TMA}-\text{CF}_3\text{Br}$.

The changes in the C–X bond length upon complexation and its correlation with the complexation shift of the C–X stretching mode are shown in Fig. 48. The results for $\text{TMA}-\text{CF}_3\text{I}$ are omitted for clarity. A striking agreement between the ab initio values, represented by a circle, and the experimental values, depicted by a triangle, can be seen. This proves the suitability of the chosen calculation method to describe accurately the halogen bond. Furthermore, it can be seen that, for the weaker CF_3Cl complexes, all C–Cl bond lengths are calculated to shorten by at least 0.0010 \AA upon complexation. This bond length shortening, however, is not always synonymous with a blue shift of the C–Cl stretching mode, in contrast to what has often been considered in the literature [151]. Although only a limited number of the CF_3Cl complexes could be studied experimentally, both red and blue shifts were observed, the largest shifts observed for the TMA and DME complexes being -3.9 cm^{-1} and $+2.0 \text{ cm}^{-1}$, respectively.

Fig. 48 Correlation of the complexation shifts of the C–X stretching vibration, calculated (*circle*) and observed (*triangle*), and C–X bond length changes upon complexation. The data for the TMA-CF₃I complex (+0.0165 Å, –24.4 cm^{–1} and –18.1 cm^{–1}) are omitted for clarity



The strong CF₃I complexes, on the other hand, are generally calculated with an elongated C–I bond length upon complexation. In the complexes with benzene, CH₃F, and C₂H₅F, however, the C–I bond length is found to shorten by –0.0005 Å, –0.0029 Å and –0.0027 Å, respectively, but only the last two are accompanied by a blue shift of +0.5 cm^{–1} and +0.2 cm^{–1}, respectively. These calculated shifts were confirmed by the experimental blue shift of +0.8 cm^{–1} and +0.6 cm^{–1}, respectively.

Finally, it can be seen that, for the intermediate CF₃Br complexes, the C–Br bond length changes are situated somewhere between the C–Cl and C–I bond length changes: about half the C–Br bond lengths are shortened, the other half are elongated. Also here, the bond length shortening is not synonymous with a blue shift of the C–Br stretching mode. This is only the case for the CH₃F and C₂H₅F complexes, which show the largest contraction, by –0.0034 Å and –0.0032 Å, respectively. They are accompanied by a respective blue shift of +1.0 cm^{–1} and +0.7 cm^{–1}. The signs of the calculated shifts were confirmed by the experimental blue shift of +1.3 cm^{–1} and +1.5 cm^{–1}, respectively.

6 Conclusions and Future Perspectives

In this chapter, typical results for blue- and red-shifting C – X . . . Y halogen-bonded complexes obtained by dissolving selected proton donors and acceptors in liquid rare gases are summarized. The results show that by recording the IR and Raman spectra of cryogenic solutions, a broad range of experimental information is obtained, which cannot be obtained by using other spectroscopic techniques, and which can be used to evaluate and further develop methodologies to describe and to predict the structural, thermodynamic, and vibrational properties of weakly-bound molecular complexes.

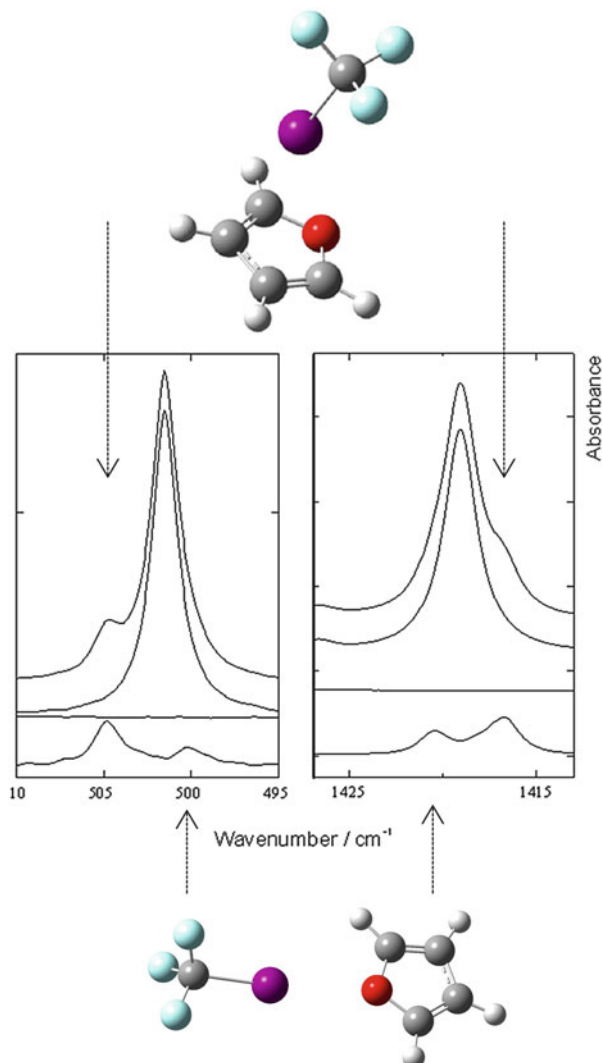
Although the amount of data available is often still limited, the experimental studies carried out so far involving cryosolutions have led to different conclusions. To shed further light on these trends, and to gain more information on the accuracy of the correlations suggested, expanding the experimental information available is of great interest. Typical Lewis bases which so far have not been investigated, but which are expected to deliver additional information, involve, amongst other compounds, trimethyl phosphine, methyl bromide, and methyl iodide. In addition, experimental information can be gained for other nitrogen-, oxygen-, or sulfur-containing Lewis bases such as pyridine, ammonia, acetone, and oxirane.

Future perspectives are concerned with expanding the series of halogen donors by including donors based on C_{sp2}-X bonds and by studying the simultaneous occurrence of and the competition between different interaction site in the donor or the acceptor molecule. In addition, by studying mixtures of hydrogen and halogen donors, and by studying the appropriate mixed proton/halogen donors, cryosolutions can be used to deliver unique experimental data on the mutual competition between hydrogen and halogen bonds.

6.1 Different Interaction Sites in the Donor Molecule

Preliminary results obtained during a recent study (Nagels and Herrebout, unpublished results) of the complexes of furane-d₄ with CF₃I are shown in Fig. 49. Close scrutiny of the data relating to subtraction procedures, in which spectra of the mixed solutions and of the respective monomers recorded at exactly the same temperature are subtracted, shows that various bands localized in either furane-d₄ or CF₃I give rise to two distinct complex bands which can be assigned to a C–I . . . O or C–I . . . π -bonded complex, respectively. The complexation enthalpies for the complexes are $-6.4(5)$ kJ mol⁻¹ for the C–I . . . O-bonded isomer and $-7.8(4)$ kJ mol⁻¹ for the C–I . . . π -bonded isomer.

Fig. 49 Infrared spectra obtained for mixed solutions in LKr containing furane-d₄ and CF₃I. In both panels, the *top trace* refers to the spectrum of the mixed solution, while the *middle spectra* refer to the rescaled spectra of monomer furane-d₄ and monomer CF₃I. The *lower traces* refer to the spectra of the complexes as obtained from the subtraction procedures. The bands assigned to the different complexes and proving the simultaneous appearance of C–I...O- and C–I... π -bonded complexes are denoted with *arrows*



6.2 Mixed Halogen/Hydrogen Donors: Simultaneous Occurrence of C–X...Y Halogen- and C–H...Y Hydrogen-Bonded Complexes

Typical examples of mixed proton/halogen donors for which competition involving C–Br...X and/or C–Cl...X halogen bonding interactions can be envisaged are halothane, CF₃CBrClH, bromodifluoromethane, CHF₂Br, and chlorodifluoromethane, CHF₂Cl. Unfortunately, experiments in which the IR or Raman spectra of mixed solutions containing these compounds and containing the appropriate

Lewis bases have been studied have so far only given evidence [64, 66–68, 112, 113, (Geboes et al., unpublished results)] for the occurrence of C–H...X hydrogen-bonded complexes. Another compound for which competition involving C–I...X halogen and C–H...X halogen bonding can be envisaged is iododifluoromethane, CHF₂I. A detailed spectroscopic study of mixed solutions containing CHF₂I and an appropriate set of Lewis bases has recently been initiated [153]. The results obtained for these systems will be presented in due course.

Acknowledgments It is a pleasure to acknowledge the contributions of my co-workers, whose names are evident from the references cited below. Without their excellent work, this review could not have been written. The research presented was carried out with financial support from the Fund for Scientific Research (FWO-Vlaanderen) and from the Flemish Community, through the Special Research Fund (BOF). The Hercules Foundation and the Flemish Supercomputing Centre (www.vscentrum.be) is acknowledged for generously providing the computing resources required.

References

1. Khriachtchev L (ed) (2011) *Physics and chemistry at low temperatures*. Pan Stanford Publishing, Singapore
2. Clark RJH, Hester RE, Bulanin MO (eds) (1995) *Molecular cryospectroscopy*. Wiley, Chichester
3. Bulanin MO (1995) Spectroscopy of molecules in liquid noble gases. *J Mol Struct* 347:73–82
4. Bulanin MO (2002) Liquefied gases as solvents for vibrational spectroscopy. In: Chalmers JM, Griffiths PR (eds) *Handbook of vibrational spectroscopy*, vol 2. Wiley, Chichester, pp 1329–1341
5. Bulanin MO, Velasco S, Hernandez AC (1996) Spectroscopic studies of diatomics in dense non-polar fluids: an overview. *J Mol Liquids* 70(2–3):107–123
6. Manzanares C, Minacamilde N, Brock A, Peng JP, Blunt VM (1995) Piezoelectric detection of vibrational overtones at cryogenic temperatures. *Rev Sci Instr* 66(3):2644–2651. doi:10.1063/1.1145603
7. McKelvy ML, Britt TR, Davis BL, Gillie JK, Lentz LA, Leugers A, Nyquist RA, Putzig CL (1996) Infrared spectroscopy. *Anal Chem* 68(12):R93–R160
8. Sennikov PG (1994) Weak H-bonding by 2nd-row (PH₃, H₂S) and 3rd-row (AsH₃, H₂Se) hydrides. *J Phys Chem* 98(19):4973–4981
9. Tokhadze KG, Tkhorzhetskaya NA (1992) Infrared-spectra of weak hydrogen-bonded complexes in cryogenic solutions. *J Mol Struct* 270:351–368
10. Turner JJ, Poliakov M, Howdle SM, Jackson SA, McLaughlin JG (1988) Infrared spectroscopy and chemistry in liquid rare-gas solvents. *Faraday Discuss Chem Soc* 86:271–284
11. Cheetham NF, McNaught IJ, Pullin ADE (1974) Donor-acceptor complexes formed by perfluoro-organo bromides and iodides with nitrogenous and other bases. 3. Qualitative examination of condensed phase spectra of CF₃I and CF₃Br and of their complexes with trimethylamine and other bases. *Austr J Chem* 27(5):973–985
12. Cheetham NF, McNaught IJ, Pullin ADE (1974) Donor-acceptor complexes formed by perfluoro-organo bromides and iodides with nitrogenous and other bases. 4. Analysis of infrared-spectra of CF₃I.N(CH₃)₃ and CF₃Br.N(CH₃)₃ and related complexes. *Austr J Chem* 27(5):987–1007
13. Cheetham NF, Pullin ADE (1967) A gas-phase donor-acceptor complex. *Chem Commun* 5:233–234

14. Cheetham NF, Pullin ADE (1971) Donor-acceptor complexes formed by perfluoro-organo bromides and iodides with nitrogenous and other bases. I. Vapor pressure measurements. *Austr J Chem* 24(3):479–487
15. McNaught IJ, Pullin ADE (1974) Donor-acceptor complexes formed by perfluoro-organo bromides and iodides with nitrogenous and other bases. 5. Comparison of liquid-phase complexes of CF_3I , $\text{C}_2\text{F}_5\text{I}$ or $\text{C}_3\text{F}_7\text{I}$ with NMe_3 , NEt_3 or NPr_3 - infrared, far-infrared and NMR-spectra. *Austr J Chem* 27(5):1009–1015
16. McNaught IJ, Robbins RJ (1985) Thermodynamic parameters of some aliphatic amine-pseudohalogen molecular-complexes. *South African J Chem* 38(3):124–128
17. Mishra B, Pullin ADE (1971) Donor-acceptor complexes formed by perfluoro-organo bromides and iodides with nitrogenous and other bases. 2. Band shapes and widths in the absorption spectrum of gaseous $\text{CF}_3\text{I}\cdot\text{N}(\text{CH}_3)_3$. *Austr J Chem* 24:2493–2507
18. Wang W, Hobza P (2008) Origin of the X-Hal (Hal=Cl, Br) bond-length change in the halogen-bonded complexes. *J Phys Chem A* 112(17):4114–4119
19. Wang W, Wang D, Zhang Y, Ji B, Tian A (2011) Hydrogen bond and halogen bond inside the carbon nanotube. *J Chem Phys* 134(5):054317/054311–054317/054317
20. Wang W, Zhang Y, Ji B (2010) On the difference of the properties between the blue-shifting halogen bond and the blue-shifting hydrogen bond. *J Phys Chem A* 114(26):7257–7260
21. Grabowski SJ (2013) Hydrogen and halogen bonds are ruled by the same mechanisms. *Phys Chem Chem Phys* 15(19):7249–7259
22. Legon AC (2009) Halogen bonds and hydrogen bonds in the gas phase: how similar are they? American Chemical Society, Washington (USA), pp ORGN-002
23. Legon AC (2010) The halogen bond: an interim perspective. *Phys Chem Chem Phys* 12(28):7736–7747
24. Lu Y, Li H, Zhu X, Liu H, Zhu W (2012) Effects of solvent on weak halogen bonds: density functional theory calculations. *Int J Quantum Chem* 112(5):1421–1430
25. Metrangolo P, Cavallo G, Resnati G, Terraneo (2013) From crystal engineering to function engineering with halogen bonding. American Chemical Society, Washington (USA), pp SERM-485
26. Priimagi A, Cavallo G, Metrangolo P, Resnati G (2013) The halogen bond in the design of functional supramolecular materials: recent advances. *Acc Chem Res* 46(11):2686–2695
27. Wolters LP, Bickelhaupt FM (2013) Halogen bonding vs. hydrogen bonding: a molecular orbital perspective. American Chemical Society, Washington (USA), pp COMP-124
28. Zeng Y, Zhang X, Li X, Zheng S, Meng L (2011) Ab initio and AIM studies on typical π -type and pseudo- π -type halogen bonds: comparison with hydrogen bonds. *Int J Quantum Chem* 111(14):3725–3740
29. Barnes AJ (2004) Blue-shifting hydrogen bonds - are they improper or proper? *J Mol Struct* 704(1–3):3–9
30. Hermansson K (2002) Blue-shifting hydrogen bonds. *J Phys Chem A* 106(18):4695–4702
31. Herrebout WA, Melikova SM, Delanoye SN, Rutkowski KS, Shchepkin DN, van der Veken BJ (2005) A cryosolution infrared study of the complexes of fluoroform with ammonia and pyridine: evidence for a C-H \cdots N pseudo blue-shifting hydrogen bond. *J Phys Chem A* 109(13):3038–3044
32. Hobza P (2002) Improper, blue-shifting hydrogen bond: theory and experiment. In: Strength from weakness: structural consequences of weak interactions in molecules, supermolecules, and crystals. NATO Science Series, II vol 68. Kluwer Academic Publishers, Dordrecht, The Netherlands, pp 281–291
33. Hobza P (2008) Noncovalent interactions with participation of hydrogen: hydrogen bond, blue-shifting hydrogen bond and dihydrogen bond. *Chem Listy* 102(10):884–888
34. Hobza P, Havlas Z (2000) Blue-shifting hydrogen bonds. *Chem Rev* 100(11):4253–4264
35. Hobza P, Havlas Z (2002) Improper, blue-shifting hydrogen bond. *Theor Chem Acc* 108(6):325–334

36. Oliveira BG, de Araujo RCMU, Ramos MN (2009) A theoretical study of blue-shifting hydrogen bonds in π weakly bound complexes. *J Mol Struct Theomchem* 908(1–3):79–83
37. Rutkowski KS, Melikova SM, Asfin RE, Czarnik-Matusewicz B, Rospenk M (2014) The gas phase FTIR studies of chloroform + B and halothane + B (B=TMA, FCD₃) mixtures. *J Mol Struct* 1072:32–37
38. Scheiner S, Kar T (2002) Red- versus blue-shifting hydrogen bonds: are there fundamental distinctions? *J Phys Chem A* 106(9):1784–1789
39. Bulanin MO, Zhigula LA, Kolomiitsova TD, Shchepkin DN (1984) Study of infrared-spectrum of CF₃I solutions in liquid argon. *Optika i Spektroskopiya* 56(4):663–669
40. Bürger H, Burczyk K, Grassow R, Ruoff A (1982) Vibrational spectra and force constants of symmetric tops: rotational analysis of the parallel bands ν_1 , ν_2 , $2\nu_1$, $2\nu_3$, $\nu_1 - \nu_3$, $\nu_1 + \nu_2$, $\nu_1 + \nu_3$, and $\nu_2 + \nu_3$ of CF₃³⁵Cl. *J Mol Spectrosc* 93(1):55–73
41. Bürger H, Burczyk K, Schulz P, Ruoff A (1982) Vibrational spectra and force constants of symmetric tops. XXIV. Vibrational and rotational analysis of parallel overtones and combination bands of CF₃Br. *Spectrochimica Acta Pt A Mol Spectrosc* 38(6):627–635
42. Anderson A, Ko YM, Smith W (1996) Infrared spectra of solid trifluoriodomethane. *Phys Status Solidi (b)* 194(2):775–782
43. Clark RJH, Ellestad OH (1975) Vapor-phase Raman-spectra, Raman band contour analyses, Coriolis coupling-constants, and e-species force constants for molecules HCF₃, ClCF₃, BrCF₃, and ICF₃. *Mol Phys* 30(6):1899–1911
44. Davidson G, Davies CL (1989) Raman-spectroscopy in liquid xenon solutions - trifluorohalomethanes. *Spectrochim Acta A Mol Biomol Spectrosc* 45(3):371–373
45. Passerini A, Baldacci A, Gambi A, Ghersetti S (1982) Vapor-phase infrared studies of bromotrifluoromethane in the range 4,000–1,800 cm⁻¹. *Gazz Chim Ital* 112(5/6):213–219
46. Scanlon K, Suzuki I, Overend J (1981) The anharmonic-force field of CClF₃ and the determination of the Coriolis coefficients and anharmonic coefficients from the infrared spectrum. *J Chem Phys* 74(7):3735–3744
47. Zhigula LA, Kolomiitsova TD, Shchepkin DN (1981) Ternary resonances in vibrational spectra of simple polyatomic molecules. *Optika I Spektroskopiya* 51(5):809–815
48. Hauchecorne D, Szostak R, Herrebout WA, van der Veken BJ (2009) C-X...O halogen bonding: interactions of trifluoromethyl halides with dimethyl ether. *Chemphyschem* 10(12):2105–2115
49. Evangelisti L, Feng G, Gou Q, Grabow JU, Caminati W (2014) Halogen bond and free internal rotation: the microwave spectrum of CF₃Cl-dimethyl ether. *J Phys Chem A* 118(3):579–582
50. Feng G, Evangelisti L, Gasparini N, Caminati W (2012) On the Cl...N halogen bond: a rotational study of CF₃Cl...NH₃. *Chem Eur J* 18(5):1364–1368
51. Gou Q, Feng G, Evangelisti L, Caminati W (2013) Lone-pair center dot center dot pi Interaction: a rotational study of the chlorotrifluoroethylene-water adduct. *Angew Chem Int Ed* 52(45):11888–11891
52. Stephens SL, Mizukami W, Tew DP, Walker NR, Legon AC (2012) The halogen bond between ethene and a simple perfluoroiodoalkane: C₂H₄...ICF₃ identified by broadband rotational spectroscopy. *J Mol Spectrosc* 280:47–53
53. Stephens SL, Walker NR, Legon AC (2011) Internal rotation and halogen bonds in CF₃I...NH₃ and CF₃I...N(CH₃)₃ probed by broadband rotational spectroscopy. *Phys Chem Chem Phys* 13(46):20736–20744
54. Stephens SL, Walker NR, Legon AC (2011) Molecular geometries of H₂S...ICF₃ and H₂O...ICF₃ characterized by broadband rotational spectroscopy. *Phys Chem Chem Phys* 13(47):21093–21101
55. Stephens SL, Walker NR, Legon AC (2011) Rotational spectra and properties of complexes B center dot center dot center dot ICF₃ (B=Kr or CO) and a comparison of the efficacy of ICl and ICF₃ as iodine donors in halogen bond formation. *J Chem Phys* 135(22):224309

56. Hawthorne B, Fan-Hagenstein H, Wood E, Smith J, Hanks T (2013) Study of the halogen bonding between pyridine and perfluoroalkyl iodide in solution phase using the combination of FTIR and 19 F NMR. *Int J Spectrosc* 2013:216510, Article ID 216518
57. Bertsev VV (1995) Experimental technique. In: Clark RJH, Hester RE, Bulanin MO (eds) *Molecular cryospectroscopy*, vol 23, *Advances in spectroscopy*. Wiley, Chichester, pp 1–19
58. Harris DC (1999) *Materials for infrared windows and domes: properties and performance*. SPIE - The International Society for Optical Engineering, Washington
59. Herrebout W, Van der Veken B, Kouzov AP, Bulanin MO (2004) Collision-induced absorption of hydrogen deuteride dissolved in liquid neon. *Phys Rev Lett* 92(2):023002
60. Herrebout WA, van der Veken BJ, Kouzov AP (2008) New line narrowing effects in the infrared collision-induced spectra of molecular hydrogens in liquid neon. *Phys Rev Lett* 101(9):093001
61. Herrebout WA, van der Veken BJ, Kouzov AP (2012) Concentration studies of collision-induced fundamental absorption of hydrogen dissolved in liquid neon. *J Chem Phys* 137(8):084509
62. Van den Kerkhof T, Bouwen A, Goovaerts E, Herrebout WA, van der Veken BJ (2004) Raman spectroscopy of cryosolutions: the van der Waals complex of dimethyl ether with fluoroform. *Phys Chem Chem Phys* 6(2):358–362
63. Dom JJJ, Michielsens B, Maes BUW, Herrebout WA, Van der Veken BJ (2009) The C-H... π interaction in the halothane/ethene complex: a cryosolution infrared and Raman study. *Chem Phys Lett* 469(1–3):85–89
64. Dom JJJ, van der Veken BJ, Michielsens B, Jacobs S, Xue ZF, Hesse S, Loritz HM, Suhm MA, Herrebout WA (2011) On the weakly C-H... π hydrogen bonded complexes of sevoflurane and benzene. *Phys Chem Chem Phys* 13(31):14142–14152
65. Herrebout WA, Nagels N, van der Veken BJ (2009) On the $\nu_1\text{CO}_2/\nu_2\text{CO}_2$ resonance dioxide with dimethyl ether. *Chemphyschem* 10(17):3054–3060
66. Michielsens B, Dom JJJ, van der Veken BJ, Hesse S, Suhm MA, Herrebout WA (2012) Solute-solvent interactions in cryosolutions: a study of halothane-ammonia complexes. *Phys Chem Chem Phys* 14(18):6469–6478
67. Michielsens B, Dom JJJ, van der Veken BJ, Hesse S, Xue ZF, Suhm MA, Herrebout WA (2010) The complexes of halothane with benzene: the temperature dependent direction of the complexation shift of the aliphatic C-H stretching. *Phys Chem Chem Phys* 12(42):14034–14044
68. Michielsens B, Verlact C, van der Veken BJ, Herrebout WA (2012) C-H...X (X=S, P) hydrogen bonding: The complexes of halothane with dimethyl sulfide and trimethylphosphine. *J Mol Struct* 1023:90–95
69. Arp Z, Herrebout WA, Laane J, van der Veken BJ (2000) Infrared and ab initio study of the relative stability and geometry of the 3-fluoropropene-hydrogen chloride van der Waals complexes. *J Phys Chem A* 104(22):5222–5229
70. Bulanin KM, Bulychev VP, Herrebout W, Schepkin DN (2014) IR spectroscopic study of the HCl...O₃ molecular complex in liquid argon. *Spectrochimica Acta Pt A Mol Biomol Spectrosc* 117:713–717
71. Everaert GP, Herrebout WA, van der Veken BJ (1999) Formation of van der Waals complexes between allene and HCl in cryosolutions. An IR and ab initio study. *Phys Chem Chem Phys* 1(2):231–238
72. Everaert GP, Herrebout WA, van der Veken BJ (2000) A cryospectroscopic and ab initio study of the cyclopropane. (HCl)_x van der Waals complexes. *J Mol Struct* 550:399–411
73. Everaert GP, Herrebout WA, van der Veken BJ (2001) Ab initio and cryospectroscopic investigation of the Van der Waals complexes of methylcyclopropane with hydrogen chloride and boron trifluoride. *J Phys Chem A* 105(39):9058–9067
74. Everaert GP, Herrebout WA, van der Veken BJ (2005) An ab initio and cryospectroscopic study of the hydrogen chloride and boron trifluoride complexes of cyclopropene. *Spectrochimica Acta Pt A Mol Biomol Spectrosc* 61(7):1375–1387

75. Herrebout WA, Everaert GP, vanderVeken BJ, Bulanin MO (1997) On the ethene/HCl Van der Waals complexes observed in liquefied argon and liquefied nitrogen. *J Chem Phys* 107 (21):8886–8898
76. Herrebout WA, Gatin A, Everaert GP, Fishman AI, van der Veken BJ (2005) A cryosolution infrared and ab initio study of the van der Waals complexes of cyclopentene with hydrogen chloride and boron trifluoride. *Spectrochimica Acta Pt A Mol Biomol Spectrosc* 61(7):1431–1444
77. Herrebout WA, van den Kerkhof T, van der Veken BJ (1999) Vibrational spectra and relative stability of the van der Waals complexes formed between 1,2-butadiene and HCl: a FTIR and density functional study. *J Mol Struct* 481:495–498
78. Herrebout WA, Van den Kerkhof T, van der Veken BJ (2000) Isomerism in van der Waals molecules: a cryospectroscopic study of the complexes of buta-1,2-diene with hydrogen chloride. *Phys Chem Chem Phys* 2(21):4925–4932
79. Herrebout WA, van der Veken BJ (1998) Vibrational spectra and relative stability of the van der Waals complexes formed between cis-2-butene, trans-2-butene, 2-methyl propene and HCl: a FTIR and density functional study. *J Mol Struct* 449(2–3):231–240
80. Herrebout WA, van der Veken BJ (2002) A cryosolution infrared and DFT study of the complexes formed between vinylacetylene and hydrogen chloride. *J Mol Struct* 642(1–3):1–13
81. Herrebout WA, Van der Veken BJ, Durig JR (1995) On the angular geometry of the CH₃Cl·HCl van der Waals complex in the gas phase and in liquefied noble gas solutions. *Theochem* 332(3):231–240
82. Herrebout WA, Van der Veken BJ (1994) Equilibrium geometry and vibrational frequencies of the 1:2 van der Waals complexes between methyl chloride and hydrogen chloride. *J Chem Soc Faraday Trans* 90(24):3601–3607
83. Herrebout WA, Van der Veken BJ (1994) Infrared-spectra and relative stability of hydrogen-chloride van der Waals complexes with various alkyl chlorides in liquefied noble gases. *J Phys Chem* 98(11):2836–2843
84. Herrebout WA, Van der Veken BJ (1995) Vibrational frequencies, relative stability and angular geometry of some vinyl halide/HCl van der Waals complexes observed in liquefied argon. *J Mol Struct* 348:481–484
85. Herrebout WA, Van der Veken BJ (1996) Vibrational analysis of the van der Waals complexes between vinyl fluoride and hydrogen chloride in liquefied argon. *J Phys Chem* 100(39):15695–15703
86. Herrebout WA, Van der Veken BJ (1997) IR spectra, relative stability and angular geometry of vinyl chloride-HCl, vinyl bromide-HCl and allyl chloride-HCl van der Waals complexes observed in liquefied argon. *J Chem Soc Faraday Trans* 93(19):3453–3461
87. Herrebout WA, Van der Veken BJ, Durig JR (1995) On the angular geometry of the CH₃Cl·HCl van der Waals complex in the gas-phase and in liquefied noble gas solutions. *Theochem J Mol Struct* 332(3):231–240
88. Sluys EJ, Herrebout WA, Van der Veken BJ (1994) On the behavior of CO, CO₂ and their complexes with HCl in liquefied argon. *J Mol Struct* 317(1–2):49–57
89. Szostak R, Herrebout WA, Van der Veken BJ (2000) On the HCl and DCl complexes of methylenecyclopropane in liquid argon. *Phys Chem Chem Phys* 2(18):3983–3991
90. Van der Veken BJ, Everaert GP, Herrebout WA (2005) An ab initio and cryospectroscopic study of the hydrogen chloride and boron trifluoride complexes of cyclopropene. *Spectrochimica Acta Pt A Mol Biomol Spectrosc* 61(7):1375–1387
91. van der Veken BJ, Sluys EJ, Herrebout WA (1998) The van der Waals molecules of carbonyl sulfide with hydrogen chloride and boron trifluoride: an infrared study in cryosolution. *J Mol Struct* 449(2–3):219–229
92. Melikova SM, Rutkowski KS, Lipkowski P, Shchepkin DN, Koll A (2007) FTIR studies of HCl dissolved in liquid CO: an harmonic effects in the weak OC...HCl complex. *J Mol Struct* 844:64–69

93. Rutkowski KS, Melikova S, Shchepkin DN, Lipkowski P, Koll A (2000) Higher-order transitions in the IR spectrum of the weak OC...HCl complex dissolved in liquid CO. *Chem Phys Lett* 325(4):425–432
94. Rutkowski KS, Melikova SM (1998) Infrared studies of weak B...HCl (B=HCl, CO, Xe N₂) complex formation in solid Kr solutions. *J Mol Struct* 448(2–3):231–237
95. Rutkowski KS, Melikova SM (1999) Vibrational spectra of OC...HCl complex in Kr solutions at liquid to solid phase transition. *J Mol Struct* 511/512:233–240
96. Bulychev VP, Mielke Z, Tokhadze KG, Utkina SS (1999) Evolution of the nHF vibrational-rotational absorption bands in the OC...HF and CO...HF complexes with increasing density. *Optics Spectrosc* 86(3):352–360
97. Rutkowski KS, Melikova SM, Koll A (1996) Features of IR bands of the CD₃F...HCl complex in liquid and solid noble gas solutions. *Electron J Theor Chem* 1:103–115
98. Everaert GP, Herrebout WA, van der Veken BJ, Lundell J, Rasanen M (1998) Vibrational analysis of the van der Waals complex between cyclopropane and boron trifluoride in liquefied inert gases. *Chem Eur J* 4(2):321–327
99. Herrebout WA, Lundell J, Van der Veken BJ (1999) Carbon-carbon triple bonds as nucleophiles: adducts of ethyne and propyne with boron trifluoride. *J Phys Chem A* 103(38):7639–7645
100. Herrebout WA, Lundell J, Van der Veken BJ (1999) Van der Waals complexes between unsaturated hydrocarbons and boron trifluoride: an infrared and ab initio study of ethyne, BF₃, propyne, BF₃ and propyne.(BF₃)₂. *J Mol Struct* 481:489–493
101. Herrebout WA, Stolov AA, Van der Veken BJ (2001) Characterization of the CH₃F.BF₃ van der Waals complex in the vapor phase. *J Mol Struct* 563:221–226
102. Herrebout WA, Szostak R, Van der Veken BJ (2000) Methylenecyclopropane-boron trifluoride van der Waals complexes; an infrared and DFT study. *J Phys Chem A* 104(37):8480–8488
103. Herrebout WA, Van der Veken BJ (1998) Behavior of boron trifluoride in cryosolutions: a combined ab initio, Monte Carlo, and FTIR investigation. *J Am Chem Soc* 120(38):9921–9929
104. Herrebout WA, Van der Veken BJ (1999) Infrared and ab initio study of the van der Waals complex formed between allene and BF₃. *Phys Chem Chem Phys* 1(15):3445–3452. doi:[10.1039/a903462e](https://doi.org/10.1039/a903462e)
105. Herrebout WA, Van der Veken BJ (2000) Vibrational spectra and relative stabilities of the van der Waals complexes of boron trifluoride with cis-2-butene, trans-2-butene and 2-methyl propene. *J Mol Struct* 550:389–398
106. Van der Veken BJ, Sluyts EJ (1995) A FTIR study of the van der Waals complexes between boron trifluoride and carbon monoxide in liquefied argon. *J Mol Struct* 349:461–464
107. Van der Veken BJ, Sluyts EJ (1997) The van der Waals complex between boron trifluoride and methyl fluoride: an infrared and ab initio study. *J Phys Chem A* 101(48):9070–9076
108. Stolov AA, Herrebout WA, Van der Veken BJ (1998) Van der Waals complexes between carbonyl fluoride and boron trifluoride observed in liquefied argon, krypton, and nitrogen: a FTIR and ab initio study. *J Am Chem Soc* 120(29):7310–7319
109. Sluyts EJ, Van der Veken BJ (1996) Van der Waals complexes between boron trifluoride and carbon monoxide in liquefied argon: an infrared study. *J Am Chem Soc* 118(2):440–445
110. Van der Veken BJ, Sluyts EJ (1997) Reversed Lewis acidity of mixed boron halides: an infrared study of the van der Waals complexes of BF_xCl_y with CH₃F in cryosolution. *J Am Chem Soc* 119(47):11516–11522
111. Van Ginderen P, Herrebout WA, Van der Veken BJ (2003) Van der Waals complex of dimethyl ether with carbon dioxide. *J Phys Chem A* 107(28):5391–5396
112. Michielsen B, Herrebout WA, Van der Veken BJ (2007) Intermolecular interactions between halothane and dimethyl ether: a cryosolution infrared and ab initio study. *Chemphyschem* 8(8):1188–1198

113. Michielsen B, Herrebout WA, Van der Veken BJ (2008) C-H bonds with a positive dipole gradient can form blue-shifting hydrogen bonds: the complex of halothane with methyl fluoride. *Chemphyschem* 9(12):1693–1701
114. van der Veken BJ, Delanoye SN, Michielsen B, Herrebout WA (2010) A cryospectroscopic study of the blue-shifting C-H...O bonded complexes of pentafluoroethane with dimethyl ether-d₆, acetone-d₆ and oxirane-d₄. *J Mol Struct* 976(1–3):97–104
115. Melikova SM, Rutkowski KS, Rodziewicz P, Koll A (2002) FT-IR studies of CH...B interactions in fluoroform containing cryosolutions. *Polish J Chem* 76(9):1271–1285
116. Melikova SM, Rutkowski KS, Rodziewicz P, Koll A (2002) Unusual spectroscopic properties of CF₃H dissolved in liquefied Ar, N₂, CO, and CO₂. *Chem Phys Lett* 352(3–4):301–310
117. Melikova SM, Rutkowski KS, Rodziewicz P, Koll A (2003) CH...B interactions in acetylene containing solutions: experimental and theoretical DFT studies. *J Mol Struct* 645(2–3):295–302
118. Melikova SM, Rutkowski KS, Rodziewicz P, Koll A (2004) Comparative studies of blue shifting and red shifting effects in fluoroform and acetylene cryogenic solutions. *J Mol Struct* 705(1–3):49–61
119. Rutkowski KS, Karpfen A, Melikova SM, Herrebout WA, Koll A, Wolschann P, Van der Veken BJ (2009) Cryospectroscopic and ab initio studies of haloform-trimethylamine H-bonded complexes. *Phys Chem Chem Phys* 11(10):1551–1563
120. Rutkowski KS, Melikova SM, Janski J, Koll A (2010) Cryospectroscopic and ab initio anharmonic studies of acetylene-trimethylamine H-bonded complex. *Chem Phys* 375(1):92–100
121. Rutkowski KS, Melikova SM, Rospenk M, Koll A (2011) Strong and weak effects caused by non covalent interactions between chloroform and selected electron donor molecules. *Phys Chem Chem Phys* 13(31):14223–14234
122. Rutkowski KS, Melikova SM, Smimov DA, Rodziewicz P, Koll A (2002) Infrared studies of acetylene dissolved in liquefied Ar, Kr, N₂, CO, and CO₂. *J Mol Struct* 614(1–3):305–313
123. Delanoye SN, Herrebout WA, Van der Veken BJ (2002) Blue shifting hydrogen bonding in the complexes of chlorofluoro haloforms with acetone-d₆ and oxirane-d₄. *J Am Chem Soc* 124(40):11854–11855
124. Delanoye SN, Herrebout WA, Van der Veken BJ (2002) Improper or classical hydrogen bonding? A comparative cryosolutions infrared study of the complexes of HCClF₂, HCCl₂F, and HCCl₃ with dimethyl ether. *J Am Chem Soc* 124(25):7490–7498
125. Delanoye SN, Herrebout WA, Van der Veken BJ (2005) Stabilities of the C–H...O bonded complexes of the haloforms HCCl_nF_{3–n} (n = 0–3) with dimethyl ether, oxirane, and acetone: an experimental and theoretical study. *J Phys Chem A* 109(43):9836–9843
126. Herrebout WA, Delanoye SN, Maes BUW, Van der Veken BJ (2006) Infrared spectra of the complexes of trifluoroethene with dimethyl ether, acetone, and oxirane: a cryosolution study. *J Phys Chem A* 110(51):13759–13768
127. Herrebout WA, Delanoye SN, Van der Veken BJ (2004) On the formation of a van der Waals complex between ethene and carbon dioxide in liquid argon. An FTIR and ab initio study. *J Mol Struct* 706(1–3):107–113
128. Herrebout WA, Delanoye SN, Van der Veken BJ (2004) Blue-shifting or red-shifting hydrogen bonding? Predictions for haloform complexes with dimethyl ether on the basis of perturbation theory. *J Phys Chem A* 108(28):6059–6064
129. Rutkowski KS, Herrebout WA, Melikova SM, Rodziewicz P, Van der Veken BJ, Koll A (2005) Infrared spectra and relative stability of the F₃CH/NH₃ H-bonded complex in liquefied Xe. *Spectrochimica Acta Pt A Mol Biomol Spectrosc* 61(7):1595–1602
130. Rutkowski KS, Herrebout WA, Melikova SM, Van der Veken BJ, Koll A (2008) A cryosolution FTIR and ab initio study of the blue shifting C–H...F hydrogen bonded complexes F₂ClCH.FCD₃ and Cl₂FCH.FCD₃. *Chem Phys* 354(1–3):71–79
131. Rutkowski KS, Melikova SM, Rodziewicz P, Herrebout WA, Van der Veken BJ, Koll A (2008) Solvent effect on the blue shifted weakly H-bound F₃CH...FCD₃ complex. *J Mol Struct* 880(1–3):64–68

132. Rutkowski KS, Rodziejewicz P, Melikova SM, Herrebout WA, Van der Veken BJ, Koll A (2005) Blue shifted $F_3CH \cdots FCD_3$ and $Cl_3CH \cdots FCD_3$ weakly H-bound complexes. Cryospectroscopy and ab initio study. *Chem Phys* 313(1–3):225–243
133. Bertsev VV, Golubev NS, Shchepkin DN (1976) Cryospectroscopic study of fluoroform-trimethylamine-argon (krypton) liquid systems. *Optika i Spektroskopiya* 40(5):951–952
134. Van der Veken BJ (1996) Measurement of enthalpy differences in cryosolutions: influence of thermal expansion. *J Phys Chem* 100(44):17436–17438
135. Hauchecorne D, Van der Veken BJ, Moiana A, Herrebout WA (2010) The C–Cl...N halogen bond, the weaker relative of the C–I and C–Br...N halogen bonds, finally characterized in solution. *Chem Phys* 374(1–3):30–36
136. Vanspeybrouck W, Herrebout WA, Van der Veken BJ, Lundell J, Perutz RN (2003) Direct measurement of the stability of the supramolecular synthon $C_6H_6 \cdots C_6F_6$. *J Phys Chem B* 107(50):13855–13861
137. Hauchecorne D, Moiana A, Van der Veken BJ, Herrebout WA (2011) Halogen bonding to a divalent sulfur atom: an experimental study of the interactions of CF_3X (X=Cl, Br, I) with dimethyl sulfide. *Phys Chem Chem Phys* 13(21):10204–10213
138. Auffinger P, Hays FA, Westhof E, Ho PS (2004) Halogen bonds in biological molecules. *Proc Natl Acad Sci USA* 101(48):16789–16794
139. Bayse CA, Rafferty ER (2010) Is halogen bonding the basis for iodothyronine deiodinase activity? *Inorg Chem* 49(12):5365–5367
140. Lu YX, Wang Y, Zhu WL (2010) Nonbonding interactions of organic halogens in biological systems: implications for drug discovery and biomolecular design. *Phys Chem Chem Phys* 12(18):4543–4551
141. Van der Veken BJ, Herrebout WA, Szostak R, Shchepkin DN, Havlas Z, Hobza P (2001) The nature of improper, blue-shifting hydrogen bonding verified experimentally. *J Am Chem Soc* 123(49):12290–12293
142. Hauchecorne D, Herrebout WA (2013) Experimental characterization of C–X...Y–C (X=Br, I; Y=F, Cl) halogen-halogen bonds. *J Phys Chem A* 117(45):11548–11557
143. Herrebout WA, Lundell J, Van der Veken BJ (1998) A cryospectroscopic study of the van der Waals complexes between vinyl fluoride and boron trifluoride: evidence for the existence of sigma and pi complexes. *J Phys Chem A* 102(49):10173–10181
144. Hauchecorne D, Nagels N, Van der Veken BJ, Herrebout WA (2012) C–X... π halogen and C–H... π hydrogen bonding: interactions of CF_3X (X=Cl, Br, I or H) with ethene and propene. *Phys Chem Chem Phys* 14(2):681–690
145. Nagels N, Hauchecorne D, Herrebout WA (2013) Exploring the C–X... π halogen bonding motif: an infrared and Raman study of the complexes of CF_3X (X=Cl, Br and I) with the aromatic model compounds benzene and toluene. *Molecules* 18(6):6829–6851
146. Wilcken R, Zimmermann MO, Lange A, Joerger AC, Boeckler FM (2013) Principles and applications of halogen bonding in medicinal chemistry and chemical biology. *J Med Chem* 56(4):1363–1388
147. Bhattacharyya S, Bhattacharjee A, Shirhatti PR, Wategaonkar S (2013) O–H...S hydrogen bonds conform to the acid-base formalism. *J Phys Chem A* 117(34):8238–8250
148. Delgado MR, Bulanek R, Chlubna P, Areato CO (2014) Bronsted acidity of H-MCM-22 as probed by variable-temperature infrared spectroscopy of adsorbed CO and N_2 . *Catal Today* 227:45–49
149. Rivera-Rivera LA, McElmurry BA, Scott KW, Lucchese RR, Bevan JW (2013) The Badger-Bauer rule revisited: correlation of proper blue frequency shifts in the OC hydrogen acceptor with morphed hydrogen bond dissociation energies in OC–HX (X=F, Cl, Br, I, CN, CCH). *J Phys Chem A* 117(35):8477–8483
150. Zhang Y, Ma N, Wang W-Z (2012) Correlation between bond-length change and vibrational frequency shift in hydrogen-bonded complexes revisited. *Wuli Huaxue Xuebao* 28(3):499–503

151. Wang W, Zhang Y, Ji B, Tian A (2011) On the correlation between bond-length change and vibrational frequency shift in halogen-bonded complexes. *J Chem Phys* 134(22):224303/224301–224303/224305
152. Nagels N, Herrebout WA (2015) A cryospectroscopic infrared and Raman study of the C–X... π halogen bonding motif: complexes of the CF₃Cl, CF₃Br, and CF₃I with ethyne, propyne and 2-butyne. *Spectrochim Acta A Mol Biomol Spectrosc* 136:16–26
153. Nagels N, Geboes Y, Pinter B, De Proft F, Herrebout WA (2014) Tuning the halogen/hydrogen bond competition: a spectroscopic and conceptual DFT study of some model complexes involving CHF₂I. *Chem Eur J* 20(27):8433–8443

Halogen Bonding in Supramolecular Synthesis

Christer B. Aakerøy and Christine L. Spartz

Abstract Supramolecular synthesis is typically limited to one-pot reactions because of the reversibility of non-covalent bonds, and to overcome this restriction we need to be able to rank the relative structural importance of such interactions and build synthetic methods to utilize synthons which can operate side-by-side without interference. Halogen bonds have characteristics (strength and directionality) which potentially make them prime candidates as critical components of effective, transferable, and versatile supramolecular synthetic strategies. In this chapter, several halogen-bond driven crystal engineering strategies for the assembly of specific architectures in molecular solids are described in detail, and the utility of halogen bonds for the synthesis of co-crystals are addressed. Finally, the structural compatibility or competition between of halogen- and hydrogen bonds in the context of supramolecular synthesis are examined.

Keywords Cocrystal · Hydrogen bond · Supramolecular architecture · Supramolecular synthesis · Synthon

Contents

1	Introduction	156
2	1-D Architectures Constructed via Halogen Bonds	158
3	Supramolecular Architectures Constructed via Multiple Halogen Bonds	165
4	Combination and Competition; Halogen Bonds vs the Rest	174
	References	180

1 Introduction

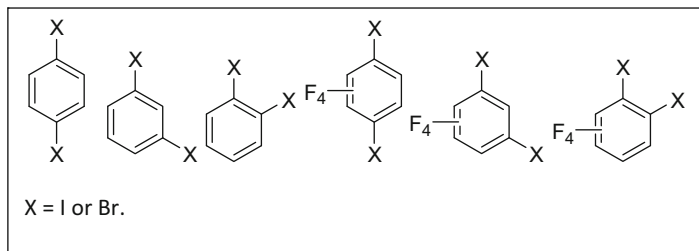
Crystal engineering is a branch of supramolecular chemistry which receives extensive attention from a broad spectrum of chemists and materials scientists. Crystal engineering is, broadly speaking, driven by “the nature and structural consequences of intermolecular forces, and the way in which such interactions are utilized for controlling the assembly of molecular building blocks into infinite architectures” [1]. However, instead of using covalent bonds to reach synthetic chemical targets, crystal engineers employ reversible non-covalent interactions, such as hydrogen bonds and $\pi \cdots \pi$ interactions, to name a few. The potential practical applications of this field span areas from biology and chemistry to materials science and nanotechnology, and crystal engineering has brought about specific and transferable insight into drug design, coordination chemistry, catalysis, fuel cells, molecular sensing, polymorphism, etc. [2]. In this chapter, we focus on some of the recent contributions which halogen bonding has made to crystal engineering and supramolecular synthesis.

One of the key goals of supramolecular chemistry is to develop methodologies and strategies which allow for the synthesis of a specific structural target which may be defined by, e.g., its topology, dimensionality, stoichiometry, chemical composition, or primary intermolecular events. In contrast to conventional covalent synthesis, which is supported by a large number of named reactions which can be relied upon to achieve a specific chemical transformation, supramolecular synthesis is still in the early stages of development. In particular, crystal engineers are seeking to identify and develop rules and guidelines relating to the structural landscape surrounding specific molecules and their functional groups. In this context, hydrogen bonding is a well-documented and thoroughly explored intermolecular force, and many reliable synthons have been discovered for use in supramolecular synthesis [3–6]. On the other hand, halogen bonding, despite being highly directional and of similar strength, has not been explored to the same extent (it has yet to make its appearance in text books on introductory chemistry!), and the supramolecular community is still seeking to develop versatile and robust synthetic strategies which take full advantage of the unique characteristics of halogen bonds.

A suitable starting point for developing crystal engineering strategies can be found by examining some of the existing structural data from the Cambridge Structural Database (CSD) (CSD ConQuest Version 1.15). A search focused on di-substituted aromatic molecules which can potentially act as halogen-bond donors (Scheme 1) produced results consistent with the relative strengths of the donor atoms.

The donor molecules were grouped into four different types (Table 1), and a search was carried out for structures containing a halogen \cdots acceptor distance less than the combined van der Waals radii. Acceptor atoms under consideration were O, N, S, Cl, Br, and I. The number of hits for each group is shown in Table 1.

Examining this narrowly defined data set of existing crystal structures for a series of halogen-bond donors, it is obvious that the field is dominated by

**Scheme 1** Family of potential halogen-bond donors**Table 1** Distribution of hits of structures containing short X...acceptor contacts in the CSD

DONOR	Number of hits	DONOR	Number of hits
1,4-Diiodobenzene	7	Tetrafluoro analogues	104
1,3-Diiodobenzene			
1,2-Diiodobenzene			
1,4-Dibromobenzene	0	Tetrafluoro analogues	16
1,3-Dibromobenzene			
1,2-Dibromobenzene			

iodo-based donors “activated” by electron-withdrawing groups which enhance the positive electrostatic potential at the end of the iodine atom. There are many more hits with iodo-based donors than with the corresponding bromo-substituted species, which reflects the relative strengths of these interactions as determined using both theory and experiment.

Although a relatively small number of structures have been reported (compared to those of hydrogen bond-based architectures), where halogen bonds have been used as the primary tool for directional assembly of molecular species within a crystalline material, the existing information may allow us to identify patterns of behavior which can be used in practical crystal engineering strategies. In this chapter we examine some of the most recent work in halogen-bond-based supramolecular synthesis from the perspective of dimensionality. First, one-dimensional assembly inevitably brings the focus onto the halogen bond itself and the way in which it creates a molecular recognition event leading to the organization of homomeric or heteromeric chain-like architectures. Next, we examine some representative studies which attempt to combine multiple recognition events for the targeted assembly of higher dimensionalities. Finally, we discuss a few examples of supramolecular synthesis which utilize a combination of halogen bonds and hydrogen bonds.

2 1-D Architectures Constructed via Halogen Bonds

The basic approach to making heteromeric 1-D architectures using halogen bonding tends to involve a ditopic halogen-bond donor, most commonly 1,4-diiodotetrafluorobenzene, and a ditopic halogen-bond acceptor with two separate acceptor sites, or an acceptor molecule which uses two electron-pairs located on the same atom. Two examples of the former are shown in Fig. 1.

In both cases, the activated diiodo species acts as a powerful XB donor, and a ditopic acceptor provides the complementary link, resulting in a 1-D chain. In the structure of 1,4-bis(3-quinoly)-1,3-butadiyne 1,4-diiodotetrafluorobenzene [7], infinite chains are propagated through $I \cdots N(\text{aryl})$ interactions, whereas in the crystal structure of 2,3,5,6-tetramethyl-1,4-benzodicyanide 1,4-diiodotetrafluorobenzene [8], the chains are held together via $I \cdots N \equiv C$ halogen bonds. These types of motifs are arguably the most common constructions found in halogen-bonded co-crystals, and the two building blocks are encoded with precise structural information specifically intended to accomplish the assembly of a 1-D chain. The exact nature of the chain itself is controlled by the relative position of the two donor/acceptor sites with respect to each other. Similar assemblies have been made using different isomers of the donor, e.g., 4,4'-bipyridine 1,3-diiodotetrafluorobenzene [9] and 4,4'-bipyridine 1,2-diiodotetrafluorobenzene [10] as well as bromo-based analogues [11, 12]. A substantial number of 1-D halogen bonded chains have also been synthesized using perfluorinated iodoalkanes as halogen bond (XB) donors (Fig 2).

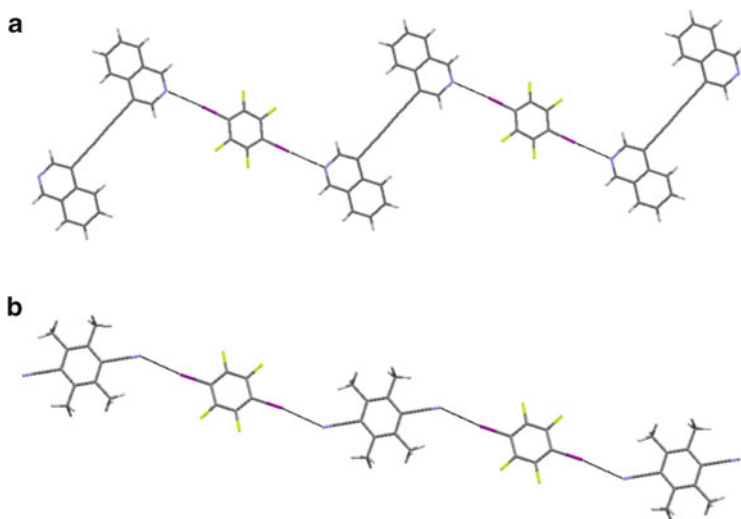


Fig. 1 (a) 1-D halogen-bonded chain in the crystal structure of 1,4-bis(3-quinoly)-1,3-butadiyne 1,4-diiodotetrafluorobenzene [7]. (b) 1-D halogen-bonded chain in the crystal structure of 2,3,5,6-tetramethyl-1,4-benzodicyanide 1,4-diiodotetrafluorobenzene [8]

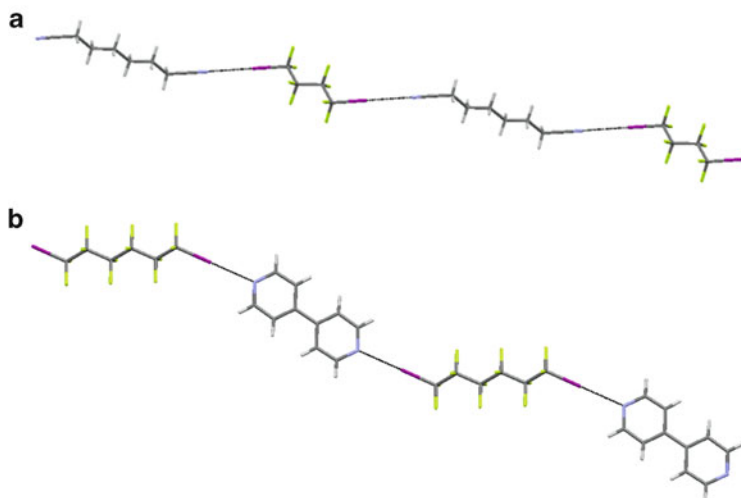


Fig. 2 (a) 1-D chain in the crystal structure of 1,6-dicyano-1,1,2,2,3,3,4,4-octafluorobutane [13]. (b) 1-D chain in the crystal structure of 4,4'-bipyridyl 1,6-diiodoperfluorohexane [14]

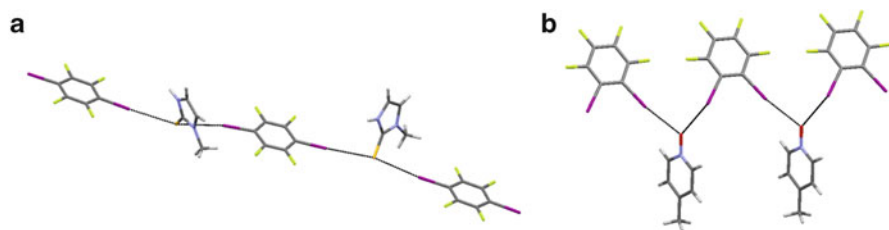
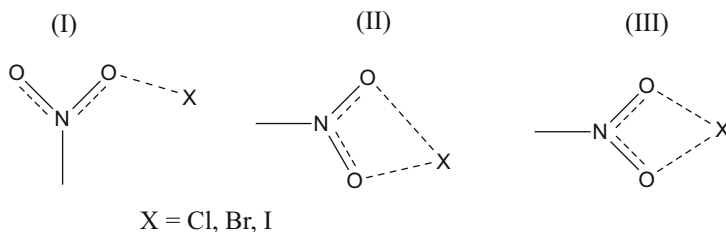


Fig. 3 1-D chains in the crystal structures of (a) 2-mercapto-1-methyl-imidazole 1,4-diiodotetrafluorobenzene [16] and 4-methylpyridine *N*-oxide 1,2-diiodotetrafluorobenzene [17]

To build heteromeric 1-D chains, it is also possible to use a single atom with two available lone-pairs as a connector between ditopic halogen-bond donors, as long as both sites become involved in halogen bonds. Although less common, the CSD does contain examples [15] of such an approach for constructing 1-D architectures (Fig. 3).

Both sulfur atoms [16] and oxygen atoms [17] with multiple accessible lone pairs can form bifurcated halogen bonds capable of promoting the formation of 1-D chains with an appropriate, ditopic, XB donor.

It is known that polarizable halogen atoms present only a relatively small region of positive electrostatic potential, the σ -hole, to its surroundings, and so are normally expected to form only one bond with a suitable electron-pair donor [18–21]. However, in some cases the σ -hole can simultaneously form two short contacts to appropriate XB acceptors, and this has been explored to develop assembly strategies for crystal engineering. Ji et al. [22] examined the frequency of occurrence of three different intermolecular motifs (Scheme 2) involving nitro groups and potential halogen-bond donors in the CSD.



Scheme 2 Three plausible $\text{NO}_2 \cdots \text{X}$ synthons

Table 2 Occurrence of single-point, asymmetric, and symmetric halogen bonds involving nitro groups

Synthon	$\text{NO}_2 \cdots \text{Cl}$	$\text{NO}_2 \cdots \text{Br}$	$\text{NO}_2 \cdots \text{I}$
I	437	180	79
II	9	13	16
III	0	2	4

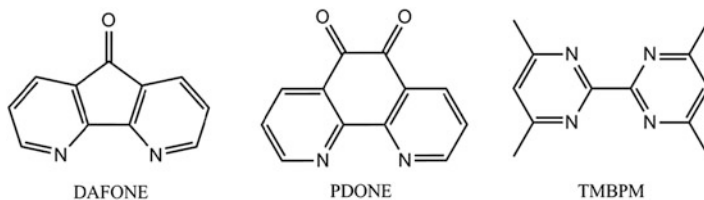
Synthon I, the single-point halogen bond, was found in 696 crystal structures, synthon II, the asymmetric bifurcated halogen bond, was found in 38 crystal structures, and synthon III, the symmetric bifurcated halogen bond, only appeared in six crystal structures (Table 2).

These observations, which indicate that linear, single-point halogen bonds are preferred, are consistent with theoretical results regarding halogen-bond geometries. A more linear assembly available in a single-point contact maximizes the XB strength; bifurcation at the point of the donor site does not allow for linearity. In response to these findings, the authors designed and examined a new set of acceptor molecules where two negative points on the molecular potential surface were locked in place in such a way as to favor the formation of a symmetric bifurcated halogen bond over a single-point halogen bond. The hypothesis was tested through co-crystallizations of symmetric halogen-bond donors 1,4-dichlorotetrafluorobenzene (DCTFB), 1,4-dibromotetrafluorobenzene (DBTFB), and 1,4-diiodotetrafluorobenzene (DITFB) with potentially symmetric halogen-bond acceptors 4,5-diazafluoren-9-one (DAFONE), 1,10-phenanthroline-5,6-dione (PDONE), and 4,4',6,6'-tetramethyl-2,2'-bipyrimidine (TMBPM) (Scheme 3).

As expected, only the iodo-based donor was capable of forming halogen bonds of sufficient strength to enable the synthesis of heteromeric co-crystals. In two of the three cases, PDONE and TMBPM, the desired bifurcated interactions were present which, in turn, produced the targeted 1-D assemblies (Fig. 4) [22].

The acceptor DAFONE also yielded 1-D chains, but through linear single-point interactions, which may have been because the two nitrogen atom-based lone pairs were too far apart to shift the balance in favor of a symmetric bifurcated interaction.

Linear heteromeric chains are probably the most commonly reported halogen-bonded architectures, further exemplified by work by Schöllhorn and co-workers who combined 1,4-diiodotetrafluorobenzene with four different nitrogen containing ditopic acceptors; two of the resulting structures are shown in Fig. 5 [23].



Scheme 3 XB acceptors utilized in the pursuit of symmetric bifurcated halogen bonds [22]

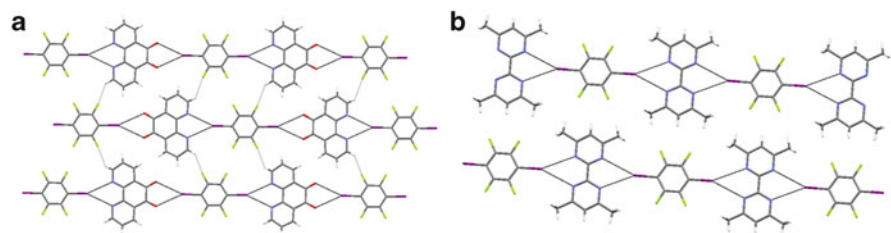


Fig. 4 (a) Bifurcated halogen bonds in the crystal structure of 1,10-phenanthroline-5,6-dione 1,4-diiodotetrafluorobenzene [22]. (b) Bifurcated halogen bonds in the crystal structure of 1,10-phenanthroline-2,9-dione 1,4-diiodotetrafluorobenzene 4,4',6,6'-tetramethyl-2,2'-bipyrimidine [22]

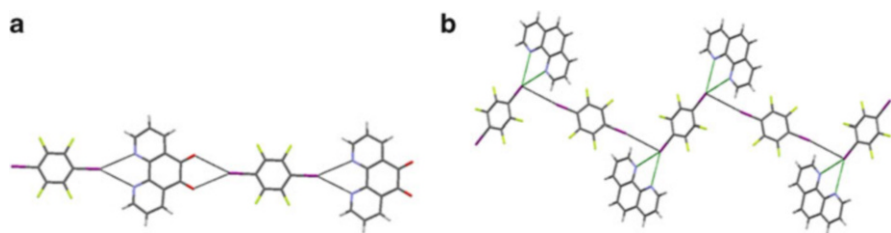


Fig. 5 (a) Bifurcated halogen bonds in 1,10-phenanthroline-5,6-dione 1,4-diiodotetrafluorobenzene [23]. (b) Bifurcated halogen bonds in 1,10-phenanthroline-2,9-dione 1,4-diiodotetrafluorobenzene [23]

The crystal structure of the co-crystal of 1,10-phenanthroline 1,4-diiodotetrafluorobenzene is particularly intriguing as it combines two different types of halogen bonds; conventional $I \cdots N$ interactions and $I \cdots I$ halogen bonds. The $C-I \cdots I$ angles are ca. 95° , which indicates that the positive potential of the iodine atom along the $C-I$ axis is interacting with the surplus electron density of the p-orbitals perpendicular to the $C-I$ axis. Schöllhorn's group also connected ferrocene-based metallacyclic building blocks into 1-D chains using $N \cdots I$ interactions (Fig. 6) [24].

The ability to target successfully the halogen-bond driven assembly of 1-D heteromeric motifs has been demonstrated on numerous occasions, and it is certainly possible to limit synthon crossover [25] (which can result in an unpredictable/unwanted architecture) by selecting building blocks capable of forming a small

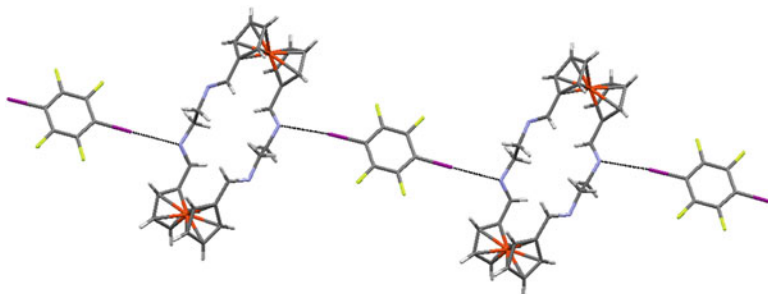


Fig. 6 1-D chain in the co-crystal of 3,6,10,13-tetra-aza-1,8(1,1')-diferrocenacyclotetradecaphane-2,6,9,13-tetraene 1,4-diodotetrafluorobenzene [24]

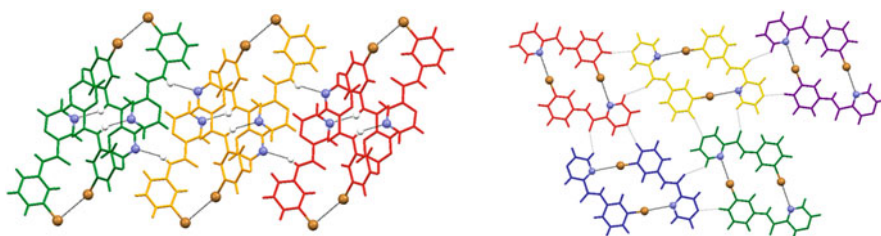


Fig. 7 Main motifs in the crystal structures of two polymorphs of *N*-(3-bromophenyl)-2-pyrazine-carboxamide [26]

number of primary structure-directing synthons. However, if the XB donor is given a choice of comparable acceptors, predictability and reliability of the synthetic process can diminish rapidly.

An interesting example of synthon crossover was found by Khavasi and Tehrani [26] in two polymorphs of *N*-(3-bromophenyl)-2-pyrazinecarboxamide. The bromo substituent has a choice of multiple possible XB acceptor sites (N, O, and Br) and in polymorph I a tetrameric assembly is created through a combination of N–H \cdots N hydrogen bonds and Br \cdots Br halogen bond. In polymorph II, adjacent molecules are brought together into dimers through two Br \cdots N(aryl) halogen bonds (Fig. 7).

In addition to the different structural features appearing in the two polymorphs, this system also represents an example of conformational polymorphism [27].

For a specific supramolecular synthetic strategy to be considered worthwhile and of real practical use, akin to a named reaction in organic synthesis, the recognition events which collectively generate the bonds required to assemble a target need to be relatively insensitive to the shape and size of the molecule to which they belong. Ideally, changing substitution the pattern of two XB donors or acceptors from 1,2 to 1,4 on a phenyl ring should not change the nature of the bonds formed, but only affect the geometric parameters characterizing the resulting assembly. Because halogen bonds are generally highly directional with a strong preference for C–X \cdots N(aryl) geometries, the angle between donor or acceptor sites on a ditopic molecule essentially determines the shape of the desired 1-D chain. An illustration

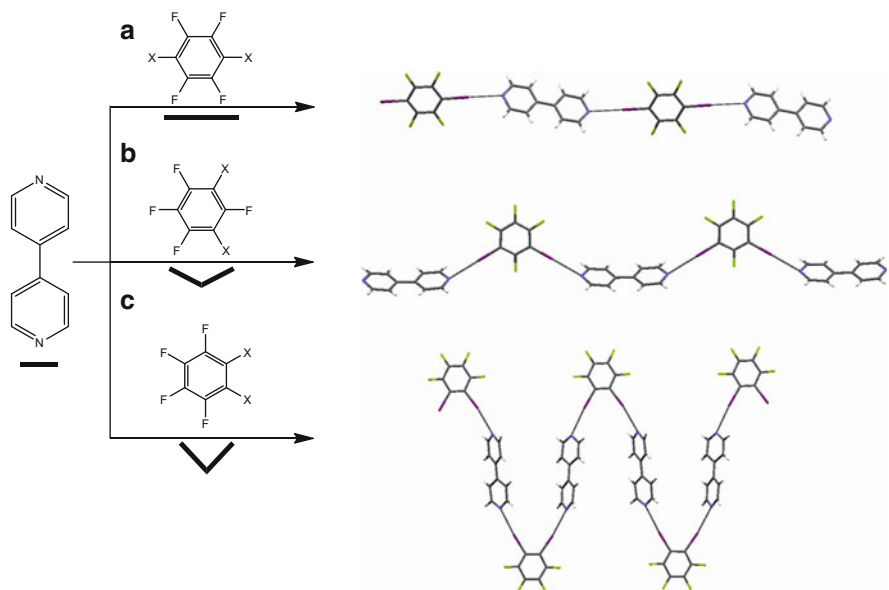


Fig. 8 Outcome of the co-crystallization of 4,4'-bipyridine with (a) 1,4-diiiodotetrafluorobenzene [28], (b) 1,3-diiiodotetrafluorobenzene [28], and (c) 1,2-diiiodotetrafluorobenzene [28]

of this can be found by examining the crystal structures obtained by combining a linear ditopic acceptor, 4,4'-bipyridine, with the three different isomers of diiodotetrafluorobenzene (Fig. 8) [28].

The 1-D chains are generated via near-linear C–I \cdots N interactions and the bending angles along the chains are close to 120° and 60°, which reflect the relative intramolecular orientation of the two iodine atoms on the three ditopic donors, respectively. An analogous outcome can be found in co-crystals of the corresponding dibromo analogues [29] as well as with other bidentate XB donors such as 1,4-diiodoethynylbenzene derivatives and its 1,3-analogue [30].

The robustness of conventional halogen bonds should also mean that, if the relative orientation of the acceptor sites were altered, the resulting supramolecular entity should reflect tecton geometries. This hypothesis was validated by Metrangola, Resnati and co-workers by co-crystallizing 3,5-bis(pyrid-4'-yl)-1,2,4-oxadiazole with two different halogen-bond donors, 1,4-diiodoperfluorobutane and 1,6-diiodoperfluorohexane [31]. It was found that the geometries of the halogen-bond acceptors (as determined by the relative orientation of the lone-pair of electrons on the halogen-bond acceptor sites) directly determine the resulting bending angles in the resulting heteromeric chains (Fig. 9).

The most common halogen-bond acceptor sites tend to involve nitrogen atoms, but ditopic acceptors using oxygen or sulfur atoms have also been used successfully for the assembly of 1-D chains with suitable XB donors (Fig. 10).

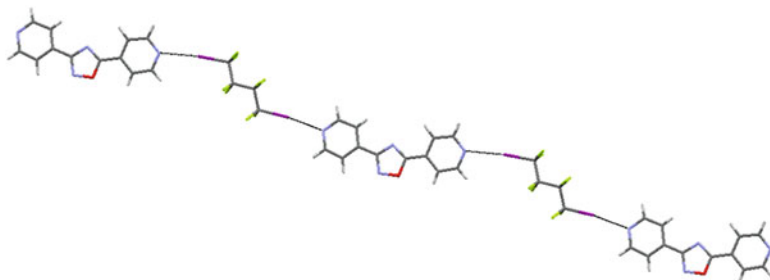


Fig. 9 Result of cocrystallizing 3,5-bis(pyrid-4'-yl)-1,2,4-oxadiazole with 1,4-diiodoperfluorobutane [31]

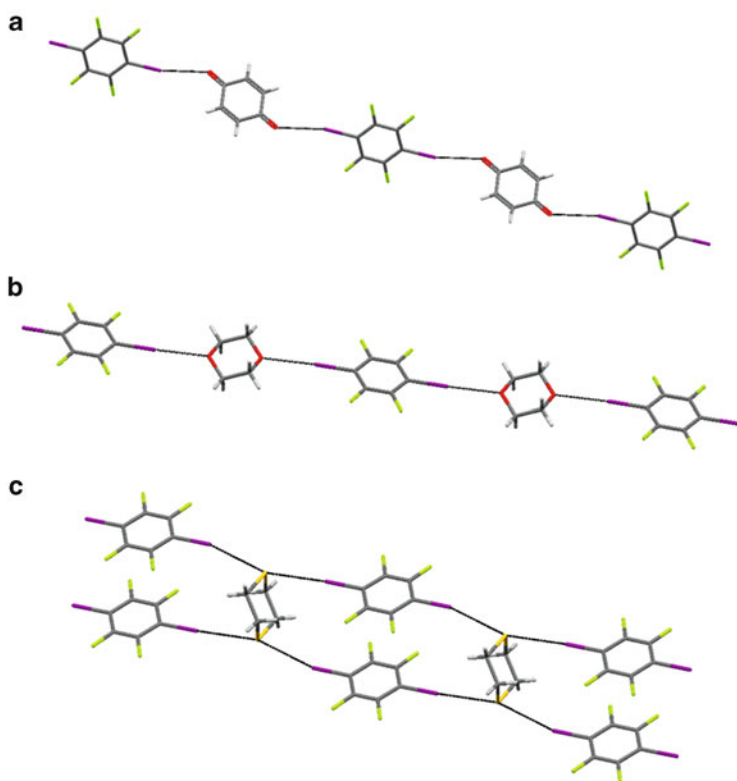


Fig. 10 Examples of 1-D chains formed from 1,4-diiodotetrafluorobenzene with (a) 1,4-benzoquinone [32], (b) 1,4-dioxane [33], and (c) 1,4-dithiane [34]

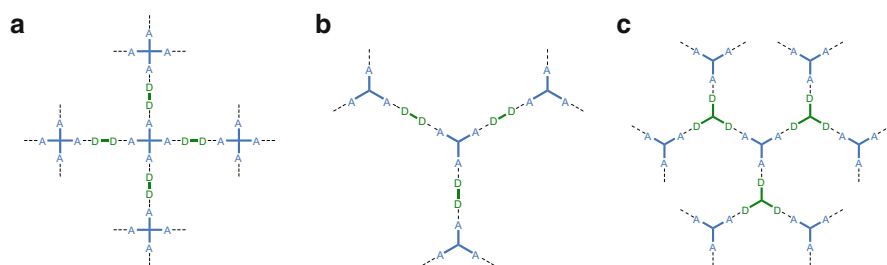
The structure involving 1,4-diiodotetrafluorobenzene 1,4-dithiane is particularly interesting since both sulfur atoms are bifurcated and accept two halogen-bond donors, resulting in the assembly of an infinite ribbon-like architecture.

3 Supramolecular Architectures Constructed via Multiple Halogen Bonds

From the discussion in the previous section, it is clear that many strategies have made use of halogen bonds for the successful construction of heteromeric chains. In principle, it should also be possible to construct architectures of higher dimensionalities simply by increasing the number of donor/acceptor sites, and by orienting them in such a way that two or three synthetic vectors remain more or less orthogonal to each other. The particular halogen bonds employed in a strategy for 2-D/3-D assembly can all be of the same type or with different donor...acceptor pairs, and the choice is frequently determined by ease/difficulty of synthesis of the tectons themselves. Several combinations of tectons could, in theory, lead to 2-D assemblies (Scheme 4).

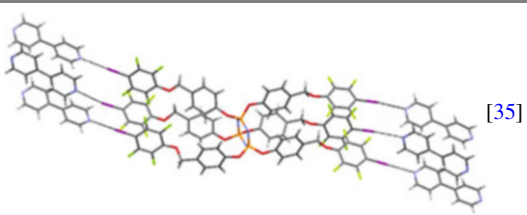
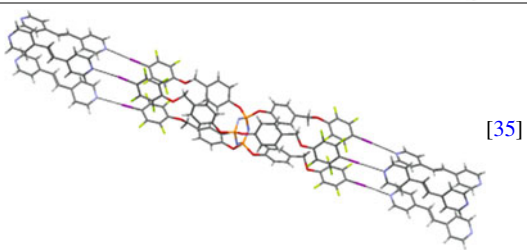
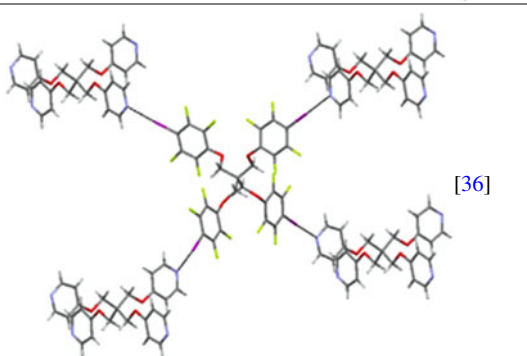
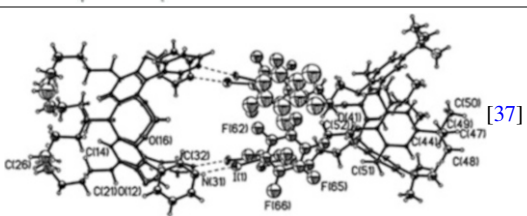
There is still a paucity of structures which exemplify the different possible assembly strategies shown in Scheme 4, and this could be because of synthetic challenges, problems with crystal growth, or, potentially, inherent problems with the proposed assembly strategy. The latest version of the CSD (November 2013) contains details of a small number of crystal structures where there is a clearly identifiable strategy in place for combining multiple X...N halogen bonds in the pursuit of a desired multidimensional architecture. In Table 3, some of the outcomes of successful co-crystallizations of donor molecules with a range of donor atoms (from two, to six; 2D–6D) combined with acceptor molecules with a range of acceptor atoms (from two to four; 2A–4A) are displayed. In principle, most of these structures could have resulted in assemblies of high dimensionality, but the outcome is also highly dependent upon the relative orientation of the donor or acceptor atoms with each molecule.

To utilize halogen bonds for organizing relatively large and complex molecules in the solid state, Aakerøy and co-workers [37] attempted to link cavitand-type molecules into discrete molecular capsules. Capsules are of considerable interest for both esthetic and practical reasons; applications for such species include drug delivery, gas encapsulation [43], and reaction chambers [44]. The use of halogen bonds as the reversible “glue” for turning “cups” into “capsules” may be advantageous under certain conditions compared to hydrogen-bond based counterparts. In this particular



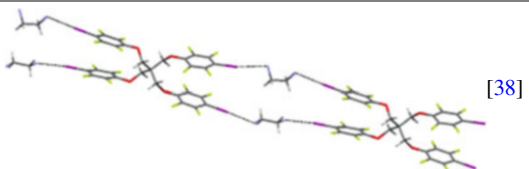
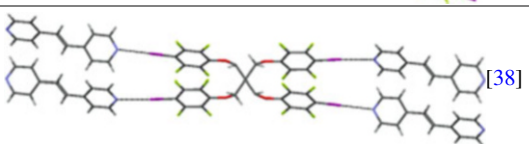
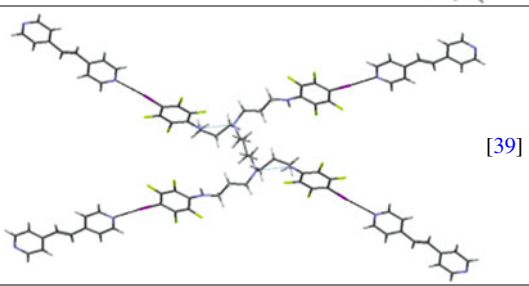
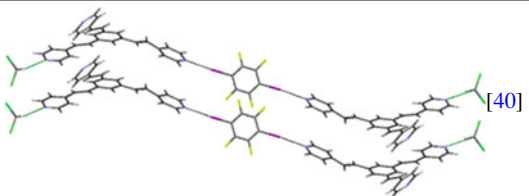
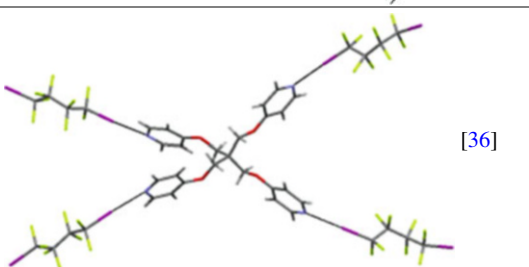
Scheme 4 Examples of synthetic strategies for the potential assembly of 2-D halogen-bonded architectures. (a) DD+AAAA (planar fourfold symmetric). (b) DD+AAA (planar threefold symmetric). (c) DDD+AAA (both planar threefold symmetric)

Table 3 Examples of motifs found in co-crystals synthesized via multiple X \cdots N halogen bonds (the last entry is the only homomeric solid)

	Architecture	Crystal Structures
6D + 2A	1-D tubes	 [35]
	1-D tubes	 [35]
4D + 4A	3-D	 [36]
	0-D capsule	 [37]

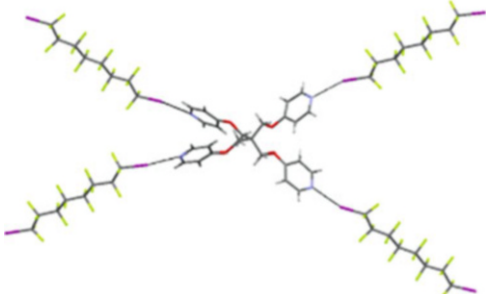
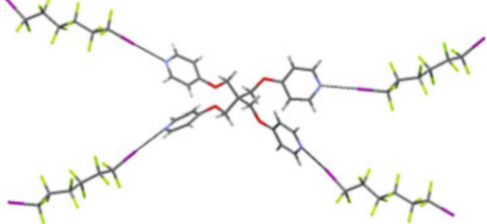
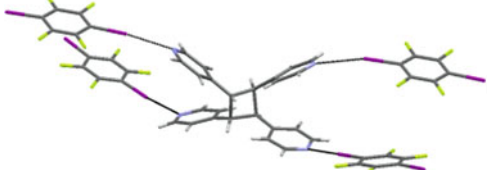
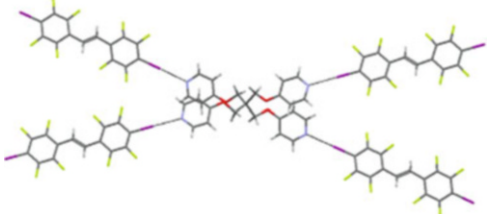
(continued)

Table 3 (continued)

	Architecture	Crystal Structures
4D + 2A	1-D ribbon	 [38]
	1-D ribbon	 [38]
	2-D layer	 [39]
2D + 3A	Discrete trimer	 [40]
2D + 4A	3-D	 [36]

(continued)

Table 3 (continued)

	Architecture	Crystal Structures
	2-D	 <p>[36]</p>
	2-D	 <p>[36]</p>
	2-D	 <p>[41]</p>
	2-D	 <p>[41]</p>

(continued)

Table 3 (continued)

	Architecture	Crystal Structures
	1-D	
DADA (single molecule)	2-D	

study, a cavitand was decorated along its rim with four pyridyl moieties suitable as XB acceptor sites. In the first attempt, 2 equiv. of this cavitand were co-crystallized with 4 equiv. of 1,4-diiodotetrafluorobenzene with the goal of making a discrete hexameric capsule. However, the desired product was not obtained and, instead, a polymeric architecture was produced (Fig. 11). It was clear that the inherent divergent nature of the relative positions of the four nitrogen atoms of the pyridyl moiety would likely prevent rigid linear connectors from yielding the capsular species.

To overcome this problem, the cavitand was instead decorated with four 3-pyridyl moieties which could, in theory, present the four acceptor sites in such a way that a capsule could be formed (while also opening the possibility for another polymer structure, should the *meta*-nitrogen atoms be oriented towards the outside of the cavitand). In addition, rigid ditopic linkers were abandoned in favor of a flexible calixarene equipped with four halogen-bond donor sites. This strategy, which takes full advantage of supramolecular chelation, did result [45] in the desired product, dimeric halogen-bonded, discrete capsules (Fig. 12). Therefore, it has been shown that it is possible to use what we know about the linearity of halogen bonds (their one-dimensional structure) and how they can interact in two dimensions to predict and develop interesting and functional three-dimensional assemblies.

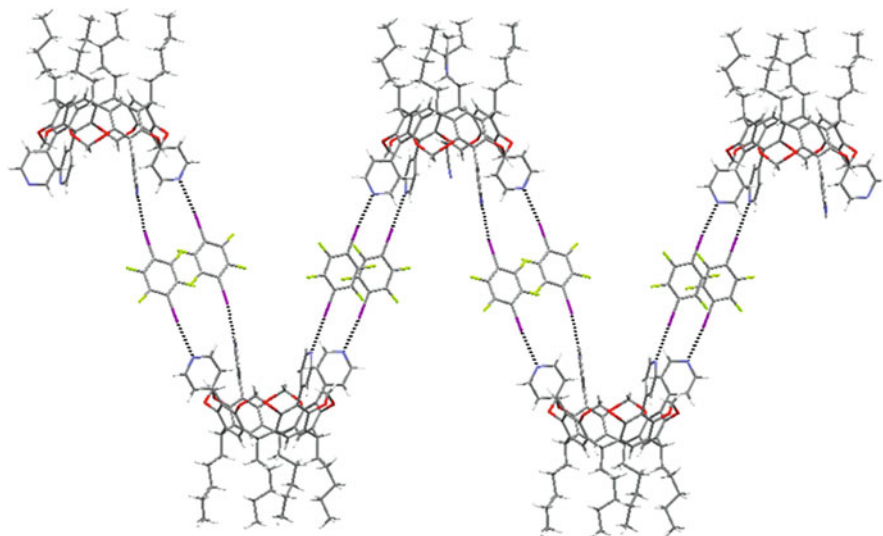


Fig. 11 Resulting cavitand chain formed from 4-pyridyl moieties along the cavitand rim [37]

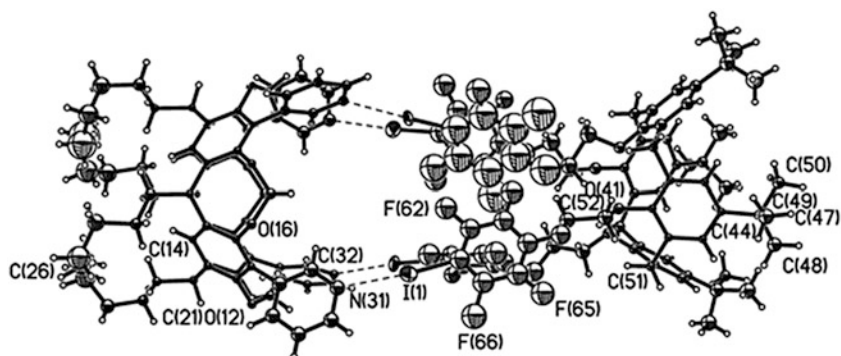
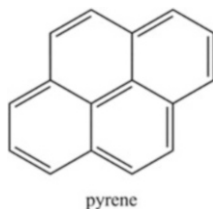


Fig. 12 Dimeric capsule constructed by four N...I halogen bonds between the calixarene *on the right*, and the cavitand *on the left* [45]

The synthesis of this dimeric capsule demonstrates that the strength and directionality of XBs can be employed as structure-directing tools for the assembly of relatively large capsular structures from suitable functionalized host-molecules. This also emphasizes that observed trends regarding intermolecular recognition between small molecules can be combined into practical guidelines for the construction of specific supramolecular architectures with the desired shape and topology comprising structurally complex building blocks.

Shen et al. utilized the strength of halogen bonds to improve the photophysical behavior of a series of pyrene-based materials. Pyrenes can display desirable phosphorescence which is subsequently utilized in bio/chemo-analyses or in



Scheme 5 Pyrene molecule displays significant phosphorescence when separated from other molecules of its kind

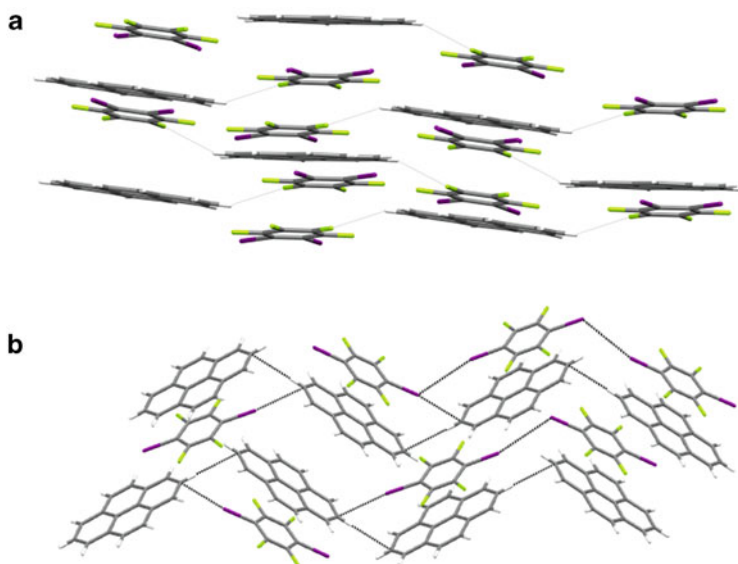
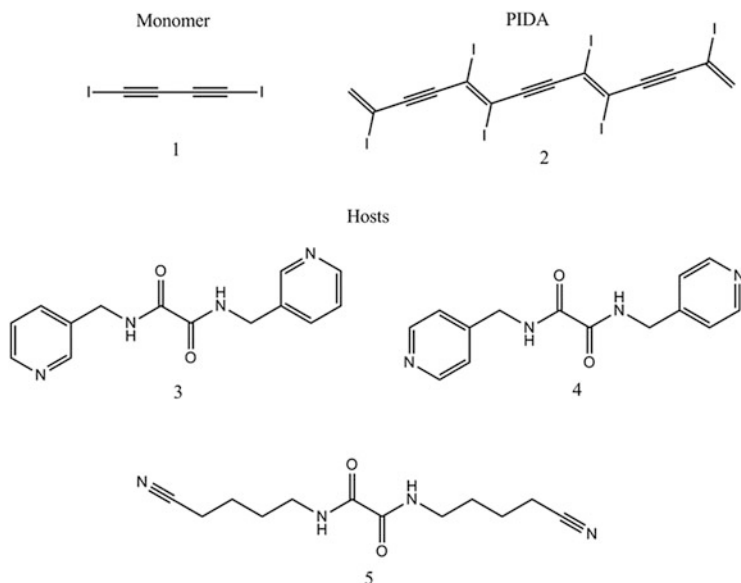


Fig. 13 Resulting cocrySTALLIZATIONS of pyrene with (a) 1,2-diiidotetrafluorobenzene and (b) 1,4-diiidotetrafluorobenzene allow for the spatial separation of pyrene molecules [54]

organic light-emitting diodes [46–53]. Unfortunately, in the solid state, the sought-after photochemistry is often hampered as a result of strong $\pi \cdots \pi$ interactions between neighboring pyrene molecules, which, in turn, diminishes the luminescence (Scheme 5).

To limit the structural influence of unfavorable $\pi \cdots \pi$ interactions which produces stacking, a set of co-crystals was prepared using XB as the synthetic vector. The two co-crystals were obtained from pyrene and 1,4-diiidotetrafluorobenzene and 1,2-diiidotetrafluorobenzene, respectively. The subsequent structure determinations showed that pyrene molecules had indeed been separated as a result of competing halogen bonds and new $\pi \cdots \pi$ and C–H \cdots F interactions. The successful prevention of pyrene–pyrene stacks resulted in maintained and substantial room-temperature phosphorescence in the solid state (Fig. 13) [54].



Scheme 6 Monomer **1**, diiodobutadiyne, the polymerization product **2**, poly(diiododiacetylene) (PIDA), and three host molecules, **3**, **4**, and **5**, used for regioselective cocrystallization [55]

In a study by Goroff and co-workers, an elegant connection between the structural influence of halogen bonds and solid-state functionality was presented [55]. This effort focused on function/reactivity induced by halogen bonding related to solid-state polymerization involving polydiacetylenes, PDAs. Such polymers, whose structures consist of alternating double and triple bonds, are greatly sensitive to changes in environment, allowing them to be useful in optical applications [56–58]. Additionally, they form robust strong, planar structures in the solid state, frequently referred to as “molecular wires.” Solution-phase chemistry of such materials can be difficult because of unwanted regioselective polymerization. Again, co-crystal technology (driven by halogen bonds), was used extensively to organize the target molecules into the appropriate alignment in the solid state. The synthetic targets in this case were co-crystals of potentially reactive monomers, diiodobutadiyne, with three different “hosts.” The desired halogen bonds effectively align the molecules to produce poly(diiododiacetylene) (Scheme 6).

When monomer **1** was co-crystallized with host **5**, solid-state polymerization to PIDA was spontaneous. However, co-crystals with **3** and **4** do not polymerize cleanly, even upon irradiation or heating. The authors suggested that the reactions did not proceed because of the steric hindrance of the pyridine rings present in **3** and **4**. As a remedy, the authors opted to use pressure to alter the structure sufficiently to allow for the polymerizations to take place. The premeditated structural change was indeed achieved successfully (Fig. 14).

As a result of the pressure-induced modification to the original crystal structure of the co-crystal of diiodobutadiyne with host **3**, a new solid phase was obtained which facilitated effective solid-state reactivity (Scheme 7).

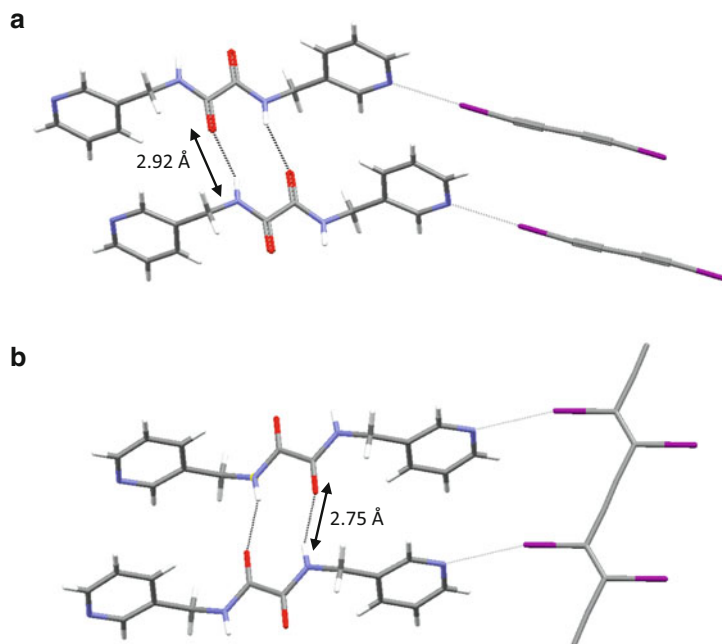
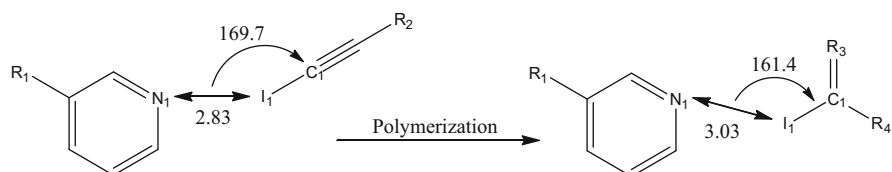


Fig. 14 Change in crystal structure with host **5** before polymerization: (a) with monomer **1**, diiodobutadiyne [59], and after polymerization (b) with PIDA [55]



Scheme 7 Pressure-induced polymerization of host **3** with diiodobutadiyne resulted in altered halogen-bond geometry between host **3** and PIDA [55]

It is important to note that the relative softness of the potential energy curve describing the strength/flexibility of a halogen bond means that such non-covalent interactions can be manipulated through external stimuli, such as temperature and pressure, and that new intermolecular geometries and arrangements can become accessible without loss of crystallinity, mechanical strength, or stability in the new solid phase.

Another interesting approach to creating highly-ordered assemblies has also been sought in two-dimensional crystal engineering on a macroscopic scale. One such example, from Jones and co-workers, involves crystal growth of a halogen-bonded co-crystal on a 2-D substrate [60]. Part of the goal of this study was to replicate the known crystal structure of 4,4'-bipyridyl 1,4-diiodotetrafluorobenzene (Fig. 15) [11].

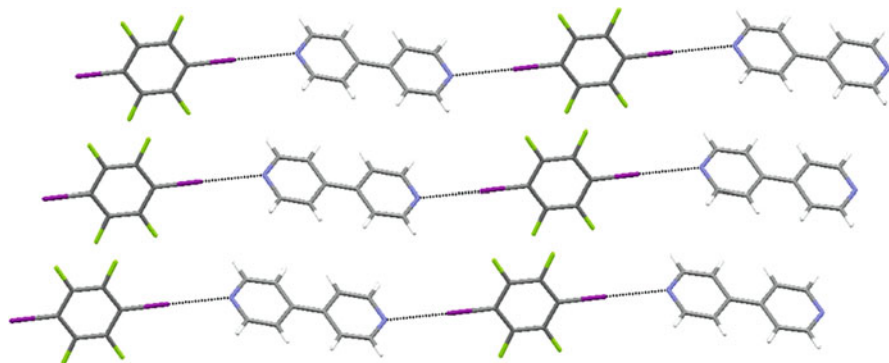
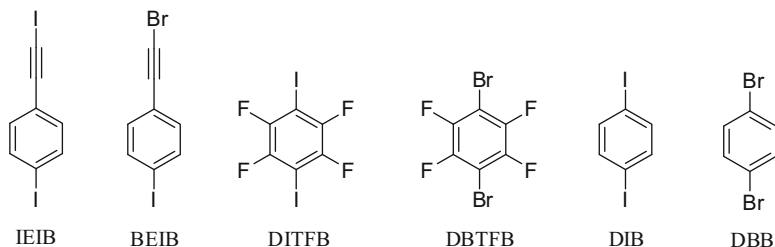


Fig. 15 Crystal structure of 4,4'-bipyridyl 1,4-diiodotetrafluorobenzene [11]

This structure is typically obtained by slow evaporation of a solution containing both components. However, Jones and co-workers were able to assemble a heteromeric 2-D architecture on a graphite surface and analyze it using synchrotron-based X-ray diffraction. The authors established that the two components interact via $I \cdots N$ halogen bonding to form infinite chains (as was observed for the 3-D crystal structure). This was the first reported analysis of a sub-monolayer structure involving halogen bonding as the primary interaction between molecules. Interestingly, the solid phase did not melt despite the fact that the reported melting point of this compound is ca. 450 K, and diffraction patterns were collected up to 470 K.

4 Combination and Competition; Halogen Bonds vs the Rest

The ground-breaking work by Etter for developing rules and guidelines for how hydrogen bonds preferentially form in the solid state remains highly relevant to present-day crystal engineering [61]. Etter and her group were able to identify rules for hydrogen-bond (HB) formation in crystal structures, including the notion that certain hydrogen-bond donors preferred certain binding patterns within a system of multiple options, regardless of the presence of many other intermolecular interactions. The “best donor–best acceptor” guideline implies that the strongest hydrogen-bond donor in a system interacts with the strongest hydrogen-bond acceptor, thus leaving sequentially weaker forces to engage with one another. This idea has become very helpful when trying to design supramolecular synthetic strategies for the assembly of a specific extended motif or architecture in the solid state [62–64]. Since hydrogen bonds and halogen bonds share many fundamental characteristics, it is natural to ask questions about whether similar guidelines are applicable to halogen bonds and, even more interestingly, how the two different



Scheme 8 Chemical structure of six potential halogen-bond donors

forces compete within the same structural arena. What does the structural landscape look like which defines the balance and competition between different hydrogen bonds and halogen bonds in the same structural arena? Only a relative limited number of studies have been published to date in this area.

Aakeröy et al. tried to establish whether a ranking based on calculated molecular electrostatic potential surfaces (MEPS) would translate into practical crystal engineering efficiency [65]. By combining structural chemistry and infrared spectroscopy, the relative structure-directing importance of different ditopic halogen-bond (XB) donors was established. Each donor was co-crystallized with over 20 XB acceptors, and the results made it possible to map out the supramolecular landscape describing the competition between I/Br – ethynyl donors, perfluorinated I/Br donors, and I/Br – phenyl-based donors.

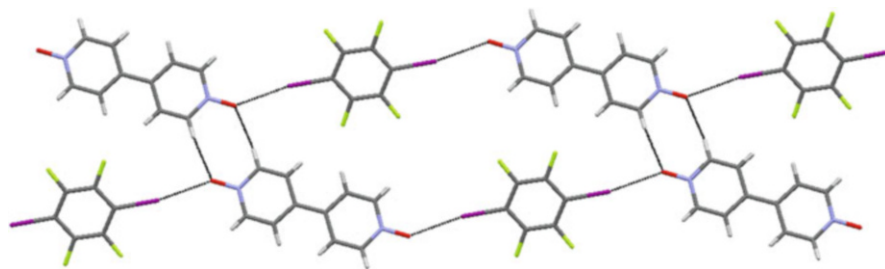
It was found that 1-iodoethynyl-4-iodobenzene (IEIB) and 1,4-diiidotetrafluorobenzene (DITFB) are XB donors of equal power, and the remaining four XB donors in this study (Scheme 8) perform according to their ranking based on the values of the electrostatic potential of the donor atoms; BEIB > DBTFB > DIB > DBB. The single-crystal X-ray diffraction studies demonstrate that the best-donor best-acceptor concept, well known from hydrogen-bonded systems, is also applicable to halogen-bonded systems with multiple and competitive XB donors; the two types of interactions have many parallel features and functions.

Recently, the result of systematic co-crystallizations of six bi-functional donor molecules (containing both a traditional hydrogen-bond donor and a halogen-bond donor) with a series of different acceptors was presented [66]. The goals of the experiment were not only to investigate competition between the interactions, but also to develop potential guidelines for their preferences in the solid state, based on their geometric/structural differences. Even though the multi-donor, multi-acceptor systems involved in this study offered the possibility of structural chaos, considerable structural consistency, in terms of primary interactions, was found for each acceptor.

The first acceptor, 3,3'-azobipyridine, exhibited OH...N interactions from the hydrogen-bond donor to the best acceptor in five of six crystal structures, creating trimers. This was clearly the dominating interaction, as the halogen-bond donors only formed weak interactions to a secondary acceptor in the five similar structures. For this reason, hydrogen bonding was found to dominate over halogen bonding five times out of six. On the other hand, the second acceptor, 4,4'-azobipyridine,

Table 4 Results of the cocrystallization study indicate that either (A) $HB > XB$, (B) $HB \approx XB$, or (C) $HB < XB$ (ox = oxime) [66]

	COOH-I	COOH-Br	OH-I	OH-Br	Ox-I	Ox-Br
3,3'-azpy	OH > I	OH > Br	OH > I	OH > Br	OH _{ox} < I	OH _{ox} > Br
	A	A	A	A	C	A
4,4'-azpy	OH=I	OH=Br	OH=I	OH=Br	OH _{ox} =I	OH _{ox} > Br
	B	B	B	B	B	A

**Fig. 16** Crystal structure of 4,4'-bipyridyl-*N,N'*-dioxide 1,4-di-iodotetrafluorobenzene [67]

exhibited both $OH \cdots N$ hydrogen bonds and $C-X \cdots N$ halogen bonds, simultaneously (in five out of six crystal structures). Both interactions were driving the co-crystal assembly. Therefore, the hydrogen-bond donors and halogen-bond donors were judged to be of equal strength and importance in five out of six crystal structures with this acceptor. The results are summarized in Table 4.

Although the results of this study gave some indication of how individual molecules may behave when confronted with competing hydrogen-bond and halogen-bond donors, they were not enough to give clear and unambiguous information about the relative ranking of such donor moieties. The relative similarity in interaction strength between some XB/HB donors can also lead to complications as far as structural analysis goes.

In this context it is interesting to explore systems in which HB and XB compete directly with one acceptor molecule, forming bifurcated halogen bonds. It seems likely that, if one type of bonding takes preference over the other, the acceptor forms bonds to the best-donor on each side of the bifurcated system. However, in the co-crystal 4,4'-bipyridyl-*N,N'*-dioxide 1,4-di-iodotetrafluorobenzene, it has been shown that an acceptor site capable of bifurcation, an *N*-oxide, simultaneously engages in one XB and one HB (Fig. 16) [67].

This result clearly indicates that the two interactions are alike both in terms of thermodynamic strength and geometric requirements, undoubtedly presenting significant issues regarding predictability in systems containing both types of donors. Structures which contain both hydrogen-bond and halogen-bond donors can exhibit structural “synthon crossover” [25] depending the different interaction possibilities. The outcome can be unclear because of the presence of unexpected or concomitant stoichiometries and by unresolvable disorder.

An example is offered in a study by Jones and co-workers [68], wherein they analyzed co-crystals exhibiting variations in crystal structure stoichiometry. The variations are thought to occur because of the competitive nature of the system. The system under investigation utilized the common halogen-bond donor, 1,4-diiodotetrafluorobenzene. In the crystal structure of this ditopic donor and methylidiphenylphosphine oxide (MDPPO), the expected halogen bonds to the oxygen atoms did not appear. Instead, the iodine molecule showed short contacts with the phenyl carbon atoms on the acceptor molecule, accompanied by self-complementary C-H \cdots O hydrogen bonds between adjacent MDPPO molecules (Fig. 17).

As a result of the unexpected intermolecular interactions, additional attempts at making co-crystals within the same system were carried out. By changing reaction conditions, a crystal structure with a 1:1 stoichiometry was found, and this time, the intended/expected I \cdots O halogen bonds were present (Fig. 18).

These two structures confirm that the balance between competing hydrogen bonds and halogen bonds can be affected dramatically by subtle changes in reaction conditions and indicates that the relative strengths of such interactions are often very similar.

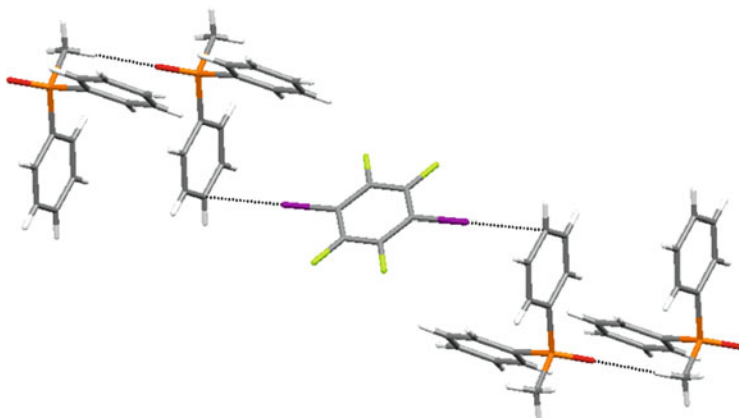


Fig. 17 Chains of 1,4-diiodotetrafluorobenzene separated by columns of MDPPO molecules in the crystal structure of MDPPO₂ · TFIB [68]

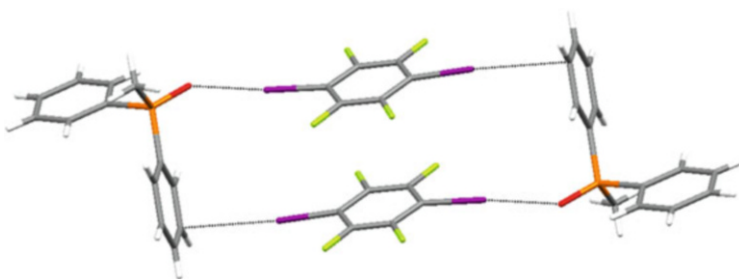
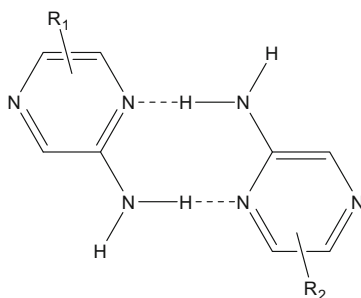


Fig. 18 Primary motif in the crystal structure of MDPPO · TFIB [69]



Scheme 9 Self-complementary homo synthon in 2-aminopyrazine [25]

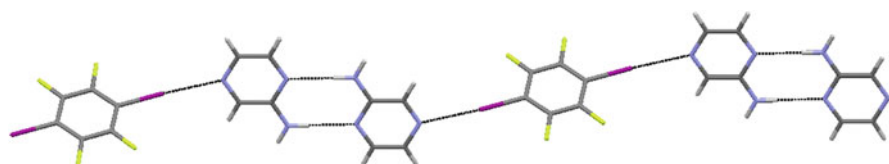


Fig. 19 Primary motif in the crystal structure of 2-aminopyrazine 1,4-diiidotetrafluorobenzene [25]

The problems associated with “synthon crossover,” or the unpredictability of intermolecular interactions as synthetic tools, have been addressed in several reports by Aakeröy and co-workers. In a recent publication [25] they attempted to assemble selectively simple linear architectures containing both halogen- and hydrogen-bond donors. The synthetic strategy involved covalent modifications to the backbone of the individual components to exploit the “best donor-best acceptor” guideline. The centerpiece of this work was 2-aminopyrazine, which is known to form self-complementary hydrogen-bonded homo synthons (Scheme 9).

An attempt was made to break this interaction with a strong XB donor, 1,4-diiidotetrafluorobenzene (DITFB). In addition, three versions of 2-aminopyrazine decorated with different substituents (to alter the electrostatic potential surface around the molecule) were examined. In none of the co-crystals, DITFB with 2-aminopyrazine, 2-amino-5-bromopyrazine, or 2-amino-3,5-dibromopyrazine, respectively, did the hydrogen-bonded homo synthon break. Instead, the halogen-bond donor in each structure had to settle for “second place” and engage with the nitrogen atom in the *para* position (Fig. 19).

While the initial goal of disrupting the self-complementary synthon was not established, this study proved to be helpful in developing patterns for “synthon crossover,” or lack thereof. Each of the three co-crystals exhibited the same general one-dimensional (linear) structure, with no deviation in secondary interactions. Subsequently [69], the same group demonstrated how HBs and XBs can be used as orthogonal synthetic vectors without structural interference as long as the

primary molecular recognition events are designed around a careful combination of geometric and electrostatic complementarity (Fig. 20).

A two-point contact is more easily incorporated within a hydrogen-based synthon, whereas the vast majority of halogen-bond interactions involve single-point halogen atom \cdots lone pair synthons. This indicates that it may be possible to build supramolecular assemblies of greater complexity with a larger number of different molecules (even ternary co-crystals are still notoriously difficult to obtain) by combining interactions which can be made to operate independently of each other, both at the level of molecular recognition, and at the level of overall structural control. The effective use of different intermolecular interaction in the synthesis of supramolecular architectures can be facilitated by ensuring that geometric complementarity minimizes possible “synthon crossover” during the assembly process.

Tothadi and Desiraju [70] utilized a combination of hydrogen-bond and halogen-bond donors in the attempted assembly of ternary co-crystals. Three-component co-crystals represent a particularly vexing synthetic challenge, but the authors succeeded through a combination of HBs and XBs supported by geometrical arguments based on the size and shape of molecules. The synthetic strategy took advantage of the well-known and robust acid \cdots amide heterosynthon, coupled with the established $I \cdots O_2N$ interaction. By combining fumaric acid (or oxalic acid), 4-nitrobenzamide, and 1,4-diiodobenzene, the desired ternary co-crystals were obtained (Fig. 21).

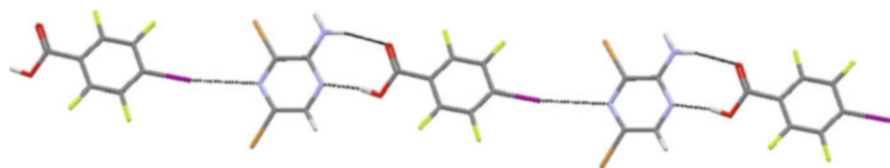


Fig. 20 Infinite 1-D chain constructed via a combination of HBs and XBs [69]

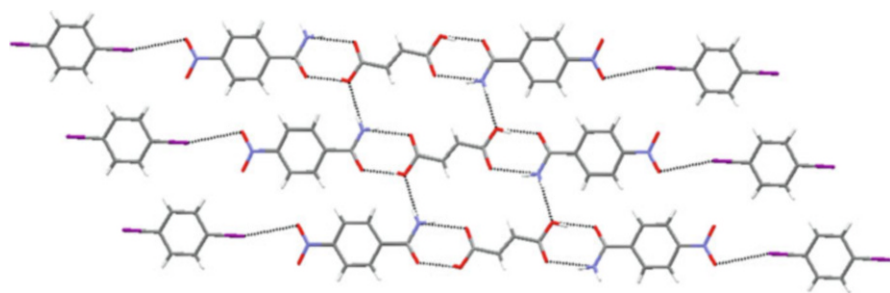


Fig. 21 Combination of acid \cdots amide and $I \cdots O_2N$ synthons produce a ternary co-crystal [70]

The fundamental nature of halogen-bond interactions has been explored with a variety of theoretical and experimental techniques, but it is obvious that our understanding of XB, especially in solution [71], is far less developed compared to those available for other non-covalent bonds (such as $\pi \cdots \pi$ and hydrogen-bond interactions) [72, 73]. The extent to which the thermodynamics of HB and XB respond to changes in solvent characteristics (e.g., polarity and dielectric constant), has not been fully explored in a systematic manner. Only a very small number of association constants for halogen-bonding interactions in the solution phase have been reported [74–77]. Clearly, this type of information is essential if we are to establish reliable and transferable metrics for evaluating and comparing hydrogen-bond and halogen-bond interactions in solution [78]. In the long run, such metrics would be invaluable for developing robust supramolecular synthetic strategies, effective host-guest systems, and new organo-catalysts.

In addition, it remains important to combine structural database analyses with systematic structural and spectroscopic studies of halogen-bonded solid-state systems to develop and refine synthetic strategies which can offer robust and versatile pathways towards the construction of desirable supramolecular architectures.

References

1. Aakerøy CB (1997) *Acta Crystallogr B* 53:569
2. Braga D (2003) *Chem Commun* 22:2751
3. Walsh RDB, Bradner MW, Fleischman S, Morales LA, Moulton B, Rodriguez-Hornedo N, Zaworotko MJ (2003) *Chem Commun* 186
4. Wenger M, Bernstein J (2006) *Angew Chem Int Ed* 45:7966
5. Lehn J-M (2002) *Science* 295:2400
6. Desiraju GR (2002) *Acc Chem Res* 35:565
7. Crihfield A, Hartwell J, Phelps D, Walsh RB, Harris JL, Payne JF, Pennington WT, Hanks TW (2003) *Cryst Growth Des* 3:313
8. Britton D, Gleason WB (2002) *Acta Crystallogr Sect E Struct Rep Online* 58:o1375
9. Metrangolo P, Meyer F, Pilati T, Resnati G, Terraneo G (2007) *Acta Crystallogr Sect E Struct Rep Online* 63:o4243
10. Liantonio R, Metrangolo P, Pilati T, Resnati G (2002) *Acta Crystallogr Sect E Struct Rep Online* 58:o575
11. Walsh RB, Padgett CW, Metrangolo P, Resnati G, Hanks TW, Pennington WT (2001) *Cryst Growth Des* 1:165
12. Cincic D, Friscic T, Jones W (2008) *Chem Mater* 20:6623
13. Metrangolo P, Pilati T, Resnati G, Stevenazzi A (2004) *Chem Commun* 1492
14. Cardillo P, Corradi E, Lunghi A, Meille SV, Messina MT, Metrangolo P, Resnati G (2000) *Tetrahedron* 56:5535
15. Syssa-Magale J-L, Boubekeur K, Schollhorn B (2005) *J Mol Struct* 737:103
16. Jay JI, Padgett CW, Walsh RDB, Hanks TW, Pennington WT (2001) *Cryst Growth Des* 1:501
17. Aakerøy CB, Wijethunga TK, Desper J (2014) *CrystEngComm* 16:28
18. Clark T, Hennemann M, Murray JS, Politzer P (2007) *J Mol Model* 13:291
19. Politzer P, Lane P, Concha MC, Ma Y, Murray JS (2007) *J Mol Model* 13:305
20. Göbell M, Tchitchanov BH, Murray JS, Politzer P, Klapötke TM (2009) *Nat Chem* 1:229
21. Politzer P, Murray JS, Clark T (2010) *Phys Chem Chem Phys* 12:7748

22. Ji B, Wang W, Deng D, Zhang Y (2011) *Cryst Growth Des* 11:3622
23. Syssa-Magalé J, Boubekeur K, Palvadeau P, Meerschaut A, Schöllhorn B (2005) *CrystEngComm* 7:302
24. Syssa-Magalé J-L, Boubekeur K, Palvadeau P, Meerschaut A, Schöllhorn B (2004) *J Mol Struct* 691:79
25. Aakeröy CB, Chopade PD, Desper J (2011) *Cryst Growth Des* 11:5333
26. Khavasi HR, Tehrani AA (2013) *CrystEngComm* 15:5813
27. Bernstein J (2002) *Polymorphism in molecular crystals*, IUCr monographs on crystallography. Clarendon Press, Oxford
28. Metrangolo P, Resnati G, Pilati T, Biella S (2008) In: Metrangolo P, Resnati G (eds) *Halogen bonding: fundamentals and applications*. Springer, Berlin, p 105
29. De Santis A, Forni A, Liantonio R, Metrangolo P, Pilati T, Resnati G (2003) *Chem Eur J* 9:3974
30. Yamamoto HM, Kosaka Y, Maeda R, Yamaura J, Nakao A, Nakamura T, Kato R (2008) *ACS Nano* 2:143
31. Saccone M, Cavallo G, Metrangolo P, Pace A, Pibiri I, Pilati T, Resnati G, Terraneo G (2013) *CrystEngComm* 15:3102
32. Liu P, Ruan C, Li T, Ji B (2012) *Acta Crystallogr Sect E Struct Rep Online* 68(Pt 5):o1431
33. Cincic D, Friščić T, Jones W (2008) *Chem Eur J* 14:747
34. Cincic D, Friščić T, Jones W (2011) *CrystEngComm* 13:3224
35. Bertani R, Chaux F, Gleira M, Metrangolo P, Milani R, Pilati T, Resnati G, Sansotera M, Venzo A (2007) *Inorg Chim Acta* 360:1
36. Metrangolo P, Meyer F, Pilati T, Proserpio DM, Resnati G (2007) *Chem Eur J* 13:5765
37. Aakeröy CB, Rajbanshi A, Metrangolo P, Resnati G, Parisi MF, Desper J, Pilati T (2012) *CrystEngComm* 14:6366
38. Caronna T, Liantonio R, Logothetis TA, Metrangolo P, Pilati T, Resnati G (2004) *J Am Chem Soc* 126:4500
39. Metrangolo P, Meyer F, Pilati T, Proserpio DM, Resnati G (2008) *Cryst Growth Des* 8:654
40. Vartanian M, Lucassen ACB, Shimon LJW, van der Boom ME (2008) *Cryst Growth Des* 8:786
41. Baldrighi M, Metrangolo P, Meyer F, Pilati T, Proserpio D, Resnati G, Terraneo G (2010) *J Fluorine Chem* 131:1218
42. Marras G, Metrangolo P, Meyer F, Pilati T, Resnati G, Vlij A (2006) *New J Chem* 30:1397
43. Scarso A, Shivanyuk A, Hayashida O, Rebek J Jr (2003) *J Am Chem Soc* 125:6239
44. Chen J, Rebek J Jr (2002) *Org Lett* 4:327
45. Aakeröy CB, Rajbanshi A, Desper J (2011) *Chem Commun* 47:11411
46. Focsaneanu K-S, Scaiano JC (2005) *Photochem Photobiol Sci* 4:817
47. Manandhar E, Broome JH, Myrick J, Lagrone W, Cragg PJ, Wallace KJ (2011) *Chem Commun* 47:8796
48. Zhang B, Sun J, Bi C, Yin G, Shi PY, Sheng L (2011) *New J Chem* 35:849
49. Xue L, Charles I, Arya DP (2002) *Chem Commun* 70
50. Okamoto A, Ochi Y, Saito I (2005) *Chem Commun* 1128
51. Nakamura M, Ohtoshi Y, Yamana K (2005) *Chem Commun* 5163
52. Østergaard M, Hrdlicka PJ (2011) *Chem Soc Rev* 40:5771
53. Figueira-Duarte TM, Mullen K (2011) *Chem Rev* 111:7260
54. Shen QJ, Wei HQ, Zou WS, Sun HL, Jin WJ (2012) *CrystEngComm* 14:1010
55. Jin H, Plonka AM, Parise JB, Goroff NS (2013) *CrystEngComm* 15:3106
56. Sharma Goel SK, Rezan SA, Misra VN, Tripathi KN (2003) *J Mater Sci Lett* 22:737
57. Chae SK, Park H, Yoon J, Lee CH, Ahn DJ, Kim JM (2007) *Adv Mater* 19:521
58. Ahn DJ, Kim JM (2008) *Acc Chem Res* 41:805
59. Goroff NS, Curtis SM, Webb JA, Fowler FW, Lauher JW (2005) *Org Lett* 7:1891
60. Clark SM, Friščić T, Jones W, Mandal A, Sun C, Parker JE (2011) *Chem Commun* 47:2526
61. Etter MC (1990) *Acc Chem Res* 23:120

62. Aakerøy CB, Epa KN, Forbes S, Desper J (2013) *CrystEngComm* 15:5946
63. Aakerøy CB, Epa KN, Forbes S, Schultheiss N, Desper J (2013) *Chem A Eur J* 19:14998
64. Aakerøy CB, Desper J, Smith MM (2007) *Chem Commun* 3936
65. Aakerøy CB, Baldrihi M, Desper J, Metrangolo P, Resnati G (2013) *Chem A Eur J* 19:16240
66. Aakerøy CB, Panikkattu S, Chopade PD (2013) *J Desper CrystEngComm* 15:3125
67. Messina MT, Metrangolo P, Panzeri W, Pilati T, Resnati G (2001) *Tetrahedron* 57:8543
68. Oh SY, Nickels CW, Garcia F, Jones W, Friščić T (2012) *CrystEngComm* 14:6110
69. Aakerøy CB, Chopade PD, Ganser C, Desper J (2011) *Chem Commun* 47:4688
70. Tothadi S, Desiraju GR (2013) *Chem Commun* 49:7791
71. Erdélyi M (2012) *Chem Soc Rev* 41:3547
72. Abraham MH (1993) *Pure and Appl Chem* 65:2503
73. Schneider H-J (2003) *Method Prin Med Chem* 19:21
74. Libri S, Jasim NA, Perutz RN, Brammer L (2008) *J Am Chem Soc* 130:7842
75. Metrangolo P, Panzeri W, Recupero F, Resnati G (2002) *J Fluorine Chem* 114:27
76. Cabot R, Hunter CA (2005) *Chem Commun* 2009
77. Laurence C, Queignec-Cabanetos M, Dziembowska T, Queignec R, Wojtkowiak BJ (1982) *Chem Soc Perkin Trans* 2 1605
78. Sarwar MG, Dragisic B, Salsberg LJ, Gouliaras C, Taylor MS (2010) *J Am Chem Soc* 132:1646

Solid-State NMR Study of Halogen-Bonded Adducts

David L. Bryce and Jasmine Viger-Gravel

Abstract Nuclear magnetic resonance (NMR) spectroscopy offers unique insights into halogen bonds. NMR parameters such as chemical shifts, quadrupolar coupling constants, J coupling constants, and dipolar coupling constants are in principle sensitive to the formation and local structure of a halogen bond. Carrying out NMR experiments on halogen-bonded adducts in the solid state may provide several advantages over solution studies including (1) the absence of solvent which can interact with halogen bond donor sites and complicate spectral interpretation, (2) the lack of a need for single crystals or even long-range crystalline order, and (3) the potential to measure complete NMR interaction tensors rather than simply their isotropic values. In this chapter, we provide an overview of the NMR interactions and experiments which are relevant to the study of nuclei which are often found in halogen bonds (RX...Y) including ^{13}C , $^{35/37}\text{Cl}$, $^{79/81}\text{Br}$, ^{127}I , ^{77}Se , and $^{14/15}\text{N}$. Experimental examples based on iodoperfluorobenzene halides, bis(trimethylammonium)alkane diiodide, and selenocyanate complexes, as well as haloanilinium halides, are discussed. Of particular interest is the sensitivity of the isotropic chemical shifts, the chemical shift tensor spans, and the halide nuclear electric quadrupolar coupling tensors to the halogen bond geometry in such compounds. Technical limitations associated with the NMR spectroscopy of covalently-bonded halogens are underlined.

Keywords Chemical shifts · Co-crystals · Halogen bonds · Nuclear magnetic resonance · Quadrupolar coupling · Solid-state NMR spectroscopy

Contents

1	Introduction	184
2	Fundamentals of Solid-State Nuclear Magnetic Resonance (SSNMR) Spectroscopy	186
2.1	Zeeman Interaction and Fundamental Properties	186
2.2	Chemical Shifts	186
2.3	The Nuclear Electric Quadrupolar Interaction	188
2.4	Spin-Spin Coupling	189
3	Applications of SSNMR to the Study of Halogen-Bonded Adducts	190
3.1	Literature Highlights	191
3.2	SSNMR of the Halogen Bond Acceptor: Halogen-Bonded Selenocyanate and Thiocyanate Complexes	192
3.3	SSNMR Studies of the Halogen Bond Acceptor: Cl^- , Br^- , and I^-	195
3.4	SSNMR and NQR Studies of the Halogen Bond Donor (R-X): Covalently-Bonded Halogens	196
3.5	SSNMR Studies of the Halogen Bond Donor (R-X): Correlation Between ^{13}C Shifts and the C-I Distance	197
4	Conclusions and Outlook	199
	References	200

1 Introduction

Nuclear magnetic resonance (NMR) spectroscopy is well known as a versatile analytical technique for studying molecular structure and dynamics. One of the strengths of NMR spectroscopy is its power to analyze samples in a variety of states, including liquids, solutions, gases, amorphous solids, crystalline solids, gels, and more. Among the advantages of solid-state NMR compared to diffraction techniques is the former's ability to provide detailed information on local structure even when long-range crystalline order is absent. NMR has proven to be a particularly useful site-specific probe of non-covalent interactions in solution and in the solid state, having provided fundamental insights into hydrogen bonding [1–4], cation- π interactions [5, 6], and CH/ π interactions [7], for example. Applications to the phenomenon of halogen bonding, where a halogen bond donor RX (X = halogen) interacts with a halogen bond acceptor, Y (Y = anion, Lewis base, π electrons, etc.), to form a halogen bond (RX...Y) hold much potential (see Fig. 1). The IUPAC definition of the halogen bond [8], informed in part by discussions held at the IUCr Satellite Workshop on “Categorizing Halogen Bonding and Other Noncovalent Interactions Involving Halogen Atoms” held in August 2011 in Sigüenza, Spain [9], states in part that “the XY halogen bond usually affects the NMR observables (e.g., chemical shift values) of nuclei in both R-X and Y, both in solution and in the solid state.” Indeed, many of the chemical elements which are involved in the formation of halogen bonds have isotopes with non-zero nuclear spin quantum numbers, making them in principle amenable to study by NMR spectroscopy (Table 1). A few examples are given in Fig. 1; these

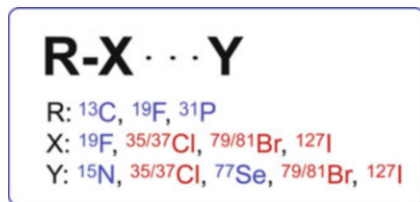


Fig. 1 Generic halogen bonding motif, $RX\cdots Y$, along with a non-exhaustive list of spin-active nuclides of interest which may be contained in the various fragments. Spin-1/2 nuclides are shown in blue; quadrupolar nuclei (spin $> 1/2$) are shown in red

Table 1 Summary of nuclear spin properties of isotopes discussed in the context of halogen bonds in this chapter [27]

Nuclide	Spin, I	Ξ (%) ^a	Q (mb) ^b	Natural abundance (%)
¹ H	1/2	100	–	99.9885
¹³ C	1/2	25.145020	–	1.108
¹⁴ N	1	7.226317	20.44	99.632
¹⁵ N	1/2	10.136767	–	0.368
¹⁹ F	1/2	94.094011	–	100
³⁵ Cl	3/2	9.797909	–81.65	75.78
³⁷ Cl	3/2	8.155725	–64.35	24.22
⁷⁷ Se	1/2	19.071513	–	7.63
⁷⁹ Br	3/2	25.053980	313	50.69
⁸¹ Br	3/2	27.006518	262	49.31
¹²⁷ I	5/2	20.007486	–696	100

^aRatio of the resonance frequency of the reference for the isotope relative to that of the protons in TMS

^bQuadrupole moment in millibarn

will be discussed in more detail in Sect. 2. Many nuclei of interest are quadrupolar, i.e., their nuclear spin quantum numbers are greater than 1/2.

Solution NMR spectroscopy has long been used to monitor the formation of halogen bonds, mainly through the analysis of chemical shift changes of nuclei such as ¹H and ¹⁹F [10–19]. Some ¹⁴N and ¹³C studies in solution have also been reported [16, 18, 20–22]. More recently, detailed studies of the thermodynamics of halogen bonding in organic solution have been analyzed with NMR by Taylor [23, 24]. Erdélyi and co-workers have also presented elegant solution NMR studies which demonstrate the symmetry of $[N-X-N]^+$ halogen bonds in solution [25, 26].

The remainder of this chapter describes NMR studies of solid halogen-bonded complexes. First, a brief overview of relevant solid-state NMR theory and various parametric definitions is given. This is followed by a discussion of selected literature on solid-state NMR studies of halogen-bonded complexes. Finally, conclusions and an outlook for future research are given.

2 Fundamentals of Solid-State Nuclear Magnetic Resonance (SSNMR) Spectroscopy

2.1 Zeeman Interaction and Fundamental Properties

NMR spectroscopy relies on the fundamental Zeeman interaction between the nuclear magnetic moment, μ , and an external applied magnetic field, B_0 . The nuclear spin quantum number, I , and the magnetic moment are related according to the magnetogyric ratio (γ) specific to the nuclide of interest:

$$\gamma = 2\pi\mu/hI$$

Each of the adjacent $2I + 1$ Zeeman states, labeled with a quantum number m_I , are separated by an energy of $h\gamma B_0/2\pi$. The associated resonance frequency, known as the Larmor frequency (ν_0), is equal to $\gamma B_0/2\pi$. For a spin-1/2 nucleus such as ^{13}C , there are two energy levels ($m_I = 1/2$ and $-1/2$). For a quadrupolar nucleus such as ^{35}Cl ($I = 3/2$), there are four energy levels ($m_I = 3/2, 1/2, -1/2$, and $-3/2$). The $1/2 \leftrightarrow -1/2$ transition is called the central transition (CT) and the $3/2 \leftrightarrow 1/2$ and $-3/2 \leftrightarrow -1/2$ transitions are called the satellite transitions.

2.2 Chemical Shifts

Not all nuclei of a given type resonate at the pure Larmor frequency. Magnetic shielding (σ) by the surrounding electronic framework alters the observed frequency as follows:

$$\nu = \gamma B_0(1 - \sigma)/2\pi$$

Magnetic shielding gives rise to the chemical shifts familiar from ^1H and ^{13}C solution NMR. The relationships between chemical shifts, magnetic shielding constants, and resonance frequencies are as follows:

$$\delta = (\sigma - \sigma_{\text{ref}})/(1 - \sigma_{\text{ref}})$$

and

$$\delta = (\nu - \nu_{\text{ref}})/(1 - \nu_{\text{ref}})$$

where σ_{ref} and ν_{ref} are the magnetic shielding constant and resonance frequency, respectively, of the primary chemical shift reference compound (i.e., TMS for ^1H and ^{13}C).

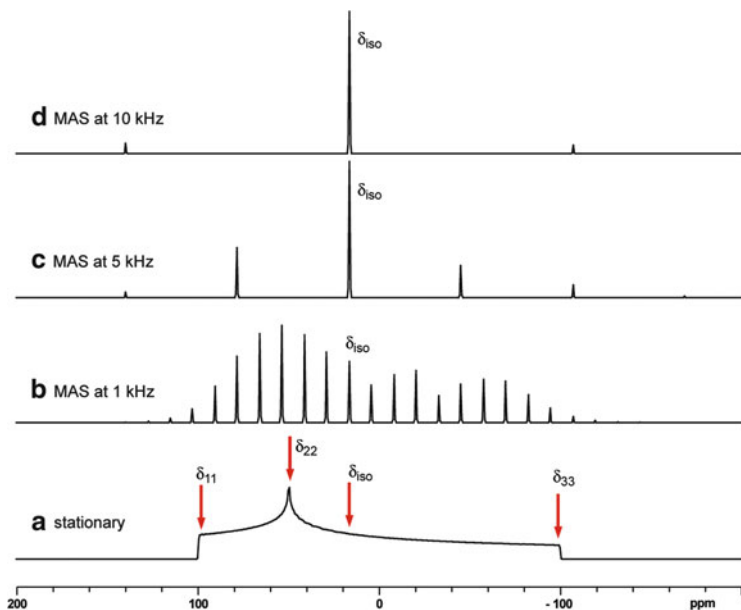


Fig. 2 Simulated solid-state NMR spectra of an isolated spin-1/2 nucleus (e.g., ^{13}C , ^{15}N , ^{31}P , ^{77}Se) under stationary (a) and magic-angle spinning (b–d) conditions. The values of the principal components of the chemical shift tensor are $\delta_{11} = 100$, $\delta_{22} = 50$, and $\delta_{33} = -100$ ppm. As the MAS rate is increased, the intensities of the spinning sidebands diminish and the peak corresponding to the true isotropic chemical shift at 16.7 ppm becomes obvious

Magnetic shielding constants, and therefore chemical shifts, are orientation-dependent anisotropic properties described by second-rank tensors with up to nine independent elements. For the chemical shift, the tensor is given by

$$\delta = \begin{bmatrix} \delta_{xx} & \delta_{xy} & \delta_{xz} \\ \delta_{yx} & \delta_{yy} & \delta_{yz} \\ \delta_{zx} & \delta_{zy} & \delta_{zz} \end{bmatrix}$$

when expressed in an arbitrary molecule-fixed axis system. In its principal axis system, the symmetric part of the tensor becomes diagonal and it is customary to describe the magnitude of the chemical shift tensor by three principal components ordered as follows: $\delta_{11} \geq \delta_{22} \geq \delta_{33}$.

The practical consequence of the above discussion is that, for a powdered sample, the nucleus of interest in each different crystallite orientation relative to B_0 will give rise to a different resonance frequency. For a stationary powder sample, the resulting NMR spectrum will be a sum of all possible resonance frequencies resulting from a random distribution of crystallite orientations. The resulting spectrum takes the form of a “powder pattern” (see Fig. 2). An alternative representation of the three independent chemical shift tensor elements gives the familiar isotropic chemical shift (δ_{iso}), the span (Ω), and the skew (κ):

$$\begin{aligned}\delta_{\text{iso}} &= (1/3)(\delta_{11} + \delta_{22} + \delta_{33}) \\ \Omega &= \delta_{11} - \delta_{33} \\ \kappa &= 3(\delta_{22} - \delta_{\text{iso}})/\Omega\end{aligned}$$

Rapidly rotating a powdered sample at the magic angle (54.74°) relative to the direction of B_0 causes the powder pattern to become resolved into a series of sharp peaks consisting of a peak at the isotropic chemical shift and a set of spinning sidebands. Relatively slow spinning results in a spectrum with many sidebands, the envelope of which mimics the shape of the powder pattern. For spin-1/2 nuclei, fast spinning can effectively remove the sidebands, giving a high-resolution spectrum consisting of peaks whose positions correspond to their chemical shifts, as is familiar from solution NMR (Fig. 2).

2.3 The Nuclear Electric Quadrupolar Interaction

Many of the nuclei involved in halogen bonds (see Table 1 and Fig. 1) have spin quantum numbers greater than 1/2 and are called quadrupolar nuclei. Indeed, the stable isotopes of chlorine, bromine, and iodine are all quadrupolar [28–30]. The NMR spectra of such nuclei are influenced by the interaction between the quadrupole moment of the nucleus (Q) and the electric field gradient (EFG) at the nucleus. The EFG is described by a second-rank tensor which can be diagonalized to give three principal components, $|V_{33}| \geq |V_{22}| \geq |V_{11}|$. The magnitude of the quadrupolar interaction is typically described by a quadrupolar coupling constant, C_Q , and an asymmetry parameter, η :

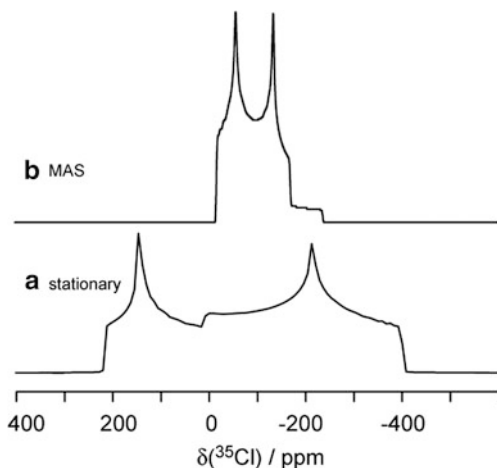
$$\begin{aligned}C_Q &= eQV_{33}/h \\ \eta &= (V_{11} - V_{22})/V_{33}\end{aligned}$$

As the quadrupolar interaction is anisotropic, the NMR powder patterns of quadrupolar nuclei will be further broadened compared to the spin-1/2 case where only anisotropic chemical shifts contribute to the powder pattern (Fig. 3). Furthermore, typically only the central transition is observed as the satellite transitions give rise to powder patterns which are even broader.

The Q values are constants for particular isotopes, and for the quadrupolar halogens they increase in the order $^{37}\text{Cl} < ^{35}\text{Cl} < ^{81}\text{Br} < ^{79}\text{Br} < ^{127}\text{I}$. This means that, for a given chemical environment (and fixed EFG), the quadrupolar coupling constant and NMR powder pattern breadth will be largest for ^{127}I and smallest for ^{37}Cl . In practice this means that ^{127}I NMR spectroscopy is extremely challenging and there are relatively few reports in the literature [30].

The EFG is determined by the arrangement of atoms and ions in the crystal lattice surrounding the nucleus of interest, and thus the measurement of quadrupolar coupling constants and asymmetry parameters can yield insight into

Fig. 3 Simulated ^{35}Cl NMR spectra of a powdered sample containing one crystallographically unique chloride ion site under stationary (a) and infinitely fast magic-angle spinning (b) conditions. Simulation parameters include a Larmor frequency of 49 MHz, quadrupolar coupling constant of 3 MHz, asymmetry parameter of 0.3, and chemical shift of 0 ppm



the local structure and crystal symmetry. For example, perfectly tetrahedral or octahedral coordination environments yield zero EFG at the center. An “isolated” closed-shell ion, such as Cl^- in solution or in a cubic salt, also experiences zero EFG. By measuring values of C_Q and η in a series of halogen-bonded complexes, one should be able to obtain insight into the influence of the halogen bond on these parameters. Ideally, once a thorough understanding of the relationship between these parameters and the XB environment has been established, one could envisage using parameters measured on new compounds to provide novel structural information.

Magic-angle spinning will reduce the line width due to the quadrupolar interaction in a powdered sample by a factor of about 3–4 only if the spinning rate is comparable to or exceeds the static breadth of the powder pattern (see Fig. 3). For covalently-bonded halogens this is impractical with current technology. In certain cases where the halogen bond acceptor is a halide ion, MAS NMR of that ion may be feasible due to the smaller C_Q values and corresponding narrower NMR powder patterns.

2.4 Spin–Spin Coupling

Indirect nuclear spin–spin (J) coupling is mediated by the intervening electronic framework. Coupling can give rise to fine structure in the NMR spectra of solids in much the same way as is observed in liquids. However, it is often the case in solids that other larger interactions (e.g., chemical shift anisotropy, quadrupolar coupling, dipolar coupling) obscure the typically smaller effects of J coupling. The measurement of J couplings across hydrogen bonds in proteins had a great impact and opened the door to measuring small J couplings in other weakly bonded systems [31]. For example, couplings have been measured in Van der Waals’ complexes

[32] and across CH- π bonds in proteins [7]. To date, no J couplings have been measured across halogen bonds. The observation of such couplings across hydrogen bonds in proteins initially led to conclusions that this indicated some degree of covalency of the hydrogen bond; however, the subsequent measurement of couplings in Van der Waals' complexes, as well as computational studies, show that the measurement of a J coupling is not a direct indicator of covalency. Nevertheless, the observation of J coupling across a halogen bond would be very interesting and the dependence of the J values on the halogen bond geometry would be particularly valuable. In principle, one would expect J couplings between both the X...Y and the $\underline{\mathbf{R}}(\mathbf{X})\cdots\underline{\mathbf{Y}}$ nuclei. In practice, these could be difficult to measure due to the strong quadrupole interactions of the X nuclei, and the expected weak coupling between the R and Y nuclei. Del Bene et al. have calculated the J couplings in the gas phase for various model halogen-bonded systems using the equation-of-motion coupled-cluster single and doubles method (EOM-CCSD) [33–35]. For example, for F-Cl...NCH, the one-bond ^{35}Cl - ^{15}N coupling constant was calculated to be -32.6 Hz and the two-bond ^{19}F - ^{15}N coupling constant was calculated to be -12.0 Hz. The authors describe several trends relating the computed coupling constants to the geometry of the halogen-bonded complexes; it will be interesting to see whether experimental measurements can be realized via NMR spectroscopy.

Dipolar coupling between nuclear spins is a through space phenomenon and it depends on the motionally-averaged inverse cube of the internuclear distance. Measurement of dipolar coupling constants can therefore, under favorable circumstances, provide bond lengths and internuclear distances. In the case of ^1H SSNMR, homonuclear dipolar coupling can result in severely broadened lines. Advanced decoupling methods can now be used to overcome such problems [36].

3 Applications of SSNMR to the Study of Halogen-Bonded Adducts

In this section we highlight briefly some reports of the application of SSNMR to the study of halogen bonded adducts. This is followed by a more detailed discussion of a few areas of application within our own laboratory. The relevance of related techniques such as nuclear quadrupole resonance (NQR) [37] is noted where appropriate. Shown in Table 2 are typical chemical shifts and quadrupolar coupling constants for some halogen bonding motifs in solids. One can see that in general it is possible to study all three components of an RX...Y halogen bond using NMR and NQR spectroscopies.

Table 2 Some typical chemical shifts and quadrupolar coupling constants for halogen-bonded (R–X...Y) solids

R–X...Y motif and nucleus studied	Compound	δ_{iso} (ppm)	C_Q (MHz)
$^{13}\text{C}\text{--I}\cdots\text{Br}^-$	(<i>n</i> -Bu ₄ PBr)(<i>p</i> -C ₆ F ₄ I ₂)	83.80, 83.00 ^a	n/a
	(<i>n</i> -Bu ₄ NBr)(<i>p</i> -C ₆ F ₄ I ₂)	84.72, 81.84 ^a	n/a
C–I... $^{77}\text{SeCN}^-$	(Me ₄ NSeCN)(<i>p</i> -C ₆ F ₄ I ₂) ₂	–158.2	n/a
	(Me ₄ NSeCN)(<i>o</i> -C ₆ F ₄ I ₂) ₂	–189.0	n/a
C–X... $^{35}\text{Cl}^-$	2-Chloroanilinium chloride	70	6.04
	2-Iodoanilinium chloride	75	2.12
C–X... $^{81}\text{Br}^-$	2-Bromoanilinium bromide	155	38.0
	2-Iodoanilinium bromide	187	12.3
C–X... $^{127}\text{I}^-$	2-Chloroanilinium iodide	340	57.50
	2-Bromoanilinium iodide	500	152.50
C- $^{127}\text{I}\cdots\text{N}$	I(CF ₂) ₂ I·NH(C ₂ H ₅) ₂	n/a	308, 834 ^b

Data are from [38–41]

^aThere are two crystallographically distinct sites

^bThese are NQR frequencies rather than C_Q values

3.1 Literature Highlights

Some ^{13}C CPMAS NMR data have been reported for a diazabicyclo[2.2.2]octane (DABCO)-CBr₄ complex by Blackstock et al. [42]. In this complex, short C–Br...N contacts were noted and the ^{13}C resonance was a slightly asymmetric singlet at 49.08 ppm. This is about 1 ppm higher than in crystalline DABCO.

Bricklebank et al. reported ^{31}P MAS NMR spectra for diiodophosphoranes with short linear I...I contacts [43]. Their results allowed them to reach some conclusions regarding the similarity between various structures with different aryl and alkyl substituents at phosphorus. Some related data have been reported by Dillon and Waddington [44].

Gervais and co-workers have described ^1H , ^{15}N , and ^{13}C SSNMR studies of imidazole- and morpholine-based model compounds exhibiting halogen bonds [45]. Some interesting ^{15}N results demonstrated the sensitivity of ^{15}N chemical shifts to halogen bonds. However, difficulties were encountered in observing some of the relevant ^{13}C signals. Weingarth et al. reported ^{15}N CP/MAS spectra as well as rotary resonance ^{15}N NMR spectra and attributed the line shape to $^{15}\text{N}\text{--}^{127}\text{I}$ dipolar coupling across the halogen bond in benzyl-di(4-iodobenzyl)amine [46]. They noted no effects attributable to $J(^{15}\text{N}, ^{127}\text{I})$ coupling.

García et al. reported ^{15}N and ^{13}C spectra in solution and in the solid state for some NH-pyrazoles exhibiting halogen bonds [47]. Bertani et al. carried out ^{13}C CP/MAS SSNMR experiments on halogen-bonded poly(4-vinylpyridine)-haloperfluorocarbon complexes [48]. The spectra revealed relatively broad lines, perhaps indicative of disorder in such compounds. Nonappa et al. have recently employed ^{15}N and ^{13}C CP/MAS NMR to study *cis*-itraconazole and the halogen-bonded itraconazole–succinic acid cocrystal [49].

Widdifield et al. [50] described a detailed multinuclear magnetic resonance study of a series of halogen-bonded decamethonium diiodide-dihalogenated benzene co-crystals as well as of the non-halogen-bonded starting materials. ^{13}C , ^{14}N , ^{15}N , ^{19}F , and ^{127}I solid-state NMR spectroscopies were utilized. They showed that such techniques were very sensitive to the formation of the co-crystals, via both chemical shifts (particularly for the spin-1/2 nuclei) and quadrupolar coupling constants. For example, ^{14}N quadrupolar coupling constants in the decamethonium moiety were found to decrease upon halogen bond formation. ^{19}F SSNMR was used to probe the nature of the disorder in some of the complexes.

Baldrighi et al. used high-resolution solid-state ^1H combined rotation and multiple pulse spectroscopy (CRAMPS), ^{13}C , and ^{15}N SSNMR to study pharmaceutical co-crystals of 3-iodo-2-propynyl-*N*-butylcarbamate [51]. The chemical shifts were useful in determining the number of molecules in the asymmetric unit, and changes in the chemical shifts were useful to monitor the formation of halogen-bonded adducts.

Garcia-Garibay and co-workers reported wideline ^1H and ^{13}C CP/MAS experiments to examine halogen-bonded ultrafast rotors with potential applications in molecular machines [52]. Of particular interest was the measurement of ^1H spin-lattice relaxation time constants (T_1) as a function of temperature to probe dynamic processes in 1,4-bis(iodoethynyl)bicyclo[2.2.2]octane, which is an ultrafast rotor with GHz rotation.

3.2 SSNMR of the Halogen Bond Acceptor: Halogen-Bonded Selenocyanate and Thiocyanate Complexes

The work of Fournigué and co-workers [53] on halogen-bonded thiocyanates prompted us to prepare and study by solid-state NMR a series of halogen-bonded thiocyanates and selenocyanates [38]. Selenium is known to participate in halogen bonds and is more attractive than sulfur from an NMR point of view. ^{33}S is a quadrupolar nucleus ($I = 3/2$) with a sizable quadrupole moment and a low natural abundance of 0.76%, rendering its study by NMR difficult. ^{77}Se is a spin-1/2 nucleus with a moderate resonance frequency and a natural abundance of 7.63%. We prepared and characterized by single-crystal X-ray diffraction the halogen-bonded complexes shown in Fig. 4: $(\text{Me}_4\text{NSeCN})(p\text{-C}_6\text{F}_4\text{I}_2)_2$, $(\text{Me}_4\text{NSeCN})(o\text{-C}_6\text{F}_4\text{I}_2)_2$, $(n\text{-Bu}_4\text{NSCN})(p\text{-C}_6\text{F}_4\text{I}_2)$, and $(\text{Me}_4\text{NSCN})(p\text{-C}_6\text{F}_4\text{I}_2)_2$. The short iodine-selenium, iodine-sulfur, and iodine-nitrogen distances and near-linearity were taken as indicative of halogen bonding. The carbon-13 chemical shifts of the thiocyanates were observed to increase in complexes exhibiting halogen bonds relative to non-halogen-bonded thiocyanates. Nitrogen-15 chemical shifts decrease slightly under the same conditions; however, the opposite trends were noted for the selenocyanates. Results from ^{77}Se CP/MAS NMR spectroscopy were more conclusive, showing a clear increase in chemical shift in halogen-bonded selenocyanates compared to Me_4NSeCN

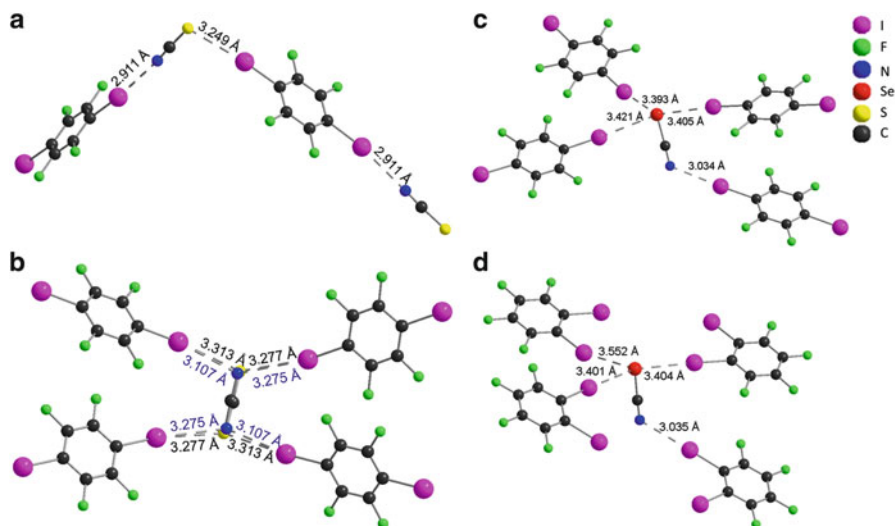


Fig. 4 Halogen bonding environments around the thiocyanate and selenocyanate anions in (a) $(n\text{-Bu}_4\text{NSCN})(p\text{-C}_6\text{F}_4\text{I}_2)$, (b) $(\text{Me}_4\text{NSCN})(p\text{-C}_6\text{F}_4\text{I}_2)_2$, (c) $(\text{Me}_4\text{NSeCN})(p\text{-C}_6\text{F}_4\text{I}_2)_2$, and (d) $(\text{Me}_4\text{NSeCN})(o\text{-C}_6\text{F}_4\text{I}_2)_2$. The R_4N^+ cations have been omitted for clarity. Reproduced with permission of the American Chemical Society. From [38]

(see Fig. 5). For example, the ^{77}Se chemical shift of Me_4NSeCN is -299.4 ppm while those of $(\text{Me}_4\text{NSeCN})(p\text{-C}_6\text{F}_4\text{I}_2)_2$ and $(\text{Me}_4\text{NSeCN})(o\text{-C}_6\text{F}_4\text{I}_2)_2$ are -158.2 ppm and -189.0 ppm, respectively.

Because SSNMR of powdered samples provided the complete ^{77}Se chemical shift tensor, insight into the reasons behind the change in the ^{77}Se isotropic chemical shift can be gleaned. As is apparent visually in Fig. 5, it is mainly the smallest component of the chemical shift tensor, δ_{33} , which changes upon halogen bonding. This change in δ_{33} in turn results in a change in δ_{iso} . How can the value of δ_{33} be related to the halogen bonding interaction? First, consider that the value of δ_{33} represents the chemical shift along the axis of the selenocyanate anion. As explained in [38], according to Ramsey's theory of paramagnetic shielding the mixing of occupied and virtual orbitals in a plane will affect the magnetic shielding along the direction perpendicular to that plane. Changes in δ_{33} for ^{77}Se in the selenocyanate anion therefore reflect perturbations to the molecular orbitals in the plane perpendicular to the anion's axis. As visualized in Fig. 4, this plane is that in which iodines engage in halogen bonding with the selenium center. Therefore, the value of δ_{33} is a good measure of the extent of halogen bonding in these complexes.

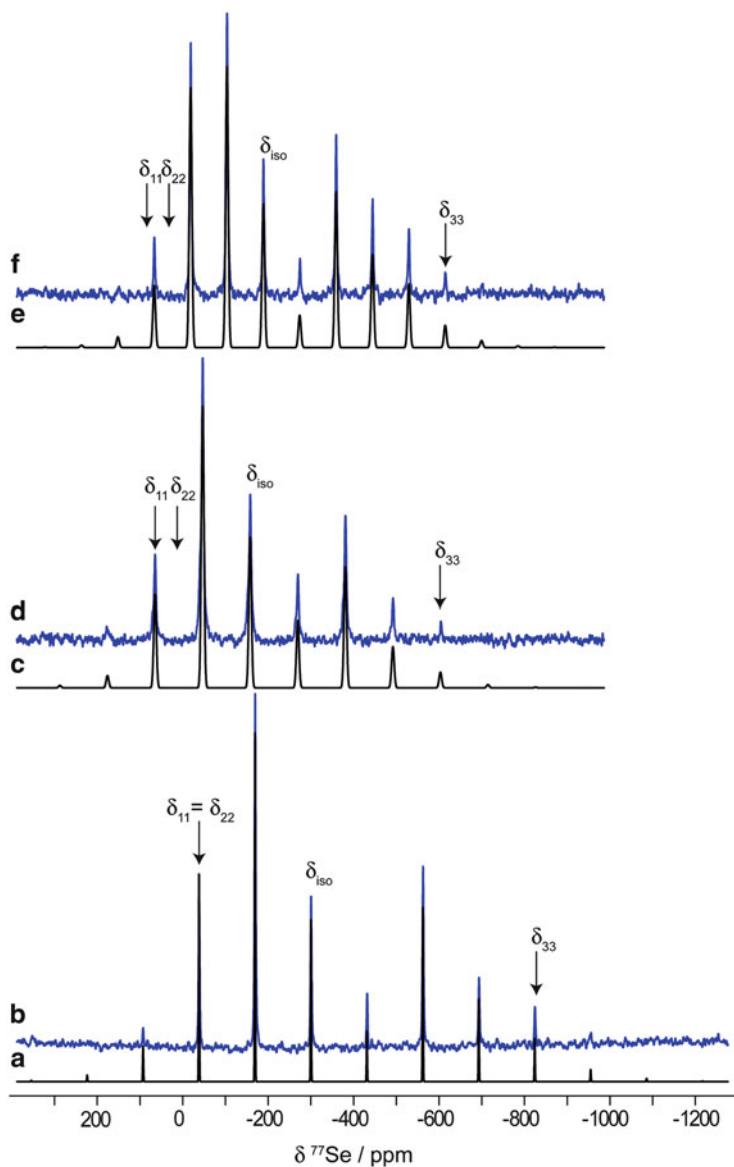


Fig. 5 ^{77}Se CP/MAS SSNMR spectra (in blue) acquired at 9.4 T for (b) non-halogen-bonded Me_4NSeCN , and halogen-bonded (d) $(\text{Me}_4\text{NSeCN})(p\text{-C}_6\text{F}_4\text{I}_2)_2$ and (f) $(\text{Me}_4\text{NSeCN})(o\text{-C}_6\text{F}_4\text{I}_2)_2$. Simulated spectra are shown in black in (a), (c), and (e), respectively. Isotropic chemical shifts are indicated (-299.9 ppm, -158.2 ppm, and -189.0 ppm, respectively). Reproduced with permission of the American Chemical Society. From [38]

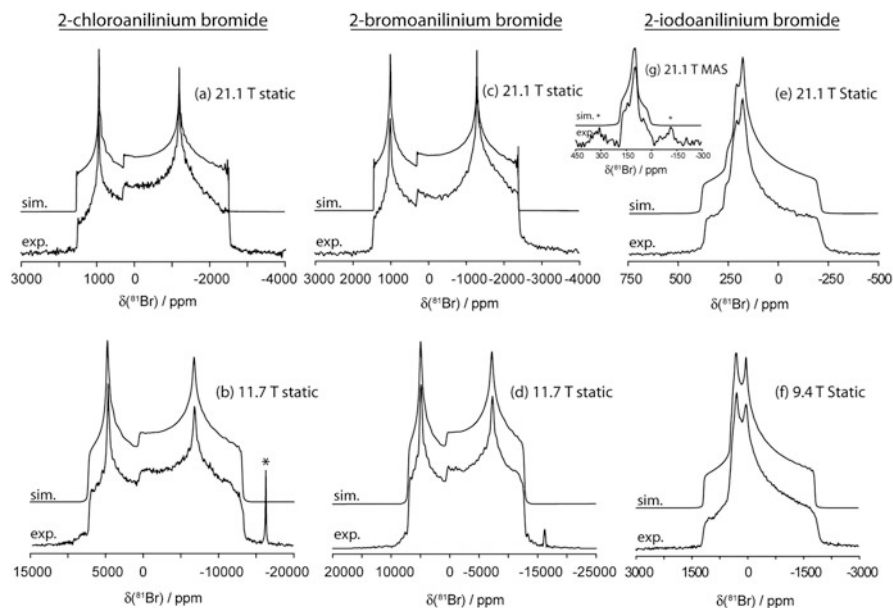


Fig. 6 ^{81}Br SSNMR spectra of the halogen-bonded bromide anions in stationary powdered samples of 2-chloroanilinium bromide (*left*), 2-bromoanilinium bromide (*center*), and 2-iodoanilinium bromide (*right*). Simulations are shown above each of the experimental spectra. Reproduced with permission of the American Chemical Society. Attrell et al. [40]

3.3 SSNMR Studies of the Halogen Bond Acceptor: Cl^- , Br^- , and I^-

Although the term “halogen bond” arises from the fact that covalently-bonded halogens are the electron acceptors (halogen bond donors), complexes can be formed wherein anionic halides (Cl^- , Br^- , and I^-) play the role of electron donor (halogen bond acceptor). One such class of compounds are the haloanilinium halides. Halogen bonding in these compounds has been discussed by Gray and Jones [54], Raatikainen et al. [55], and Attrell et al. [40]. The reduced distance parameter, R_{XB} , varies from a minimum of 0.88 for 2-iodoanilinium bromide to a maximum of 1.03 in 3-chloroanilinium bromide, indicating that the halogen bonds are weak at best in such complexes.

^{35}Cl , ^{81}Br , and ^{127}I SSNMR spectra were recorded on powdered samples of various haloanilinium halides. Note that, due to the extremely large breadth of the NMR spectra of the covalently-bonded halogens, only the spectra of the halide anions were recorded. Examples for ^{81}Br are shown in Fig. 6. The spectra were fit to determine the relevant quadrupolar coupling constants and asymmetry parameters. In favorable cases some information on the chlorine and bromine chemical shift tensors was also available, as a result of the high magnetic field (21.1 T) used in this study. The quadrupolar data for several compounds were indicative of

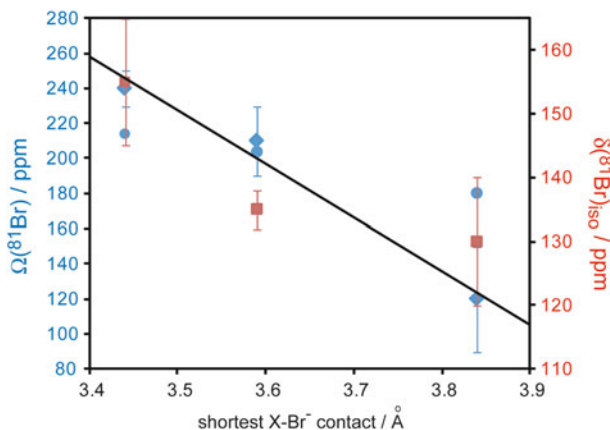


Fig. 7 Plot of experimental bromine chemical shifts (*red squares*), bromine chemical shift tensor spans (*blue diamonds*), and gauge-including projector-augmented wave DFT calculated spans (*blue circles*) as a function of the shortest X–Br[−] distance (d) in 2-chloroanilinium bromide, 2-bromoanilinium bromide, and 3-chloroanilinium bromide. The line indicates a linear fit to the experimental span data; $\Omega/\text{ppm} = -310d/(\text{\AA}) + 1,313$; correlation coefficient $R = 0.99$. Reproduced with permission of the American Chemical Society. Attrell et al. [40]

whether or not they packed in the same space group. In one isostructural series of compounds, the halide quadrupolar coupling constant was found to increase as the halogen bond weakens. The most interesting correlation in this study is shown in Fig. 7, where, for 2-chloroanilinium bromide, 2-bromoanilinium bromide, and 3-chloroanilinium bromide, it is seen that the bromine isotropic chemical shift and the bromine chemical shift tensor span both increase with decreasing halogen–bromide distance. The observed trends were corroborated by quantum chemical calculations; however, the authors were also careful to point out the possible competing influence of hydrogen bonds on the bromine NMR parameters.

Overall, no completely general spectral signature for the presence or absence of a halogen bond was found in this study, likely due to their weakness in the chosen compounds, and also due to the presence of competing hydrogen bonds. In future studies it would be very useful to examine halogen-bonded halide anions using similar methods, but in more strongly-halogen bonded environments without competing hydrogen bonds.

3.4 SSNMR and NQR Studies of the Halogen Bond Donor (R–X): Covalently-Bonded Halogens

We have discussed above some studies of the NMR parameters of the halogen bond acceptor, Y, in solids. Clearly it would be advantageous to be able to probe directly the halogen bond donor itself using NMR spectroscopy. As mentioned,

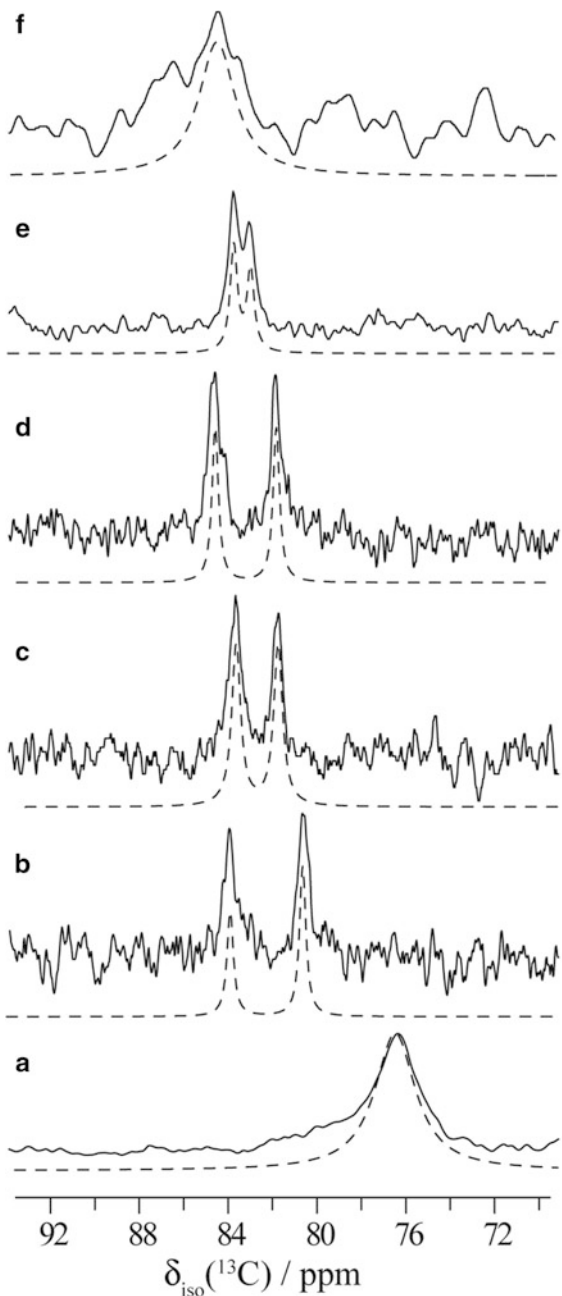
the NMR spectroscopies of chlorine, bromine, and iodine are difficult, mainly due to the large quadrupole moments of their NMR-active isotopes and the resulting extremely broad powder patterns. Even for halide anions, where the closed-shell electronic configuration means that the EFG will be relatively low at the nucleus (zero in the limit of an isolated anion), powder patterns covering at least tens of kHz (for $^{35/37}\text{Cl}$) and up to more than a MHz (for ^{127}I) in breadth are obtained. Spectra of covalently-bonded halogens will be much broader than this due to the larger EFGs imposed by the substantially more anisotropic local environment (i.e., a strong directional σ -bond). Generally speaking, therefore, it is highly impractical to record SSNMR spectra of covalently-bonded bromine or iodine nuclei; indeed, there are no examples in the literature. Very recently, Perras and Bryce reported the first direct observation of $^{35/37}\text{Cl}$ SSNMR spectra of covalently-bonded chlorine atoms in powdered samples, thus opening the door for similar studies of halogen-bonded co-crystals in the future [56]. Still, these spectra spanned up to 8 MHz in a magnetic field of 21.1 T and required several transmitter offsets to piece together the complete spectra.

Due to the large quadrupole interactions, in particular for $^{79/81}\text{Br}$ and ^{127}I nuclei when bromine or iodine is involved in a covalent bond, nuclear quadrupole resonance (NQR) may be better suited to their study. There are some older reports in the literature demonstrating the shifts in quadrupole frequency which have been attributed to charge-transfer. For example, Semin et al. reported changes in the ^{127}I NQR frequencies of $\text{I}(\text{CF}_2)_2\text{I}$ when it halogen bonds with $\text{NH}(\text{C}_2\text{H}_5)_2$ [41]. Bowmaker has also made significant contributions in this area [57–60].

3.5 SSNMR Studies of the Halogen Bond Donor ($R-X$): Correlation Between ^{13}C Shifts and the $C-I$ Distance

Aside from the atoms X and Y directly involved in the $\text{RX}\cdots\text{Y}$ halogen bond, insight may also be gained by studying the other NMR signals in the fragment RX. Indeed, this has typically been the approach in solution NMR, where ^1H or ^{19}F are sensitive probes of halogen bonding. In a series of *p*-diiodotetrafluorobenzene (*p*-DITFB) co-crystals we investigated the relationship between the ^{13}C SSNMR signals of the carbon atoms directly bonded to iodine [39]. Such experiments can be challenging for various reasons. First, as there are typically no nearby protons, one cannot efficiently carry out cross-polarization experiments, nor can one rely on dipolar relaxation of the ^{13}C spins with protons. Spin-lattice relaxation times tend to be long. The impact of the iodine which is directly bonded to carbon may cause rapid T_2 relaxation and/or residual dipolar broadening of the ^{13}C signals. Finally, the appropriate hardware for decoupling ^{19}F may not always be available. Nevertheless, presented in Fig. 8 are selected regions of the ^{13}C CP/MAS SSNMR spectra (21.1 T) of (*n*-Bu $_4$ NCl)(*p*-DITFB), (*n*-Bu $_4$ PCl)(*p*-DITFB), (*n*-Bu $_4$ NBr)(*p*-DITFB), (*n*-Bu $_4$ PBr)(*p*-DITFB), (EtPh_3PBr) $_2$ (*p*-DITFB), and the parent non-halogen bonded

Fig. 8 Experimental (*solid line*) and simulated (*dashed line*) ^{13}C CP/MAS SSNMR spectra for the region of the carbon covalently bonded to iodine. The spectra were recorded at 21.1 T with a MAS speed of 18 kHz and correspond to *p*-DITFB (a), (*n*-Bu₄NCl) (*p*-DITFB) (b), (*n*-Bu₄PCl) (*p*-DITFB) (c), (*n*-Bu₄NBr) (*p*-DITFB) (d), (*n*-Bu₄PBr) (*p*-DITFB) (e), (EtPh₃PBr)₂ (*p*-DITFB) (f). Reproduced by permission of the Royal Society of Chemistry. From [39]



compound *p*-DITFB. The signals are weak for the reasons described above. Nevertheless, the signals of interest are well-resolved from the rest of the ^{13}C NMR spectrum due to the unique chemical shifts of carbon atoms which are directly bonded to a heavy nucleus like ^{127}I . This is due to a relativistic spin-orbit-induced

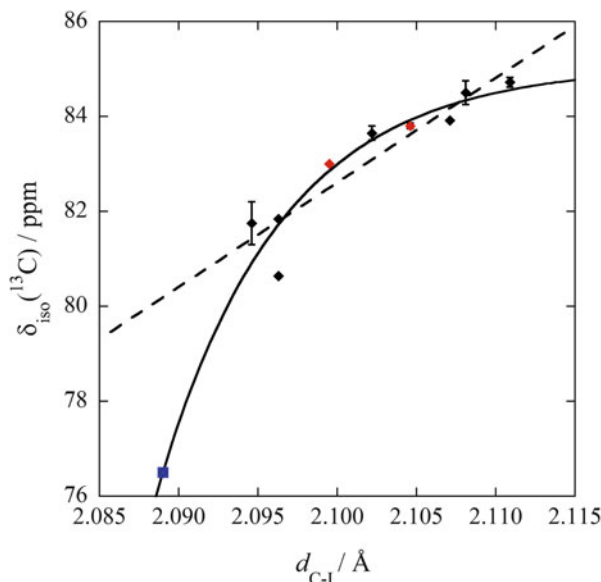


Fig. 9 Plot of experimental values of $\delta_{\text{iso}}(^{13}\text{C})$ as a function of the corresponding carbon–iodine distance, $d_{\text{C-I}}$, for carbons directly bonded to iodine for the compounds described in Fig. 8. The best fit represented by a *black line* is an exponential function: $\delta_{\text{iso}}(^{13}\text{C}) = 8.5629 \times (1 - \exp(-128.96\Delta d)) + 76.5$, Pearson correlation coefficient $R^2 = 0.9613$, where $\Delta d = d_{\text{C-I}}(\text{XB compound}) - d_{\text{C-I}}(p\text{-DITFB})$. A linear fit to the data for the halogen bonded complexes (*blue square* corresponding to *p*-DITFB excluded from fit) is described by: $\delta_{\text{iso}}(^{13}\text{C}) = 220.15d - 379.71$, $R^2 = 0.859$. Reproduced with permission of the Royal Society of Chemistry. From [39]

shielding effect [22]. For example, the range of shifts observed in Fig. 8 is 76.5–84.5 ppm, whereas protonated aromatic carbon resonances always exceed 100 ppm, and are typically closer to 140 ppm.

When plotted as a function of the C–I distance, a clear trend is observed (Fig. 9). As the C–I distance increases, so does the ^{13}C chemical shift. This general trend was reproduced using density functional theory calculations [39]. Interestingly, a clear correlation between the chemical shift and the reduced distance parameter, R_{XB} , was not obtained. However, as the C–I bond is known to lengthen upon halogen bonding, in this context the ^{13}C chemical shift is diagnostic of the strength of the halogen bond.

4 Conclusions and Outlook

NMR spectroscopy is a versatile site-specific probe of halogen bonding interactions in solids. As a result of the continued advances in NMR technology, more and more of the spin-active isotopes of the periodic table are becoming accessible for study.

In principle, NMR is capable of providing direct information on all three fragments of the halogen bond, namely the R, X, and Y components. This chapter has surveyed some of the results available for ^1H , ^{13}C , ^{77}Se , $^{14/15}\text{N}$, $^{35/37}\text{Cl}$, $^{79/81}\text{Br}$, and ^{127}I . Of particular interest is the correlation between the C–I distance and the ^{13}C chemical shift in halogen-bonded C–I \cdots Y motifs. The selenium chemical shift tensor is also a sensitive probe of halogen bonding in selenocyanate complexes.

The properties of the quadrupolar halogens render them amenable to study by NMR spectroscopy, but only under favorable conditions. In high magnetic fields it is feasible to record and interpret $^{35/37}\text{Cl}$ and $^{79/81}\text{Br}$ SSNMR spectra of chloride and bromide anions; ^{127}I SSNMR spectra of iodide anions are more challenging to acquire. With regard to covalently-bonded halogens, it is possible to record $^{35/37}\text{Cl}$ SSNMR spectra in very high magnetic fields, while recording NMR spectra for covalently-bonded bromine and iodine atoms is highly impractical if not impossible. $^{35/37}\text{Cl}$, $^{79/81}\text{Br}$, and ^{127}I SSNMR results obtained to date for halide anions involved in halogen bonds show the utility of the data in identifying isostructural compounds, and, in the case of bromine, a correlation between the chemical shift tensor and the X \cdots Br $^-$ halogen bond distance.

Future directions worthy of exploration include revisiting the spectroscopy of chloride, bromide, and iodide anions in compounds with stronger halogen bonds and in the absence of competing hydrogen bonds. Solid-state NMR studies of compounds containing halogen bonds remain relatively sparse to date, and it is clear that there are a wealth of opportunities for applying standard (e.g., ^{13}C CP/MAS, high-resolution ^1H) and advanced (e.g., correlation spectroscopy, ultrawide-line spectroscopy, high-resolution spectroscopy of quadrupolar nuclei) SSNMR techniques to the characterization of such compounds. The characterization of covalently-bonded chlorine atoms involved in halogen bonds via $^{35/37}\text{Cl}$ SSNMR should be pursued. Finally, one can envisage the possibility of measuring J couplings across halogen bonds in the solid state and in solution, analogous to what has been done in the case of hydrogen bonds. Such measurements, if successful, would provide a valuable new probe of halogen bonds.

Acknowledgements We are grateful to the Natural Sciences and Engineering Research Council of Canada for supporting our research in this area. J. V.-G. thanks the “Fonds de recherche du Québec – Nature et technologies” for a graduate scholarship.

References

1. Alkorta I, Elguero J, Denisov GS (2008) A review with comprehensive data on experimental indirect scalar NMR spin-spin coupling constants across hydrogen bonds. *Magn Reson Chem* 46:599
2. Aliev AE (2004) Probing hydrogen bonding in solids using solid state NMR spectroscopy. *Struct Bond* 108:1
3. Brunner E, Sternberg U (1998) Solid-state NMR investigations on the nature of hydrogen bonds. *Prog Nucl Magn Reson Spectrosc* 32:21

4. Wu G, Freure CJ, Verdurand E (1998) Proton chemical shift tensors and hydrogen bond geometry: a ^1H - ^2H dipolar NMR study of the water molecule in crystalline hydrates. *J Am Chem Soc* 120:13187
5. Bryce DL, Adiga S, Elliott EK, Gokel GW (2006) Solid-state ^{23}Na NMR study of sodium lariat ether receptors exhibiting cation- π interactions. *J Phys Chem A* 110:13568
6. Lee PK, Chapman RP, Zhang L, Hu J, Barbour LJ, Elliott EK, Gokel GW, Bryce DL (2007) K-39 quadrupolar and chemical shift tensors for organic potassium complexes and diatomic molecules. *J Phys Chem A* 111:12859
7. Plevin MJ, Bryce DL, Boisbouvier J (2010) Direct detection of CH/ π interactions in proteins. *Nat Chem* 2:466
8. Desiraju GR, Ho PS, Kloo L, Legon AC, Marquardt R, Metrangolo P, Politzer P, Resnati G, Rissanen K (2013) Definition of the halogen bond (IUPAC recommendations 2013). *Pure Appl Chem* 85:1711
9. Bryce DL (2012) Halogen bonding. *Chem Int* 34:27
10. Larsen DW, Allred AL (1965) Halogen complexes. III. The association of 2,4,6-trimethylpyridine and trifluoroiodomethane. *J Phys Chem* 69:2400
11. Bruno TJ, Martire DE, Harbison MWP, Nikolić A, Hammer CF (1983) Gas-liquid chromatographic and nuclear magnetic resonance study of haloform + di-*n*-alkyl ether + *n*-alkane mixtures at 30°C. *J Phys Chem* 87:2430
12. Martire DE, Sheridan JP, King JW, O'Donnell SE (1976) Thermodynamics of molecular association. 9. An NMR study of hydrogen bonding of CHCl_3 and CHBr_3 to di-*n*-octyl ether, di-*n*-octyl thioether, and di-*n*-octylmethylamine. *J Am Chem Soc* 98:3101
13. Green RD, Martin JS (1968) Anion-molecule complexes in solution. I. Nuclear magnetic resonance and infrared studies of halide ion-trihalomethane association. *J Am Chem Soc* 90:3659
14. Bertrán JF, Rodríguez M (1979) Detection of halogen bond formation by correlation of proton solvent shifts. 1. Haloforms in *n*-Electron Donor Solvents. *Org Magn Reson* 12:92
15. Bertrán JF, Rodríguez M (1980) Detection of halogen bond formation by correlation of proton solvent shifts. II - Methylene Halides in *n*-Electron Donor Solvents. *Org Magn Reson* 14:244
16. Messina MT, Metrangolo P, Panzeri W, Ragg E, Resnati G (1998) Perfluorocarbon-hydrocarbon self-assembly. Part 3. Liquid phase interactions between perfluoroalkylhalides and heteroatom containing hydrocarbons. *Tetrahedron Lett* 39:9069
17. Metrangolo P, Panzeri W, Recupero F, Resnati G (2002) Perfluorocarbon-hydrocarbon self-assembly. Part 16. ^{19}F NMR study of the halogen bonding between halo-perfluorocarbons and heteroatom containing hydrocarbons. *J Fluor Chem* 114:27
18. Messina MT, Metrangolo P, Navarini W, Radice S, Resnati G, Zerbi G (2000) Infrared and Raman analyses of the halogen-bonded non-covalent adducts formed by α , ω -diiodoperfluoroalkanes with DABCO and other electron donors. *J Mol Struct* 524:87
19. Tiers GVD (2000) Detection of oriented association via NMR dilution shifts in tetramethylsilane solvent. 4. Temperature coefficients for perfluoroalkyl halide systems. *J Fluor Chem* 102:175
20. Löhr H-G, Engel A, Josel H-P, Vögtle F, Schuh W, Puff H (1984) Three-dimensional linkage by electron donor-acceptor interactions: complexes of organic ammonium halides with triiodomethane. *J Org Chem* 49:1621
21. Rege PD, Malkina OL, Goroff NS (2002) The effect of Lewis bases on the ^{13}C NMR of iodoalkynes. *J Am Chem Soc* 124:370
22. Glaser R, Chen N, Wu H, Knotts N, Kaupp M (2004) ^{13}C NMR study of halogen bonding of haloarenes: measurements of solvent effects and theoretical analysis. *J Am Chem Soc* 126:4412
23. Sarwar MG, Dragisic B, Salsberg LJ, Gouliaras C, Taylor MS (2010) Thermodynamics of halogen bonding in solution: substituent, structural, and solvent effects. *J Am Chem Soc* 132:1646

24. Sarwar MG, Dragisic B, Sagoo S, Taylor MS (2010) A tridentate halogen-bonding receptor for tight binding of halide anions. *Angew Chem Int Ed* 49:1674
25. Carlsson A-CC, Gräfenstein J, Laurila JL, Bergquist J, Erdélyi M (2012) Symmetry of [N-X-N]⁺ halogen bonds in solution. *Chem Commun* 48:1458
26. Carlsson A-CC, Gräfenstein J, Budnjo A, Laurila JL, Bergquist J, Karim A, Kleinmaier R, Brath U, Erdélyi M (2012) Symmetric halogen bonding is preferred in solution. *J Am Chem Soc* 134:5706
27. Harris RK, Becker ED, Cabral de Menezes SM, Goodfellow R, Granger P (2001) NMR nomenclature. Nuclear spin properties and conventions for chemical shifts. *Pure Appl Chem* 73:1795
28. Bryce DL, Widdifield CM, Chapman RP, Attrell RJ (2011) Chlorine, bromine, and iodine solid-state NMR. *eMagRes*. doi:10.1002/9780470034590.emrstm1214
29. Chapman RP, Widdifield CM, Bryce DL (2009) Solid-state NMR of quadrupolar halogen nuclei. *Prog Nucl Magn Reson Spectrosc* 55:215
30. Widdifield CM, Chapman RP, Bryce DL (2009) Chlorine, bromine, and iodine solid-state NMR spectroscopy. *Annu Rep Nucl Magn Reson Spectrosc* 66:195
31. Grzesiek S, Cordier F, Jaravine V, Barfield M (2004) Insights into biomolecular hydrogen bonds from hydrogen bond scalar couplings. *Prog Nucl Magn Reson Spectrosc* 45:275
32. Ledbetter MP, Saielli G, Bagno A, Tran N, Romalis MV (2012) Observation of scalar nuclear spin-spin coupling in van der Waals complexes. *Proc Natl Acad Sci U S A* 109:12393
33. Del Bene JE, Alkorta I, Elguero J (2008) Spin-spin coupling across intermolecular F-Cl · · · N halogen bonds. *J Phys Chem A* 112:7925
34. Del Bene JE, Alkorta I, Elguero J (2010) Ab initio study of ternary complexes A···NCH···C with A, C = HCN, HF, HCl, ClF, and LiH: energetics and spin-spin coupling constants across intermolecular bonds. *J Phys Chem A* 114:8463
35. Alkorta I, Sanchez-Sanz G, Elguero J, Del Bene JE (2012) FCl:PCX complexes: old and new types of halogen bonds. *J Phys Chem A* 116:2300
36. Vinogradov E, Madhu PK, Vega S (2005) Strategies for high-resolution proton spectroscopy in solid-state NMR. *Top Curr Chem* 246:33
37. Lucken EAC (1969) Nuclear quadrupolar coupling constants. Academic, London
38. Viger-Gravel J, Korobkov I, Bryce DL (2011) Multinuclear solid-state magnetic resonance and X-ray diffraction study of some thiocyanate and selenocyanate complexes exhibiting halogen bonding. *Cryst Growth Des* 11:4984
39. Viger-Gravel J, Leclerc S, Korobkov I, Bryce DL (2013) Correlation between ¹³C chemical shifts and the halogen bonding environment in a series of solid *para*-diiodotetrafluorobenzene complexes. *CrystEngComm* 15:3168
40. Attrell RJ, Widdifield CM, Korobkov I, Bryce DL (2012) Weak halogen bonding in solid haloanilinium halides probed directly via chlorine-35, bromine-81, and iodine-127 NMR spectroscopy. *Cryst Growth Des* 12:1641
41. Semin GK, Babushkina TA, Khrlakyan SP, Pervova EY, Shokina VV, Knunyants IL (1971) I¹²⁷ NQR spectra of fluorinated α, ω-diiodoalkanes and complexes with amines. *Theor Exp Chem* 4:179
42. Blackstock SC, Lorand JP, Kochi JK (1987) Charge-transfer interactions of amines with tetrahalomethanes. X-Ray crystal structures of the donor-acceptor complexes of quinuclidine and diazabicyclo[2.2.2]octane with carbon tetrabromide. *J Org Chem* 52:1451
43. Bricklebank N, Godfrey SM, Mackie AG, McAuliffe CA, Pritchard RG, Kobryn PJ (1993) Diiodophosphoranes. Synthesis and structure in the solid state and in solution. *J Chem Soc Dalton Trans* 1993:101
44. Dillon KB, Waddington TC (1971) Structures of some dihalotriphenylphosphorus(V) compounds. *Nat Phys Sci* 230:158
45. Bouchmella K, Dutremez SG, Alonso B, Mauri F, Gervais C (2008) ¹H, ¹³C, and ¹⁵N solid-state NMR studies of imidazole- and morpholine-based model compounds possessing halogen and hydrogen bonding capabilities. *Cryst Growth Des* 8:3941

46. Weingarth M, Raouafi N, Jouvelet B, Duma L, Bodenhausen G, Boujlel K, Schöllhorn B, Tekely P (2008) Revealing molecular self-assembly and geometry of non-covalent halogen bonding by solid-state NMR spectroscopy. *Chem Commun* 5981
47. García MA, Cabildo P, Claramunt RM, Pinilla E, Torres MR, Alkorta I, Elguero J (2010) The interplay of hydrogen bonds and halogen bonds in the structure of NH-pyrazoles bearing C-aryl and C-halogen substituents. *Inorg Chim Acta* 363:1332
48. Bertani R, Metrangolo P, Moiana A, Perez E, Pilati T, Resnati G, Rico-Lattes I, Sassi A (2002) Supramolecular route to fluorinated coatings: self-assembly between poly(4-vinylpyridines) and haloperfluorocarbons. *Adv Mater* 14:1197
49. Nonappa, Lahtinen M, Kolehmainen E, Haarala J, Shevchenko A (2013) Evidence of weak halogen bonding: new insights in itraconazole and its succinic acid cocrystal. *Cryst Growth Des* 13:346
50. Widdifield CM, Cavallo G, Facey GA, Pilati T, Lin J, Metrangolo P, Resnati G, Bryce DL (2013) Multinuclear solid-state magnetic resonance as a sensitive probe of structural changes upon the occurrence of halogen bonding in co-crystals. *Chem Eur J* 19:11949
51. Baldrighi M, Cavallo G, Chierotti MR, Gobetto R, Metrangolo P, Pilati T, Resnati G, Terraneo G (2013) Halogen bonding and pharmaceutical cocrystals: the case of a widely used preservative. *Mol Pharm* 10:1760
52. Lemouchi C, Vogelsberg CS, Zorina L, Simonov S, Batail P, Brown S, Garcia-Garibay MA (2011) Ultra-fast rotors for molecular machines and functional materials via halogen bonding: crystals of 1,4-bis(iodoethynyl)bicyclo[2.2.2]octane with distinct gigahertz rotation at two sites. *J Am Chem Soc* 133:6371
53. Cauliez P, Polo V, Roisnel T, Llusar R, Fourmigué M (2010) The thiocyanate anion as a polydentate halogen bond acceptor. *CrystEngComm* 12:558
54. Gray L, Jones PG (2002) Secondary bonding interactions in some haloanilinium halides. *Z Naturforsch* 57b:61
55. Raatikainen K, Cametti M, Rissanen K (2010) The subtle balance of weak supramolecular interactions: the hierarchy of halogen and hydrogen bonds in haloanilinium and halopyridinium salts. *Beilstein J Org Chem* 6:4. doi:10.3762/bjoc.6.4
56. Perras FA, Bryce DL (2012) Direct investigation of covalently bound chlorine in organic compounds by solid-state ³⁵Cl NMR spectroscopy and exact spectral line-shape simulations. *Angew Chem Int Ed* 51:4227
57. Bowmaker GA (1976) Nuclear quadrupole resonance of charge transfer complexes. Part 3.-A ¹⁴N and ³⁵Cl N.Q.R. study of the 1:1 complex of 3,5-dichloropyridine with iodine monochloride. *J Chem Soc Faraday Trans 2* 72:1964
58. Bowmaker GA, Hacobian S (1968) Nuclear quadrupole resonance of charge transfer complexes. I. The trihalide ions. *Aust J Chem* 21:551
59. Bowmaker GA, Hacobian S (1969) Nuclear quadrupole resonance of charge-transfer complexes. II. The amine halogen complexes. *Aust J Chem* 22:2047
60. Bowmaker GA, Boyd PDW (1987) An SCF-MS-X α study of the bonding and nuclear quadrupole coupling in 1:1 complexes of amines with diatomic halogens and interhalogens. *J Chem Soc Faraday Trans 2* 83:2211

Anion Transport with Halogen Bonds

Andreas Vargas Jentzsch and Stefan Matile

Abstract This review covers the application of halogen bonds to transport anions across lipid bilayer membranes. The introduction provides a brief description of biological and synthetic transport systems. Emphasis is on examples that explore interactions beyond the coordination with lone pairs or hydrogen bonds for the recognition of cations and anions, particularly cation- π and anion- π interactions, and on structural motifs that are relevant for transport studies with halogen bonds. Section 2 summarizes the use of macrocyclic scaffolds to achieve transport with halogen bonds, focusing on cyclic arrays of halogen-bond donors of different strengths on top of calixarene scaffolds. This section also introduces methods to study anion binding in solution and anion transport in fluorogenic vesicles. In Sect. 3, transport studies with monomeric halogen bond-donors are summarized. This includes the smallest possible organic anion transporter, trifluoroiodomethane, a gas that can be bubbled through a suspension of vesicles to turn on transport. Anion transport with a gas nicely illustrates the power of halogen bonds for anion transport. Like hydrogen bonds, they are directional and strong, but compared to hydrogen-bond donors, halogen-bond donors are more lipophilic. Section 3 also offers a concise introduction to the measurement of ion selectivity in fluorogenic vesicles and conductance experiments in planar bilayer membranes. Section 4 introduces the formal unrolling of cyclic scaffolds into linear scaffolds that can span lipid bilayers. As privileged transmembrane scaffolds, the importance of hydrophobically matching fluorescent *p*-oligophenyl rods is fully confirmed. The first formal synthetic ion channel that operates by cooperative multiion hopping along transmembrane halogen-bonding cascades is described. Compared to homologs for anion- π interactions, transport with halogen bonds is clearly more powerful.

A. Vargas Jentzsch and S. Matile (✉)
Department of Organic Chemistry, University of Geneva, Geneva, Switzerland
e-mail: stefan.matile@unige.ch

Keywords Anion binding · Anion- π interactions · Calixarenes · Halogen bonds · Ion carriers · Ion channels · Ion transport · Lipid bilayers · Macrocycles · Membranes · Oligomers · *p*-Oligophenyls · Rigid-rod molecules · Vesicles

Contents

1	Introduction	206
2	Cyclic Oligomers	210
2.1	Concept	210
2.2	Synthesis	211
2.3	Ion Binding in Solution	211
2.4	Ion Transport Across Membranes	212
2.5	Computational Simulations	215
3	Monomers	216
3.1	Concept	216
3.2	Ion Transport in Vesicles	217
3.3	Ion Selectivity	219
3.4	Conductance Experiments in Planar Bilayers	220
3.5	Phase Behavior and Co-transporters	223
3.6	Computational Simulations	224
3.7	Crystal Structures	226
4	Linear Oligomers	227
4.1	Concept	227
4.2	Synthesis	229
4.3	Ion Transport in Vesicles	230
4.4	Structural Studies in Vesicles	232
5	Summary	235
	References	236

1 Introduction

The first synthetic ion channel was reported almost exactly four decades ago [1]. Since then, impressive progress with synthetic transport systems has led to the emergence and growth of an interdisciplinary field that is firmly rooted in organic synthesis but contributes significantly to a variety of current topics in chemical, biological, medicinal, and materials sciences. The current standing of the field has just been summarized for the first time in a special issue of *Acc Chem Res* [2]. The following introduction is thus kept to a minimum and focuses particularly on systems that are relevant for the topic of this review, i.e., the use of halogen bonds to transport anions across lipid bilayer membranes.

In the beginning, the transport of cations received much more attention than anion transport, perhaps because of the importance of this process for signal transduction in the nervous system. Selective ion transport can be achieved by ion carriers, ion channels, pores, or more complex systems. The smaller carriers

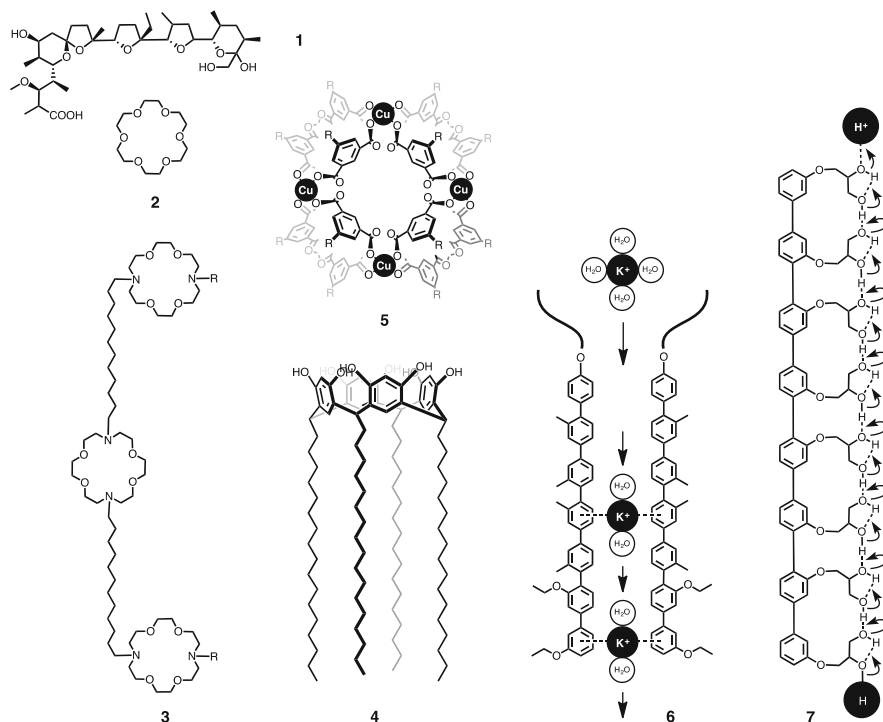


Fig. 1 Selected synthetic and biological cation transporters

move like ferries across the membrane during transport, whereas larger channels achieve the same result but much faster and without moving. Biological cation carriers and channels usually recognize cations by coordination to a preorganized array of multiple oxygen lone pairs. For structural motifs beyond peptide chemistry, monensin **1**, a marvelous polyketide natural product, can be cited as an example of a biological sodium carrier (Fig. 1). The best known synthetic cation carriers are crown ethers, such as **2**. In one of the first synthetic ion channels, three of these crown ethers have been linked together to provide a membrane-spanning scaffold with multiple cation-binding sites [3]. Cations could thus hop from crown to crown across the bilayer, while ion channel **3** does not have to move to mediate transmembrane cation transport. Since then, many other examples have been realized with crown ethers attached along transmembrane scaffolds of different natures [1, 2]. The construction of synthetic ion channels with calixarene macrocycles has been realized first with ion channel **4** [4]. Long alkyl chains have been attached at one face of the resorcinarene, whereas the other face contains hydrophilic hydroxy groups. This example is relevant for the topic of this review because unorthodox interactions are used in combination with calixarenes to achieve cation selectivity. The question as to whether or not the selection occurs while potassium cations pass through the π -basic macrocycle at the membrane–water interface has provoked

healthy discussion in the field. Similar cation- π interactions account for potassium selectivity with the metallorganic polyhedron **5**, while in cation- π slides **6**, the cyclic array of π -basic aromatics in **4** has been unrolled into a transmembrane scaffold for multiion hopping along the aromatic binding sites [5]. The same rigid *p*-oligophenyl rods were used as privileged scaffold to construct transmembrane hydrogen-bonded chains (HBCs) in proton transporters **7** [6].

This system has provided unprecedented access to the so-called Onsager mechanism, a cooperative hop-turn process that is thought to be essential in bioenergetics and related biological processes but has been difficult to explore within the context of synthetic transport systems [6]. In a first step, the proton ready to move across the membrane binds covalently to the acceptor at one end of the HBC. The proton bound to this acceptor is released and hops to the next acceptor, which releases the original proton for the next acceptor, and so on until the proton at the other end of the proton wire is released at the other side of the membrane (**7**, Fig. 1). In a second step, all alcohols involved in the HBC have to rotate 180° around their C–O bonds to return to the resting state and be ready to transport another proton in the same direction across the membrane. As with cooperative cation hopping along cation- π slides **6** (or in biological potassium channels), the proton entering the HBC **7** at one side of the membrane is not the same that exits at the other side. This cooperative multiion hopping across lipid bilayer membranes is essential to combine selectivity with speed, is ubiquitous in biological ion channels, and was the key to creating the first anion channel that operates with halogen bonds (see below).

More recently, the transport of anions across bilayer membranes has moved more into focus, the reasons including possible medicinal use with regard to cystic fibrosis and related channelopathies [7–11]. Other attractive applications of anion transport include separation and purification systems, sensing [12], artificial photosynthesis [13, 14], catalysis [15], drug delivery [16], and so on. The leading nonpeptide example from biology for anion transport is prodigiosin **8**, a red pigment produced by certain bacteria (Fig. 2) [7–11]. Many prodigiosin mimics have been reported. They all bind anions with multiple hydrogen-bond donors. Isophthalamides such as **9** and **10** have been very successful [17, 18]. Systematic simplification of the scaffolds leads to squaramides **11**, hydroxyamides **12**, or ureas and thioureas **13**, all remarkably active anion carriers despite their structural simplicity [9, 10, 19–21]. Among more sophisticated scaffolds, cholates as in **14** are most popular [22]. The self-assembly into anion channels has been demonstrated for isophthalamides **10** [11, 17] and the partial-cone configured calixarene **15** [23, 24]. As in all other examples, multiple hydrogen bonds have been proposed to account for the anion selectivity of anion channel **15**. Several other interactions have been explored to achieve anion transport across lipid bilayer membranes. A complete set of monomers **16** [25], cyclic oligomers **17** [26], and linear oligomers **18** [27] is available for transport with anion- π interactions. Larger architectures have been required to explore other interactions for anion transport. These include anion-macrodipole interactions in peptide urea nanotubes [28],

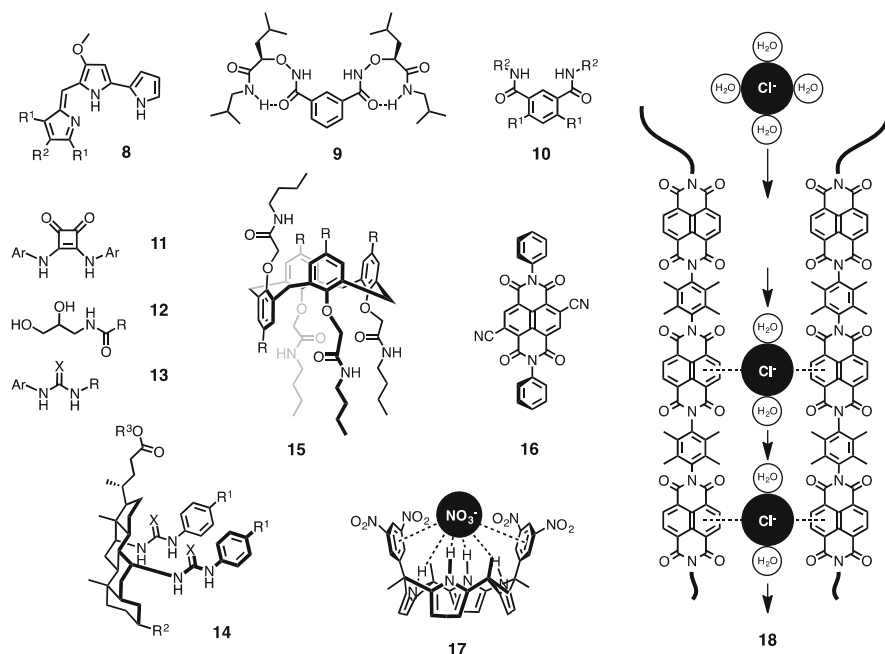


Fig. 2 Selected synthetic and biological anion transporters

multivalent ion pairing in artificial β -barrels [29], and aromatic electron donor–acceptor interactions in transmembrane π -stacks [13, 30].

Halogen bonds have not been used for transport until recently [31–33]. This is surprising because they appear ideal for this task. As elaborated in detail in this volume of *Top Curr Chem* [34], halogen bonds are strong and directional like hydrogen bonds [34–38]. However, halogen-bond donors are more lipophilic than hydrogen-bond donors. This intrinsic lipophilicity suggests that anion transport with halogen bonds could be very efficient. The functional relevance of halogen bonds has been demonstrated extensively for activities other than anion transport. Initial systematic studies focused on crystal engineering [34–39]. Wonderful applications to functional materials such as responsive hydrogels [40], imprinted polymers [41], foldamers [42], or capsules [43] followed. Rational drug design increasingly considers halogen bonds [44–46], and examples of biological relevance today go far beyond tyroxine, the thyroid, and the iodination of our cooking salt [45–47]. Several receptors for anion binding with halogen bonds in solution have been designed, synthesized, and evaluated [48–54]. The first explicit example of the application of halogen bonds to catalysis appeared in 2008 [55]. Recent progress with halogen-bonding catalysis indicates that this topic could grow rapidly in the near future [56–63]. In the following, the use of halogen bonds to transport anions across lipid bilayer membranes will be reviewed comprehensively. To facilitate reading and stimulate further use in a community

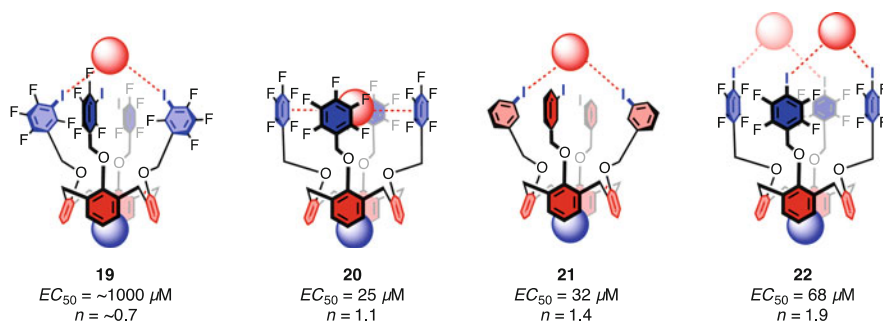


Fig. 3 Schematic structure of TMACl complexes of cyclic oligomers made to study transport with halogen bonds in combination with cation- π and anion- π interactions. *Red spheres* indicate chloride anions, *blue spheres* TMA cations, electron-rich regions are in *red*, electron-poor ones in *blue*. The effective concentration EC_{50} and the Hill coefficient n refer to transport activity in the HPTS assay

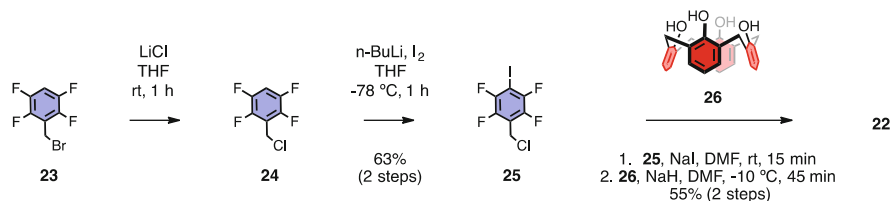
with little experience on the topic, the most important methods to characterize ion transport are briefly introduced when they appear first in the text, and background information is provided as appropriate. More detailed descriptions of analytical methods in the field can be found elsewhere [64].

2 Cyclic Oligomers

2.1 Concept

The rational design of the first anion transporter that operates with halogen bonds, i.e., calixarene **19**, was an almost complete failure (Fig. 3) [31]. The idea was to place four strong halogen-bond donors on top of a calix[4]arene scaffold. Perfluorophenyl groups were the obvious choice, iodination in the *meta* position being ideal to capture anions at the focal point of the activated halogen-bond donors above the macrocycle. Anion binding by halogen bonds would be supported by counterions bound within the calixarene macrocycle. Tetramethylammonium (TMA) would fit very well. The extent and exact nature of the contributions of cation- π interactions to TMA recognition within calix[4]arenes have been discussed extensively, including the crystal structures of the inclusion complexes that exist [31, 65–68]. The ditopic nature of calixarene **19** appeared ideal for the transport of an anion and a cation at the same time in the same direction. This process is referred to as symport, and the complementary anion or cation exchange across the membrane is referred to as antiport [64].

Calixarenes **20–22** were designed as control molecules. In **20** the iodines in **19** are replaced by fluorines. Without strong halogen-bond donors, anion binding by calixarene **20** could occur only by anion- π interactions [15, 25]. In **21**, the fluorines



Scheme 1 Synthesis of transporter **22**

in **19** are replaced by hydrogens. Anion recognition by halogen bonding should thus be weaker than with calixarene **19**. The same is true with the regioisomer **22**. Unfocused halogen bonds in the *para* position should be weaker anion binders. Moreover, the unfocused binding sites should be moved away from the counterion within the calixarene macrocycle.

2.2 Synthesis

The synthesis of the macrocyclic transporters **19–22** was embarrassingly easy. For the preparation of **22**, for example, the commercially available benzylbromide **23** was first inactivated by Finkelstein substitution with chloride (Scheme 1). The benzylchloride **24** obtained was iodinated, and the resulting iodoarenes **25** were attached to the calixarene scaffold **26** by routine Williamson ether synthesis.

2.3 Ion Binding in Solution

Anion binding in solution was measured by ^{19}F NMR spectroscopy [31]. All spectra were recorded in dry acetone- d_6 with α,α,α -trifluorotoluene ($\delta = -63.72$ ppm) as internal standard (Fig. 4a). The ^{19}F NMR spectrum of transporter **19** showed four distinct fluorine resonances with the expected coupling pattern (Fig. 4a, bottom line). In the presence of increasing concentrations of tetrabutylammonium chloride (TBACl), all four signals shifted upfield (the solubility of tetramethylammonium chloride (TMACl) was insufficient for titrations under these conditions). The observed shifts were plotted as a function of the concentration of TBACl, and the resulting curves were fitted to a 1:1 isotherm. For higher stoichiometries, good fitting was possible but not significant because the first K_D was already very weak. A $K_D = 18$ mM was obtained for **19**. A similar $K_D = 13$ mM was found for the *para* isomer **22**, whereas anion binding by the iodine-free anion- π receptor **20** was not detectable under these conditions. Similarly modest values have been reported previously for anion binding with halogen-bond donors in competing acetone.

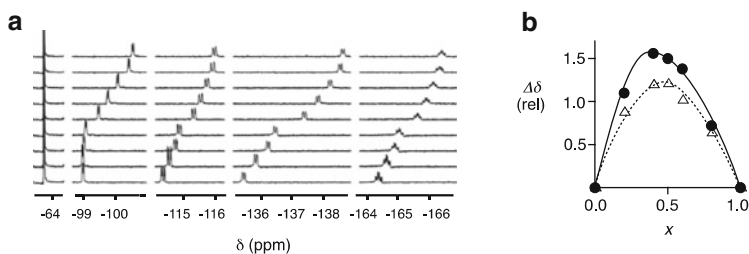


Fig. 4 (a) ^{19}F NMR spectra of **19** and α,α,α -trifluorotoluene (-63.7 ppm) in acetone- d_6 in the presence of increasing concentrations of TBACl. (b) Job plots for TBACl binding by **19** (open triangles) and **22** (filled circles), $x = [\text{TBACl}]/([\text{TBACl}] + [\text{transporter}])$. Adapted with permission from [31]. Copyright 2011 Wiley)

Whereas the binding isotherms for regioisomers **19** and **22** were nearly the same, their Job plots [69] showed subtle differences. TBACl binding under identical conditions in acetone- d_6 gave a 1:1 stoichiometry for *meta* isomer **19** (Fig. 4b, open triangles). The maximum around $x = 0.33$ in the Job plot of *para* isomer **22** supported the formation of a 2:1 complex (Fig. 4b, filled circles). This finding was in excellent agreement with the expectation that the halogen-bond donors in *meta* isomer **19** could focus on one anion, whereas the peripheral position of the halogen-bond donors in *para* isomer **19** are out of focus and could thus associate with two chloride anions (Fig. 3).

2.4 Ion Transport Across Membranes

The ideal method for initial screens on transport activity in lipid bilayers is the so-called HPTS assay [64] (Fig 5a). In this assay, large unilamellar vesicles (LUVs) are loaded with the pH-sensitive fluorophore 8-hydroxy-1,3,6-pyrenetrisulfonate (HPTS) [70]. For routine screens, egg yolk phosphatidylcholine (EYPC) is used. This is a mixture of lipids with the same, zwitterionic headgroup and different tails. The dominance of unsaturated tails affords bilayers in the liquid-disordered (L_d) phase, also referred to as liquid-crystalline or fluid phase. The obtained vesicles can be abbreviated as EYPC-LUVs \supset HPTS.

HPTS is the fluorescent probe of choice because of the complementary response of the two maxima in the excitation spectrum to changes in pH around the $pK_a \sim 7.3$ [64, 70]. One band decreases, the other increases. With the resulting possibility to detect pH changes ratiometrically, false positives can be excluded. To detect transport, a base pulse is applied to EYPC-LUVs \supset HPTS. This creates a pH gradient across the membrane. Then the transporter is added and the ability to accelerate the dissipation of the pH gradient is measured. Several transport processes can lead to this result (Fig. 5a). The intravesicular pH can increase due to either facilitated proton efflux or facilitated influx of OH^- . Proton efflux can be

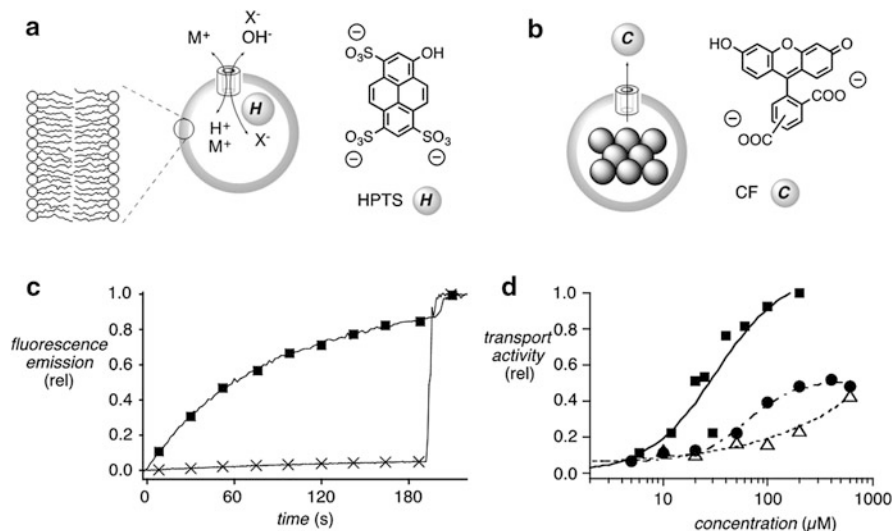


Fig. 5 Standard configuration of transport experiments in (a) the HPTS assays and (b) the CF assay in large unilamellar vesicles, compare text. (c) Original kinetics for “halogen-bonding” transporter **21** characterized with the HPTS assay (filled squares, 60 μM) and the CF assay (crosses, 600 μM). At 200 s, the vesicles are destroyed for calibration. (d) Dose response curve for **19** (open triangles), **21** (filled squares) and **22** (filled circles). Adapted with permission from [31]. Copyright 2011 Wiley

compensated either by cation antiport or anion symport. The same is true for the influx of OH^- . Finally, the efflux of the HPTS probe itself will increase the local pH around the probe as well. It is this failure of the HPTS assay to discriminate between all these processes that makes the method ideal for an initial screen for activity: almost everything can be seen. The possibility to discriminate between different processes with the same HPTS assay will be described later on.

Original fluorescence kinetics for transporter **21** at concentrations of 60 μM are shown in Fig. 5c, filled squares. The transporter is added at time zero. The steady increase in ratiometric HPTS emission demonstrates that **21** is active at concentrations of 60 μM . At the end of the experiment, the EYPC-LUVs \supset HPTS are destroyed with a detergent to determine the maximal possible emission intensity. This value is then used to calibrate the kinetic traces.

With evidence for transport activity in hand, the next question to ask concerns non-specific transport, i.e., leakage through more drastic defects in the bilayer membrane. This question can be addressed with the CF assay (Fig. 5b) [64]. In this assay, EYPC LUVs are loaded with CF at concentrations high enough for self-quenching to occur. CF efflux then reduces the local concentration and results in fluorescence recovery. Application of the CF assay to transporter **21** at ten times higher concentrations than that used in the HPTS assay, i.e., 600 μM , did not cause fluorescence recovery (Fig. 5c, crosses). This result demonstrated that the transport activity of **21** observed in the HPTS assay does not arise from non-specific defects

in the membrane. This implies that the activity originates from specific anion or cation symport or antiport. The same clean, defect-free transport activity was found for all other “halogen-bonding” transporters described in this review.

To quantify ion transport activity, dose response curves are recorded (Fig. 5d). The increase in the fractional transport activity Y with increasing concentration c_M of the monomeric transporter is fitted to the Hill equation (1):

$$Y = Y_{\text{MAX}} + (Y_{\text{MIN}} - Y_{\text{MAX}}) / \{1 + (c_M / \text{EC}_{50})^n\} \quad (1)$$

In the Hill equation, the EC_{50} , the effective concentration, describes the monomer concentration needed to reach 50% of the maximal detectable activity Y_{MAX} [64, 71]. Y_{MIN} is the activity observed without addition of the transporters. The Hill coefficient n describes the number of monomers needed to observe activity *as long as the active suprastructure is unstable* [72–74]. With stable supramolecules as active structures, $n = 1$ is observed because the Hill equation is not applicable in this form. Instead of the irrelevant monomer concentration c_M , the concentration of the dominant supramolecule c_S has to be inserted, with the result being necessarily $n = 1$. Interpretation of the frequently found $n < 1$ in terms of stoichiometry or stability of the active suprastructure is obviously nonsense. This situation is caused by the emergence of an inactivation mechanism at high monomer concentration. Usually, $n < 1$ indicates that the molecular or supramolecular transport system starts to precipitate at high concentrations before reaching the bilayer membrane. This behavior often coincides with $Y_{\text{MAX}} < 1$, indicating that not all vesicles can be reached by the transport system, i.e., irreversible partitioning due to excessive lipophilicity.

Hill analysis revealed that the rationally designed halogen-bonding transporter **19** is quite inactive (Fig. 5d open triangles). An $\text{EC}_{50} \sim 1$ mM is high under the conditions used in the HPTS assay (Fig. 3). Replacement of the iodines in halogen-bonding transporter **19** by fluorines in “anion- π ” transporter **20** caused, according to an $\text{EC}_{50} = 25$ μM , a 40-fold increase in activity (Fig. 3). Detectability of anion binding by halogen-bonding transporter **19** but not by anion- π transporter **20** in solution (see Sect. 2.3) suggested that anion recognition by halogen bonds in transporter **19** is too strong rather than too weak for transport. The dependence of transport activity on binding follows the “Goldilocks principle” because insufficient binding and insufficient release are both inhibitory [75].

This interpretation suggested that weakening of the halogen bonds in transporter **19** would increase activity. Replacement of the fluorines in transporter **19** by hydrogens in transporter **21** reduces the electron deficiency of the iodines and thus the magnitude of their σ hole [76]. This weakening of the halogen-bond donors in transporter **21** restored transport activity of the system. The most convincing dose response curve of the series gave an $\text{EC}_{50} = 32$ μM and a $Y_{\text{MAX}} = 1.0$ (Fig. 5, filled squares). This corresponds to a 31-fold increase in activity compared to the overachieving calixarene **19**.

The characteristics of the regioisomer **22** were most interesting. The loss of focus at the maintained strength of the halogen bonds resulted in a significant

increase in activity to an $EC_{50} = 68 \mu\text{M}$ (Fig. 3). However, inspection of the dose response curve reveals a low Y_{MAX} , suggesting that the *para* isomer presumably starts precipitating at higher concentrations. Moreover, a Hill coefficient of $n = 1.9$ was found, whereas all other macrocyclic transporters were consistent with monomeric active structures. Importantly, this Hill coefficient $n = 1.9$ does not correspond to the 2:1 stoichiometry found in the Job plot. The Job plot indicates that the *para* isomer **22** can bind two chloride anions in solution (acetone). The Hill coefficient $n = 1.9$ indicates that an unstable dimer of *para* isomer **22** accounts for anion transport across the bilayer membranes. Both complexes, 1:2 in solution and 2:1 in the membrane, are a direct consequence of the lack of focus of the halogen-bond donors in calixarene **22**.

In summary, the rational design of anion binding at the focal point of four strong halogen-bond donors in cyclic oligomers **19** provides anion transporters with poor activity. Increasing transport activity with weaker halogen bonds in **21** or less focused halogen bonds in **22** implies that the poor activity of **19** originates from too strong anion binding (i.e., poor dissociation) rather than too weak anion binding (i.e., poor association). A more dramatic way to reduce the strength of halogen bonding in anion transporters will be described in Sect. 3 on monomers. Before that, computational insights on anion binding by cyclic oligomers will be briefly summarized.

2.5 Computational Simulations

Computational simulations of anion transporters **19–21** revealed a delightfully complex situation (Fig. 6). The general trends were in full agreement with experimental results. Density functional theory (DFT) modeling afforded the highest binding energy of $-70.9 \text{ kcal mol}^{-1}$ for the TMACl complex of the overachiever **19**. Binding energies dropped to $-58.3 \text{ kcal mol}^{-1}$ with the anion- π interactions in transporter **20** and to $-59.7 \text{ kcal mol}^{-1}$ with the weakened halogen bonds in transporter **21**. These results provided support for the interpretation that the transport activity of calixarene **19** is poor because anion binding is too strong.

On the structural level, however, the DFT models of the TMACl complexes were less ordered than expected. In the overachieving complex **19**, only two out of the four focused halogen bonds contribute to anion binding (Fig. 6a). The other two iodines turn away from the anion, probably because of steric hindrance, with their electron-deficient σ holes [76] nicely visible as blue circles on top of the two atoms. The same is found for anion- π interactions in complex **20**. Only one of the π -acidic phenyls binds the chloride at the center (Fig. 6b). Two show more peripheral contacts; the fourth ring is far from the anion.

The most interesting structure is found for the most active halogen-bonding transporter **21**. Two vicinal iodophenyls participate in halogen bonding with the correct linear geometry. The other two iodines are turned away from the anion and reveal the presence of a significant σ hole although the iodine is not particularly

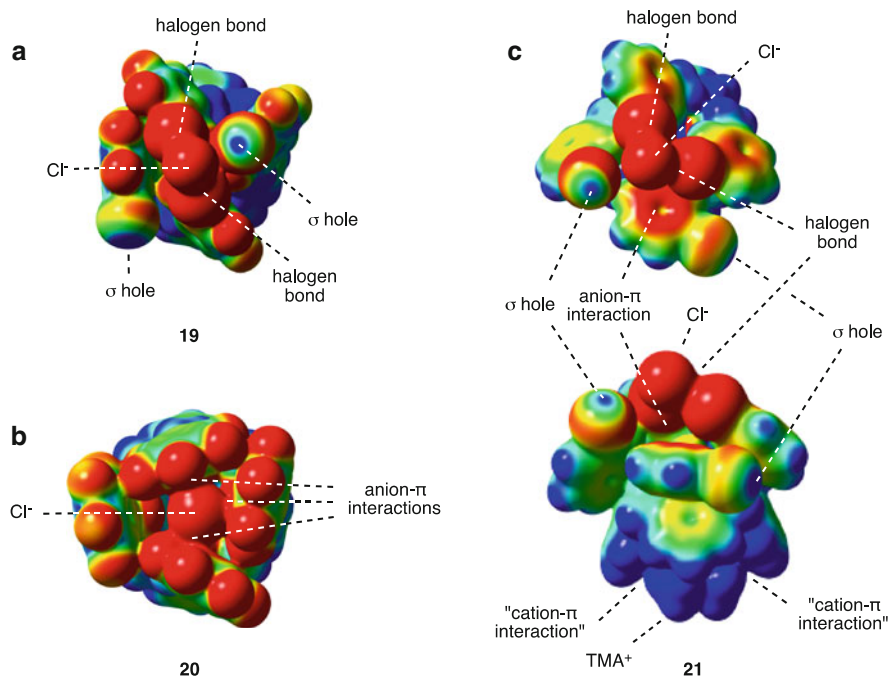


Fig. 6 Electrostatic potential surfaces of DFT-minimized TMACl complexes of transporters **19**, **20**, and **21** in top view and **21** also in side view (*blue* positive, *red* negative). Adapted with permission from [31]. Copyright 2011 Wiley

electron deficient. The iodine closer to the anion receives electron density through a non-classical lateral contact with the anion. Most interesting is the contact of the anion with the surface of one phenyl ring. The red aromatic surface demonstrates that some of the negative charge of the anion is transferred. This is remarkable because this phenyl ring is π -basic and thus intrinsically repulsive for anions. Transporter **21** thus provides another example that anion- π interactions with π -basic aromatics are possible, presumably due to the polarizability of the aromatic system.

3 Monomers

3.1 Concept

Halogen bonds are particularly promising for anion transport across lipid bilayer membranes because they are strong and directional like hydrogen bonds, but halogen-bond donors are intrinsically more hydrophobic than hydrogen-bond

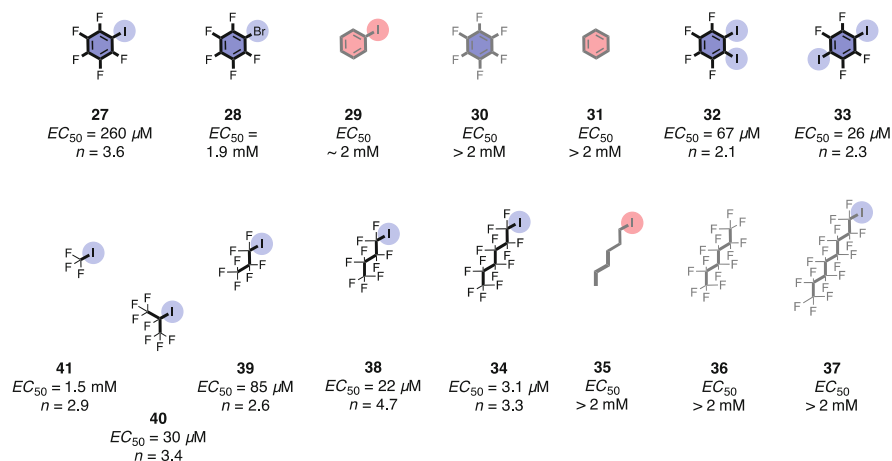


Fig. 7 Monomeric halogen-bond donors and controls used to study transport with halogen bonds in combination with cation- π and anion- π interactions. Electron-rich regions are in red, electron-poor ones in blue, EC_{50} and n refer to transport activity in the HPTS assay

donors. Results with rationally designed halogen-bonding arrays in cyclic oligomers **19** suggest that preorganized anion recognition by multiple strong halogen bond donors is already too good for efficient transport (Fig. 3). One solution to achieve anion transport is to weaken the strength of the halogen-bond donors in cyclic oligomers **21** and **22**. Another, more dramatic solution to weaken halogen bonding is to remove the entire calixarene in **19** and use monomeric halogen-bond donors instead. To elaborate on this idea, a fairly large collection of small, commercially available molecules including **27–41** was tested for transport activity in fluorogenic vesicles (Fig. 7). The results were both surprising and quite remarkable [32].

3.2 Ion Transport in Vesicles

The ability of small, monomeric halogen-bond donors and controls **27–41** to transport anions across lipid bilayer membranes was tested first with the HPTS and the CF assay as described in Sect. 2.4 (Fig. 7) [32]. With an $EC_{50} = 260 \mu\text{M}$, pentafluoriodobenzene **27** was four times more active than the rationally designed cyclic array of the same perfluorinated iodophenyls in the cyclic oligomer **19**. This quite remarkable finding confirmed that the activity of calixarene **19** is poor because anion binding is too strong and, most importantly, that halogen bonds are ideal to transport anions across lipid bilayers. All controls were in agreement that the activity of pentafluoriodobenzene **27** originates from halogen bonding. Weakening of halogen bonds in **28** and **29** reduced activity. The anion- π and cation- π controls **30** and **31** were inactive. Phenol as a minimalist

hydrogen-bonding homolog was also inactive. Divalent halogen-bond donors **32** and **33** were most active. Particularly the high activity of the *para* diiodobenzene **33**, equipped with two halogen-bond donors that can never bind to the same anion, supported the existence of higher-order active structures.

Highest activities were found in the alkyl rather than in the aryl series. With an $EC_{50} = 3.1 \mu\text{M}$, perfluoroiodohexane **34** was the most active halogen-bonding transporter observed so far. Controls **35** and **36** with weakened and absent halogen bonds confirmed that halogen bonds account for the high activity of **34**. Homologs such as **37** with longer perfluoroalkyl tails were inactive. This result confirmed that, with longer chains, self-assembly and eventual precipitation dominate over the partitioning into the lipid bilayers. With shorter tails, activities decreased gradually from the perfect perfluoroiodohexane **34** with $EC_{50} = 3.1 \mu\text{M}$ over perfluoroiodobutane **38** with $EC_{50} = 22 \mu\text{M}$ to perfluoroiodopropane **39** with still respectable $EC_{50} = 85 \mu\text{M}$. The branched *iso*-propane **40** was, with an $EC_{50} = 30 \mu\text{M}$, about three times more active than the linear isomer **39**. High Hill coefficients up to $n = 4.7$ for perfluoroiodobutane **38** and decreasing activity with decreasing tail length suggested that for transport, at least five halogen-bond donors bind around one anion and thus encapsulate the hydrophilic anion within a lipophilic shell (see Sects. 3.5 and 3.6). The branched tails in **40** are presumably better suited to shield the anion from the hydrophobic environment of the membrane than the linear tails in isomer **39**.

Transport activity was still detectable for trifluoroiodomethane **41**. This finding was remarkable because trifluoroiodomethane **41** is by definition the smallest possible organic anion transporter, composed of one carbon atom and five atoms in total. With a boiling point of -22°C , the gas was bubbled through a suspension of fluorogenic vesicles to turn on transport. Considering the peculiar experimental conditions, the found $EC_{50} = 1.5 \text{ mM}$ could be considered as a likely underestimate. In any case, although very weak, the anion transport mediated by trifluoroiodomethane **41** was clearly detectable in the HPTS assay. This perfect “atom efficiency” with the smallest possible organic anion transporter provides a marvelous illustration of the power of halogen bonds to transport anions across lipid bilayer membranes. Methanol as a hydrogen-bonding homolog is inactive.

Iodide and bromide transporters composed of even less atoms than trifluoroiodomethane are molecular iodine and also bromine [77, 78]. Although contributions from halogen bonds to this process are likely, the situation is more complex and presumably dominated by covalent bonds in I_3^- and the like. However, without carbon atoms, iodine and bromine are not organic transporters, and, in contrast to the gaseous trifluoroiodomethane (boiling point -22°C), they are liquids (bromine: boiling point 59°C) or even solids (iodine, melting point 114°C [79]).

Weaker halogen bonds, as in pentafluorobromobenzene **28**, gave very poor activity. Inhalational general anesthetics such as halothane, i.e., 2-bromo-2-chloro-1,1,1-trifluoroethane, did not act as anion transporters. This is consistent with the fact that the bromine in halothane is not essential.

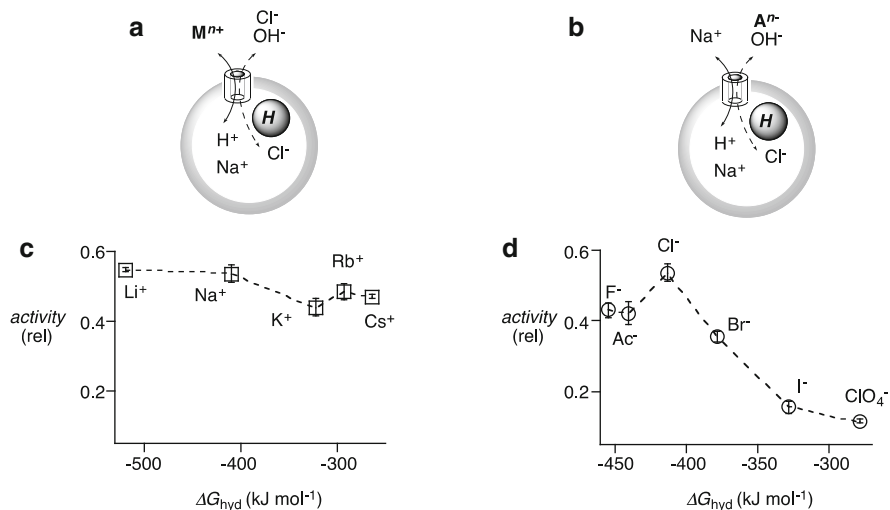


Fig. 8 (a) In the HPTS assay, dependence of transport activity on external cation exchange reveals cation selectivity. (b) The complementary dependence of transport activity on external anion exchange reveals anion selectivity. (c) Independence of the transport activity on the hydration energy ΔG_{hyd} of external cations indicates that transporter **32** is not a cation transporter (100 mM MCl, inside 100 mM NaCl). (d) An anti-Hofmeister selectivity topology indicates that **32** is an anion transporter and that anion binding to the transporter overcompensates the cost of anion dehydration (100 mM NaX, inside 100 mM NaCl). Adapted from [32] with permission, © 2012 Nature Publishing Group

3.3 Ion Selectivity

Transport activity in the HPTS assay originates either from anion transport, cation transport, or non-specific leakage through larger defects (Fig. 5a). Occurrence of the latter could be excluded by inactivity in the CF assay (Fig. 5b). Discrimination between anion and cation transport is of course vital for the characterization of synthetic transport systems that operate with halogen bonds. Namely, operational halogen bonds require anion selectivity, and the selective transport of cations would exclude significant contributions from halogen bonds.

In the HPTS assay the selectivity of ion transport is determined by external ion exchange (Fig. 8) [64]. To determine the influence of cations on transport, the original sodium cations are replaced by lithium, potassium, rubidium, and cesium cations, and changes in activity are recorded (Fig. 8a). In so-called cation selectivity topologies, these changes are plotted as a function of the hydration energy of the cations [64, 80–83]. For the diiodobenzene **32**, transport activities in the HPTS assay did not change much in response to external cation exchange (Fig. 8c). This result suggested that cations are presumably not involved in transport.

The influence of anions on the transport activity of diiodobenzene **32** was determined by external anion exchange (Fig. 8b). In sharp contrast to the

insensitivity toward external cation exchange, external anion exchange influenced the activity of diiodobenzene **32** significantly (Fig. 8d). Except for fluoride and acetate, transport activities decreased with decreasing cost of anion dehydration. Results for fluoride and acetate have to be interpreted with caution because these comparably strong bases can temporarily bind a proton and cross the bilayer membrane as neutral conjugate acids [84]. Anion selectivity topologies characterized by decreasing activities with decreasing cost of dehydration are referred to as “anti-Hofmeister” topologies [64]. In Hofmeister selectivity topologies, activities are exclusively determined by the cost of dehydration [64, 81]. In the complementary anti-Hofmeister topologies, the cost of dehydration is overcompensated by anion binding to the transporter. The anti-Hofmeister topologies found for diiodobenzene **32** and other transporters tested thus supported the importance of anion binding to the transporters, i.e., existence and significance of halogen bonds at work.

3.4 Conductance Experiments in Planar Bilayers

Because of the exceptional significance of the results obtained with the HPTS assay in vesicles, the transport activity of small monomers that operate with halogen bonds was further investigated in planar bilayer conductance experiments [64]. These experiments use two chambers named *cis* and *trans* that are both filled with buffer and are separated by a wall (Fig. 9a). This wall contains a tiny hole, with a diameter in micrometers, the smaller the better, connecting the two chambers. In this hole, the planar lipid bilayer is formed. The two chambers are then connected to electrodes to apply a potential. In the absence of ion carriers, channels, or pores, current cannot flow between the electrodes because the lipid bilayer membrane acts as an insulator. With the help of ion carriers, channels, or pores, the electrolytes can cross the hydrophobic barrier and connect the two electrodes. The resulting currents can then be used to characterize the involved transporters.

In response to the addition of pentafluoroiodobenzene **27** to one of the two chambers, a current started to flow across the planar lipid bilayer (Fig. 9b). This current gradually increased until saturation was reached after about 20 min. This behavior is characteristic for ion carriers. Conductance experiments in planar lipid bilayers with ion channels are special because the currents flowing through single ion channels can be detected. An example of single-channel measurements with a synthetic ion channel composed of folate quartets is shown in Fig. 9c [85]. With time, the opening and closing of single ion channels is observed as the instantaneous appearance and disappearance of new current levels. These opening and closing events occur with the irregular patterns that are characteristic for the stochastic behavior of single molecules [64, 86]. The occurrence of current levels with different magnitudes demonstrates the co-existence of different active structures (Fig. 9c, inset). From the single-channel conductance, the inner diameter of the active structure can be estimated. The average lifetime of an open single

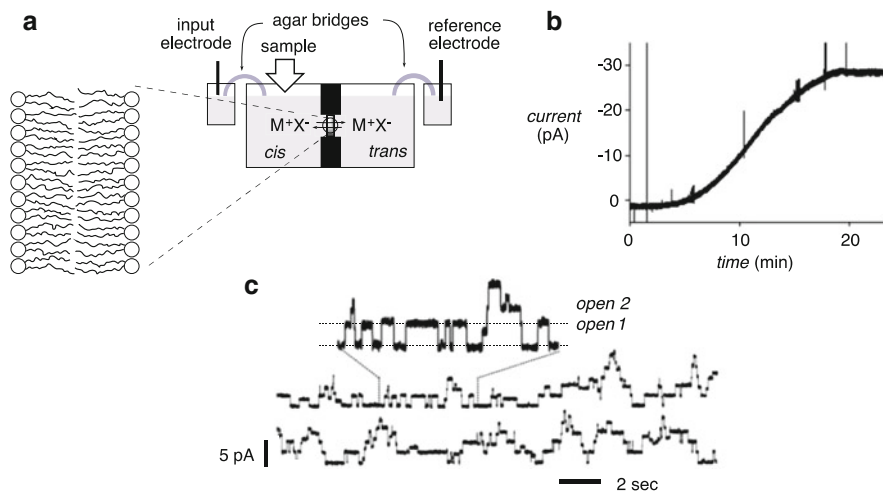


Fig. 9 (a) Standard configuration of conductance experiments in planar lipid bilayers. (b) Current flowing across planar lipid bilayers in response to the addition of pentafluoroiodobenzene **27** to the *cis* chamber and the application of a voltage of $V = -50$ mV (2 M KCl *cis* and *trans*). Adapted from [32] with permission, © 2012 Nature Publishing Group. (c) Characteristic single-channel currents measured for synthetic transport systems composed of folate quartets. Reproduced with permission from [85]. Copyright 2006 American Chemical Society

channel reveals the kinetic stability of the active structure; the thermodynamic stability is given by the open probability. For pentafluoroiodobenzene **27** and other small monomeric halogen-bonding transporters tested, these characteristics of ion channels could not be observed. This absence of single-channel currents supports the presence of ion carriers, although it does not prove that ion channels do not exist.

In conductance experiments, it is obviously very straightforward to determine the dependence of the activity on the external voltage applied to the planar bilayer. For pentafluoroiodobenzene **27** and related small monomeric halogen-bonding transporters, this voltage dependence was not linear (Fig. 10a). In other words, these very small ion carriers violate Ohm's law. Such non-ohmic ion transporters are described by (2):

$$Y \propto \exp(z_g eV/kT) \quad (2)$$

where Y is the measured activity, usually the current, e the elementary charge, k the Boltzmann constant, T the absolute temperature, and V the applied voltage [64]. The gating charge z_g is obtained from exponential curve fit. For small monomeric halogen-bonding transporters such as **27**, gating charges up to $z_g = 0.41$ were determined. Voltage dependence is a key characteristic of biological ion channels. It is essential for neural signal transduction and is thus optimized to much higher gating charges with highly sophisticated gating mechanisms. Synthetic anion

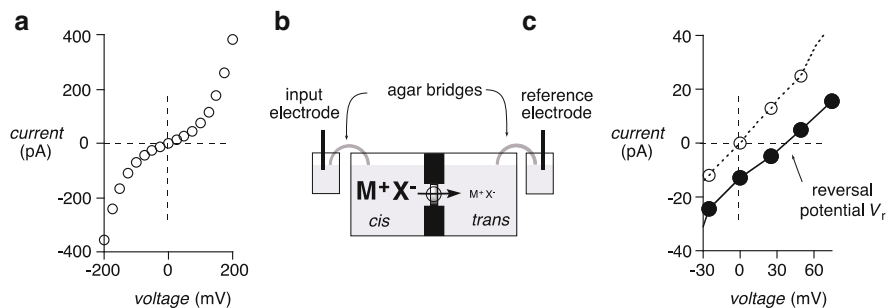


Fig. 10 Voltage dependence and ion selectivity of monomeric halogen-bonding transporters in planar bilayer conductance experiments. (a) Dependence of the current on the applied voltage V after the addition of pentafluoriodobenzene **27** to the *cis* chamber (2 M KCl *cis* and *trans*). (b) Configuration of conductance experiments in planar lipid bilayers to determine anion/cation selectivity. (c) I - V profile for **27** with 2 M KCl *cis* and *trans* (open circles) or 2 M KCl *cis* and 0.25 M KCl in *trans* (filled circles). Adapted from [32] with permission, © 2012 Nature Publishing Group

channels with much higher gating charges have been reported as well [87]. However, gating charges up to $z_g = 0.41$ are significant values for ion carriers [88, 89]. They imply that association and dissociation at the membrane surface is fast compared to translocation, and that ion selectivity is very high. In this situation, high gating charges originate from the direct acceleration of the translocation of the loaded carrier across the membrane; that is true current rectification.

The implication that non-ohmic minimalist halogen-bonding transporters such as **27** operate with high anion selectivity was confirmed quantitatively. Ion selectivity experiments in the HPTS assay give quantitative results for anion or cation selectivity topologies but only qualitative insights for the selectivity between anions and cations (see Sect. 3.3). To measure the selectivity between anions and cations quantitatively, conductance experiments in planar bilayers are perfect. An excess electrolyte, e.g., KCl, is added in one of the two chambers to generate a current also without the application of voltage (*cis* in Fig. 10b) [64]. The sign of this “zero current” already shows if anions or cations are transported across the membrane. The negative zero current found for pentafluoriodobenzene **27** demonstrated that anions are transported, i.e., it confirms the results from the HPTS assay and thus the existence of operational halogen bonds (Fig. 10c, filled circles). To quantify anion selectivity in conductance experiments, the voltage needed to stop the zero current from flowing is determined. The measured reversal potential V_r is then inserted into the Goldman–Hodgkin–Katz (GHK) voltage equation (3):

$$P_{A^-}/P_{M^+} = [a_{M^+cis} - a_{M^+trans} \exp(-V_r F/RT)]/[a_{A^-cis} \exp(-V_r F/RT) - a_{A^-trans}] \quad (3)$$

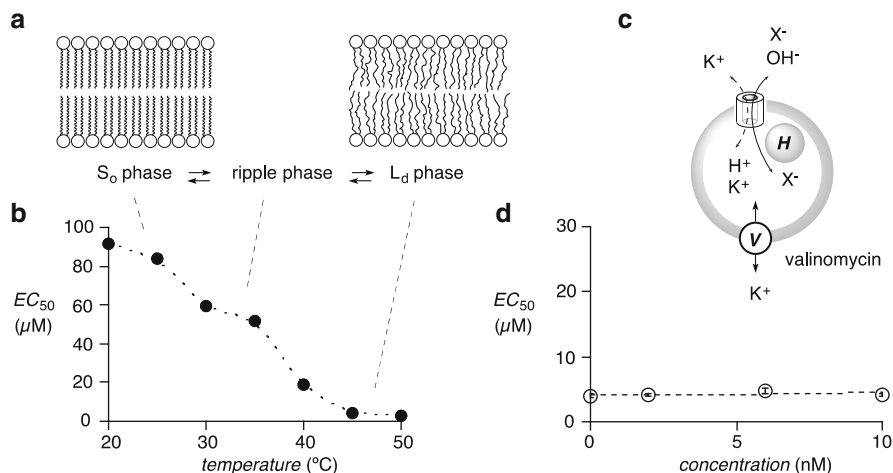


Fig. 11 (a) Upon heating, DPPC membranes change from the solid-ordered (S_o) phase to the ripple phase around 34°C and to the liquid-disordered (L_d) phase at 41°C . (b) Dependence of the EC_{50} of nonafluoro-1-iodobutane **38** in DPPC-LUVs \supset HPTS as a function of temperature. (c) Addition of the cation-carrier valinomycin V can clarify transport mechanisms in the HPTS assay. (d) Dependence of the EC_{50} of perfluoroiodohexane **34** in EYPC-LUVs \supset HPTS on the concentration c of valinomycin. Adapted from [32] with permission, © 2012 Nature Publishing Group

In this equation, $a_{M\text{cis}}$ and $a_{M\text{trans}}$ are the cation activity in *cis* and *trans* chambers, $a_{A\text{cis}}$ and $a_{A\text{trans}}$ the anion activity in *cis* and *trans*, R the gas constant, T the absolute temperature, and F the Faraday constant [64, 88]. For minimalist halogen-bonding transporters including **27**, anion/cation permeability ratios up to $P_{A^-}/P_{M^+} = 37$ have been determined. These are exceptional values. They demonstrate that halogen-bonding transporters operate by a clean anion antiport mechanism. High anion/cation selectivity is not unusual for ion carriers [90], whereas the combination of selectivity with speed is one of the central challenges with ion channels. Biological anion channels operate with $P_{A^-}/P_{M^+} \sim 5$ [91].

3.5 Phase Behavior and Co-transporters

The characterization of synthetic transport systems in lipid bilayer membranes can be an endless story. A fine balance between depth and breadth is often critical to develop a meaningful study. More interesting systems will naturally call for more experiments. For minimalist halogen-bonding transporters, the dependence of activity on membrane phase behavior and co-transporters nicely illustrates what else can be done and learned (Fig. 11).

The temperature dependence of ion transport in EYPC LUVs vesicles is usually not very interesting because these membranes exist in the same liquid-disordered

(L_d) phase at all easily accessible temperatures. The temperature dependence of ion transport in DPPC (dipalmitoyl phosphatidylcholine) vesicles is much more interesting because DPPC membranes exist in different phases at different temperatures (Fig. 11a). Above their main transition at 41°C, DPPC membranes exist like EYPC membranes in the liquid-crystalline L_d phase [92, 93]. Below 41°C, DPPC membranes first cool into a so-called ripple phase and then into the crystalline solid-ordered (S_o) phase. Decreasing activity with decreasing membrane fluidity was found for the halogen-bonding transporter **38** (Fig. 11b). This phase dependence is often considered to support a carrier mechanism because ion carriers should move easier through L_d membranes, whereas ion channels should be stabilized in S_o membranes [64]. In most cases this interpretation is incorrect. Low activities in S_o membranes usually originate from hindered partitioning and are observed for both carriers and channels [94]. However, for minimalist halogen-bonding transporters, evidence is increasing that they really act as carriers, including the absence of single-channel currents in planar bilayers. The observed temperature dependence in DPPC membranes certainly does not argue against this conclusion (see Sect. 3.4, Fig. 9b). The ripple phase was also detectable as a distinct shoulder in the temperature profile of the transporter **38** (Fig. 11b). Both pretransition and main phase transition of DPPC can be identified as sharp changes in activity. In the L_d phase of DPPC above 45°C, transport activity was roughly independent of temperature.

Further insights on the transport process can be obtained from additives. This is particularly true for co-transporters. For example, the presence of selective proton transport can be identified in the HPTS assay only with the addition of valinomycin, a selective potassium transporter [6] (Fig. 11d). Selective proton transport in one direction can then be compensated by selective potassium transport in the other, leading to accelerated dissipation of the pH gradient monitored in the HPTS assay. In this situation, a huge increase in activity is observed in the presence of valinomycin [6]. The activity of minimalist halogen-bonding transporters in EYPC vesicles was independent of the presence of valinomycin (Fig. 11d). This result supported the suggestion that halogen-bonding transporters operate with a clean and efficient anion antiport, i.e., cations are not involved in the process, and facilitated cation transport is insufficiently effective to turn on additional anion–cation symport. This conclusion was consistent with all results on ion selectivity, including very high anion/cation permeability ratios in conductance experiments (see Sects. 3.3 and 3.4), and with poor activity in anionic vesicles.

3.6 Computational Simulations

The main origin of halogen bonds has been attributed the σ hole that appears on top of electron deficient halogen atoms [76]. The textbook example is the iodine atom in trifluoroiodomethane **41**, the smallest possible organic halogen-bond donor that, with this work [32], is also the smallest organic anion transporter that exists

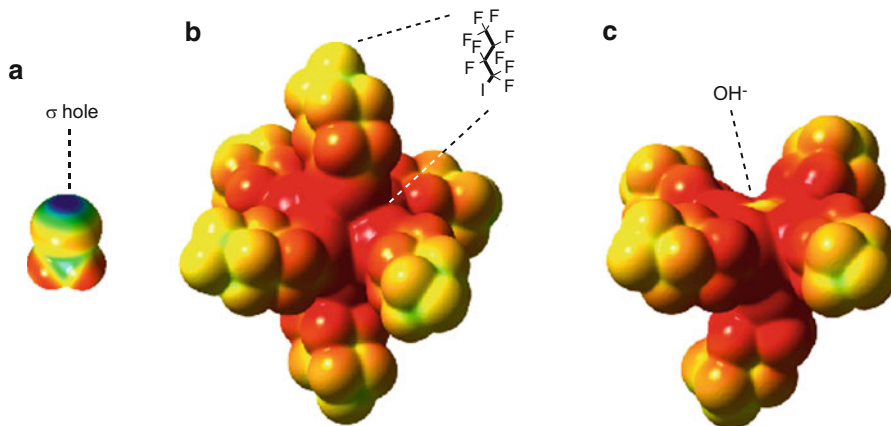


Fig. 12 DFT optimized structures of halogen-bonded transport systems. (a–c) Electrostatic potential surfaces of (a) CF_3I **41** and DFT optimized structures of halogen-bonded transport systems composed of (b) six perfluoro-1-iodobutanes **38** surrounding a chloride and (c) five transporters **38** surrounding a hydroxide anion (blue positive, red negative). Adapted from [32] with permission, © 2012 Nature Publishing Group

(Figs. 7 and 12a). The highly localized electron deficient area functions as halogen-bond donor that can interact strongly and directionally with electron-rich centers such as lone pairs of carbonyls, nitrogens, or, naturally, anions. The size of the σ hole determines the strength of the halogen bond. They are strongest with the most electron-deficient iodines in perfluorinated arenes or alkanes. Iodines in unfluorinated arenes, as in the hormone tyroxine or transporter **21** (Fig. 6c), or bromines and chlorines in perfluorinated arenes or alkanes, have smaller σ holes and thus form weaker halogen bonds.

To explain how simple perfluoroiodoalkanes can transport anions across lipid bilayers, several σ holes were docked onto an anion (Fig. 12b). In the most stable complex, the iodines form an almost perfect octahedron around the anion. With the characteristic angle of 180° between the halogen bond and the iodine-carbon bond, the perfluoroalkyl chains extend this quasi-octahedral geometry to encapsulate the anion with a hydrophobic shell. DFT calculations in the “membrane-mimetic” gas phase [25] gave increasingly stable complexes with an increasing number of transporters bound around the anion. Six halogen-bonded ligands **38** placed around one chloride gave a binding energy of $-376.9 \text{ kJ mol}^{-1}$. Only five ligands **38** could be placed around one hydroxide because position six in the octahedron around the oxygen is occupied by the hydrogen atom (Fig. 12c). This stoichiometry of the active structure was in good agreement with Hill coefficients up to $n = 4.7$ found for perfluoro-1-iodobutane **38**. An active structure with five to six minimalist halogen-bonding transporters wrapping around the anions provides also good arguments to explain why transport activities in the alkyl series decrease with decreasing length and why branched alkyls are better than linear ones (Fig. 7).

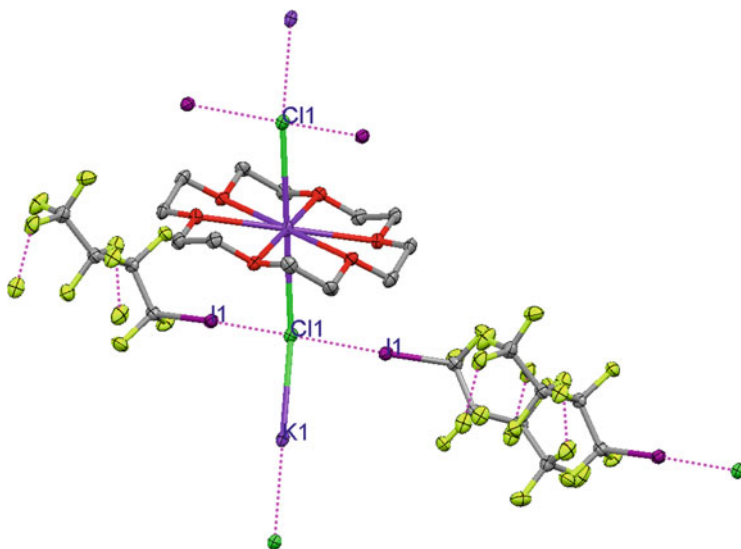


Fig. 13 Part of the crystal structure of the complex of two nonafluoro-1-iodobutanes **38** bound to chloride with potassium in 18-crown-6 as counterion. Hydrogen atoms are omitted for clarity, carbons are gray, oxygens red, fluorines light green, chlorines green, potassiums violet, and iodines purple. Adapted from [32] with permission, © 2012 Nature Publishing Group

The substitution of the five to six halogen-bond donors around the anions with the same number of water molecules reduced the binding energies. This result was consistent with the observed anti-Hofmeister selectivity topology (Fig. 8d). Weaker halogen bonds generated by the substitution of iodine by bromine as in pentafluoro-bromobenzene **28** or by arene defluorination as in iodobenzene **29** were correctly reflected by reduced stability of the respective quasi-octahedral active structures. This result confirmed insufficient halogen bonding as the origin of the poor activity of these control molecules (Fig. 7), and thus provided corroborative support that halogen bonds account for the observed anion transport activity.

3.7 Crystal Structures

A crystal structure of transporter **38** was obtained together with KCl and 18-crown-6 (Fig. 13). Two perfluoroiodobutane donors bind to the same chloride anion. The Cl–I distances of 3.0 Å and the Cl–I–C angles of 177.5° revealed beautiful halogen bonds that fulfill all structural prerequisites to perfection. In the ternary co-crystal, the binding sites for the other four halogen bond donors observed in molecular models (Fig. 12b) are occupied by the potassium counterion, bound within 18-crown-6 ligands. Although the dynamic situation during anion transport across lipid bilayers is not comparable with structures in the solid state, direct

evidence for halogen bonds between anion and transporter further supported the idea that the same interactions also account for function. Moreover, the halogen-bonded structure found in the solid state was fully compatible with the active structure obtained by molecular modeling (Fig. 12b).

4 Linear Oligomers

4.1 Concept

Anion transport with monomeric halogen-bond donors as well as with cyclic oligomers revealed the unique power of halogen bonds to perform this task. Namely, directional and strong like hydrogen bonds, halogen-bond donors are intrinsically more hydrophobic. However, the activities found to support this bold claim were not that convincing. The smallest possible organic transporter was discovered, yes, but the $EC_{50} = 1.5$ mM for trifluoroiodomethane **41** is very weak (Fig. 7). The rationally designed cyclic oligomer **19** was, with an $EC_{50} = 1.0$ mM, not much better (Fig. 3). The best activities with cyclic oligomers were found with weakened halogen bonds ($EC_{50} = 32$ μ M for **21**), and activities obtained with anion- π interactions in cyclic oligomers remained superior compared to halogen bonds ($EC_{50} = 25$ μ M for **20**, Fig. 3). The best activities observed with halogen-bond donors were obtained with minimalist monomers in the alkyl series at intermediate length ($EC_{50} = 3.1$ μ M for perfluoro-1-iodohexane **34**, Fig. 7). Maximal performance at intermediate length reveals that activity depends on a subtle balance between increasing anion encapsulation by up to six transporters (Fig. 12b, $n = 3.3$) and decreasing miscibility with longer perfluorinated tails. In the aryl series, the best activities were obtained with the divalent tetrafluoro-1,4-diiodobenzene **33** ($EC_{50} = 26$ μ M, Fig. 7). As the two halogen-bond donors in transporter **33** cannot bind to the same anion, this high activity implies the occurrence of a more complex anion transport mechanism.

To confirm the high expectations concerning anion transport with halogen bonds in reality, the cyclic overperformers **19** (Fig. 3) were formally unrolled into linear oligomers of increasing length, i.e., dimer **42**, tetramer **43**, hexamer **44**, and octamer **45** (Fig. 14). Rigid-rod *p*-oligophenyls were selected as a classical scaffold to create transport systems that can span a lipid bilayer membrane. *p*-Oligophenyl rods were introduced in 1997 [95] and used later on to build potassium transporters **6** with transmembrane cation- π slides [5], proton transporters **7** with transmembrane hydrogen-bonded chains (Fig. 1) [6], artificial β -barrels [96, 97], and π -stack architectures [13, 30]. The formal unrolling of cyclic into linear oligomers has been successfully applied before for cation- π transporters **4–6** (Fig. 1) [3–5]. With anion- π transporters, the full evolution from monomers **15** to cyclic oligomers **17** and linear oligomers **18** has been accomplished (Fig. 2) [25–27]. Linear oligomers that can span the membrane are top candidates to achieve high activity because they

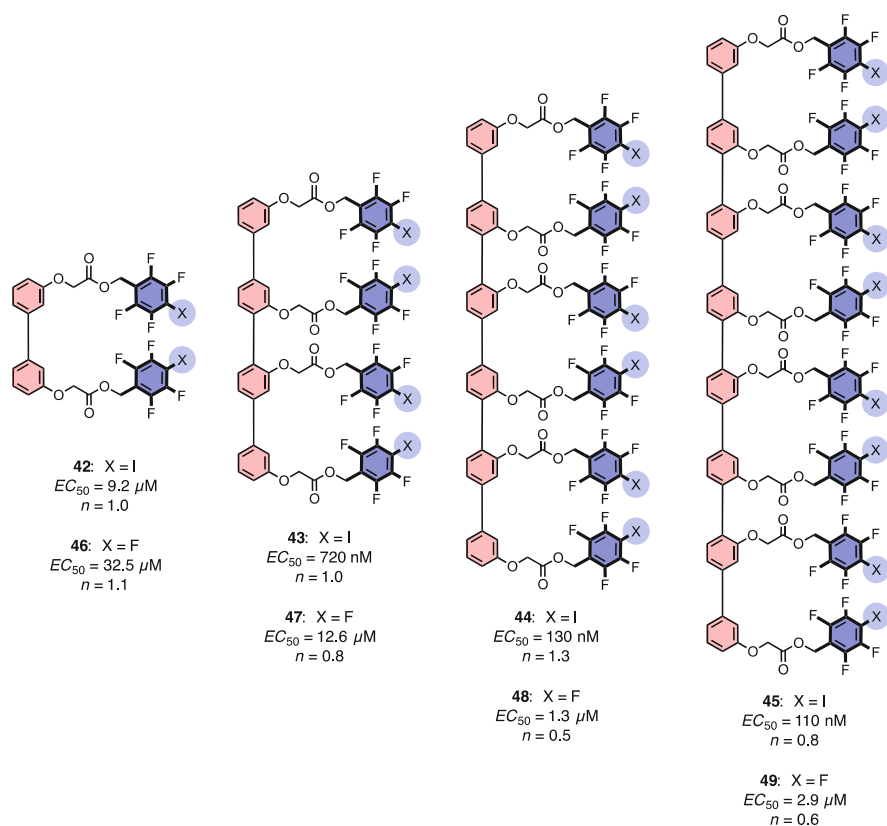
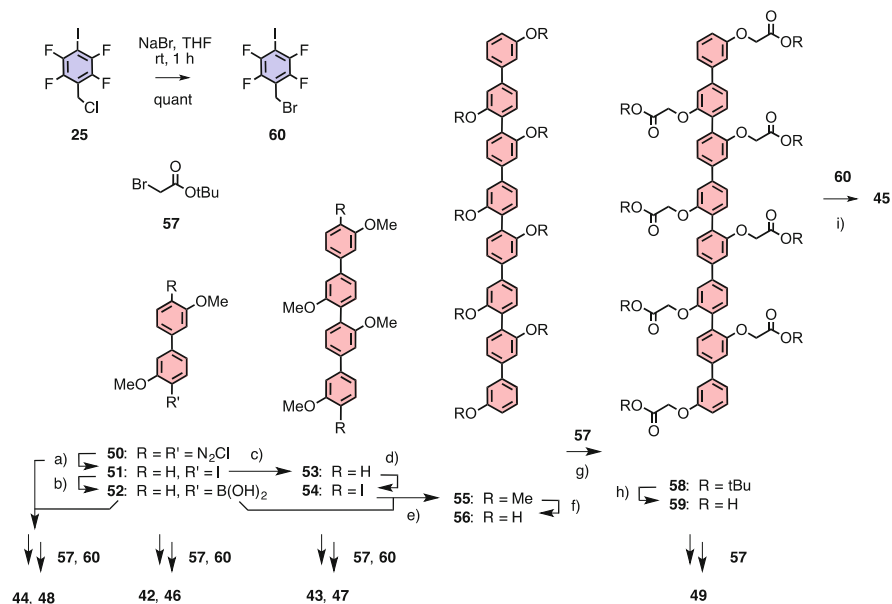


Fig. 14 Linear oligomers made to study transport with halogen bonds (**42–45**) in comparison to anion- π interactions (**46–49**). Electron-rich regions are in red, electron-poor ones in blue, EC_{50} and n refer to transport activity in the HPTS assay

are expected to operate by a different transport mechanism, i.e., a cooperative multiion hopping that is essential to combine selectivity and speed in synthetic and biological ion channels.

The downside with linear oligomers is that they are usually only accessible after quite significant synthetic efforts. The use of rigid-rod *p*-oligophenyls as privileged scaffolds was also attractive because their synthesis is very well developed [95, 96]. For cooperative anion hopping along transmembrane cascades of halogen-bond donors, *p*-octiphenyl **45** was envisioned. In **45**, strong perfluoriodophenyl halogen-bond donors are attached along the membrane-spanning scaffold. To complete the series, the shorter homologs **42–44** were needed. As additional controls, the oligomer series **46–49** with anion- π donors in place of halogen-bond donors in **42–45** were prepared as well. As in the cyclic series with the less active halogen-bonding transporter **19** and more active anion- π transporter **20** (Fig. 3), access to halogen-bonding oligomers **42–45** and anion- π oligomers **46–49** was



Scheme 2 Synthesis of halogen-bonding ion channel **45**. (a) 1. KI, 70%, 2. *n*-BuLi, 67%. (b) 1. *n*-BuLi, 2. B(*O-i*-Pr)₃, 3. HCl, 75%. (c) 1. *n*-BuLi, 2. CuCl₂, 64%. (d) 1. *t*-BuLi, 2. I₂, 29%. (e) Pd(PPh₃)₄, Na₂CO₃, 66%. (f) BBr₃. (g) Cs₂CO₃, 62% (2 steps). (h) TFA. (i) DIPEA, Na₂SO₄, DMF, μ W, 170°C, 15 min, 40%

interesting to compare directly the two unorthodox interactions in the context of multiion hopping across lipid bilayers (Fig. 14). In the following, the synthesis of the rationally designed halogen-bonding channel **45** is briefly summarized. All other compounds were made analogously.

4.2 Synthesis

The *p*-oligophenyl scaffolds for transporters **42–49** were prepared following the original procedure developed in 1997 [95] (Scheme 2). Namely, the commercially Fast Blue Salt B **50** was readily iodinated with KI and partially deiodinated with *n*-butyl lithium. The monoiodinated biphenyls **51** were either converted into the boronic acids **52** or subjected to oxidative coupling with CuCl₂ to give the *p*-quaterphenyl **53** in 64% yield. Most critical is the regioselective diiodination of both termini in *p*-quaterphenyl **54**, achieved as on the dimer level with the bulky but highly flammable *tert*-butyl lithium. As with the biphenyls, monoiodinated side products and unreacted starting material could be recycled. Suzuki coupling of the diiodotetramer **54** with the biphenyl boronic acids **52** gave the *p*-octiphenyl **55** in good 66% yield.

On the octamer level, the methyl groups in **55** were removed with BBr_3 . The resulting polyphenol **56** was subjected to Williamson ether synthesis with the activated bromoacetate *tert*-butyl ester **57**. This reaction works particularly well in DMF that is saturated with Cs_2CO_3 . Essential for success is the use of the *tert*-butyl ester **57**. The same reaction with the corresponding methyl ester gave completely insoluble material [98]. The dramatic difference between the octa-*tert*-butyl ester **58** and the complementary octamethyl ester – the latter totally intractable, the former a pleasure to work with – nicely illustrates the power of solubilizing groups in organic synthesis [99].

To introduce the halogen-bond donors along the rigid-rod scaffold, the *tert*-butyl solubilizers were removed with TFA. The resulting octaacid **59** did not react well enough with the activated benzyl chloride **25** that was used to prepare the cyclic oligomers (Scheme 1). The benzyl chloride **25** was thus activated first by Finkelstein substitution with NaBr. Anhydrous microwave conditions for 15 min at 170°C were best to react the obtained benzyl bromide **60** with the eight acids along the scaffold of rigid rod **59**. The final transporter **45** was obtained in 40% yield.

4.3 Ion Transport in Vesicles

The transport activity of the linear oligomers **42–49** was determined with the HPTS assay as described in Sect. 2.4 (Fig. 5a). Inactivity in the CF assay excluded the occurrence of non-specific leakage for the reasons described in Sect. 2.4 (Fig. 5b). Insensitivity to external cation exchange in the HPTS assay demonstrated that octamer **45** is an anion transporter (Figs. 5a and 15c). A somewhat erratic anion selectivity topology demonstrated that selective anion binding to the transporter overcompensates for dehydration costs and dominates transport (Figs. 5c and 15d). If we exclude the basic fluoride as unreliable, decreasing activities with decreasing dehydration penalty, i.e., anti-Hofmeister behavior, can be seen in the halide series. This interpretation supports the notion that anion binding overcompensates dehydration costs. Most interesting and so far not understood is the high nitrate selectivity of octamer **45** (Fig. 5c). It could imply contributions from anion- π interactions to anion selectivity in the active anion channel architecture [25, 26].

The activity of linear oligomers increased with their length. For halogen-bonding oligomers, significant nanomolar activity of $\text{EC}_{50} = 110 \text{ nM}$ was found for octamer **45** (Fig. 14). The dependence of activity on oligomer repeats N followed (4) [33] (Fig. 15a, b, filled circles):

$$\text{EC}_{50} \propto N^{-m} \quad (4)$$

The resulting cooperativity coefficient $m = 3.37$ found for halogen-bonding transporters **42–45** was unusually high. For standard contributions from multivalency with oligomers and polymers, $1 < m < 2$ would be expected [100].

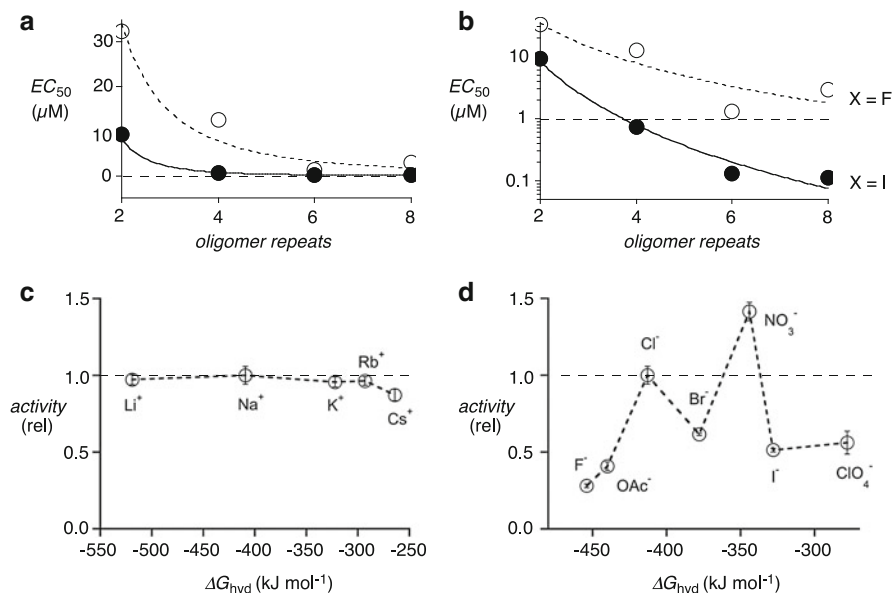


Fig. 15 (a) Transport activity EC_{50} as a function of the oligomer repeats in halogen-bonding transporters **42–45** (filled circles) and anion- π transporters **46–49** (open circles) with curve fit to (4). (b) Same with logarithmic scale. (c) Independence of the transport activity on the hydration energy ΔG_{hyd} of external cations indicates that octamer **45** does not transport cations. (d) Dependence of the transport activity on the hydration energy ΔG_{hyd} of external anions indicates that **45** transports anions. Adapted with permission from [33]. Copyright 2013 American Chemical Society

The complementary anion- π transporters **46–49**, clearly less active, still gave a cooperativity coefficient $m = 2.13$ (Fig. 15a, b, open circles). The exceptionally high activity and cooperativity with halogen-bonding cascades in **44** and **45** provided quantitative evidence for the occurrence of transmembrane multianion hopping. As a result, octamer **45** with an $EC_{50} = 110 \text{ nM}$ is 2,364-times (!) more active than monomer **27** with an $EC_{50} = 260 \text{ }\mu\text{M}$. Transporters operating with anion- π interactions are not competitive with halogen-bonding transporters in this context. This inferiority originates presumably from the poor π -acidity of the pentafluorophenyl modules used. This interpretation is also supported by the inactivity of monomeric hexafluorobenzene **30**, which contrasts nicely with the $EC_{50} = 260 \text{ }\mu\text{M}$ measured for the halogen-bonding pentafluoroiodobenzene **27** (Fig. 7). Increasing quadrupole moments from the $Q_{zz} = +9.5 \text{ B}$ (Buckinghams) for hexafluorobenzene **30** to $Q_{zz} = +19 \text{ B}$ with naphthalenediimides gives linear oligomers **18** with excellent activity [27], and a further increase to $Q_{zz} = +39 \text{ B}$ with core-substituted naphthalenediimides gives monomeric transporter **15** with an exceptional $EC_{50} = 300 \text{ nM}$ (Fig. 2) [25].

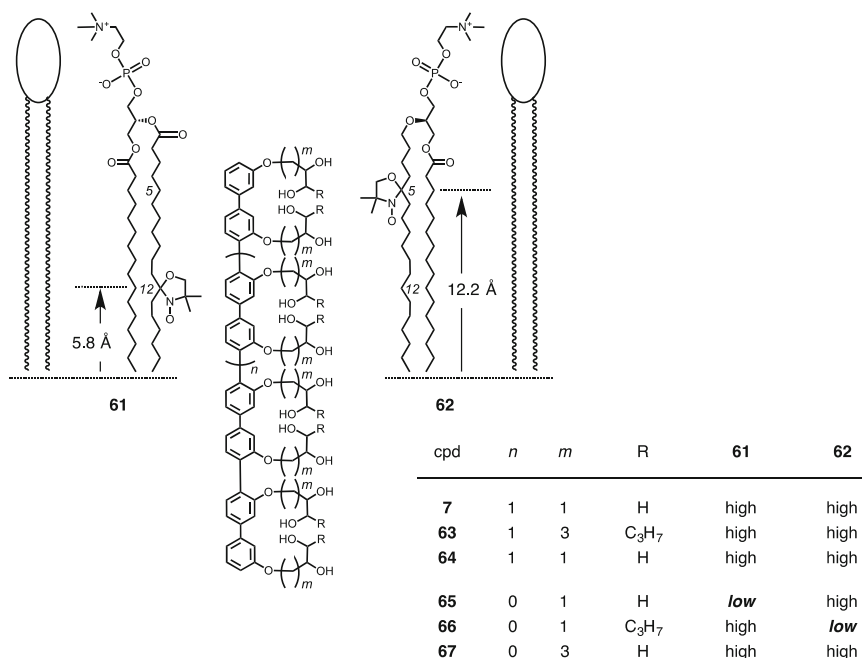


Fig. 16 Fluorescence depth quenching results for fluorescent rods **7** and **63–67**. Quenching by 12-DOXYL-PC **61** and 5-DOXYL-PC **62** is indicated as high or low, 12-DOXYL > 5-DOXYL indicates central, 12-DOXYL < 5-DOXYL interfacial and 12-DOXYL = 5-DOXYL transmembrane rod orientation

4.4 Structural Studies in Vesicles

The determination of active structures of synthetic transporters in lipid bilayers is challenging for many reasons [101]. They often exist only as minority components at high dilution and are thus undetectable by normal methods. An exceptionally powerful method for structure determination under relevant conditions is fluorescence depth quenching [6, 102–107]. Oligophenyl rods are privileged scaffolds not only because they provide a unique platform for the construction of transmembrane architectures but also because they can be seen by fluorescence depth quenching [6, 105–107]. For depth quenching, lipid bilayers are labeled with lipids that contain DOXYL quenchers at defined positions in their hydrophobic tails. Most common are 12-DOXYL-PC **61** and 5-DOXYL-PC **62** (Fig. 16).

For fluorescent rods, depth quenching rules with these two probes are the following: 12-DOXYL > 5-DOXYL quenching efficiencies indicate that the fluorescent rod is closer to position 12 than to position 5 in the bilayer. This finding directly implies that, first, the fluorescent rod adapts a “horizontal” orientation parallel to the membrane plane and, second, it resides at the center of the membrane between the two leaflets. Complementary to this central rod location with

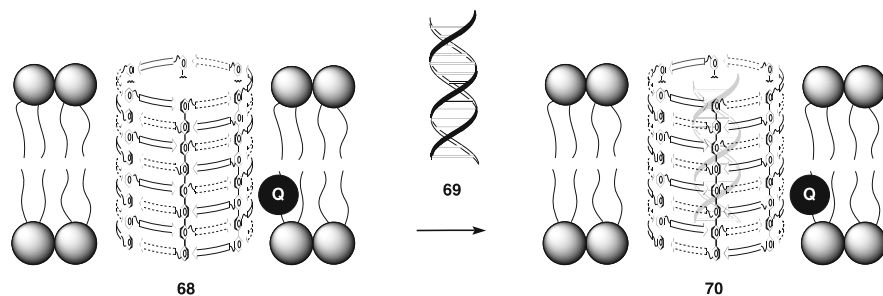


Fig. 17 Rapid inactivation but unchanged fluorescence depth quenching upon addition of DNA duplex **69** to the artificial β -barrel pore **68** demonstrates the formation of the transmembrane inclusion complex **70**

12-DOXYL > 5-DOXYL is the interfacial location with 12-DOXYL < 5-DOXYL. The only explanation for this selective quenching efficiency implies that rods are lying flat at the surface of the bilayer. Transmembrane orientation of fluorescent rods is demonstrated with 12-DOXYL = 5-DOXYL, the independence of the quenching efficiency on the location of the quencher.

The orientation of oligophenyl rods in lipid bilayers has been studied in the greatest detail. *p*-Octiphenyls were most attractive because their length of 34 Å roughly matches the thickness of the hydrophobic core of standard lipid bilayers. Hydrophobically matching [106] *p*-octiphenyls reliably adapt transmembrane orientation. This preference is independent of the substituents placed along the scaffold and at both termini. Examples include not only small HBCs as in **7**, **63**, and **64** (Fig. 16) [105] but also the giant artificial β -barrel pore **68** exposed to blockage by DNA duplex **69** (Fig. 17) [107]. Since the artificial β -barrel **68** was constructed based on the same *p*-octiphenyl scaffold used in HBC **7** or halogen-bonding transporter **45**, fluorescence depth quenching could be used to clarify the mechanism of pore blockage. As for HBC **7**, comparison of efficiencies by 12-DOXYL-PC **61** and 5-DOXYL-PC **62** confirmed that the β -barrel pore **68** exists in transmembrane orientation. Addition of the blocker **69** caused rapid disappearance of transport activity in single-channel conductance experiments, whereas fluorescence quenching remained unchanged. This demonstrated that the duplex **69** enters into intact transmembrane pores **68**, the formation of the transmembrane inclusion complex **70**.

Whereas the transmembrane orientation of hydrophobically matching *p*-octiphenyl rods was general, the positioning of mismatched rods in lipid bilayers was determined by the nature of the substituents along their scaffolds [105]. The original, truncated *p*-sexiphenyl HBC **65** showed weak quenching with the central quencher **61** and is thus localized flat at the surface of the membrane (Fig. 16) [6]. Hydrophobic tails added after the HBC in *p*-sexiphenyl **66** produced weak quenching with the interfacial quencher **62** and thus caused “horizontal” rod

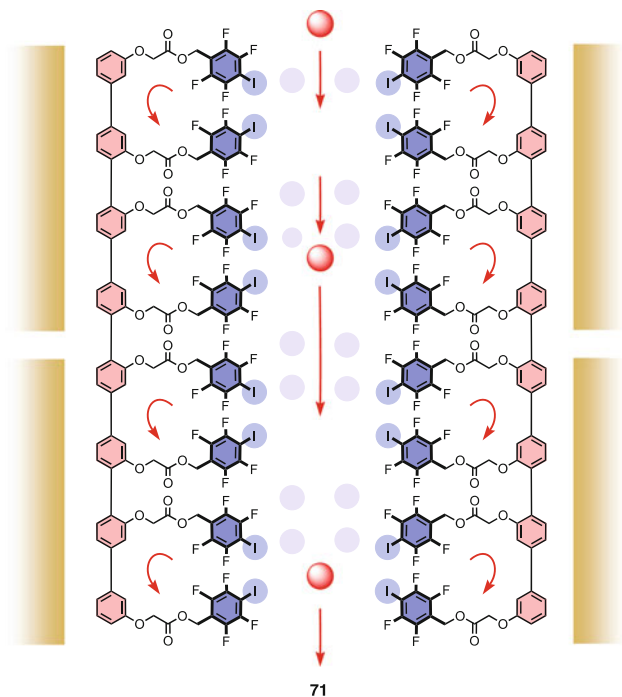


Fig. 18 Schematic active structure **71** of the ion channel formed by transmembrane bundles of **45** with internal arrays of halogen-bond donors for cooperative anion hopping across the membranes

accumulation in the middle of the membrane [105]. However, hydrophobic chains inserted between *p*-sexiphenyl scaffold and HBC in **67** gave independence of quenching efficiency on quencher location, i.e., transmembrane *p*-sexiphenyls despite a hydrophobic mismatch. This result suggested that, with the additional spacers, the terminal diols can reach out toward the interfacial region, a more polar region rich in electron-rich hydrogen-bond acceptors, and thereby anchor the rod in a membrane-spanning orientation. Equipped with similarly long sidechains with halogen-bond donors or π -acids, such anchoring could also occur with *p*-sexiphenyls **44** and **48**, enforce transmembrane orientation of the mismatched scaffold, and thus account for their high activity (Fig. 14).

The consistently transmembrane orientation of hydrophobically matching *p*-octiphenyl scaffolds seen by fluorescent depth quenching suggests that at least transporter **45** offers a transmembrane array of halogen-bond donors. Most likely, the transmembrane rods assemble into bundles **71** to hide the superhydrophobic halogen-bond donors from the surrounding the membrane (Fig. 18). Hill coefficients $n = 0.8$ suggest that these bundles are thermodynamically very stable [74]. Insights from earlier structural studies further support the existence of an active suprastructure **71** that is composed of bundles of transmembrane rigid-rod scaffolds with a central array of halogen-bond donors for the cooperative anion

hopping across the membrane (Fig. 17). Although single-channel currents have not yet been reported, this active structure, immobile during anion transport, can arguably be classified as the first synthetic ion channel that operates with halogen bonds. The creation of this halogen-bonding channel with transmembrane rigid-rod scaffolds confirms the general validity and practical relevance of a concept introduced in 1997 [95].

5 Summary

The unique power of halogen bonds to transport anions across lipid bilayers has been disclosed in a comprehensive trilogy of concise communications [31–33]. The objective of this review was to put this breakthrough in a broader context and add the background and explanations needed to enable and encourage readers with more or less expertise to appreciate, enjoy, and exploit the findings. Directional and strong but more hydrophobic than hydrogen bonds, halogen bonds are ideal for anion transport. The activity of halogen-bond donors has been explored as monomers [32], as oligomers in cyclic arrays that can bind around an anion [31], and as linear oligomers that are long enough to span a lipid bilayer membrane [33].

The discovery of the smallest possible organic anion transporter perfectly illustrates the unique power of halogen bonds to transport anions [32]. Trifluoroiodomethane, composed of one carbon and five atoms in total, can be bubbled through a suspension of vesicles to turn on transport ($EC_{50} = 1.5$ mM). The best monomeric halogen-bond donor, i.e., perfluoro-1-iodohexane, shows significant activities ($EC_{50} = 3.1$ μ M), whereas comparably “atom-efficient” monomers that could transport ions with anion- π interactions, hydrogen bonds, ion pairing, or cation- π interactions are less active, and often inactive.

Because of the unique power of halogen bonds to transport anions, the rational design of cyclic halogen-bonding arrays for preorganized multivalent anion recognition was a failure [31]. Transport activities were disappointing because anion binding was too good ($EC_{50} = 1.0$ mM). Transport activities could be restored by weakened halogen bonds ($EC_{50} = 32$ μ M), and control macrocycles that operate with the weaker anion- π interactions were better anion transporters.

To secure experimental evidence for the unique power of halogen bonds to transport anions, the overachieving cyclic oligomers were unrolled into linear oligomers that can span a lipid bilayer membrane ($EC_{50} = 110$ nM) [33]. This activity is 2,364-times better than that of the corresponding monomeric halogen-bond donor monomers. Transmembrane arrays of halogen-bond donors transported anions with the highest cooperativity coefficient ever observed in this context ($m = 3.37$). This finding confirmed the occurrence of cooperative multiion hopping along halogen-bonding cascades across the membrane, which is the successful creation of the first synthetic ion channel that works with halogen bonds. The control channels that work with anion- π interactions were less cooperative and less active ($m = 2.13$, $EC_{50} = 2.9$ μ M).

The significant activities obtained with the formal unrolling of overachieving cyclic oligomers into transmembrane linear oligomers – culminating in the first synthetic ion channel that operates with halogen bonds and unprecedented cooperativity – were of highest importance for two other reasons: (1) the rational design of larger architectures remains essential for the creation of significant function and (2) synthetic efforts to make them are worthwhile.

The studies summarized in this review cover comprehensively anion transport with halogen bonds. The results encourage the highest expectations and provide all the information needed to develop future applications. The next big step with transmembrane ion transport will concern pumps, i.e., active transport. Other promising directions include separation and purification systems, sensing [12], cellular uptake [16], and so on. With anion- π interactions, evidence for the stabilization of anions in the ground state during transport called for the stabilization of anionic transition states in catalysis because catalysis with anion- π interactions has never been seen before [12]. With halogen bonds, contributions to catalysis were discovered before transport [55]. Nevertheless, this reverse chronology does not change the fact that the application of halogen bonds in catalysis is of the highest importance [55–63]. The discovery of their unique power for anion transport provides a further incentive to develop “halogen-bonding” catalysis in the broadest sense, particularly in non-polar environments.

Acknowledgments We warmly thank all past and present coworkers and collaborators for their contributions, particularly the groups of Jiri Mareda (Geneva) and Pierangelo Metrangolo and Giuseppe Resnati (Milano), and the University of Geneva, the European Research Council (ERC Advanced Investigator), the National Centre of Competence in Research (NCCR) Chemical Biology, and the Swiss NSF for financial support.

References

1. Sakai N, Matile S (2013) *Langmuir* 29:9031–9040
2. Matile S, Fyles T (2013) *Acc Chem Res* 46:2741–2742
3. Gokel GW, Daschbach MM (2008) *Coord Chem Rev* 252:886–902
4. Tanaka Y, Kobuke Y, Sokabe M (1995) *Angew Chem Int Ed* 34:693–694
5. Tedesco MM, Ghebremariam B, Sakai N, Matile S (1999) *Angew Chem Int Ed* 38:540–543
6. Weiss LA, Sakai N, Ghebremariam B, Ni C, Matile S (1997) *J Am Chem Soc* 119:12142–12149
7. Davis AP, Sheppard DN, Smith BD (2007) *Chem Soc Rev* 36:348–357
8. Davis JT, Okunola O, Quesada R (2010) *Chem Soc Rev* 39:3843–3862
9. Gale PA, Pérez-Tomás R, Quesada R (2013) *Acc Chem Res* 46:2801–2813
10. Busschaert N, Gale PA (2013) *Angew Chem Int Ed* 52:1374–1382
11. Yau KH, Mak JC, Leung SW, Yang D, Vanhoutte PM (2012) *PLoS One* 7:e45340
12. Takeuchi T, Matile S (2013) *Chem Commun* 49:19–29
13. Bhosale S, Sisson AL, Talukdar P, Fürstenberg A, Banerji N, Vauthey E, Bollot G, Mareda J, Röger C, Würthner F, Sakai N, Matile S (2006) *Science* 313:84–86
14. Perez-Velasco A, Gorteau V, Matile S (2008) *Angew Chem Int Ed* 47:921–923

15. Zhao Y, Domoto Y, Orentas E, Beuchat C, Emery D, Mareda J, Sakai N, Matile S (2013) *Angew Chem Int Ed* 52:9940–9943
16. Bang EK, Gasparini G, Molinard G, Roux A, Sakai N, Matile S (2013) *J Am Chem Soc* 135:2088–2091
17. Li X, Shen B, Yao XQ, Yang D (2009) *J Am Chem Soc* 131:13676–13680
18. Santacroce PV, Davis JT, Light ME, Gale PA, Iglesias-Sanchez JC, Prados P, Quesada R (2007) *J Am Chem Soc* 129:1886–1887
19. Busschaert N, Bradberry SJ, Wenzel M, Haynes CJE, Hiscock JR, Kirby IL, Karagiannidis LE, Moore SJ, Wells NJ, Herniman J, Langley GJ, Horton PN, Light ME, Marques I, Costa PJ, Felix V, Frey JG, Gale PA (2013) *Chem Sci* 4:3036–3045
20. Busschaert N, Karagiannidis LE, Wenzel M, Haynes CJE, Wells NJ, Young PG, Makuc D, Plavec J, Jolliffe KA, Gale PA (2014) *Chem Sci* 5:1118–1127
21. Moore SJ, Wenzel M, Light ME, Morley R, Bradberry SJ, Gomez-Iglesias P, Soto-Cerrato V, Perez-Tomas R, Gale PA (2012) *Chem Sci* 3:2501–2509
22. Valkenier E, Davis AP (2013) *Acc Chem Res* 46:2898–2909
23. Sidorov V, Kotch FW, Abdrakhmanova G, Mizani R, Fettinger JC, Davis JT (2002) *J Am Chem Soc* 124:2267–2278
24. Seganish JL, Santacroce PV, Salimian KJ, Fettinger JC, Zavalij P, Davis JT (2006) *Angew Chem Int Ed* 45:3334–3338
25. Dawson RE, Hennig A, Weimann DP, Emery D, Ravikumar V, Montenegro J, Takeuchi T, Gabutti S, Mayor M, Mareda J, Schalley CA, Matile S (2010) *Nat Chem* 2:533–538
26. Adriaenssens L, Estarellas C, Vargas Jentzsch A, Martinez Belmonte M, Matile S, Ballester P (2013) *J Am Chem Soc* 135:8324–8330
27. Gorteau V, Bollot G, Mareda J, Perez-Velasco A, Matile S (2006) *J Am Chem Soc* 128:14788–14789
28. Hennig A, Fischer L, Guichard G, Matile S (2009) *J Am Chem Soc* 131:16889–16895
29. Sakai N, Sordé N, Das G, Perrottet P, Gerard D, Matile S (2003) *Org Biomol Chem* 1:1226–1231
30. Talukdar P, Bollot G, Mareda J, Sakai N, Matile S (2005) *Chem Eur J* 11:6525–6532
31. Vargas Jentzsch A, Emery D, Mareda J, Metrangolo P, Resnati G, Matile S (2011) *Angew Chem Int Ed* 50:11675–11678
32. Vargas Jentzsch A, Emery D, Mareda J, Nayak SK, Metrangolo P, Resnati G, Sakai N, Matile S (2012) *Nat Commun* 3:905
33. Vargas Jentzsch A, Matile S (2013) *J Am Chem Soc* 135:5302–5303
34. Metrangolo P, Resnati G (2014) *Top Curr Chem*, This volume
35. Metrangolo P, Meyer F, Pilati T, Resnati G, Terraneo G (2008) *Angew Chem Int Ed* 47:6114–6127
36. Priimagi A, Cavallo G, Metrangolo P, Resnati G (2013) *Acc Chem Res* 46:2686–2695
37. Hassel O (1970) *Science* 170:497–502
38. Rissanen K (2008) *CrystEngComm* 10:1107–1113
39. Metrangolo P, Carcenac Y, Lahtinen M, Pilati T, Rissanen K, Vij A, Resnati G (2009) *Science* 323:1461–1464
40. Foster JA, Piepenbrock MOM, Lloyd GO, Clarke N, Howard JAK, Steed JW (2010) *Nat Chem* 2:1037–1043
41. Takeuchi T, Minato Y, Takase M, Shinmori H (2005) *Tetrahedron Lett* 46:9025–9027
42. You LY, Chen SG, Zhao X, Liu Y, Lan WX, Zhang Y, Lu HJ, Cao CY, Li ZT (2012) *Angew Chem Int Ed* 51:1657–1661
43. Sarwar MG, Ajami D, Theodorakopoulos G, Petsalakis ID, Rebek J (2013) *J Am Chem Soc* 135:13672–13675
44. Hardegger LA, Kuhn B, Spinnler B, Anselm L, Ecabert R, Stihle M, Gsell B, Thoma R, Diez J, Benz J, Plancher JM, Hartmann G, Banner DW, Haap W, Diederich F (2011) *Angew Chem Int Ed* 50:314–318
45. Lu Y, Liu Y, Xu Z, Li H, Liu H, Zhu W (2012) *Expert Opin Drug Discov* 7:375–383

46. Wilcken R, Zimmermann MO, Lange A, Joerger AC, Boeckler FM (2013) *J Med Chem* 56:1363–1388
47. Auffinger P, Hays FA, Westhof E, Ho PS (2004) *Proc Natl Acad Sci U S A* 101:16789–16794
48. Cavallo G, Metrangolo P, Pilati T, Resnati G, Sansotera M, Terraneo G (2010) *Chem Soc Rev* 39:3772–3783
49. Beale TM, Chudzinski MG, Sarwar MG, Taylor MS (2013) *Chem Soc Rev* 42:1667–1680
50. Mele A, Metrangolo P, Neukirch H, Pilati T, Resnati G (2005) *J Am Chem Soc* 127:14972–14973
51. Spence GT, Beer PD (2013) *Acc Chem Res* 46:571–586
52. Sarwar MG, Dragisic B, Salsberg LJ, Gouliaras C, Taylor MS (2010) *J Am Chem Soc* 132:1646–1653
53. Zapata F, Caballero A, White NG, Claridge TDW, Costa PJ, Felix V, Beer PD (2012) *J Am Chem Soc* 134:11533–11541
54. Walter SM, Kniep F, Rout L, Schmidtchen FP, Herdtweck E, Huber SM (2012) *J Am Chem Soc* 134:8507–8512
55. Bruckmann A, Pena MA, Bolm C (2008) *Synlett* 2008:900–902
56. Lenoir D, Chiappe C (2003) *Chem Eur J* 9:1036–1044
57. Kraut DA, Churchil MJ, Dawson PE, Herschlag D (2009) *ACS Chem Biol* 4:269–273
58. Coulembier O, Meyer F, Dubois P (2010) *Polym Chem* 1:434–437
59. Walter SM, Kniep F, Herdtweck E, Huber SM (2011) *Angew Chem Int Ed* 50:7187–7191
60. Lindsay VNG, Lin W, Charette A (2011) *J Am Chem Soc* 131:16383–16385
61. Lindsay VNG, Charette AB (2012) *ACS Cat* 2:1221–1225
62. Kniep F, Rout L, Walter SM, Bensch HK, Jungbauer SH, Herdtweck E, Huber SM (2012) *Chem Commun* 48:9299–9301
63. Kniep F, Jungbauer SH, Zhang Q, Walter SM, Schindler S, Schnapperelle I, Herdtweck E, Huber SM (2013) *Angew Chem Int Ed* 52:7028–7032
64. Matile S, Sakai N (2012) The characterization of synthetic ion channels and pores. In: Schalley CA (ed) *Analytical supramolecular chemistry*, 2nd edn. Wiley, Weinheim, pp 711–742
65. Abraham W (2002) *J Incl Phen Macrocycl Chem* 43:159–174
66. Araki K, Shimizu H, Shinkai S (1993) *Chem Lett* 1993:205–208
67. Harrowfield JM, Ogden M, Richmond WR, Skelton BW, White AH (1993) *J Chem Soc Perkin Trans 2* 1993:2183–2190
68. Salonen LM, Bucher C, Banner DW, Haap W, Mary JL, Benz J, Kuster O, Seiler P, Schweizer WB, Diederich F (2009) *Angew Chem Int Ed* 48:811–814
69. Renny JS, Tomasevich LL, Tallmadge EH, Collum DB (2013) *Angew Chem Int Ed*, doi: 10.1002/anie.201304157
70. Kano K, Fendler JH (1978) *Biochim Biophys Acta* 509:289–299
71. Hill AV (1913) *Biochem J* 7:471–480
72. Stadler E, Dedek P, Yamashita K, Regen SL (1994) *J Am Chem Soc* 116:6677–6682
73. Litvinchuk S, Sordé N, Matile S (2005) *J Am Chem Soc* 127:9316–9317
74. Bhosale S, Matile S (2006) *Chirality* 18:849–856
75. Behr JP, Kirch M, Lehn JM (1985) *J Am Chem Soc* 107:241–246
76. Clark T, Hennemann M, Murray JS, Politzer P (2007) *J Mol Model* 13:291–296
77. Klotz KH, Benz R (1995) *Biochim Biophys Acta* 1235:378–386
78. Klotz KH, Benz R (1993) *Biophys J* 65:2661–2672
79. Küpper FC, Feiters MC, Olofsson B, Kaiho T, Yanagida S, Zimmermann MB, Carpenter LJ, Luther GW III, Lu Z, Jonsson M, Kloo L (2011) *Angew Chem Int Ed* 50:11598–11620
80. Eisenman G, Horn R (1983) *J Membr Biol* 76:197–225
81. Wright EM, Diamond JM (1977) *Physiol Rev* 57:109–156
82. Hartzell C, Putzier I, Arreola J (2005) *Annu Rev Physiol* 67:719–758
83. Lindsell P (2001) *J Physiol* 531:51–66
84. Gorteau V, Bollot G, Mareda J, Matile S (2007) *Org Biomol Chem* 5:3000–3012

85. Sakai N, Kamikawa Y, Nishii M, Matsuoka T, Kato T, Matile S (2006) *J Am Chem Soc* 128:2218–2219
86. Hille B (2001) *Ionic channels of excitable membranes*, 3rd edn. Sinauer, Sunderland, MA
87. Sakai N, Houdebert D, Matile S (2003) *Chem Eur J* 9:223–232
88. Läuger P (1972) *Science* 178:24–30
89. Chen W (2006) *Phys Rev E* 73:021902-1-021902-7
90. Hansen SP, Fyles TM (2011) *Chem Commun* 47:6428–6430
91. Franciolini F, Nonner W (1987) *J Gen Physiol* 90:453–478
92. Koynova R, Caffrey M (1998) *Biochim Biophys Acta* 1376:91–145
93. Connell SD, Smith DA (2006) *Mol Membr Biol* 23:17–28
94. Otto S, Osifchin M, Regen SL (1999) *J Am Chem Soc* 121:10440–10441
95. Sakai N, Brennan KC, Weiss LA, Matile S (1997) *J Am Chem Soc* 119:8726–8727
96. Sakai N, Mareda J, Matile S (2005) *Acc Chem Res* 38:79–87
97. Sakai N, Mareda J, Matile S (2008) *Acc Chem Res* 41:1354–1365
98. Sakai N, Majumdar N, Matile S (1999) *J Am Chem Soc* 121:4294–4295
99. Ravikumar V, Fin A, Sakai N, Matile S (2011) *Supramol Chem* 23:69–73
100. Hennig A, Gabriel GJ, Tew GN, Matile S (2008) *J Am Chem Soc* 130:10338–10344
101. Baudry Y, Bollot G, Gorteau V, Litvinchuk S, Mareda J, Nishihara M, Pasini D, Perret F, Ronan D, Sakai N, Shah MR, Som A, Sordé N, Talukdar P, Tran DH, Matile S (2006) *Adv Funct Mater* 16:169–179
102. London E, Ladokhin AS (2002) *Curr Top Membr* 52:89–115
103. Ladokhin AS (1997) *Methods Enzymol* 278:462–473
104. Abrams FS, London E (1992) *Biochemistry* 31:5312–5322
105. Ni C, Matile S (1998) *Chem Commun* 33:755–756
106. Ghebremariam B, Sidorov V, Matile S (1999) *Tetrahedron Lett* 40:1445–1448
107. Sakai N, Baumeister B, Matile S (2000) *ChemBioChem* 1:123–125

Biomolecular Halogen Bonds

P. Shing Ho

Abstract Halogens are atypical elements in biology, but are common as substituents in ligands, including thyroid hormones and inhibitors, which bind specifically to proteins and nucleic acids. The short-range, stabilizing interactions of halogens – now seen as relatively common in biology – conform generally to halogen bonds characterized in small molecule systems and as described by the σ -hole model. The unique properties of biomolecular halogen bonds (BXBs), particularly in their geometric and energetic relationship to classic hydrogen bonds, make them potentially powerful tools for inhibitor design and molecular engineering. This chapter reviews the current research on BXBs, focusing on experimental studies on their structure–energy relationships, how these studies inform the development of computational methods to model BXBs, and considers how BXBs can be applied to the rational design of more effective inhibitors against therapeutic targets and of new biological-based materials.

Keywords Drug design · Medicinal chemistry · Molecular engineering · Molecular interactions · Protein-inhibitor interactions

Contents

1	Introduction	243
2	The Halogen Bond, A Bird's Eye View	246
3	Occurrence of Biomolecular Halogen Bonds	247
3.1	BXB Donors and Acceptors	248
4	Geometry of BXBs	252
4.1	Approach of BXB Acceptor to Donor (Θ_1)	253
4.2	Approach of BXB Donor to Acceptor (Θ_2)	254
4.3	Relationship Between X-Bonds and H-Bonds in Biomolecules	256

P.S. Ho (✉)

Department of Biochemistry and Molecular Biology, Colorado State University, Fort Collins, CO 80523-1870, USA

e-mail: shing.ho@colostate.edu

5	Energies of Interaction	256
5.1	Measuring BXB Energies in Crystals	257
5.2	Measuring BXB Energies in Solution	259
5.3	Measuring BXB Energies in Protein–Ligand Complexes	261
6	Computational Models	263
7	Perspectives and Conclusions	266
7.1	BXBs as Molecular Tools for Rational Drug Design	266
7.2	Potential Application of BXBs in Biomolecular Engineering	268
7.3	Why Are Halogens Hydrophobic?	269
7.4	Conclusions	269
	References	270

Abbreviations

Å	Ångstrom (10^{-10} m)
A	Adenosine
Asn	Asparagine
Asp	Aspartic acid
Arg	Arginine
BXB	Biomolecular halogen bond
Br	Bromine
BrTyr	Bromotyrosine
^{Br} U	5-Bromouridine
C	Cytidine
C=O	Carbonyl group
C–X	Carbon–halogen bond
Cl	Chlorine
DFT	Density functional theory
DNA	Deoxyribonucleic acid
DSC	Differential scanning calorimetry
e	Exponential (2.7182...)
<i>E</i>	Energy
F	Fluorine
G	Guanosine
<i>G</i> [°]	Standard state Gibbs free energy
Gln	Glutamine
Glu	Glutamic acid
<i>h</i> -BXB	Shared halogen–hydrogen bond
<i>H</i> [°]	Standard state enthalpy
H-bond	Hydrogen bond
His	Histidine
I	Iodine
ⁱ C	5-Iodocytidine
IC50	Concentration for half maximal inhibition

kcal	Kilocalorie (4.18 kJ)
K_D	Dissociation constant
K_i	Inhibition constant
μM	Micromolar (10^{-6} M)
MD	Molecular dynamics
MM	Molecular mechanics
mol	Mole (6.02×10^{23} particles)
N	Nitrogen
N–H	Nitrogen–hydrogen bond
NCI	National Cancer Institute
ND	Not determined
nM	Nanomolar (10^{-9} M)
O	Oxygen
P	Probability of interaction
PDB	Protein Data Bank
Phe	Phenylalanine
QM	Quantum mechanics
r_{DA}	Distance between donor and acceptor
R_{vdW}	van der Waals radius
$\sum R_{vdW}$	Sum of van der Waals radii of two interacting atoms
S	Sulfur
S°	Standard state entropy
SA	Surface area
T	Thymidine
T3	3,5,3'-Triiodo-L-thyronine (liothyronine)
T4	3,5,3,5'-Tetraiodo-L-thyronine
TR	Thyroid hormone receptor
Tyr	Tyrosine
U	Uridine
X-bond	Halogen bond
^XU	5-Halouridine

1 Introduction

The unique chemical interactions of halogens in covalent compounds have been recognized for nearly two centuries. Their ability to serve as Lewis acids (acceptors of lone-pair electrons) has been known since the 1800s [1] and in short-range, stabilizing interactions with electron-rich Lewis bases (called charge transfer bonds) since the 1970s [2–4]. The use of the term “halogen bond” (X-bond) started to appear significantly in publications on materials chemistry in the late 1990s [5, 6]. Thus, there is a rich history of studies on the stabilizing interactions involving halogens in chemistry.

X-bonding had been largely unrecognized in the life sciences community, primarily because halogens are not commonly found in naturally occurring proteins or nucleic acids. In 1996, the drug design group at Bristol-Myers Squibb, Co, headed by Patrick Lam, had applied the concept of halogen bonding to design an iodinated inhibitor against clotting factor Xa as a potential anticoagulant [7]. The strategy was to replace an amidine group with an iodine to interact with the carboxylate of Asp189 in the protein. The structure of the protein with the new inhibitor analogue showed an I...O interaction that was 0.3 Å shorter than the sum of the standard van der Waals radii of the two atoms. That particular product never made it to market, but was likely the first example of the most practical application of X-bonds in biology – the rational design of new inhibitors and drugs against therapeutic protein targets. Still, there was at that time no understanding for whether X-bonding was generally important in biological systems.

The basic concept of X-bonding was introduced to the biological community with the first survey in 2004 of their occurrence in the structures of biological molecules [8]. The survey was prompted by two studies in 2003. A study by Muzet et al. [9] had identified a short (3.0 Å) contact from the bromine of the halogenated inhibitor *IDD594* to the hydroxyl group of Thr133 in the enzyme aldose reductase. In addition, our lab showed that a similarly short interaction from a brominated uracil induces a four-stranded DNA junction [10], replacing a stabilizing hydrogen bond (H-bond) in the structure. Neither of these individual studies had recognized the existence of X-bonds, which, again, emphasized the lack of knowledge of this class of interaction in the biological community. The 2004 PDB survey, however, demonstrated that X-bonds are indeed prevalent in biomolecular structures [8]. Although halogens are uncommon in biological molecules, halogens are being added to proteins and nucleic acids to help to solve their X-ray structures [11], and into compounds that serve as ligands recognized and bound by these molecules [12–14]. Today, X-bonds are included along with classic H-bonding, π - π stacking, π -charge, and other “weak” interactions in the analysis of biomolecular structures [15–17].

For this discussion, we will focus on X-bonds found in biological systems, and will refer to these as biomolecular X-bonds (BXBs) to emphasize their distinctive nature, as compared to those in small molecule complexes [18, 19]. In particular, we will explore the unique geometries and structure–energy relationships imposed on BXBs by their molecular contexts and aqueous environments (Fig. 1). We should note here that the interacting partners will be named based on their strong analogous roles in H-bonds: the halogen that serves as the Lewis acid will be called the X-bond donor, while the electron-rich Lewis base will be the X-bond acceptor [21].

How important is it to understand and accurately model the structure–energy relationships of BXBs? For many medicinal chemists, the starting point in trying to identify potential lead compounds against therapeutic targets is to look towards repositories of molecules that are readily available for testing. In one popular repository, the National Cancer Institutes’ Diversity Set IV (a list of organic

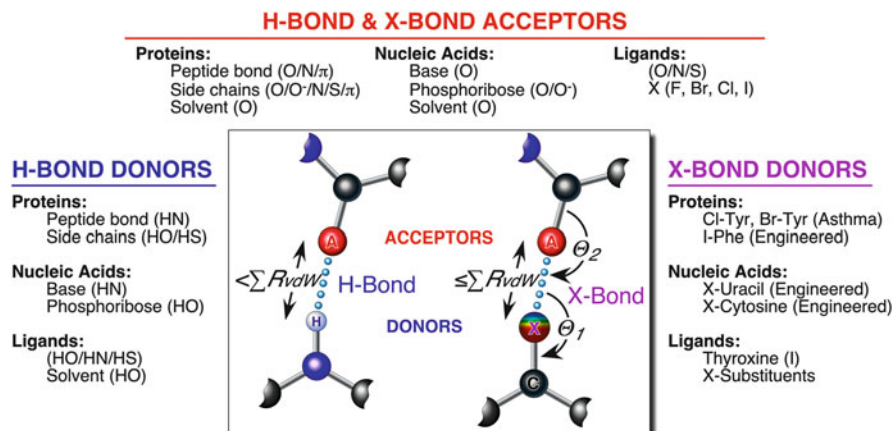


Fig. 1 Comparison of donors and acceptors between hydrogen bonds (H-bonds) and halogen bonds (X-bonds) (adapted from Scholfield et al. [20])

molecules available as potential lead compounds for high throughput screening as anticancer agents [22], 22% of the compounds are halogenated and nearly 20% include halogens (Cl, Br, and I) that can potentially form BXBs. A computational medicinal chemist would, for example, start with this list of structures to perform large scale virtual docking studies as a first screen for compounds that could bind with dissociation constants (K_D s) in the micromolar to nanomolar range. The standard docking algorithms, with their preprogrammed properties for halogens, would not only be incapable of modeling an X-bond [23], they would in fact have the halogen and its Lewis base partner repelling each other. As a result, the loss of one BXB interaction could push the calculated K_D from nanomolar to micromolar and, worse yet, micromolar to millimolar. In short, 20% of potential lead compounds could be discarded in the first screen simply because the current docking programs do not treat BXBs properly. This is one of the primary reasons to study and understand the structural and thermodynamic properties and, from these, develop accurate computational models of X-bonds in biomolecules. The focus of this chapter, therefore, will be on the current advances made in these topics, with particular attention paid towards experimental studies.

Before delving into the features of BXBs, we will start by summarizing the underlying model that explains the principle of X-bonds. Once established, this model will serve as the basis for our understanding of the nature of BXBs, including the types of atoms or groups of atoms that serve as X-bond acceptors, their unique geometries in relation to classic H-bonds, and the structure–energy relationships that can eventually serve to establish BXBs as a molecular tool for designing new materials and drugs.

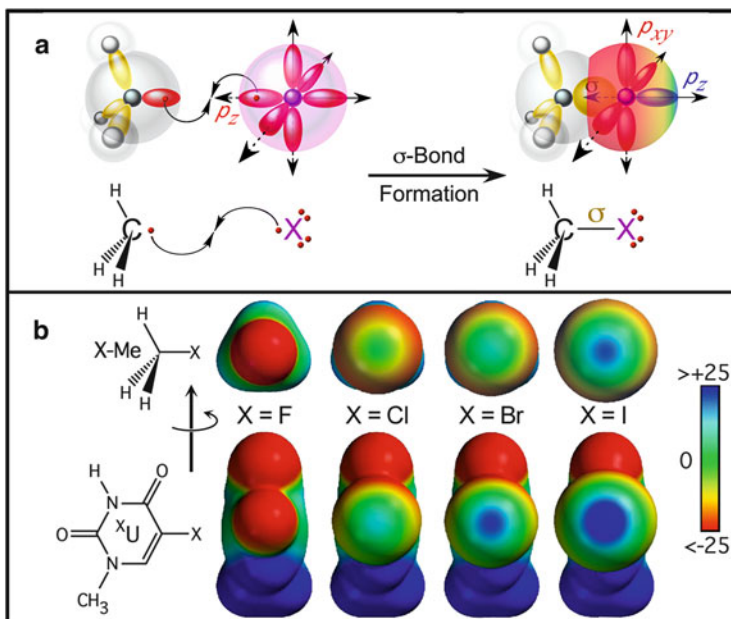


Fig. 2 (a) The σ -hole model for halogen bonding (adapted from Scholfield et al. [20]). (b) Effects of polarizability and electron-withdrawing groups on electrostatic potential (adapted from Auffinger et al. [8])

2 The Halogen Bond, A Bird's Eye View

The physicochemical principles that help explain the existence of X-bonds are extensively covered in other chapters in this book. Here, we will provide a brief overview of the prevailing electrostatic model (the σ -hole model [24–29]), without any comment on its accuracy or completeness – it is currently the most intuitive description for how the interaction arises (Fig. 2a). The basic principle starts with the electronic configuration of the Group VII atoms: all halogens have five electrons filling the three valence p-atomic orbitals (p_x , p_y , and p_z), just one short of the maximum to fill the full octet (s- and p-orbitals) of a stable atom. To form a covalent or σ -bond, we pair one of these valence p-electrons with, for example, another halogen (to form F_2 , Cl_2 , Br_2 , or I_2) or to a carbon (for a C–X type bond). By convention, this electron comes from the p_z -orbital, which is aligned in the direction of the resulting σ -bond. Consequently, the p_z -orbital becomes depleted of electron density, exposing the charge of the nucleus. This depletion is manifested as an electropositive crown (called the σ -hole) at the surface diametrically opposed to the σ -bond. It is this σ -hole, serving as the X-bond donor, which interacts electrostatically with an electron-rich X-bond acceptor. The depopulation of the p_z -orbital further reduces the electron–electron overlap associated with steric repulsion in this

direction, resulting in polar flattening of the atom, contributing to the close approach of the acceptor in the direction of the σ -hole. The resulting short-range, electrostatic interaction is what has now been defined as the halogen bond [19, 21].

The σ -hole model predicts that any atom which forms a covalent bond should experience an electropositive crown opposite that bond. Indeed, there is evidence to suggest that this is the case for many atoms, including those outside the Group VII column of elements [25, 28, 29]. Thus, the more general class of interactions can be considered to be σ -hole bonding, with X-bonds being a subset of this larger group [28]. What makes the halogen unique, however, is that there are no additional covalent bonds or sets of non-bonding molecular orbitals to restrict access, either sterically or electronically, to the σ -hole.

The size of the σ -hole and, consequently, the strength of the X-bond is dependent on a number of factors, including the polarizability of the halogen and the electron-withdrawing capacity of the atom or groups of atoms that the halogen is covalently bonded to [5, 29]. As we proceed down the Group VII column from F to I for the common halogens, the atoms become larger as we fill atomic orbitals at higher quantum levels (Fig. 2b). These higher-level electrons are more susceptible to redistribution as the σ -hole becomes established. Thus, the strength of X-bonds follows the size of the atom, with $F < Cl < Br < I$. For the most part, fluorine is not particularly polarizable and does not form X-bonds, except under exceptional circumstances [30, 31]; consequently, we will focus primarily on Cl, Br, and I in BXBs for the remainder of this chapter. The σ -hole becomes further exaggerated when the halogen is attached to strongly electron-withdrawing groups, for example an aromatic ring, and the addition of electron-withdrawing substituents on the ring can be used to tune further the strength of the X-bond [32, 33]. A commonly used physical organic measure of the electron-withdrawing capacity of substituents is the Hammett constant [34], which has been shown to be linearly related to the calculated strength of X-bonds [33]. With this general model which describes the anisotropic distribution of charge and the resulting short, stabilizing interactions of halogenated compounds, we can now start to explore some of the unique features of X-bonds in the biomolecular context (the BXBs).

3 Occurrence of Biomolecular Halogen Bonds

The first indication that X-bonds play a generally important role in biomolecular systems came from a survey in 2004 [8] of the Protein Data Bank (PDB) [35]. The results of the PDB survey showed that BXBs were fairly prevalent, even as they had been largely ignored in the prior analyses of the individual structures. This initial survey of BXBs was prompted by two studies showing unusually short Br...O distances in their structures. First concerned the 0.6-Å resolution structure of the IDD594 inhibitor with aldose reductase [9] and the second a 1.3-Å structure of a four-stranded DNA Holliday junction [10] – neither had recognized these interactions as X-bonds. In the reductase study, the Br of the inhibitor was seen to be

within 3.0 Å of the hydroxyl group of a Thr side chain [9]. A density function theory (DFT) calculation of the electrostatic potential of the complex attributed the 1,000-fold increase in the specificity of the inhibitor for this enzyme over the closely related aldehyde dehydrogenase [36] to this short bromine–oxygen interaction.

The second study was part of a larger effort to find all sequences that stabilize Holliday junctions (the four-stranded intermediate associated with genetic recombination and recombination dependent mechanisms, including DNA repair and integration) [37]. In this study, a thymine in the sequence CCAGTACTGG was replaced with a 5-bromouracil (^{Br}U, as in the sequence CCAGTAC^{Br}UGG) to help phase the X-ray diffraction data. The brominated sequence was seen to form a four-stranded junction, while the structure of the parent sequence (and the analogous non-halogenated uracil-containing sequence) was eventually solved as a standard B-DNA duplex. The bromine of the ^{Br}U structure was observed to form a short interaction to the formally negatively charged oxygen of the phosphodeoxyribose, substituting for an analogous essential H-bond in a native junction [38]. The simplistic understanding of halogens by us, as biologists, was at odds with the observation that this electron-rich atom formed such a close interaction with a formally negatively charged oxygen, and that it would replace a stabilizing H-bond – the X-bond concept was absent.

The 2004 PDB survey [8] mimicked earlier studies of X-bonds in small molecule complexes [18, 39], and applied the same criteria for identifying the chemical interaction: (1) acceptor atoms that are classic Lewis bases (O, N, S); (2) distances between donor/acceptor atoms less than the sum of their van der Waals radii ($r_{\text{DA}} \leq \sum R_{\text{vdW}}$); and (3) an angle of approach of the acceptor to the donor (Θ_1) that is nearly linear to the σ -bond ($\Theta_1 \geq 120^\circ$). Using these criteria, the study found 113 examples of BXBs in 66 unique crystal structures (at resolutions limited to 3.0 Å or better), with the majority of the structures being complexes of proteins with halogenated ligands.

More recent surveys of the PDB show BXBs to be even more prevalent, with now over 600 examples (and growing) [20, 40–42]. In addition, the geometries are more broadly distributed than initially thought, as discussed in greater detail in Sect. 4 of this chapter. The significant factors in the expansion of recognized BXBs come from a growing recognition of the interaction by structural biologists and the extension of types of atoms and geometries (beyond those seen in small molecules) that serve as BXB acceptors.

3.1 BXB Donors and Acceptors

As the list of BXBs grows, so must the types of molecular moieties that constitute the donors and acceptors (Fig. 1). Within BXBs themselves, the varieties of donors are necessarily small, since halogens are not common elements in biomolecules. There are specific instances, however, where halogenated amino acids or nucleic acids do or could serve as BXB donors. Halogens are introduced into proteins and polynucleotides to help phase X-ray diffraction data from single crystals [11, 43, 44].

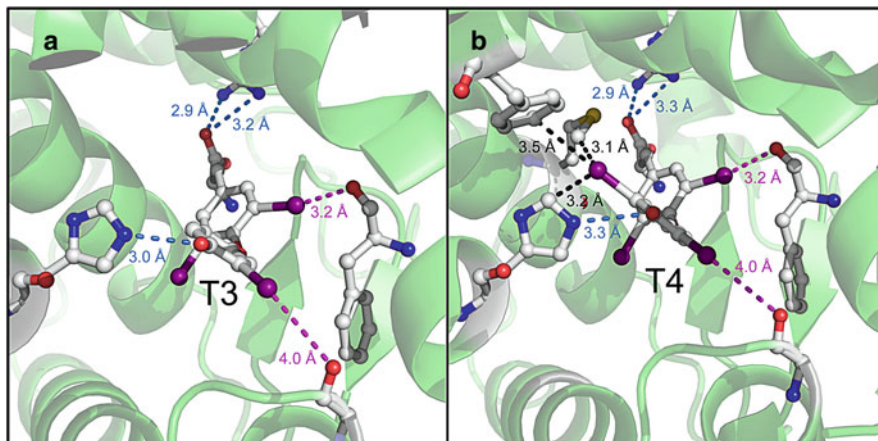


Fig. 3 Interactions of thyroid hormone receptor TR β : (a) with 3,5,3'-triiodo-L-thyronine (T3) (PDB code 1XZX); (b) with 3,5,3',5'-tetraiodo-L-thyronine (T4) (PDB code 1Y0X) [51]

In the specific case of the sequence CAGTAC^{Br}UGG, as described above, a pair of Br-BXBs forces the DNA into a four-stranded Holliday junction. A more dramatic example of the effect that X-bonds can have on molecular conformation is seen with the sequence G^ICGAAAGCT, where the I-BXB formed by the iodocytosine (^IC) shifts the structure from a parallel intercalated-duplex to a hexameric complex [45, 46]. Halogenated amino acids in proteins, particularly chloro- and bromotyrosines resulting from oxidative halogenation by myeloperoxidases [47] and eosinophil peroxidases [48], respectively, are markers for asthma [49]. Although not yet implicated as BXB donors, these halogenated proteins are distinguishable by polyclonal antibodies [50], suggesting a role of X-bonds in their recognition.

Halogenated ligands are the most common and wide-ranging BXB donors. Examples of naturally occurring donors are the thyroxine-class of hormones from the thyroid [8, 42]. Thyroxines can occur in the more stable and, thus, more commonly found tetraiodinated (T4) or the more potent triiodinated (T3) forms. The regulation of metabolism by T3 and T4 is mediated by a set of thyroid hormone receptors (TRs, Fig. 3). The selectivity of the TR α over TR β for T3 was suggested to be from a shorter and presumably stronger BXB [52]. In contrast, transthyretin, an extracellular protein responsible for the transport of thyroxine hormones, has a higher affinity for T4 than for T3. A structural analysis shows that T4 makes two BXBs to the transthyretin backbone, while T3 has two binding modes, both of which isolate the iodine, leaving the hydroxyl group to form H-bonds to these same protein sites (Fig. 4) [53]. Finally, the deiodination of T4 to T3 by iodothyronine deiodinase is seen to involve formation of an X-bond to a sulfur or selenium, which helps to elongate the susceptible C–I bond prior to cleavage [54]. Thus, BXBs play roles in the recognition by receptors and transport proteins, and in the chemistry that converts between the two functional forms of the hormone.

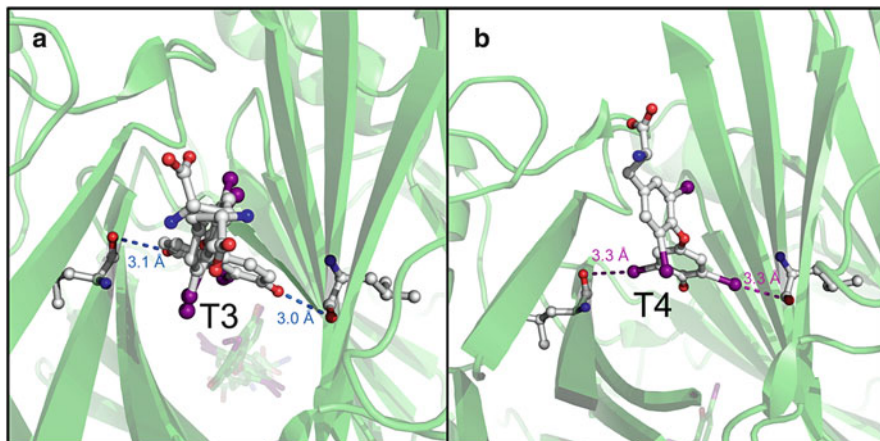


Fig. 4 (a) H-bonding interactions of the transporter protein transthyretin to T3 (PDB code 1SN5). (b) X-bonds to T4 (1SN0) [53]

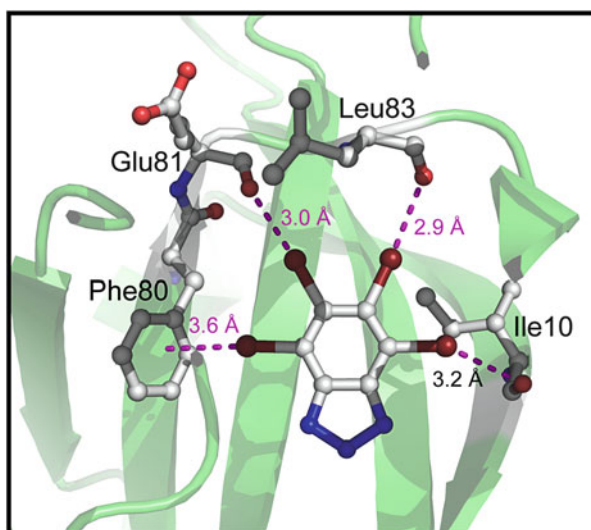


Fig. 5 Protein kinase CDK2 complex with the inhibitor 4,5,6,7-tetrabromo-benzotrazole (PDB code 1P5E) [57]

The largest single class of BXB donor molecules is the inhibitors to protein targets [8, 42, 55], many of which have pharmacological potential [13, 56] (Fig. 5). The halothane anesthetics and some non-steroidal anti-inflammatory drugs involve BXB interactions in protein binding [42, 58]. More specific inhibitors include triclosan, which targets the enoyl-acyl carrier protein reductase associated with fatty acid chain elongation in various microorganisms [42, 59]. Perhaps more

important than any single example or single category is the fact that halogenated molecules represent a large proportion of pharmacological compounds clinically used or in clinical trials, and incorporated into screening libraries to search for lead compounds as potential inhibitors against therapeutically important targets [13, 14, 60, 61].

Among the interesting targets for X-bonding inhibitors, protein kinases are a large group where BXBs have been observed [60, 62] (Fig. 5) and are being introduced [63]. This important class of proteins contains leading targets for treatments against chronic inflammatory diseases, neurodegenerative disorders, viral infections, unicellular parasites, cardiovascular disease, and cancer [60]. There is, however, a growing list of therapeutically important targets where BXBs are or will be playing a role, including: HIV reverse transcriptase [64]; integrins, which are targets for treatments against T- and B-cell lymphomas [65]; human cathepsin L, implicated in various pathologies, including metastasis of many common human cancers [66–70]; and aldose reductase, described above, which is associated with diabetic hyperglycemia.

BXB acceptors includes all possible H-bond acceptors, starting with the standard Lewis bases found along the backbone and the side chains of polypeptide and polynucleotide chains, and extending to aromatic systems, other halogens, and finally to the ubiquitous water solvent (Fig. 1). The most common acceptor type, particularly in ligand complexes, is the peptide carbonyl oxygen (C=O) of protein backbone (Fig. 5) [8, 20, 41, 55, 71]. In some ways, this observation was not surprising, but in others it was very surprising. Since the peptide C=O is the most common type of oxygen found in polypeptides (every amino acid has one), it is perhaps not unexpected that it is also the most common BXB acceptor in protein–inhibitor complexes. However, the atoms along the backbone of folded proteins are largely inaccessible, protected by packing of side chains; thus, it was unexpected to find that the most prevalent BXBs in the PDB are to the peptide carbonyls. Perhaps a better question may be: why are there so few BXBs to side chains? Polar side chains (Asp, Asn, Glu, Gln, and His [72]) are more exposed (and H-bonded) to solvent and more dynamic, thereby resulting in both steric and solvent entropic costs to forming BXBs.

The aromatic side chains in proteins are an interesting set of BXB acceptors. Even before X-bonds were recognized in biology as a general class of molecular interactions, it had been recognized that halogen–aromatic interactions are important. In small molecule complexes, for example, so-called C–X \cdots π interactions have been seen in host–guest and other crystalline systems [73]. In biological systems, the bromines of several inhibitors against protein kinases are seen to form BXBs to Phe side chains of CK2 and CDK2 (Fig. 5) [60]. More comprehensive surveys [74, 75] show that such BXBs extend to a broad range of aromatic side chains and may be associated with up to 2.5 kcal/mol in stabilizing interaction energy to the system [75].

In addition to aromatic rings, BXBs have been seen to other delocalized π -electron systems, including the guanido-group of Arg [20, 72] and, most commonly to the peptide bond itself [8, 76]. We can thus categorize each of these to a more general class of π -X-bonds or, in biology, π -BXBs.

Water molecules are amphipathic, being capable of serving as both H-bond donors and acceptors. Furthermore, when interacting with halogens, waters can serve as X-bond acceptors or as H-bond donors, depending on whether they are aligned into or perpendicular to the σ -hole. An interesting concept is that waters can serve as bridges between X-bond donors and H-bond acceptors in a set of so-called halogen–water–hydrogen interactions [77]. This class of X-bonds would be uniquely found in biomolecules, because of their aqueous environment. However, the amphipathic nature of water masks the specificity of X-bonds in such a tripartite system.

4 Geometry of BXBs

The geometry of X-bonds is perhaps the most important property for identifying the interaction in the crystal structures of biomolecular systems [8, 21]. BXBs are now being incorporated into computational programs to help structural biologists identify and understand how halogens affect the structure and function of these systems [15–17]. For the most part, the geometric criteria in such programs have adapted the geometric constraints defined in small molecules and the 2004 PDB survey. If, however, the biomolecule imposes unusual structural constraints on the interaction, the standard geometric parameters may not be entirely accurate in identifying BXBs.

The most immediately obvious indicator for the presence of a BXB is seen as an unusually short distance (shorter than the sum of the respective van der Waals radii, $\sum R_{vdw}$) between a halogen and a Lewis base atom (Fig. 1) [8, 18, 21, 39]. It is tempting to assign every contact $\leq \sum R_{vdw}$ as a BXB. That, however, would overstate the occurrence of the interaction, since many contacts at or near the $\sum R_{vdw}$ could simply be van der Waals-type interactions. For example, consider the distributions of short distance contacts between halogens and acceptor atoms from a 2012 survey of the PDB (Fig. 6). For iodine, the distribution peaks at 95–97% $\sum R_{vdw}$, as one would expect for a strong X-bonding interaction, suggest that this is the optimal distance (balancing the electrostatic attraction against steric repulsion) for the I-BXB. We see, however, that the distribution of Cl contacts drops off exponentially rather than peaking at a value $< \sum R_{vdw}$. However, if a reasonable angle cut-off is applied (where the electrostatic charge of the halogen surfaces switches to negative, see Sect. 4.1), even the Cl distribution also shows a peak (at ~92–94% of $\sum R_{vdw}$), suggesting that many of the contacts at or near the $\sum R_{vdw}$ are van der Waals type contacts. Although we would consider any contact with $\sum R_{vdw} \leq 100\%$ to be a potential X-bond, we can start to define distance criteria ($\sum R_{vdw} \leq 96\%$ for Cl, $\sum R_{vdw} \leq 97\%$ for Br, and $\sum R_{vdw} \leq 98\%$ for I) where we would have the greatest confidence that a contact is a BXB.

X-bonds are highly directional, both in terms of the donor and acceptor, as defined by the electronic properties of the halogen and the Lewis base. In the crowded environments of proteins and polynucleotides, the geometries of BXBs are further restricted by the accessibility of the interacting atoms, along with the

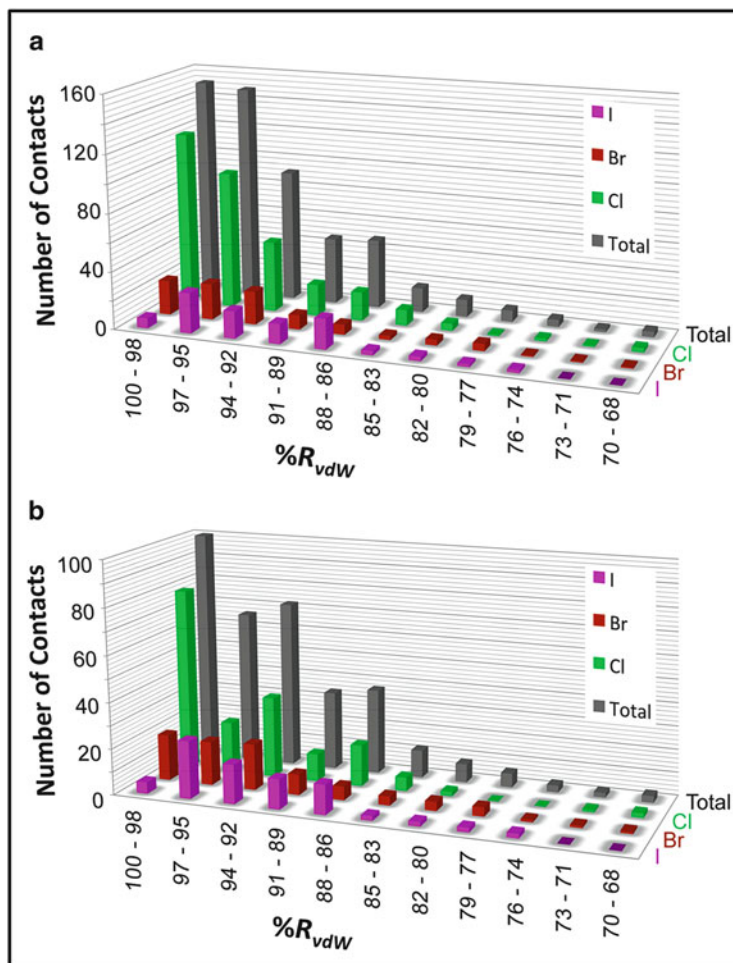


Fig. 6 Contact distances of halogens to acceptors: (a) all contacts; (b) limited to $\Theta_1 \geq 120^\circ$

multitude of other weak electrostatic and steric interactions of the rest of the molecule. The angular directionality provides additional evidence for an X-bonding interaction [21].

4.1 Approach of BXB Acceptor to Donor (Θ_1)

The σ -hole model imposes a strong directionality in the distribution of electrostatic potential across the halogen surface; thus, there is a strong directionality to the geometry of X-bonds in terms of the approach of the acceptor towards the halogen [8, 18, 39]. The angular approach of the acceptor (A) is measured relative to the

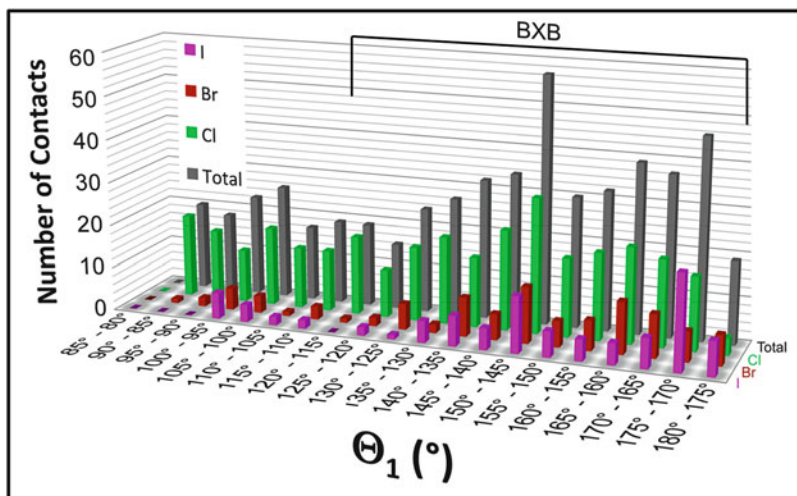


Fig. 7 Numbers of halogen-acceptor contacts as a function of the Θ_1 -angle, with contacts considered to be BXBs bracketed

carbon–halogen ($C-X\cdots A$), and is designated the Θ_1 -angle (Fig. 1). Since the σ -hole is diametrically opposed to the $C-X$ bond, one would expect the most energetically favorable approach would be at $\Theta_1 = 180^\circ$. However, we must also consider the area of the halogen surface available for interaction. If the electrons distributed across the halogen were isotropic, the most probable angle of approach would be $\Theta_1 = 90^\circ$, since this angle provides the largest available surface area for contact. Combining the energy of the electrostatic potential (E) with the angular dependence of the contact surface area (SA) yields a probability for interaction (1) that is maximized at $\Theta_1 = 170^\circ$ [33]; the distribution of BXB contacts in the PDB relative to Θ_1 for Cl, Br, and I generally bears this out (Fig. 7), and is consistent with the preferred Θ_1 -angle seen for small molecule complexes in the Cambridge Database [18, 39].

$$P = SAe^{(-E/kT)} \quad (1)$$

shows the BXB probability (P) as a function of the accessible surface area (SA) and energy of interaction (E).

4.2 Approach of BXB Donor to Acceptor (Θ_2)

The angular approach of the halogen towards the BXB acceptor, designated as the Θ_2 -angle (Fig. 1), is defined by the arrangement of available electronegative molecular orbitals on the acceptor atom. For the most part, these are the

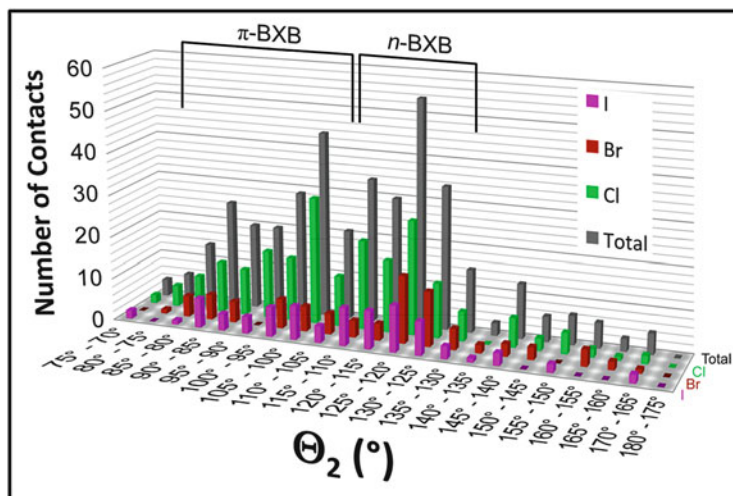


Fig. 8 Numbers of halogen-acceptor contacts as a function of the Θ_2 -angle, with BXBs to π -orbitals (π -BXB) or non-bonding orbitals (n -BXB) of carbonyl oxygens are bracketed above the bars

nonbonding n -orbitals of oxygen, nitrogen, and sulfur and the π -orbitals of aromatic systems. In general, the Θ_2 -angles for structures in the PDB fall around 120° relative to, for example, an O=C bond; this would be consistent with the BXBs involving primarily the n -orbitals in the plane of a carbonyl oxygen or in the tetrahedral geometry of sp^3 -type atoms. However, in going from the smaller Cl to the larger I donors, it was found that $\Theta_2 = 90^\circ$ becomes a distinct class (Fig. 8). A more detailed analysis of the BXBs to the carbonyl oxygens of peptide bonds in proteins (the largest class of acceptors in the PDB) showed that the majority of X-bonds to ligands had an $X \cdots O=C-N$ dihedral angle of 90° relative to the peptide plane (defined by O=C-N) [8]. This perpendicular approach indicated that BXB interactions are primarily to the π -electrons rather than to the n -electrons of the peptide bond – subclasses of π -BXBs [8, 76]. This specific geometry is rarely seen in small molecule complexes, and only when there are significant steric constraints restricting access to the n -electrons of the X-bond acceptor [18]. The rationale for the perpendicular orientation of BXBs relative to the peptide plane comes from the relationship between X-bonds and H-bonds in proteins, as we will discuss in Sect. 4.3.

A similar angle of approach is defined for π -BXBs to aromatic rings. In this case, the delocalized nature of the π -electrons in the aromatic ring imposes a less stringent angular geometry to the approach of the halogen to the aromatic acceptor [74, 75].

4.3 Relationship Between X-Bonds and H-Bonds in Biomolecules

The strong correspondence between X-bonds and H-bonds means that their relationships can be very complex. Since they both share common Lewis bases as acceptors, the interactions can compete against each other; this competition has been exploited as a means to control the formation of small molecule complexes in crystals and in solution [78, 79], and have been used as tools to control the conformation of DNA [80]. H- and X-bonds can also complement each other, as seen with amphipathic acceptors, such as water, which can act as bridges between X-bond donors and H-bonds acceptors [77]. Halogens themselves are amphipathic, serving as X-bond donors along the σ -hole and H-bond acceptors perpendicular to the σ -hole [78].

In protein–ligand complexes, BXBs and H-bonds are most notably seen in orthogonal relationships, both in terms of their geometric alignments and their independent behavior when sharing common acceptors (we have called these *h*-BXBs, X-bonds sharing a common H-bond acceptor) [55]. This orthogonal relationship was first posed as a hypothesis to rationalize the unique geometries of *h*-BXBs to the peptide bonds of proteins (Fig. 9). The most immediate thought when considering the perpendicular alignment of the BXBs to the peptide plane is that the in-plane *n*-orbital electrons of the carbonyl oxygen are not available for an X-bond because they are typically involved in an H-bond to the N–H of another peptide, particularly in ubiquitous α -helices and β -sheets of proteins. However, a detailed analysis of *h*-BXBs shows there is a very strong orthogonal geometry relating $\text{--X}\cdots\text{O}\cdots\text{H--}$, even when the H-bond is not exactly in the peptide plane. This was most notable with α -helices, where the H-bonds are commonly $\sim 40^\circ$ out of the peptide plane, while the *h*-BXBs are seen to be 50° from the opposite side of the common peptide plane. In addition, calculations on sets of H-bonded and X-bonded model complexes suggest that adding or removing an X-bond from a pair of H-bonded peptides does not affect the energies of the H-bonds, and that the energy of the added X-bond is independent of the presence or absence of the H-bond. This concept of orthogonal interactions has important implications for how BXBs can be used to design rationally more effective halogenated inhibitors, as we will discuss later in Sect. 7.

5 Energies of Interaction

X-bonds, as with H-bonds, fall into the category of “weak” molecular interactions – stabilizing energies below ~ 12 kcal/mol [81]. The question is, how weak are X-bonds in a biological context? From melting studies on small molecule complexes, X-bonds have been estimated to have energies ranging from 1 to 5 kcal/mol [82]. The effect of halogens on the affinity and associated binding energies of inhibitors are in about the same range expected for BXBs.

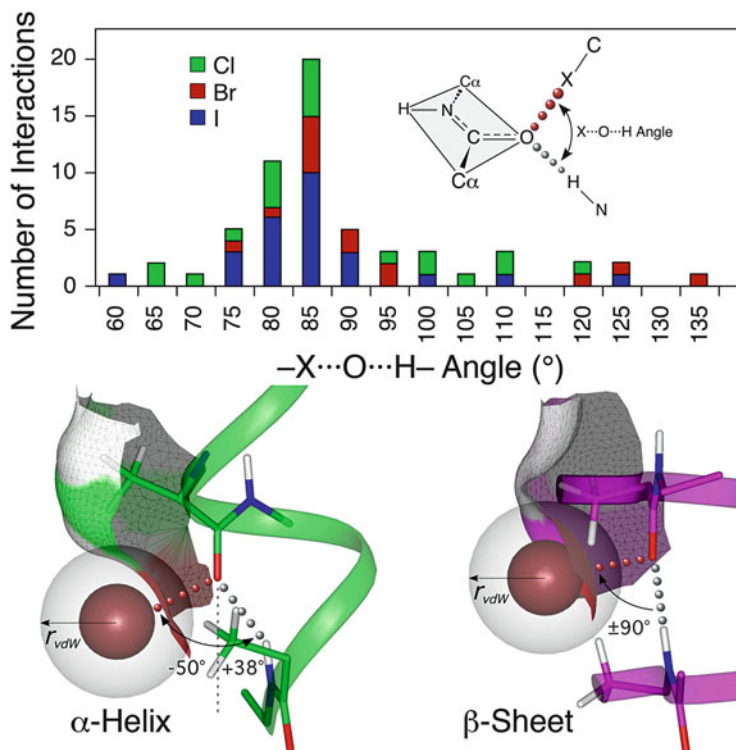


Fig. 9 Orthogonal relationship between H-bonds and BXBs in protein–ligand complexes, seen in the $\sim 90^\circ$ for the $-X\cdots O\cdots H-$ angle (top), and in α -helices and β -sheets (bottom) [55]

The energies of X-bonds and H-bonds, however, are strongly dependent on their geometries and, therefore, it is important to be able to relate directly the detailed structure of these interactions with the stabilizing potential – their structure–energy relationships. There are few direct experimental measurements of the structure–energy relationships of BXBs, but they are important as validation tools in the development of computational methods to model these interactions.

5.1 Measuring BXB Energies in Crystals

The most direct way to determine explicit structure–energy relationships is to study single crystals of X-bonded complexes. In a small molecule example, Corradi et al. [82] crystallized a bipyridine acceptor with either an iodine-containing X-bond donor or an OH-type H-bond donor. A calorimetric analysis for the melting of the crystals after structure determination by X-ray diffraction estimated a ~ 3.5 kcal/mol difference energy to the near linear $I\cdots O$ X-bond as compared to

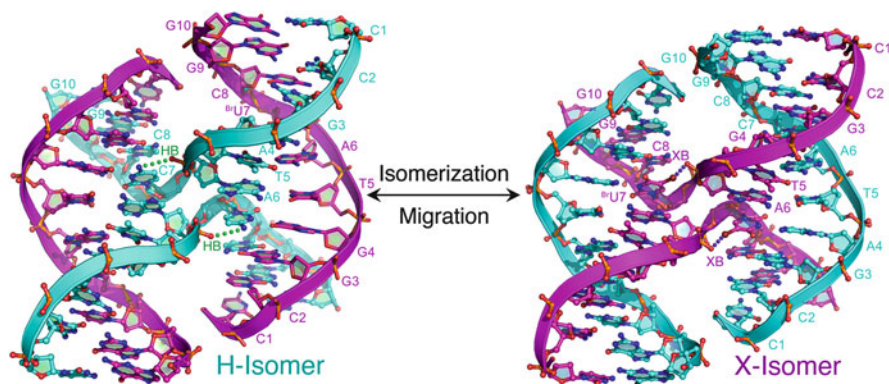


Fig. 10 Competition between H-bond (*cyan strand*) and X-bond (*magenta strand*) in a four-stranded DNA junction requires conversion between an H-bond stabilized isomer and X-bonded isomer [80]

the O–H...N H-bond, with the X-bond being more stable. This energy difference was sufficient to allow the X-bonding donor to outcompete the H-bonding donor, on an equal molar basis, when crystallized with this same acceptor.

An analogous X- vs H-bond competition was performed using DNA as the experimental platform [80] to study the structure–energy relationship of BXBs. Unlike the small molecule systems, we cannot simply melt the crystals to analyze the energies of the molecular interactions, due to the many forces and factors, including the solvent, which contribute to the stability of the lattice and the macromolecular conformations in crystals. In this case, the study exploited a set of H-bonds which are important for the stabilization of a four-stranded DNA complex called the Holliday junction (Fig. 10). A junction was constructed from two unique strands: one which could form an N–H...O H-bond between a cytosine base and the phosphate backbone where the DNA formed a U-turn, and a second which could form a competing Br...O from a bromouracil (^{Br}U). The conversion between the two simply required isomerization of the junction to place either the N–H substituent at the junction center (which would mean the junction was stabilized by an H-bond, so this is the H-isomer) or the Br at the junction center to form an X-bond (the X-isomer). By crystallographically determining the position of the Br atom (through a crystallographic titration assay) [80, 83, 84], the study could determine whether the H- or X-bond was more stabilizing. When sequences were designed to measure the competition of one X- against two H-bonds, the ratio of X- to H-isomers observed in the crystal was 85:15, reflecting a ~2 kcal/mol greater stability of the X-bond (with a 3.3 Å Br...O distance) relative to the competing H-bond (when accounting for the competing molar X- to H-bond ratio). As expected, when the competition was changed to a 2:2 ratio of X- vs H-bonds, only the Br was observed at the junction center, indicating that the X-bond was more stabilizing. In this latter case, the Br...O distance was shorter (at 2.9 Å), associated with ~5 kcal/mol in stabilizing energy assigned to this X-bond vs its competing H-bond.

Table 1 Geometries and energies of BXBs ($X\cdots O^{-1/2}$) as determined in a four-stranded DNA junction [85]

Halogen	X:H ratio	X \cdots O $^{-1/2}$ distance		C–X \cdots O $^{-1/2}$ (Θ_1)	E_{BXB} (kcal/mol)
		Å	% $\sum R_{\text{vdW}}$		
F	2:2	3.20	107	153.5°	–0.5
Cl	1:2	2.95	90.2	152.0°	–0.8
	2:2	2.88	88.1	146.0°	–0.8
Br	1:2	3.32	98.5	167.2°	–2.3
	2:2	2.87	85.2	163.2°	ND
I	1:2	2.92	83.4	164.4°	≤ -2.1
	2:2	3.01	86.0	170.7°	ND

By extending the DNA competition assay, the BXB energies of all the halogens (F, Cl, Br, and I) could be estimated along with their geometries (Table 1). The two Cl-containing junctions allowed an energy for the competing H-bond to be estimated and, therefore, the energies listed in the table are absolute rather than relative energies for BXBs in this system. It is clear from the analysis that the order of energies follows the size and polarizability of the halogens (F through I). Furthermore, as the X-bonds become more stable, the geometries become more ideal in terms of the shorter distances of interaction and more linear angle of approach of the acceptor.

Thus, by carefully designing the experimental system, accurate structure–energy relationships can be determined for BXB from crystals. The energies measured in this manner are most directly related to the enthalpies of interaction, since there is not expected to be significant entropy differences between the X- and H-isomeric forms in the crystals.

5.2 Measuring BXB Energies in Solution

A number of methods have been successfully applied to studying the energies of X-bonds of chemical complexes in solution, including UV-visible, infrared, Raman, and NMR spectroscopy [86]. It is more challenging to determine the structure energy relationships of BXBs in aqueous solution, because of the difficulty in isolating the signals associated with specific molecular interactions in large biomolecular systems by solution methods. Furthermore, it is currently impossible to determine the geometric features of the interactions to the same level of detail as seen from X-ray structures. The two examples discussed here rely on correlations of the solution-state energies back to structural methods (X-ray diffraction or NMR spectroscopy) to derive their structure–energy relationships.

The same DNA junction system used to determine the structure–energy relationships in crystals was also applied to measuring BXB energies in solution. In these studies, differential scanning calorimetry (DSC) was used to monitor the heat

Table 2 Stabilizing energies of Br and I type BXBs determined in DNA junctions in aqueous solution (pH 7.0, 25°C) by DSC [84, 85]

BXB	$\Delta\Delta H^\circ_{X-H}$ (kcal/mol)	$\Delta\Delta S^\circ_{X-H}$ (cal mol ⁻¹ K ⁻¹)	$\Delta\Delta G^\circ_{X-H}$ (kcal/mol)
Br...O ^{-1/2}	-3.6	+4.2	-4.8
I...O ^{-1/2}	-5.9	-12.0	-2.3

Table 3 Stabilizing energies of π -BXBs determined by van't Hoff analysis of thermal melting of β -hairpins in aqueous solution, as monitored by NMR [87]

π -BXB	ΔH° (kcal/mol)	ΔS° (cal mol ⁻¹ K ⁻¹)	ΔC_p° (cal mol ⁻¹ K ⁻¹)
F...Phe	-4.2	-14.6	-90
I...Phe	-6.3	-20.1	-60
I ₂ ...Phe	-8.9	-27.2	-20

required to melt the DNA junction. By judiciously controlling sequence and substituent effects on the major interactions that stabilize DNA (base pairing H-bonds and base stacking interactions), the specific energies of the BXBs could be isolated in terms of the enthalpic ($\Delta\Delta H^\circ_{X-H}$), entropic ($\Delta\Delta S^\circ_{X-H}$), and corresponding free energy ($\Delta\Delta G^\circ_{X-H}$) differences between the X-bonds and comparable H-bonds in the system (Table 2).

The solution energies of BXBs indicate that, consistent with the σ -hole model and the crystal-state energies, the larger halogen I shows a more stabilizing enthalpic component compared to Br. What is interesting, however, is that there is an entropic cost associated with lodging the large atom into the molecular structure; consequently, Br is the “optimum” halogen for forming a BXB in this DNA junction system, as reflected in the overall $\Delta\Delta G^\circ_{X-H}$. Thus, for any particular system, it is important to consider not only the enthalpic energies from the electrostatic attraction between the σ -hole and the BXB acceptor, but also the effects of conformational crowding on the dynamics of the overall molecule which must be considered when incorporating halogen interactions into a biomolecule to affect its stability.

In an earlier study, Tatko and Waters [87] designed a β -hairpin peptide to study interactions between the aromatic side chains of a natural and iodinated Phe by NMR. The halogen was shown to be interacting directly with the ring of the neighboring Phe, providing -0.54 kcal/mol of stabilization for the mono-iodinated Phe and -1.01 kcal/mol for the diiodinated construct. By monitoring the chemical shifts during thermal melting of the peptide, the authors determined the ΔH° and ΔS° for the interactions (Table 3), with the enthalpy following the polarizabilities of the F and I π -BXB, while the entropy loss presumably following the loss of conformational dynamics of the side chain. The negative heat capacities (ΔC_p°) are inconsistent with this being a hydrophobic effect.

5.3 Measuring *BXB* Energies in Protein–Ligand Complexes

Given that the majority of *BXB*s seen in surveys of the PDB are in protein–ligand complexes and, thus, the most direct application of *BXB* will be for the rational design of halogenated inhibitors, it would seem natural to attempt to correlate the structures of protein–ligand complexes with their K_D , inhibition constants (K_i), or their dose responses (IC50s). There are several complexities which come into play, however, in such studies. First, although a K_D can be directly correlated with energies through a standard Boltzmann relationship (2), K_i and IC50 may not be. Perhaps more importantly, the energy of binding a ligand to a protein involves a multitude of interactions and dynamic effects, and this complexity may mask or distort the apparent effects of a single *BXB* in the system. In the simplest case, consider the equilibrium between a protein in its unbound and bound forms. The energy of interaction for ligand binding (E_{bind}) would be a simple relationship (3) between the energies of the bound (E_{PL}) and unbound forms of the protein (E_{P}) and the ligand components (E_{L}). It is also easy to see how (2) and (3) are related to each other. However, for this simplest set of equations to work, there is the implicit assumption that the only difference between the ligand-bound protein (PL) and the unbound protein (P), and the protein-bound ligand and the unbound ligand (L) is the interaction energy of the ligand in the binding pocket. Lost in this are any differences in structures between the various forms and, perhaps more importantly, their interactions with solvent. Still, such comparisons can be used as a first approximation, particularly if we focus primarily on, for example, how the addition of a halogen to the ligand or the substitution of another substituent with a halogen changes the K_D , K_i , or IC50.

$$K_D = \frac{[\text{P}][\text{L}]}{[\text{PL}]} = e^{E_{\text{bind}}/RT} \quad (2)$$

gives K_D , as defined by concentrations of unbound protein [P] and ligand [L] vs the protein–ligand complex [PL], and by the Boltzmann relationship for the binding energy (E_{bind}).

$$E_{\text{bind}} = E_{\text{PL}} - (E_{\text{P}} + E_{\text{L}}) \quad (3)$$

gives the relationship between the binding energy (E_{bind}) and the energies of the protein–ligand complex (E_{PL}) and the unbound protein (E_{P}) and ligand (E_{L}).

The binding pocket in protein kinases is formed at the cleft between two distinct domains, which provides a significant number of contact points and buried surface areas which help provide specificity for a particular inhibitor. The accessibility of these contact points depends on the capacity of the ligand to open the cleft and expose these atomic surfaces. Thus, it is not sufficient simply to have a structure of the protein–inhibitor complex and the K_D in order to determine structure–energy relationship for a *BXB*. We need to have several such structures with different halogen or nonhalogen substituents and their associated K_D s in order to control for

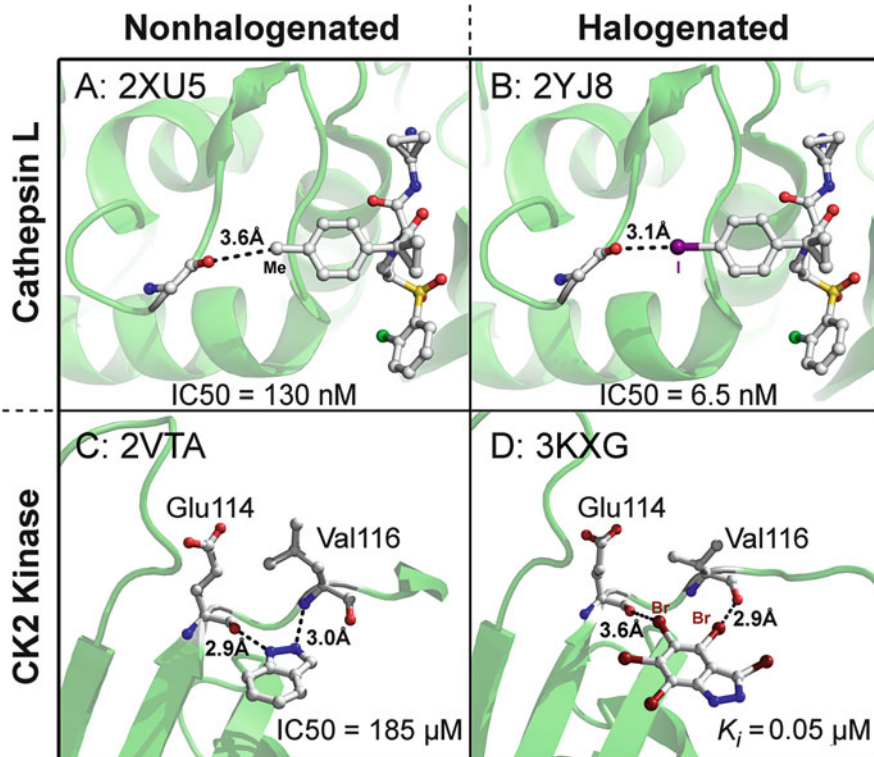


Fig. 11 Structures of cathepsin L (*top row, a, b* [88]) and the CK2 protein kinase (*bottom row, c* [89] and *d* [90]) with nonhalogenated (*left column, a, c*) and halogenated (*right column, b, d*) inhibitors

the accessibility of the binding pocket, possible rearrangement of side chains within the pocket, contributions from hydrophobic effects, and potential inductive effects on other interactions, including neighboring H-bonding substituents. There are limited numbers of such comprehensive studies available, and even then, the results are mostly qualitative.

In one particular systematic study by Hardegger et al. [88], the structures along with the IC₅₀s have been determined for cathepsin L in complex with various halogenated and unhalogenated inhibitors (Fig. 11a, b). The nonhalogenated inhibitor places a methyl group within 3.6 Å of the peptide carbonyl oxygen of residue Gly61, while the halogenated inhibitor places a Cl, Br, or I within BXB distances from this same oxygen. The reduction of the IC₅₀ from 130 nM to 22 nM for Cl, 12 nM for Br, and 6.5 nM for I (equivalent to ~1–2 kcal/mol increase in the binding energy) could readily be attributed to the short X···O BXBs in this system, since the overall structures are nearly identical and the steric effects required to make the binding pocket available are present in all constructs. This systematic study also showed significant inductive effects when various electron-withdrawing groups

Table 4 Structures and binding free energies (ΔG_{Exp} , in kcal/mol are calculated from their K_i s or, in the case of 2VTA, the IC50) of CK2 kinase with various tetrabrominated inhibitors [91]

Structure	Inhibitor	ΔG_{Exp}
1J91 [92]	4,5,6,7-Tetrabromobenzotriazole	-8.84
1ZOE [93]	4,5,6,7-Tetrabromo- <i>N,N</i> -dimethyl-1 <i>H</i> -benzimidazole-2-aminebenzotriazole	-10.2
1ZOG [93]	4,5,6,7-Tetrabromo-2-(methylsulfanyl)-1 <i>H</i> -benzimidazole	-9.88
1ZOH [93]	5,6,7,8-Tetrabromo-1-methyl-2,3-dihydro-1 <i>H</i> -imidazo[1,2- <i>a</i>]benzimidazole	-9.67
2OXD [94]	4,5,6,7-Tetrabromo-1 <i>H</i> ,3 <i>H</i> -benzimidazol-2-one	-9.43
2OXX [94]	4,5,6,7-Tetrabromo-1 <i>H</i> ,3 <i>H</i> -benzimidazol-2-thione	-9.25
2OXY [94]	4,5,6,7-Tetrabromo-benzimidazole	-9.01
3KXG [90]	3,4,5,6,7-Pentabromo-1 <i>H</i> -indazole	-10.1
2VTA [89]	1 <i>H</i> -Indazole	-5.16
3KXN [90]	4,5,6,7-Tetraiodo-1 <i>H</i> -benzimidazole	-10.6

were added to the ring system of the BXB donor, showing how the interactions can be fine tuned through classic substituent effects, as discussed above.

A more difficult analysis is seen with the protein kinases. There are a large number of structures of kinases in complex with halogenated and nonhalogenated inhibitors, and an even greater number of measurements of K_D , K_i , and IC50 values. Unfortunately, they are not always correlated. A particularly well-studied case is the CK2 kinase with various tetrahalogenated benzimidazole inhibitors (Table 4). It is clear from this list that the dominant interactions defining the affinity are the two X...O BXBs which each inhibitor forms with the carbonyl oxygen of the kinase backbone; however, there are variations of upwards of 1.4 kcal/mol in their binding energies. A comparison of 2OXY and 3KXN suggests that the I-BXBs contribute up to 1.6 kcal/mol (0.8 kcal/mol per interaction) binding energy over the Br-BXBs.

One must be cautioned, however, when comparing between halogenated and nonhalogenated inhibitors, even when they are very similar. An example is seen in the structures of CK2 with 1*H*-indazole compared to pentabromo-1*H*-indazole (Fig. 11c, d). The brominated complex has a K_i that is more than three orders of magnitude lower than the IC50 of the unhalogenated ligand (comparable to ~5 kcal/mol difference in binding energy); however, even though both have identical ring structures, the inhibitors are completely flipped in the binding site. Thus, it would be difficult to attribute the loss in binding energy of the unhalogenated inhibitor simply to the BXBs.

6 Computational Models

We have focused to this point on experimental studies that elucidate the structure–energy relationships of BXBs and have left the more comprehensive treatment of the theory behind X-bonding in particular and σ -hole bonding in general to others. The BXB concept, however, can only be fully exploited as a molecular tool if it can

be computationally modeled in, for example, the rational design of inhibitors against therapeutic targets. This has been the focus of several research groups in the past few years, each taking a different approach to the problem. A more comprehensive discussion of these methods is presented in a different chapter, but it is worth mentioning a few examples that serve as starting points for rational molecular design of BXBs.

At one end of the computational modeling spectrum is quantum mechanical (QM) calculations, which is highly accurate for modeling X-bonds in general, but is cumbersome and much too time intensive to be applied to any but the smallest biomolecular systems. At the opposite end are the atomistic molecular mechanics (MM) and molecular dynamics (MD) methods, which are not as accurate but can reasonably be applied to model systems as large as the ribosome. The latter case requires that the force fields defining the classical Newtonian force equations must be modified or re-derived in order to accommodate the specific properties of halogens which allow for the formation of stabilizing X-bonds – two strategies to this approach will be discussed later.

One approach to marrying the two general computational methods is a hybrid QM/MM calculation. In this method, most of the biological molecule is modeled using a standard MM/MD treatment, but those parts of the molecule not properly treated by standard force equations are treated quantum mechanically. This hybrid approach has been successfully used, for example, to model an enzyme reaction pathway [95], allowing the breaking and formation of covalent bonds, which cannot be modeled by MM/MD force fields. Applying QM/MM to BXBs in protein–inhibitor complexes, MM force fields are applied to the majority of atoms of the protein, with the groups immediately around the X-bonding acceptor(s) and donor(s) treated by QM. Lu et al. [61] showed how QM/MM calculations can accurately reproduce the geometries of BXBs for halogenated ligands to the carbonyl oxygens of proteins in complexes. Success in modeling the interaction energies, however, depended on how the QM component was implemented, but they do qualitatively follow the trends expected for BXBs.

In standard MM/MD methods, halogens are assigned an isotropic electronegative charge and, therefore, any attempts to model the geometry or the interaction energies of X-bonds are doomed to failure. One very straightforward strategy to incorporating X-bonds into programs that simulate energies of biological macromolecules, such as AMBER [96] or OPLS-AA [97], is the positive extra point (PEP) approach [98, 99]. In this method, the halogen retains an overall negative charge at the atom center, but a positive pseudoatom is added at or near the atomic surface to mimic the positive crown of the σ -hole (Fig. 12). By implementing the PEP approach [98, 102], Ibrahim showed that interaction energies calculated from AMBER for various halogenated inhibitors in complex with CK2 kinase correlated well with energies from experimental K_D , K_i , or IC50 values [102]. The geometries modeled in this way, however, tended to be ~ 0.3 Å longer than seen in the crystal structures. Hobza's group [101] has shown that by moving the PEP pseudoatom closer to the halogen center (for Br, it is placed 1.5 Å from the atom center), the

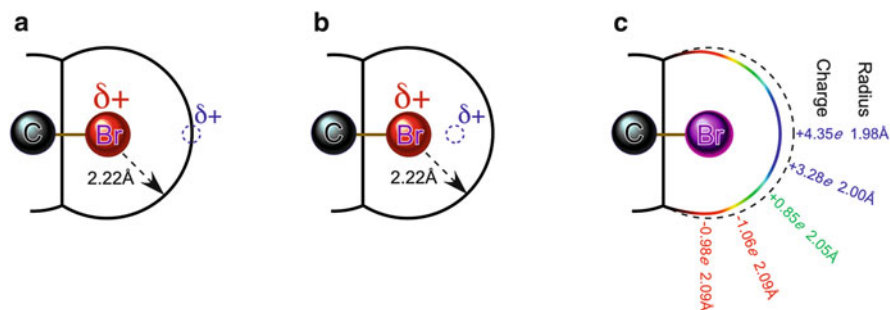


Fig. 12 Strategies for modeling σ -hole in the AMBER [96] force field for MM/MD simulation by: (a) the PEP (with the pseudo atom at the halogen center and charges assigned using restrained electrostatic potential approach [100]); (b) the enhanced PEP (with the pseudo atom placed 1.2 Å from the halogen center [101]); (c) the ffBxB (charges and R_{vdw} assigned according to Θ_1 [33]) methods

X-bond distance becomes closer and is in significantly better agreement with the X-ray structures. Indeed, there is a strong correlation between the position of the PEP relative to the halogen center and the approach distance of the BXB acceptor to the halogen [98].

In a completely different approach, our group set out to derive a set of MM/MD force field equations (a force field for BXBs, or ffBxB) based solely on the physical properties of covalently bonded halogens, starting with Br [33]. The result was a set of potential energy functions (for the Coulombic and Lennard–Jones potentials) that describe both the effective charge and the effective shape (R_{vdw}) of Br as angular dependent functions of Θ_1 . The ffBxB properly models the QM calculated and experimentally measured structure–energy relationships for the BXBs in the DNA junction model system, and is expected to be applicable to modeling BXBs as well as H-bonds to halogens in protein–inhibitor complexes, once incorporated into MM/MD programs like AMBER.

Finally, Liu et al. [103] have applied a knowledge-based approach to deriving a set of scoring functions, based on statistical distributions of the geometries (Figs. 6, 7, and 8), to help identify BXBs in protein–ligand complexes. One must be careful, however, to insure when applying population studies to infer probability functions that the datasets sample the overall population broadly, but without redundancy. For example, the number of I-BXBs is small relative to Cl and Br, and is dominated by contacts of thyroxine in various protein contexts. Similarly, the Br-BXB dataset may be over-represented by inhibitors to particular protein kinases. Although each example within these classes of interactions may be unique in themselves, the binding environments may show significantly similarities and, consequently the binding modes may be related. Thus, the balance between having a sufficient number and the uniqueness of the structures could depend on how such force fields are derived. Such population distributions, however, may be particularly useful for validating and comparing the various competing computational approaches to modeling BXBs.

7 Perspectives and Conclusions

We have now started to dissect the details of the structure and energies of BXBs and to develop methods to incorporate accurately the concept into molecular simulation programs to model their effects on molecular folding and binding interactions.

The question has been raised as to why we should care about BXBs and invest so much creative energy into measuring and modeling such weak interactions [104]. For most chemists, interactions at or near thermal fluctuations ($k_B T$, ~ 0.6 kcal/mol at room temperature) could be considered to be inconsequential. Why should we care about X-bonds and H-bonds, which in biology are at most an order of magnitude above $k_B T$? The reason is that, in biology, the difference between a folded (and thus functional native) conformation and an unfolded denatured form typically is not so far from $k_B T$. For example, the functional KIX domain of the CREB binding protein (a transcriptional activator) is only 97% folded and 3% unfolded under standard solution conditions at 27°C [105], translating to $\Delta G^\circ \approx 2$ kcal/mol ($\sim 3 k_B T$). Even the most stable protein or polynucleic acid is held together by a sum of multiple weak interactions, each contributing no more than a few kcal/mol. Thus, although the sums are greater than the individual parts, not all parts are equal; an interaction at or near binding recognition or catalytic sites may have an inordinately large influence on functional specificity, even if it contributes only minimally to structural stability.

We can consider, for example, the effect of a single weak interaction on ligand binding. We have already seen that the contribution of 4 kcal/mol is equivalent to a 1,000-fold increase in specificity. Consider a case where a lead compound is being developed as a potential drug. That compound may have a K_D in the micromolar range, which means that it could not be sent forward for clinical trials. Adding a “weak” 4 kcal/mol BXB, however, would reduce the K_D to the nanomolar range, which would then render it a potential drug candidate. In many cases, even a 50-fold reduction in K_D (equivalent to ~ 2 kcal/mol interaction, in the range of a Cl- or Br-BXB) can make the difference between a viable and a dead-end compound for a medicinal chemist.

The unique geometry and energetic properties, particularly when compared to the more ubiquitous H-bond, make BXBs important tools for rational design of halogenated compounds in macromolecular engineering.

7.1 BXBs as Molecular Tools for Rational Drug Design

We have already seen that BXBs are most prevalent in protein–ligand complexes and in these complexes the geometries are uniquely defined by the complex environment of the binding pocket. Where the BXB concept is seen to have its greatest potential and its greatest challenge is towards the rational design of ligands against therapeutic targets – drug design. Indeed, a large fraction of drugs already

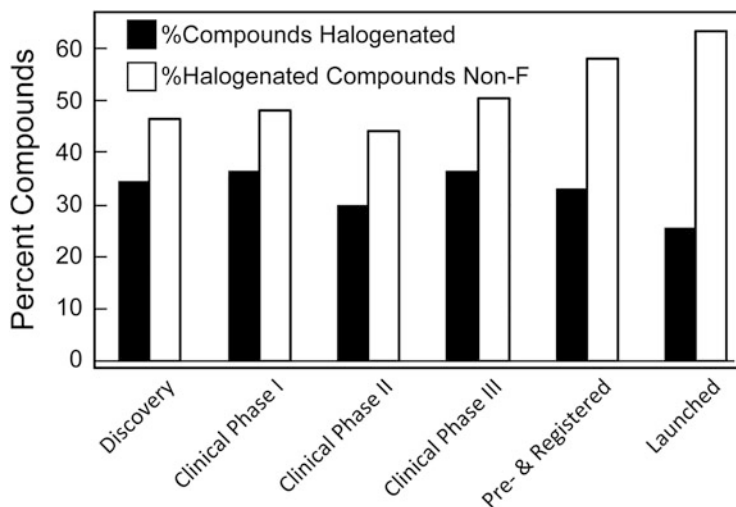


Fig. 13 Percent of organic compounds that are halogenated (*solid bars*) and percent of halogenated compounds that are not fluorinated (*open bars*) from the initial discovery stage, through clinical trials, and to the end point of launch as a new drug (from Xu et al. [106])

on the market or in clinical trials (~40%) are halogenated and, prior to the “re-discovery” of X-bonds, it was not entirely clear why. Now we know the why, we just need to determine how.

How can we exploit this concept to rationally design more effective drugs? The most obvious application is that the BXB principle, when incorporated into docking programs, will allow the various halogenated compounds in libraries to be properly treated in virtual screens. It should be remembered that ~20% of the molecules in the NCI Diversity IV group contain a halogen which can potentially form BXBs. In a survey of the role halogens play in drug design, Xu et al. [106] showed that, in general, compounds making it through various points along the pathway for drug development start at ~35% being halogenated at the initial discovery stage and end with ~25% being halogenated at the end of the pipeline (at launch). However, the attrition of halogenated compounds is primarily of fluorinated molecules – those with BXB potential, particularly Cl, tend to persist to the end (Fig. 13).

The current docking algorithms that do not incorporate BXBs, however, would be incapable of covering the contribution of the halogens towards the affinity/specificity of these compounds to potential target proteins (thus losing up to 20% of possible lead compounds). There has been some success with incorporating an explicit σ -hole (ESH, similar to the PEP strategy of MM/MD simulations) [23] into the University of California at San Francisco DOCK program [107], which is an important first step towards attacking this problem.

A more focused strategy would be to take advantage of the unique geometries and directionality of the BXBs to optimize the efficacy of unhalogenated lead compounds [108]. For example, consider the fairly common situation where you

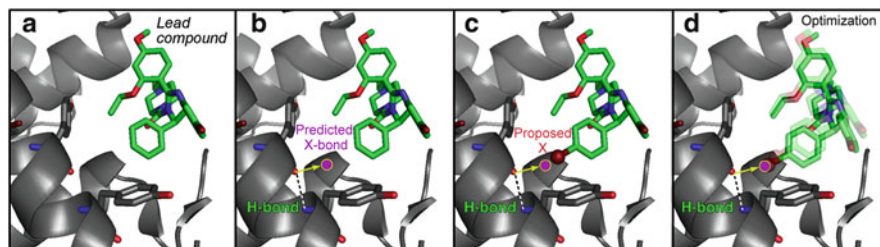


Fig. 14 Proposed application of BXBs for lead compound optimization, starting from structure of a lead compound (a), to the principle of orthogonal X- and H-bonds (b), to guiding placement of a halogen substituent on the lead compound (c), and finally, optimization of the new halogenated compound to predict the effect on binding/specificity (d) (adapted from [109])

have the structure (either an experimental crystal structure or a computational model from a virtual screening and docking study) of a compound with the potential to be a potent inhibitor against a protein target (Fig. 14); however, the K_D for this ligand (in the micromolar range) is insufficient to make this a clinically viable inhibitor. Introducing a halogen substituent which forms a BXB could provide the two to three orders of magnitude change in K_D , and be the difference when making the “go or no-go” decision to continue development of that compound. However, where should that substituent be added and how much improvement can be expected? Applying the orthogonality concept of BXBs and H-bonds to the pattern of structural H-bonds of the protein [55], it is now possible to predict the positions for where a halogen can be placed within the binding site to form a stabilizing BXB. These potential BXB positions can then help guide the design by medicinal chemists of halogenated variants of the lead compound. Finally, applying either QM/MM or MM/MD methods (with a PEP or f BXB correction) would allow one to predict the effects of the halogen substituent on the geometry and affinity of the new protein–inhibitor complex.

7.2 Potential Application of BXBs in Biomolecular Engineering

The application of X-bonds (exploiting the stabilizing potential, directionality, and their competitive or complementary relationships with H-bonds [78]) to chemical engineering in the design and construction of sensors, liquid crystals, organic conductors, and other materials is now fairly well established [6, 110, 111]. This is not true with BXBs, which opens a completely new and unexplored area in the field. The studies of BXBs in DNA junctions shows a glimpse of what is possible – the conformations of the junction arms were shown to be controlled through competition between H- and X-bonds. DNA junctions are, themselves, the basic building blocks for many biomolecular engineering applications [112], including DNA origami [113] and structured two-dimensional and three-dimensional lattices

[114, 115], to name just a few, because their assembly can be controlled by sequence design. The introduction of BXBs would allow control of the three-dimensional shape of the junction [80], using BXBs to define the spatial relationship between the DNA arms.

For protein engineering, BXBs have the potential to introduce more directed and specific interactions in hydrophobic regions, for example at binding sites for new ligands – an inverse application to the design of halogenated inhibitors [116]. The ability to introduce unnatural amino acids (including many halogenated amino acids) site-specifically into proteins [117, 118] also provides opportunities to control stability of domains or entire proteins, or to design new protein–protein interfaces.

7.3 *Why Are Halogens Hydrophobic?*

Finally, we need to address a fundamental question about halogens in the aqueous environment. Why are halogens, particularly the larger elements Br and I, hydrophobic? The conundrum is that halogens are involved in electrostatic interactions (X-bonds as well as H-bonds, and perhaps other convolutions of these), and the larger the atom the more polarizable and more enthalpically stabilizing the BXBs are. As such, we may consider them to be similar in many respects to a hydroxyl group, which also shows similar amphipathic properties (being both donors and acceptors of H-bonds). There clearly are solvent effects on the energies of X-bonds [83, 85, 119–122], but the studies to date have focused only on the effects on electrostatics (enthalpic components). The current understanding is that hydrophobicity is primarily associated with the loss of entropy of solvent around substituent groups; however, as with H-bonds, there is a delicate balance between the entropy and the electrostatic properties of the waters around the donor atom [123–125]. Thus, to tackle this question, it is imperative that the field develops accurate models for halogens and for waters [126–129] that interact with them. Without an understanding of why halogens as substituents in covalent compounds are hydrophobic, it would be difficult to utilize BXBs fully in, for example, the design of more effective drugs, since the binding and specificity of inhibitors depends not only on the energies of the protein complex, but also on the competing energies of each component in solution [62].

7.4 *Conclusions*

Over the past decade, X-bonding has become accepted, if not fully recognized, by the biological community, particularly in its role in the binding specificity of halogenated inhibitors against protein targets and to affect molecular conformation.

BXBs are becoming well characterized through structural database surveys, and computational and experimental studies on their structure–energy relationships. They have been found to parallel in many cases, but extend in others, the basic physical principles seen in small molecule complexes. Their unique properties, including the relationships with H-bonds and the aqueous environment, will allow BXBs to evolve beyond being a simple curiosity to becoming a powerful molecular tool for the rational engineering of new pharmaceutically important compounds and biological-based materials. For the medicinal chemist, BXBs are now a regular if not common tool in the molecular design toolbox. There remain, however, many audiences in which the question of “Who has heard of halogen bonds?” is met with deadly silence. Thus, there is still work to be done for the evangelist to spread the word of this molecular interaction which has been long neglected, but which has great potential in the biological arena.

Acknowledgements The studies on halogen bonds from the Ho laboratory have been supported by grants from the Fulbright Association and the National Science Foundation (CH 1152494), and funds from Colorado State University. I am indebted to the current and former undergraduates and graduates students who have contributed to the studies through their creative and intellectual capabilities, particularly my current students (M. Scholfield, C. Vander Zanden, and M. Ford) for proof reading the current manuscript.

References

1. Guthries F (1863) On the iodide of iodammonium. *J Am Chem Soc* 16:239–244
2. Flurry RL Jr, Politzer P (1969) Molecular orbital theory of electron donor-acceptor complexes. III. The relationship of state energies and stabilization energies to the charge-transfer transition energy. *J Phys Chem* 73:2787–2789
3. Hassel O (1970) Structural aspects of interatomic charge-transfer bonding. *Science* 170:497–502
4. Hassel O (1972) Structural aspects of interatomic charge-transfer bonding. In: Nobel lectures, chemistry. Elsevier, Amsterdam, pp 1963–1970
5. Metrangolo P, Neukirch H, Pilati T, Resnati G (2005) Halogen bonding based recognition processes: a world parallel to hydrogen bonding. *Acc Chem Res* 38:386–395
6. Metrangolo P, Meyer F, Pilati T, Resnati G, Terraneo G (2008) Halogen bonding in supramolecular chemistry. *Angew Chem Int Ed* 47:6114–6127
7. Lam PYS, Clark CG, Smallwood AM, Alexander RS (2009) Structure-based drug design utilizing halogen bonding: factor Xa inhibitors. In: Metrangolo P, Resnati G (eds) The 238th ACS national meeting. ACS, Washington, DC, p 58
8. Auffinger P, Hays FA, Westhof E, Ho PS (2004) Halogen bonds in biological molecules. *Proc Natl Acad Sci U S A* 101:16789–16794
9. Muzet N, Guillot B, Jelsch C, Howard E, Lecomte C (2003) Electrostatic complementarity in an aldose reductase complex from ultra-high-resolution crystallography and first-principles calculations. *Proc Natl Acad Sci U S A* 100:8742–8747
10. Hays FA, Vargason JM, Ho PS (2003) Effect of sequence on the conformation of DNA Holliday junctions. *Biochemistry* 42:9586–9597
11. Vallejos M, Auffinger P, Ho P (2012) Halogen interactions in biomolecular crystal structures. In: Himmel DM (ed) *Int Tables Cryst* vol F, pp 23–26

12. Riu A, Grimaldi M, le Maire A, Bey G, Phillips K, Boulahtouf A, Perdu E, Zalko D, Bourguet W, Balaguer P (2011) Peroxisome proliferator-activated receptor gamma is a target for halogenated analogs of bisphenol A. *Environ Health Perspect* 119:1227–1232
13. Lu Y, Liu Y, Xu Z, Li H, Liu H, Zhu W (2012) Halogen bonding for rational drug design and new drug discovery. *Expert Opin Drug Discov* 7:375–383
14. Wilcken R, Liu X, Zimmermann MO, Rutherford TJ, Fersht AR, Joerger AC, Boeckler FM (2012) Halogen-enriched fragment libraries as leads for drug rescue of mutant p53. *J Am Chem Soc* 134:6810–6818
15. Zou JW, Lu YX, Yu QS, Zhang HX, Jiang YJ (2006) Halogen bonding: an AIM analysis of the weak interactions. *Chin J Chem* 24:1709–1715
16. Tiwari A, Panigrahi SK (2007) HBAIT: a complete package for analysing strong and weak hydrogen bonds in macromolecular crystal structures. *In Silico Biol* 7:0057
17. Schreyer A, Blundell T (2009) Credo: a protein-ligand interaction database for drug discovery. *Chem Biol Drug Des* 73:157–167
18. Ouvrard C, Le Questel JY, Berthelot M, Laurence C (2003) Halogen-bond geometry: a crystallographic data-base investigation of dihalogen complexes. *Acta Cryst B* 59:512–526
19. Politzer P, Lane P, Concha MC, Ma Y, Murray JS (2007) An overview of halogen bonding. *J Mol Model* 13:305–311
20. Scholfield MR, Vander Zanden CM, Carter M, Ho PS (2013) Halogen bonding (X-bonding): a biological perspective. *Protein Sci* 22:139–152
21. Desiraju GR, Ho PS, Legon AC, Marquardt R, Metrangolo P, Politzer P, Resnati G, Rissanen K (2013) Definition of the halogen bond (IUPAC recommendations 2013). *Pure Appl Chem* 85:1711–1713
22. NCI/NIH (2014) Developmental therapeutics program. <http://dtp.nci.nih.gov/index.html>
23. Kolar M, Hobza P, Bronowska AK (2013) Plugging the explicit sigma-holes in molecular docking. *Chem Commun (Camb)* 49:981–983
24. Clark T, Hennemann M, Murray JS, Politzer P (2007) Halogen bonding: the sigma-hole. Proceedings of “Modeling Interactions in Biomolecules II”, Prague, September 5th–9th, 2005. *J Mol Model* 13:291–296
25. Murray JS, Lane P, Clark T, Politzer P (2007) Sigma-hole bonding: molecules containing group VI atoms. *J Mol Model* 13:1033–1038
26. Politzer P, Murray JS, Lane P (2007) Sigma-hole bonding and hydrogen bonding: competitive interactions. *Int J Quantum Chem* 107:3046–3052
27. Murray JS, Riley KE, Politzer P, Clark T (2010) Directional weak intermolecular interactions: sigma-hole bonding. *Aust J Chem* 63:1598–1607
28. Murray JS, Lane P, Clark T, Riley KE, Politzer P (2012) Sigma-holes, pi-holes and electrostatically-driven interactions. *J Mol Model* 18:541–548
29. Politzer P, Riley KE, Bulat FA, Murray JS (2012) Perspectives on halogen bonding and other sigma-hole interactions: *lex parsimoniae* (Occam’s razor). *Comput Theor Chem* 998:2–8
30. Metrangolo P, Murray JS, Pilati T, Politzer P, Resnati G, Terraneo G (2011) Fluorine-centered halogen bonding: a factor in recognition phenomena and reactivity. *Cryst Growth Des* 11:4238–4246
31. Metrangolo P, Murray JS, Pilati T, Politzer P, Resnati G, Terraneo G (2011) The fluorine atom as a halogen bond donor, viz. a positive site. *CrystEngComm* 13:6593–6596
32. Riley KE, Murray JS, Fanfrlik J, Rezac J, Sola RJ, Concha MC, Ramos FM, Politzer P (2011) Halogen bond tunability I: the effects of aromatic fluorine substitution on the strengths of halogen-bonding interactions involving chlorine, bromine, and iodine. *J Mol Model* 17:3309–3318
33. Carter M, Rappe AK, Ho PS (2012) Scalable anisotropic shape and electrostatic models for biological bromine halogen bonds. *J Chem Theor Comput* 8:2461–2473
34. Hammett LP (1937) The effect of structure upon the reactions of organic compounds. Benzene derivatives. *J Am Chem Soc* 59:96–103

35. Berman HM, Westbrook J, Feng Z, Gilliland G, Bhat TN, Weissig H, Shindyalov IN, Bourne PE (2000) The protein data bank. *Nucleic Acids Res* 28:235–242
36. Howard EI, Sanishvili R, Cachau RE, Mitschler A, Chevrier B, Barth P, Lamour V, Van Zandt M, Sibley E, Bon C, Moras D, Schneider TR, Joachimiak A, Podjarny A (2004) Ultrahigh resolution drug design I: details of interactions in human aldose reductase-inhibitor complex at 0.66 Å. *Proteins* 55:792–804
37. Hays FA, Teegarden A, Jones ZJR, Harms M, Raup D, Watson J, Cavaliere E, Ho PS (2005) How sequence defines structure: a crystallographic map of DNA structure and conformation. *Proc Natl Acad Sci U S A* 102:7157–7162
38. Eichman BF, Vargason JM, Mooers BHM, Ho PS (2000) The Holliday junction in an inverted repeat sequence: sequence effects on the structure of four-way junctions. *Proc Natl Acad Sci U S A* 97:3971–3976
39. Lommerse JPM, Stone AJ, Taylor R, Allen FH (1996) The nature and geometry of intramolecular interactions between halogens and oxygen or nitrogen. *J Am Chem Soc* 118:3108–3116
40. Panigrahi SK, Desiraju GR (2007) Strong and weak hydrogen bonds in the protein-ligand interface. *Proteins* 67:128–141
41. Zhou P, Tian F, Zou J, Shang Z (2010) Rediscovery of halogen bonds in protein-ligand complexes. *Mini Rev Med Chem* 10:309–314
42. Parisini E, Metrangolo P, Pilati T, Resnati G, Terraneo G (2011) Halogen bonding in halocarbon-protein complexes: a structural survey. *Chem Soc Rev* 40:2267–2278
43. Xie J, Wang L, Wu N, Brock A, Spraggon G, Schultz PG (2004) The site-specific incorporation of p-iodo-l-phenylalanine into proteins for structure determination. *Nat Biotechnol* 22:1297–1301
44. Beck T, Gruene T, Sheldrick GM (2010) The magic triangle goes mad: experimental phasing with a bromine derivative. *Acta Crystallogr D Biol Crystallogr* 66:374–380
45. Sunami T, Kondo J, Hirao I, Watanabe K, Miura K, Takenaka A (2004) Structures of d(GCGAAGC) and d(GCGAAGC) (tetragonal form): a switching of partners of the sheared G.A pairs to form a functional G.AxA.G crossing. *Acta Crystallogr D Biol Crystallogr* 60:422–431
46. Sunami T, Kondo J, Hirao I, Watanabe K, Miura KI, Takenaka A (2004) Structure of d(GCGAAAGC) (hexagonal form): a base-intercalated duplex as a stable structure. *Acta Crystallogr D Biol Crystallogr* 60:90–96
47. Domigan NM, Charlton TS, Duncan MW, Winterbourn CC, Kettle AJ (1995) Chlorination of tyrosyl residues in peptides by myeloperoxidase and human neutrophils. *J Biol Chem* 270:16542–16548
48. Wu WJ, Chen YH, d'Avignon A, Hazen SL (1999) 3-Bromotyrosine and 3,5-dibromotyrosine are major products of protein oxidation by eosinophil peroxidase: potential markers for eosinophil-dependent tissue injury in vivo. *Biochemistry* 38:3538–3548
49. Wu W, Samoszuk MK, Comhair SAA, Thomassen MJ, Farver CF, Dweik RA, Kavuru MS, Erzurum SC, Hazen SL (2000) Eosinophils generate brominating oxidants in allergen-induced asthma. *J Clin Invest* 105:1455–1463
50. Kambayashi Y, Ogino K, Takemoto K, Imagama T, Takigawa T, Kimura S, Hibino Y, Hitomi Y, Nakamura H (2009) Preparation and characterization of a polyclonal antibody against brominated protein. *J Clin Biochem Nutr* 44:95–103
51. Sandler B, Webb P, Aprelletti JW, Huber BR, Togashi M, Cunha Lima ST, Juric S, Nilsson S, Wagner R, Fletterick RJ, Baxter JD (2004) Thyroxine-thyroid hormone receptor interactions. *J Biol Chem* 279:55801–55808
52. Valadares NF, Salum LB, Polikarpov I, Andricopulo AD, Garratt RC (2009) Role of halogen bonds in thyroid hormone receptor selectivity: pharmacophore-based 3D-QSSR studies. *J Chem Inf Model* 49:2606–2616
53. Eneqvist T, Lundberg E, Karlsson A, Huang S, Santos CR, Power DM, Sauer-Eriksson AE (2004) High resolution crystal structures of piscine transthyretin reveal different binding modes for triiodothyronine and thyroxine. *J Biol Chem* 279:26411–26416

54. Manna D, Mugesh G (2012) Regioselective deiodination of thyroxine by iodothyronine deiodinase mimics: an unusual mechanistic pathway involving cooperative chalcogen and halogen bonding. *J Am Chem Soc* 134:4269–4279
55. Voth AR, Khuu P, Oishi K, Ho PS (2009) Halogen bonds as orthogonal molecular interactions to hydrogen bonds. *Nat Chem* 1:74–79
56. Hernandes MZ, Cavalcanti SM, Moreira DR, de Azevedo Junior WF, Leite AC (2010) Halogen atoms in the modern medicinal chemistry: hints for the drug design. *Curr Drug Targets* 11:303–314
57. De Moliner E, Moro S, Sarno S, Zagotto G, Zanotti G, Pinna LA, Battistutta R (2003) Inhibition of protein kinase CK2 by anthraquinone-related compounds - a structural insight. *J Biol Chem* 278:1831–1836
58. Liu R, Loll PJ, Eckenhoff RG (2005) Structural basis for high-affinity volatile anesthetic binding in a natural 4-helix bundle protein. *FASEB J* 19:567–576
59. Heath RJ, Su N, Murphy CK, Rock CO (2000) The enoyl-[acyl-carrier-protein] reductases FabI and FabL from *Bacillus subtilis*. *J Biol Chem* 275:40128–40133
60. Voth AR, Ho PS (2007) The role of halogen bonding in inhibitor recognition and binding by protein kinases. *Curr Top Med Chem* 7:1336–1348
61. Lu Y, Shi T, Wang Y, Yang H, Yan X, Luo X, Jiang H, Zhu W (2009) Halogen bonding—a novel interaction for rational drug design? *J Med Chem* 52:2854–2862
62. Wasik R, Lebska M, Felczak K, Poznanski J, Shugar D (2010) Relative role of halogen bonds and hydrophobic interactions in inhibition of human protein kinase CK2 alpha by tetrabromobenzotriazole and some C(5)-substituted analogues. *J Phys Chem B* 114:10601–10611
63. Fedorov O, Huber K, Eisenreich A, Filippakopoulos P, King O, Bullock AN, Szklarczyk D, Jensen LJ, Fabbro D, Trappe J, Rauch U, Bracher F, Knapp S (2011) Specific CLK inhibitors from a novel chemotype for regulation of alternative splicing. *Chem Biol* 18:67–76
64. Bollini M, Domaal RA, Thakur VV, Gallardo-Macias R, Spasov KA, Anderson KS, Jorgensen WL (2011) Computationally-guided optimization of a docking hit to yield catechol diethers as potent anti-HIV agents. *J Med Chem* 54:8582–8591
65. Carpenter RD, Natarajan A, Lau EY, Andrei M, Solano DM, Lightstone FC, DeNardo SJ, Lam KS, Kurth MJ (2010) Halogenated benzimidazole carboxamides target integrin alpha(4) beta(1) on t-cell and b-cell lymphomas. *Cancer Res* 70:5448–5456
66. Joseph LJ, Chang LC, Stamenkovich D, Sukhatme VP (1988) Complete nucleotide and deduced amino acid sequences of human and murine preprocathepsin L. An abundant transcript induced by transformation of fibroblasts. *J Clin Invest* 81:1621–1629
67. Maciewicz RA, Wardale RJ, Etherington DJ, Paraskeva C (1989) Immunodetection of cathepsins B and L present in and secreted from human pre-malignant and malignant colorectal tumour cell lines. *Int J Cancer* 43:478–486
68. Watanabe M, Higashi T, Hashimoto M, Tomoda I, Tominaga S, Hashimoto N, Morimoto S, Yamauchi Y, Nakatsukasa H, Kobayashi M et al (1987) Elevation of tissue cathepsin B and L activities in gastric cancer. *Hepatogastroenterology* 34:120–122
69. Rozhin J, Wade RL, Honn KV, Sloane BF (1989) Membrane-associated cathepsin L: a role in metastasis of melanomas. *Biochem Biophys Res Commun* 164:556–561
70. Yamaguchi N, Yamamura Y, Koyama K, Ohtsuji E, Imanishi J, Ashihara T (1990) Characterization of new human pancreatic cancer cell lines which propagate in a protein-free chemically defined medium. *Cancer Res* 50:7008–7014
71. Wilcken R, Zimmermann MO, Lange A, Zahn S, Boeckler FM (2012) Using halogen bonds to address the protein backbone: a systematic evaluation. *J Comput Aid Mol Des* 26:935–945
72. Kortagere S, Ekins S, Welsh WJ (2008) Halogenated ligands and their interactions with amino acids: implications for structure-activity and structure-toxicity relationships. *J Mol Graph Model* 27:170–177
73. Prasanna MD, Guru Row TN (2000) C-halogen- π interactions and their influence on molecular conformation and crystal packing: a database study. *Cryst Eng* 3:135–154

74. Saraogi I, Vijay V, Das S, Sekar K, Guru Row T (2003) C-halogen... π interactions in proteins: a database study. *Cryst Eng* 6:69–77
75. Matter H, Nazare M, Gussregen S, Will DW, Schreuder H, Bauer A, Urmann M, Ritter K, Wagner M, Wehner V (2009) Evidence for C-Cl/C-Br... π interactions as an important contribution to protein-ligand binding affinity. *Angew Chem Int Ed* 48:2911–2916
76. Paulini R, Muller K, Diederich F (2005) Orthogonal multipolar interactions in structural chemistry and biology. *Angew Chem Int Ed* 44:1788–1805
77. Zhou P, Lv J, Zou J, Tian F, Shang Z (2010) Halogen-water-hydrogen bridges in biomolecules. *J Struct Biol* 169:172–182
78. Aakeröy C, Despera J, Helfrich BA, Metrangolo P, Pilatic T, Resnati G, Stevenazzi A (2007) Combining halogen bonds and hydrogen bonds in the modular assembly of heteromeric infinite 1-D chains. *Chem Commun* 4236–4238
79. Aakeröy CB, Fasulo M, Schultheiss N, Desper J, Moore C (2007) Structural competition between hydrogen bonds and halogen bonds. *J Am Chem Soc* 129:13772
80. Voth AR, Hays FA, Ho PS (2007) Directing macromolecular conformation through halogen bonds. *Proc Natl Acad Sci U S A* 104:6188–6193
81. van Holde K, Johnson WJ, Ho PS (2006) Principles of physical biochemistry, 2nd edn. Pearson Prentice Hall, Upper Saddle River, NJ
82. Corradi E, Meille SV, Messina MT, Metrangolo P, Resnati G (2000) Halogen bonding versus hydrogen bonding in driving self-assembly processes. *Angew Chem Int Ed* 39:1782–1786
83. Carter M, Ho PS (2011) Assaying the energies of biological halogen bonds. *Cryst Growth Des* 11:5087–5095
84. Vander Zanden CM, Carter C, Ho PS (2013) Determining thermodynamic properties of molecular interactions from single crystal studies. *Methods* 64:12–18
85. Carter M, Voth AR, Schofield MR, Rummel B, Sowers LC, Ho PS (2013) Enthalpy - entropy compensation in biomolecular halogen bonds measured in DNA junctions. *Biochemistry* 52:4891–4903
86. Erdelyi M (2012) Halogen bonding in solution. *Chem Soc Rev* 41:3547–3557
87. Tatko CD, Waters ML (2004) Effect of halogenation on edge-face aromatic interactions in a beta-hairpin peptide: enhanced affinity with iodo-substituents. *Org Lett* 6:3969–3972
88. Hardegger LA, Kuhn B, Spinnler B, Anselm L, Ecabert R, Stihle M, Gsell B, Thoma R, Diez J, Benz J, Plancher JM, Hartmann G, Banner DW, Haap W, Diederich F (2011) Systematic investigation of halogen bonding in protein-ligand interactions. *Angew Chem Int Ed* 50:314–318
89. Wyatt PG, Woodhead AJ, Berdini V, Boulstridge JA, Carr MG, Cross DM, Davis DJ, Devine LA, Early TR, Feltell RE, Lewis EJ, McMenamin RL, Navarro EF, O'Brien MA, O'Reilly M, Reule M, Saxty G, Seavers LC, Smith DM, Squires MS, Trewartha G, Walker MT, Woolford AJ (2008) Identification of n-(4-piperidiny)-4-(2,6-dichlorobenzoylamino)-1 H-pyrazole-3-carbox-amide (at7519), a novel cyclin dependent kinase inhibitor using fragment-based X-ray crystallography and structure based drug design. *J Med Chem* 51:4986–4999
90. Sarno S, Papinutto E, Franchin C, Bain J, Elliott M, Meggio F, Kazimierczuk Z, Orzeszko A, Zanotti G, Battistutta R, Pinna LA (2011) ATP site-directed inhibitors of protein kinase CK2: an update. *Curr Top Med Chem* 11:1340–1351
91. Dobs P, Rezac J, Fanfrlik J, Otyepka M, Hobza P (2011) Semiempirical quantum mechanical method PM6-DH2X describes the geometry and energetics of CK2-inhibitor complexes involving halogen bonds well, while the empirical potential fails. *J Phys Chem B* 115:8581–8589
92. Battistutta R, De Moliner E, Sarno S, Zanotti G, Pinna LA (2001) Structural features underlying selective inhibition of protein kinase CK2 by ATP site-directed tetrabromo-2-benzotriazole. *Protein Sci* 10:2200–2206
93. Battistutta R, Mazzorana M, Sarno S, Kazimierczuk Z, Zanotti G, Pinna LA (2005) Inspecting the structure-activity relationship of protein kinase CK2 inhibitors derived from tetrabromo-benzimidazole. *Chem Biol* 12:1211–1219

94. Battistutta R, Mazzorana M, Cendron L, Bortolato A, Sarno S, Kazimierczuk Z, Zanotti G, Moro S, Pinna LA (2007) The ATP-binding site of protein kinase CK2 holds a positive electrostatic area and conserved water molecules. *ChemBiochem* 8:1804–1809
95. Monard G, Prat-Resina X, Gonzalez-Lafont A, Lluch JM (2003) Determination of enzymatic reaction pathways using QM/MM methods. *Int J Quantum Chem* 93:229–244
96. Case DA, Cheatham TE 3rd, Darden T, Gohlke H, Luo R, Merz KM Jr, Onufriev A, Simmerling C, Wang B, Woods RJ (2005) The amber biomolecular simulation programs. *J Comput Chem* 26:1668–1688
97. Jorgensen WL, Schyman P (2012) Treatment of halogen bonding in the OPLS-AA force field: application to potent anti-HIV agents. *J Chem Theor Comput* 8:3895–3901
98. Ibrahim MA (2011) Molecular mechanical study of halogen bonding in drug discovery. *J Comput Chem* 32:2564–2574
99. Rendine S, Pieraccini S, Forni A, Sironi M (2011) Halogen bonding in ligand-receptor systems in the framework of classical force fields. *Phys Chem Chem Phys* 13:19508–19516
100. Bayly CI, Cieplak P, Cornell WD, Kollman PA (1993) A well-behaved electrostatic potential based method using charge restraints for deriving atomic charges - the RESP model. *J Phys Chem* 97:10269–10280
101. Kolar M, Hobza P (2012) On extension of the current biomolecular empirical force field for the description of halogen bonds. *J Chem Theor Comput* 8:1325–1333
102. Ibrahim MA (2012) Amber empirical potential describes the geometry and energy of noncovalent halogen interactions better than advanced semiempirical quantum mechanical method PM6-DH2X. *J Phys Chem B* 116:3659–3669
103. Liu Y, Xu Z, Yang Z, Chen K, Zhu W (2013) A knowledge-based halogen bonding scoring function for predicting protein-ligand interactions. *J Mol Model* 19:5015–5030
104. Gavezzotti A (2013) The “sceptical chymist”: intermolecular doubts and paradoxes. *CrystEngComm* 15:4027–4035
105. Schanda P, Brutscher B, Konrat R, Tollinger M (2008) Folding of the KIX domain: characterization of the equilibrium analog of a folding intermediate using (15)N/(13)C relaxation dispersion and fast (1)H/(2)H amide exchange NMR spectroscopy. *J Mol Biol* 380:726–741
106. Xu Z, Yang Z, Liu Y, Lu Y, Chen K, Zhu W (2014) Halogen bond: its role beyond drug-target binding affinity for drug discovery and development. *J Chem Inf Model* 54:69–78
107. Kuntz ID, Blaney JM, Oatley SJ, Langridge R, Ferrin TE (1982) A geometric approach to macromolecule-ligand interactions. *J Mol Biol* 161:269–288
108. Xu Z, Liu Z, Chen T, Wang Z, Tian G, Shi J, Wang X, Lu Y, Yan X, Wang G, Jiang H, Chen K, Wang S, Xu Y, Shen J, Zhu W (2011) Utilization of halogen bond in lead optimization: a case study of rational design of potent phosphodiesterase type 5 (PDE5) inhibitors. *J Med Chem* 54:5607–5611
109. Ho PS (2014) From Holliday junctions to biomolecular halogen bonds: how biology informs us about complex chemistry. *F&M Scientist* 2:28–54
110. Fourmigué M (2009) Halogen bonding: recent advances. *Curr Opin Solid State Mater Sci* 13:36–45
111. Priimagi A, Cavallo G, Metrangolo P, Resnati G (2013) The halogen bond in the design of functional supramolecular materials: recent advances. *Acc Chem Res* 46:2686–2695
112. Seeman NC (2005) From genes to machines: DNA nanomechanical devices. *Trends Biochem Sci* 30:119–125
113. Rothemund PW (2006) Folding DNA to create nanoscale shapes and patterns. *Nature* 440:297–302
114. Mao C, Sun W, Seeman NC (1999) Designed two-dimensional DNA Holliday junction arrays visualized by atomic force microscopy. *J Am Chem Soc* 121:5437–5443
115. Paukstelis PJ, Nowakowski J, Birktoft JJ, Seeman NC (2004) Crystal structure of a continuous three-dimensional DNA lattice. *Chem Biol* 11:1119–1126

116. Jackson JC, Duffy SP, Hess KR, Mehl RA (2006) Improving nature's active site with genetically encoded unnatural amino acids. *J Am Chem Soc* 128:11124–11127
117. Wang L, Brock A, Herberich B, Schultz PG (2001) Expanding the genetic code of *Escherichia coli*. *Science* 292:498–500
118. Young TS, Schultz PG (2010) Beyond the canonical 20 amino acids: expanding the genetic lexicon. *J Biol Chem* 285:11039–11044
119. Sarwar MG, Dragisic B, Salsberg LJ, Gouliaras C, Taylor MS (2010) Thermodynamics of halogen bonding in solution: substituent, structural, and solvent effects. *J Am Chem Soc* 132:1646–1653
120. Lu Y, Li H, Zhu X, Zhu W, Liu H (2011) How does halogen bonding behave in solution? A theoretical study using implicit solvation model. *J Phys Chem A* 115:4467–4475
121. Lu YX, Li HY, Zhu X, Liu HL, Zhu WL (2012) Effects of solvent on weak halogen bonds: density functional theory calculations. *Int J Quantum Chem* 112:1421–1430
122. Chudzinski MG, Taylor MS (2012) Correlations between computation and experimental thermodynamics of halogen bonding. *J Org Chem* 77:3483–3491
123. Rose GD, Wolfenden R (1993) Hydrogen bonding, hydrophobicity, packing, and protein folding. *Annu Rev Biophys Biomol Struct* 22:381–415
124. Karplus PA (1997) Hydrophobicity regained. *Protein Sci* 6:1302–1307
125. Lum K, Chandler D, Weeks JD (1999) Hydrophobicity at small and large length scales. *J Phys Chem B* 103:4570–4577
126. Duffy EM, Jorgensen WL (2000) Prediction of properties from simulations: free energies of solvation in hexadecane, octanol, and water. *J Am Chem Soc* 122:2878–2888
127. Lu YP, Wang RX, Yang CY, Wang SM (2007) Analysis of ligand-bound water molecules in high-resolution crystal structures of protein-ligand complexes. *J Chem Inf Model* 47:668–675
128. Michel J, Tirado-Rives J, Jorgensen WL (2009) Energetics of displacing water molecules from protein binding sites: consequences for ligand optimization. *J Am Chem Soc* 131:15403–15411
129. Ross GA, Morris GM, Biggin PC (2012) Rapid and accurate prediction and scoring of water molecules in protein binding sites. *PLoS One* 7:e32036

Index

A

Ab initio calculations, 43, 101
Aldehyde dehydrogenase, 248
Alkenes, 126
Alkyl chlorides, 121
Alkyl fluorides, 121
Alkynes, 126
2-Amino-3,5-dibromopyrazine, 178
2-Aminopyrazine
 1,4-diiidotetrafluorobenzene, 178
Angular and radial geometry, 43
Anion binding, 205
Anion–cation symport, 224
Anion– π interactions, 205
Anion transport, halogen bonds, 208
Argon, 81
Aromatic compounds, 126
Astatine, 4
3,3'-Azobipyridine, 175

B

Basis set superposition error (BSSE), 102
Benzene, 135
1,4-Benzoquinone, 8
Best donor–best acceptor, 174
Binding strength, 70
Biomolecular halogen bonds (BXBs), 241
4,4'-Bipyridine 1,3-diiidotetrafluorobenzene, 158
4,4'-Bipyridyl 1,4-diiidotetrafluorobenzene, 173
4,4'-Bipyridyl-*N,N'*-dioxide
 1,4-di-iodotetrafluorobenzene, 176
Bis(trimethylammonium)alkane diiodide, 183

1,4-Bis(iodoethynyl)bicycle[2.2.2]octane, 192
1,4-Bis(3-quinolyl)-1,3-butadiyne
 1,4-diiidotetrafluorobenzene, 158
Bis(pyrid-4'-yl)-1,2,4-oxadiazole, 163
Blue-shifting, 142
Bromine bond, 12
2-Bromoanilinium bromide, 195
2-Bromo-2-chloro-1,1,1-trifluoroethane, 218
Bromodifluoromethane, 145
5-Bromouracil, 248
2-Butyne, 132

C

Calixarenes, 205, 210
Capsules, 165, 209
Cation– π interactions, 184
Cation selectivity, 219
Cation transporters, 207
CCSD(T)(F12b)/VTZ, 66
Centrifugal distortions constants, 51
Cesium, 219
Channelopathies, 208
Charge transfer, 33
Chemical shifts, 183, 186
Chlorine bond, 12
2-Chloroanilinium bromide, 195
Chlorodifluoromethane, 145
CK2 kinase, 263
Cocrystals, 155, 183
Combined rotation and multiple pulse spectroscopy (CRAMPS) 192
Complexation enthalpies, 98, 139
Complex bands, 95
Cotransporters, 223

Coulomb law/interactions, 19, 20, 32
 Counterpoise (CP), 102
 Cryosolutions, 79
 infrared spectroscopy, 83
 Raman spectroscopy, 90
 Crystal engineering, 1, 156

D

Decamethonium diiodide-dihalogenated
 benzene, 192
 Density functional theory (DFT), 215, 248
 Diazabicyclo[2.2.2]octane (DABCO), 191
 4,5-Diazafluoren-9-one (DAFONE), 160
 Dibromine, 5
 Dibromotetrafluorobenzene (DBTFB), 160
 Dichlorotetrafluorobenzene (DCTFB), 160
 Difluorine, 4
 Diidobutadiene, 172
 Diiodobenzene, 219
 Diiodooctafluorobutane, 159
 Diiodoperfluorohexane, 163
 1,2-Diiodotetrafluorobenzene, 158
 1,4-Diiodotetrafluorobenzene (DITFB), 8, 169,
 175, 178, 197
 1,4-Diiodotetrafluorobenzene 1,4-dithiane,
 164
 Dimethyl ether (DME), 93, 112
 Dimethyl sulfide (DMS), 112, 116
 Dioxane, 8
 4,4'-Dipyridine, 8
 Distributed multipole analysis, 60
 1,4-Dithiane, 164
 DNA duplex, 233
 DNA junctions, 244, 259
 DNA origami, 268
 Doppler doublet, 48
 DOXYL quenchers, 232
 DPPC (dipalmitoyl phosphatidylcholine)
 vesicles, 224
 Drug design, 241

E

Egg yolk phosphatidylcholine (EYPC), 212,
 223
 Electric charge rearrangement, 71
 Electric field gradients (EFG), 54, 188
 Equation-of-motion coupled-cluster single and
 doubles method (EOM-CCSD), 190
 Ethene, 127
 Ethyl chloride, 121
 Ethyl fluoride, 121

F

Fabry-Perot cavity, 47, 49
 Fast Blue Salt B, 229
 Finkelstein substitution, 211
 Fluorine, 3
 bonds, 12
 Fluoroform, 141
 Foldamers, 209
 Fourier-transform microwave spectroscopy,
 chirped-jet, 49
 pulsed-jet, 47

G

Goldman-Hodgkin-Katz (GHK) voltage
 equation, 220

H

Haloanilinium halides, 183, 195
 Halocarbons, 2
 Halogen bonds/bonding, 1, 12, 19, 28, 79, 183,
 205, 243
 biomolecular, 241
 Halogen/hydrogen donors, 145
 Halophilic reactions, 7
 Halothane (2-bromo-2-chloro-
 1,1,1-trifluoroethane), 135, 139, 145,
 218, 250
 Hellmann-Feynman theorem, 19, 20, 32
 Heptafluoro-2-iodopropane, 107
 Hexafluorobenzene, 231
 Hofmeister selectivity, 220
 σ -Hole bonding, 19
 Holliday junctions, 247
 Hydrogels, responsive, 209
 Hydrogen bonding, 19, 34, 155, 174
 Hydrophobicity, 269
 8-Hydroxy-1,3,6-pyrenetrisulfonate (HPTS),
 212

I

IDD594, 244, 247
 Inert gases, liquified, 81
 Infrared spectroscopy, 79, 83
 Intermolecular stretching, force constants, 43,
 51, 67
 Iodine bond, 12, 43
 Iodine monochloride, 43
 2-Iodoanilinium bromide, 195
 1-Iodoethynyl-4-iodobenzene (IEIB), 175
 Iodoperfluoroalkanes, 142

Iodoperfluorobenzene halides, 183
3-Iodo-2-propynyl-N-butylcarbamate, 192
Iodo-trifluoromethane, 43
Ion binding, in solution, 211
Ion carriers, 205
Ion channels, 205
Ion selectivity, 219
Ion transport, 205
 membranes, 212
 vesicles, 217, 230
Isophthalamides, 208
Itraconazole–succinic acid, 191

K

Krypton, 81

L

Large unilamellar vesicles (LUVs), 212
Lennard–Jones potentials, 103
Lewis bases, 19, 28, 43, 45, 79, 121, 243
Light-emitting diodes, 171
Lipid bilayer membranes, 205, 208
Liquid argon (LAr), 81
Liquid krypton (LKr), 81
Liquid xenon (LXe), 81
Lithium, 219

M

Macrocycles, 205
Magnetic shielding constants, 187
Matrix isolation spectroscopy, 81
Medicinal chemistry, 241
Membrane-mimetic gas phase, 225
Membranes, 205
2-Mercapto-1-methyl-imidazole
 1,4-diiodotetrafluorobenzene, 159
Methyl chloride, 121
Methyldiphenylphosphine oxide (MDPPO),
 177
Methyl fluoride, 121
4-Methylpyridine N-oxide
 1,2-diiodotetrafluorobenzene, 159
Molecular capsules, 165
Molecular electrostatic potential surfaces
 (MEPS), 175
Molecular engineering, 241
Molecular interactions, 241
Molecular wires, 172
Monomers, 216
 bands, 95

Monte Carlo-free energy perturbation
 (MC-FEP), 102
Multiion hopping, 205, 208, 228, 235

N

Nonafluoro-1-iodobutanes, 226
Noncovalent interactions, 1
Nuclear electric quadrupolar interaction, 188
Nuclear magnetic resonance (NMR), 183
 solid-state, 183
Nuclear quadrupole resonance (NQR), 190,
 197
 coupling constants, 53
 hyperfine components, 53
Nucleic acids, 241

O

Occam's Razor, 37
p-Octiphenyl, 229
Oligomers, 205
 cyclic, 210
 linear, 227
p-Oligophenyl rods, 205, 208, 227
Onsager mechanism, 208
Optimized potentials for liquid simulation, 103

P

Pauli repulsion, 20
Pentafluorobromobenzene, 218, 226
Pentafluoroiodobenzene, 217, 221, 231
Peptide urea nanotubes, 208
Perfluoroalkyl iodides, 83
Perfluorocarbon/amine, 5
Perfluoroiodobutane, 218, 226
Perfluoroiodohexane, 218, 227
Perfluoroiodopropane, 218
Perfluorophenyl groups, 210
Phase behavior, 223
 1,10-Phenanthroline-5,6-dione (PDONE), 160
Polar flattening, 22
Polydiacetylenes (PDAs), 172
Poly(diiododiacetylene) (PIDA), 172
Polyiodide alkaloids, 2
Poly(4-vinylpyridine)-haloperfluorocarbon,
 191
Potassium transporters, 219, 227
Potential energy functions, 43
Prodigiosin, 208
Propene, 127
Protein-inhibitor interactions, 241

Protein–ligand binding, 126
Protein–ligand complexes, 261
Proteins, 241
Proton transporters, 208, 227
Pyrene, 171

Q

Quadrupolar nuclei/coupling, 183, 188
Quantum numbers, 52
p-Quaterphenyl, 229
Quinoline/iodoform adduct, 2

R

Radial geometry, 66
Raman spectroscopy, 79, 90
Rational drug design, 209
Red-shifting, 82, 142
Relative stabilities, 111, 120
Rigid-rod molecules, 205
Ripple phase, 224
Rotational angular momentum, 53
Rotational constants, 50
Rotational spectroscopy, 43, 46
Rubidium, 219

S

Selenides, 29
Selenocyanates, 183
 halogen-bonded, 192
Self assembly, 1
Sevoflurane, 139
p-Sexiphenyl, 233
Sodium carriers, 207
Solute–solvent interactions, 103
Spin–spin (J) coupling, 189
Strychnine triiodide, 2
Sulfides, 29
Supramolecular architectures/synthesis, 1, 155,
 165

Synthons, 155
 crossover, 176

T

Tetra-aza-1,8(1,1')-
 diferrocenacyclotetradecaphane-
 tetraene 1,4-diiodotetrafluorobenzene,
 162
Tetrabutylammonium chloride (TBACl), 211
Tetramethylammonium (TMA), 210
Tetramethyl-1,4-benzodicyanitrile
 1,4-diiodotetrafluorobenzene, 158
Tetramethyl-2,2'-bipyrimidine (TMBPM), 160
Thermodynamic stability, 36, 101
Thiocyanates, halogen-bonded, 192
Thiourea, 8
Thyroid hormones, 241
Toluene, 135
Townes–Dailey model, 54
Transmembrane hydrogen-bonded chains
 (HBCs), 208
Transmembrane scaffolds, 205, 207
Transporter, halogen-bonding, 214
Trifluorohalomethanes, 45, 79, 82
Trifluoriodomethane, 218, 224
Trimethylamine (TMA), 82, 101, 106
Triphenylphosphineselenide, 8
Tyroxine, 209, 225

V

Vesicles, 205
Vibrational satellites, 58

W

Williamson ether synthesis, 211

X

Xenon, 81